The University of Sheffield

Department of Mechanical Engineering

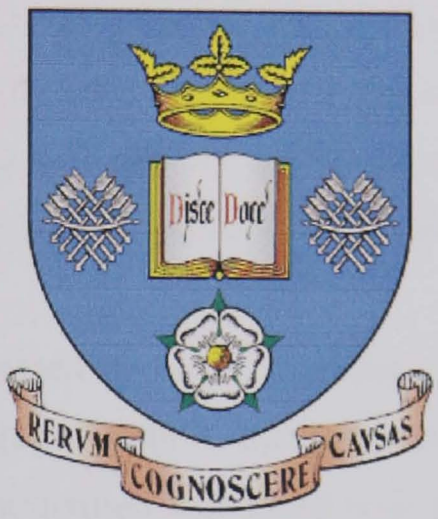

Supersonic Ejector Simulation and Optimisation

For the Degree of
Doctor of Philosophy (PhD) in Mechanical Engineering

John H Hart

September 2002

Abstract

The aims of this project were the implementation of Computational Fluid Dynamics (CFD) to the study of supersonic ejectors, and the investigation of the flow processes that occur. The conventional ejector has been in existence for more than a century yet the design has remained largely unchanged and is difficult to optimise. This has been attributed to a lack of understanding of the complex flow processes and phenomena that occur. CFD provides the ability to study these processes, and to rapidly assess geometrical influence upon operational performance.

The CFD model was assessed through systematic appraisal of the numerical parameters that influence solution stability and simulation accuracy. Two proprietary CFD codes were utilised; a structured segregated code and an adaptive mesh coupled code. Assessed parameters included; mesh dependency, discretisation schemes, turbulence models, and boundary layer models that are shown highly influential. Simulation was validated through comparison of predicted and experimental entrainment values.

Simulations of an ejector that is part of a steam-jet refrigeration cycle were used to assess the influence of geometry and operating conditions. The structured code was found suitable for geometrical studies however the coupled code was required for detailed flow analysis. Geometrical studies showed current ejector design guidelines to be well set. Operational studies highlighted the dominant influence of motive fluid flow rate upon entrainment levels. Shock systems and flow processes could be clearly identified. Simulations of ejectors utilised in vacuum and thrust augmenting applications were also conducted in assessment of the general applicability of CFD.

CFD has the potential to be an effective and powerful tool in simulating and understanding ejectors. Qualitative and quantitative results can be obtained dependent upon the optimisation and validation of the mathematical model. This however can only be performed properly if the user fully understands the flow physics and applied numerics.

Acknowledgements

The Author would like to take this opportunity to express his gratitude to several people and organisations that have made this work possible:

- Firstly to my supervisor Dr S B Chin, for his guidance and encouragement throughout, and the time and effort he has put in.
- All involved in the CFD side of the ThermoFluids group, that was, for bouncing ideas off on and advice. Including Dr E Munyebvu, Mr R Nunez, Mr A P Wong, Dr B Lim, and Mr W A Bullough.
- Dr S B M Beck, for his interesting and useful range of advice, and for his assistance in and from consultancy work.
- Dr A Yoxall, for assisting me in and pushing consultancy work my way during my writing-up year.
- Dr I W Eames of the University of Nottingham for the provision of experimental data.
- The financial support from the EPSRC, without which this work would not have been possible.
- Finally, to my family, Ben Bradbrook, and the friends I have been blessed with. Thank you for being there, I'm more in debt to you than you could know.

Contents

Nomenclature

Symbol	Quantity	SI Unit
a	Speed of Sound	(m/s)
A	Area	(m^2)
A*	Area of Nozzle Throat	(m^2)
AR	Nozzle Throat to Ejector Throat Area Ratio	Dimensionless
C	Constant	Dimensionless
Cp	Specific Heat at Constant Pressure	(kJ/kg·K)
$\overline{C}p$	Molar Specific Heat at Constant Pressure	(kJ/kmol·K)
Cv	Specific Heat at Constant Volume	(kJ/kg·K)
$\overline{C}v$	Molar Specific Heat at Constant Volume	(kJ/kmol·K)
COP_R	Coefficient of Performance	(Dimensionless)
d	Diameter	(m)
D	Throat Diameter	(m)
E	Empirical Constant	(Dimensionless)
F	Convection	($kg/m^2 \cdot s$)
h	Enthalpy	(kJ/kgmol)
k	Kinetic Energy	(m^2/s^2)
k	Thermal Conductivity	(kW/m·K)
l, lμ, lε	Turbulence Length Scales	(m)
L	Characteristic Length	(m)
$\dot{m}$	Mass Flow Rate	(kg/s)
m_i,	Mass Fraction	(Dimensionless)
M	Mach Number	(Dimensionless)
M_i,	Molecular Weight	(kg/kmol)
P	Pressure	(Pa)
Pe	Peclet Number	(Dimensionless)
Q	Heat Transfer	(kJ)
r	Radius	(m)
Re	Reynolds Number	(Dimensionless)
Re_y	Turbulent Reynolds Number	(Dimensionless)

R_m	Entrainment	(Dimensionless)
R_u	Universal Gas Constant	(kJ/kmol·K)
S	Source Term	(Dimensionless)
t	Time	(s)
u	Velocity Component	(m/s)
U	Velocity	(m/s)
U*	Free Stream Velocity	(m/s)
v	Velocity Component	(m/s)
V	Volume	(m^3)
w	Velocity Component	(m/s)
Y	Distance	(m)
y^+, y^*	Non Dimensional Distance	(Dimensionless)
α	Under-Relaxation Factor	(Dimensionless)
ε	Eddy Dissipation	(m^2/s^3)
ϕ	Flow Variable	(Dimensionless)
γ	Specific Heat Ratio	(Dimensionless)
κ	Von Karman's Constant	(Dimensionless)
μ	Viscosity	(kg/ms)
ν	Kinematic Viscosity	(m^2/s)
θ	Angle	(Degree)
ρ	Density	(kg/m^3)
σ	Turbulent Prandtl Number	(Dimensionless)
τ	Shear Stress	(N/m^2)
Γ	Diffusion Coefficient	(Dimensionless)

Subscript

1	Primary	t	Turbulent
2	Secondary	v	Vapour
3	Outlet	boiler	Boiler
a	Atmosphere	cond	Condenser
c	Convective	evap	Evaporator
f	Liquid	gen	Generator
o	Stagnation		

Chapter 1 - Introduction

An ejector is essentially a flow device with no moving parts. Instead the ejector relies upon the momentum of a high velocity primary fluid to entrain and pump a low energy secondary fluid. Dating from the 1800's, the ejector found its first notable use in vacuum breaking systems on railway trains[1]. The ejector driven by waste steam from the locomotive was used to entrain air maintaining a partial vacuum within the breaking cylinders fitted to the carriages. In 1902 the profile of the ejector was further raised when Parsons[2] designed his "vacuum augmentor", another name for an ejector. Parsons used his vacuum augmentor on the steam turbine systems he was developing to eject air from within the condensing plants. These were cheap and efficient to operate as they again utilised surplus steam as the primary motive fluid.

The combination of simplicity of design, and the ability to utilise a surplus gas as the motive fluid, means the ejector has always had the potential for utilisation in a wide variety of applications. This has been widely recognised within industry and ejectors today can be found in many guises and uses. In particular the ejector has found a home within the petrochemical and food industries. However over the last century the design of the ejector has not altered significantly, and no real improvements have been made to their operational efficiency.

Even though the ejector is physically simplistic the flow processes within the unit are complex and not fully understood. The lack of understanding, coupled with the fact that slight changes to ejector geometry or operating conditions severely influence operational performance, lead to difficulties in design. New ejector configurations are therefore mostly conceived and based around existing designs, acquired knowledge, and published guidelines such as those by ESDU[3]. This knowledge however is no guarantee that a newly designed ejector will be effective, and this cannot be determined until a costly model has been constructed. The adoption of a technique which could accurately predict ejector performance without the use of a model would be highly desirable.

It is believed that computational fluid dynamics (CFD) could perform this task and at the same time explain some of the mysteries that shroud ejector operation. The application of CFD techniques to ejectors is not a new concept. Hedges & Hill[4], who were pioneers in early CFD techniques, developed and applied a 2D finite-difference model to the problem in 1974. However until recently the application of CFD to the study of ejectors has been limited.

The main aims of this project therefore are; the implementation of CFD to the study of supersonic ejectors, and the investigation of the flow processes that occur within it.

CFD has a number of advantages over other analytical and experimental techniques. Principally CFD can provide information on flow processes that cannot be obtained through other means, which is of particular importance to the study of ejectors. The motive jet in an ejector is typically supersonic to ensure the stable operation of the device as discussed in Chapter 2. Mixing and entrainment processes are therefore complicated due to the complex confined interaction between the supersonic primary stream and subsonic secondary stream. Intrusive experimental methods could alter or destroy aspects of the flow structure, whilst non-intrusive methods are highly complex. CFD can visualise and provide experimental data on the flow easily, without affecting the flow. Additionally CFD can provide results quickly and economically compared to experimental methods. Geometrical and operational influence can thus be rapidly assessed.

The method however does have some disadvantages. CFD attempts to solve the governing equations using mathematical models that describe different aspects of flow behaviour. Simulation results can be susceptible to numerical errors, and many of the mathematical models contain experimentally determined empirical constants that can create uncertainty.

The different solver formulations and numerical models that describe flow phenomena and mechanisms within a CFD code are discussed in Chapters 3 and 4. These have certain capabilities and limitations which can create further uncertainty in obtained results. In choosing suitable numerics it is therefore important to have

some understanding of the basic mechanisms and phenomena which will be involved or may be encountered. To ensure meaningful results the chosen numerics must be validated and verified, and the degree of uncertainty considered, as discussed in Chapter 5.

In this investigation CFD has been used to model a selection of steam/gas supersonic ejectors. The majority of studies are based upon an ejector which is part of a steam jet refrigeration cycle currently under investigation at the University of Nottingham by Eames et al[5]. This has been designed to operate with a primary nozzle Mach number of M = 4. The use of ejectors in refrigeration is becoming one of the most heavily researched ejector applications, perhaps only surpassed by thrust augmentation. This is due to the growing demand for environmentally friendly and economic refrigeration. Other simulated ejectors included a vacuum ejector[1], thrust augmenting ejector[6], and a constant area ejector[7]. These were simulated to investigate the general applicability of CFD to ejector simulation.

Geometrical investigations of the Eames[5] ejector mixing chamber and throat have been conducted, based upon ejector design guidelines stipulated by ESDU[3]. Operating condition studies have been performed for all simulated ejectors. The majority of studies conducted were two dimensional with an axisymmetric approximation. This saved computational resources and permitted detailed study of the flow processes. A limited number of three dimensional simulations of the Eames ejector were also conducted to verify the axisymmetric assumption.

1.1 – Experimental Geometry

The basic geometry of the Eames[5] ejector is outlined in Fig 1.1. Two slightly different motive nozzles were used in this study. The original nozzle configuration, shown in Fig 1.2a, had been used in previously conducted CFD studies[86,89] of the Eames ejector. Assumptions had been made regarding the radii and length of the respective nozzle convergent and divergent sections. As more information on the nozzle design came to light, the dimensions of these sections were adapted as shown in Fig 1.2b. Critical nozzle dimensions at the throat and nozzle exit were maintained.

However it will be shown that this alteration had negligible influence upon predicted ejector performance.

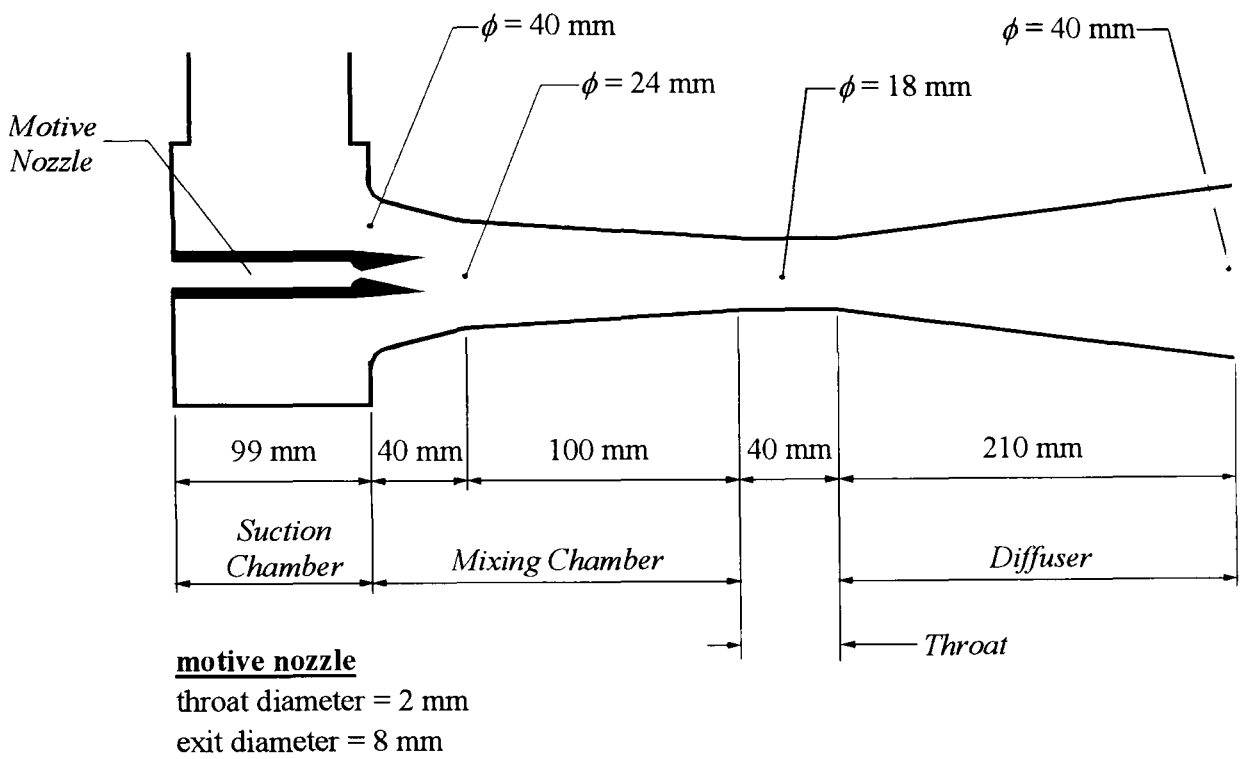

motive nozzle
throat diameter = 2 mm
exit diameter = 8 mm

Figure 1.1 - Schematic of Eames Ejector

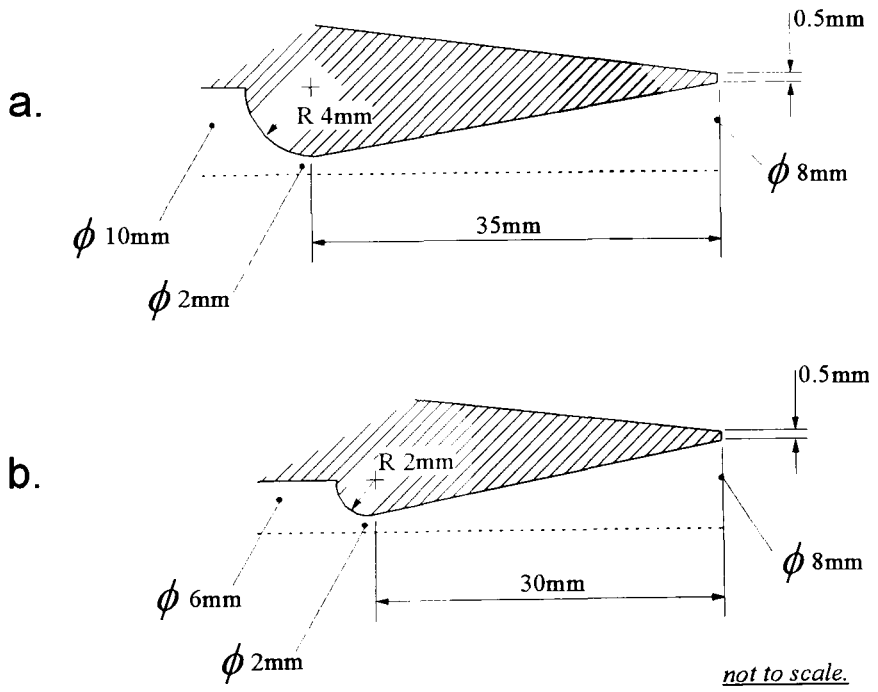

Fig 1.2 – Modelled Nozzle Geometry:
a. Original Geometry, b. Modified Geometry.

Chapter 2 - Principles & Applications of Ejector Pumps

This chapter describes ejector theory, applications & flow structure. The chapter begins with a basic description of the operation of a supersonic steam ejector, before moving onto ejector applications. The flow structure within ejectors is then discussed. Flow phenomena which may be expected to occur within supersonic ejectors are identified. Research that has been conducted into the understanding of the flow physics both experimentally and computationally is also discussed.

2.1 – The Ejector

Regardless of design all supersonic ejectors operate under the same principle. A high pressure, high velocity jet of fluid is used to entrain and pump a low pressure, low velocity fluid. Although the operational principle appears simplistic, the design process for an ejector is complex. This relies largely upon empirical design guidelines such as those formulated by ESDU[3] which cover the various designs.

There are different styles of ejector including the popular constant pressure design, constant area, annular[8], pulse[8,9], and the more recent pressure-exchange design[10,11]. Each of the designs share four common components; motive nozzle, mixing chamber, secondary inlet, and diffuser. It is the design of the mixing chamber and motive nozzle that differentiates the styles.

2.1.1 – Constant-Pressure / Constant-Area Ejectors

The constant pressure ejector is the most commonly encountered design due to its ease of manufacture, and reliable performance characteristics. Essentially the design consists of a venturi with a single centrally mounted motive nozzle, Fig 2.1. The optimisation of the geometry of the venturi poses a particular problem to designers when trying to ensure constant pressure mixing. It is this design of ejector which this study primarily concentrates upon, with occasional reference to the similar constant area design.

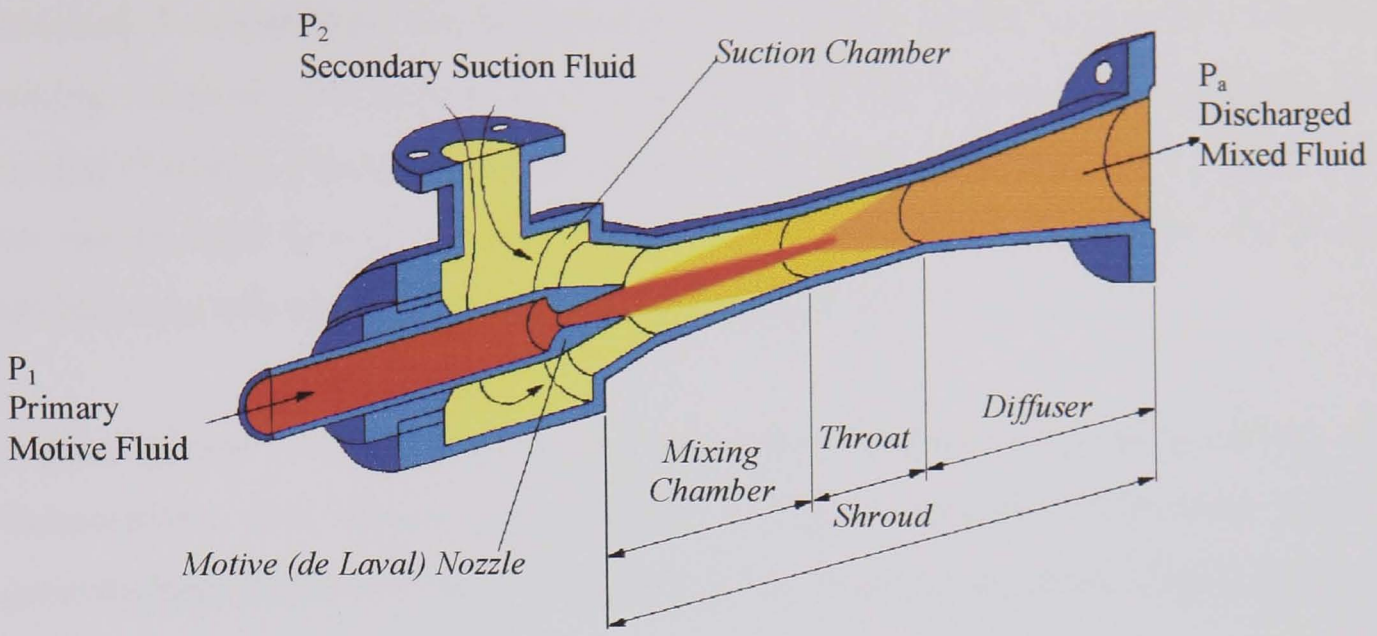

Figure 2.1 – Constant Pressure Ejector Schematic

The constant area ejector is a simple design, the mixing chamber is a length of uniform bore pipe, Fig 2.2, with again a single centrally mounted nozzle. However the application of constant area ejectors to compressible flow problems is rare. This could be due in part to the work of Keenan et al[12] which demonstrated analytically that the constant pressure design offers superior operational performance. ESDU[3] however claim that there is no reason to assume that one design is more efficient than the other.

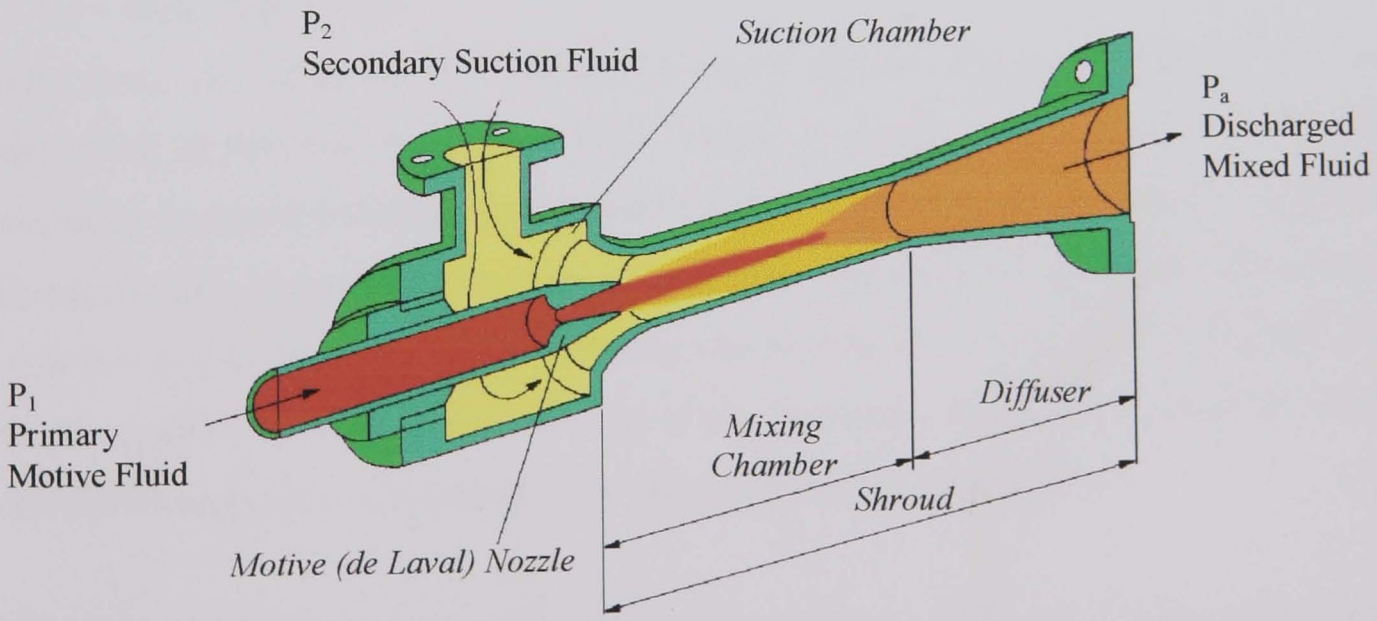

Figure 2.2 – Constant Area Ejector Schematic

2.1.2 – Alternative Designs

The following alternative ejector designs are worth mentioning. Annular[8] or coanda[8,13] ejectors utilise angled motive nozzles. Normally these are centrally

mounted, however they can be included in the ejector shroud and angled into the mixing chamber. The annular design generates a high degree of swirl within the mixing chamber. This results in the rapid mixing of the secondary fluid, and allows the use of short mixing sections. However their efficiency is less than that of an ejector using a single centrally mounted de Laval nozzle.

A pulse ejector[8,9] does not imply a specific design characteristic, but an operational characteristic. The motive jet is pulsed at regular intervals. This again should generate large degrees of swirl within the mixing chamber resulting in rapid mixing.

The pressure exchange ejector is a relatively new concept, currently under investigation by Garris et al[10,11]. This ejector departs from a key concept of conventional design through the inclusion of moving parts. A free-spinning rotor is placed centrally within the mixing chamber, in an attempt to lift the performance of the ejector to that of turbomachinery. Driven by the primary jet, the rotor forces secondary fluid through the mixing chamber to the diffuser. The pressure exchange design however is yet to exhibit any significant improvements in performance over conventional ejectors.

2.1.3 – Basic Operation

The basic operation of the constant pressure ejector shown in Fig 2.1 can be described as follows. A primary fluid, steam, is supplied to a motive (de Laval) nozzle at constant pressure. As the steam travels the length of the nozzle it expands isentropically, accelerating to supersonic speeds. Secondary fluid enters the suction chamber and is entrained into the mixing chamber by the momentum of the primary fluid. A small increase in the velocity of the secondary fluid is noticeable at entry, but this is negligible compared to the velocity of the primary stream.

The two fluids then mix in an irreversible process within the mixing chamber. Primary fluid momentum decreases with a corresponding increase in that of the secondary fluid. Mixing occurs along the entire length of the mixing chamber but is assumed to be complete by the throat. The mixed fluids then enter the diffuser where fluid velocity is reduced and pressure recovered prior to discharge.

2.1.4 – Ejector Performance

The performance of an ejector is typically categorised by its mass flow characteristics. The entrainment ratio (R_m) gives a direct indication of operational performance. This is the ratio of suction mass flow rate ($\dot{m}_2$), to motive mass flow rate ($\dot{m}_1$). The higher this value the more efficient the ejector generally is.

$$R_m = \dot{m}_2 / \dot{m}_1 \tag{2.1}$$

However if the ejector is used within a vacuum application it is more common to refer to the suction characteristics of the unit, and not the entrainment ratio. This will include maximum vacuum obtainable at various motive and discharge pressures.

2.2 – Ejector Applications

Ejector is essentially a generic name used to describe a flow device which utilises a jet of fluid to entrain and pump a secondary fluid. However ejectors are also known as jet pumps, eductors, vacuum augmentors, thrust augmentors, thermocompressors, and injectors. These names are generally more descriptive of what the ejector is used for. Jet pump or eductor refers to an ejector which uses as the motive fluid, or pumps, an incompressible fluid, whereas vacuum augmentor, thrust augmentor, thermocompressor, or if the term "ejector" is actually used, generally refers to a compressible flow device utilising vapours or gases. An injector is essentially an ejector except it is used to feed the secondary fluid to a device rather than to solely extract the secondary fluid.

Throughout this study we will only concern ourselves with ejectors dealing with compressible flow. The use of the compressible flow ejector within industry is far more widespread than the jet pump. ESDU[3] list a selection of applications, and many more can be found in Bonnington[14], who provided a review of ejector related literature predating 1976. Further applications, particularly related to refrigeration cycles, can be found in Sun & Eames[15]. A selection of the most common ejector applications are as follows.

2.2.1 – Refrigeration

Ejectors have been used within refrigeration systems for more than a century. In 1901 Parsons[16] designed the first steam jet refrigeration cycle, using steam as the system coolant. The ejector is the heart of the cycle, Fig 2.3, used to both pump and compress the coolant. Driven by primary high pressure steam raised within the generator, the ejector supplies a vacuum to the evaporator. This entrains secondary steam vapour from the evaporator producing a cooling effect. The primary and secondary vapours are combined, compressed within the diffuser, and exhausted to the condenser. Here the combined steam vapours are condensed and returned to the generator via a feed pump, and evaporator through an expansion valve.

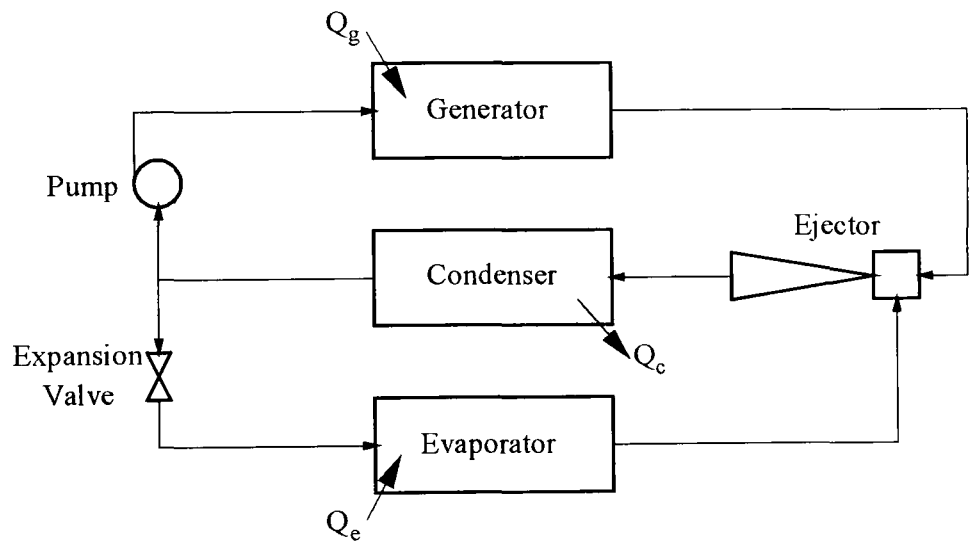

Figure 2.3 – Schematic of a Steam Jet Refrigeration System[5]

The efficiency of the ejector governs the overall system efficiency. Calculation of the predicted coefficient of performance of the refrigeration system (COP_R), a technique used by Eames et al[5], demonstrates this. This is the ratio of evaporator heat load, and energy input to the generator, multiplied by the ejector entrainment ratio. The evaporator heat load, and energy input to the generator, are determined by subtracting the enthalpy of the steam in its liquid state within the condenser ($h_{f,cond}$), from the respective vapour enthalpies within the evaporator ($h_{v,evap}$) and generator ($h_{v,gen}$).

$$COP_R = R_m \left[\frac{h_{v,evap} - h_{f,cond}}{h_{v,gen} - h_{f,cond}} \right] \qquad (2.2)^{[5]}$$

Steam jet refrigeration quickly became popular for air conditioning large buildings, and industrial refrigeration. The cycle never found real use within the domestic environment, probably due to the size of the systems. With the introduction of mechanical vapour compression cycles the popularity of the systems waned, steam jet refrigeration all but disappeared. However the cycle is once more gaining interest due to the growing demand for environmentally friendly and economic refrigeration.

Application of ejectors to refrigeration processes has now become one of the largest fields of ejector research, probably only surpassed by the study of thrust augmenting ejectors in aerospace applications. Recently the most notable work into steam jet refrigeration has come from Eames[5,17] and his co-workers Sun[18], and Aphornratana[19]. The influence of operational parameters upon the performance of steam jet cycles has been studied by Aphornratana & Eames[19], and Eames et al[17]. These studies included information regarding the influence which motive nozzle position has upon ejector performance. Information on the influence of throat area ratios for the motive nozzle and diffuser, was also provided by Eames et al[17]. Analytical methods, verified with experimental data, have also been developed by Eames et al[5] and Sun[18]. These have been used to predict the performance of steam ejector systems.

Huang et al[20], have also studied the geometrical influence of an ejector within a steam jet cycle. However Huang[21,22] has conducted more research upon the influence of the geometry of ejectors within refrigeration cycles using halocarbon compounds. The use of halocarbons in refrigeration allows cooling at sub zero temperatures, an obvious limitation for a steam jet cycle.

There are a number of additional refrigeration cycles that the ejector lends itself to, including; solar powered refrigeration, and combined ejector-absorption cycles. These will not be recounted here, but are described in depth by Sun & Eames[15].

2.2.2 – Vacuum Augmentation

The ejector has a long history of use within vacuum applications. As mentioned in Section 1 the ejector found its first notable use in railway vacuum breaking systems[1], and later within the condensing plants of turbine systems[2]. The use of ejectors within vacuum applications is particularly prevalent within the petrochemical industries which generally possess a significant supply of surplus steam. Here ejectors are used to maintain vacuum within chemical reactors and distillation columns. Extraction of potentially explosive vapours can be performed. The likelihood of accidental ignition is slight, as the lack of moving parts means there is little chance of a spark being generated.

A single ejector designed for vacuum augmentation can typically "pull down" to approximately 0.98 bar, however ejectors can be coupled in series to obtain lower pressures. As an example a five stage series can pull vacuums as low as 0.033 mbar abs. This typically involves using ejectors interspersed with condensers to reduce the pumping demand applied to the later ejector stages in the series. Fig 2.4 shows a typical three stage ejector set used to evacuate a chemical reactor.

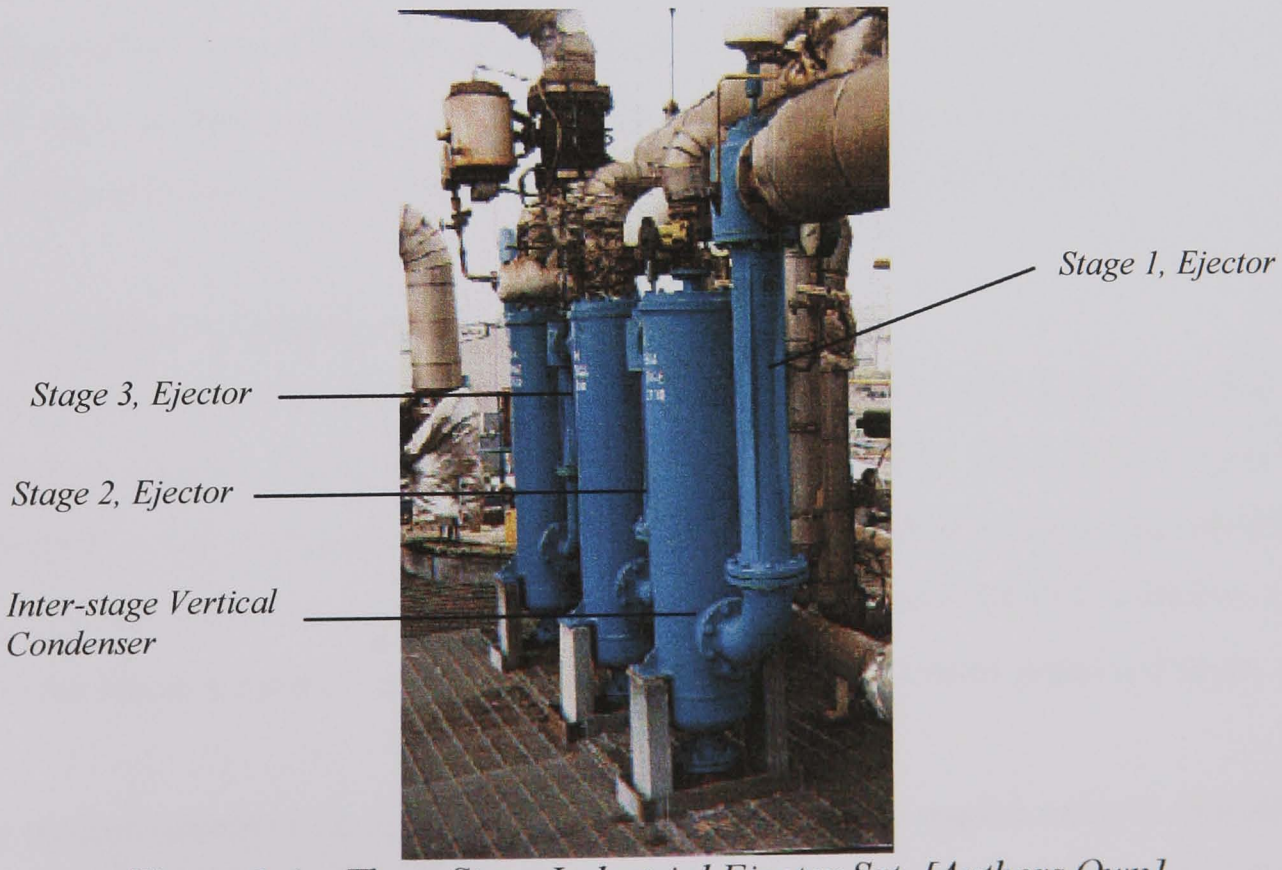

Figure 2.4 – Three Stage Industrial Ejector Set. [Authors Own]

2.2.3 – Thermocompressor

Steam is widely utilised within the food processing, petrochemical, & pharmaceutical industries, within process equipment including evaporators, reactors, & crystallisers. These processes tend to use steam at intermediate pressures (25-30 psig) and vent off waste steam at lower pressures (10-15 psig). Rather than condensing this waste steam or venting it to atmosphere, it can be reclaimed and boosted back to a higher pressure through the use of a thermocompressor, Fig 2.5. Using high pressure make up steam as the motive fluid, vented process waste steam is entrained. This is combined and recompressed within the mixing chamber and diffuser of the thermocompressor prior to discharge, ready for reuse.

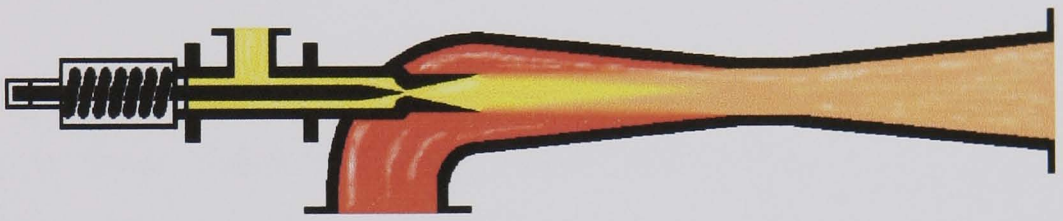

Figure 2.5 – Thermocompressor

Thermocompressors can also be used to accurately mix two fluids in place of a gas mixing valve. Typically fitted with an actuator and needle to control the motive mass flow rate, accurate control of either the final discharge pressure, if used in a reclamation process, or composition of discharged fluid, can be obtained.

2.2.4 – Thrust Augmentation

The use of ejectors in thrust augmentation is probably the most heavily researched ejector application, being predominantly used upon VSTOL (very short take-off & landing) aircraft. Research into the application of the ejector to thrust augmentation began in the 1960's as aircraft manufacturers tried to evolve VSTOL systems away from the single centrally mounted engine. This has still not been improved upon.

The ejector consists of a short shroud mounted around the engine exhaust, benefiting the suppression of noise, and augmentation of thrust. Thrust augmenting ejectors are characteristically short to save both space and weight. Research has therefore mainly been concentrated on the design of the shroud, to prevent flow separation[23], and

nozzle[24-26], to ensure that mixing is rapid and ideally complete before the shroud exit is reached.

Ejectors have also been fitted to jet exhaust systems in an attempt to mask the infra red signature of the exhaust[27]. The advantages of applying such technology to military aircraft are obvious. The technology translates to other forms of military transport other than just aircraft. Infra red reduction systems are also used upon tanks and within naval vessels[28,29]. As with the thrust augmenting ejector the units tend to entrain vast quantities of secondary fluid in an attempt to mask the exhaust.

2.3 – Designing Ejectors

The flow conditions within an ejector are determined by its application. For a fixed design it is these conditions which principally govern the ejectors operational performance. When designing an ejector it is common practice to use these conditions as the starting point in the design calculation process. The geometry is then configured to give the ejector a set level of operational performance. Many geometrical parameters need to be taken into account when conducting this task. Each one in turn has the potential to influence performance significantly.

Ejectors are mainly designed through the use of one-dimensional methods. Flűgel[30] provided the first recognised design method in 1939. This was followed by the analysis of Elrod[31], and the similar analysis of Keenan & Neumann[32] for constant area ejectors. Keenan et al[12] followed up this work in 1950 with an analysis of constant pressure designs. This questionably assumed that frictional effects were negligible and that flow was isentropic. The influential effect of fluid species[33,34] upon ejector performance was also neglected.

The work of Keenan et al[12] however, has provided the basis for the majority of one-dimensional methods since derived. This has been improved through the removal of some of the assumptions and constraints made. Improvements have included analysis which incorporate frictional effects[5], and the proposal of theories for the influence of choking[35] which previously could not be accounted for.

One-dimensional methods assume constant profiles across the ejector and therefore do not accurately represent mixing processes. Two-dimensional methods have been used in an attempt to resolve this problem[36-38]. These use integral methods with the application of fixed profiles at various sections of the ejector. However the assumption of fixed profiles is limiting, and prompted the development of techniques omitting their need. This eventually led to the work of Hedges and Hill[4,39], and a move into the realms of CFD analysis which will be discussed further in Section 2.6.

Nevertheless one dimensional methods have been shown proficient for ejector design. Though they mostly prove capable of determining area ratios of the ejector throat and motive nozzle. Occasionally suggestions are made for determining appropriate dimensions of other components. Therefore the detailed design of an ejector is performed mostly through the use of empirical results formulated into design guidelines. The best known, and most detailed guidelines as mentioned are those produced by ESDU[3]. ESDU outline the complex nature of the design process and discuss influential components and parameters. Geometrically this again can be split into four common ejector components; motive nozzle, mixing chamber, secondary inlet, & diffuser.

2.3.1 – Motive Nozzle

One dimensional design methods yield area ratios for the motive nozzle which govern the mass flow rate and exit velocity. Other geometrical features are best designed through the use of guidelines. ESDU suggest appropriate radii and angle for the respective convergent-divergent portions of the nozzle. The importance of the design of these sections is further emphasised by Hopkins[40]. The angle of these sections at the throat can effect the flow field within the transonic region. Additionally when designing the nozzle it is generally accepted that the nozzle lip should be as sharp as possible. This ensures immediate interaction and mixing between the two streams.

Nozzle position at the mixing chamber entrance is an important consideration. Currently no method is available which determines the best position. This has to be discovered through experiment. ESDU state that slight alterations of ± 1mm in

positioning can lead to appreciable changes in operational performance. This was borne out in the work of Keenan et al[12], Hogarth[41], Eames et al[17], and Aphornratana & Eames[19]. Hogarth[41] demonstrated marked improvement in operational performance through moving the motive nozzle into the mixing chamber.

Keenan et al[12] demonstrated that optimum nozzle position is dependant upon the design of the mixing chamber entrance and that determining optimum nozzle position is a careful balancing act. Withdrawl of the nozzle affects the nozzle expansion and thus entrainment. Advancement of the nozzle into the chamber will eventually cause entrainment to fall, due to the constriction in the area between the nozzle and chamber wall, through which secondary fluid flows.

2.3.2 – Mixing Chamber

The mixing chamber is perhaps the most important component for consideration during the design process. One dimensional analysis[12] can provide the minimum cross sectional area of this section, through the calculation of area ratios. In a constant pressure ejector this will be at the throat, for a constant area design the cross-sectional area of the chamber itself. Empirical results are relied upon for the determination of the chamber length to ensure optimum mixing. If the ejector is of the constant pressure design, there are further complications. An appropriate convergent angle needs to be determined for the chamber. Additionally an appropriate length of parallel throat is required. ESDU[3] again provide recommendations for these dimensions.

2.3.3 – Secondary Inlet

This is perhaps one of the least researched areas of ejector design. It is generally accepted that the secondary inlet must be generously sized so as to limit the secondary inlet velocity and thus the level of swirl within the mixing chamber. ESDU recommend that the inlet velocity at this section should be less than 100m/s. ESDU also mention how the angle of the inlet can be influential, however no guidelines or further information is provided upon this.

2.3.4 – Diffuser

The design of diffusers is well documented[42] and the design of the diffuser in an ejector is no special case. The angle of course should be maintained in the region of 3°-7° to limit the influences of friction and flow separation upon pressure recovery. The angle of the diffuser only becomes a real issue where space is a consideration, as this section is the largest component of the ejector.

Without guidelines the design of a new ejector would become difficult and somewhat haphazard. The requirement for the guidelines stems from a lack of understanding of the operational phenomena which occur within the unit. A design process which renders guidelines obsolete will not be a reality until either the influence of the phenomena are fully understood or a numerical method which can deal with these phenomena is formulated.

2.4 – Supersonic Flow Phenomena

The compressible flow ejector offers an interesting challenge to ejector designers. Although simplistic in design the flow physics within the ejector are anything but simplistic. The design of ejectors has been studied since the early 1900's in an attempt to reveal and comprehend some of their operational secrets. Yet to this day even though a much better picture of ejector operation is held, the actual processes are still not fully understood. The combination of subsonic-supersonic mixing, and the influence of expansion fans and shockwaves embedded within the supersonic motive jet, complicate matters considerably. The process is further complicated by the influential effect which the proximity of the shroud wall imposes. Compressible mixing is once again an area of intense research. Renewed interest in scramjet engines has arisen over the last decade, and the study of actual mixing processes within ejectors is beginning to grow with it.

2.4.1 – Supersonic Jet Behaviour

As the motive jet within the ejector is supersonic the observance of a number of flow phenomena can be expected. Dependant upon design, the de Laval nozzle may operate in a number of ways. Isentropic expansion of the nozzle is unlikely, even if

the nozzle has been designed to operate isentropically. This is due to the influence the ejector shroud has upon the motive jet. Additionally ejectors tend to be configured to operate at design conditions. Deviation in the operation of an ejector away from the original design conditions will also result in the occurrence of non-isentropic expansion processes. The result will be the presence of either an under-expanded or over-expanded motive jet within the mixing chamber, both of which possess distinct and different characteristics.

Under-expanded operation results when the exit pressure of the jet is higher than the back pressure of the surrounding environment which it issues into. As a result a set of expansion fans form at the nozzle exit as the jet attempts to attain equality of pressure with the surrounding environment, Fig 2.6. However as the jet expands it overshoots, reaching a pressure lower than that of the back pressure. The consequence of this is the occurrence of a reflected shock wave within the flow, and a rapid pressure rise which results with the jet again having a higher pressure than the surrounding environment. Thus a sinusoidal pressure pattern is established, and the characteristic "barrelling" effect can be observed, with the formation of a series of reflected expansion and compression waves. These decrease in strength due to frictional effects within the flow, and the dissipation of energy from the momentum change across the shocks, until equality of pressure is attained between the jet and surrounding environment.

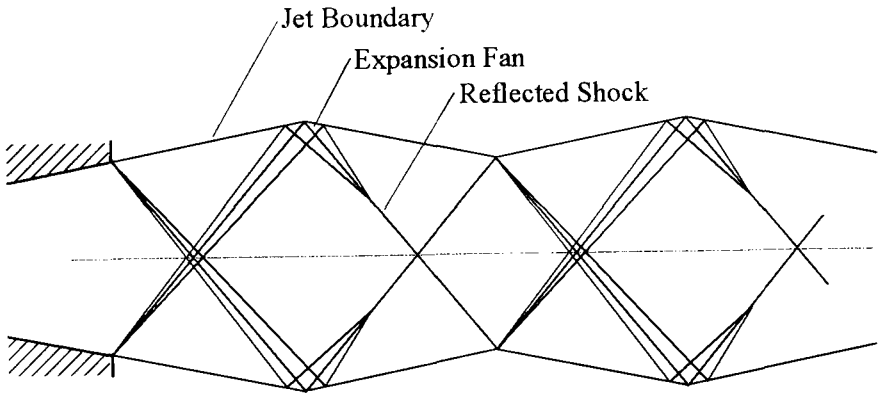

Figure 2.6 – An Under-Expanded Jet

Over-expanded flow occurs when the jet exit pressure is lower than the back pressure, resulting in the formation of a shock at the nozzle exit. Two forms of shock pattern may be observed dependant upon the severity of over-expansion. With a

low/moderately over-expanded nozzle a reflected shock system forms. This is then followed by the characteristic "barrelling" effect in the same manner as an under-expanded jet, Fig 2.7.

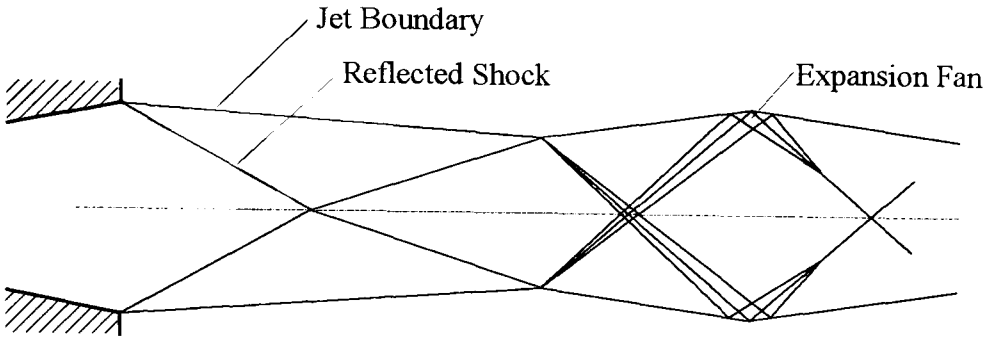

Figure 2.7 – Low/Moderately Over-Expanded Jet

A highly over-expanded flow will exhibit a mach reflection at the nozzle exit with the formation of a Mach disk, Fig 2.8. This can cause the rapid break up of the jet[43]. Ejector designers have been known to try to design ejectors with motive nozzles which over-expand. It has been claimed that an over-expanded jet produces a good vacuum with stable ejector operation[1].

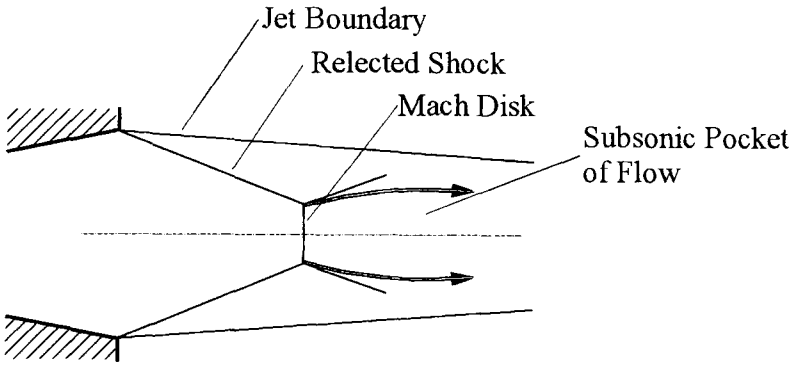

Figure 2.8 – Highly Over-Expanded Jet

2.4.2 – Choking: Modes of Operation

Regardless of design all supersonic ejectors operate within one of two modes, either pressure independent[44] or pressure dependent[44]. An ejector termed pressure independent is deemed to be choked within the throat. A shock system stands within the throat, effectively sealing the mixing chamber from the diffuser pressure.

The form of this shock is of interest as it is a normal shock. These were categorised by Shapiro[45] to occur within constant area ducts in three main styles dependant upon boundary layer thickness. Shapiro[45] stated that when the boundary layer

within a duct is thin a single normal shock can be observed. This shock has forked ends due to boundary layer separation, Fig 2.9a. As the boundary layer thickens this single shock develops into multiple normal shocks, Fig 2.9b. Eventually with very thick boundary layers the forked ends of the shocks disappear and a normal reflective shock without a Mach disk exists. Each of these shock systems can be observed within the throat of a supersonic ejector dependent upon operation.

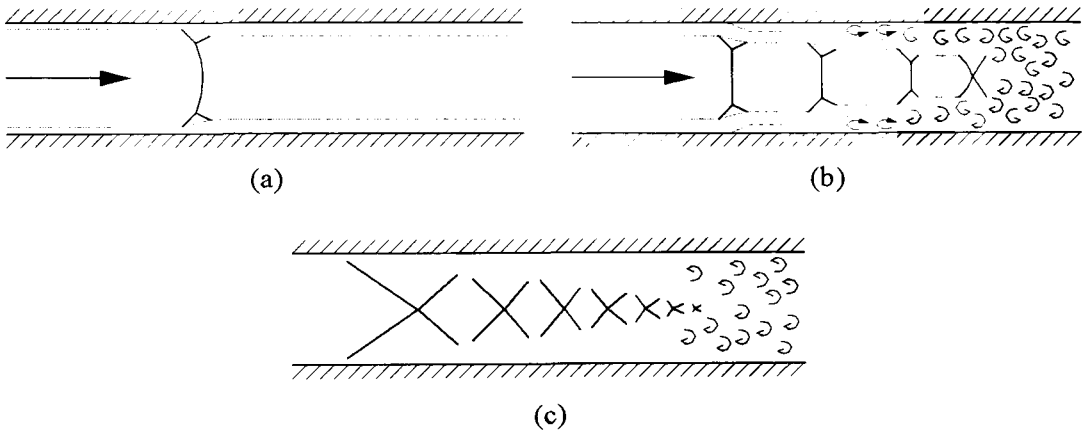

Figure 2.9 – Normal Shock Systems[45]

Pressure dependent operation occurs when the ejector throat is either partially or fully unchoked. As a result entrainment becomes a function of diffuser pressure (P_a). See Fig 2.10. Pressure dependant operation can be attributed to a number of causes. Either the motive jet pressure is to low, or diffuser pressure to high, for the formation of a choke. Alternatively a rise in diffuser pressure can unseat an established choke, forcing the shock system out of the throat and back into the mixing chamber. An ejector throat of inappropriate length can be a further cause[46].

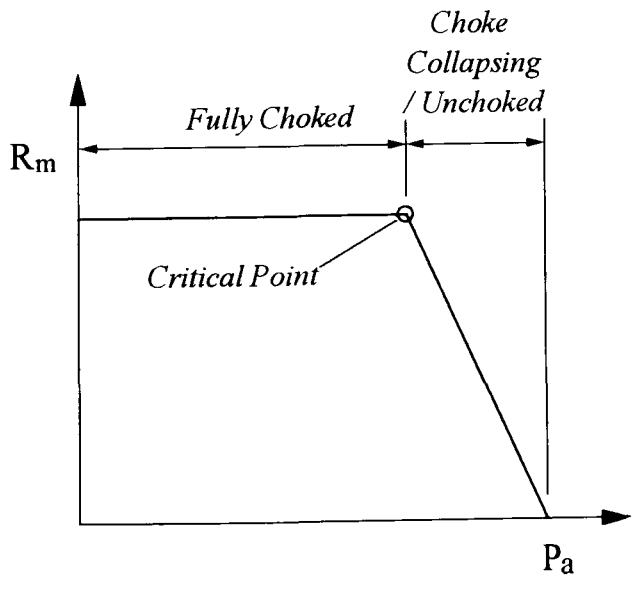

Figure 2.10 – Entrainment V's P_a

A second choke also exists within the ejector, situated within the motive nozzle. This also can be unseated by a rise in diffuser pressure. However a reverse flow condition rendering the ejector inoperable normally exists before this can occur. The flow structure within an ejector alters considerably between either mode, as shown by Addy[43] and Matsuo[47,48].

It is these choking phenomena which give ejectors their well documented constant capacity characteristics[19,20,35], and stable operation. Reducing diffuser back pressure will aid the formation of a choke within the ejector throat. However once the throat is fully choked, a further reduction in back pressure will not influence operational performance. Entrainment becomes independent of diffuser pressure, and the constant capacity characteristic is observed as shown in Fig 2.10.

Whether pressure dependency is a help or hindrance to ejector operation however is dependent upon the ejectors intended application. If the ejector is used in a refrigeration cycle or for vacuum augmentation, where secondary inlet pressure is low in comparison to diffuser pressure, then pressure dependent operation is not ideal. However in thrust augmentation, secondary inlet pressure can be comparable to diffuser pressure, and the entrainment of vast quantities of secondary fluid desirable. Pressure independent operation can thus become unwanted as the formation of a choke can limit the degree of secondary mass flow through the ejector.

2.4.3 – Shear Mixing Layers

A shear mixing layer will form along the edge of the supersonic jet. Fig 2.11 and 2.12. Subsonic fluid is entrained into this region and subsequently mixed with the supersonic jet, causing the layer to increase in thickness. Interaction between the layer, expansion fan and shockwave structure will generate additional turbulence encouraging the layer to thicken further. Eventually the layer grows in sufficient thickness to completely engulf the supersonic jet. This causes shock structure within the jet to diminish in strength due to viscous damping effects[49].

The structure of a supersonic mixing layer differs considerably compared to a subsonic layer. Subsonic layers are dominated by clearly defined large scale Brown-

Roshko[50] structures comparable in diameter to the layer thickness, which are initiated by Kelvin-Helmholtz instabilities. It is these structures which give subsonic layers their high entrainment characteristics and rapid growth rates, Fig 2.13.

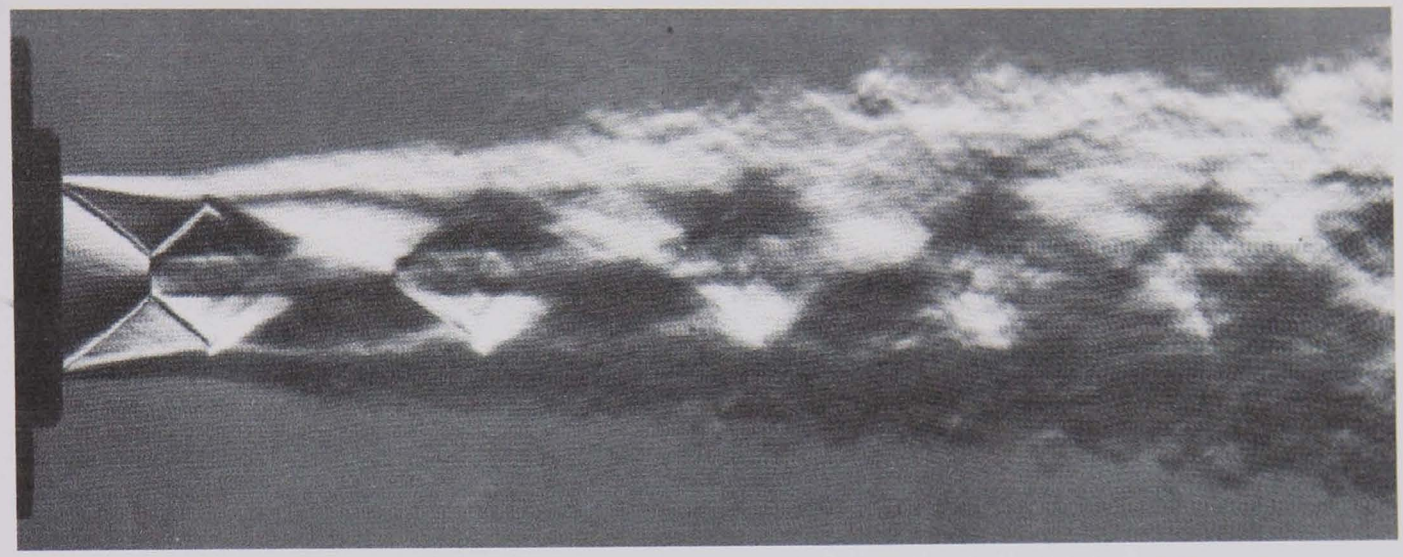

Figure 2.11 - Schlieren Image of An Over-Expanding Jet[51]

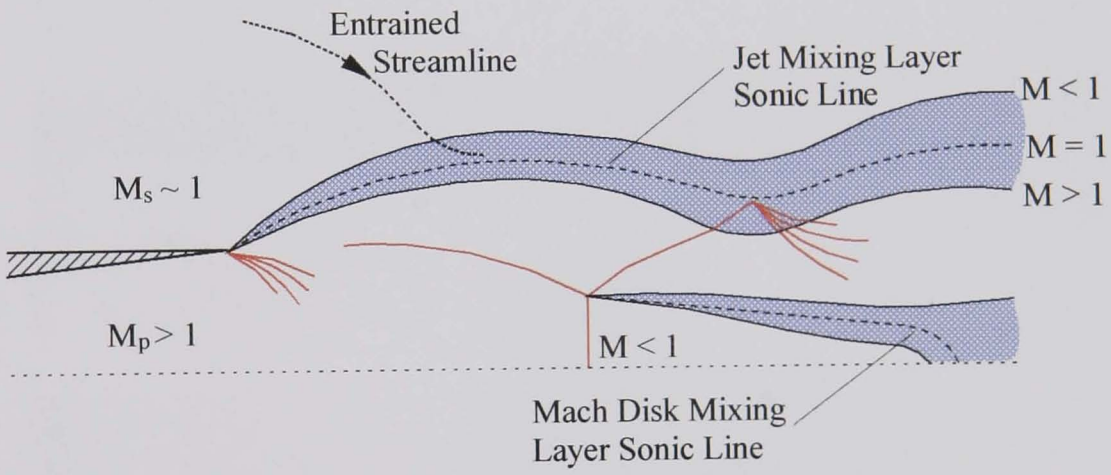

Figure 2.12 - Schematic of Jet Near Field Structure[49]

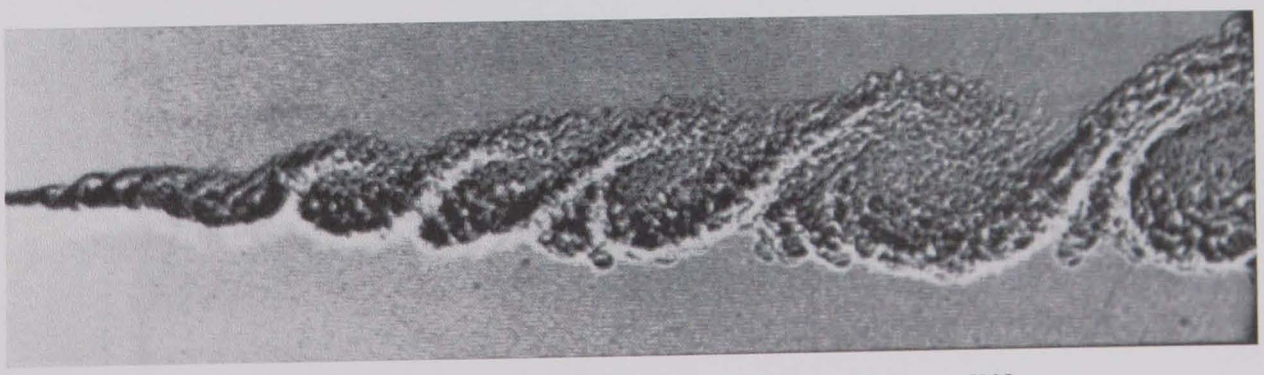

Figure 2.13 – Subsonic Plane Shear Layer.[50]

The structure of a supersonic mixing layer is governed by the compressibility within the layer. Mixing layer compressibility can be evaluated through calculation of the convective Mach number, M_c, as proposed by Bogdanoff[52]. Supersonic plane shear

layers at M_c = 0.15, 0.54, and 0.96 are shown in Fig 2.14. It has been shown that plane mixing layers, axisymmetric mixing layers and jets have very comparable flow structure[50,53]. In particular the initial mixing region at the boundary of an axisymmetric jet approximates well to that of a plane mixing layer[50]. Large scale structures like those observed in subsonic layers are visible at M_c = 0.15, however at higher M_c this structure diminishes and disappears. This diminishing large scale structure is attributable to compressibility and not the extremely high Reynolds number which accompany these flows.

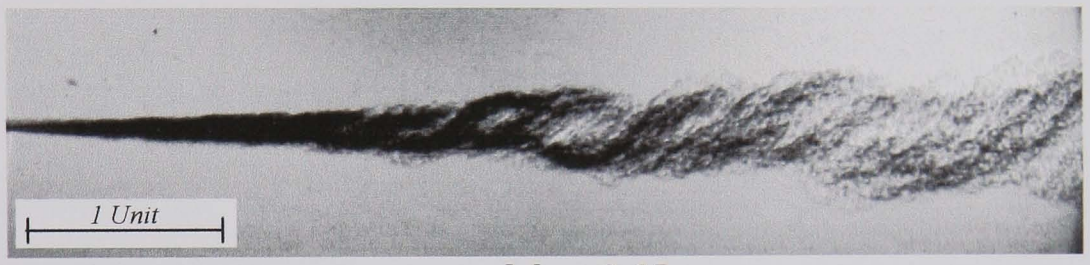

a. – M_c = 0.15

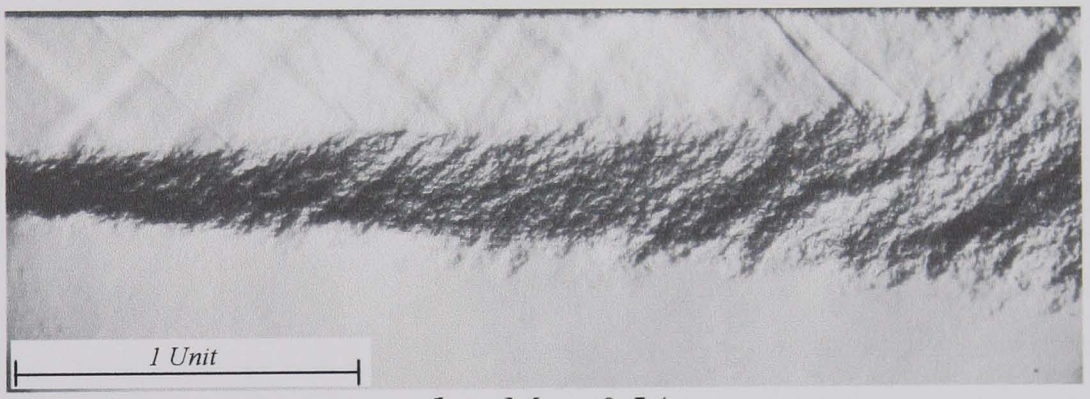

b. – M_c = 0.54

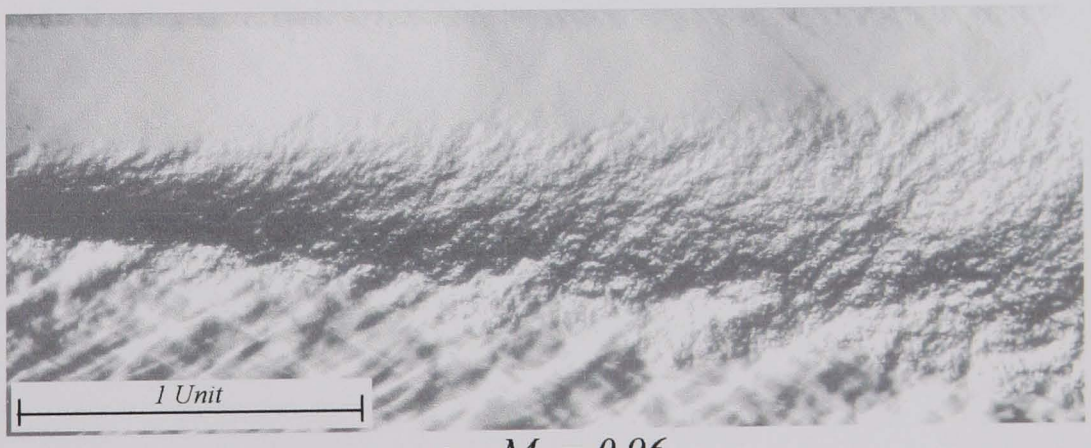

c. – M_c = 0.96

Figure 2.14 – Compressible Plane Shear Layers
At Increasing Convective Mach Number[54]

What is not clear from the images is that as compressibility levels increase the structures within the layer change from being two dimensional in nature to exhibiting a full three dimensional behaviour[53,55]. Two dimensional vortex pairings disappear

as do the roller like structures which accompany them. Such behaviour has also been observed in supersonic jets[7].

Although at high M_c large scale structure is not evident Clemens[55] has suggested that it is still present. Clemens[55] claims that researchers occasionally fail to observe this large scale structure due to the positioning of the knife edge used in the schlieren technique. Desevaux[7] also discussed how three dimensional structures fail to appear due to spatial integration, an intrinsic component of the schlieren technique.

2.4.4 - Entrainment

Entrainment is the process by which irrotational (non-turbulent) fluid is incorporated into a turbulent flow. In contrast this can also be the diffusion of a turbulent flow within an ambient environment. Although the definition of entrainment is widely accepted the actual mechanism of entrainment is an area of considerable debate.

Originally entrainment was thought of as a "nibbling" process by which irrotational fluid was ingested by the turbulent flow[57]. This occurred within a viscous super-layer, a thin interface between rotational and irrotational fluid driven by the shear forces which would exist between the fluids. The layer was assumed essentially homogeneous and isotropic in nature[58], with thickness comparable in order of magnitude to the Kolmogorov[58] length scale.

This explanation is now thought too simplistic, and theories which describe entrainment as a "gulping" process have been proposed[50,59]. Irrotational fluid is engulfed by large scale turbulent structures, Fig 2.15. Small scale structures embedded within the large scale turbulence then digest and mix entrained fluid into the main body of turbulent flow. Finally diffusive processes could then possibly occur mixing at a molecular level. However Roshko[60] suggested that nibbling processes may exist at the edges of the large scale structure complimenting the engulfing processes.

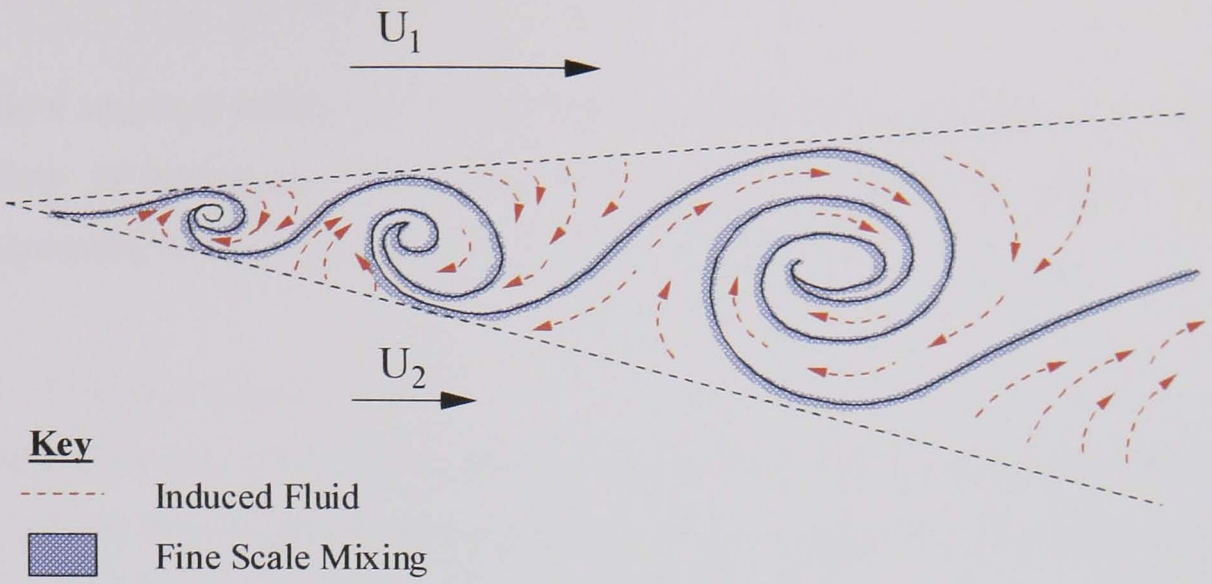

Figure 2.15 - Entrainment Into A Shear Layer[59]

Fluid entrained into the shear layer causes the layer to spread and develop. Subsonic shear layers have the highest growth rates, and correspondingly the highest entrainment due to the large scale structure within them. As the convective Mach number of the layer increases the growth and entrainment rate decreases.

Additional turbulent structures particular to supersonic jets have been claimed to assist entrainment[61]. Streamwise vortices have been observed at the boundary of under-expanded jets. Krothpalli[61] has suggested that these structures play an important role in the entrainment of fluid into spreading supersonic jets.

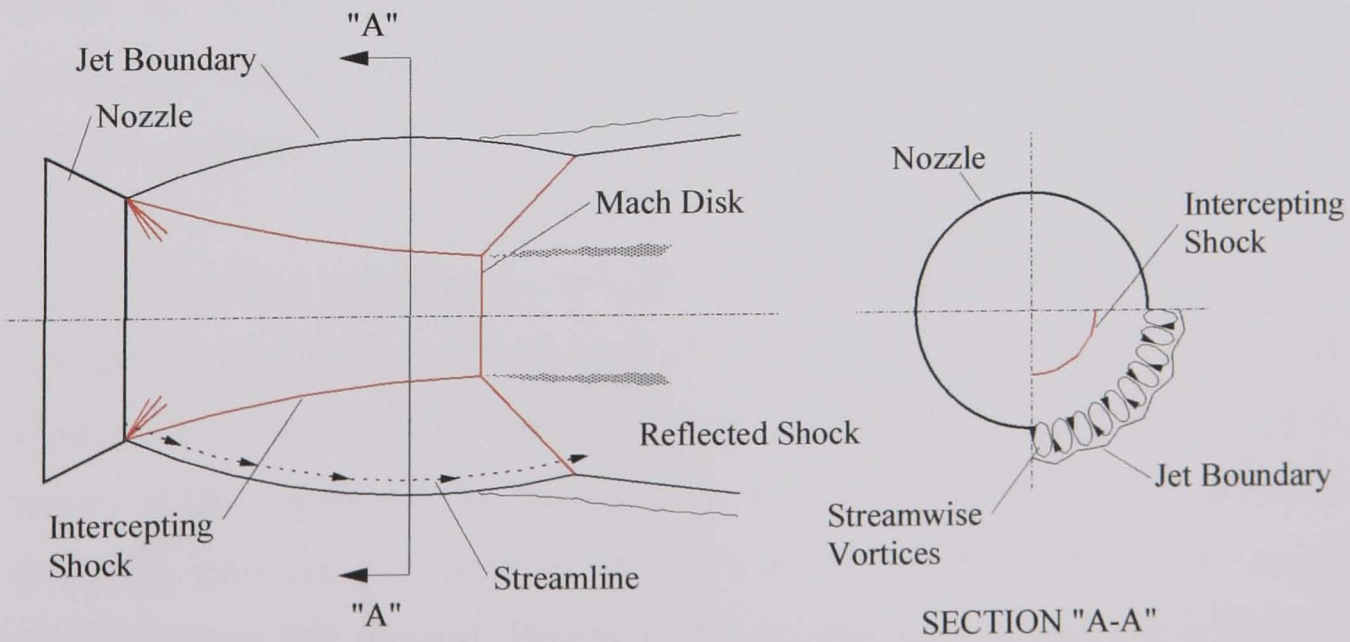

Figure 2.16 - Streamwise Vortices In An Under-Expanded Jet[61]

2.5 – Ejector Flow Structure

The flow structure within ejectors has been the subject of considerable study utilising a variety of techniques. These can be primarily split into two groups, pressure measurement, and visualisation.

2.5.1 – Pressure Measurement

Both intrusive and non-intrusive pressure measurement techniques have been used to study ejector flow structure. Non-intrusive pressure measurement is easily conducted by simply taking static pressure readings at tappings placed along the ejector shroud wall. This is a popular technique and has been used extensively[6,39]. Although this method reveals pressure variation along a mixing section, it does not often reveal what is occurring within the flow channel. Static tappings can be used to locate shock systems within the ejector. Though this is only possible if the shock extends to the ejector shroud, and the tappings are placed with sufficient frequency.

Intrusive methods provide far more detailed information on the mixing process, but at the risk of causing flow disturbances. The insertion of a probe into a small space could destroy or influence flow phenomena. This could include the formation of shocks at the probes surface. Pitot tube methods[6,39] have been employed, which provide useful information on pressure distribution, and in turn, velocity distribution across the width of the mixing chamber. These methods allow study of the interaction between the primary and secondary streams through identifying the velocity gradient.

Search tubes have been used by both Watson[1] and Desevaux[62]. The technique uses a length of tube, with a static tapping, which is passed along the central axis of the ejector. The technique has been useful in the provision of information relating to the nature of the supersonic jet issuing from the motive nozzle. Information on the existence, position, and strength of shock structures within the flow can all be obtained using this method. However search tubes have a number of limitations, principally related to the possible occurrence of tube resonance.

To prevent vibration the search tube must be either rigid or supported at both ends. Both approaches have disadvantages. A search tube of sufficient dimensions to prevent resonance could disturb flow patterns considerably. Supporting the tube at either end, and in tension, allows the probe to be thinner. Desevaux[62] used this configuration to study the flow in constant area ejectors. The tube however needs to be fed through the entire length of the ejector, from the motive nozzle inlet to the diffuser outlet. This limits the method to the study of ejectors of short length. A supported tube, of sufficient length to axially traverse the ejector, will also be prone to oscillations. Additionally the motive nozzle throat needs to be generously sized as the tube passes through this section. Desevaux[62] claimed however that the presence of the search tube did not significantly affect the flow, having compared flow visualisations with and without the probe.

2.5.2 – Visualisation

The best insight into ejector operation has been provided by flow visualisation studies, mostly conducted using the schlieren technique. Watson[1] used schlieren visualisations when studying constant-pressure vacuum ejectors to explain the operational performance through the expansion structure of the jet. Keenan et al[12] presented a limited number of visualisations demonstrating the influence which diffuser exhaust pressure has upon the flow structure within a constant area ejector. The images revealed some of the complicated shock structure that can occur within the shroud, including reflected expansion waves and shocks. Most notable is the work of Bauer[63] who presented numerous visualisations of the flow. Predominantly taken within constant area ejectors, the images were combined with static pressure data obtained along the shroud wall. A limited selection of visualisations within constant pressure ejectors were also shown.

Desevaux[62,64] used a laser light sheet to visualise flow within constant area ejectors. As part of the visualisation the fluids need seeding, oil drop tracer particles were injected into the secondary stream. This was not necessary with the primary stream as the expansion processes caused the formation of condensation which worked in the same manner as the oil drops. The technique though is complex, and has a number of disadvantages. The light sheet is focused up along the length of the ejector from the diffuser outlet. This prevents the ejector under study from forming part of a

closed system. Additionally the images obtained are of poor quality, revealing only basic detail, unlike schlieren images.

Flow visualisation has been used to try to explain ejector operation, by the identification of common flow patterns that occur within different performance regimes. These regimes have been generally delineated by the degree of secondary mass flow. Fabri & Sienstrunck[65] and more recently Matsuo[48], presented a series of operational performance curves which plotted entrainment vs P_2/P_a. The nature of the curves was explained by the observed flow structure within the ejector.

Fabri & Sienstrunck[65] provided the first real flow visualisation study within ejectors which linked observed structure to operational performance. Utilising a constant area air-air ejector Fabri identified four key flow patterns, Fig 2.17; supersonic flow, saturated supersonic flow, mixed flow, and mixed flow with separation. Supersonic and saturated supersonic flow patterns are pressure independent, the supersonic secondary flow within the mixing tube forming a choke. The potential entrainment level of the supersonic flow pattern is greater than that of the saturated flow pattern. This is because the entrainment in the saturated supersonic flow regime is limited by the formation of a choke within the secondary flow at the motive nozzle exit. Mixed flow with and without separation is pressure dependent, the secondary flow stream never attains sonic velocities, preventing the formation of a choke.

The relevance of the flow structure within a constant area ejector to the study of a constant pressure design may be questioned. However Matsuo[48] identified similar flow patterns within constant pressure style rectangular ejectors. Matsuo[48] also observed that the flow pattern can be dependant upon the area ratio between the throat of the ejector and motive nozzle in a constant pressure design.

Matsuo[48] also identified four distinct sets of flow structure in a constant pressure style ejector; fully supersonic, choked secondary, "shock between throats", and double choked flow, Fig 2.18. Fully supersonic and "shock between throats" flow patterns are comparable respectively to the supersonic and mixed flow patterns identified by Fabri & Siestrunck[65]. Double choked structure was only observed for small ratios of nozzle-to-ejector throat area ratio, (AR).

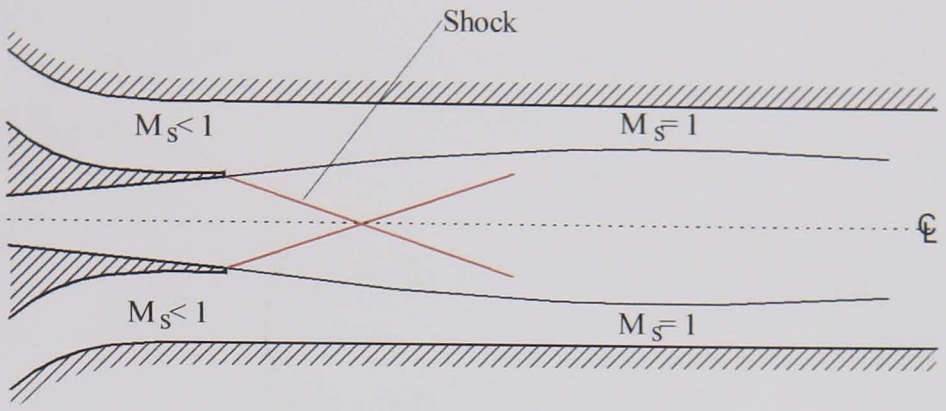

a. – Supersonic Flow

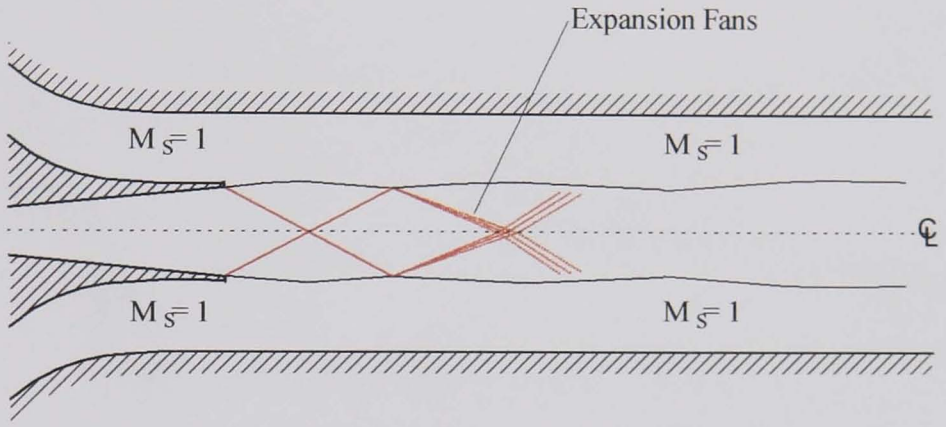

b. – Saturated Supersonic Flow

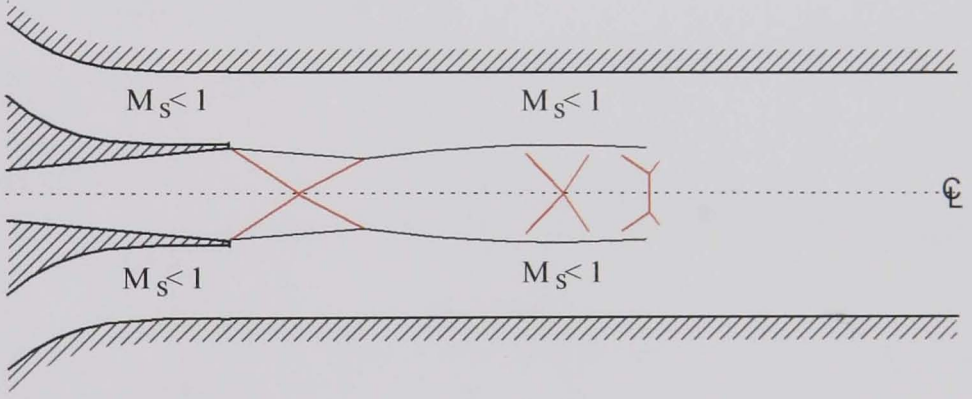

c. – Mixed Flow

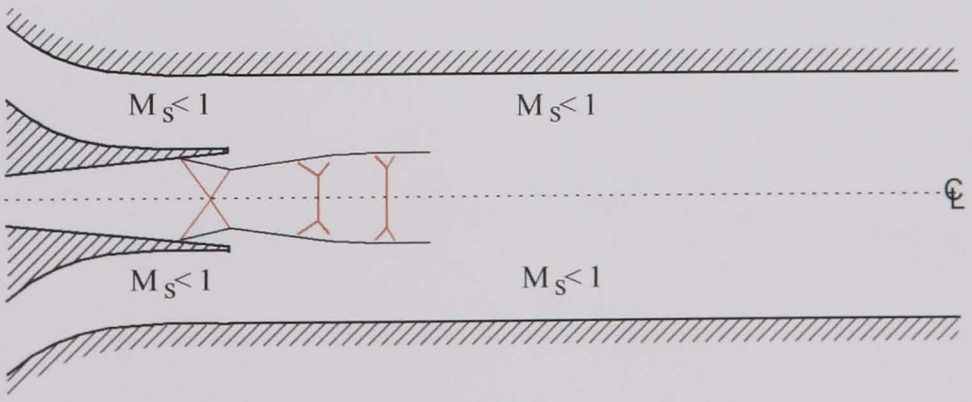

d. – Mixed Flow With Separation

Figure 2.17 – Fabri & Siestrunck[65] Classification of Internal Flows

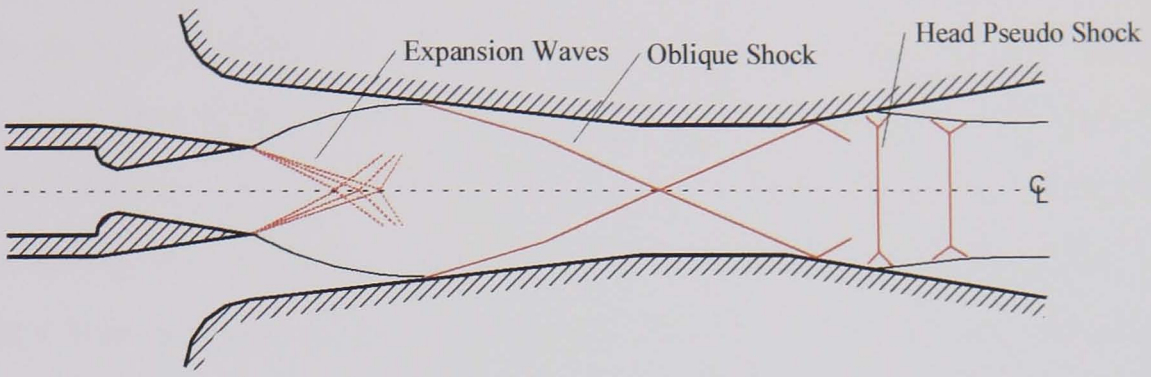

a. – Fully Supersonic

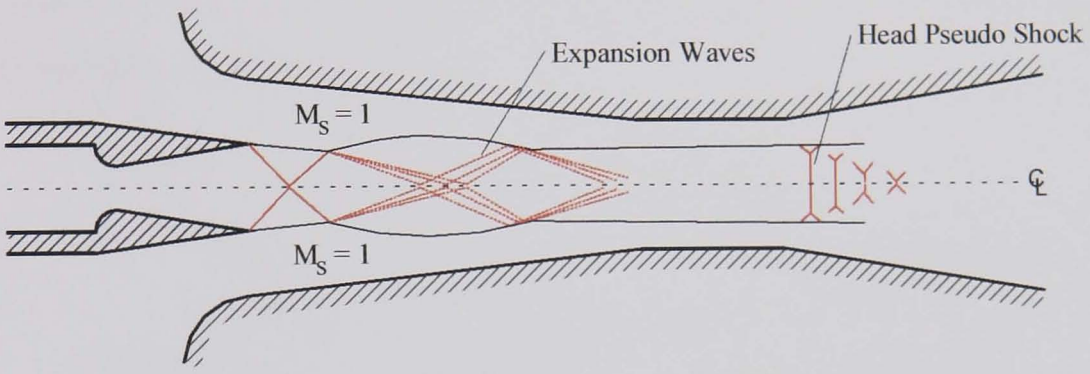

b. – Choked Secondary Flow

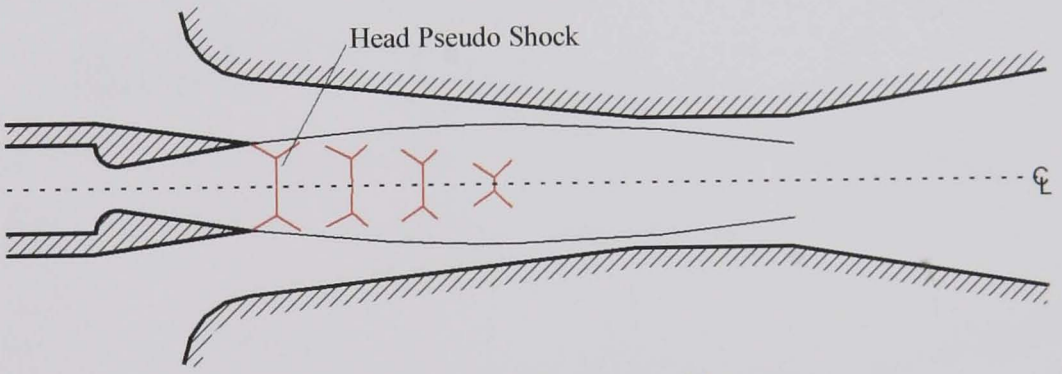

c. –Shock Between Throats

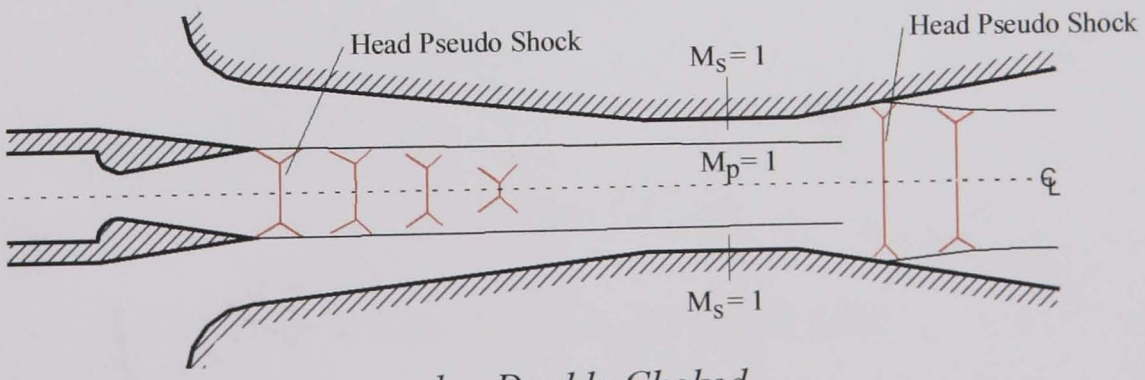

d. – Double Choked

Figure 2.18 – Matsuo's Classification of Internal Flows[48]

The flow patterns again can be split between pressure independent and pressure dependant operation. All are pressure independent with the exception of the shock between throats structure which is pressure dependant. The double choked and choked secondary flow patterns exhibited a higher entrainment level than the fully supersonic pattern. This is due to the secondary flow remaining distinct from the primary stream throughout the ejector. However this only occurs for higher levels of secondary inlet pressure. Therefore the observed flow pattern is not only dependent upon diffuser pressure, but also upon secondary inlet pressure. This can also be seen in the work of Addy[44] who prior to Matsuo had performed an analysis of constant pressure supersonic ejectors.

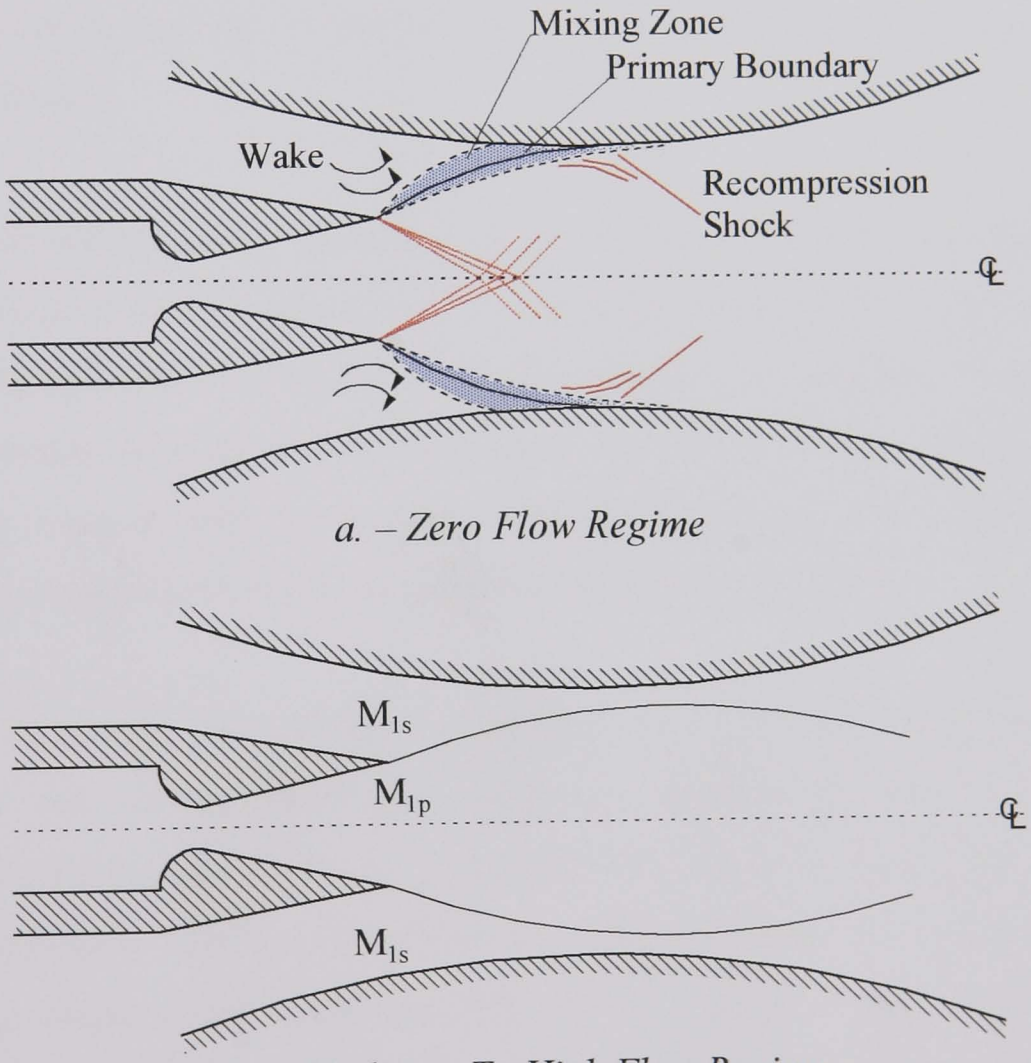

a. – Zero Flow Regime

b. – Moderate To High Flow Regime

Figure 2.13 – Addy's Classification of Internal Flows[44]

Addy[44] classified ejector performance principally on pressure dependency and then by secondary mass flow characteristics. These were split between three mass flow regimes; zero secondary flow, low secondary flow, moderate to high secondary flow, Fig 2.13. With the choked state Addy stipulates that for a zero flow regime to occur, primary flow expands within the mixing chamber choking the ejector throat with a recompression shock system. Whereas for moderate to high regimes the two streams are stated to essentially remain distinct. Secondary fluid attains sonic velocities and chokes the throat. It is claimed that the low flow regime operates somewhere between the zero and moderate regimes.

With unchoked flow, in all flow regimes, the choke within the throat collapses. The primary jet shock structure recedes towards the motive nozzle until the nozzle throat is itself unchoked.

Addy's description of the spreading of the motive jet within the zero/low flow regime is echoed in a theory proposed by Munday & Bagster[35]. This explains the constant capacity characteristics of ejectors in refrigeration systems. They postulated that the primary jet of the motive nozzle fans out into the mixing section, forming a converging channel with the shroud wall. The secondary fluid flows down the channel eventually reaching sonic velocities which form the choke.

The study of ejector flow structure is not easily accomplished. To obtain an overall picture of the mixing processes occurring, information from a number of experimental techniques should be combined. This should include pressure data and flow visualisations. The use of a technique which could provide all this data in a single step would be advantageous. PIV (Particle Image Velocimetry) maybe of some use but is highly complex. The best alternative method for obtaining this combination of data with images is to use CFD in an attempt to model and predict the ejector flow structure.

2.6 CFD Studies

It was Keenan et al[12] who stated in 1950:

"*No analytical device has been found for determining under all circumstances the mixing processes corresponding to optimum ejector performance*"

Keenan et al[12]

It is believed that computational fluid dynamics might provide a solution to this problem. The application of CFD to the study of ejectors is not a new concept. In 1974 Hedges & Hill[4], who were forerunners in CFD, developed a 2-D finite difference flow model. This used the governing equations in conservation form, with a mixing length model providing turbulence closure. The model was used to calculate the mixing of a compressible jet in plane and axisymmetric variable area ducts. However the model was basic compared to modern codes being incapable of dealing with recirculation and strong shock waves. Both of these phenomena have been shown through visualisation studies to occur within ejectors operating under certain flow conditions, [63,65]. However when used to simulate air-air ejectors experimentally tested by Helmbold[66] and Hickman et al[6], the model was shown to produce results which compared well to experiment.

The model was further validated by Hedges & Hill[4] with yet another experimental geometry and again found to perform well. Combined within the results is a study of the influence of turbulence model parameters. Hedges concluded that more advanced turbulence models using kinetic energy equations may be beneficial in the simulation of ejectors operating with different types of flow. This appears to be a belief demonstrated by other researchers in his time [67,68].

In the same era other studies into different forms of ejector were also being conducted. Croft & Lilley[67] worked on a finite difference program utilising the k–ε model to deal with turbulence. However they only applied the technique to incompressible flow in a jet pump. A 3-D parabolic finite difference method was developed by De Joode & Patankar[68] to model the hypermixing characteristics of a

thrust augmenting ejector. They also rejected the use of a mixing length model to provide turbulence closure as they felt it was not sophisticated enough to deal with the complex 3-D mixing processes within this style of ejector. Instead they also chose the k–ε model of Launder & Spalding[69].

More than a decade after Hedges & Hill, Nilavalagen et al[70] presented a similar technique for analysing the mixing within a compressible flow ejector. A finite-difference technique proposed by Patankar-Spalding[71], and modified to deal with axisymmetric flow was implemented. A mixing length model was again adopted to provide turbulence closure of the governing equations. This appears somewhat of a step back in progress. Although the model has been shown to be capable of predicting flow within specific ejectors its general applicability is questionable. Consequently the model suffered from similar problems as the work of Hedges & Hill[4] and was incapable of dealing with recirculation. The method was capable of studying flow throughout the entire ejector, however studies were confined to the mixing section, the diffuser being omitted. Modelling the ejector in part only is not uncommon. As an example Neve[72] dealt only with the diffuser. It is only recently that simulations of the whole ejector have been conducted. This is most likely due to the continuing increase in computing power.

Over the last decade the study of ejectors utilising CFD has taken a new direction. The use of in-house developed codes written specifically to resolve the flow problems within ejectors has all but disappeared, with perhaps the exception of research concerned with the evaluation of thrust augmenting ejectors. Instead researchers are now turning their attention towards commercially available codes such as Fluent to simulate the ejector. Commercial codes have now evolved to a stage where they are widely applicable to the resolution of many flow problems, and can be used to accurately predict ejector performance. This could signal a departure away from academic based study of the units, to industrial use of the technique in the design process.

Caution must however be exercised in the use of commercial codes. The wide applicability of the codes can lead to problems in obtaining a decent answer, unlike

in the use of specifically written codes. To write a code capable of predicting flow within an ejector it is necessary to possess an understanding of the numerics required to predict the phenomena which occur. A deep understanding of the numerics is not required to obtain some form of solution from a commercial code. However if the obtained results are to be quantitative, or even just qualitative, the numerics of the code must be fully understood by the user and then applied carefully and correctly. It is therefore perhaps now more important than ever that CFD is calibrated and validated so that the colourful pictures which result can be believed and used.

The majority of studies conducted using commercial software have been of ejectors used within refrigeration and air-conditioning cycles. Both of these cycles typically entrain vapour at relatively low pressures, using constant pressure design units. Riffat et al[73] conducted a three-dimensional study of an ejector within a refrigeration cycle, claiming that as the ejector geometry is asymmetric, axisymmetric approximations should not be adopted if flow interaction is to be predicted accurately. The study was used to determine the influence of motive nozzle shape, and the ejector simulated operating with a variety of refrigeration vapours.

The accuracy of these results must be questioned, and at best they may only be viewed as qualitative. The computational mesh comprised only 36855 cells, which is coarse for a three-dimensional flow problem. This however was a result of computational constraints. These constraints would also have prevented a mesh dependency test, an important factor. Most questionable though is the assumption that the working fluids were incompressible. An assumption imposed due to encountered computational difficulties. Finally, no experimental validation is offered.

An incompressible flow assumption was again imposed by Smith & Riffat et al[74] in the simulation of a supersonic steam ejector using Fluent. Once more computational constraints played an important role in the quality of the simulation and limited the mesh to 60000 computational cells. Simulation stability is always a consideration in

CFD and to ensure this a power law discretisation scheme was adopted, along with the k-ε turbulence model. However yet again no numerical validation was presented.

The influence of nozzle position & motive fluid temperature were combined in the study. The accuracy of results seen to vary somewhat (13%–40%) dependant upon nozzle position. This can be attributed to mesh, and modelling assumptions. Smith concluded that the incompressible flow assumption may need to be dropped if a more accurate result was to be obtained.

Finally in 1997 Chin et al[75] presented a paper which studied the application of commercial CFD codes to the simulation of supersonic ejectors. Comparisons were drawn between simulations performed using two commercially available finite volume codes, a segregated pressure based solver and a fully coupled solver. See Section 4.2. Discretisation and interpolation schemes were discussed and assessed for there applicability to the problem, as were other issues such as convergence criteria and numerical diffusion error.

Chin[75] modelled the ejector as a simplified two-dimensional axisymmetric geometry. This is possible by assuming that the secondary stream has negligible velocity at inlet. The motive nozzle was also modelled representatively. Instead of modelling the internals of the nozzle these were omitted and an inlet boundary condition was specified at the nozzle exit. Boundary conditions were specified having been calculated from one-dimensional compressible flow theory. This assumed tenuously that the expansion processes occurring within the nozzle were isentropic. As the nozzle and mixing chamber back pressure in turn influence each other the occurrence of this is unlikely. The predicted barrelling flow patterns further support this argument.

It was demonstrated however that CFD could prove a useful tool in the simulation of ejectors. Also shown was the importance of careful selection of numerical parameters. Chin[75] stated that failure to do this could result in predicted values with an error of 65% in respect to experiment. However if the numerics are chosen

carefully it was claimed that the ejector could be simulated accurately. The fully coupled solver was shown to outperform the segregated pressure based solver.

The use of segregated solvers still appears prevalent which is most likely due to the availability of the codes. Riffat & Everitt[76] used the segregated solver Fluent 4.32 to simulate an ejector in an air conditioning system. The simulation was once more three-dimensional. Although the mesh is relatively coarse, 65000 cells, this is justified as a trade-off between computational accuracy, and computational time. This is an important issue if CFD is to be adopted within an industrial setting. CFD can be CPU time consuming. If a coarse mesh can be used to obtain qualitative results which are sufficiently accurate, what benefit is gained from running a time consuming highly refined study ?

With this study Riffat & Everitt[76] took compressibility effects into account. However they still failed to predict a shock, shown by experiment to be present within the ejector throat. When Chin et al[75] studied the use of segregated solvers a shock system within the throat was only predicted with the use of the higher order QUICK discretisation scheme. Riffat & Everitt[76] used the Power Law discretisation scheme, the accuracy of which lies somewhere between 1st order and higher order schemes. The use of this scheme may account for the failure in prediction of this shock phenomena.

A brief study of the turbulence model applied is also discussed. Riffat & Everitt[76] criticise the limitations of the standard k-ε model including its inability to deal with rapidly strained flows and use of constant Prandtl number. Therefore the RNG k-ε model and RSM model are tested. It is concluded that there is little difference in the predicted results between the RNG and RSM methods apart from the increased computational demands of the RSM. Unfortunately there is no comparison of, or results from, tests with the standard k-ε model to confirm its unsuitability to this problem, and inferiority compared to RNG.

The applicability of various turbulence models to the simulation of ejectors has been studied by other researchers. Zhou et al[27] simulated an ejector, used in the

suppression of gas turbine infra red exhaust signature, using Fluent 5. This was an incompressible flow study of an ejector fitted with an annular motive nozzle. Various degrees of swirl were simulated within the ejector. The three k-ε turbulence models (Standard, RNG, Realisable) offered by Fluent were tested alongside RSM. It was shown that moderate degrees of swirl are best modelled using either RNG or RSM. High swirl cases should be modelled by RSM. However for zero or weak swirl cases Zhou states that reasonable results can be obtained by using any of the k-ε models.

Other studies of ejectors have also been conducted utilising proprietary software. Al-Khalidy[77] has studied a refrigerant ejector in two-dimensions. This used an unstructured tetrahedral mesh. The application of such a mesh to a flow problem with a predominant flow direction is questionable. However the work presented is in the early stages and shows only initial attempts at applying CFD methodology to the problem.

The application of commercial CFD codes to the study of ejectors still appears to be in its infancy. This is apparent in the simplifications, being made by researchers to maintain numerical stability. Inappropriate incompressible assumptions have been applied to the study of supersonic flows. The use of numerically diffusive lower order interpolation schemes combined with coarse mesh is also common. There is however an argument for the use of coarse mesh if qualitative results are attainable with such mesh and are sufficiently accurate. The majority of studies seem content with obtaining such results. Additionally to date no real studies have been presented of the entire flow structure within the ejector and the mixing processes which are occurring. Studies have been more concerned with simulating the ejector and using the results to predict the performance of the system within which it is situated.

Chapter 3 - Mathematical Model

This chapter describes the mathematical model assembled in this study. The chapter begins with the basics of the governing equations, the heart of all CFD codes. Turbulence modelling and additional numerical models are discussed in turn. The application of boundary conditions and physical properties is covered.

3.1 – The Governing Equations

The Navier-Stokes equations provide the foundation upon which all computational fluid dynamics software is based. They describe the three fundamental physical criteria upon which all fluid dynamics is founded. In 3-D, cylindrical time-averaged co-ordinates:-

Conservation of Mass: *What goes in must come out.*

$$\frac{\partial \rho}{\partial t} + \frac{\partial (\rho u)}{\partial x} + \frac{1}{r}\frac{\partial (r\rho v)}{\partial r} + \frac{1}{r}\frac{\partial (\rho w)}{\partial \theta} = 0 \qquad (3.1)$$

Conservation of Momentum: *(Newton's Second Law) The rate of change in momentum of a fluid particle is the sum of the forces acting upon that particle.*

$$\begin{aligned}&\frac{\partial}{\partial t}(\rho u)+\frac{\partial}{\partial x}(\rho uu)+\frac{1}{r}\frac{\partial}{\partial r}(r\rho vu)+\frac{1}{r}\frac{\partial}{\partial \theta}(\rho wu)=-\frac{\partial p}{\partial x}+\frac{\partial(\tau_{xx})}{\partial x}+\frac{1}{r}\frac{\partial(r\tau_{xr})}{\partial r}\\&+\frac{1}{r}\frac{\partial(\tau_{x\theta})}{\partial \theta}+\frac{\partial}{\partial x}(-\rho\overline{u}'\overline{u}')+\frac{1}{r}\frac{\partial}{\partial r}(-r\rho\overline{v}'\overline{u}')+\frac{1}{r}\frac{\partial}{\partial \theta}(-\rho\overline{w}'\overline{u}')\end{aligned} \qquad (3.2)$$

$$\begin{aligned}&\frac{\partial}{\partial t}(\rho v)+\frac{\partial}{\partial x}(\rho uv)+\frac{1}{r}\frac{\partial}{\partial r}(r\rho vv)+\frac{1}{r}\frac{\partial}{\partial \theta}(\rho wv)=-\frac{\partial p}{\partial x}+\frac{\rho w^2}{r}+\frac{\partial(\tau_{xr})}{\partial x}+\frac{1}{r}\frac{\partial(r\tau_{rr})}{\partial r}\\&+\frac{1}{r}\frac{\partial(\tau_{r\theta})}{\partial \theta}-\frac{\tau_{\theta\theta}}{r}+\frac{\partial}{\partial x}(-\rho\overline{u}'\overline{v}')+\frac{1}{r}\frac{\partial}{\partial r}(-r\rho\overline{v}'\overline{v}')+\frac{1}{r}\frac{\partial}{\partial \theta}(-\rho\overline{w}'\overline{v}')\end{aligned} \qquad (3.3)$$

$$\frac{\partial}{\partial t}(\rho w)+\frac{\partial}{\partial x}(\rho uw)+\frac{1}{r}\frac{\partial}{\partial r}(r\rho vw)+\frac{1}{r}\frac{\partial}{\partial \theta}(\rho ww)=-\frac{1}{r}\frac{\partial p}{\partial \theta}-\frac{\rho vw}{r}+\frac{\partial(\tau_{x\theta})}{\partial x}$$
$$+\frac{1}{r^2}\frac{\partial(r^2\tau_{r\theta})}{\partial r}+\frac{1}{r}\frac{\partial(\tau_{\theta\theta})}{\partial \theta}+\frac{\partial}{\partial x}(-\rho\overline{u}'\overline{w}')+\frac{1}{r}\frac{\partial}{\partial r}(-r\rho\overline{v}'\overline{w}')+\frac{1}{r}\frac{\partial}{\partial r}(-\rho\overline{w}'\overline{w}') \quad (3.4)$$

where τ_{xx}, τ_{rr}, τ_{xr}, are Reynolds stresses,

$$\tau_{xx}=2\mu_t\frac{\partial u}{\partial x}-\frac{2}{3}\mu_t\left(\frac{\partial u}{\partial x}+\frac{1}{r}\frac{\partial(rv)}{\partial r}\right) \quad (3.5)$$

$$\tau_{rr}=2\mu_t\frac{\partial v}{\partial r}-\frac{2}{3}\mu_t\left(\frac{\partial u}{\partial x}+\frac{1}{r}\frac{\partial(rv)}{\partial r}\right) \quad (3.6)$$

$$\tau_{\theta\theta}=2\mu_t\left(\frac{1}{r}\frac{\partial w}{\partial \theta}+\frac{v}{r}\right)-\frac{2}{3}\mu\left(\frac{\partial u}{\partial x}+\frac{1}{r}\frac{\partial(rv)}{\partial r}+\frac{1}{r}\frac{\partial w}{\partial \theta}\right) \quad (3.7)$$

$$\tau_{xr}=\mu_t\left(\frac{\partial u}{\partial r}+\frac{\partial v}{\partial x}\right) \quad (3.8)$$

$$\tau_{x\theta}=\mu_t\left(\frac{1}{r}\frac{\partial u}{\partial \theta}+\frac{\partial w}{\partial x}\right) \quad (3.9)$$

$$\tau_{r\theta}=\mu_t\left(\frac{1}{r}\frac{\partial v}{\partial \theta}+r\frac{\partial}{\partial r}\left(\frac{w}{r}\right)\right) \quad (3.10)$$

Conservation of Energy: *(The First Law of Thermodynamics) Energy can neither be created nor destroyed, it can only be transformed from one form to another.*

$$\rho c_p\left[\frac{\partial T}{\partial t}+\left(v\frac{\partial}{\partial r}+u\frac{\partial}{\partial x}+\frac{1}{r}w\frac{\partial}{\partial \theta}\right)T\right]=kT\left[\frac{1}{r}\frac{\partial}{\partial r}\left(r\frac{\partial}{\partial r}\right)+\frac{1}{r^2}\frac{\partial^2}{\partial \theta^2}+\frac{\partial^2}{\partial x^2}\right]$$
$$+\mu\left[2\left(\varepsilon_{rr}^{\ 2}+\varepsilon_{xx}^{\ 2}+\varepsilon_{\theta\theta}^{\ 2}\right)+\varepsilon_{xr}^{\ 2}+\varepsilon_{\theta x}^{\ 2}+\varepsilon_{r\theta}^{\ 2}\right] \quad (3.11)$$

where:-

$$\varepsilon_{rr}=\frac{\partial v}{\partial r} \qquad \varepsilon_{xx}=\frac{\partial u}{\partial x} \qquad \varepsilon_{\theta\theta}=\left(\frac{1}{r}\frac{\partial w}{\partial \theta}+v\right)$$
$$\varepsilon_{xr}=\frac{\partial v}{\partial x}+\frac{\partial u}{\partial r} \qquad \varepsilon_{\theta x}=\frac{1}{r}\frac{\partial u}{\partial \theta}+\frac{\partial w}{\partial x} \qquad \varepsilon_{r\theta}=\frac{1}{r}\left(\frac{\partial v}{\partial \theta}-w\right)+\frac{\partial w}{\partial r} \quad (3.12)$$

The preceding equations (3.1)-(3.4) and (3.11) have been described as the Navier-Stokes equations, however historically this is not strictly correct. Originally only the conservation of momentum equations, modified to deal with viscous flow, were termed Navier-Stokes equations. Over time however the description Navier-Stokes equations has been expanded to include all flow equations (momentum, continuity and energy) used in the solution of viscous flow problems. The practice of using the term in this manner is now widespread within modern CFD and fluids literature, and is therefore continued within this thesis.

The Navier-Stokes equations were first derived by Claude-Luis Navier in 1822, and then independently by George Gabriel Stokes in 1845. When combined with Benoit Clayperon's perfect gas law they provided a description of the pressure and velocity fields within a moving fluid. This presented an alternative to the potential flow theory, previously used to describe flows, and accounted for the effects it omitted. Potential flow theory assumed that flow was incompressible, irrotational, and inviscid, making its use inappropriate for many practical flow problems. Ironically although Stokes understood viscous flow, Navier had not been trying to develop equations that would describe this property, had no understanding of viscosity, and yet somehow still managed to account for the effects in his equations[78].

The Navier-Stokes equations however were far too complex to be solved for all but the simplest of flows. No real progress was therefore made in their use until the early 1900's when Ludwig Prandtl, a German mechanical engineer, produced a description of the flow within a boundary layer, (see Section 3.3). Prandtl's work led to the simplification of the Navier-Stokes equations by showing that the viscous effects are important only within the boundary layer for many flows. Potential flow theory could still then be used to describe the majority of the flow field.

Mathematical progress has been made over the last century. However the fact remains that even today the Navier-Stokes equations can still only be fully resolved for a handful of special cases. The problem remains that to fully describe a three-dimensional flow there are six unknowns; pressure, density, temperature, and velocities in the x-y-z directions. Unfortunately the Navier-Stokes equations,

describing mass, momentum, and energy conservation, only produce five partial differential equations. Hence an equation of state, such as the perfect gas law, must be implemented to provide the final link. The use of an equation of state is permissible through the assumption of thermodynamic equilibrium. Although the fluid momentum may be large it is assumed that it will still be low enough for a fluid particle to adjust almost instantaneously to the new thermodynamic conditions it encounters as it moves from one point in space to another.

Additionally the equations are non-linear, highly coupled partial differential equations, and therefore highly dependent upon each other. This means that they cannot be solved independently one at a time. The mathematical behaviour of the equations is also dependant upon whether they are applied to a subsonic or supersonic flow. In subsonic flow the equations behave in an elliptical manner, however the application to supersonic flow results in hyperbolic behaviour. This complicates the mathematical process considerably when a flow problem combines both types of flow. To further complicate matters, the solution of the equations at one point in a body of fluid is dependent upon the solution of the equations at every other point in that body.

It is the above problems that are the main source of difficulty in solving the Navier-Stokes equations. Therefore to allow the application of the equations in a wide range of flow problems they have to be manipulated. The way in which this is achieved, and that they are applied in computational fluid dynamics, is dependent upon the choice of solution method or solver. This will be discussed in Section 4.2.

3.2 – Turbulence Models – The Closure Problem

The simulation of turbulent flow creates additional complication in the solution of the governing equations. This is due to the fluctuating velocity fields, and flow properties, which are distinct characteristics of turbulence. These fluctuations at the smallest turbulent scales occur rapidly with a high frequency. The solution of the governing equations for an engineering flow problem, at each instantaneous small scale turbulent fluctuation would require computational power not currently

available. Therefore a method has to be adopted which allows the simulation of turbulence using the governing equations. Three approaches exist; time averaging, LES (Large Eddy Simulation), DNS (Direct Numerical Simulation).

LES solves the governing equations for the largest eddies within a flow. Small scale eddies and the effects of viscosity are representatively modelled. The method is computationally expensive and not suitable for many industrial flows. At high Reynolds number even the largest eddies can be small resulting in large computational demands, this restricts its use. DNS goes a step further than LES and actually solves the governing equations for each turbulent fluctuation. As has been stated the solution of each instantaneous small scale turbulent fluctuation in a flow problem would not be possible due to computational power that would be required. Hence this restricts DNS to a research environment, small Reynolds number and simple geometrical flows. For these reasons it is unlikely that DNS will ever become a useful engineering tool. LES & DNS were therefore not considered for this investigation, time averaging methods were adopted.

The governing equations (3.1)-(3.4) & (3.11) are written in time-averaged form. Time averaging removes the instantaneous small scale turbulent fluctuations through the use of time averaged values for flow properties. This procedure is applied not only to the velocity components in the momentum equations but also to pressure and other scalars. The time-averaging process however creates a further problem. Additional unknowns, the Reynolds stresses, now appear within the governing equations. A turbulence model therefore has to be used to predict the Reynolds stresses, and the additional scalar transport terms which accompany them.

There are two approaches to dealing with Reynolds stresses, either direct solution using Reynolds stress models (RSM), or the application of models based upon the Boussinesq hypothesis. In 1877 Boussinesq hypothesised that an analogy could be drawn between the action of the viscous stresses and the Reynolds stresses in a flow. This was based upon Newtons law of viscosity (3.13) , where viscous stress is taken to be proportional to the rate of deformation upon a fluid element.

$$\tau_{ij} = \mu\left(\frac{\partial u_i}{\partial x_j} + \frac{\partial u_j}{\partial x_i}\right) \tag{3.13}$$

Applying the hypothesis to the Reynolds stresses in the governing equations we obtain equations (3.5)-(3.10). These formulae are the same in respect to (3.13) with the exception of the appearance of μ_t, turbulent viscosity. It is the value of this property which turbulence models attempt to obtain.

The simplest method of deriving μ_t is through the use of the Prandtl mixing length model. This well documented model attempts to derive μ_t through the use of simple algebraic formula. Other approaches include; one equation models (Spalart-Allmaras) and two equation models (k-ε formulations). The Boussinesq hypothesis however is disadvantaged by the assumption that μ_t is isotopic. This is not the case for many flows, though the approximation is acceptable for the majority of industrial flows. When this is not acceptable Reynolds Stress models (RSM) can be used to resolve the individual Reynolds stresses. RSM is computationally intensive, requiring up of 50% more computational time than turbulence models which use the Boussinesq approach. For this reason Reynolds stress models were not considered within this investigation. Studies by Riffat & Everitt[76] have also shown they provide no additional benefit to the simulation of ejectors.

The one-equation Spalart-Allmaras[79,80] model, and two equation k-ε models (Standard, RNG, & Realisable) were considered. The Spalart-Allmaras model is a relatively new model now appearing within commercial CFD codes, however the standard k-ε model and its derivatives are well established. Originally proposed by Launder & Spalding[81], the k-ε model has achieved widespread use. This is due to its applicability to the simulation of many industrial flows, coupled with its economic and robust performance characteristics. Two variants of the standard model have evolved, RNG (Renormalisation Group Theory)[82], and the Realisable[83] formulation. The in depth numerics of the individual models used will not be recounted here as they have been well documented. However it is sufficient to outline the following points.

3.2.1 – Spalart-Allmaras

Spalart-Allmaras[80] is a one equation low Reynolds number model, developed for wall bounded flows, particularly related to aerospace applications. As the model is still relatively new its performance is somewhat of an unknown quantity. One equation models are known to have difficulty in dealing with turbulence length scales, and the prediction of the decay of homogeneous isotropic turbulence.

As the model is a low Reynolds number formulation, the viscous sublayer within the boundary layer needs resolving which can be computationally intensive. Adaptions which allow the model to utilise wall functions can be made avoiding this need. See Section 3.3. The model calculates turbulent viscosity (3.13) based upon a viscous damping function (f_{v1}) and a transport equation for turbulent kinematic viscosity (ν), equation 3.15.

$$\mu_t = \rho\tilde{\nu}f_{v1} \tag{3.14}$$

$$\rho\frac{D\tilde{\nu}}{Dt} = G_\nu + \frac{1}{\sigma_{\tilde{\nu}}}\left[\frac{\partial}{\partial x_j}\left\{(\mu+\rho\tilde{\nu})\frac{\partial\tilde{\nu}}{\partial x_j}\right\} + C_{b2}\rho\left(\frac{\partial\tilde{\nu}}{\partial x_j}\right)^2\right] - Y_\nu \tag{3.15}$$

3.2.2 – Standard k-ε Model

The Standard model[81] is the simplest "complete" turbulence model, allowing for the production/destruction of turbulence, and the effects of mean flow and diffusion upon the transport of fluid properties. Calculating the turbulent kinetic energy (3.16) and dissipation rate (3.17), turbulent viscosity is derived from the simple formula (3.18).

$$\rho\frac{Dk}{Dt} = \frac{\partial}{\partial x_i}\left[\left(\mu+\frac{\mu_t}{\sigma_k}\right)\frac{\partial k}{\partial x_i}\right] + 2\mu_t S_{ij}S_{ij} - \rho\varepsilon - Y_M \tag{3.16}$$

(I) (II) (III) (IV) (V)

$$\rho\frac{D\varepsilon}{Dt} = \frac{\partial}{\partial x_i}\left[\left(\mu+\frac{\mu_t}{\sigma_\varepsilon}\right)\frac{\partial\varepsilon}{\partial x_i}\right] + C_{1\varepsilon}\frac{\varepsilon}{k}2\mu_t S_{ij}S_{ij} - C_{2\varepsilon}\rho\frac{\varepsilon^2}{k} \tag{3.17}$$

(I) (II) (III) (IV)

$$\mu_t = \rho C_\mu \frac{k^2}{\varepsilon} \tag{3.18}$$

$$Y_M = \rho\varepsilon 2\frac{k}{a^2} \tag{3.19}$$

Where the terms are; (I) convection, (II) diffusion, (III) production, (IV) dissipation. Term (V) is Sarkar's proposal for dilation dissipation[84] (3.19). This is an important characteristic of compressible flows, related to jets, wakes, and shear layers. As the degree of compressibility involved increases the rate at which the jet, wake or shear layer spreads decreases correspondingly.

3.2.3 – RNG k-ε Model

The RNG[82] model offers improved capabilities in dealing with rapidly strained flows, and can account for low Reynolds number effects. It performs this by including an additional (R) term within the dissipation equation (3.21) which yields a lower turbulent viscosity. Low Reynolds number effects can be accounted for through the implementation of a differential viscosity model. This describes how the effective turbulent transport will vary with eddy scale.

$$\rho\frac{Dk}{Dt} = \frac{\partial}{\partial x_i}\left(\alpha_k \mu_{eff}\frac{\partial k}{\partial x_i}\right) + 2\mu_t S_{ij}S_{ij} - \rho\varepsilon - Y_M \tag{3.20}$$

$$\rho\frac{D\varepsilon}{Dt} = \frac{\partial}{\partial x_i}\left(\alpha_\varepsilon \mu_{eff}\frac{\partial \varepsilon}{\partial x_i}\right) + C_{1\varepsilon}\frac{\varepsilon}{k}2\mu_t S_{ij}S_{ij} - C_{2\varepsilon}\rho\frac{\varepsilon^2}{k} - R \tag{3.21}$$

$$R = \frac{C_\mu \rho \eta^3 (1-\mu/\mu_o)}{1+\beta\eta^3}\frac{\varepsilon^2}{k} \tag{3.22}$$

Where $\eta \equiv Sk/\varepsilon$, $\eta_o = 4.38$, $\beta = 0.012$.

Additionally the RNG model calculates Prandtl number, instead of using a constant value. However this comes at the cost of 10~15% more computational time than the standard model. Turbulent viscosity is still calculated in the same manner as the standard model, using equation (3.18).

3.2.4 – Realisable k-ε Model

The realisable[83] model has comparable computational demands to that of the standard model. However it is claimed to have improved abilities in predicting the rate of spread of axisymmetric and planar jets. This could be a useful characteristic when simulating the flow within the ejector. The main numerical difference between the realisable model and other turbulence models is its use of a new transport equation for dissipation (the kinetic energy equation is identical to that of the standard model), and its modified calculation of turbulent viscosity.

$$\rho\frac{Dk}{Dt}=\frac{\partial}{\partial x_i}\left[\left(\mu+\frac{\mu_t}{\sigma_k}\right)\frac{\partial k}{\partial x_i}\right]+2\mu_t S_{ij}S_{ij}-\rho\varepsilon-Y_M \qquad (3.23)$$

$$\rho\frac{D\varepsilon}{Dt}=\frac{\partial}{\partial x_i}\left[\left(\mu+\frac{\mu_t}{\sigma_\varepsilon}\right)\frac{\partial \varepsilon}{\partial x_i}\right]+\rho C_1 S_\varepsilon-\rho C_2\frac{\varepsilon^2}{k+\sqrt{\upsilon\varepsilon}} \qquad (3.24)$$

Equation (3.18) is still used to determine μ_t however whereas the Standard and RNG models use a constant value for $C\mu$, the realisable model calculates $C\mu$. This is a function of the rate of mean strain and rotation, and the production/dissipation turbulence fields, within the flow.

3.3 – Wall Models

The use of a wall model is a requisite when dealing with flows containing boundary layers, as k-ε turbulence models are incapable of accurately predicting the flow behaviour within them. k-ε models work best well away from walls as they are not designed to deal with low Re number. Any attempt to use them in the proximity of a wall without the implementation of a wall model would result in inaccurate k-ε profiles. This could cause problems as turbulent flows are greatly affected by walls.

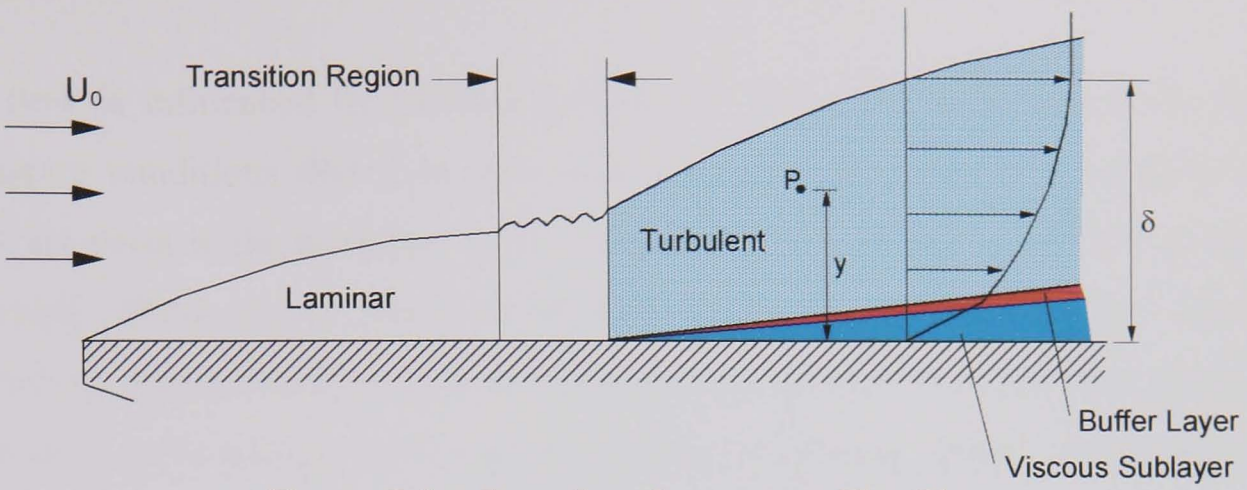

Figure 3.1 – Boundary Layer on a Flat Plate

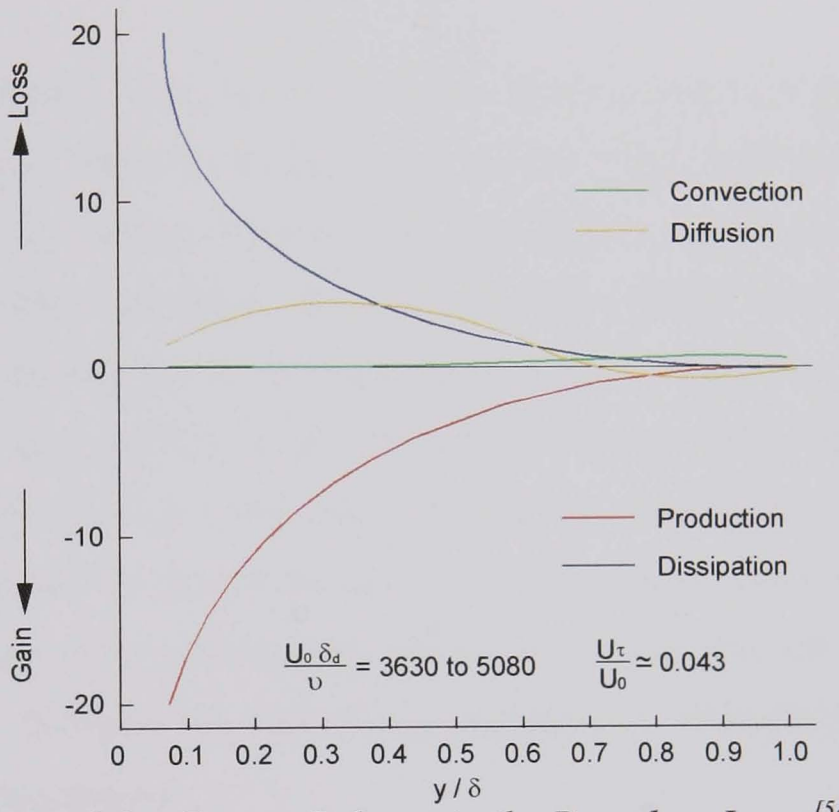

Figure 3.2 – Energy Balance in the Boundary Layer[58]

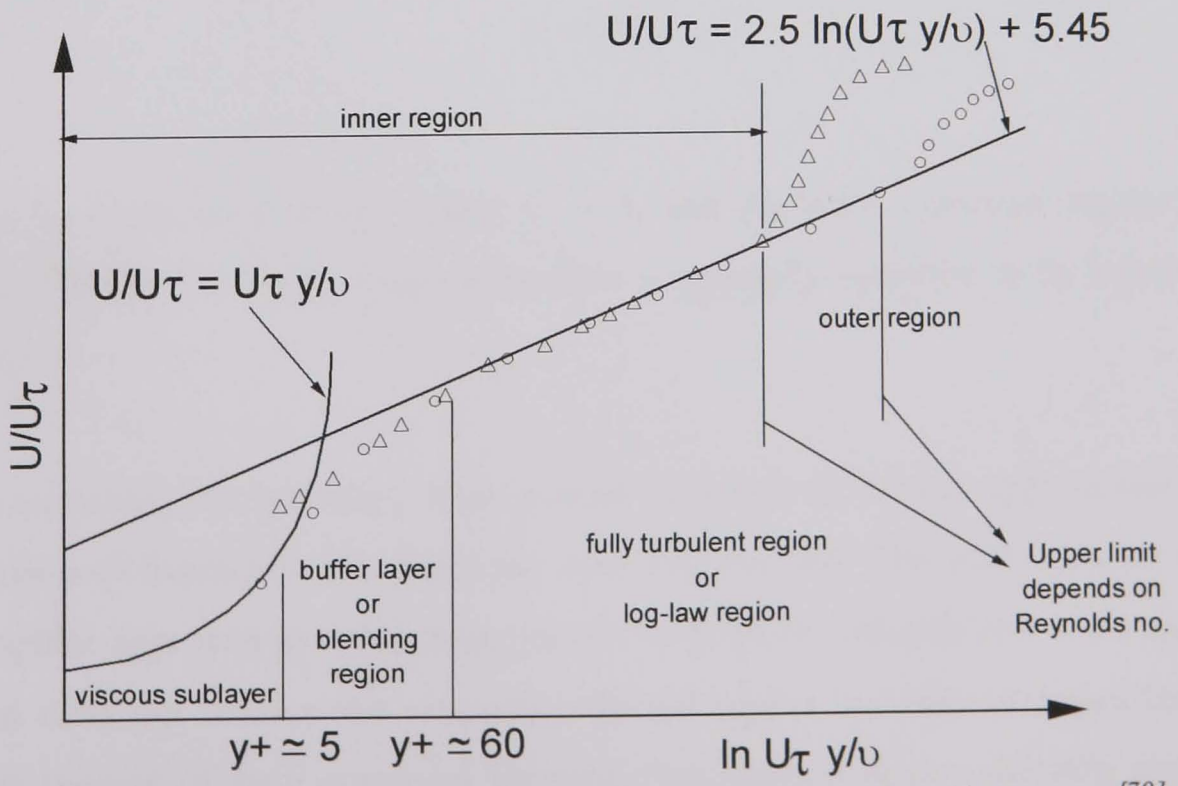

Figure 3.3 – Layers in Near Wall Regions and Corresponding Laws[79]

All flow is influenced by velocity gradient as fluid is brought to rest by no-slip boundary conditions that exist at a walls surface. Also turbulence intensity at an arbitrary point in the boundary layer is affected by the distance y from that point to the wall. Close to the wall turbulence is reduced by viscous effects. However further out in the boundary layer towards the free-stream the enhanced production of turbulent kinetic energy due to high mean velocity gradient results in the rapid rise of turbulence levels.

Experiment has shown that turbulent boundary layers consist of three distinct layers, a viscous sub-layer, buffer or blending region, and a fully turbulent region. Due to one of the most interesting characteristics of boundary layers the extent of these regions can be easily identified. Basically boundary layers behave in a universal manner, as long as they are in full equilibrium and not subject to flow separation. When dimensionless velocity is plotted against dimensionless distance y^+ (3.25) across a boundary layer on a flat plate, the obtained profile will remain the same regardless of whether the plate is the size of a postage stamp or the size of the city of Sheffield. Because of this phenomena, y^+ can be used to describe the limits of the different regions. Different laws describing the behaviour of the flow in each of these regions can then be applied.

$$y^+ = \frac{\rho u y}{\mu} \tag{3.25}$$

The viscous sub-layer occurs when $y^+ < 5$, and the fully turbulent region begins around $y^+ > 60$. The buffer region therefore is generally accepted to lie between $5 < y^+ < 60$.

When modelling the boundary layer within CFD two numerical approaches can be used, the wall function method and the near wall method. The wall function method is a popular approach as it has been shown to be fairly reliable and economic. The method does not resolve the viscosity affected region but instead spans this zone through the use of semi empirical formula, thus leading to considerable savings in computational time and effort. The near wall approach, in contrast, resolves the

viscosity affected region and viscous sub-layer to the wall surface, through the use of a refined mesh. This in turn leads to an increase in the amount of computational time required.

Both techniques have been compared in the present study, through the use of a *Standard Wall Function* as proposed by Launder & Spalding[69], and through the use of a near wall approach, the *Two Layer Zonal Method*[85].

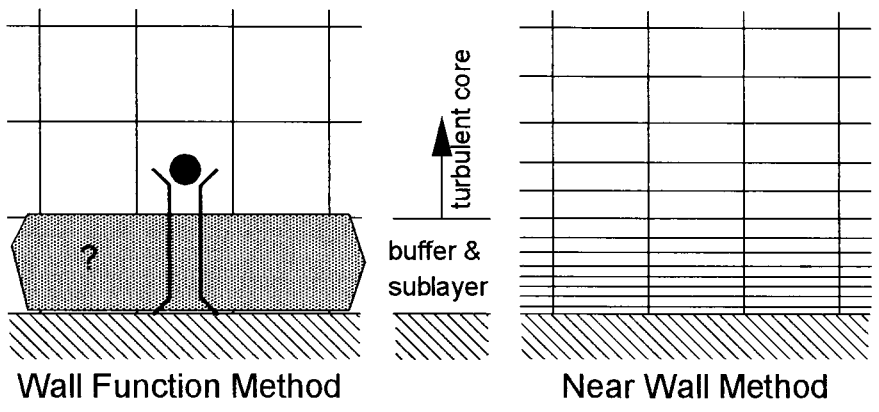

Figure 3.4 – Near Wall Methods[79]

3.3.1 – Standard Wall Function

As has been stated the standard wall function was designed to span the viscosity affected region at a wall through the use of empirical formulae, avoiding the problem of resolving this region. It performs this task through the implementation of either a laminar stress-strain relationship or log law to provide profiles of momentum transfer within this zone, dependant upon a calculated y^* value which is similar in nature to y^+.

$$y^* = \frac{\rho C_\mu^{1/4} k_p^{1/2} y_p}{\mu} \tag{3.26}$$

Where y_p is the distance from the cell centre adjacent to the wall and the wall surface. This can have severe implications for the simulated boundary layer, and as will become apparent it is therefore essential that a suitable mesh is used in the vicinity of walls for the accurate solution of a problem.

When equation (3.26) yields a $y^* > 11.25$ a log law is used to describe mean fluid velocity U^*, thus imposing a boundary layer profile.

$$U^* = \frac{1}{\kappa} ln(Ey^*) \tag{3.27}$$

For $y^* < 11.25$ a laminar stress-strain relationship is applied.

$$U^* = y^* \tag{3.28}$$

The implications of the above are that the size of the cell adjacent to the wall determines the thickness of the boundary layer. This can prove problematic as will be shown. Also if the modelled cells adjacent to the wall are too thin, returning a y^* value below 11.25, the wall function model will create a purely laminar boundary layer with no turbulent transition which is physically unrealistic in a turbulent layer.

3.3.2 – Two Layer Zonal Method

The two layer zonal model abandons the use of functions which span the viscosity affected region. Instead the viscosity affected region is resolved right down to the wall surface, through the use of a refined mesh. This approach allows the boundary layer to grow, unlike the standard wall function where the boundary layer thickness is dictated by the cell height adjacent to the wall. As with the standard wall function the two layer model splits the near wall region into two zones, viscosity affected, and fully turbulent. It accomplishes this by computing a turbulent Reynolds number, Re_y, based upon wall distance, for each computational cell.

$$\mathrm{Re_y} \equiv \frac{\rho\sqrt{k}y}{\mu} \tag{3.29}$$

When the turbulent Reynolds number of a cell is $Re_y > 200$ the cell is classed as lying in the fully turbulent zone, and the k–ε equations are applied in their unmodified form. However when $Re_y < 200$ the one equation turbulence model of Wolfstein[85] is implemented, as the cell is classed as being within the viscosity affected region. This returns the momentum and kinetic energy equations in standard

form, however a modified equation for turbulent viscosity is used, and eddy dissipation is represented algebraically.

$$\mu_t = \rho C_\mu \sqrt{k} l_\mu \tag{3.30}$$

$$\varepsilon = \frac{k^{3/2}}{l_\varepsilon} \tag{3.31}$$

When using the two layer model the y^+ value is again highly important. Cells at the wall should return a value of at least $y^+ < 5$, and ideally a value of $y^+ < 1$. A further requirement is that the viscosity affected region should be spanned by 5 ~ 10 cells, to provide adequate representation of this region. This results in the use of a highly refined mesh, which can lead to a considerable increase in computational time.

3.4 – Constitutive Equations

The Navier-Stokes equations and turbulence models are required to describe the physics of general fluid flow. However where more complex flow problems are encountered, any additional flow phenomena must also be considered in the mathematical model. This is accomplished through the adoption of additional equations which describe the behaviour of the phenomena.

In the study of ejectors there are three additional phenomena which need to be considered; compressibility, heat transfer, phase change.

3.4.1 – Compressibility

To describe the influence of compressibility the ideal gas law must be adopted. The CFD solvers used in this study use a slightly modified version of this law.

$$\rho = \frac{p_{op} + p'}{R_u T \sum_{i'} \frac{m_{i'}}{M_{i'}}} \tag{3.32}$$

where $m_{i'}$, & $M_{i'}$ are respectively the mass fraction and molecular weight of species i'. The pressure terms in equation (3.32) are the gauge local static pressure, p', relative to the operating pressure, p_{op}, as specified by the user.

The operating pressure is added to the computed relative static pressure to yield the absolute static pressure required for the calculation of density. Operating pressure is used to reduce the relative pressure within the domain as much as possible. The purpose of this is to assist in the reduction of numerical round-off error within the pressure-correction equation (see Section 4.2.2).

When setting up a compressible flow problem, the operating pressure must be subtracted from the boundary pressures. Thus gauge pressures are specified at flow boundaries to retain the correct absolute pressure. The choice of CFD solver (see Section 4.2) determines the operating pressure. When using the coupled solver the operating pressure can be set to zero, as the coupled solver does not use a pressure correction equation. Absolute pressure values are then specified at flow boundaries. When using the segregated solver, an operating pressure of 1000 Pa was specified, as had been used in previous studies by Hart[86], and Hunt[87]. Pressure values were set accordingly, relative to this value.

3.4.2 – Heat Transfer

A number of heat transfer processes will occur within the ejector. Energy transfer will exist between the primary and secondary fluids, and between the fluids and the ejector body. The energy equation and turbulence models account for energy transfer between the primary and secondary fluids. Wall functions within Fluent account for thermal gradient and heat transfer between wall surfaces and fluid, however these do not account for radiation.

Radiation of heat from the ejector walls into the primary and secondary fluids will occur. The supersonic jet within the ejector reaches temperatures as low as –80°C and acts as a heat sink. Due to the fact that steam has an opacity to radiation, heat will be transferred to the high speed ejector stream. This despite the fact that the steam near the walls is at an elevated temperature. A cooling effect is thus created at

the walls which has been observed to produce temperatures low enough for the formation of ice upon the external surface of the mixing chamber. Modelling radiation processes within the ejector is a complicated process, requiring the opacity of the fluids to be specified. Additionally to model such a process is computationally intensive, therefore radiation was not considered in this investigation.

If heat transfer across the ejector walls was to be considered, additional equations describing the heat conduction process would be required. Thermal behaviour of surfaces would also need to be specified appropriately i.e. heat flux, conduction, or external radiation condition which is computationally expensive and can lead to numerical instabilities. Heat transfer through the ejector body was not considered. The ejector which this study is predominantly based upon, is well insulated from the surrounding environment.

3.4.3 – Phase Change

The occurrence of phase change within the ejector is a possibility, when steam is involved as either the primary or secondary fluid[88]. Pressures and temperatures within the de Laval nozzle and mixing chamber can fall lower than the triple point of water.

If condensation formed within the de Laval nozzle a shock would occur which would alter nozzle performance. Nozzle exit Mach number would reduce whilst a corresponding increase in exit pressure would be observed. If ice particles were to form these could adhere to and accumulate upon the nozzle walls which would also be detrimental to performance. The build-up of ice upon the mixing chamber walls is also a possibility if the secondary fluid is a vapour, and the walls are well insulated.

To model droplet nucleation or phase change from solid directly to gas it would have been necessary to write a subroutine. This would have been outside the scope of this current project. The residence time of the vapours within the ejector is also extremely short. It is therefore doubtful whether there is sufficient time for the nucleation of water/ice droplets within the de Laval nozzle. It is also likely that any droplets which formed within the mixing chamber would quickly be destroyed. This would be due to the action of shear forces within the chamber, impact on the

chamber wall, or through a rapid rise in temperature and pressure. For the above reasons phase change was therefore not considered in this investigation.

3.5 – Physical Properties

The way in which the physical properties of the modelled fluid are defined is as important a consideration as the choice of boundary conditions. Dependant upon the numerical models applied, different properties will be required. As the current studies are based upon compressible flow the following properties need to be specified; density, viscosity, specific heat capacity, thermal conductivity. The properties can be specified in a number of ways; constant value, temperature dependant polynomials, piecewise linear functions, composition dependent, etc.

To simplify the mathematical model constant values for properties were always adopted, with the exception of density that was calculated using the ideal gas law (see Section 3.4.1). Although it is accepted that properties will be a function of pressure and temperature. Attempts were made to use temperature dependant steam properties, see Section 5.6, however the obtained results were unsatisfactory. The adoption of the ideal gas law requires the molecular weight of the fluid to be specified. The standard method of specifying fluid properties only allows for a single fluid to be modelled. If multiple fluids are present in the problem then species equations have to be adopted.

3.6 – Species Equations

Species equations allow simulation of the interactions between fluids of dissimilar properties. These interactions may be pure mixing and transport, however chemical reactions can also be simulated. The fluids within the ejector are inert, the species equations in their simplest form for convection/diffusion are used (3.33). These determine the local mass fraction ($m_{i'}$) of each fluid species.

$$\frac{\partial}{\partial t}(\rho m_{i'}) + \frac{\partial}{\partial x_i}(\rho u_i m_{i'}) = -\frac{\partial}{\partial x_i}\left[-\left(\rho D_{i',m} + \frac{\mu_t}{Sc_t}\right)\frac{\partial m_{i'}}{\partial x_i}\right] \qquad (3.33)$$

The physical properties of the individual fluids are required for the calculations. Again these can be input as constant values, or based upon thermal or composition laws. Constant values were used for fluid properties, in ejector simulations where species calculations were included. Density was specified using the ideal gas law, requiring the molecular weight of each fluid to be defined. It is necessary to specify three individual fluid species when simulating the ejector; primary, secondary, & outlet. The specification of an outlet species is required to accommodate the possibility of a reverse flow condition existing at the diffuser exit.

A mixture template is used to relate the composition of individual species where composition dependent properties are required either in calculation or post-processing. The specification of relationships between corresponding physical properties of the individual species are required. Within this investigation ideal gas mixing laws were applied for viscosity and thermal conductivity, mixture properties were then conducted using kinetic theory. This was inline with the use of the ideal gas mixing law for the determination of density. Specific heat capacity of the mixed species was determined using a mass fraction average as an ideal gas mixing law was not available for this property.

3.7 – Boundary Conditions

The choice and implementation of boundary conditions is perhaps the most important considerations when assembling a CFD simulation. Used to specify the flow and thermal characteristics at the boundaries of a problem they can be applied in a number of ways. Of particular importance is the choice of flow boundaries. However the available experimental and physical data for the ejector constrains this choice. The location of flow boundaries must also be considered.

3.7.1 – Flow Inlets

Flow inlets can be modelled through the specification of velocity, pressure, or mass flux boundary conditions. Pressure inlet boundary conditions were used in this investigation due to available experimental data. This required the specification of pressure, thermal, and turbulence characteristics.

The specification of both total and static pressure values is required. An inlet velocity can be obtained from these values. This will determine how the values are applied and used in the solution process. If the flow velocity is supersonic, isentropic flow equations can be used to calculate the initial flow characteristics. A subsonic velocity will result in the use of only the total pressure value in the solution procedure. In this investigation static pressure and total pressure at a flow inlet were fixed with the same value, relative to the operating pressure, see Section 3.3.1.

Thermal values must be applied at the inlet. Fixed values were used which correspond to the saturation temperature of the specified pressure unless otherwise stated.

The solver requires that turbulence characteristics of the flow are specified. This can be accomplished in a number of ways, including the insertion of actual values for turbulent kinetic energy and dissipation, or through the use of turbulence intensity and length scale techniques. The latter method was chosen in this study.

Choosing an appropriate value for turbulence intensity is somewhat of an arbitrary procedure in this case, due to the lack of flow data at the ejector inlets. However a turbulence intensity value, based upon the route mean square of velocity fluctuations, of 1% is considered low and 10% or more high. Turbulence intensities of 1% were applied, as inlet flow is essentially considered stationary through the application of identical static and total pressure values. Turbulence length scale (l) was based upon equation (3.34), where L, characteristic length, was based on the height of the inlet.

$$l = 0.07\mathrm{L} \tag{3.34}$$

The location of a flow inlet must be chosen to ensure sufficient distance for the occurrence of flow development. Flow inlets can effectively create a developed flow immediately at entrance from specified boundary conditions, however it is still beneficial to include a short section of lead-up from the inlet on occasions to ensure the boundary layer forms correctly.

3.7.2 – Flow Outlets

Numerical constraints dictate that a pressure outlet boundary condition is applied at the flow outlet, as pressure boundaries have been used at flow inlets. Flow conditions are specified in much the same manner as a pressure inlet. However only a static pressure value is required, as there should be no flow originating from the boundary. Values for temperature and turbulence characteristics are required, but only implemented if a reverse flow exists at the exit. A turbulence intensity of 8% was applied.

The location of a flow outlet is an important consideration. To ensure solution accuracy flow should be fully developed at exit, hence no recirculation across the boundary. If the flow at exit does not meet this criteria, then a length of uniform bore pipe may be added to move the boundary further downstream. The pressure boundary condition applied can cope with reverse flow, however it is still good practice to ensure that the flow is fully developed with no recirculation.

3.7.3 – Walls

Thermal conditions need to be specified for wall surfaces. Walls may be set with a fixed, heat flux, radiation, or conduction condition. As stated in Section 3.4.2 heat transfer was not considered. All walls were assumed adiabatic, with a fixed temperature of 10°C, to simplify the mathematical model. A no-slip condition is assumed at the surface of each wall.

3.7.4 – Symmetrical Boundaries

If the modelled geometry of a problem can be simplified through the use of symmetrical boundaries, large savings in the amount of computational resources required can be made. The ejectors in this study were primarily modelled using an axisymmetric assumption. A limited number of three-dimensional studies were conducted to ensure that this assumption was valid. If the modelled ejector has planes of symmetry it may be possible to construct either a half or quarter three-dimensional model, conserving computational resources. No conditions have to be specified when an axis or symmetrical boundary condition is applied. It is assumed that all velocities and gradients normal to the boundary plane have a zero flux.

Chapter 4 - Numerical Method

This chapter describes the numerical methods used in the solution of the assembled equations in the mathematical model. Topics including choice of discretisation scheme and solver formulation are covered. Two commercially available solvers have been used, a segregated solver and a coupled solver, both written by Fluent. Additional solution concerns are addressed including minimising the required computational resources, and the important consideration of ascertaining convergence. Finally post-processing techniques implemented are discussed.

4.1 – Discretisation

CFD solvers are designed to perform a number of key tasks which enable the solution of a flow problem. They are used to discretise the governing equations over a finite number of grid points. This is performed by substitution of approximations into the differential governing equations for unknown flow variables described in terms of functions. The resulting set of algebraic equations can then be solved.

Most CFD codes fall within one of three distinct numerical groups; finite difference/finite volume, finite element, or spectral methods. Although these methods are all designed to resolve the governing equations they are distinct from each other through the way they discretise and approximate the unknown flow variables. The methods will not be described in depth as they are well documented [90,91].

The choice of method used to solve the governing equations is dependent upon the available commercial CFD software, unless a new code is being written by or for the intended user. The most popular solution method used in CFD today is the finite volume method, a special formulation of the finite difference technique. This has been adopted by all the major CFD companies (Fluent, Adapco (StarCD), and AEA Technology (CFX)) as the base solution technique which their software is written around.

4.1.1 – Finite Volume Method

The finite volume method was developed specifically to resolve equations for heat transfer and fluid flow [92]. The technique relies upon the use of a computational mesh fitted to the region of interest. Instead of discretising the governing equations directly across the grid of nodes, the finite volume technique uses non-overlapping control volumes of finite dimensions. These are traditionally centred around each node. See Fig 4.1.

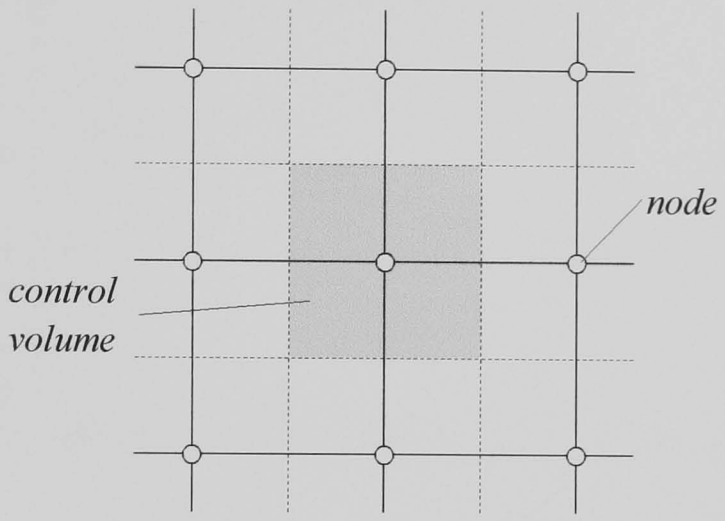

Figure 4.1 – Control Volume

The governing equations are integrated across each control volume to yield algebraic equations for the unknown variables ϕ, which can then be solved iteratively. During this study only Fluent codes were utilised. What now follows will deal specifically with the techniques that these codes employ.

Fluent codes specify control volumes in a slightly different manner, compared to the traditional node centred method outlined in most CFD text books [90]. The approach illustrated in Fig 4.2 is used, where nodes specified in the computational mesh locate the vertices of each control volume. When viewed the computational mesh not only shows the location of nodes, but also the dimensions and shape of the individual volumes. This proves a useful aide in ensuring the generation of a high quality mesh, an important criteria to fulfil if the solution of a problem is to be accurate. This approach simplifies the generation of control volumes, and thus the discretisation process. The simplification is considerable if the mesh is unstructured or hybrid in

nature, where the fitting of control volumes around central nodes would be a complex procedure.

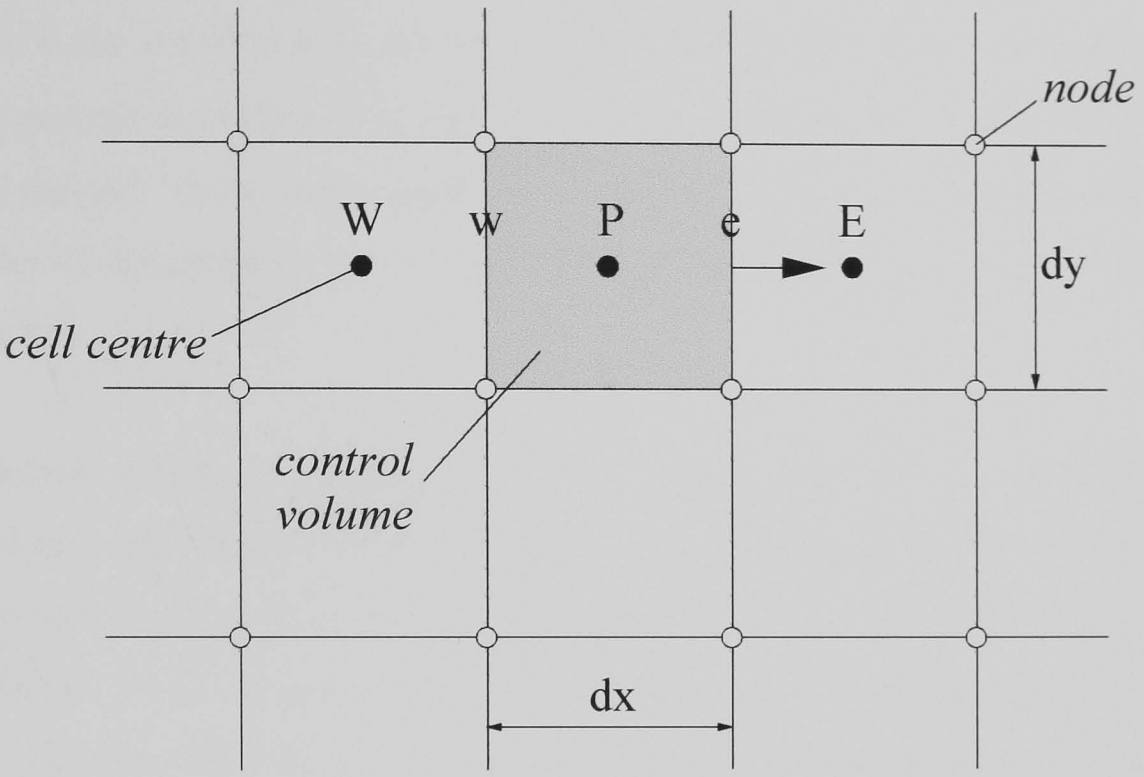

Figure 4.2 – Nodes, Control Volumes, & Cell Centres in Fluent

All values of computed variables are stored at the centre of each cell. These are interpolated to the cell faces, where they are required, during the solution procedure through the use of a user specified discretisation procedure.

4.1.2 – Discretisation Procedures

The basic discretisation procedure utilised with the control volume approach is well portrayed by considering the one dimensional steady state diffusion of a variable ϕ. This is described by the equation:-

$$\frac{d}{dx}\left(\Gamma\frac{d\phi}{dx}\right)+S=0 \qquad (4.1)$$

where Γ and S are a diffusion coefficient and source term for ϕ respectively. This is applied to all cells in the computational mesh. Integrating eqn (4.1) for a chosen cell in Fig 4.2:-

$$\int_{\Delta V}\frac{d}{dx}\left(\Gamma\frac{d\phi}{dx}\right)dV+\int_{\Delta V}SdV=\left(\Gamma A\frac{d\phi}{dx}\right)_e-\left(\Gamma A\frac{d\phi}{dx}\right)_w+\overline{S}\Delta V=0 \qquad (4.2)$$

where A is the cell face area, ΔV cell volume, and $\overline{S}$ the average of S. During the solution process the values of Γ and $d\phi/dx$ are required at the east (e) and west (w) faces of the cell. These values must be interpolated from the cell centre to the face. The order of interpolation used during this process largely governs the accuracy of the solution.

Interpolation schemes must posses three basic properties; conservativeness, boundedness, and transportiveness. Without these properties the obtained numerical results could be physically unrealistic. Conservativeness is the extent to which an interpolation scheme ensures the conservation of ϕ throughout a computational domain. The flux of ϕ out of a computational cell should be equivalent to the flux of ϕ into an adjacent cell. Thus the same expression must be used to describe the flux across adjacent control volumes. Schemes that do not satisfy conservation of ϕ do not therefore possess conservativeness.

The computed values of ϕ should be bounded or constrained by boundary conditions. Hence in the absence of source terms it should not be possible to obtain values greater or less than boundary values of ϕ. So long as this is ensured the interpolation scheme is said to possess boundedness. Finally the interpolation scheme should possess the property of transportiveness, being able not only to deal with diffusion but also convection and the accompanying directionality. The relative strength of convection and diffusion in a flow can be determined from the Peclet number (4.3) calculated at a point *"P"*, Fig 4.3, with a constant source of ϕ.

$$Pe=\frac{F}{D}=\frac{\rho u}{\Gamma/dx} \qquad (4.3)$$

When Pe = 0 pure diffusion processes with no convection occur, as Pe $\rightarrow \infty$ the flow is dominated by pure convection. Thus as Pe increases contours of ϕ change from being circular to elliptical in shape. At high Pe therefore point *E* would be strongly

influenced by *P*, which in turn would feel little or no influence from *E*. It is important that the interpolation scheme can account and deal with this.

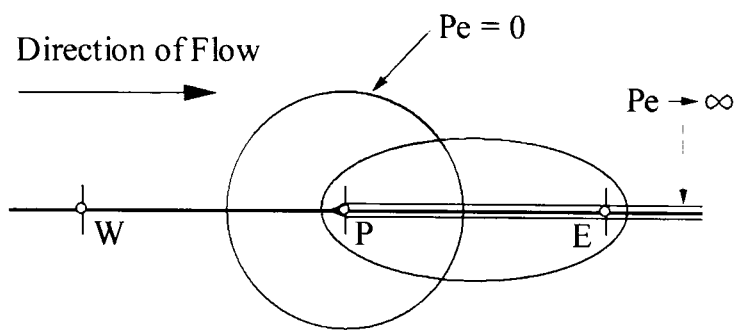

Figure 4.3 – Influence of Pe Upon Contours of ϕ Around a Node.[93]

The simplest interpolation scheme is the central differencing scheme, Fig 4.4. This calculates the face values and gradient using a linear approximation between neighbouring cells. Unfortunately this scheme can not account for the direction of flow. Most importantly central differencing is only stable and accurate for diffusion dominated flows as it cannot relate the strength of convection to diffusion. The scheme is only bounded for Pe < 2 which is impractical for engineering simulations.

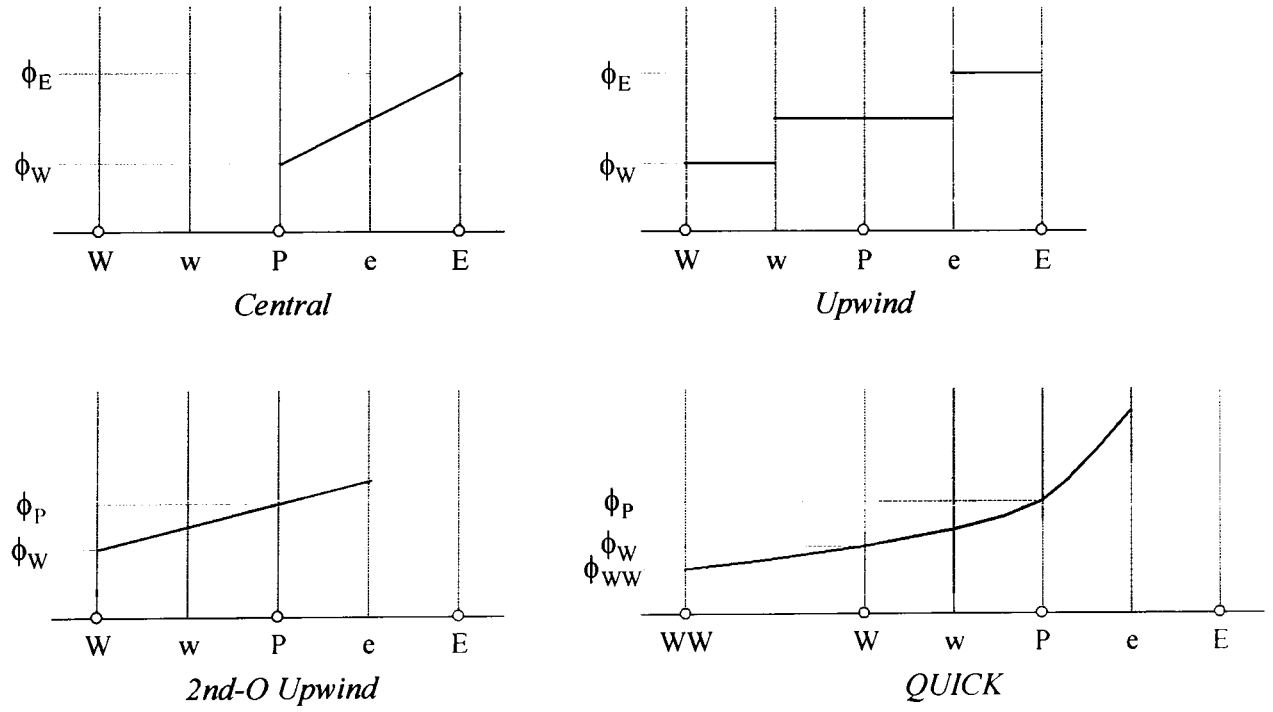

Figure 4.4 – Discretisation Schemes

The standard approach applied by the majority of CFD software is first order upwinding, which sets face values (with the face determined by local flow direction) as equal to cell centre values. This can account for the influence of convection and the direction of flow. However as the scheme is only first order accurate, errors will

occur if the flow is not aligned with the mesh effectively smearing the values of flow variables. This is equivalent to introducing a numerical diffusion coefficient to the flow.

Alternative schemes are available. The Power Law[90] scheme interpolates variables using either central differencing or upwinding dependent upon calculated Peclet number. This determines whether convection or diffusion dominates the flow.

Higher order schemes such as Second Order Upwind[79], and the quadratic QUICK[94] scheme of Leonard, can also be used. These afford a higher degree of numerical accuracy by taking more neighbouring nodes into account, however this is generally at the expense of numerical stability. Second Order Upwind is fairly stable in most situations, however the QUICK scheme can become unstable. Under certain flow conditions the coefficients of the quadratic functions can become negative and highly unrealistic values of ϕ may be produced, for example negative energy values. Numerical limiters[95] can be used to rectify this problem. The detailed numerics of these schemes are well documented [96] and therefore their workings will not be recounted here.

Throughout this study both of these higher order schemes were used. However first order schemes were still required in the early stages of calculation. The solution is particularly unstable for the first few hundred iterations. However once steady convergence is reached, the more accurate higher order schemes can be implemented.

4.1.3 – Implicit & Explicit Approaches

Discretisation schemes are numerical tools used in the solution of the governing equations. The actual solution methods which utilise these tools will be discussed in Section 4.2. All methods of solution for the discretised equations fall into one of two approaches, either an implicit or explicit approach. These differ primarily in how they compute unknown flow variables in each computational cell. The two approaches can be explained simply by considering a one dimensional heat

conduction equation (4.4). It is easier to consider this equation and its manipulation than the full governing equations.

$$\frac{\partial \phi}{\partial t} = \alpha \frac{\partial^2 \phi}{\partial x^2} \tag{4.4}$$

Applying a forward difference to $\partial\phi/\partial t$ and a second order central difference to $\partial^2\phi/\partial x^2$ equation (4.5) is obtained.

$$\frac{\phi_i^{n+1} - \phi_i^n}{\Delta t} = \frac{\alpha\left(\phi_{i+1}^n - 2\phi_i^n + \phi_{i-1}^n\right)}{(\Delta x)^2} \tag{4.5}$$

Rearranging (4.6)

$$\phi_i^{n+1} = \phi_i^n + \alpha \frac{\Delta t}{(\Delta x)^2}\left(\phi_{i+1}^n - 2\phi_i^n + \phi_{i-1}^n\right) \tag{4.6}$$

A marching solution can be used to solve this equation which can be explained as follows. Consider the computational domain shown in Fig 4.5. The solution in the domain is obtained by starting with a set of initial conditions specified at boundary *abcd*, and progressively marching across the computational mesh towards the far boundary *efgh*. Marching intervals are designated by a marching variable.

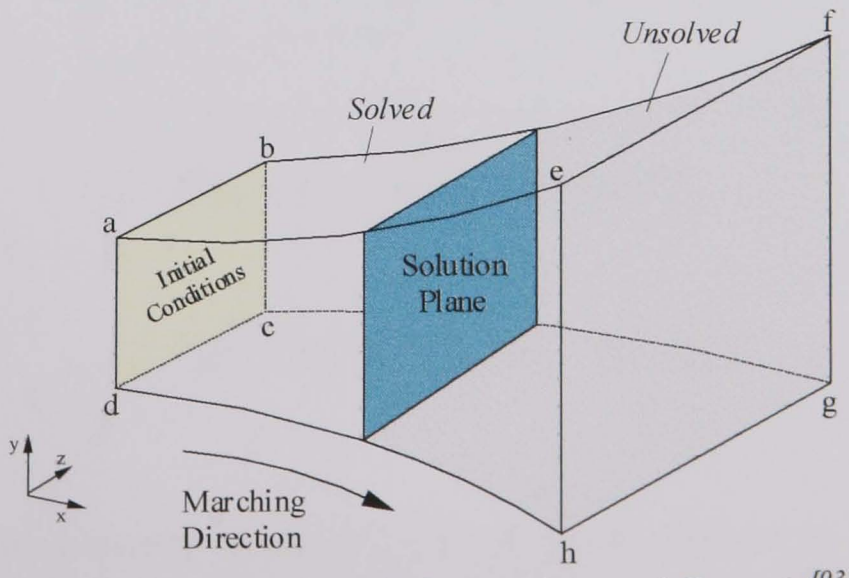

Figure 4.5 – Marching Solution Across A Domain[93]

In (4.6) the marching variable is time, t, see Fig 4.6. Assuming that ϕ is known at all points at time level n, values of ϕ at level n+1 can be determined from these values. Values at n+2 can then be obtained, and so on.

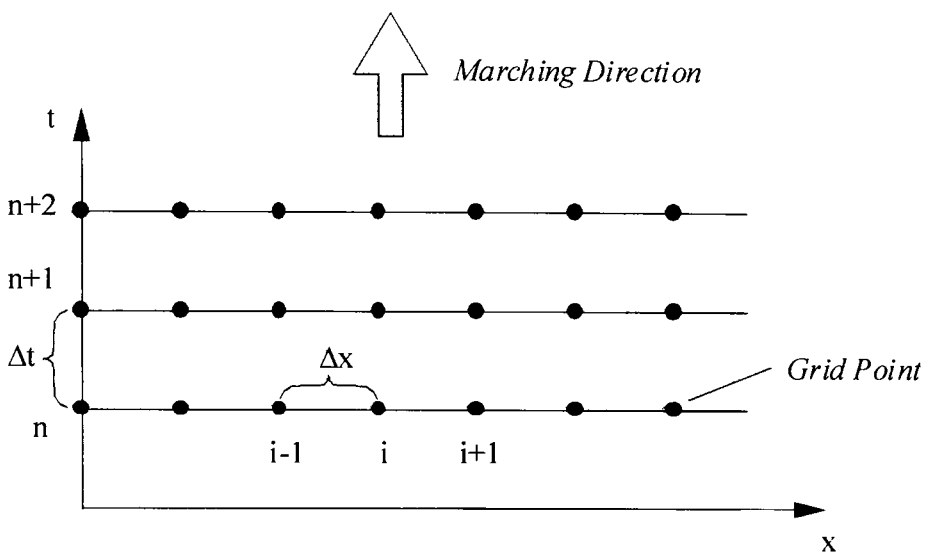

Figure 4.6 – Time Marching[93]

Only a single unknown appears in (4.6), ϕ_i^{n+1} which allows the value to be determined immediately from the values at level n. Considering Fig 4.7, to solve point three at level n+1 (4.6) becomes.

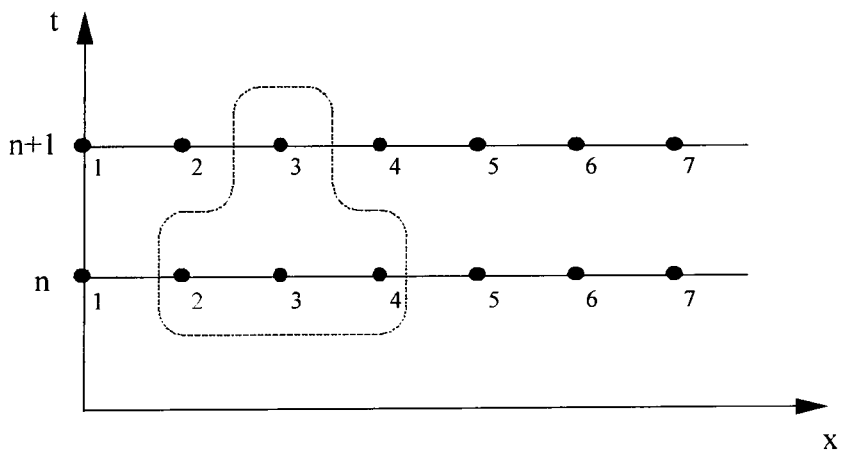

Figure 4.7 – Explicit Scheme[93]

$$\phi_3^{n=1} = \phi_3^n + \alpha \frac{\Delta t}{(\Delta x)^2}\left(\phi_4^n - 2\phi_3^n + \phi_2^n\right) \tag{4.7}$$

All values can be obtained sequentially at all points, this is an explicit scheme. Basically the explicit approach however is "explicit" in dependant variables only. This means that the value of ϕ in a cell is dependant only upon existing values of ϕ.

An implicit scheme can be described as follows. Rewriting (4.4) this time with average values, (4.8) is obtained.

$$\frac{\phi_i^{n+1}-\phi_i^n}{\Delta t}=\alpha\frac{\frac{1}{2}\left(\phi_{i+1}^{n+1}+\phi_{i+1}^{n}\right)+\frac{1}{2}\left(-2\phi_i^{n+1}-2\phi_i^{n}\right)+\frac{1}{2}\left(\phi_{i-1}^{n+1}+\phi_{i-1}^{n}\right)}{(\Delta x)^2} \qquad (4.8)$$

The unknown ϕ_i^{n+1} is not only described by values of ϕ at level n, but also at level n+1. Hence three unknowns appear in (4.8) ϕ_i^{n+1}, ϕ_{i+1}^{n+1}, and ϕ_{i-1}^{n+1}, and the equation can not be solved by itself. Equation (4.8) must therefore be written for all points in the solution domain resulting in a system of algebraic equations which must be solved simultaneously. Considering Fig 4.8, and rewriting (4.8) so that the unknowns and knowns are separate.

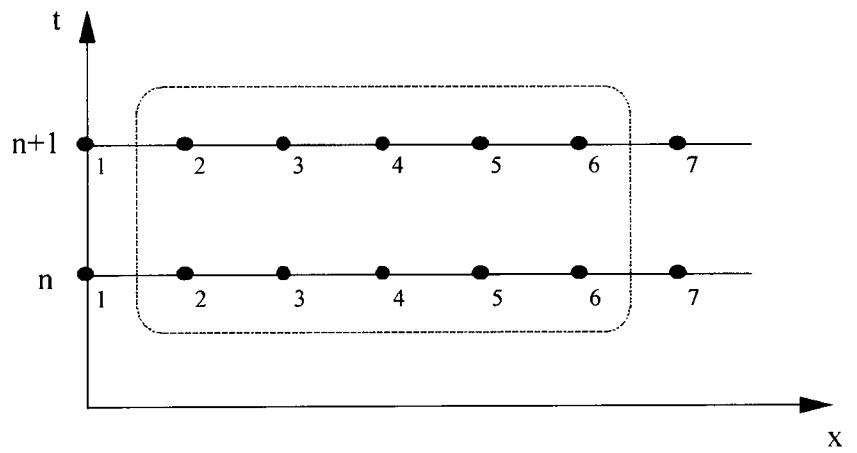

Fig 4.8 – Implicit Scheme[93]

$$\frac{\alpha\Delta t}{2(\Delta x)^2}\phi_{i-1}^{n+1}-\left[1+\frac{\alpha\Delta t}{(\Delta x)^2}\right]\phi_i^{n+1}+\frac{\alpha\Delta t}{2(\Delta x)^2}\phi_{i+1}^{n+1}=-\phi_i^n-\frac{\alpha\Delta t}{2(\Delta t)^2}\left(\phi_{i+1}^n-2\phi_i^n+\phi_{i-1}^n\right) \qquad (4.9)$$

Splitting (4.8) into quantities A, B, and K_i, (4.10) is obtained.

$$A=\frac{\alpha\Delta t}{2(\Delta x)^2} \qquad B=\left[1+\frac{\alpha\Delta t}{(\Delta x)^2}\right] \qquad K_i=-\phi_i^n-\frac{\alpha\Delta t}{2(\Delta t)^2}\left(\phi_{i+1}^n-2\phi_i^n+\phi_{i-1}^n\right)$$

$$A\phi_{i-1}^{n+1}-B\phi_i^{n+1}+A\phi_{i+1}^{n+1}=K_i \qquad (4.10)$$

Writing (4.10) for grid points 2 to 6 sequentially in Fig 4.8.

$$A\phi_1 - B\phi_2 + A\phi_3 = K_2 \tag{4.11}$$

$$A\phi_2 - B\phi_3 + A\phi_4 = K_3 \tag{4.12}$$

$$A\phi_3 - B\phi_4 + A\phi_5 = K_4 \tag{4.13}$$

$$A\phi_4 - B\phi_5 + A\phi_6 = K_5 \tag{4.14}$$

$$A\phi_5 - B\phi_6 + A\phi_7 = K_6 \tag{4.15}$$

Assuming grid points 1 and 7 are on designated boundaries with known values, (4.11) and (4.15) can be rewritten as.

$$-B\phi_2 + A\phi_3 = K_2 - A\phi_1 = K_2' \tag{4.16}$$

$$A\phi_5 - B\phi_6 = K_6 - A\phi_7 = K_6' \tag{4.17}$$

Equations (4.12) to (4.14), (4.16) and (4.17) the five equations which contain five unknowns can be written as a tridiagonal matrix (4.18). This can be solved sequentially line by line.

$$\begin{bmatrix} -B & A & 0 & 0 & 0 \\ A & -B & A & 0 & 0 \\ 0 & A & -B & A & 0 \\ 0 & 0 & A & -B & A \\ 0 & 0 & 0 & A & -B \end{bmatrix} \begin{bmatrix} \phi_2 \\ \phi_3 \\ \phi_4 \\ \phi_5 \\ \phi_6 \end{bmatrix} = \begin{bmatrix} K_2' \\ K_3 \\ K_4 \\ K_5 \\ K_6' \end{bmatrix} \tag{4.18}$$

Basically the implicit approach solves for an unknown variable ϕ in a computational cell by considering both existing and unknown values of ϕ in neighbouring cells simultaneously.

The choice of interpolation scheme is largely dependant upon time constraints and available computational resources. To maintain the stability of an explicit scheme a

small time step, Δt, has to be adopted. Many calculations are therefore required with an explicit scheme resulting in long computational runtimes, however the scheme is not demanding on computational resources. Implicit schemes can be fast as they can utilise large time steps whilst maintaining stability. Fewer time steps are therefore required to obtain a solution. However as implicit schemes calculate all values simultaneously, the required computational runtime for a single time step is greater than for explicit schemes. The demand on computational resources is correspondingly much larger.

4.2 – Solution Methods: Solver Formulations

The discretisation of the governing equations creates a set of linear algebraic equations. These can be solved using one of two solution methods; direct solution, or iterative solution. The use of direct solution methods such as gaussian elimination is not feasible due to prohibitively large computational demands. Iterative solution methods are therefore used in CFD programmes. These methods repeatedly apply an algorithm until a converged solution is obtained. The number of repetitions to reach a converged solution is unpredictable however often high.

There are two different iterative solution methods in the finite volume technique, a segregated method and a coupled method. Both are now available in Fluent V5. However previously at the beginning of this project the segregated method was that used originally by Fluent / Fluent UNS, whilst Rampant used the coupled method.

4.2.1 – The Segregated Solver

The segregated solver employs an implicit method, often referred to as a pressure based solver. This was originally designed for the solution of incompressible flows, though it has evolved to deal with compressible flows by considering density a function of pressure. The governing equations are solved in a sequential manner but an equation updating pressure is required in the solution process. This is not available explicitly in the conservation of mass or momentum equations, as density is not linked to pressure. Hence a pressure correction algorithm has to be utilised to generate a pressure field that yields velocities from the momentum equations which

satisfy the continuity equation, e.g. SIMPLE, SIMPLER[92], SIMPLEC[98], and PISO[99].

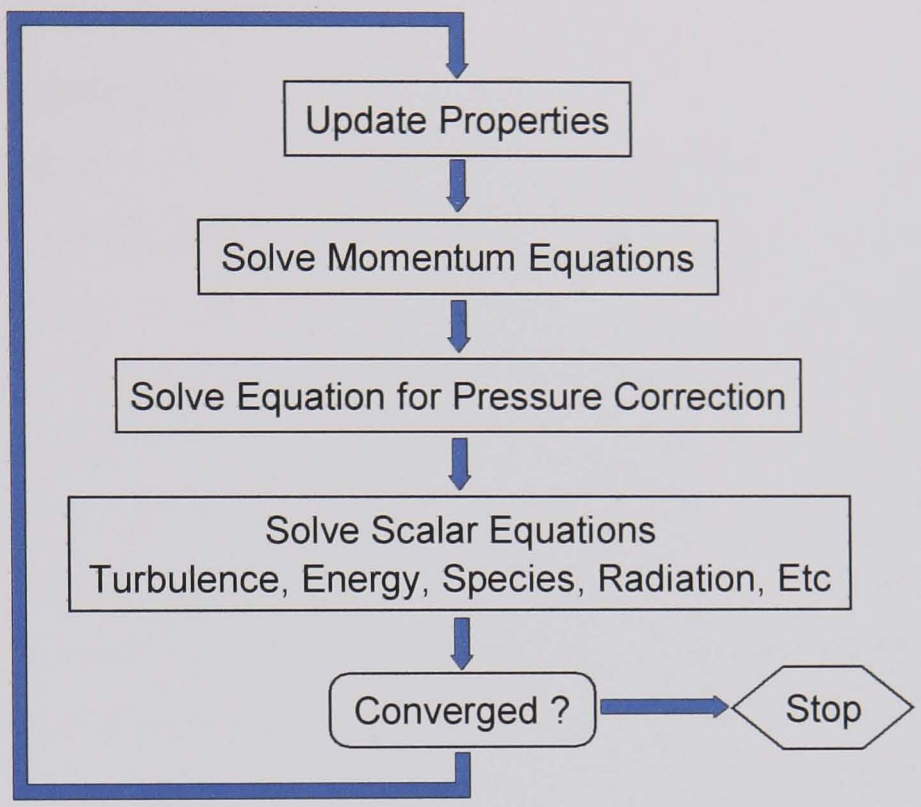

Figure 4.9 – Segregated Solver Solution Procedure[79]

The interpolation of cell faced pressure values from the stored cell centred ones during the iteration process on a co-located storage scheme may generate unrealistic oscillatory pressure fields. In a worst case scenario; may result in a chequer board distribution of pressure values between cells, (using central differencing schemes, to interpolate pressure). The simplest way of avoiding this problem is the use of a staggered grid scheme. This stores pressure values at cell centres and velocity components at staggered node points located on cell faces.

However a staggered scheme is inappropriate if the orientation of the grid lines are not aligned with the velocity components, which is often the case with body fitted co-ordinate mesh. Therefore the co-located storage scheme has to be used, and a method that prevents the oscillations has to be adopted. This can be accomplished by using a scheme proposed by Rhie & Chow[78], which uses momentum equation coefficients in the pressure interpolation to prevent oscillatory behaviour. This technique however may be deficient in dealing with sudden changes in pressure across a cell, such as a shockwave. In such circumstances it is more beneficial to use

an alternative interpolation method such as a linear pressure interpolation[95]. This simply computes the cell face pressure value as an average across the two adjacent cells.

4.2.2 – The Coupled Solver

The coupled solver is also known as a density based solver, or compressible flow solver. Density now appears explicitly within the governing equations to provide a direct link between the momentum and mass conservation equation. Pressure can thus be linked directly to density through the use of an equation of state, such as the perfect gas law or other appropriate theorem. A numerical algorithm to link the pressure-velocity fields of the problem, and to thus satisfy the continuity equation, is therefore no longer required. The use of this method for a compressible flow problem should therefore result in a more accurate solution. Representation of the physics is better as these would be coupled in reality.

The coupled method solves the governing equations in the manner illustrated in Fig 4.10. The continuity, momentum, and where appropriate energy and species equations, are all solved simultaneously as a set of vector equations. Additional scalar equations, and turbulence models are solved sequentially in a segregated manner.

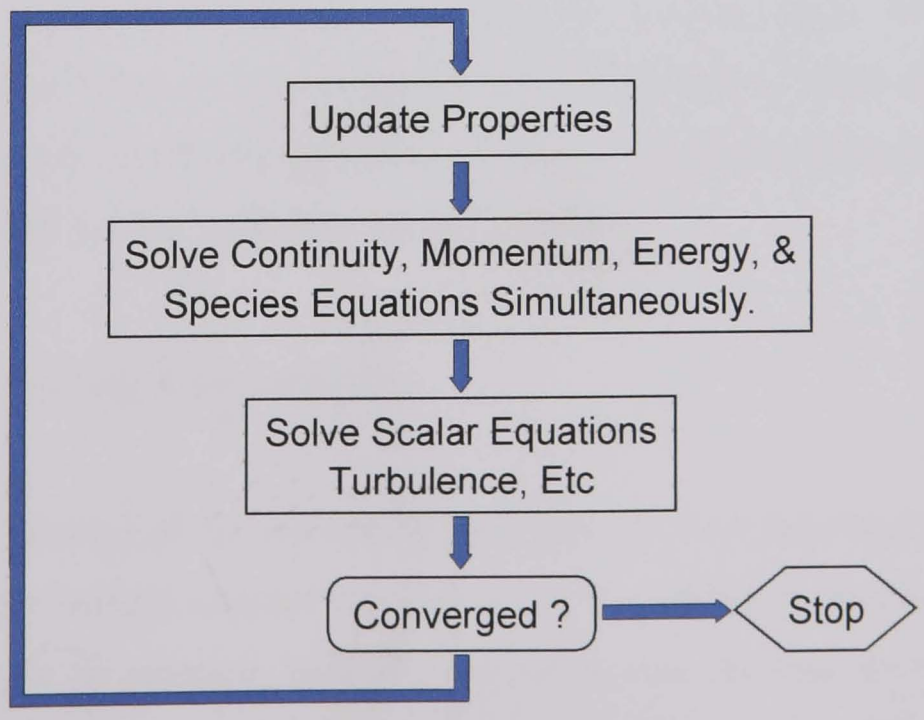

Figure 4.10 – Coupled Solver Solution Procedure[79]

The equations can be solved in either an explicit or implicit manner. As stated in Section 4.1.3 the explicit approach is a slower solution method than the more computationally intensive implicit method. However it was found inherently more stable than the implicit approach when simulating the ejector in the initial iterations. For this reason when the coupled solver was adopted the explicit approach was used. The number of iterations required to obtain a solution with the explicit method can be reduced through the use of a multi-grid scheme, which accelerates the solver, see Section 4.3.2.

As with the governing equations for incompressible flow, the solution of the governing equations in compressible form also presents numerical difficulties. When presented with a flow at low mach number, the equations become what is known as numerically "stiff". This is due to the large difference between fluid velocity and the speed of sound. When using the coupled solver for the solution of incompressible flows the problem worsens as the speed of sound becomes infinite, resulting in the infinite propagation speed of pressure waves. The consequence of this problem is that the rate of convergence falls considerably, and attaining convergence can become difficult. Numerical stiffness however can be alleviated through the use of a method termed time-derivative preconditioning.

Time-derivative preconditioning alleviates numerical stiffness at low mach number, and with incompressible flow, by re-scaling the acoustic speed of the system of equations. This is achieved by multiplying the time derivative terms of the governing equations with a preconditioning matrix. The actual numerics of preconditioning will not be recounted, but are well documented in [79].

4.3 – Accelerating Convergence

The iterative solution of the discretised equations can be a time consuming process, especially when using a coupled explicit solver. The ability to accelerate the rate of convergence for a problem is highly advantageous. In this investigation three methods have been found from trial and error to accelerate the solution process. An initial guess for calculated variables were patched into the computational mesh of the

model flow field. Under-relaxation factors of the governing equations were optimised, and a multi-grid scheme was implemented.

4.3.1 – Initialisation & Patching Variables

Iterative solution methods require an initial guess of the variables in all computational cells. The segregated solver sets zero values at each cell, however the coupled solver prompts the user for initialisation values which are then used throughout the entire solution domain. An estimated average value should be used for this purpose. This should converge a solution quicker than a zero value.

Patching further flow variables into specific areas of the computational mesh with values near those of the final flow field can accelerate the solution process considerably. In this investigation this practice was found not only beneficial, but a necessity to prevent solution divergence. Unless the de Laval nozzle was patched with a suitable guess solution divergence occurred within the first few hundred iterations. The convergent section of the nozzle was patched with the inlet boundary values. From 1-D isentropic compressible flow calculation values of flow variables at the nozzle exit were patched within the divergent section of the nozzle.

The remainder of the ejector was patched with flow values equal to those of the secondary flow inlet. There was no benefit to be gained from patching a detailed flow field external to the de Laval nozzle. It was determined that this was only destroyed by the solution process, before being recalculated.

4.3.2 – Under-relaxation and Stability Criterion

Under-relaxation factors, α, are required to control the rate of change of calculated variables, ϕ, based upon the change in the value $\Delta\phi$ and the old value ϕ_{old}, (4.19). This is necessary due to the non-linearity of the governing equations. Although used to enhance the stability of a solution, values which are too conservative will reduce the convergence rate of a problem. So long as stability can be maintained it is therefore possible to increase the under-relaxation factors to speed convergence.

$$\phi = \phi_{old} + \alpha\Delta\phi \tag{4.19}$$

The selection of under-relaxation factors are dependant upon the adopted solver formulation. Segregated solvers require the specification of relaxation factors for every calculated equation or variable. The coupled solver uses a stability criterion termed a Courant[93] number, (4.20).

$$C = c\frac{\Delta t}{\Delta x} \tag{4.20}$$

The Courant number controls the time step used in the solution of the continuity, momentum, and energy equations. As the turbulence equations are uncoupled from the governing equations separate under-relaxation factors are used for turbulence related variables, i.e. k, ε, μ.

It was found that the default values for all these factors were generally too large for use when simulating the ejector, particularly in the early stages of a solution. However it was possible to increase these values, in the later stages of a simulation once the initial transient stage in the calculation process had been passed.

4.3.3 – Multi-grid

Multi-grid is used to accelerate the solution process through the reduction of low frequency global errors which prohibit convergence. It performs this task by using a series of consecutively coarser mesh. These coarser mesh are constructed from the specified computational mesh and used to rapidly compute corrections which are then passed back down to the original computational mesh. Used with both the segregated and coupled solvers the application of the technique proved invaluable. This was particularly noticeable for the coupled solver. The use of four levels multi-grid, with the coupled solver and a computational mesh of 18000 cells, reduced the number of iterations required to obtain a solution from approximately 40000 to 7000.

The number of mesh levels which multi-grid creates needs to be specified carefully by the user. If too many levels are specified, computational performance is affected with no additional benefit upon convergence acceleration. In the current studies up to four levels of multi-grid were used with two dimensional simulations, and six levels

for three dimensional simulations. The settings for the multi-grid solver should not be altered unless severe computational difficulties are being encountered.

4.4 – Computational Mesh

Both three dimensional and two dimensional axisymmetric simulations of the ejector have been conducted in this investigation. Specific details of individual mesh will not be recounted here, but discussed later in the relevant sections. Mesh were generated using the following software packages; PreBFC, GeoMesh, and Gambit. PreBFC allows for the generation of simple mesh through the use of a text based menu system. GeoMesh and Gambit are more powerful mesh generation tools with built-in (albeit basic) CAD tools. Both packages were used due to changing license agreements with software providers.

The quality of the computational mesh is extremely important to the solution process. The grid points are used to form a computational domain which describes not only the flow field, but also divides it up into more manageable domains for the calculation process. It is important to ensure that cells are not skewed against the flow direction and that the cell aspect ratios are within the limits recommended by the CFD solvers, and numerical models employed.

Ideally when modelling supersonic flows, computational cell aspect ratio should be maintained as near to 1:1 as possible. This was shown in the work of Issa & Lockwood[99], and must be attempted due to the way in which discretisation schemes work across cells. If a cell is elongated in the x-direction so that dx>>dy, neighbouring cells in the y-direction have a greater influence upon computed cell values than cells immediately up or downstream in the x-direction, Fig 4.11. This can result in the weaker resolution of shock systems within supersonic flows. Where it is not possible to maintain an aspect ratio of 1:1 efforts were made to keep aspect ratios within the limits outlined in Fig 4.12.

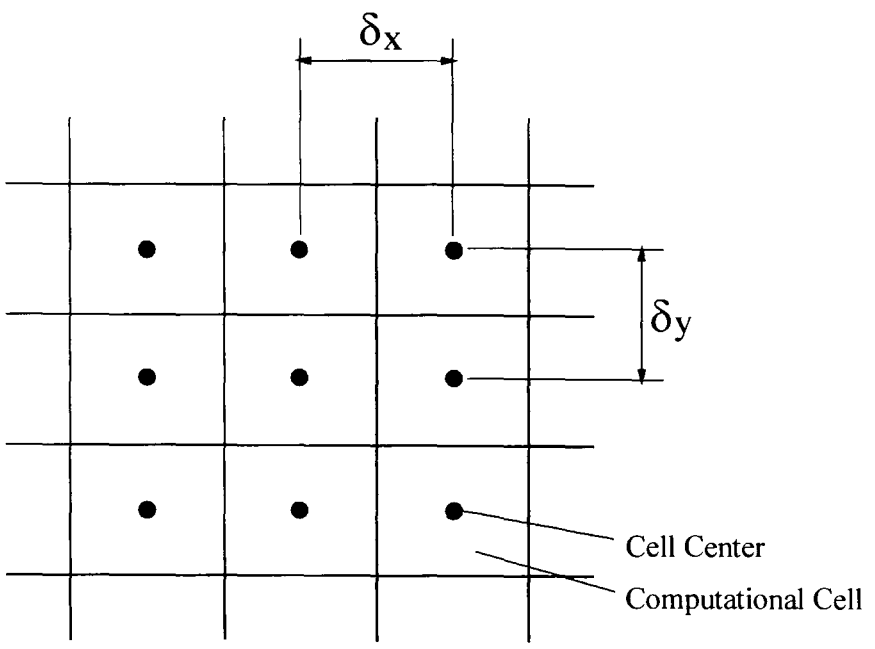

Figure 4.11 – Relationships Between Cells

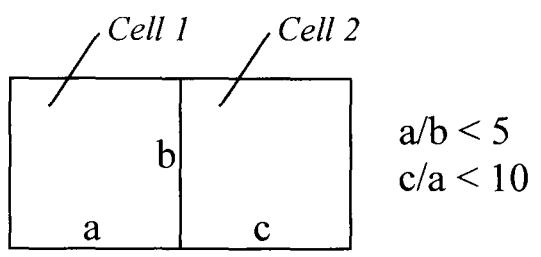

Figure 4.12 – Recommended Cell Aspect Ratios

Attempts were made to generate mesh which only used quadrilateral or hexahedral cells, as these produce higher quality mesh. This was feasible for the two dimensional simulations, however the use of triangular and tetrahedral cells within sections of the 3D studies was occasionally unavoidable. Although triangular/tetrahedral mesh are easier to generate, as they are created using automatic meshing tools, they can suffer from numerical diffusion. This is a particular problem when flow is not aligned to the mesh. With a triangular mesh of course this will never be fully possible, Fig 4.13. The ejector is essentially a long converging-diverging duct with a dominant axial flow direction. It is preferable to use quadrilateral/hexahedral mesh in such circumstances, as the mesh can be aligned to the dominant flow direction.

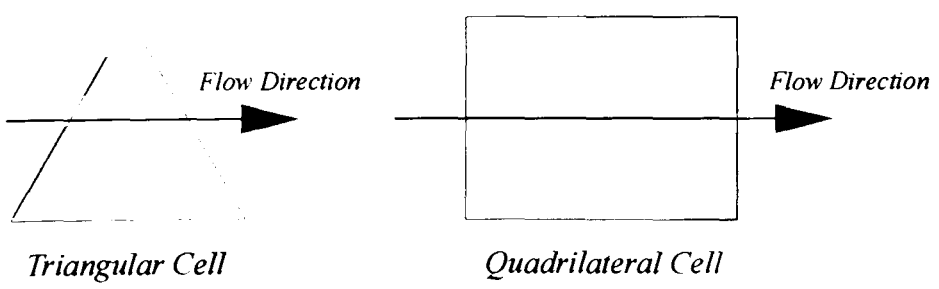

Figure 4.13 - Mesh Alignment With Flow Direction

Axisymmetric studies of the ejector were permitted by the assumption that secondary fluid velocity at entry is negligible to that of the primary fluid exiting the de Laval nozzle. Secondary inlet area was not found to be of critical importance, so long as a generously sized inlet was used.

The de Laval nozzle was modelled in full. It is possible to representatively model the nozzle, and to apply boundary conditions at its exit based upon flow relations calculated from isentropic relationships. However this was felt unsuitable as the nozzle is exhausting into a confined space. Thus the mixing chamber back pressure will not only affect the nozzle exit conditions, but in turn will be affected by the nozzle exit conditions. It is therefore doubtful that the nozzle will operate in an isentropic manner.

As has been stated three dimensional studies of the ejector were performed. These were used to verify the two dimensional axisymmetric approximations. The ejector has a plane of symmetry extending its length, therefore only a half model is required. This leads to considerable savings in computational time required as opposed to conducting a full three dimensional simulation. A combination of hexahedral, tetrahedral and wedge cells were used in the mesh. The use of tetrahedral cells was limited to the suction chamber where no predominant flow direction exists.

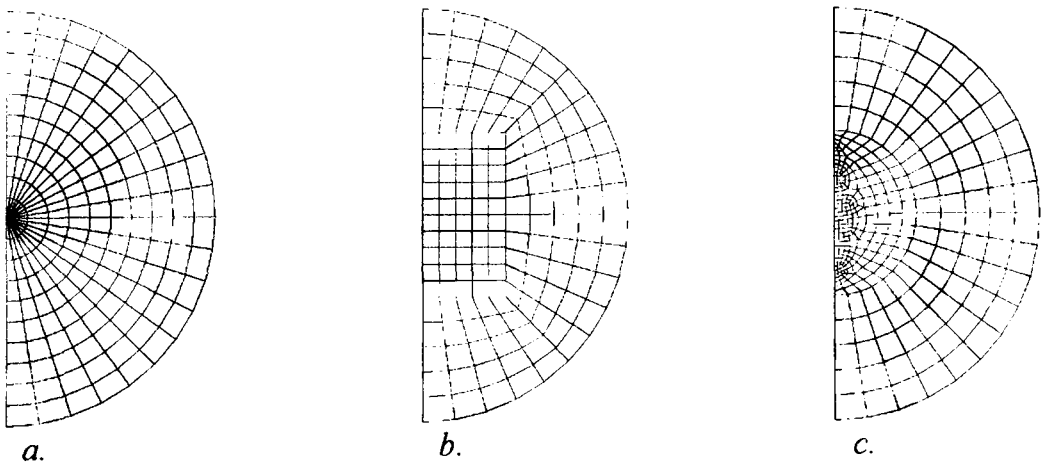

Figure 4.14 - a. Hexahedral With Central Wedge Cells, b. Structured Hexahedral, c. Unstructured Hexahedral.

The mixing chamber and diffuser can be meshed in three different ways. Hexahedral cells can be purely used in either a structured or unstructured manner. Alternatively a single row of wedge cells, aligned to a central axis, can be used in combination with

hexahedrals. Fig 4.14. The use of a combination of wedge and hexahedral cells was adopted, as the mesh is simpler to assemble than a purely hexahedral mesh. Wedge cells although prism shaped do not suffer from the same numerical diffusion problems of tetrahedral cells as they are aligned with the flow direction.

4.4.1 – Mesh Adaption

A prohibitive feature of the segregated code used in this study, is that it is a structured solver. This means that mesh refinement will result in the need for complete mesh regeneration, or/and a mesh which is over refined in unnecessary areas. The adopted coupled code possesses unstructured mesh capabilities and a built-in mesh adaption tool. This allows mesh to be selectively adapted upon obtained numerical results, or a geometrical basis. Selective refinement allows computational resources to be conserved, and concentrated on particular areas of interest in a simulation. Mesh adaption was used extensively within these studies to reduce the cell height at walls, an important consideration as mentioned earlier for near wall modelling. The tool was also used to refine the mesh in areas of high pressure gradient, thus increasing the resolution of the expansion and shock structure of the supersonic flow.

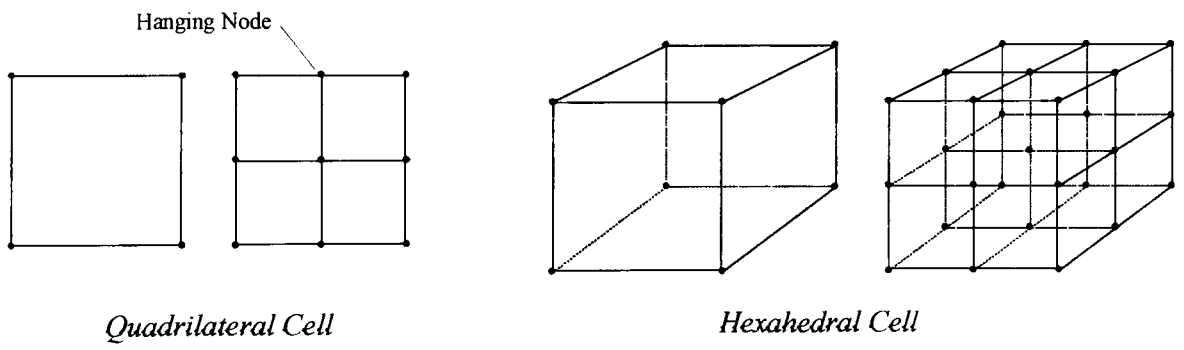

Figure 4.15 - Cell Adaption

The adaption procedure uses the hanging node technique. Cells to be adapted have an extra node placed on each vertice. These nodes are then linked with additional vertices splitting the cell. Thus a quadrilateral cell is spilt into four new cells and a hexahedral cell is split eight ways.

4.5 – Judging Convergence

The attained level of convergence is an extremely important factor to the computational accuracy of a solution. Convergence is an issue in CFD due to the iterative procedures adopted in the solution process. During the iterative process an imbalance exists within the governing equations. As the solution progresses the imbalance falls. This imbalance is also termed the residual.

Convergence is declared once the residual has decreased by an order of magnitude set by the user, as there is no mathematical proof of any convergence criterion. The order of magnitude which a residual must fall for convergence to be declared varies depending upon the equation it is representing. The standard requirement for a qualitative solution for flow equations is a reduction of three orders of magnitude, for thermal equations six orders of magnitude. Convergence is also dependent upon the accuracy required of the variable.

The fact that the residuals have decreased to a set convergent level is not indicative that a converged solution has definitely been obtained. So long as the residuals continue to fall, convergence has not been attained. This will not occur until the residuals have levelled off, ceasing to change. The danger is that the solution may still be changing, even though the set level of convergence has been reached.

This was found to be the case in the simulation of the ejector using the coupled flow solver. The default convergence criteria for all residuals was $1x10^{-3}$, this was reduced to $1x10^{-6}$. However the residuals may not always fall six orders of magnitude before convergence is attained, and at low values may begin to oscillate. Fig 4.16. Alternatively residuals may not fall three orders of magnitude before levelling out. This can occur when the values of the variables in the initialised flow field are close to those of the final calculated flow field. It is therefore necessary to monitor the history of variables within the problem in addition to the residuals.

It is possible to monitor the history of any variable at any point in the computational mesh. However in this study this approach was abandoned and instead the average

mass flow rates through the inlets and outlet were monitored. Fig 4.17. Convergence was declared once these values had ceased to change.

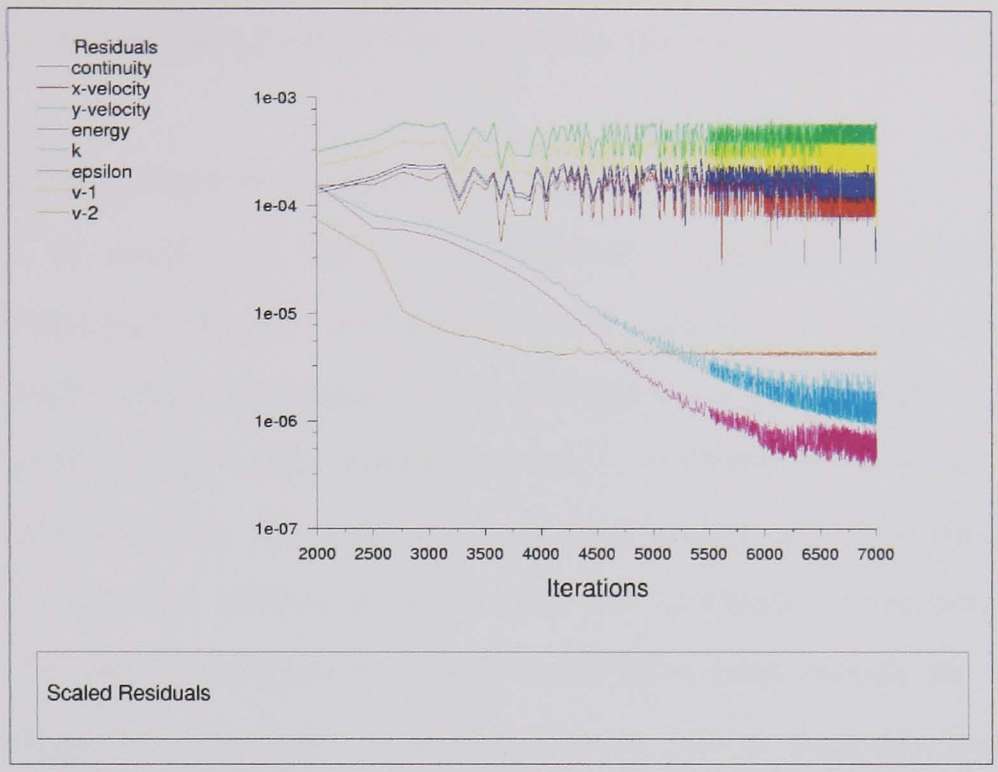

Figure 4.16 – Typical Residual History Plot With Oscillatory Residuals

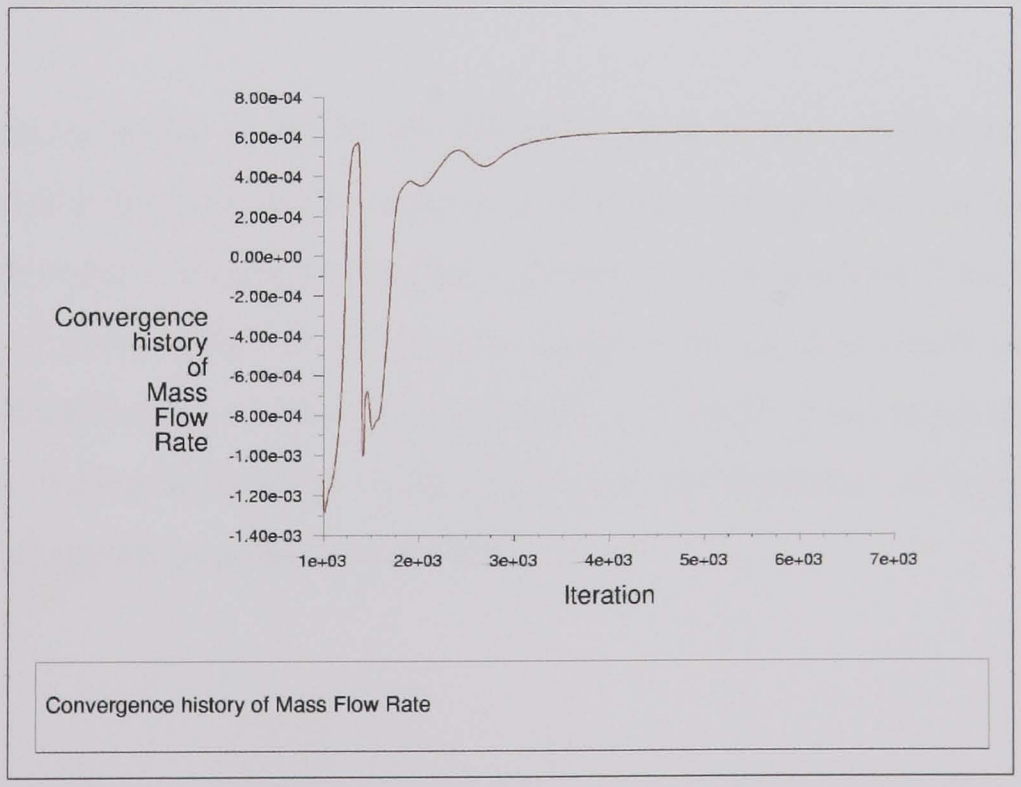

Figure 4.17 – Typical Variable History Plot of a Converged Solution

4.6 – Post-processing

Post-processing techniques are used to assemble and interpret calculated flow field data. The post-processed output can be either numerical or graphical. Graphical output was heavily relied upon in this investigation, proving an essential tool in the

understanding of flow structure and processes within the ejector. Five different methods have been used in the presentation of this data; xy plots, contour plots, vectors & streamlines, mesh plots, & combined plots of the preceding. Graphics of flow variables and properties were obtained using each of these techniques.

4.6.1 – Visualising Supersonic Flow Phenomena

Visualisation of supersonic flows is commonly performed using the schlieren technique developed by the German scientist August.J.I.Topler in 1867. CFD provides us with similar capabilities. It is possible to write subroutines or programs which can generate artificial schlieren images. Limited commercial software is available which conducts this task, however that which was available would have been unsuitable for this investigation. To use this technique the author would have had to write the required program, which would have been outside the scope of this current investigation. However it is possible to use a post-processing variable available in the coupled code, strain rate, to produce contour plots which display similar information.

The schlieren technique works by identifying regions of high density gradient, such as those found in the presence of supersonic flow features and mixing layers. Where these regions occur it is common to find a similar velocity gradient. This is shown by a high rate of strain within the fluid. The visualisation of fluid strain rate therefore allows the identification of basic expansion fan and shock wave structure within the flow stream. Additionally shear mixing layers and the formation of boundary layers along internal surfaces can also be viewed.

Chapter 5 – Optimisation of Numerical Parameters

The following chapter describes the optimisation of the numerical technique developed in this study. For CFD to be useful the numerics need to be verified, validated, and calibrated[101] or optimised. Verification determines that equations are solved correctly and is primarily the responsibility of the software programmer. The individual numerical models need to be validated in determination of their applicability to the complex phenomena they are designed to predict, which has normally also been performed by the programmer. However these must then be calibrated to specific problems and situations which is the responsibility of the user.

In the calibration/optimisation procedure it is important to consider uncertainty which is discussed firstly in this chapter. Discussion then progresses to the calibration of specific numerics. Both segregated and coupled solvers have been assessed. The choice and application of discretisation schemes, turbulence models, and physical parameters are discussed. Additionally the application of mesh adaption, and the consequences of geometrical simplifications are covered.

5.1 - Uncertainty in Computational Fluid Dynamics

"Uncertain: - adj. not sure or confident of."

OED[102]

The field of computational fluid dynamics is riddled with uncertainties, all of which need to be identified and quantified. Indeed if we do not have some grasp, or concept of the level of uncertainty involved within simulations then CFD becomes little more than a tool for producing "colourful fluid dynamic" pictures. Uncertainties arise from a myriad of sources that can generally be categorised. Cole[103] stated that CFD uncertainties fall into two simple categories; numerical, and modelling. This was echoed by Mehta[104] who defined these uncertainties as; computational, and fluid dynamic. Mehta[104] went a stage further however and suggested that human factors also contribute. Fig 5.1. Each of these can be addressed in turn for the current study.

5.1.1 – Computational Uncertainties

Computational uncertainties within the current study can be identified to an extent, but the ability to remove or reduce them is limited. This is mainly due to the use of commercial CFD codes. These uncertainties fall into two categories; equivalence, and numerical accuracy. In this study there was more control over uncertainties of numerical accuracy, including; discretisation, computational mesh, convergence criteria, and presentation/interpretation of graphical results.

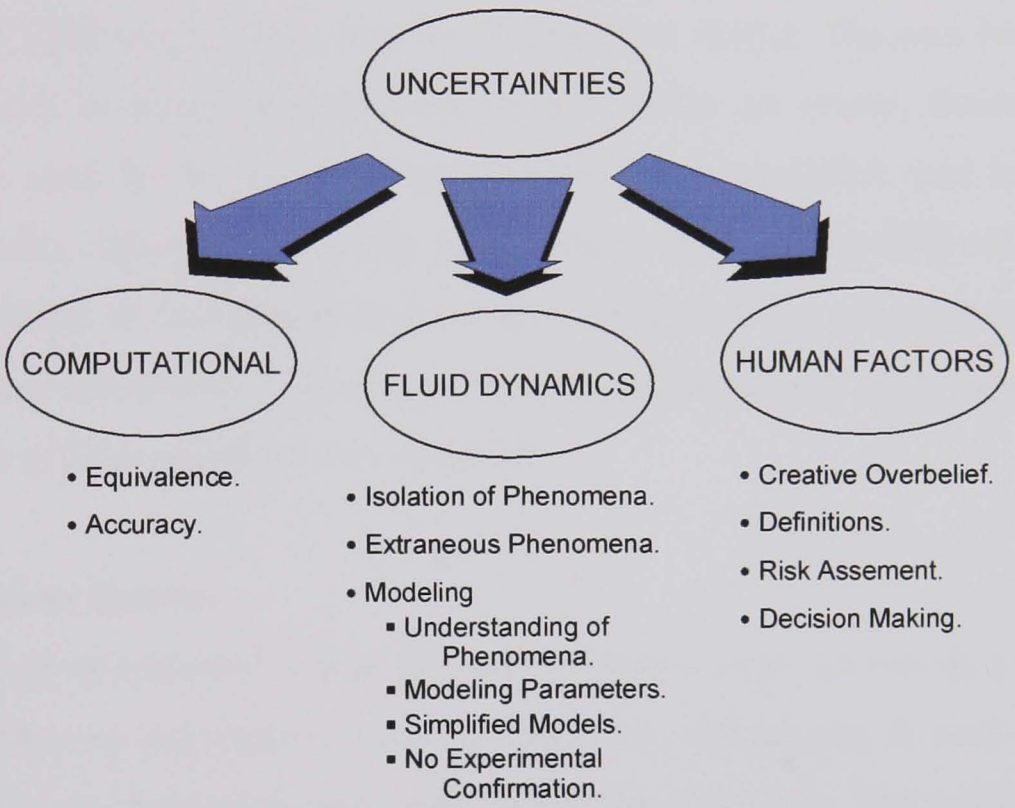

Figure 5.1 - Uncertainties in CFD [104]

The choice of discretisation scheme is at the discretion of the user, as is the convergence criteria. Uncertainty in this area can be minimised through the application of numerical schemes of comparable order accuracy. The computational mesh upon which the discretisation is performed must possess a sufficient resolution to capture flow details properly. Performing a mesh dependency study however can reduce errors attributable to the coarseness of a mesh. Unfortunately there is no other means of determining the uncertainty within a computational mesh without conducting this lengthy procedure. The initial level of uncertainty however can be reduced through insight of expected flow phenomena and the experience of the CFD user.

The reduction of convergence criteria values can also lead to improvements in accuracy. This was an important point to the current study. As stated in Section 4.5 the default convergence criteria within the coupled solver are relatively high values. Residuals need only reduce by three orders of magnitude to obtain convergence. It is possible to obtain, a numerically converged solution where the flow physics are continuing to change. Convergence values of residuals should not be solely relied upon when monitoring the accuracy of simulations. Flow variables, at various positions in the flow, also need to be monitored in ascertaining convergence.

Analysis of CFD results relies heavily on graphical output. The user has to rely on the software's accurate interpretation of the results to screen, however display parameters, such as the viewed variable range, and resolution, can be altered to enhance clarity. Alternatively where the graphical output of the CFD software is not adequate, values of variables in each computational cell can be exported to external programs and interpreted. This was performed in the current study where xy plots and profiles of flow variables were required.

5.1.2 – Human Factors

Four types of uncertainty related to human factors exist according to Mehta[104], however only two are really relevant to this study; definitions, & decision making. Uncertainty over definitions can cause numerous problems. The majority of CFD users rely on the software user guide to provide information upon the applicability and workings of numerical models. However these guides can be somewhat ambiguous with regards how models really work and assumptions which have been made. The problem can be alleviated by sourcing the original papers upon which the numerical schemes employed within the code are based.

Because of this problem there are two schools of thought on CFD usage[101]. A view purported by some academics is that users who are fully versed in the detailed workings of the code and numerics should only operate CFD software. This is only a minority view however, the more widespread belief is that users should be trained more specifically in fluid flow phenomena than the actual in-depth workings of numerical techniques. Without understanding flow phenomena it is not possible to

choose numerical models for simulation purposes. So in-turn training would also be beneficial to decision making.

Uncertainty as a result of decision making is more difficult to deal with than definitions. This is caused by a lack of information regarding the problem being studied, particularly a lack of experimental data. As Mehta states, it is not possible to determine some of the computational and fluid dynamic uncertainties without this data. Experience will reduce uncertainty to an extent, however further methods of minimising this uncertainty have to be adopted as discussed in Section 5.1.3.

5.1.3 – Fluid Dynamic Uncertainties

Uncertainty related to fluid dynamic phenomena will be a problem when simulating ejectors. It may be possible that some flow phenomena are isolated due to lack of knowledge of the actual flow physics occurring within the specific ejectors. However isolation, or even the possible introduction of extraneous phenomena, are not areas for great concern. Of greater importance are the uncertainties that have been introduced within the modelling process.

One of the aims of this study was to try and unravel the operational physics surrounding supersonic steam ejectors. Although a lack of understanding of the flow phenomena existed, it was expected that certain phenomena would be encountered. It was known that both supersonic and subsonic fluid would coexist, separated by a shear mixing layer, and that some shock phenomena would be present. However how all this would completely fit together was not known, though the flow visualisations of Fabri[65], Bauer[63], Keenan & Neumann[12], etc, provide an indication of how the phenomena may interact.

Suitable numerical modelling parameters, capable of dealing with such phenomena, can be applied. Studies of applied numerical parameters when modelling ejectors are few, authors appear too keen to just present results, which often have questionable numerics and no obvious ground work. However a degree of uncertainty in the application of numerical parameters, can be removed. This is possible through referring to validation studies of similar situations to the ejector, i.e. compressible shear mixing, supersonic flow, etc. Solver parameters for the governing equations,

turbulence model, and wall model can thus be set appropriately. The choice and application of boundary conditions can also benefit.

Simplification of the computational model can also lead to problems. With regards simplifications within the individual applied numerical models, made by programmers, little can be done. However it is important to bear in mind the simplifications they contain, e.g. k-ε turbulence models simplify matters by considering turbulence as being isentropic. Wall model simplifications with the inherent assumptions they contain become important as was found, see Section 5.5.1.

Computational model simplifications which can be dealt with easily, include the modelled geometry. The ejector was simplified by applying an axisymmetric assumption. Application of such an assumption could prevent the detection of asymmetric phenomena, and therefore needed to be verified, but was found acceptable. Additional assumptions with regards fluid properties were made which in turn were also validated. Initially the model considered only a single species fluid with identical properties at all flow boundaries. This was later adapted to separate fluid species at each flow boundary with properties set specifically to that boundary condition.

The easiest way to determine the importance of simplifications is through the use of experimental confirmation. In this investigation only limited opportunities for this existed. The only experimental data available within the majority of studies conducted were mass flow rates. Unfortunately this study is of structure and mixing processes, the experimental data offers no confirmation of this. Instead a different approach had to be adopted. As stated visualisation studies[12,63,65] of comparable ejector studies were referred to, to try and ascertain that nothing too untoward appeared within the simulation results.

The importance of this was shown when a study of different QUICK limiter schemes was conducted for the segregated solver, Section 5.4.1. Comparable mass flow characteristics to experiment were obtained, however each study produced a different flow and shock pattern. The knowledge of the CFD user comes into play at this

point, determining whether the flow appears qualitatively correct. It is a fact that any person with minimal training can conduct a CFD simulation, within reason. The skill involved is in the interpretation of the obtained results, of knowing the capabilities of the software, and thus identifying the occasions when results look plausible but are actually misleading.

5.2 – History of Solver Use

Segregated and coupled solver formulations have both been used in this investigation. Although coupled solvers are more ideally suited to the simulation of ejectors, [75], a segregated solver was initially adopted. This was unavoidable due to the available CFD software.

At the commencement of this investigation segregated solver formulations were more readily available than coupled codes. If an industrial company already possessed CFD capabilities, it was therefore more likely this would be through a segregated code. As one of the most important aims of this study is demonstrating the ability of CFD in the simulation of ejectors, it was still important to determine whether segregated codes could be optimised to produce reasonable answers. If a segregated code could be proved capable of producing accurate results this would remove the necessity of a costly upgrade to a coupled code.

The use of the segregated code revealed problems with regards mesh dependency. Both the work of Hart[86], and Warren[89] have demonstrated the concerning trait of a reduction in predicted entrainment for increasing mesh refinement. At first this was assumed to be attributable to the numerics of the segregated code. However it can now be stated with confidence that this behaviour can be attributed to the chosen wall model, see Section 5.5.1. It was found that although the segregated code could be used in the simulation of ejectors the mesh has to be carefully optimised to operate correctly with the numerics. The structured nature though of segregated codes at this time did not make the code suitable for anything other than the generation of qualitative results.

Changing software license agreements eventually allowed for the evaluation of a coupled code. The powerful unstructured mesh adaption capabilities of the code, and its ability to produce not only qualitative but also quantitative results, led to the adoption of this code in place of the segregated solver.

5.3 – Validation Source Material

The work of Eames et al[5] provided the experimental data used in the validation of the mathematical model assembled for simulating ejectors in this study. The ejector is part of a steam jet refrigeration system. Both the primary and secondary fluids are steam. The boundary conditions listed in Table 5.1 were used in all validation studies. This combination of conditions resulted in an experimental $COP_R = 0.5862$ for the ejector.

	Primary Inlet	Secondary Inlet	Outlet	Walls
Pressure (Pa)	198500	1227	3800	n/a
Temperature (K)	393	283	301	283

Table 5.1 – Validation Boundary Conditions

5.3.1 – One-Dimensional Nozzle Analysis

A one dimensional analysis of the de Laval nozzle has been performed to determine the theoretical operational characteristics. These were then used in comparison with CFD predicted values. The ratio of specific heats γ, of the motive steam was calculated from Eqn (5.1) and determined as $\gamma = 1.318$.

$$\gamma = \frac{\overline{C}p}{\overline{C}v} \tag{5.1}$$

Molar specific heat values at constant pressure $\overline{C}p$, and constant volume $\overline{C}v$, were determined from (5.2) and (5.3) respectively, where R_u is the universal gas constant.

$$\overline{C}p = a + bT + cT^2 + dT^3 \tag{5.2}$$

$a = 32.24$ $b = 0.1923 \times 10^{-2}$ $c = 1.055 \times 10^{-5}$ $d = -3.595 \times 10^{-9}$

$$\overline{C}p = \overline{C}v + R_u \tag{5.3}$$

The theoretical de Laval nozzle mass flow rate $\dot{m}$ was determined from (5.4).

$$\dot{m} = A^* \frac{P_o \sqrt{\frac{\gamma}{RT_o}}}{\left[\frac{\gamma+1}{2}\right]^{\left[\frac{\gamma+1}{2(\gamma-1)}\right]}} \tag{5.4}$$

Where A^* is the critical area of the nozzle, the nozzle throat. The de Laval nozzle Mach number at exit was determined iteratively from (5.5), and inserted into (5.6) to yield exit pressure. All calculated values are presented in Table 5.2.

$$\frac{A}{A^*} = \frac{1}{M}\left[\frac{1+\left(\frac{\gamma-1}{2}\right)M^2}{1+\left(\frac{\gamma-1}{2}\right)}\right]^{\left[\frac{\gamma+1}{2(\gamma-1)}\right]} \tag{5.5}$$

$$\frac{P_o}{P} = \left[1+\left(\frac{\gamma-1}{2}\right)M^2\right]^{\left[\frac{\gamma}{\gamma-1}\right]} \tag{5.6}$$

Mach Number	Mass Flow Rate (g/sec)	Exit Pressure (Pa)
4.081	1.245	929.4

Table 5.2 – de Laval Nozzle Theoretical Operational Characteristics

5.4 – Discretisation

The choice of interpolation scheme used in the discretisation of the governing equations when simulating the ejector was tested. Two different mesh were used, Msh001 with the segregated solver, and Msh003 with the coupled solver. See Section 5.7. A basic mathematical model incorporating the ideal gas law, a standard k-ε turbulence model, and standard wall function was adopted.

5.4.1 – Segregated Solver

The segregated solver requires the specification of interpolation schemes for spatial discretisation (interpolation of pressure, velocity, & turbulence values), and density discretisation. 1st-Order, 2nd-Order, and QUICK schemes are available for spatial and density discretisation. A linear pressure interpolation scheme is also offered. Discretisation schemes were tested, with and without linear-pressure-interpolation. The numerics of these individual schemes are detailed in Section 4.1.2. Results are presented in Table 5.3.

Nº	Spatial Discretisation	Density Discretisation	QUICK Limiter	Linear Pressure Interpolation	R_m	COP_R	% Error
V01	1st – Order	1st – Order	n/a	No	0.430	0.398	-32.1
V02	2nd – Order	2nd – Order	n/a	No	0.591	0.547	-6.7
V03	2nd – Order	2nd – Order	n/a	Yes	0.665	0.616	+5.1
V04	QUICK	QUICK	UMIST	Yes	0.657	0.610	+4.1
V05	QUICK	QUICK	MUSCL	Yes	0.677	0.630	+7.5
V06	QUICK	QUICK	SUPERBEE	Yes	0.680	0.630	+7.5
V07	QUICK	QUICK	Compressible MINMOD	Yes	0.655	0.607	+3.6

Table 5.3 - Influence of Discretisation Scheme Upon Predicted Entrainment

1st-Order accuracy is unsuitable for simulation of the ejector, it is not even possible to obtain a qualitative solution with this scheme. Although the most stable of the schemes it is known to be numerically diffusive producing a 32% difference in R_m with respect to experiment results. 2nd-Order and 3rd-Order QUICK schemes, used in conjunction with linear-pressure-interpolation, produced results of comparable accuracy.

The computed COP_R for the higher order schemes suggests that the choice of scheme, and where appropriate limiter, may be somewhat arbitrary. However it can be seen that QUICK (UMIST) and QUICK (Compressible MINMOD) produced the lowest error. It is necessary to base the choice of scheme therefore not only on computed accuracy, but also upon predicted flow structure. Fig 5.2 shows the predicted shock structures within the ejector dependant upon discretisation scheme.

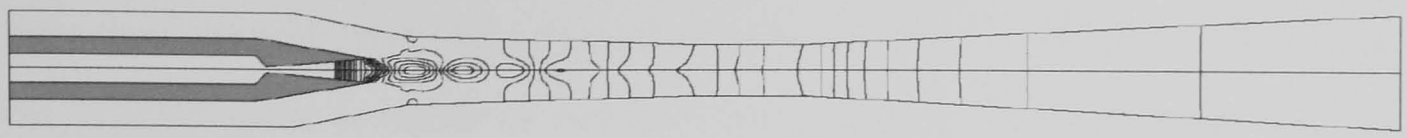

a. – V01

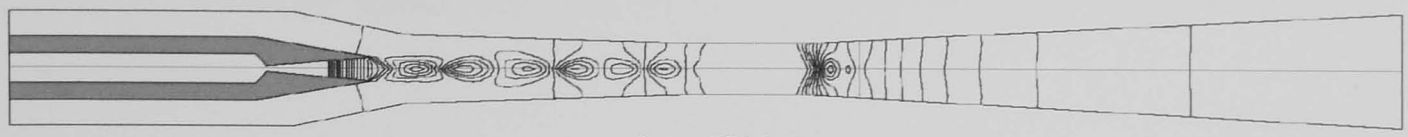

b. – V02

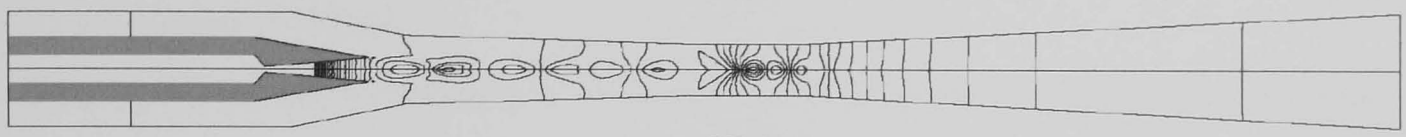

c. – V03

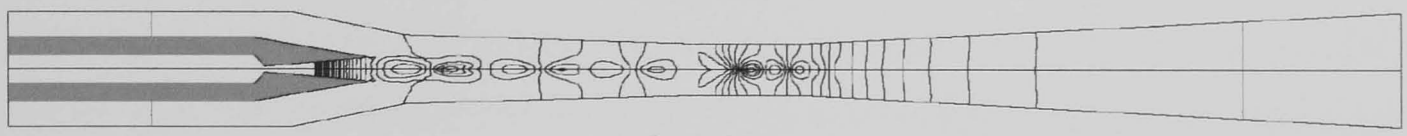

d. – V04

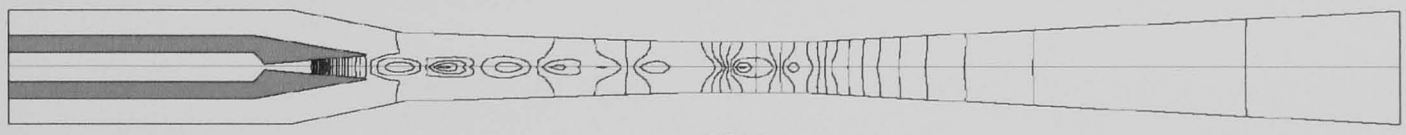

e. – V05

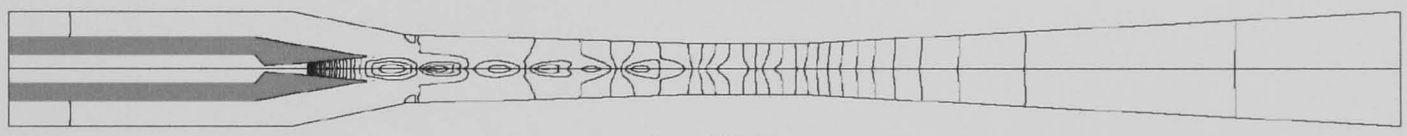

f. – V06

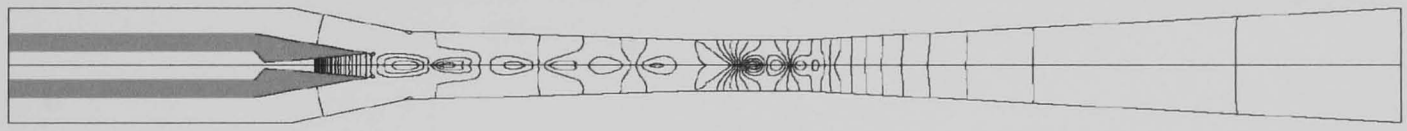

g. – V07

Figure 5.2 – Isobars Showing Predicted Shock Systems:

It can be seen that the predicted shock system differs with the interpolation scheme. Unfortunately no experimental verification of the flow field is available. However from visualisation studies of similar ejectors[12,63,65] it is known that a strong shock system generally resides within the throat. This is evident with the 2nd-Order, QUICK (UMIST), and QUICK (Compressible MINMOD) schemes, which all show tightly packed isobars within this region.

The final decision of which scheme to adopt was taken upon simulation stability. Although converged results had been obtained with the QUICK schemes, the solution process was not particularly easy compared to 2nd-Order. The decision was therefore taken to use 2nd-Order accurate schemes with linear-pressure-interpolation for all further studies conducted with the segregated solver. The predicted primary

mass flow rate with this combination of schemes was $\dot{m}_1$ = 0.946 g/sec, compared to $\dot{m}_1$ = 1.245 g/sec. It would be expected that this value should be lower than 1D theory as the actual throat area will be less than the calculated throat area, due to viscous effects in this region.

5.4.2 – Coupled Solver

The coupled solver, Section 4.2.2, requires the specification of interpolation schemes for flow (pressure, density, and velocity values) and turbulence equation discretisation. 1st-Order, 2nd-Order, Power Law, and QUICK schemes were tested. Power Law and QUICK are only available for use with the turbulence equations. Specification of a QUICK limiter is not required. Results are presented in Table 5.4.

Nº	Discretisation Scheme			R_m	COP_R	% Error
	Flow Equations	Turbulent k Equation	Turbulent ε Equation			
V08	1st Order	1st Order	1st Order	-0.339	-0.315	-153.75
V09	2nd Order	2nd Order	2nd Order	0.571	0.529	-9.687
V10	2nd Order	Power Law	Power Law	0.572	0.530	-9.539
V11	2nd Order	QUICK	QUICK	0.581	0.539	-7.968

Table 5.4 – Specification of Discretisation Schemes

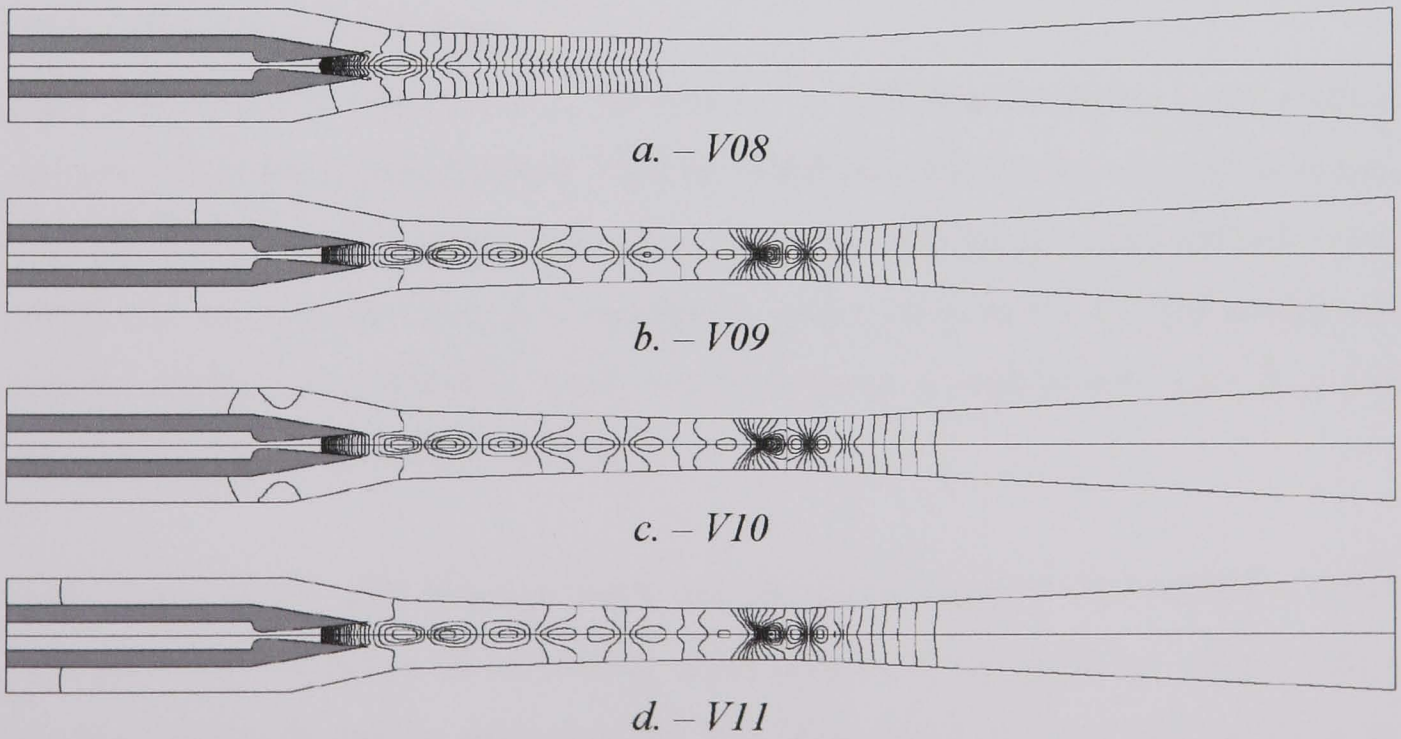

a. – V08

b. – V09

c. – V10

d. – V11

Figure 5.3 – Isobars Showing Predicted Shock Systems

1st-Order Upwind is again clearly unsuitable for simulation of the ejector, unable to predict even a qualitative solution. Simulations using the 2nd-Order Upwind scheme

for flow equations, used in conjunction with any of the higher order schemes for the turbulence equations, were found to perform well. All combinations of the higher order discretisation schemes however produced comparable results. Differences in the predicted flow structure are also negligible, Fig. 5.3. The decision was therefore taken to use 2^{nd}-Order Upwind discretisation for both flow and turbulence equations, maintaining the same order discretisation for all equations. The predicted primary mass flow rate with this combination of schemes was $\dot{m}_1 = 0.99$ g/sec. Again this value is less than predicted by 1D theory as would be expected.

5.5 – Turbulence Modelling

The choice of turbulence parameters has been assessed. Firstly the influence of near wall modelling methods were tested for both the segregated and coupled codes. This utilised computational mesh Msh003-Msh007, and also served as a mesh dependency study. The results of the near wall study were then applied to the investigation of the applicability of turbulence models available within the coupled code to the simulation of ejectors.

5.5.1 – Near Wall Modelling

Both the standard wall function, Section 3.3.1, and the two layer zonal method, Section 3.3.2, have been assessed. Only the standard wall function was used with the segregated solver. The mesh requirements of the two layer zonal method would make its use with the structured segregated solver uneconomical. Additionally the quality of the computational mesh would become a significant issue if it was designed to be used with this method.

The results of the wall function study are shown in Fig 5.4. The influence of the choice of wall model, with increasing mesh density, upon predicted entrainment is clearly visible. It can be seen that the two layer zonal method out performs the standard wall function for both solvers. Predicted entrainment clearly rises, towards the experimental value, with increasing mesh refinement. This value is nearly constant above 18000 computational cells, indicating that a mesh independent result has been obtained.

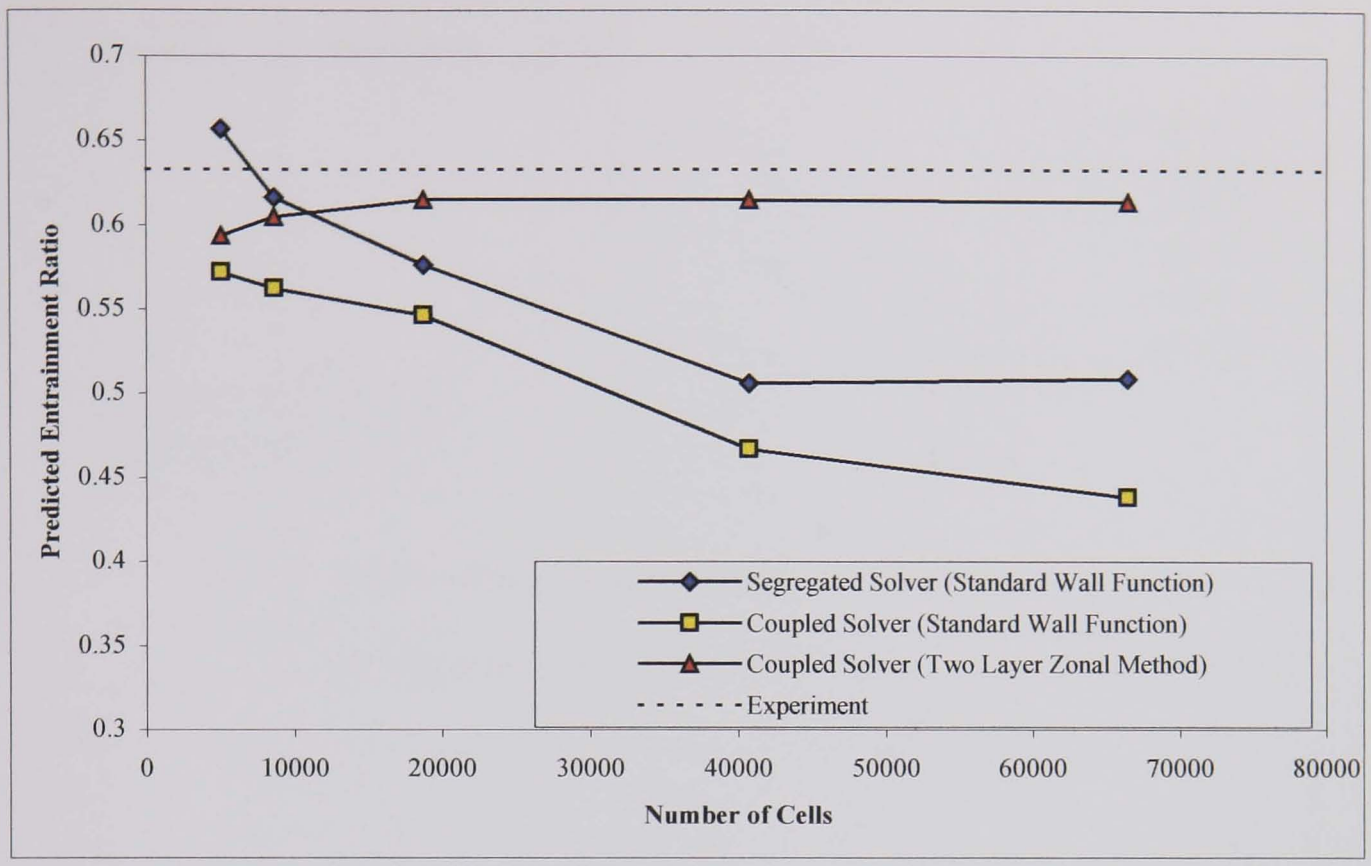

Figure 5.4 - Results of Wall Model Study

The standard wall function performs badly, predicted entrainment falls steadily with increasing mesh refinement. The reasons for the decrease in predicted entrainment when the standard wall function is used with the segregated solver, are the same as those when it is used with the coupled solver. For this reason from now on comparisons will be drawn only between the results obtained with the coupled solver.

The poor performance of the standard wall function can be explained by Fig. 5.5a – 5.5c. These show the y* values for the cells at the wall. See Section 3.3.1. It is clear from the y* values that the depth of the cells adjacent to the wall is inappropriate for use with the standard wall function. As the computational mesh was refined, the net effect was to further invalidate the use of the standard wall function. This is a major problem with structured mesh, it is impossible to maintain y* values during refinement. Hence global grid dependency studies with structured mesh can become meaningless once y* values have dropped below valid levels.

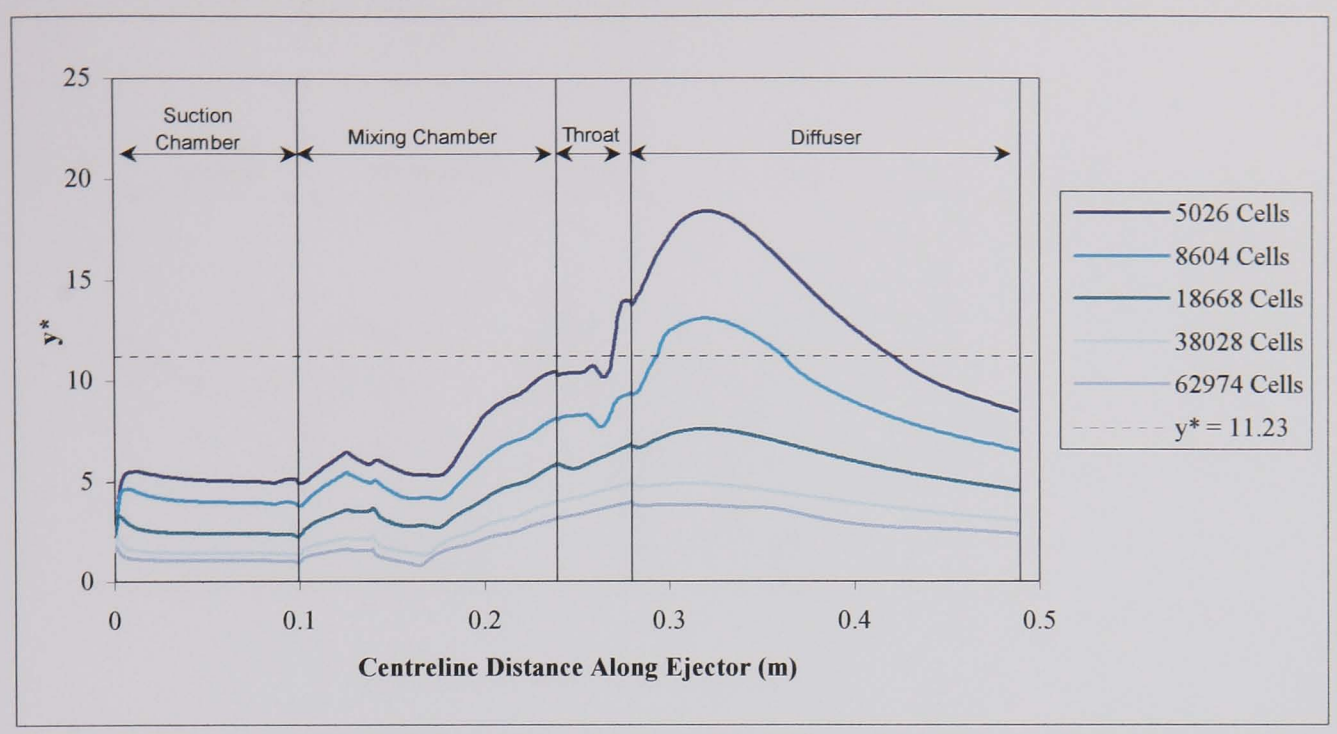

a. - y Values Along Ejector Outer Shroud*

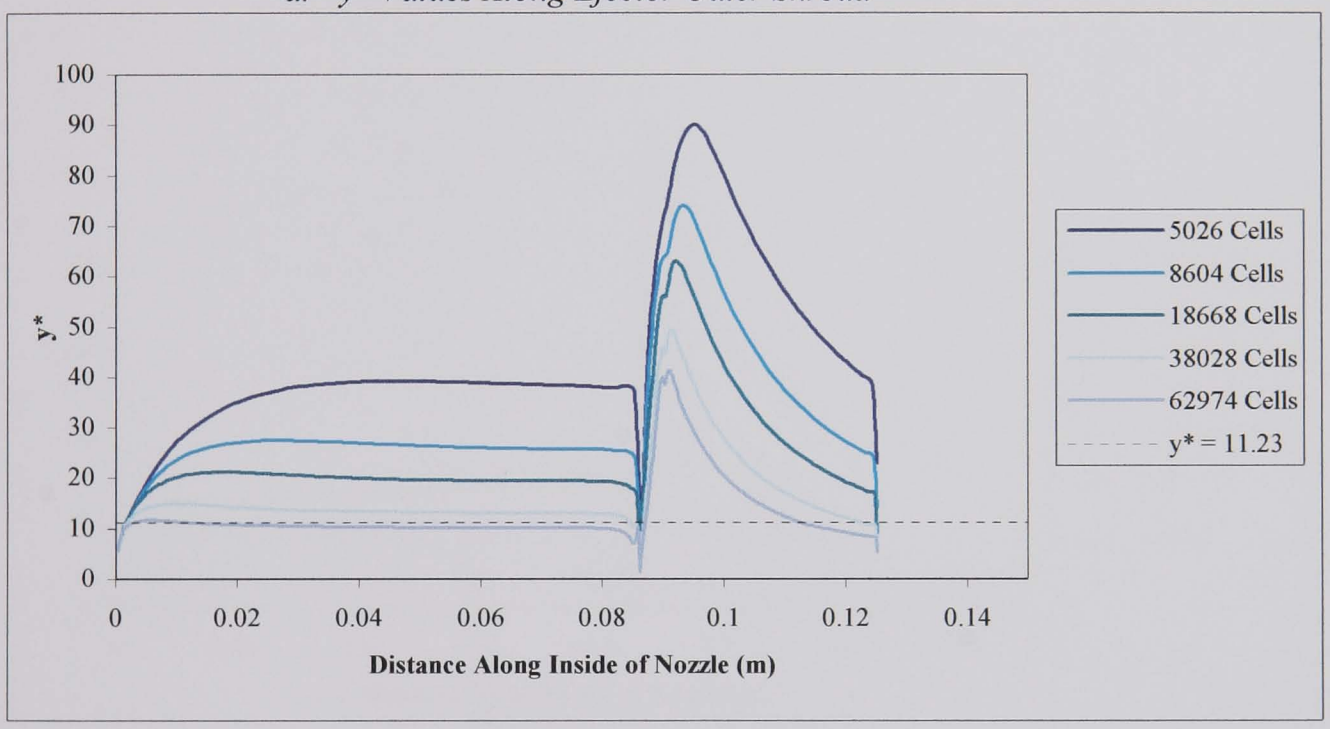

b. - y Values Along Nozzle Inner Wall*

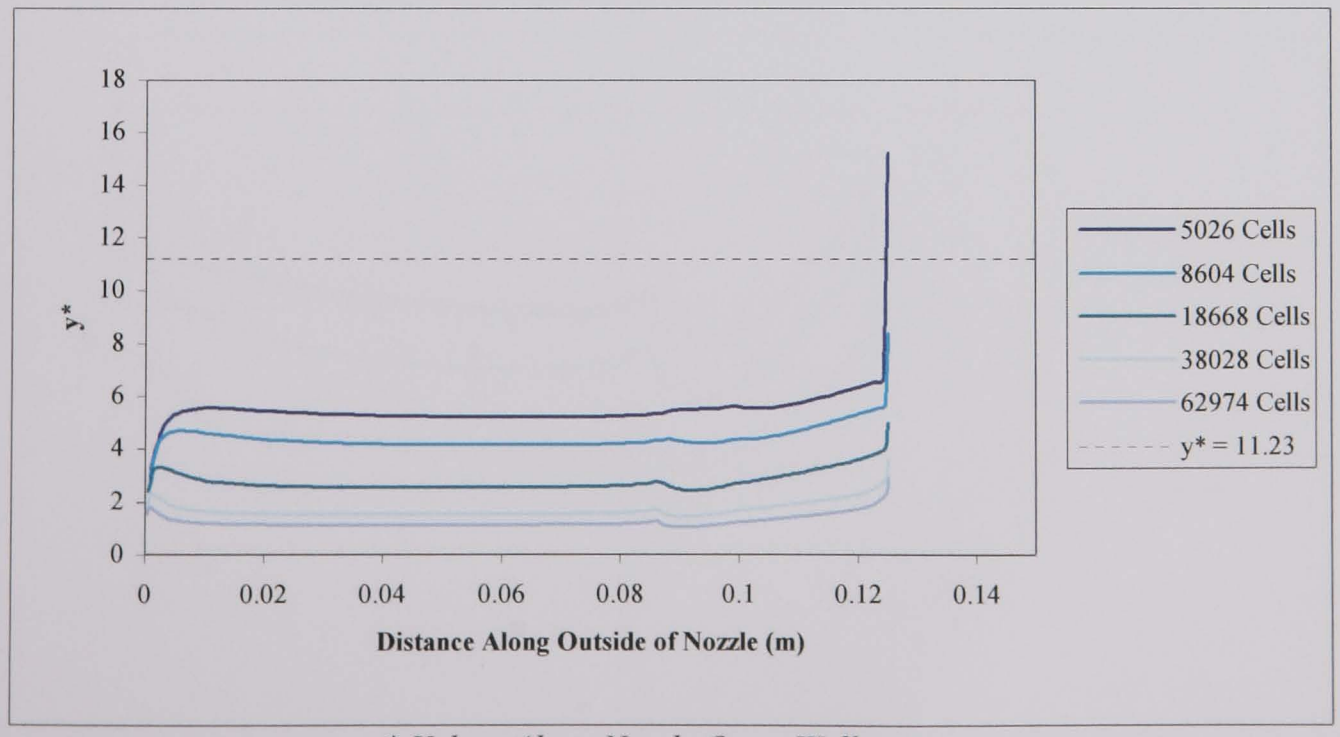

c. - y Values Along Nozzle Outer Wall*

Figure 5.5 - y Values Predicted Using Two Layer Zonal Method*

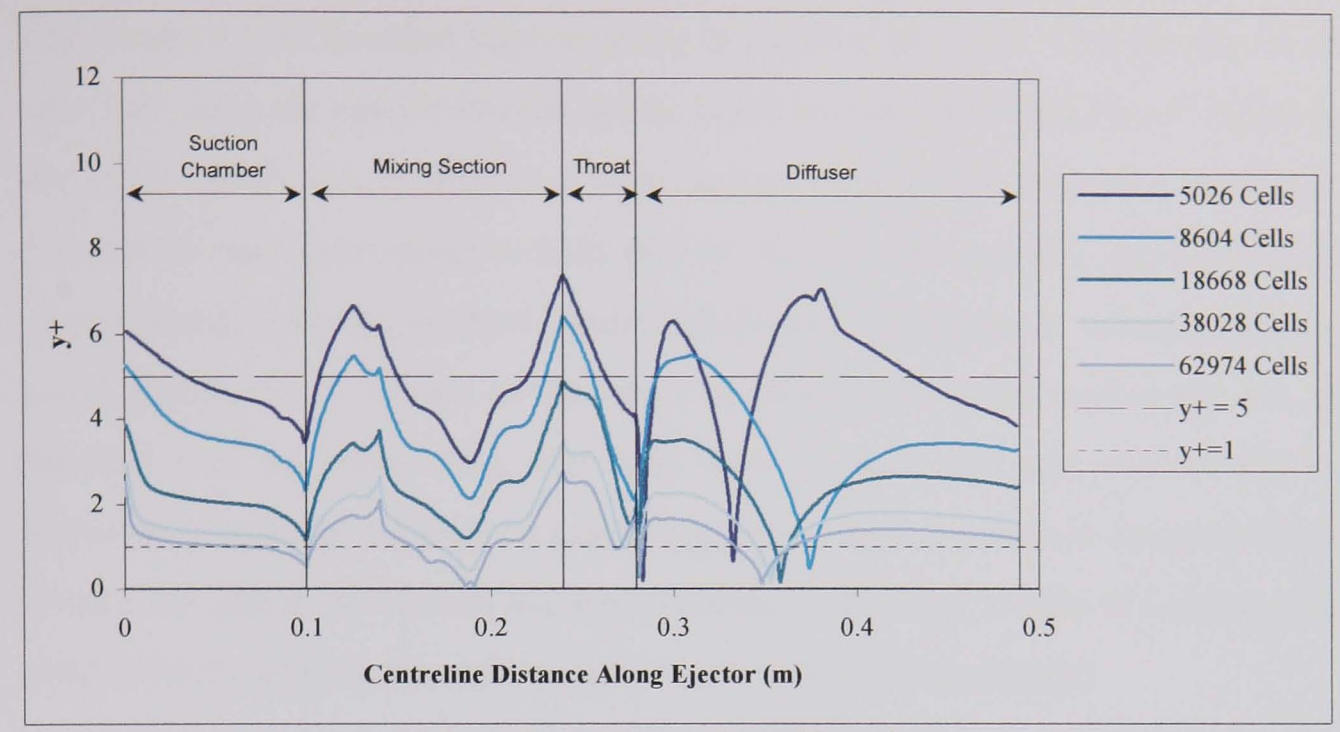

a. - y+ Values Along Ejector Outer Shroud

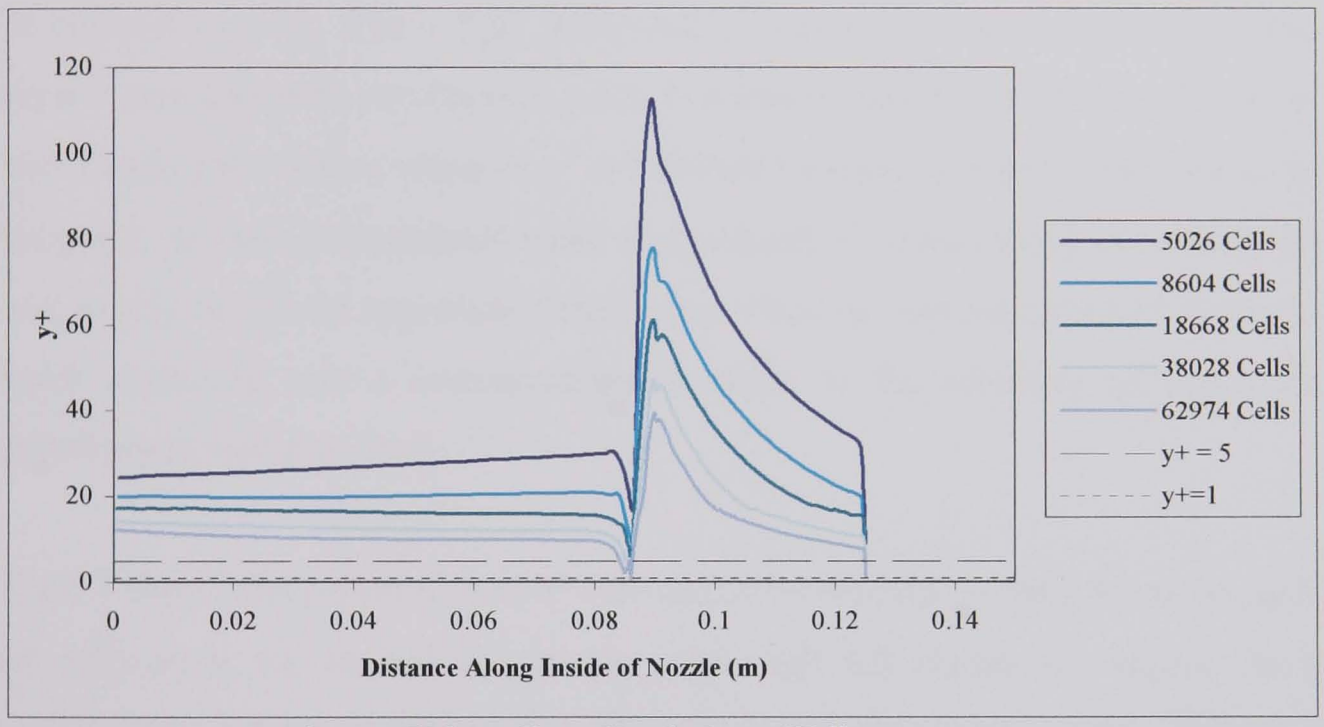

b. - y+ Values Along Nozzle Inner Wall

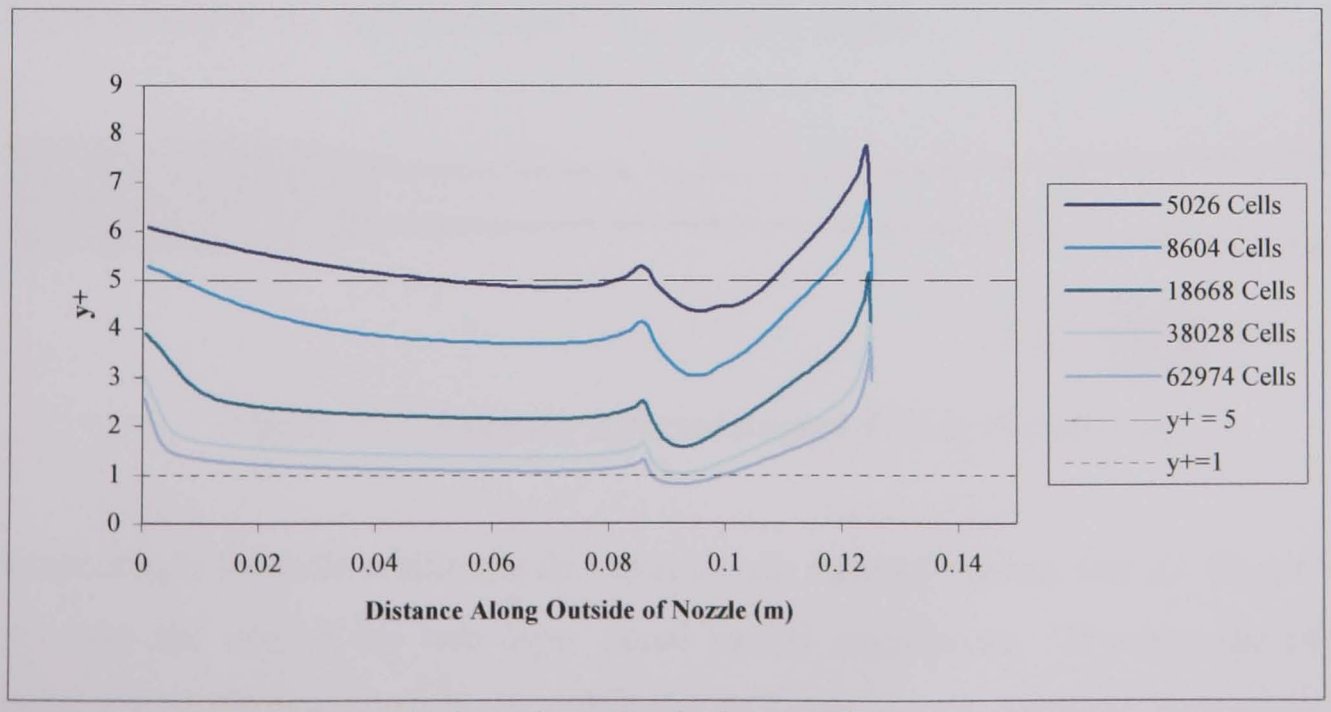

c. - y+ Values Along Nozzle Outer Wall

Figure 5.6 - y+ Values Predicted Using Two Layer Zonal Method

The standard wall function imposes a log law for values of $y^* < 11.25$ only. It can be seen that along the ejector shroud and de Laval nozzle outer wall the y* values are of the order which would impose a laminar law. Indeed the use of a standard wall function is only appropriate within part of the diffuser and the end section of the ejector throat, with the mesh of lowest cell density. However y* values within the de Laval nozzle, Fig 5.5b, are of the order of magnitude which makes the use of the standard wall function valid. The only way to make the use of a standard wall function completely valid when modelling the ejector would be to increase the depth of the cells along the shroud and outer nozzle walls. This would be inappropriate to conduct as the cells at the wall would extend well into the channel.

In comparison Fig. 5.6a – 5.6c show cell y^+ values for simulations using the two layer zonal approach, see Section 3.3.2. It is known that the model is valid for $y^+ < 5$ and ideally cells with a value of $y^+ \leq 1$ should be used to resolve the viscous region properly. As the computational mesh was refined, y^+ values along the ejector shroud and nozzle outer wall approached this value. Thus the representation of the boundary layer improved, and a corresponding increase in the accuracy of the predicted entrainment was perceived.

Fig 5.7 shows the region treated as viscosity affected ($Re_y < 200$). It can be seen that all cells along the shroud and nozzle outer wall fall within this region. As mesh density was increased the number of cells within this region grew, leading to an improvement in the representation of the viscous region.

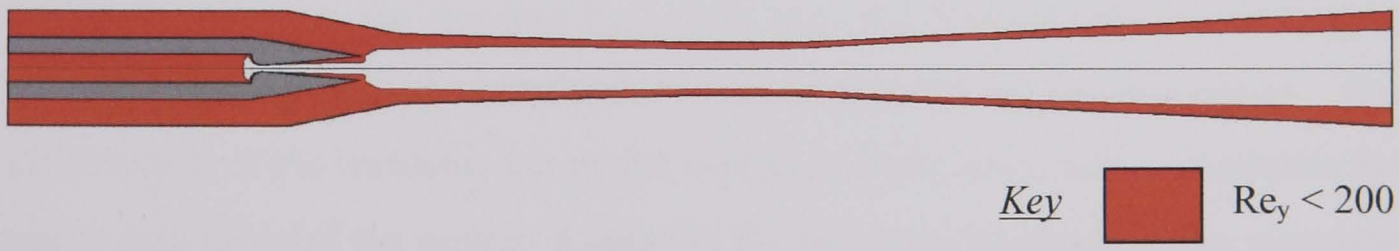

Figure 5.7 - Viscosity Affected Region Within The Ejector

Interestingly the cells within the de Laval nozzle return y^+ values that are far too high to make the use of the two layer zonal model appropriate. However the overall influence of the boundary layer within the de Laval nozzle appeared unimportant in these simulations. Comparison of velocity and pressure profiles at the nozzle exit

between the standard wall function and two layer zonal method are negligible. Hence it is believed that it is the boundary layers formed along the shroud and nozzle outer wall which play a dominant role in ejector operation.

5.5.2 – Turbulence Models

A turbulence model study was conducted using the coupled solver only. The choice of turbulence model with the segregated solver had been previously validated, [87]. The study was conducted using Msh005 an 18668 cell mesh, and the two layer zonal model to resolve the boundary layer. The wall model study had shown that above 18000 cells there was no appreciable increase in predicted entrainment. Msh005 was therefore adopted as a base mesh for the simulations.

The coupled solver has mesh adaption capabilities, and these were utilised to reduce y^+ at the walls. Mesh refinement was conducted until all y^+ values were equal to, or less than, one. In all nine refinements were required resulting in a mesh of approximately 43000 cells. Each refinement was interspersed with computations, so that the solution could adjust to the new mesh. The results of the turbulence model study are shown in Table 5.5

N°	Turbulence Model	R_m	COP_R	% Error
V12	k-ε	0.608	0.564	-3.803
V13	k-ε RNG	0.606	0.562	-4.119
V14	k-ε Realisable	0.305	0.283	-51.74
V15	Spalart-Allmaras	0.655	0.607	+3.634

Table 5.5 - Influence of Turbulence Model on Predicted Entrainment

It can be seen that the standard k-ε, RNG k-ε, and Spalart-Allmaras turbulence models return predicted entrainment values comparable to experiment. The performance of the realisable k-ε model was particularly poor, and is unsuitable for use in simulation of the ejector. Realisable k-ε has been designed to give improved prediction in the rate of spread of supersonic flows, caused by dilation dissipation. k-ε models tend to over-predict this phenomena, however in this case the Realisable model appears to over compensate for the degree of spread. Hence the ejector throat fails to choke with the application of this model. This can be seen in Fig. 5.8a-d.

The influence of the cell refinement, in reduction of y^+, upon predicted entrainment is shown in Fig. 5.9. Nine separate refinements were required in total, to reduce all y^+ values to less than 1. However the refinement process had a negligible influence on predicted entrainment after the second refinement had been conducted. Therefore two y^+ refinements are sufficient, further refinement would only waste computational resources.

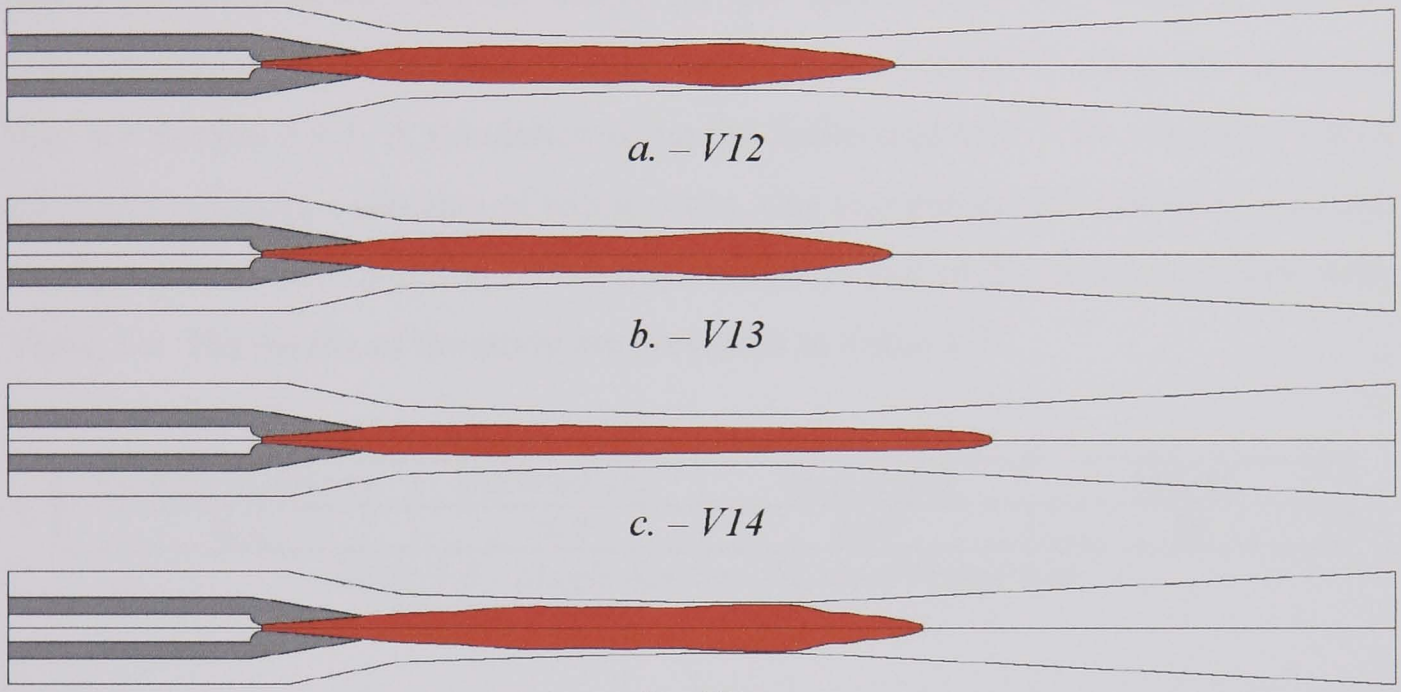

Figure 5.8 – Predicted Supersonic Region Within Ejector.

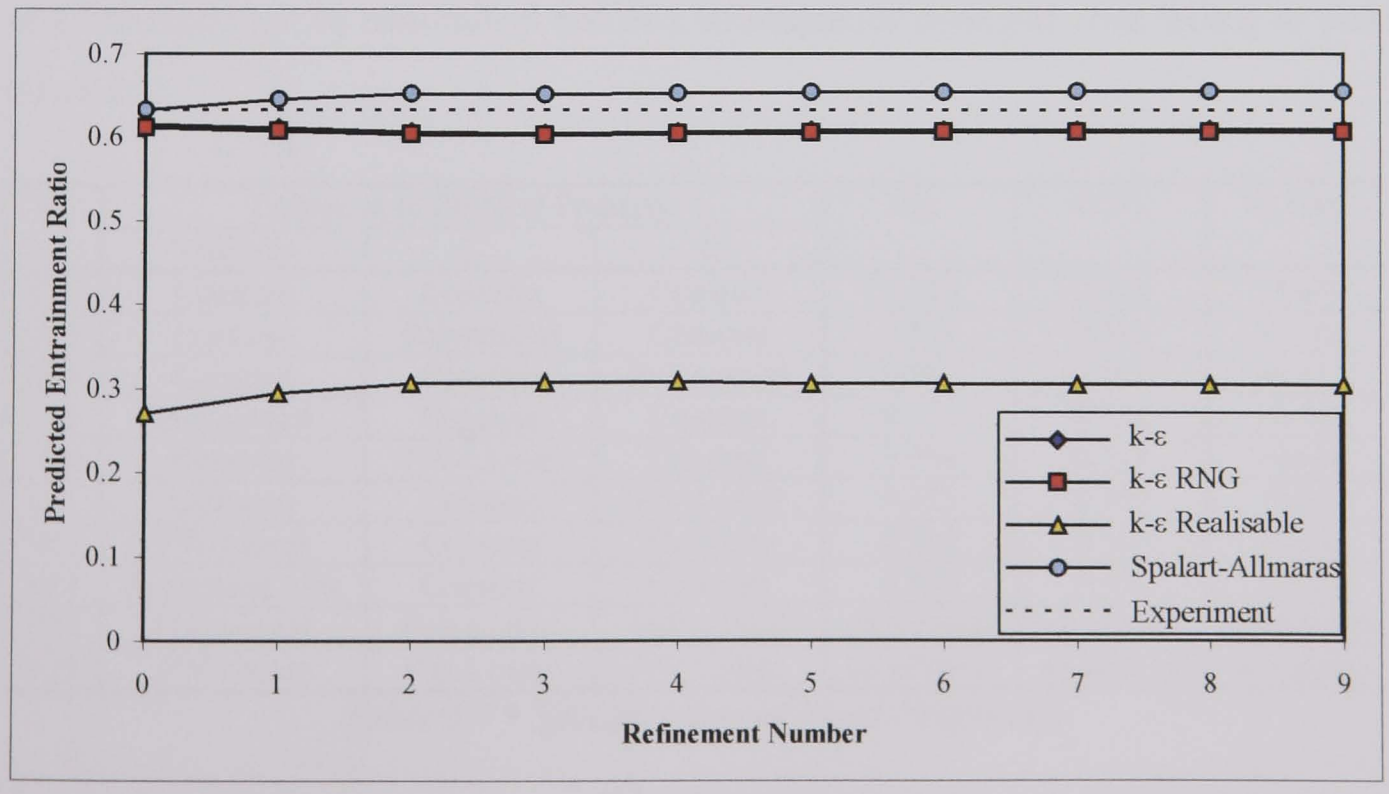

Figure 5.9 - Predicted Entrainment For Increasing Adaptive Mesh Refinement

5.6 – Physical Properties

The choice and application of physical properties were studied for the coupled solver. Physical parameters for the segregated solver had previously been validated by Hart[86]. A number of options for specifying the properties of a single species fluid were investigated. Constant values, temperature dependent polynomials, and piecewise linear laws were all tested for the specification of; viscosity, thermal conductivity, and specific heat. Density was always modelled using the ideal gas law, see Section 3.4.1. A simulation using the Sutherland law[79] for viscosity, which considers viscosity a function of temperature, was also performed. Specified constant fluid properties were based upon the physical properties of the primary motive fluid, Table 5.6. The results of the study are presented in Table 5.7.

Viscosity (kg/ms) E-6	k (kW/mK) E-6	Cp (kJ/kgK)	Mol Wt.
12.8	26.8	2090	18

Table 5.6 - Single Species Physical Properties

It can be seen that there are no additional benefits to be gained through the use of polynomials or piecewise linear functions. The use of the Sutherland viscosity law also produced poor results. Attempts to use polynomials or piecewise linear functions for the specification of all fluid properties were unsuccessful. Solution stability could not be maintained and as a consequence diverged, thus failing to yield a result.

N°	Treatment of Physical Property			R_m	COP_R	% Error
	Viscosity	C_p	k			
V16	Constant	Constant	Constant	0.595	0.551	-5.889
V17	Constant	Polynomial	Constant	0.574	0.532	-9.141
V18	Constant	Constant	Polynomial	0.593	0.550	-6.111
V19	Polynomial	Constant	Constant	0.574	0.532	-9.138
V20	Constant	PW-Linear	Constant	0.584	0.541	-7.668
V21	Constant	Constant	PW-Linear	0.595	0.552	-5.842
V22	PW-Linear	Constant	Constant	0.593	0.550	-6.146
V23	Sutherland Law	Constant	Constant	0.574	0.532	-9.228
V24	Polynomial	Polynomial	Polynomial	no solution	no solution	no solution
V25	PW-Linear	PW-Linear	PW-Linear	no solution	no solution	no solution

Table 5.7 - Specification of Fluid Properties

5.6.1 – Species

A study into the application of multiple fluid species was conducted. Individual fluid physical properties were held constant, Table 5.8. Ideal gas mixing laws were adopted to describe the viscosity and thermal conductivity of the mixed species. A mass weighted mixing law was used to describe specific heat composition. Specific details of the mixing laws can be found in [79]. The result of the species simulation is listed in Table 5.9.

Species	Viscosity (kg/ms) E-6	k (kW/mK) E-6	Cp (kJ/kgK)	Mol Wt.
Primary	12.8	26.8	2090	18
Secondary	8.83	17.1	1860	18
Outlet	9.52	18.7	1880	18

Table 5.8 - Species Physical Properties

N°	Mixing Laws			R_m	COP_R	% Error
	Viscosity	Cp	k			
V26	Ideal Gas Mixing Law	Mass Weighted Mixing Law	Ideal Gas Mixing Law	0.608	0.564	-3.8

Table 5.9 - Mixing Laws Used With Species

The use of species produced superior results compared to the single fluid studies. Species modelling was therefore adopted for all further simulations conducted using the coupled solver.

5.7 – Computational Mesh

In total nine two-dimensional computational mesh were generated for the Eames[5] ejector during the validation process. The basic details of these mesh are listed in Table 5.10. Graphics of each mesh are located in Appendix B.

Msh001 was based upon mesh previously used by Hart[86], and Warren[89]. This was used in the validation of the segregated solver mathematical model and numerics. The quality of this mesh was improved with Msh002, which was then adopted as the base mesh in all other studies involving the segregated solver post validation. Msh003-Msh007 were generated for validating the mathematical model for the coupled code. The results obtained from these mesh led to the generation of Msh008,

which possessed an improved cell quality. This mesh was then used to assess the suitability of the chosen combined numerics of the coupled code. Msh009 was created based upon additionally obtained information regarding the de Laval nozzle geometry as discussed in Section 3.8.

Mesh	N°. of Cells	Used With Solver	Nozzle Geometry	Nozzle Throat
Msh001	4410	Segregated	Original	Straight
Msh002	5012	Segregated	Original	Straight
Msh003	5026	Segregated / Coupled	Original	Curved
Msh004	8604	Segregated / Coupled	Original	Curved
Msh005	18668	Segregated / Coupled	Original	Curved
Msh006	38028	Segregated / Coupled	Original	Curved
Msh007	62974	Segregated / Coupled	Original	Curved
Msh008	18118	Coupled	Original	Curved
Msh009	18118	Coupled	Modified	Curved

Table 5.10 – Computational Mesh Used in Validation

5.7.1 – Geometrical Influence

The adoption of the coupled solver highlighted the importance of the accuracy of the modelled geometry. Initial attempts at using the coupled code with mesh Msh002 yielded results that were extremely poor. It was not even possible to predict a positive flow entrainment (R_m = -0.079, a -112.5% difference), as the ejector throat did not choke. The use of this mesh previously with the segregated solver had produced a +4% difference. Doubling the mesh led to an increase in predicted entrainment, however a 50% difference with respect to experiment still existed. The cause of this problem was traced to a geometrical simplification applied to the convergent section of the de Laval nozzle. This had been made to aide mesh generation. Although this section is radiused a linear simplification had been applied. Fig 5.10a.

a. b.

Figure 5.10 - Mesh Detail of the de Laval Nozzle: a. linear throat, b. curved throat.

The convergent section of a de Laval nozzle has a considerable influence upon the operational performance of the nozzle. Hopkins[40] showed how the curvature of this section influence the transonic flow region. Shapiro[45] discussed how this section must be designed to eliminate the possibility of flow separation or thick boundary layers. The linear approximation had to be abandoned, and the convergent section modelled with an appropriate curve. Fig 5.10b. Mesh Msh002 was modified and returned a predicted entrainment of $R_m = 0.568$, -10% difference. Doubling this mesh returned an entrainment of $R_m = 0.545$. This decrease in predicted R_m can be attributed to the chosen near wall model, see Section 5.6.1.

5.7.2 – Mesh Adaption

As mentioned in Section 4.4.1 the coupled solver has built-in mesh adaption facilities. Mesh adaption was not used within the near wall model study, Section 5.6.1, as this served as a mesh dependency study. It is important to determine the minimum mesh density required to obtain the essential features of a flow prior to adaption. The use of structured mesh, with increasing mesh density, in the near wall model investigation presented an opportunity to determine this. However as has been seen the technique was used in the turbulence model study to reduce y^+ values.

Mesh adaption has also been used to improve the resolution of shock systems within the ejector, which play a dominant role in its operational performance. At best a shock is always going to appear as a smear across a set of computational cells, however the clarity of the shock can be enhanced through selective cell refinement.

Selective refinement of the shock system was performed by identifying regions of high pressure gradient. It was found that only two refinements were often necessary to enhance the resolution of the shock system before mesh dependency was obtained. See Fig 5.11 & 5.12. Iterations were performed between each refinement allowing the solution to adapt to the new computational mesh. Approximately 4000 cells were adapted with each refinement.

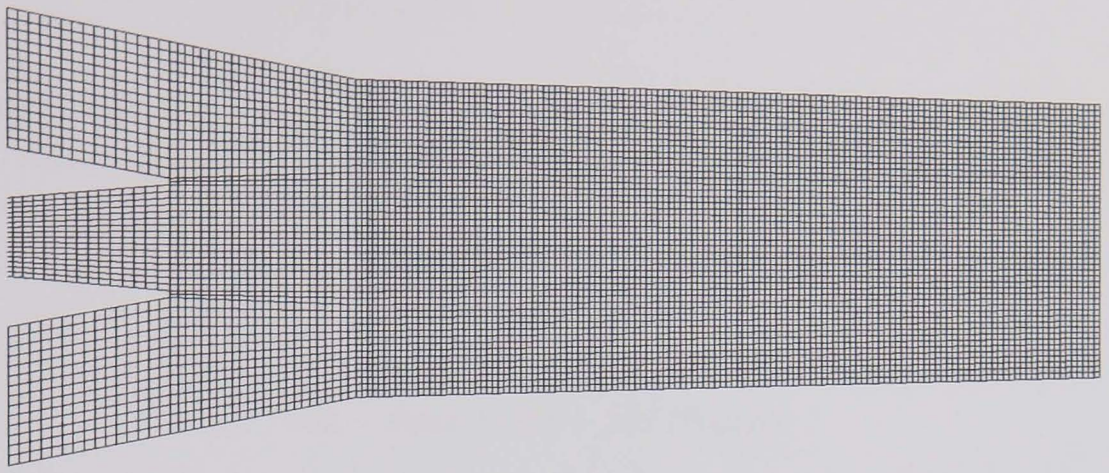

a. - Base Mesh – 18118 cells

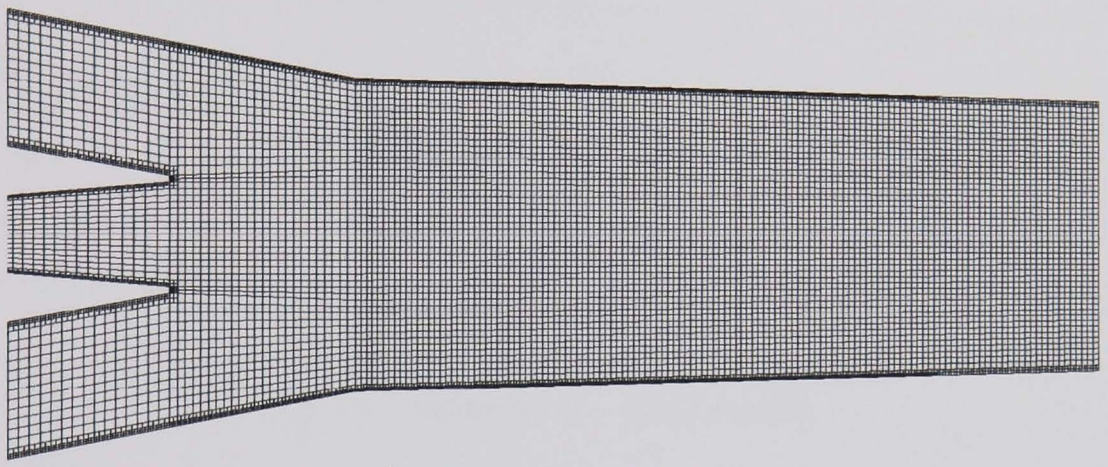

b. - y^+ refinement – 27421 cells

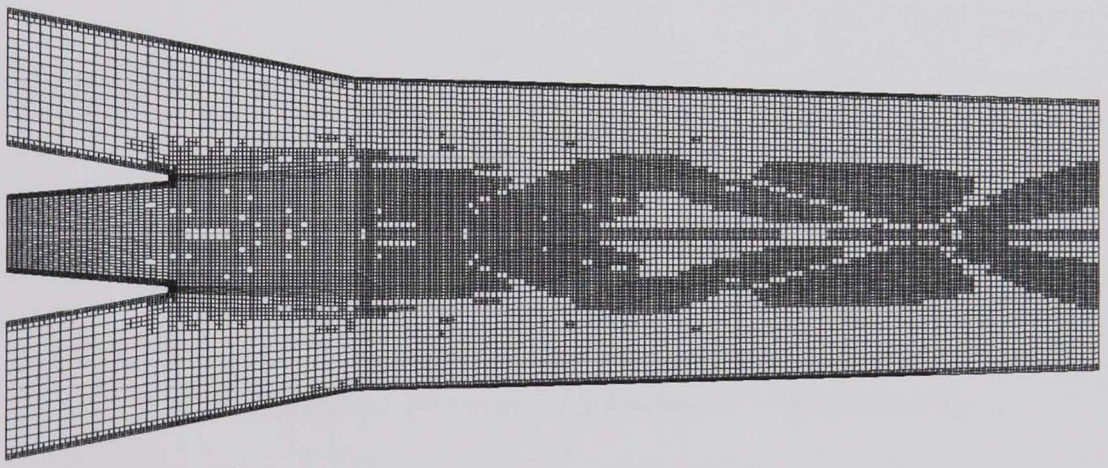

c. - 1st Adaptive Pressure Refinement – 38209 cells

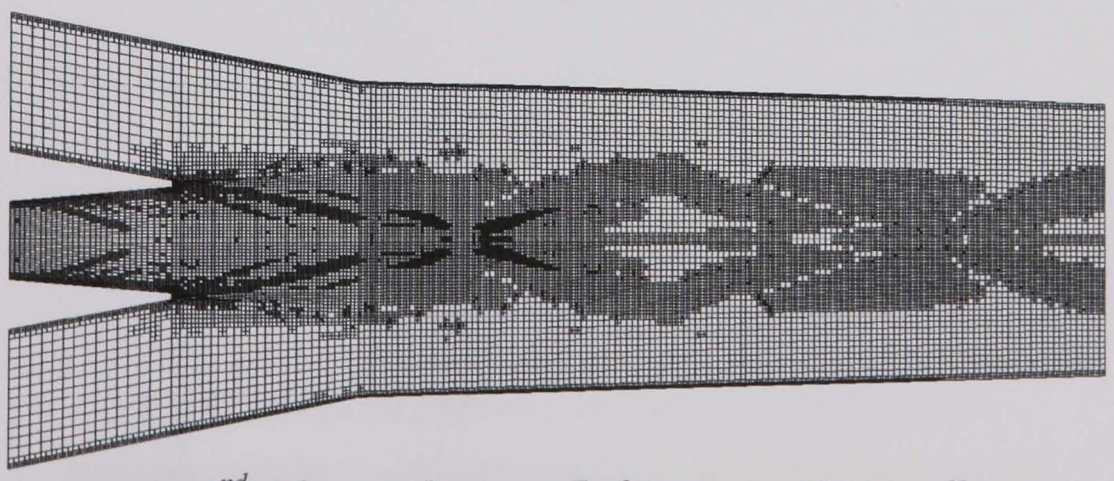

d. - 2nd Adaptive Pressure Refinement – 50014 cells

Figure 5.11 - Computational Mesh For Increasing Adaptive Mesh Refinement

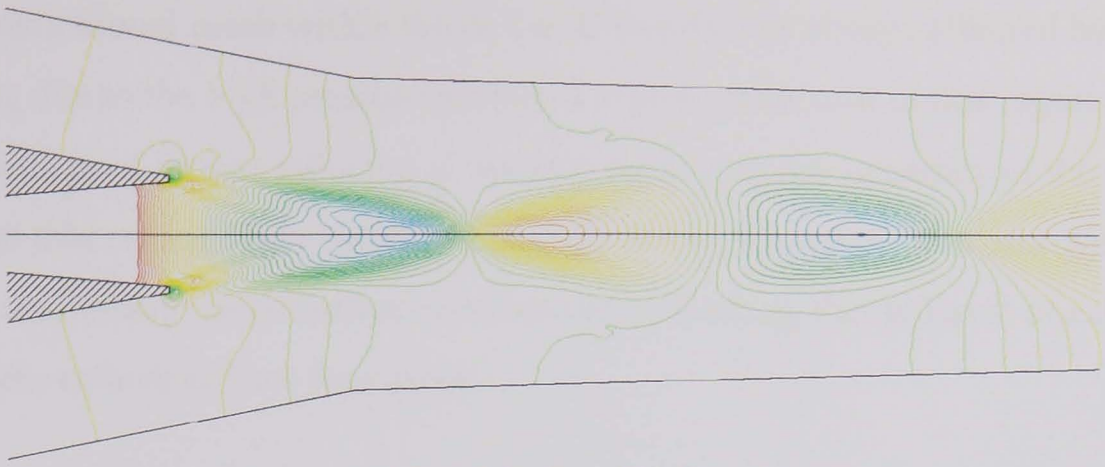

a. - Base Mesh – 18118 cells

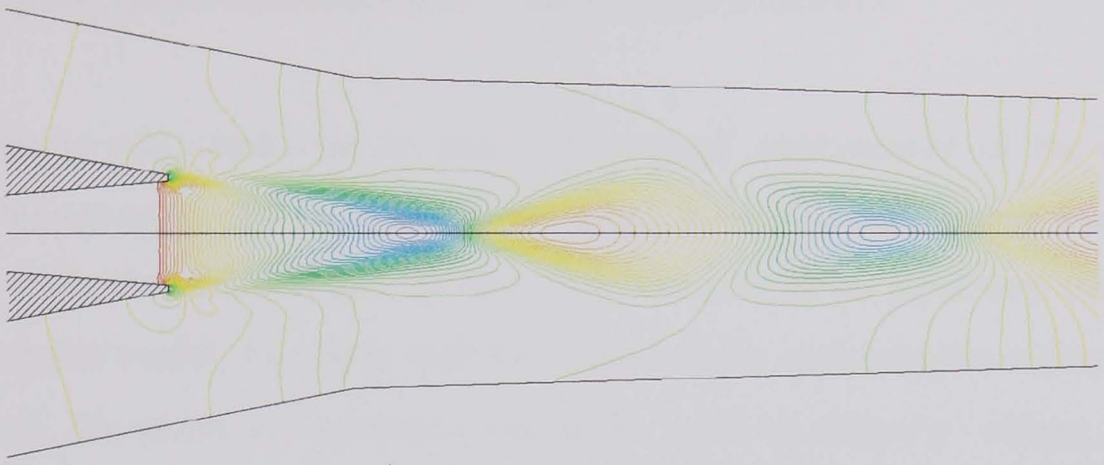

b. - y^+ refinement – 27421 cells

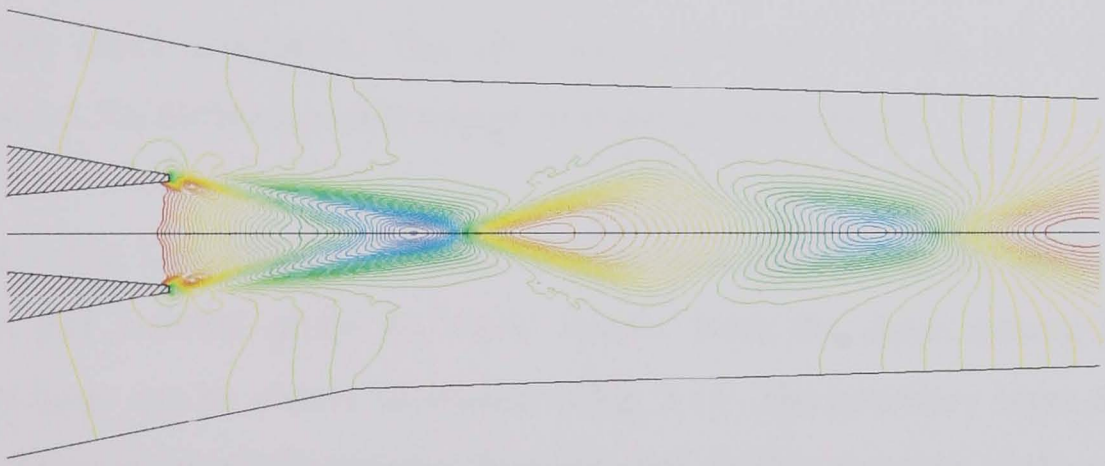

c. - 1st Adaptive Pressure Refinement – 38209 cells

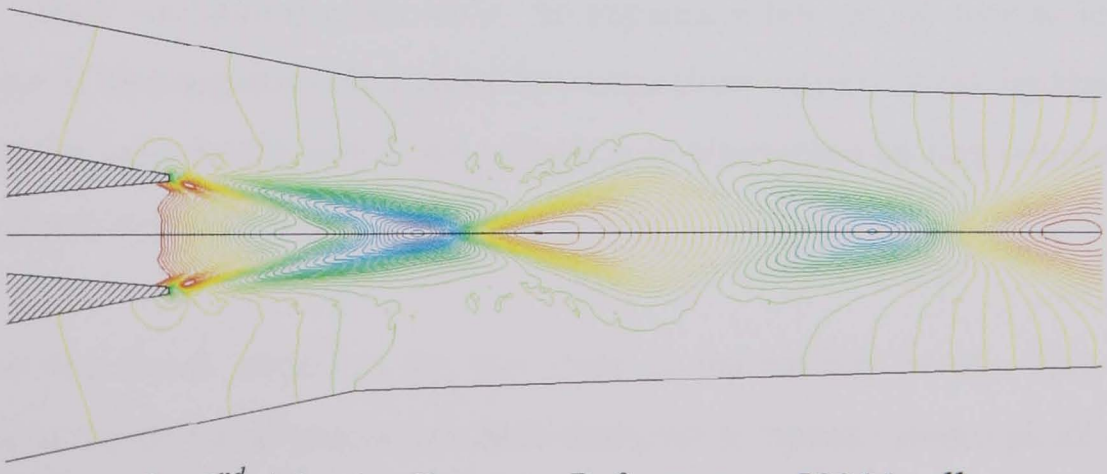

d. - 2nd Adaptive Pressure Refinement – 50014 cells

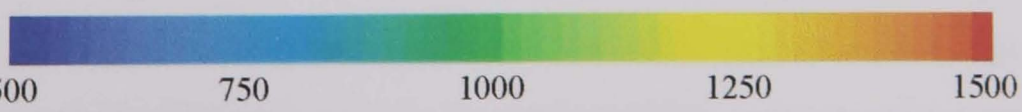

Figure 5.12 - Static Pressure Isobars (Pa) For Increasing Adaptive Mesh Refinement

The computational mesh within the de Laval nozzle was always affected by the mesh adaption, due to the high pressure gradients which reside within this region. This had the advantage of further reducing y^+ values, improving the accuracy of the near wall model in this region. Thus when refinement through pressure gradient was coupled with y^+ refinement the net effect was that the cells along the de Laval nozzle internal walls were refined at least four times.

5.8 – Optimised Numerics For The Coupled Solver

A simulation was conducted to assess the overall performance of the optimised chosen numerics for the coupled solver, using mesh Msh008. Hence a simulation with second order discretisation for both flow and turbulence equations, the standard k-ε turbulence model, two layer wall function, species, and adaptive refinement was performed. The mesh was adapted twice at the walls to reduce y^+ values. A further two adaptions were performed on the mesh as a whole, based upon pressure gradient to enhance shock resolution. The simulation predicted a COP_R of 0.578 which produced a 1.3% difference with respect to experimental values.

Fig 5.13 - Fig 5.16 show the predicted flow structure within the ejector mixing chamber, just external of the de Laval nozzle. Both the shear mixing layer and boundary layer can be clearly identified in Fig 5.13. The boundary layer appears to grow in thickness along the mixing chamber wall. Within the core of the supersonic jet some shock structure is observable. An expansion fan can be seen to form at the nozzle exit. It also appears that a secondary expansion wave or weak lip shock is also formed at the exit. As the initial fan reflects it is intersected by this secondary wave and appears to dissipate.

The observed shock structure for this case is particularly weak. This is to be expected, as the de Laval nozzle has been designed to operate isentropically with the applied combination of boundary conditions. The nozzle is however under-expanding slightly, which is confirmed by the static pressure plot, Fig. 5.15. The position of the shear mixing layer can be confirmed by referring to a contour plot of

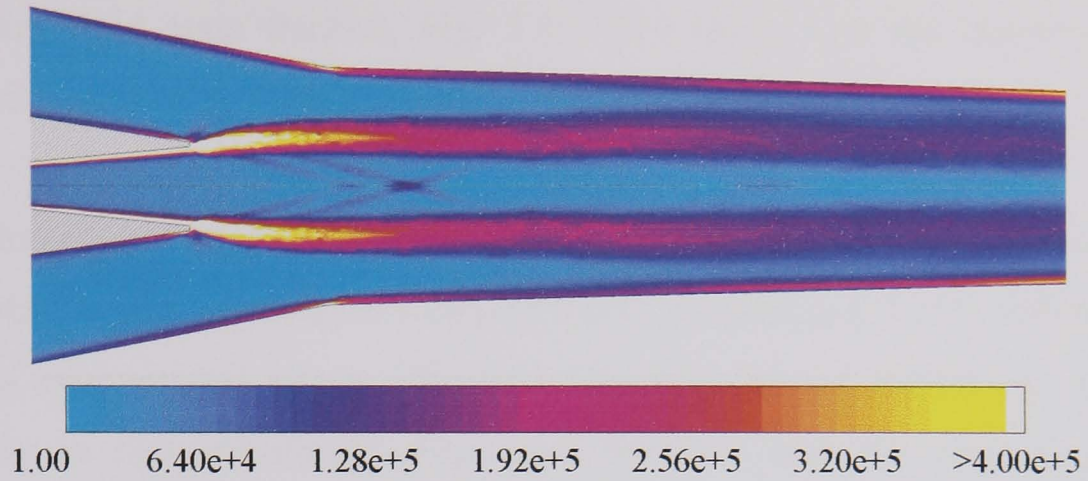

Figure 5.13 – Predicted Strain Rate (1/s) Within the Ejector

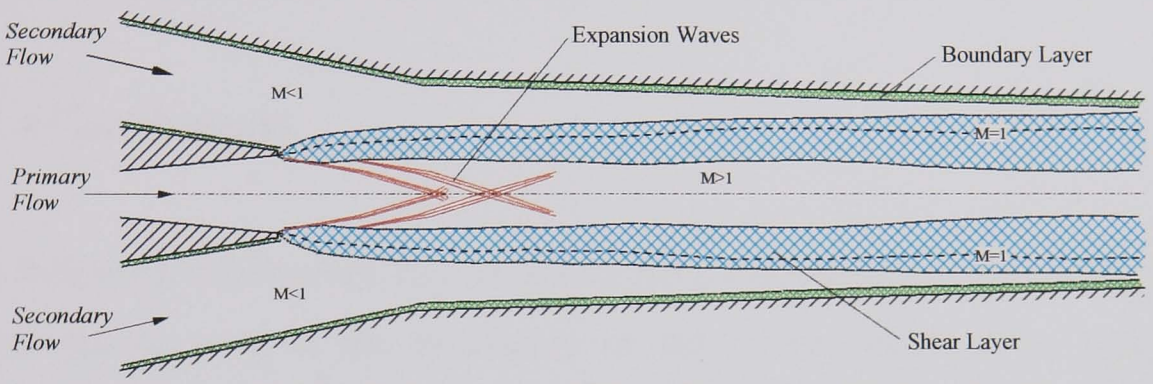

Figure 5.14 – Schematic of Flow Structure Within the Ejector

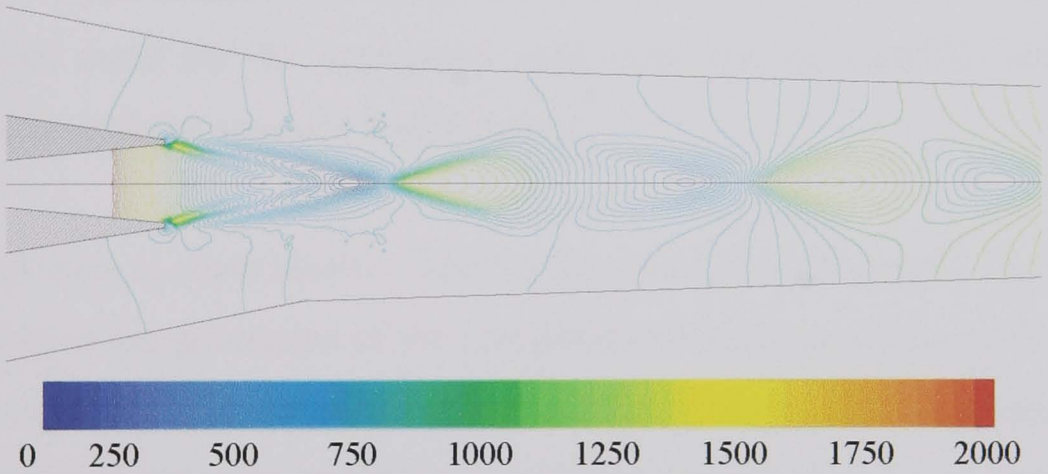

Figure 5.15 – Static Pressure Isobars (Pa) Within the Ejector

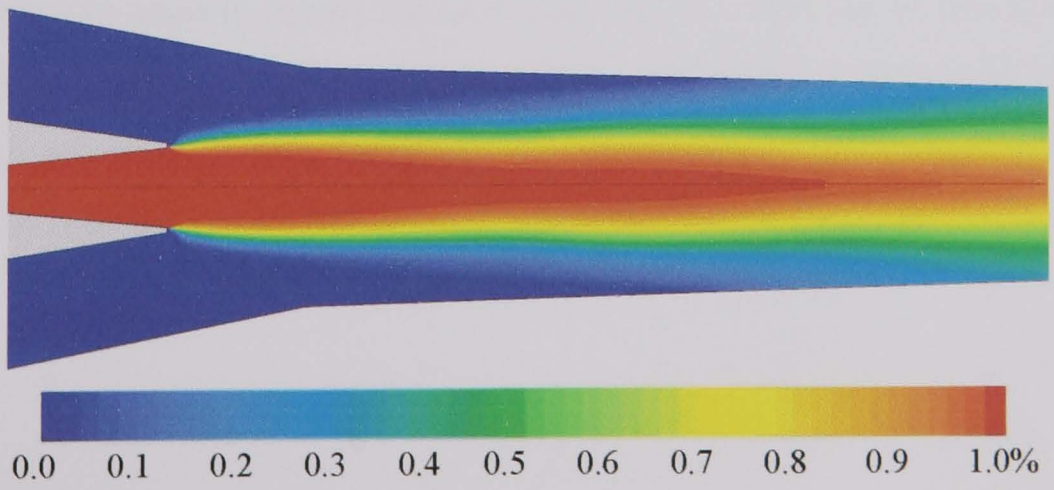

Figure 5.16 – Distribution of Primary Fluid Mass Fraction Within the Ejector

the primary fluid mass fraction, Fig. 5.16. This shows that the majority of fluid mixing will occur on or around the sonic line as observed in Fig. 5.13.

The optimised numerics were also tested for the modified nozzle geometry using mesh Msh009. This predicted a COP_R of 0.585, producing a 0.25% difference with respect to experimental values. The flow structure did not exhibit any significant differences to that calculated using mesh Msh008 with the original geometry. Msh009 was therefore used as the base mesh for all further two dimensional simulations of the Eames[5] ejector performed with the coupled solver.

5.9 – Conclusions

The following conclusions can be drawn from the validation study. The segregated solver can be used in the simulation of the ejector however its capabilities are limited. Only the generation of qualitative results are probable and realistic. Higher order discretisation schemes and linear interpolation for pressure are a requisite. The computational mesh for the segregated code must also be carefully optimised to work properly with the standard wall function.

The coupled code is more ideally suited to the simulation of ejectors. However care must be taken in the generation of the computational mesh, as it has been shown that the code is sensitive to geometrical approximations. The coupled numerics have been shown capable of not only predicting qualitative results, but also indicate that the generation of quantitative results is possible. To achieve this the two layer zonal approach must be used to model the near wall regions. The use of this low viscosity model is made economical by the unstructured mesh adaption abilities of the coupled code. Mesh adaption is also beneficial to the economic refinement of the mesh, avoiding the need for computationally expensive global refinement.

Chapter 6 – Results

The following chapter presents the results of all simulations conducted in this investigation. These predominantly comprise the results of a number of individual studies conducted upon the Eames[5] ejector. Geometrical and physical operating condition studies have been performed. The geometrical studies were conducted using the segregated solver, in completion of the validation of the ESDU[3] ejector design recommendations commenced by Hart[86] and Warren et al[89]. Studies into the influence of operating conditions upon ejector performance, and flow structure, were conducted using the coupled solver.

A three dimensional study of the Eames[5] ejector, simulated using the coupled solver, is also presented. The results of this study highlight the significant influence of the secondary inlet upon operational performance.

Additional studies of alternative ejector designs are presented which determine the general applicability of CFD to the simulation of ejectors, and further aide understanding of flow processes. These comprise the vacuum ejector of Watson[1], and the thrust augmenting ejector of Hickman et al[6]. A constant area type ejector, Desevaux[7], is included to provide comparison of operation with the constant pressure design.

6.1 – Geometrical Studies

Geometrical studies of the Eames[5] ejector mixing section have been conducted in further validation of the ESDU[3] design recommendations for supersonic ejectors as commenced by Hart[86] and Warren et al[89]. Both the influence of throat length and mixing section angle have been considered. Boundary conditions listed in Table 6.1 were used in all geometrical studies. Corresponding physical properties are listed in Table D.1 in Appendix D. Ejector geometry was based on the standard Eames ejector geometry as described in Section 3.8. this was modified accordingly in each study. Computational mesh Msh002 was chosen as a reference mesh, with the nodal distribution suitably modified within the throat and mixing chamber to maintain cell

aspect ratio with each geometrical change. The numerical model corresponded to simulation V03 in Table 5.3, Section 5.4.1, with a standard wall function and standard k-ε turbulence model.

Pressure (Pa)			Temperature (°C)		
Primary	Secondary	Outlet	Primary	Secondary	Outlet
198500	1227	3800	120	10	28

Table 6.1 – Boundary Conditions

6.1.1 – Influence of Throat Length

This study concentrated on a small but critical part of the ejector. The throat plays an important role in ensuring the stable operation of a constant pressure ejector. See Section 2.4.2. Although work has been conducted into the influence of throat diameter, [20,48], there is little work concerning the length of this section. ESDU[3] do however provide guidelines suggesting that an appropriate length should be between 2-4 throat diameters (D). Simulations have been conducted to verify this statement. The ejector throat was varied in length from 0mm-180mm (0D-10D). The current experimental throat length of the Eames ejector is 40mm (2.22D). The lengths of the convergent mixing chamber, and diffuser were held constant as detailed in Section 3.8.

The results of the study are shown in Fig. 6.1. Maximum entrainment can be clearly seen to occur with a throat length of between 2D-5.8D. These two points will be termed the *lower* and *upper limits* of the throat length, respectively. Reduction of the throat length below the lower limit results in a rapid linear loss in entrainment, reducing from a maximum value of $R_m = 0.67$ to $R_m = 0.28$ for zero length. The throat in effect was still present as the narrowest part of the mixing chamber/diffuser assembly. This was a 58% loss in entrainment for a reduction in length of two throat diameters. The level of entrainment is also seen to fall rapidly between 6D-7D, however after the initial abrupt decline the entrainment curve is seen to level off and exhibits almost a linear reduction in entrainment. Once the imposed limit of 10D is reached entrainment has fallen by 52% to $R_m = 0.32$.

It can be clearly seen that the ESDU guidelines fall comfortably within the plateau indicative of maximum entrainment. The ESDU guidelines could be described as

conservative for this ejector configuration. However it is probable that optimum throat length will differ for various ejector configurations. Therefore the ESDU guidelines are probably well set. It can also be seen that there is no benefit to be gained from using a throat length longer than 4D, in this experimental set-up. This would only take up what might be classed as valuable space in the operational environment of the ejector.

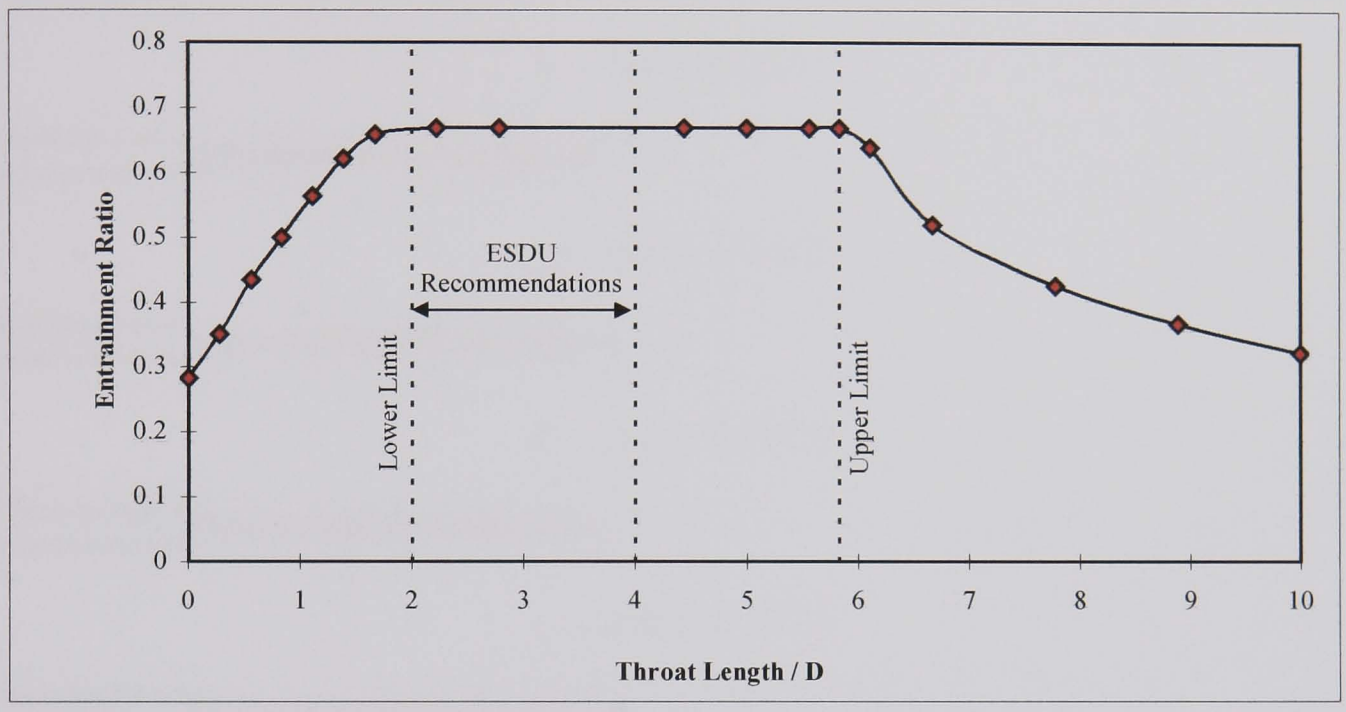

Figure 6.1 – Results of Throat Length Study

The influence of the throat upon ejector performance can be explained through the flow structure within this region. The most important flow characteristic is the extent of the supersonic region within the throat, as this is indicative of the degree of choking, Fig 6.2. It can be seen that as throat length increases, the supersonic region grows in length and diameter. Once the lower limit is reached the supersonic flow has expanded to fill the throat and the ejector is fully choked. Hence ejector performance is optimum at this point. A further increase in throat length initially led to an increase in the extent of the supersonic region, however as the ejector is already fully choked, the entrainment level is not further enhanced. Above the upper limit the length of the throat becomes excessive and the choke collapses. The supersonic region decreases correspondingly.

The influence of the throat upon formation of the choke can be explained through plots of centreline pressure distribution along the ejector, and by referring to the work of Shapiro[45]. Fig 6.3 show selective plots of centreline pressure distribution.

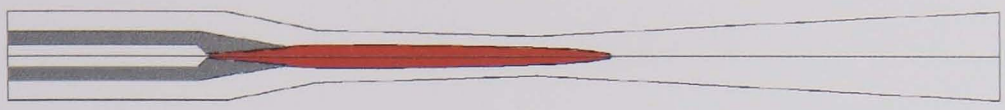

a. – Throat Length = 0mm (0D)

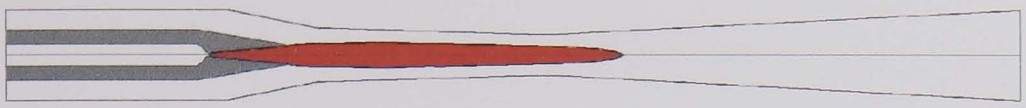

b. – 5mm (0.28D)

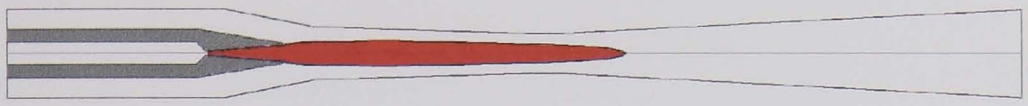

c. – 10mm (0.56D)

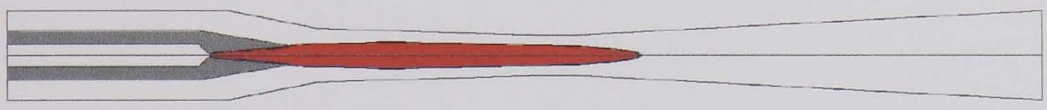

d. – 15mm (0.83D)

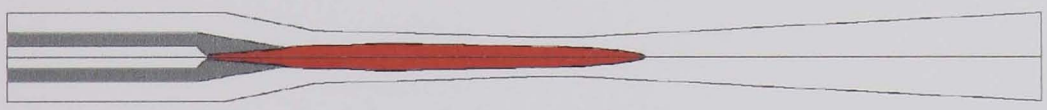

e. – 20mm (1.11D)

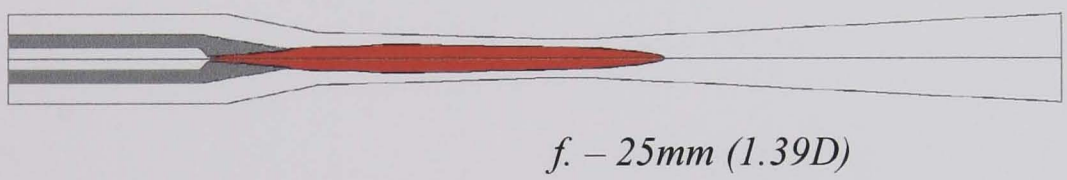

f. – 25mm (1.39D)

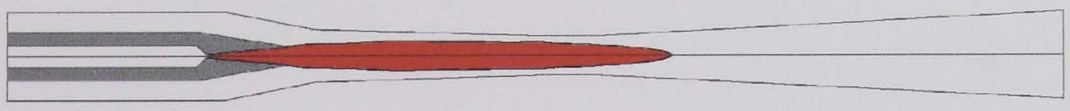

g. – 30mm (1.67D)

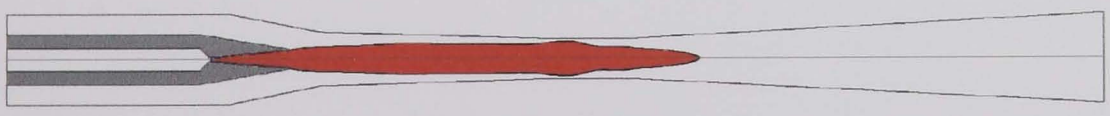

h. – 40mm (2.22D) (current experimental length)

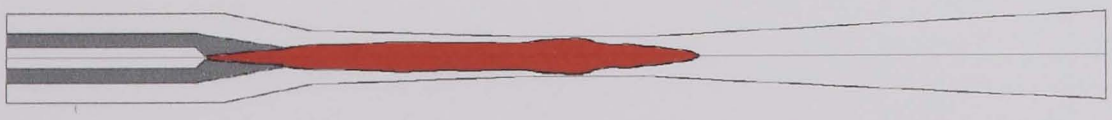

i. – 50mm (2.78D)

Key M > 1

Fig 6.2 (a-i) – Effects Of Throat Length On The Extent Of Supersonic Region Within Ejector

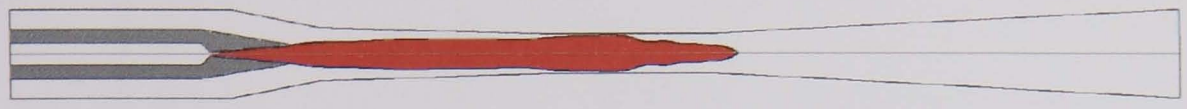

j. – 80mm (4.44D)

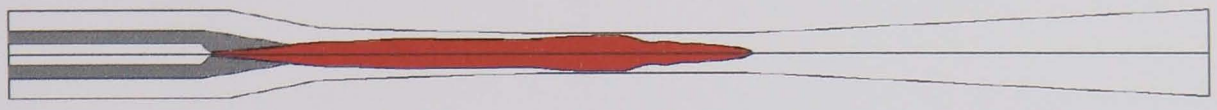

k. – 90mm (5D)

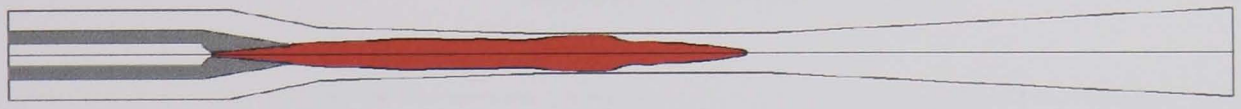

l. – 100mm (5.56D)

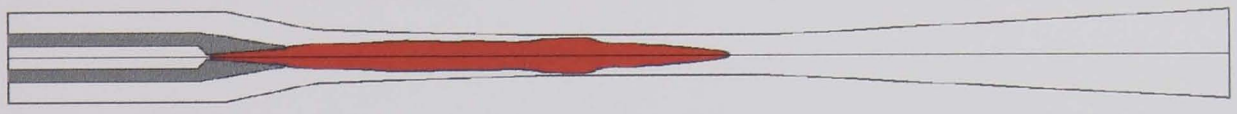

m. – 105mm (5.83D)

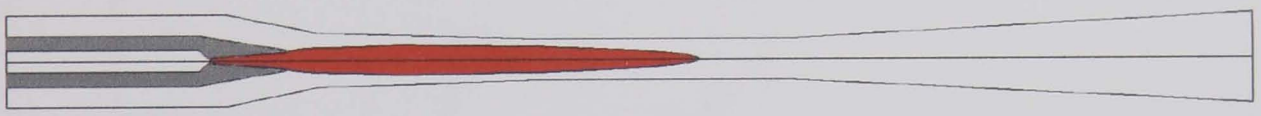

n. – 110mm (6.11D)

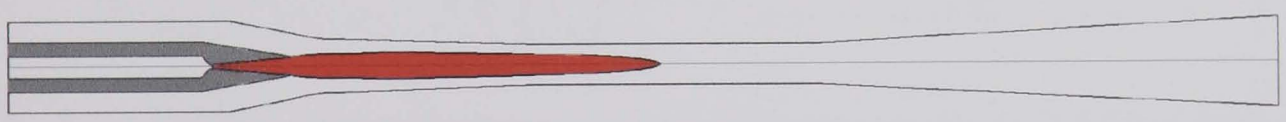

o. – 120mm (6.67D)

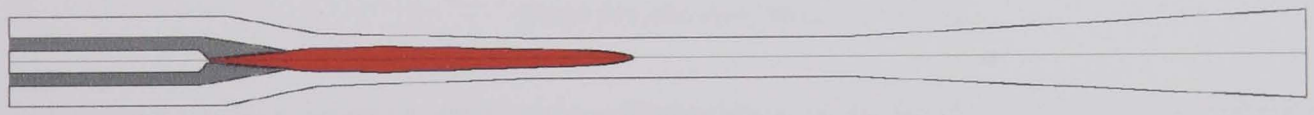

p. – 140mm (7.78D)

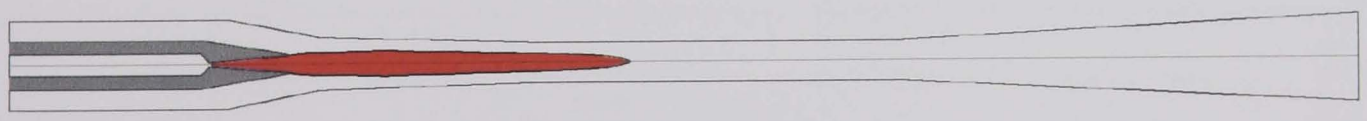

q. – 160mm (8.89D)

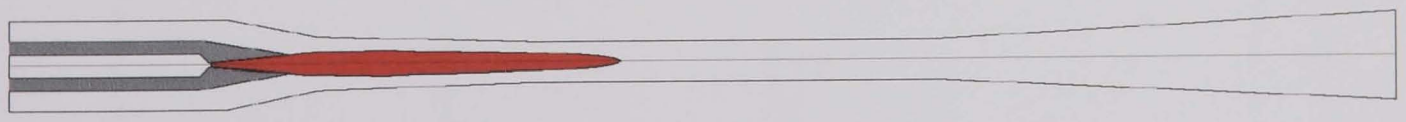

r.– 180mm (10D)

Fig 6.2 (j-r) – Effects Of Throat Length On The Extent Of Supersonic Region Within Ejector

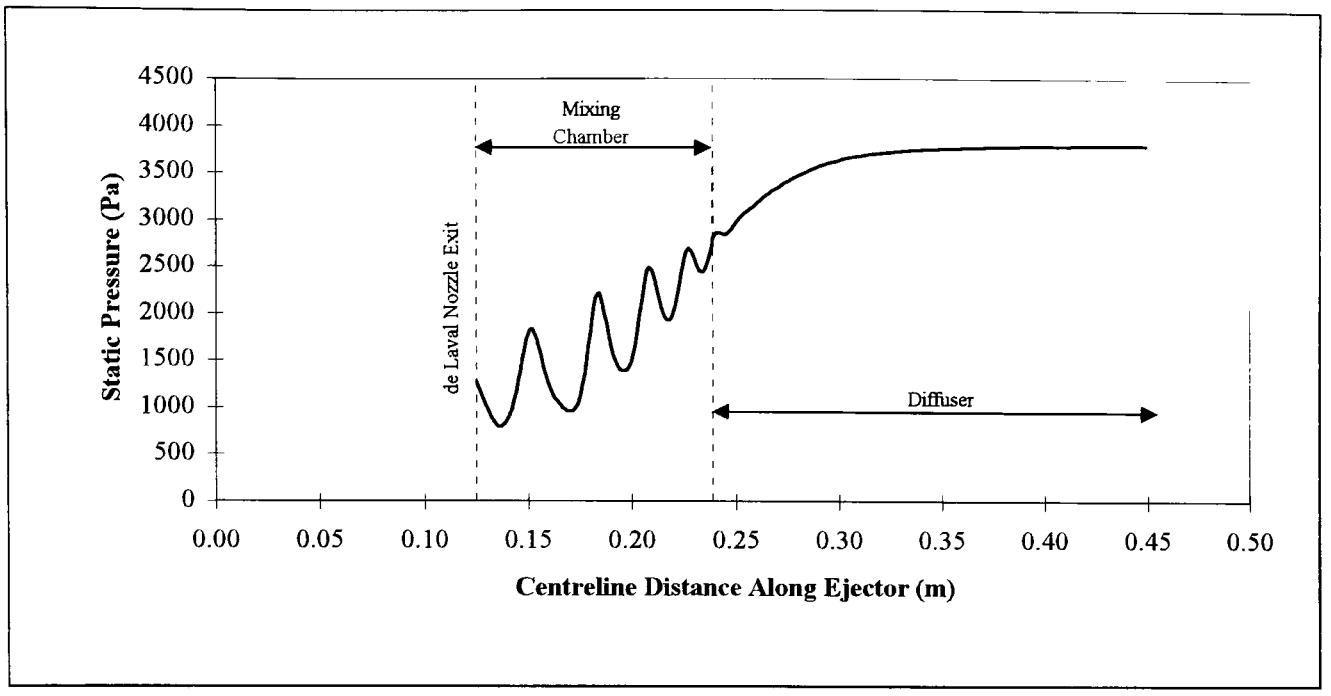

a. - Throat Length = 0mm (0D)

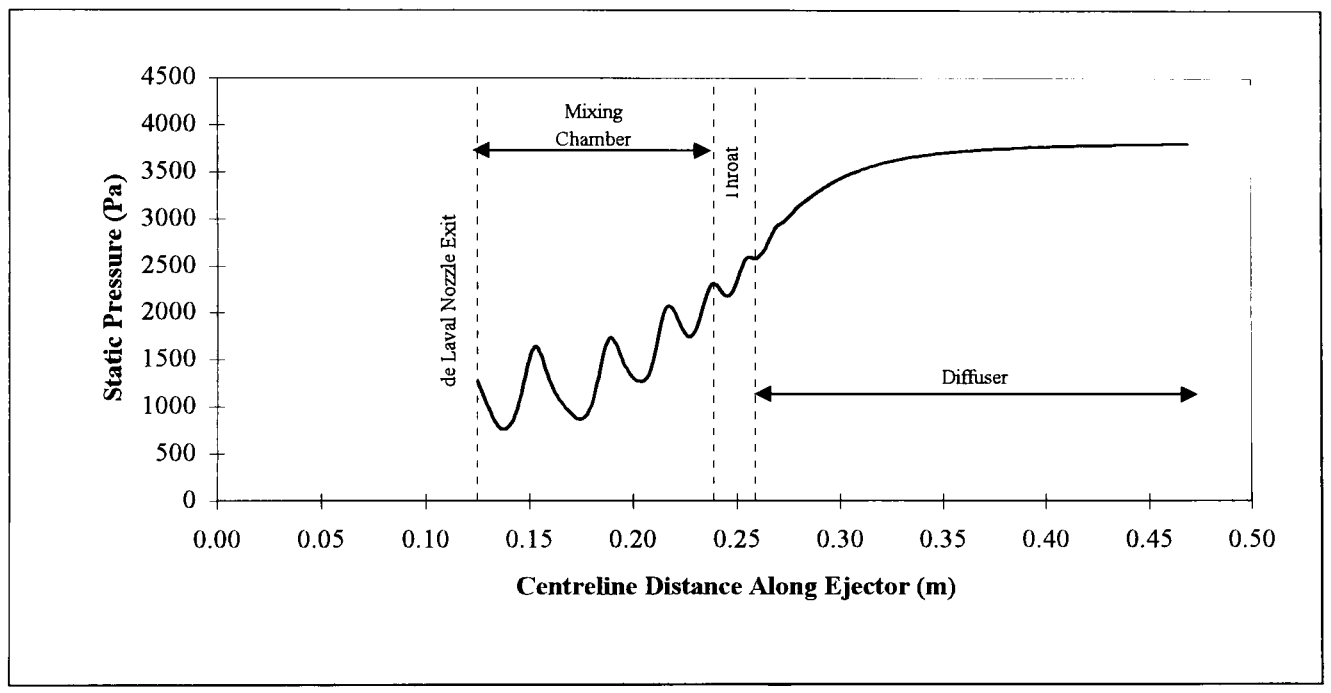

b. - Throat Length = 20mm (1.11D)

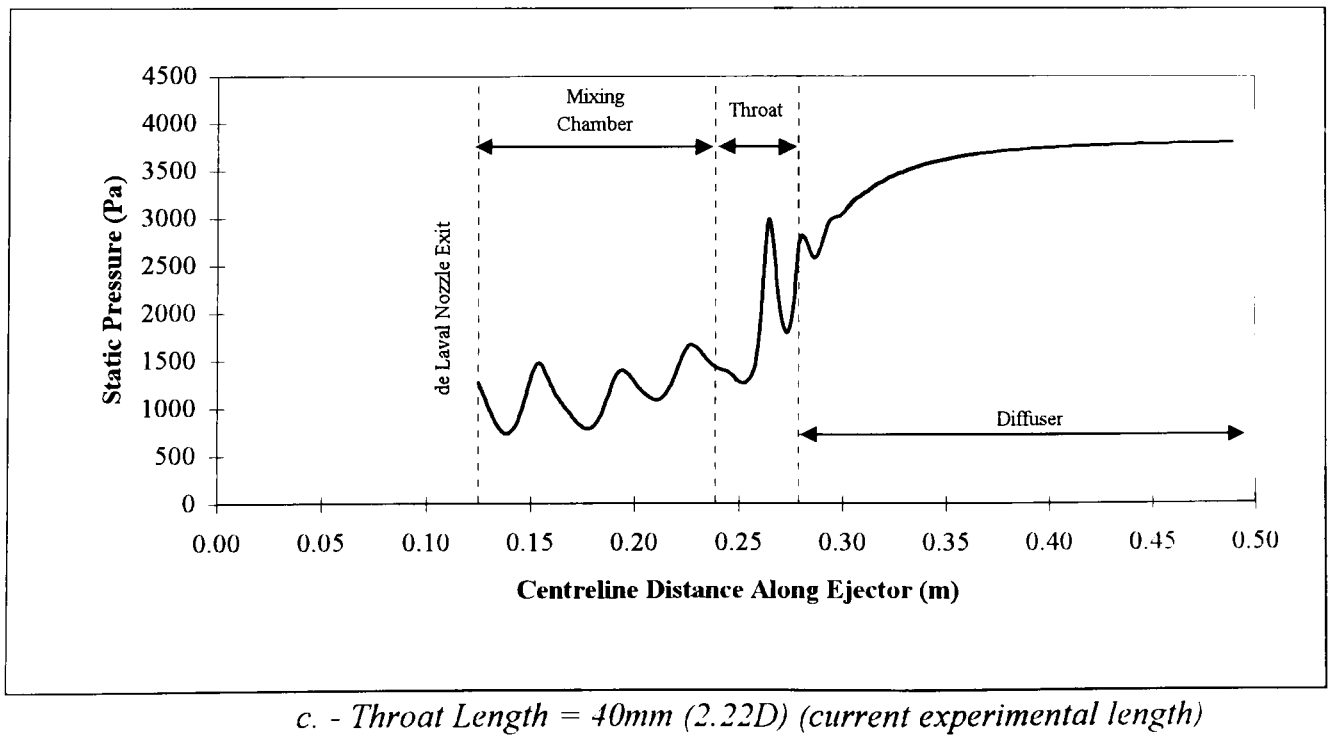

c. - Throat Length = 40mm (2.22D) (current experimental length)

Figure 6.3 (a-c) - Effect Of Throat Length On Centreline Pressure Distribution

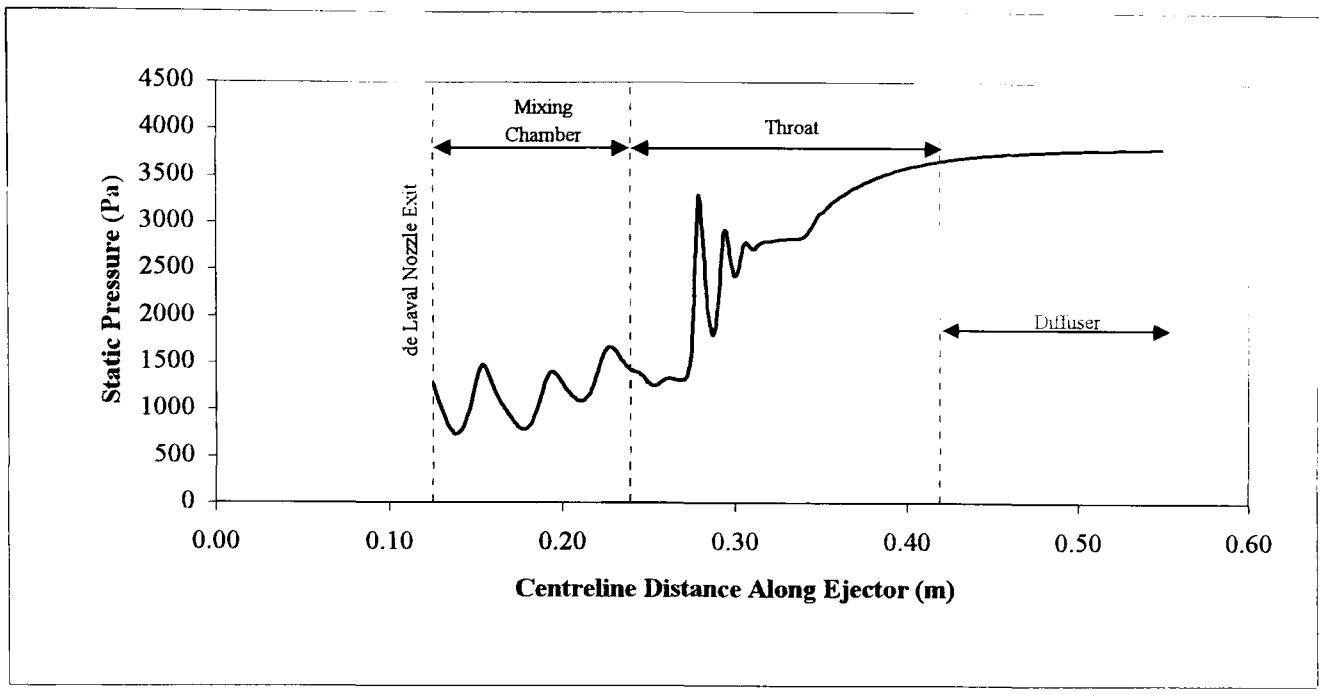

d. - Throat Length = 100mm (5.56D)

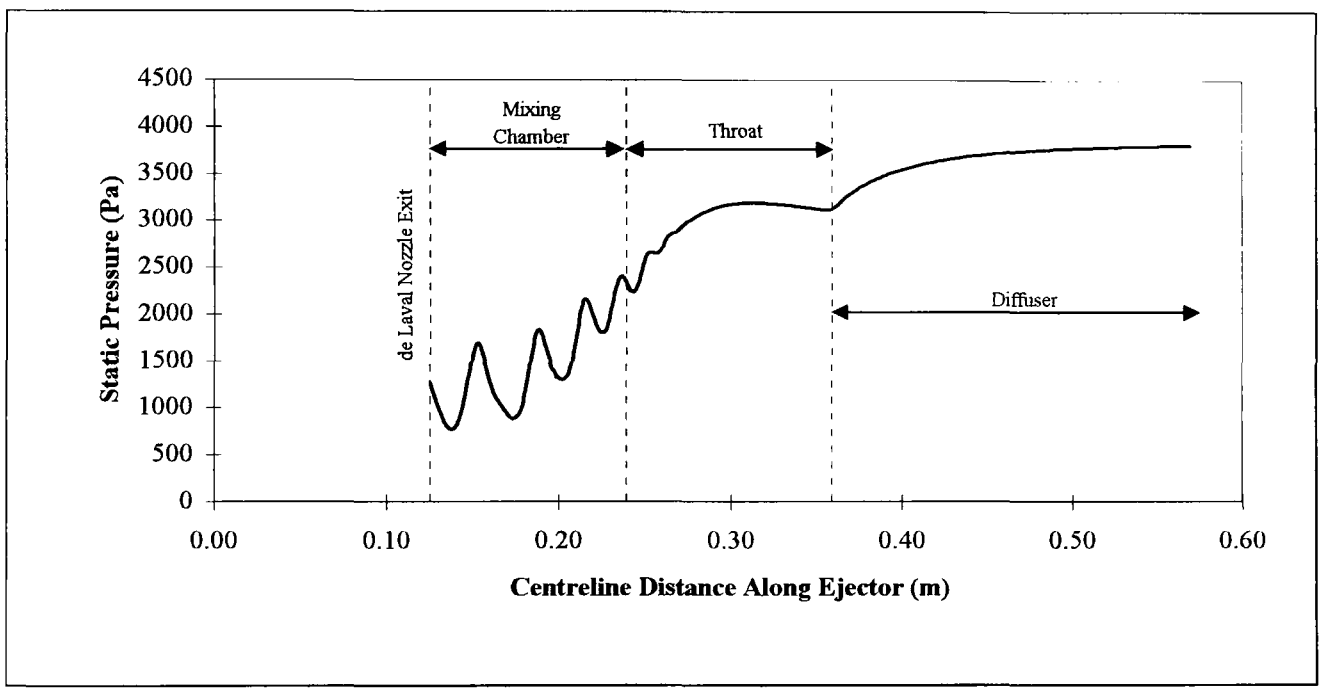

e. - Throat Length = 120mm (6.67D)

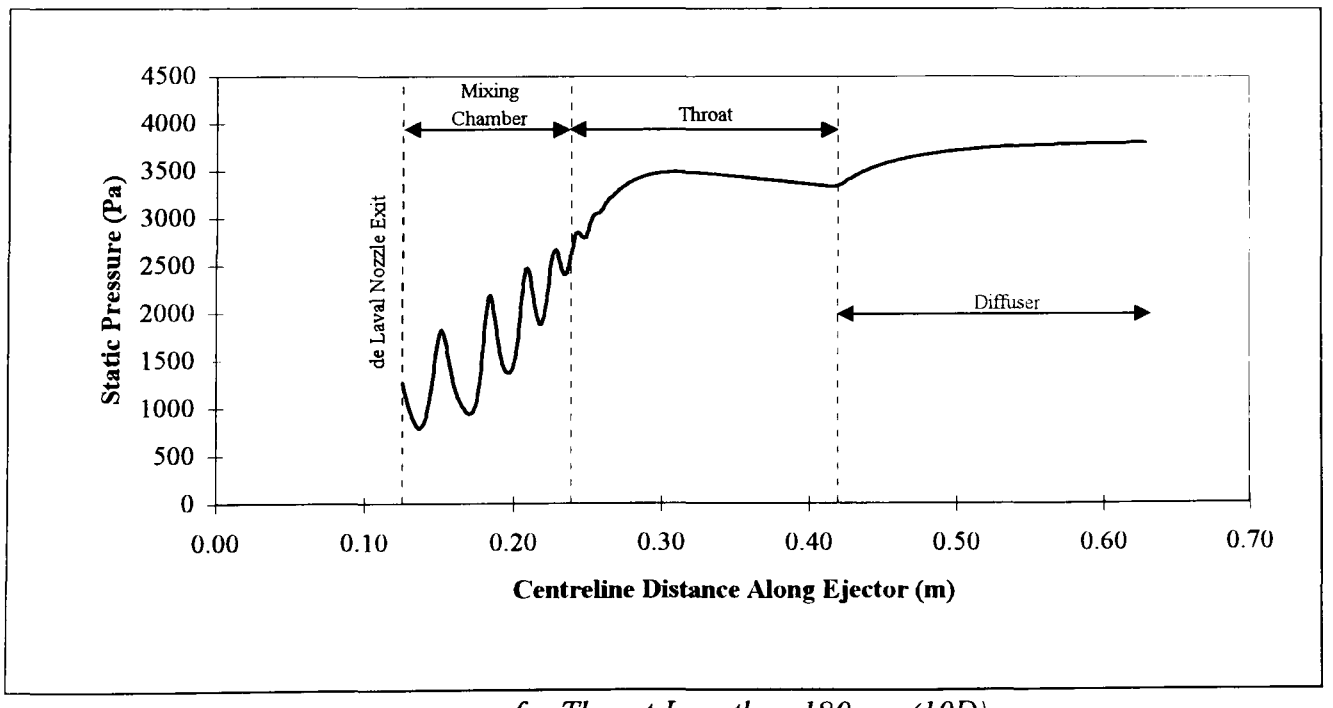

f. - Throat Length = 180mm (10D)

Figure 6.3 (d-f) - Effect Of Throat Length On Centreline Pressure Distribution

The pressure distribution for throats below the lower limit are shown in Fig 6.3a and 6.3b. It can be seen that the flow pressure, although oscillatory due to expansion waves, rises steadily along the mixing chamber and throat. An important operational phenomena is seen to appear within Fig 6.3c and Fig 6.3d for throats of optimum length within the ESDU recommendations. A large pressure spike resides within the ejector throat, followed by a rapid climb in pressure. This spike is indicative of a strong shock within the throat indicating that the throat is fully choked. This is confirmed in Fig 6.2h and Fig 6.2l, the corresponding plots of supersonic flow within the ejector. A normal shock system results as categorised by Shapiro[45], who studied shocks in ducts of constant area, and detailed within Section 2.4.2.

Throats in excess of the upper limit are shown in Fig 6.3e and 6.3f. A pressure loss can be seen to occur within the throat as a result of wall friction. It can be seen that the pressure at the entrance to the throat is higher than that at the exit to the diffuser. This suggests that the pressure rise within the mixing section is not only due to diffuser back pressure, but is also a result of the deceleration of the supersonic stream. Thus the total pressure rise within the mixing section is a combination of diffuser back pressure, and pressure rise due to fluid deceleration.

Shapiro[45] showed that as a duct fed by a supersonic stream is increased in length, a stationary shock within the duct will travel upstream as a direct result of the increasing effect of pipe friction. A similar phenomenon was observed in this study. As the throat length was increased above the upper limit, a frictional pressure loss is noted. The growing frictional effects in the throat cause the extent of the supersonic region/degree of choking to decrease, and the normal shock system disappears.

In comparison failure to provide a throat of sufficient length will also be detrimental, as a certain length is required to cause flow development which leads to the choke and normal shock system. Throat length of the ejector must therefore be carefully chosen to ensure choking. The choke will guarantee that the mixing chamber pressure remains low enough to ensure the occurrence of maximum entrainment.

6.1.2 – Influence of Mixing Chamber Angle

A study into the influence of mixing chamber half angle, ϕ_1, upon the operational performance of constant pressure design ejectors has been conducted. Although the design of the mixing chamber has been the subject of extensive study in constant area ejectors, the angle and thus length of the constant pressure ejector chamber has been particularly neglected. Few studies exist of the influence of the chamber design, and these have generally been for a limited number of designs. This is probably due to the expense of producing a wide selection of chambers. CFD can be used to analyse a wide range of chamber angles for limited cost.

ESDU[3] provide guidelines on the appropriate angle for this section, stating that for a gas-gas ejector, $\phi_1 = 1^o$-10^o. Simulations have been conducted to verify this statement. Mixing chamber half angle has been varied from $\phi_1 = 1^o$-10^o. The current experimental angle of the Eames[5] ejector is $\phi_1 = 1.718^o$ (mixing chamber length, L_m = 100mm).

Results of the study are shown in Fig. 6.4. The results of the mixing chamber angle study indicate that there is no obvious range of ϕ_1 which will guarantee optimum entrainment. This is in contrast to the throat length study where a clearly defined range of throat length would produce maximum entrainment.

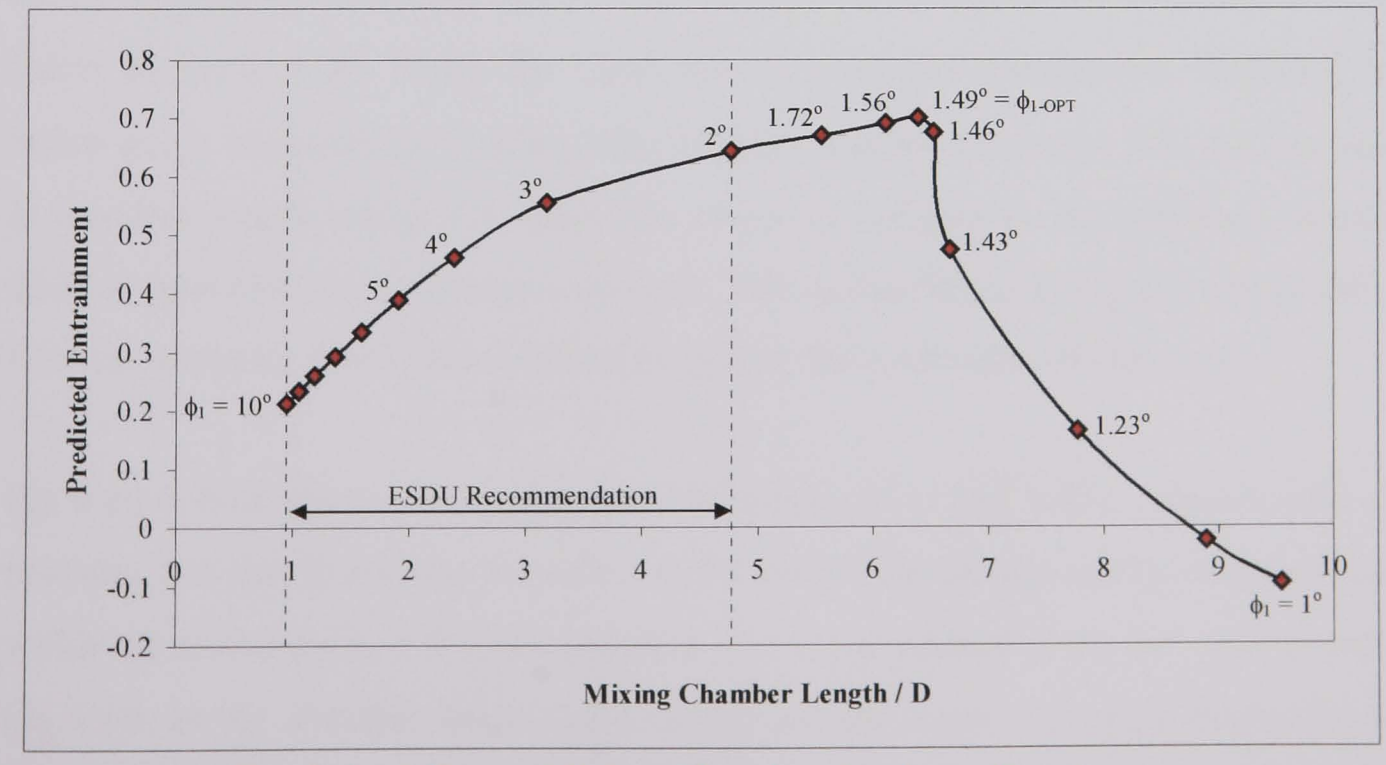

Fig 6.4 – Effect of Mixing Chamber Angle on Entrainment

The study shows that the optimum half angle for the Eames[5] ejector at the modelled operating conditions lies just outside the ESDU[3] recommendations. Optimum half angle, $\phi_{1\text{-OPT}}$, was found to be approximately $\phi_{1\text{-OPT}} = 1.49^{o}$. If the angle is reduced below this value the loss of entrainment is drastic, 114% for a half degree. However the smaller ϕ_1 the longer the chamber is, and for small values of ϕ_1 the increase in chamber length is great. In contrast increasing the angle into the ESDU recommended range results in a gradual loss in entrainment, 67% for increasing ϕ_1 from 2^{o}-10^{o}.

As with the throat study the ESDU recommendations are probably well set, however slightly wide. The benefit of reducing ϕ_1 below 2^{o} is slight, and as has been shown if ϕ_1 is reduced too much detrimental to operational performance. It is likely that the angle of $\phi_{1\text{-OPT}}$, at which entrainment begins to fall, will vary with fluctuations in operating conditions. A value of 2^{o} is probably far enough away from $\phi_{1\text{-OPT}}$ to guarantee an acceptable level of entrainment if conditions do fluctuate. The wide range of recommended angle is most likely set to cover the wide range of possible ejector designs and conditions which will produce optimum entrainment.

The influence of ϕ_1 upon the supersonic region, and choking within the ejector can be seen in Fig 6.5. A reduction in ϕ_1 below 1.5^{o} or an increase above 2^{o} causes the choke to collapse within the throat. The collapse of the choke for a reduction in ϕ_1 below $\phi_{1\text{-OPT}}$ is rapid, hence the rapid loss in predicted entrainment. Reducing ϕ_1 below $\phi_{1\text{-OPT}}$ increases the length of the mixing chamber markedly. It is this increase in chamber length which will cause the choke to collapse as the influence of wall friction upon the flow is greatly enhanced. This is confirmed in Fig 6.6 which show the axial pressure distribution within the ejector, for a selection of chambers.

Fig 6.6a & 6.6b show mixing chamber half angles of 1^{o} and 1.432^{o}, respectively. A pressure loss due to friction is evident at the end of the ejector mixing chamber and within the throat for $\phi_1 = 1^{o}$. This pressure loss is not evident in the $\phi_1 = 1.432^{o}$ plot, Fig 6.6b, as the chamber length has reduced and the supersonic jet is beginning to move into the throat where a choke will form. However as the jet is not sufficiently advanced within the throat the choke does not form. Figs 6.6c & 6.6d

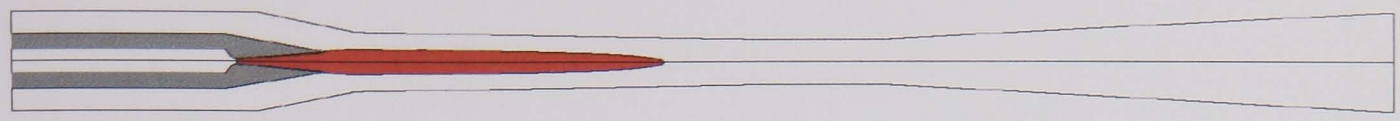

a. $-\phi_1 = 1^o$

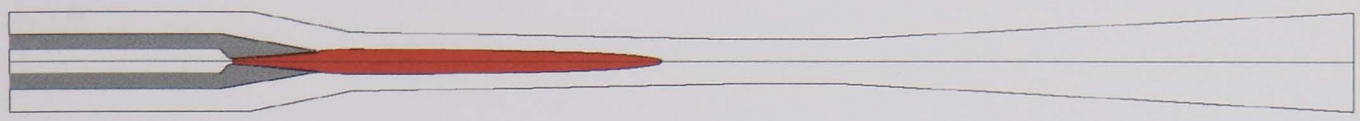

b. $- 1.07^o$

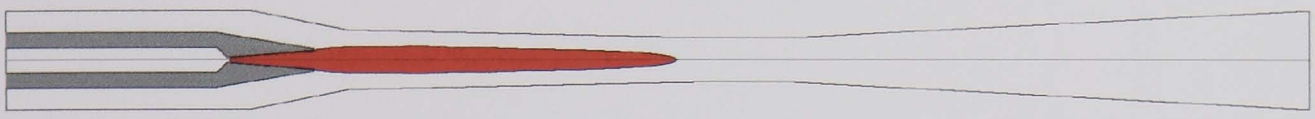

c. $- 1.228^o$

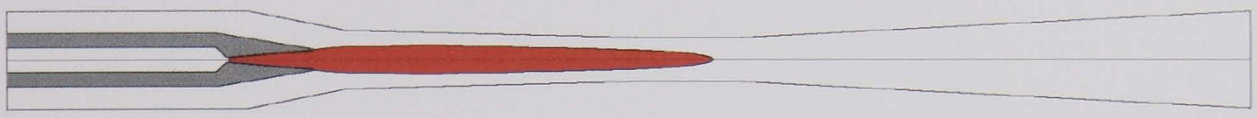

d. $- 1.432^o$

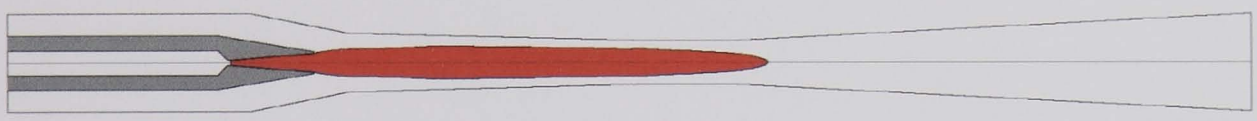

e. $- 1.463^o$

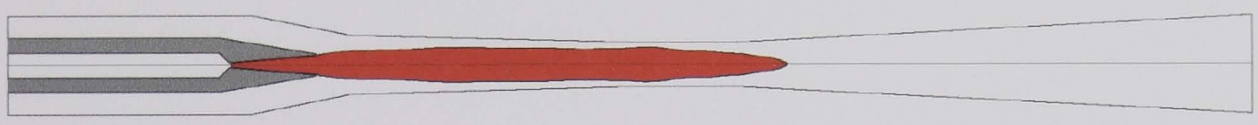

f. $- 1.494^o$

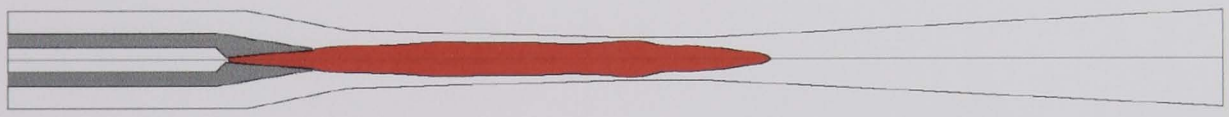

g. $- 1.562^o$

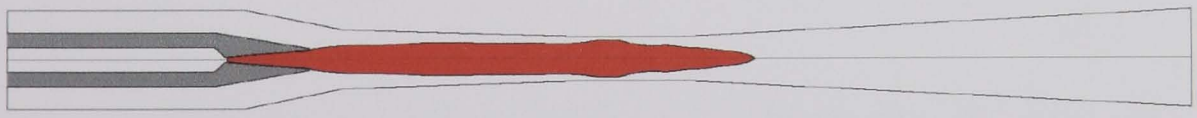

h. $- 1.718^o$ *(current experimental angle)*

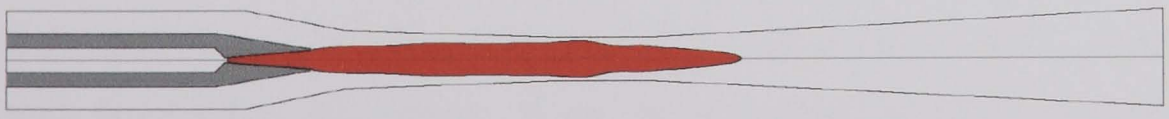

i. $- 2^o$

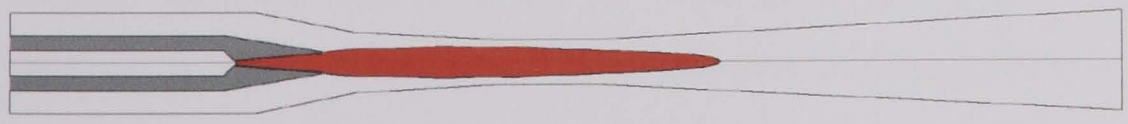

j. $- 3^o$

Key M > 1

Fig 6.5 (a-j) – Effect of ϕ_1 Upon Supersonic Region Within Ejector

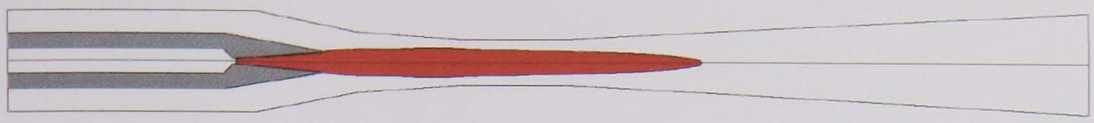

k. – 4^o

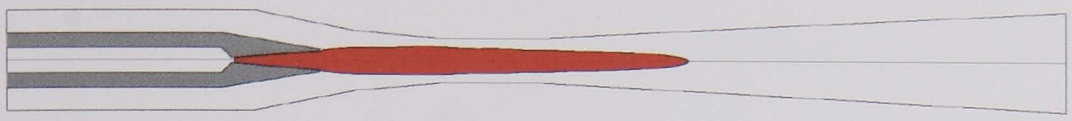

l. – 5^o

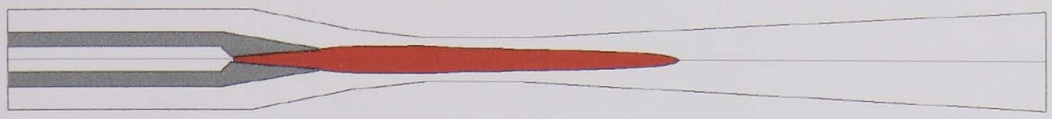

m. – 6^o

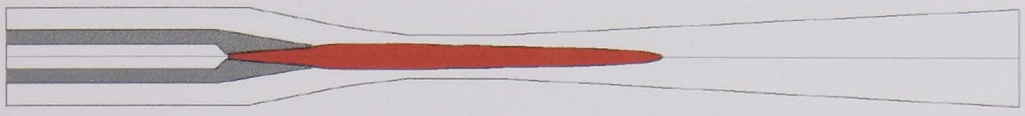

n. – 7^o

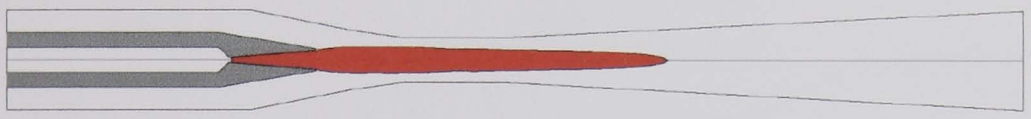

o. – 8^o

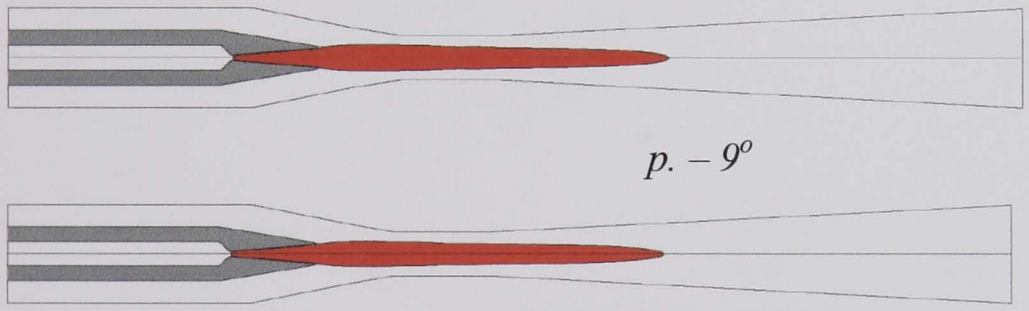

p. – 9^o

q. – 10^o

Key M > 1

Fig 6.5 (l-q) – Effect of ϕ_1 Upon Supersonic Region Within Ejector

show the pressure distribution for chambers with a choked throat. Entrainment is at a high level when this occurs. It can be seen that the pressure within the mixing section, although oscillating as the supersonic jet barrels, remains essentially constant. A normal shock system[45] stands within the ejector throat.

When $\phi_1 > 2^o$ the choke collapses and entrainment falls gradually, Figs 6.6e and 6.6f show the pressure distributions for $\phi_1 = 5^o$ & 10^o respectively. Pressure rises along the mixing chamber and continues to do so throughout the throat. Although the supersonic jet passes through the throat, a choke does not form, hence no shock system is observed within the pressure plots.

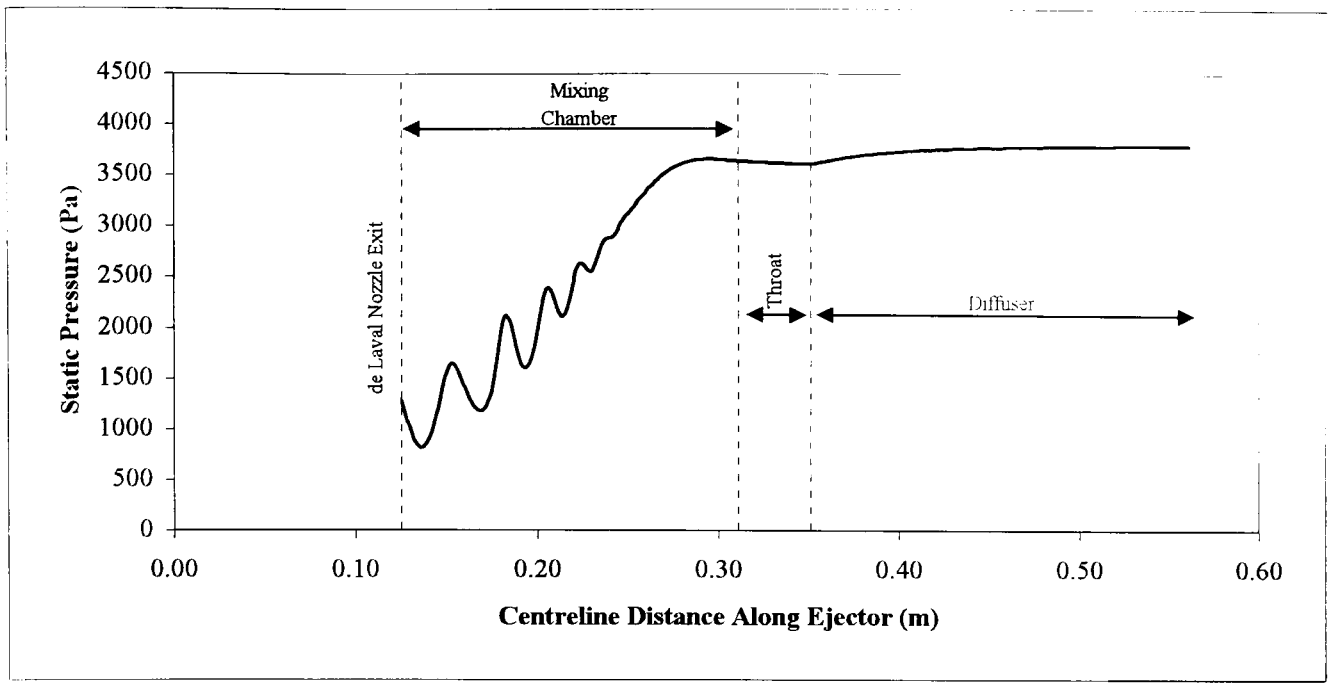

a. - Mixing Chamber Half Angle = 1°

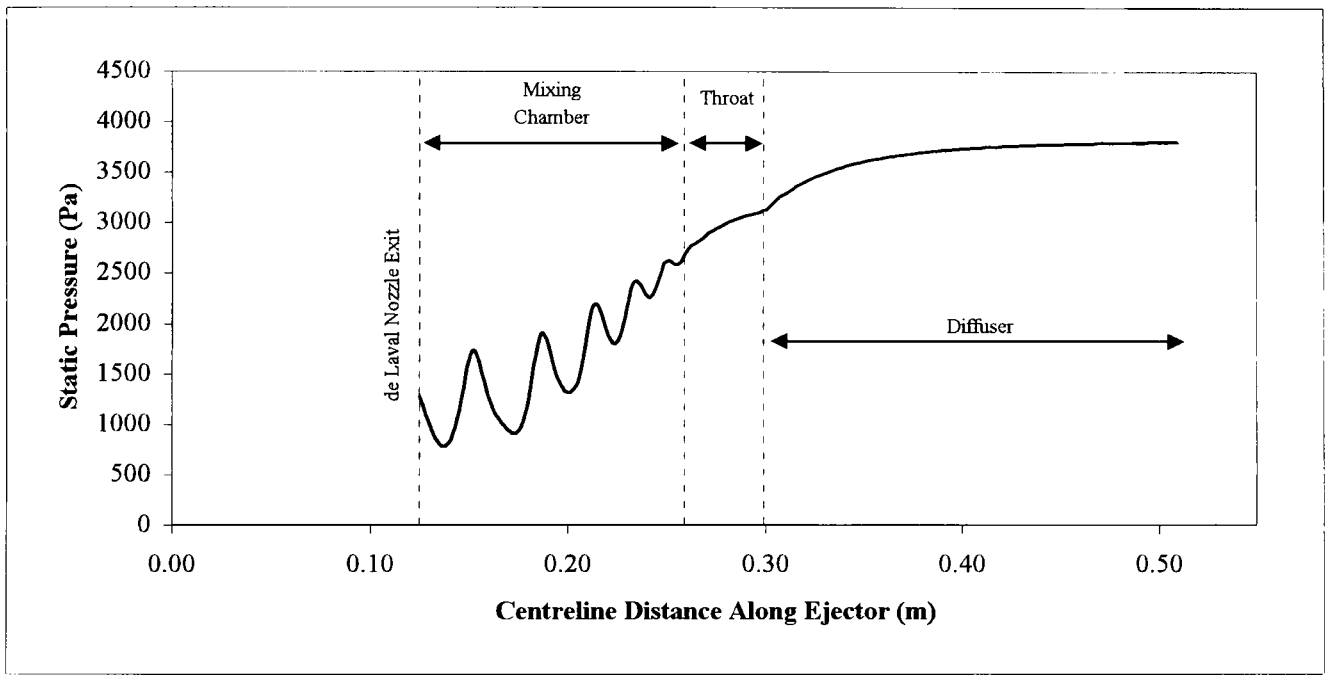

b. - Mixing Chamber Half Angle = 1.432°

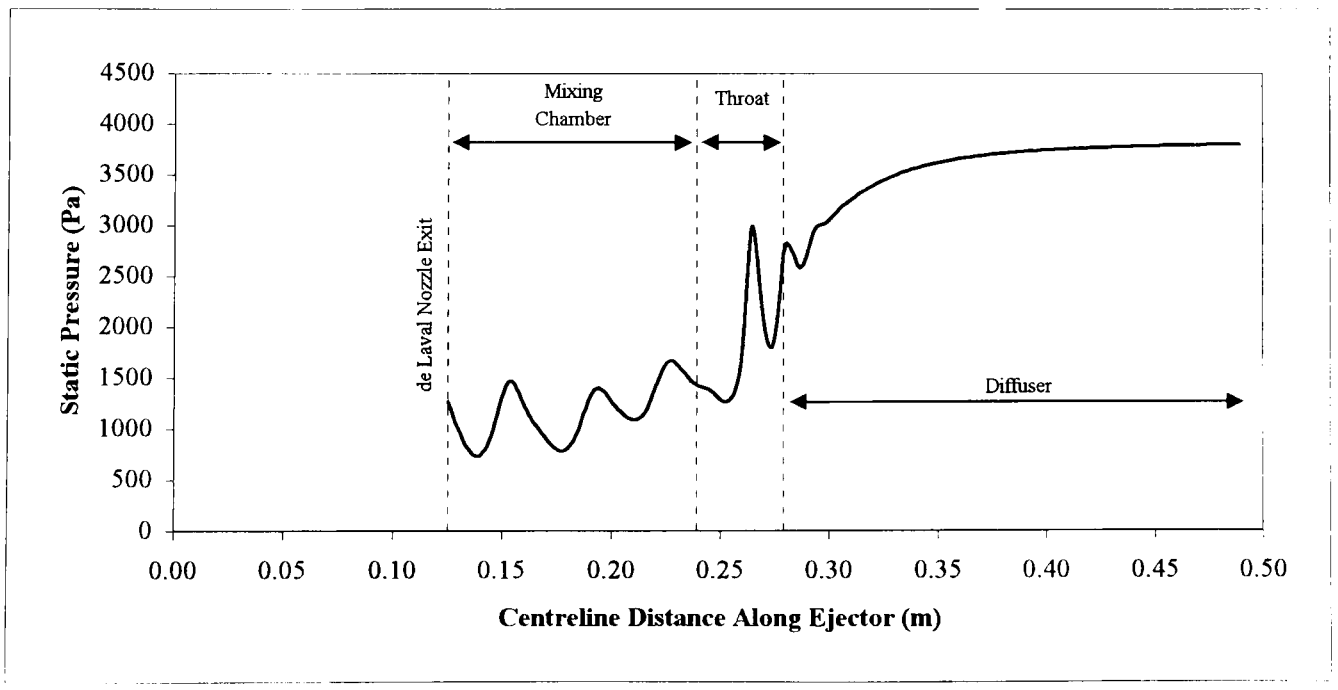

c. - Mixing Chamber Half Angle = 1.718°
(current experimental angle)

Figure 6.6 (a-c) - Effect Of ϕ_1 On Centreline Pressure Distribution

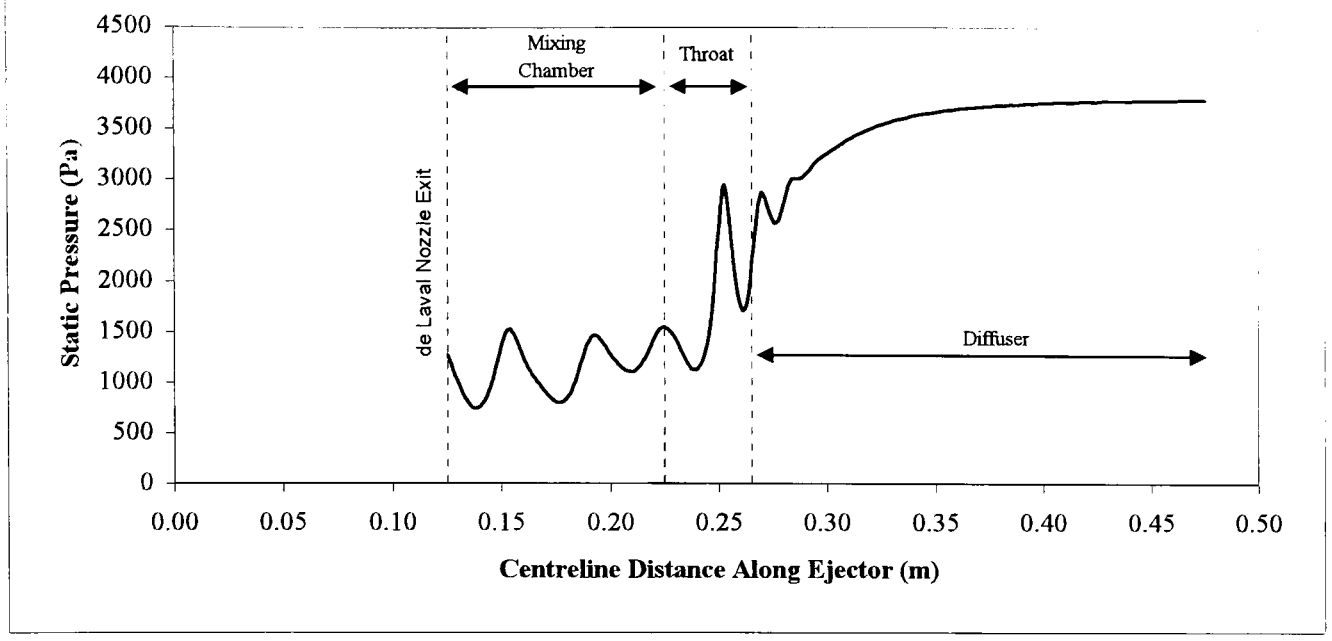

d. - Mixing Chamber Half Angle = 2°

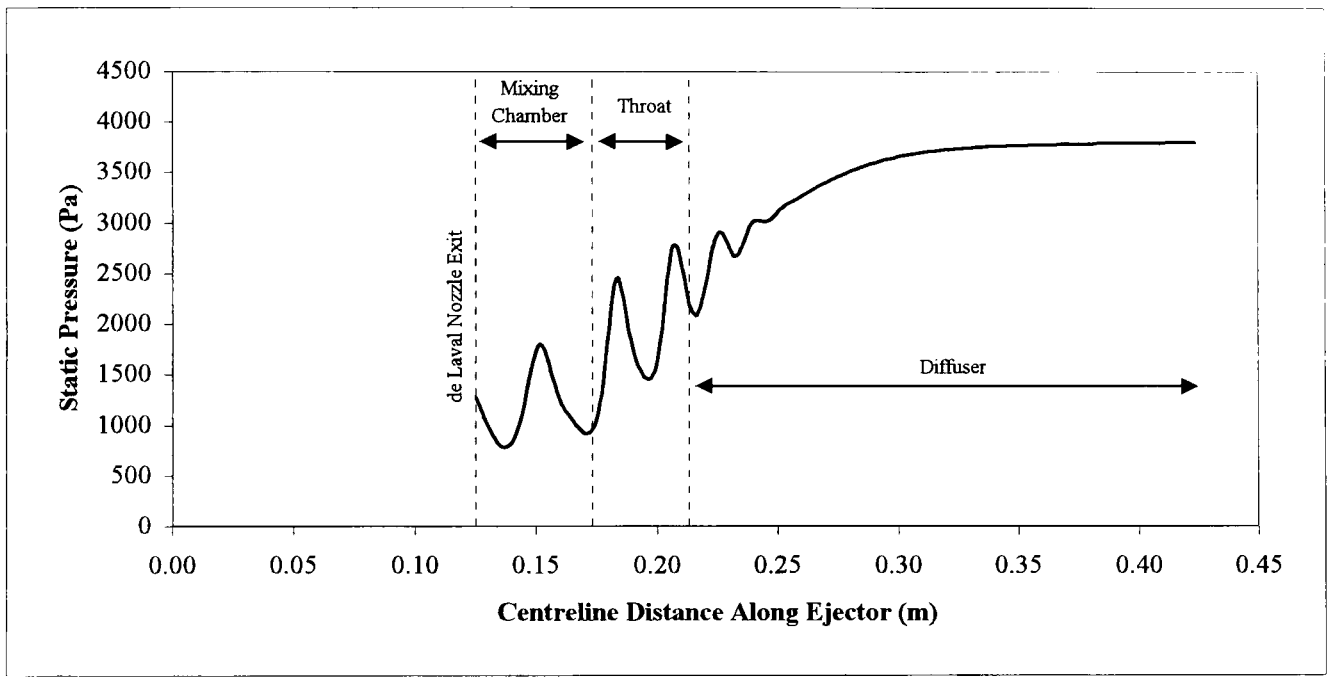

e. - Mixing Chamber Half Angle = 5°

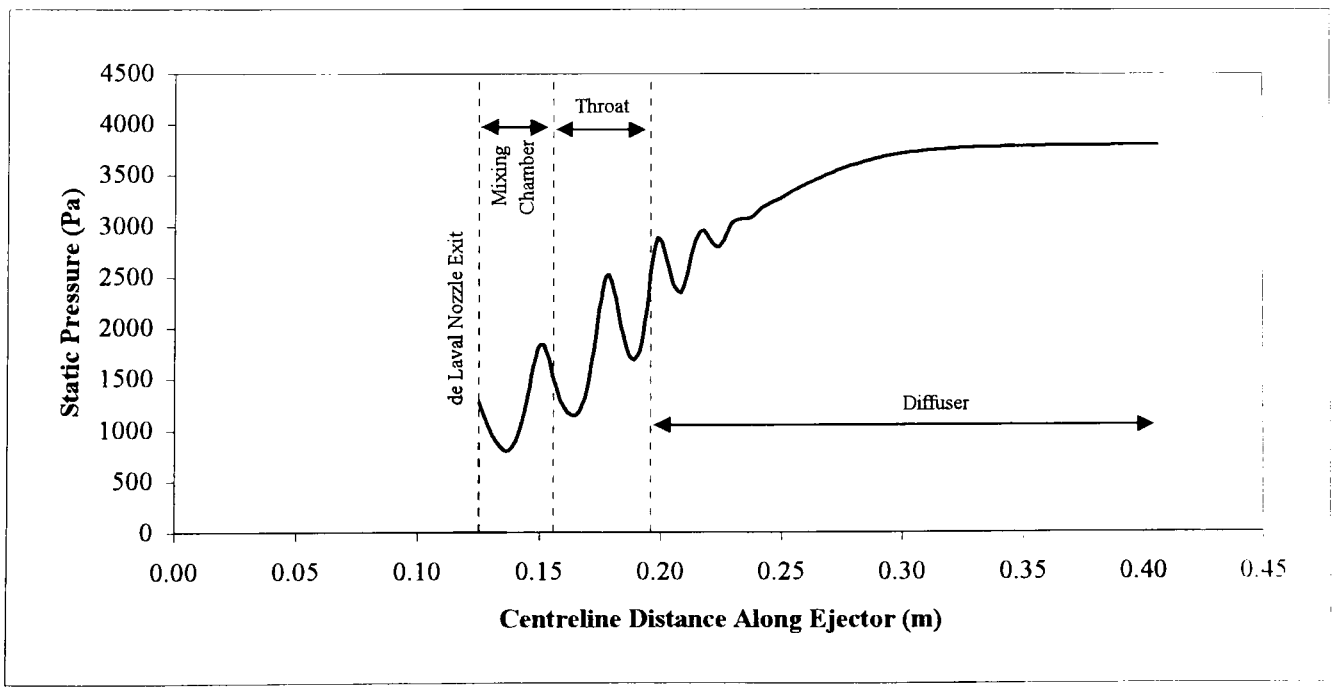

f. - Mixing Chamber Half Angle = 10°

Figure 6.6 (d-f) - Effect Of ϕ_1 On Centreline Pressure Distribution

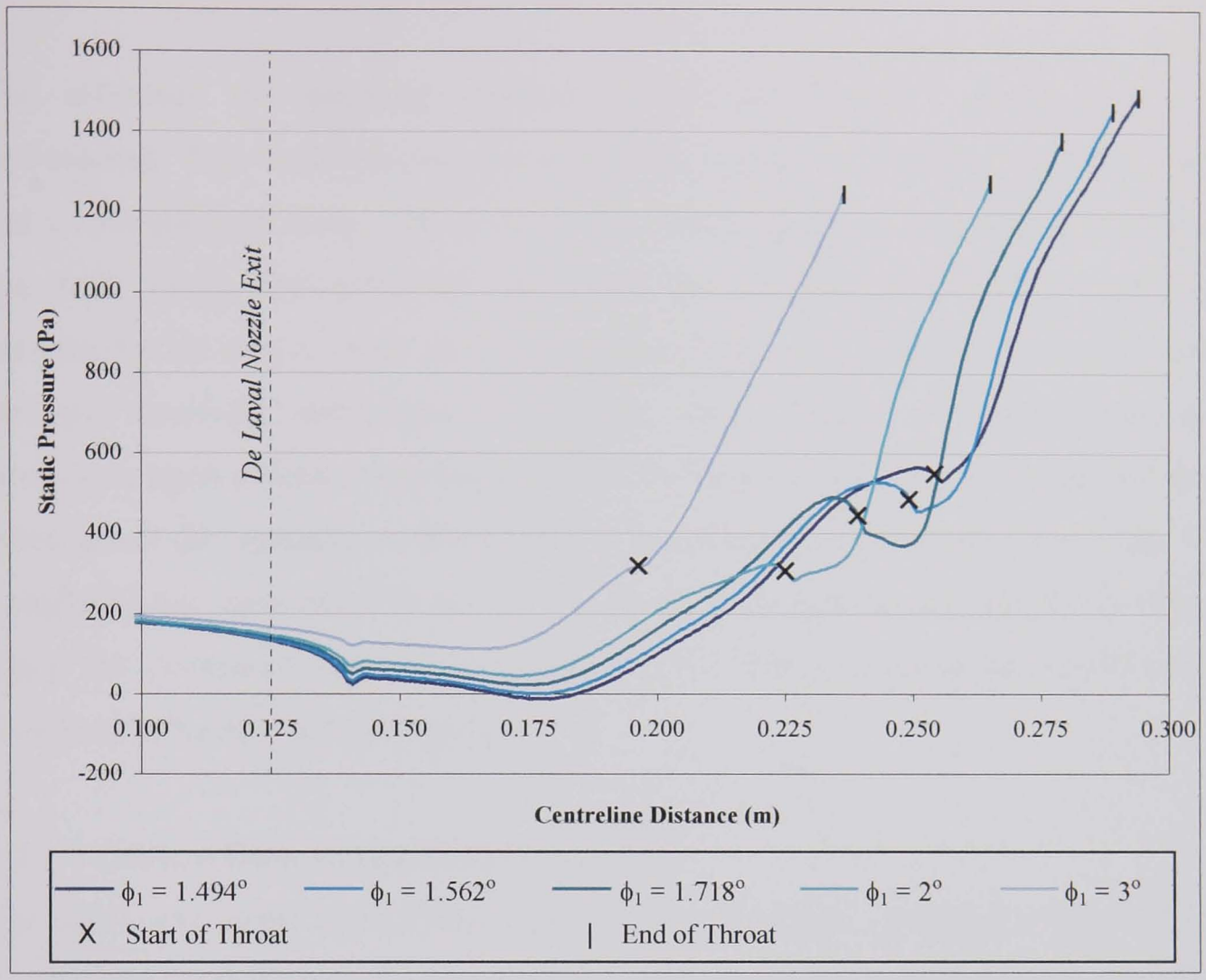

Figure 6.7 – Static Pressure Distribution Along Mixing Chamber And Throat Walls

The collapse of the choke when $\phi_1 > 2^o$ can be explained by studying the pressure distribution within the mixing chamber whilst the throat is choked as ϕ_1 increases. Fig 6.7 shows static pressure along the mixing chamber and throat walls. As ϕ_1 is increased the pressure within the mixing chamber can be seen to rise. The velocity and thus momentum of the fluid surrounding and entrained into the motive jet is reduced. When $\phi_1 > 2$ the surrounding fluid has insufficient momentum to attain sonic velocities and the jet width does not fill the throat. The jet therefore passes straight through the throat without the formation of a choke. However as there is a core of supersonic fluid passing through the throat the decrease in entrainment is not as abrupt as when ϕ_1 is reduced.

Mixing chamber half angle should be carefully chosen. If ϕ_1 is too large frictional affects become excessive. Increasing ϕ_1 increases mixing chamber pressure preventing the formation of a choke.

6.2 – Operating Condition Studies

The influence of operating conditions upon the Eames[5] ejector has been investigated. Two studies have been performed, a critical operating condition study, and a low pressure study. The aims of the critical operating conditions study were two fold. Firstly the numerical set up of the coupled solver, which had been optimised with only a single set of operating conditions could be observed at other settings. Secondly and more importantly the influence of current operating conditions upon ejector performance could be investigated. The low pressure study investigated the operation of the ejector at evaporator temperatures lower than 5°C. Computational mesh Msh009 was used in these investigations and adaptively refined using the procedure outlined in Section 5.7.2. The optimised numerical model described in Section 5.8 was applied.

6.2.1 – Critical Operating Conditions Study

The study was based upon fifteen separate sets of critical operating conditions, see Section 2.4.2, taken from the experimental work of Eames et al[5]. Details of applied boundary conditions can be found in Table 6.3, and physical properties in Appendix D, Table D.2. Results of the study are presented within Table 6.3 and Fig. 6.8. The numerical model had been optimised with evaporator and boiler temperatures of 10°C and 120°C respectively, simulation Nº 1 in Table 6.3. This set of conditions produced a predicted ejector performance extremely close to experiment. Simulations of the ejector at other sets of operating conditions produced results of varying agreement with experiment.

Setting an evaporator temperature of 10°C within the simulations yielded the closest results to experiment. As the evaporator temperature was reduced the extent to which the simulations over predict the operational performance increased. This was due to an under prediction in the rate at which the supersonic jet spreads within the mixing chamber. It is hypothesised that this may be related to either the axisymmetric flow assumptions, or the fixed thermal boundary conditions applied at the walls. A fixed temperature of 10°C was imposed at all wall boundaries, in all simulations. This may have produced a slight rise in the pressure of the secondary stream flowing from the

evaporator. However it is believed that any discrepancies between the computational and experimental results will fall within experimental error bar.

Nº	Temperature (°C)			Pressure (Pa)	R_m	COP_R	
	Evaporator	Boiler	Condenser	Condenser	CFD	CFD	Experiment[5]
1	10	120	28.3	3800	0.630	0.585	0.586
2		125	30.0	4200	0.559	0.518	0.537
3		130	31.9	4700	0.489	0.452	0.473
4		135	34.0	5300	0.425	0.393	0.389
5		140	36.3	6000	0.366	0.335	0.309
6	7.5	120	27.3	3600	0.555	0.514	0.500
7		125	29.5	4100	0.491	0.453	0.418
8		130	31.5	4600	0.427	0.393	0.355
9		135	33.4	5100	0.356	0.328	0.296
10		140	35.3	5700	0.291	0.266	0.233
11	5	120	26.5	3400	0.489	0.452	0.404
12		125	27.8	3700	0.417	0.385	0.344
13		130	30.8	4400	0.345	0.317	0.276
14		135	33.4	5100	0.279	0.257	0.251
15		140	34.4	5400	0.231	0.211	0.177

Table 6.3 - Results of Operating Conditions Study

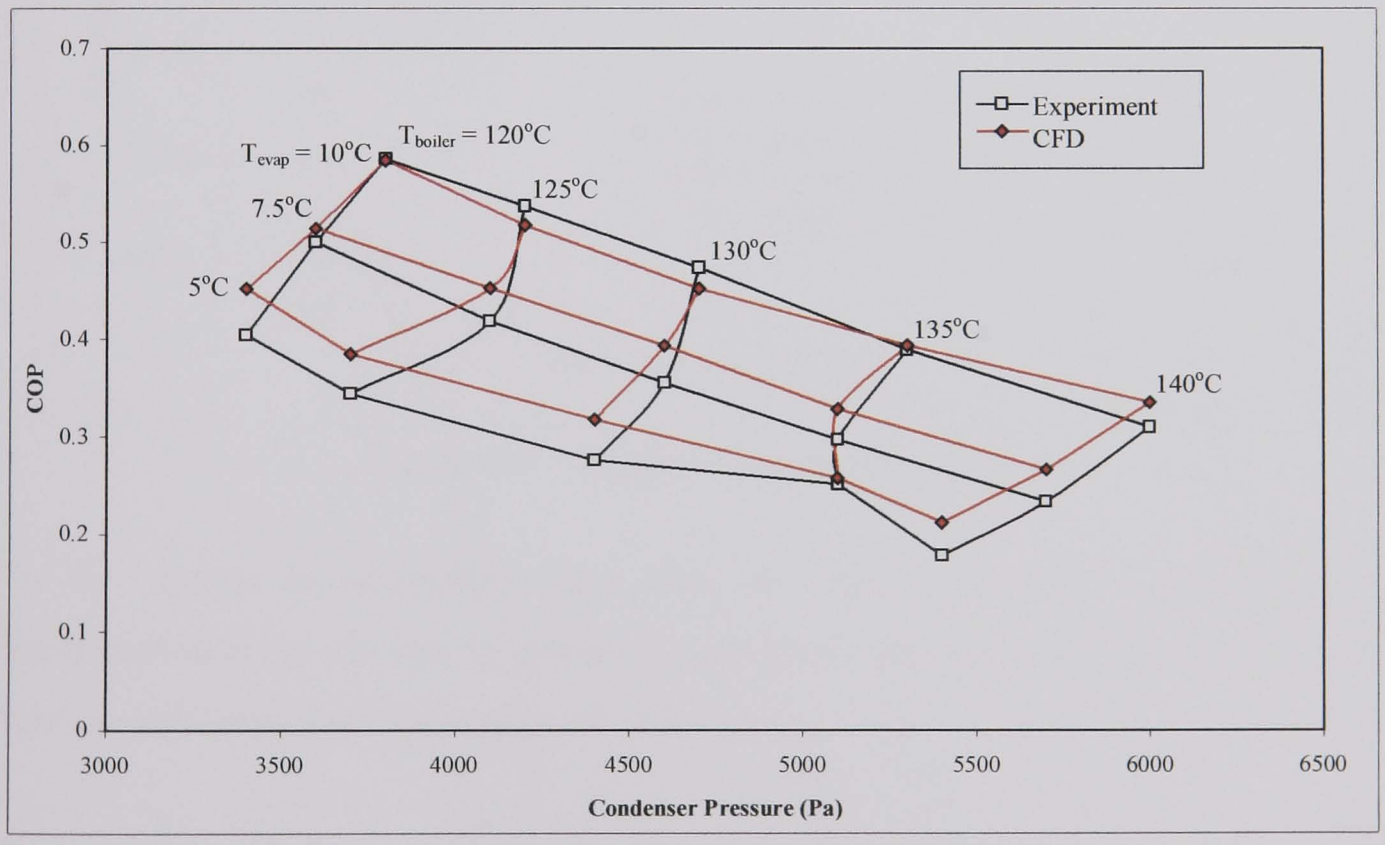

Figure 6.8 - Results of Operating Conditions Study

It can be clearly seen from Fig 6.8 that an increase in boiler temperature or decrease in evaporator temperature will lead to a fall in entrainment and thus predicted COP_R. Plots of mass flow rate through the primary and secondary flow inlets however prove interesting, Fig 6.9. It is clear that an increase in boiler temperature has little influence upon the induced flow from the evaporator. At evaporator temperatures of

10°C and 7.5°C a slight rise in secondary mass flow can be observed for increasing boiler temperature. However the effect is short lived and once boiler temperature is raised above 130°C the secondary mass flow rate begins to fall. An increase in boiler temperature for a fixed evaporator temperature of 5°C has no beneficial influence upon the level of induced flow.

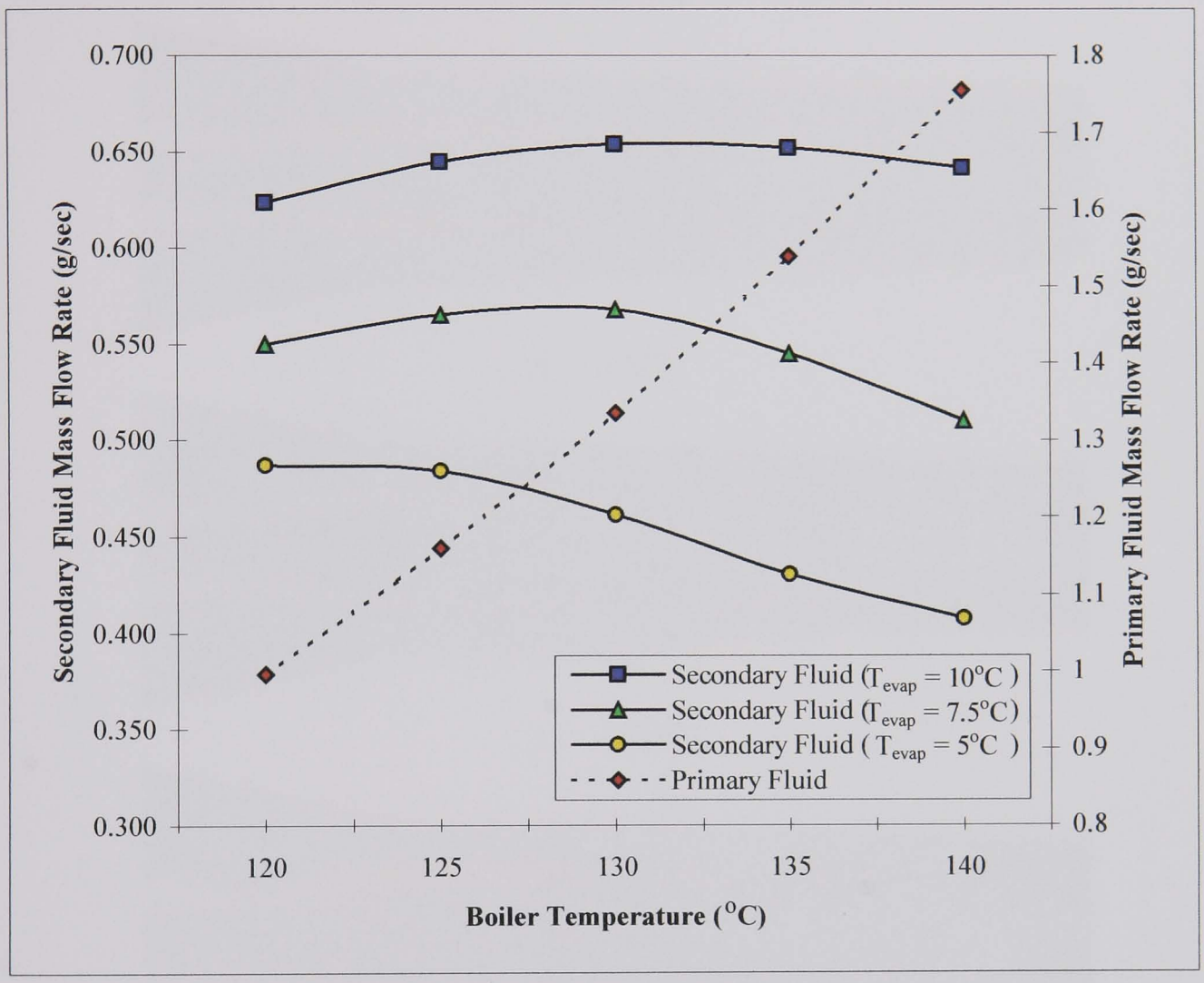

Figure 6.9 – Predicted Mass Flow Rates

As the change in secondary mass flow for increasing boiler temperature is disproportionate to the rise in primary mass flow, any potential benefits are lost. Thus overall ejector performance will fall.

Figs. 6.10 – 6.12 show contour plots of strain rate, see Section 4.6.1, which can be used to identify key flow structure within the mixing chamber of the supersonic ejector. The shear layer, boundary layers, and embedded shock cell structure within the supersonic jet, can all be identified. It can be seen that as the boiler temperature is increased the strength of the shock structure within the flow grows. The expansion fans visible at the nozzle exit increase in strength, showing that the nozzle is becoming increasingly under-expanded in relation to the mixing chamber back

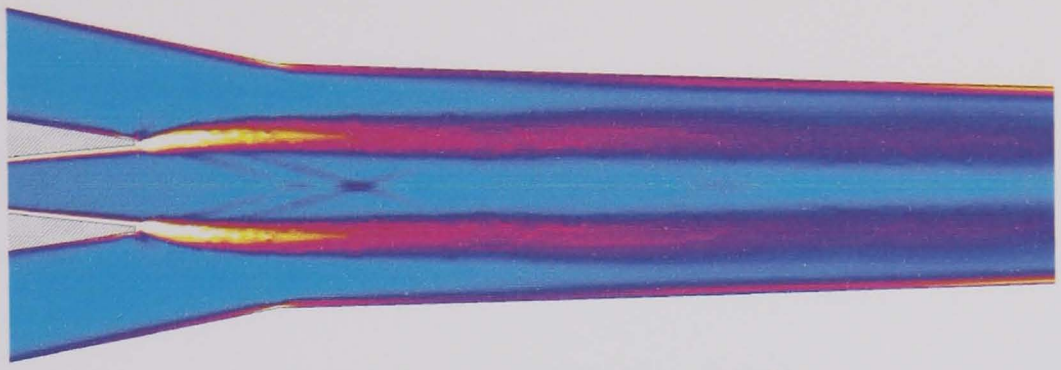

a. – Boiler Temperature = 120°C

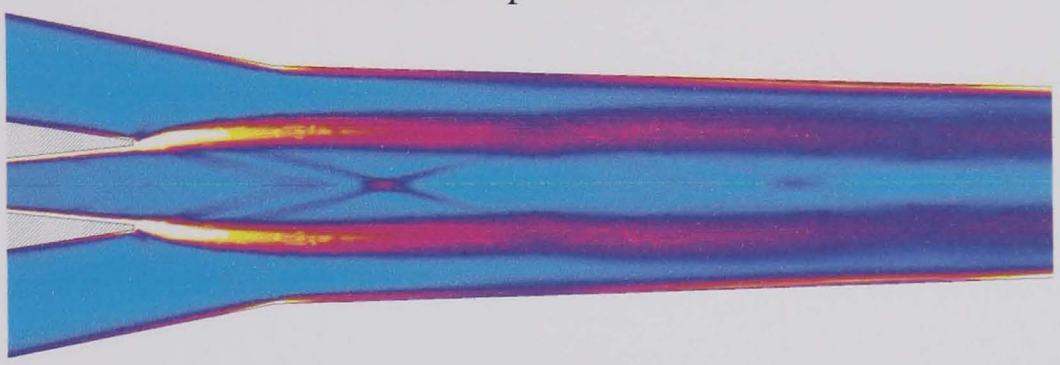

b. – 125°C

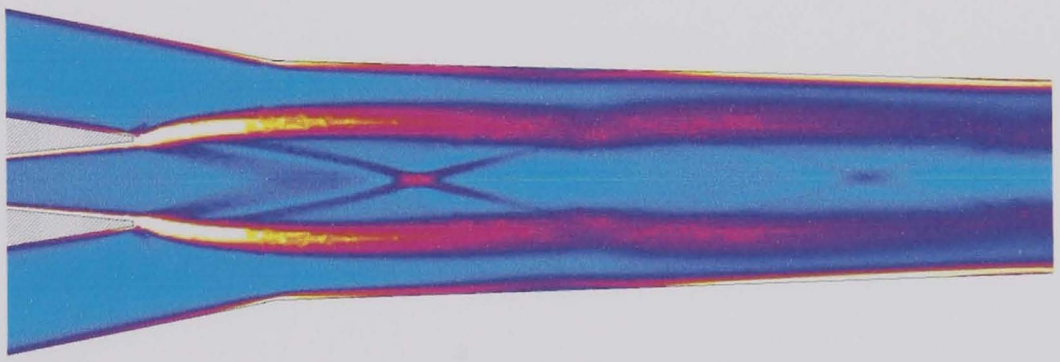

c. – 130°C

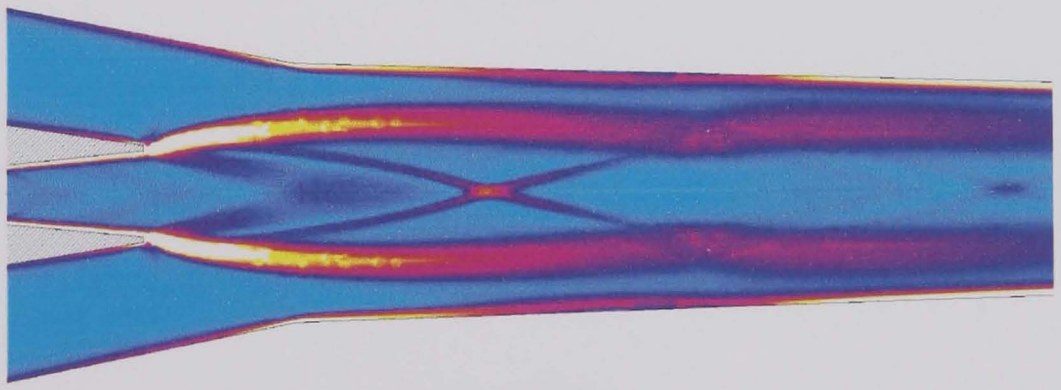

d. – 135°C

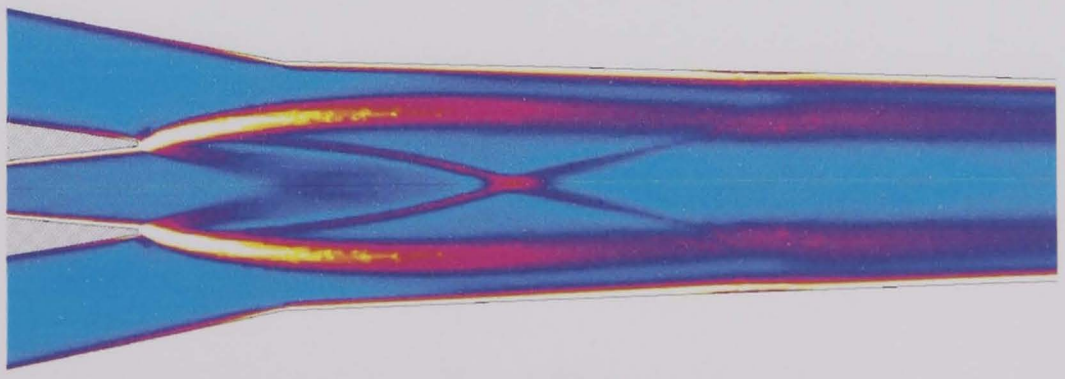

e. – 140°C

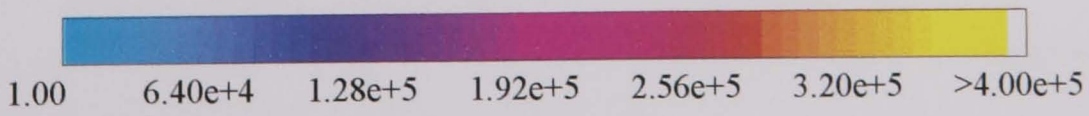

Figure 6.10 – Predicted Strain Rate (1/s) Within Ejector Evaporator Temperature = 10°C

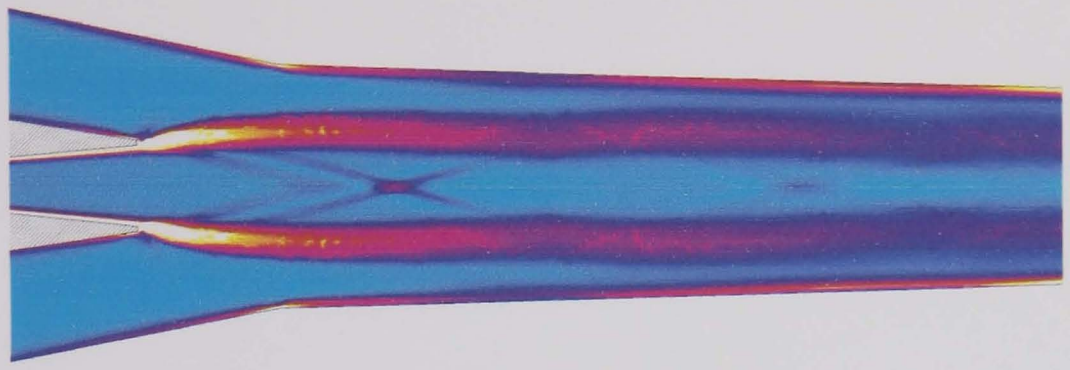

a. – Boiler Temperature = 120°C

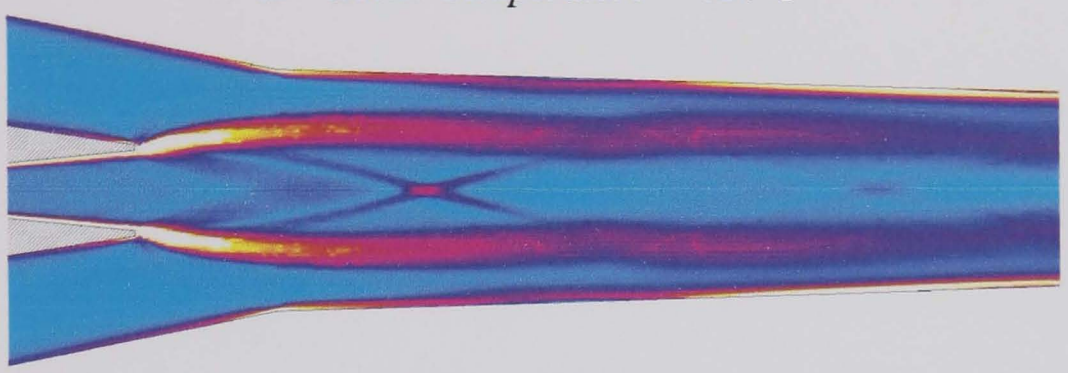

b. – 125°C

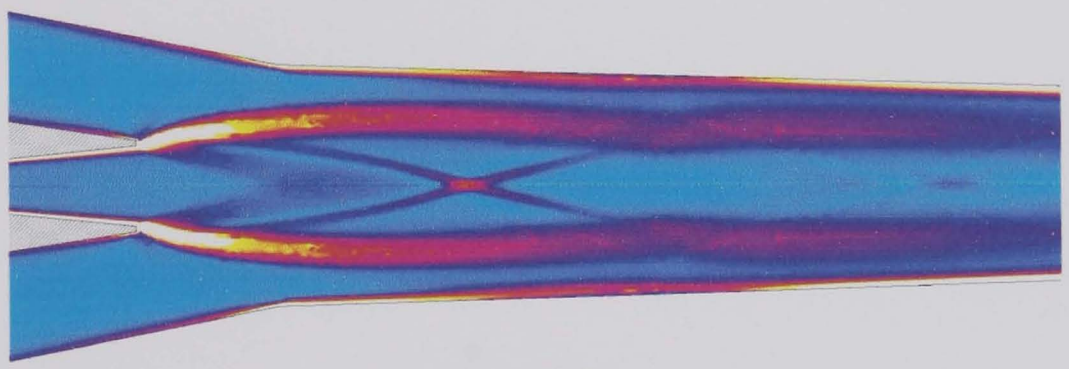

c. – 130°C

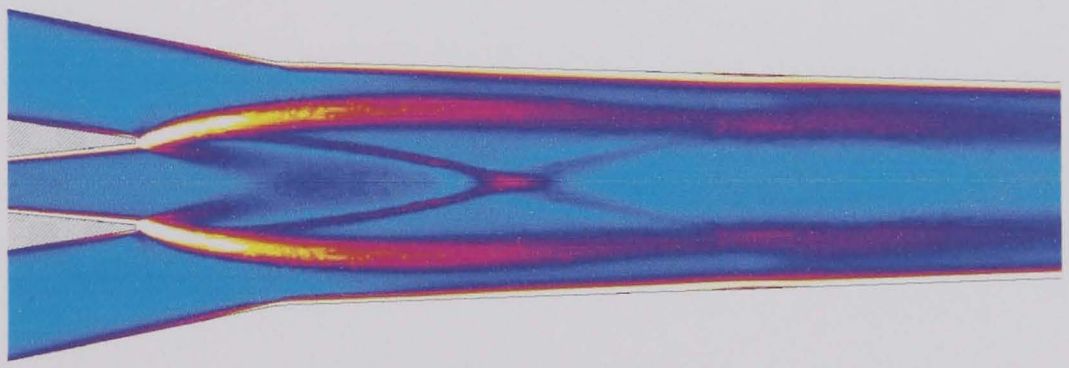

d. – 135°C

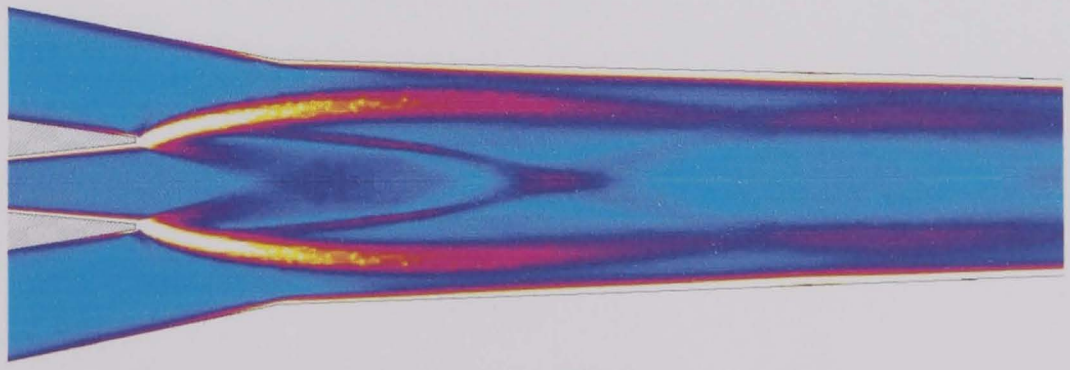

e. – 140°C

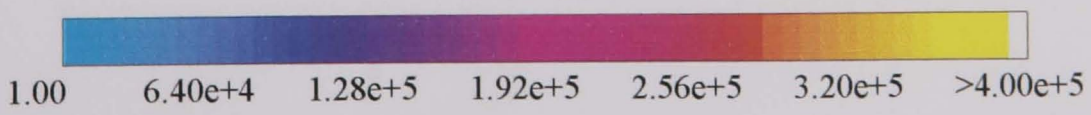

Figure 6.11 – Predicted Strain Rate (1/s) Within Ejector Evaporator Temperature = 7.5°C

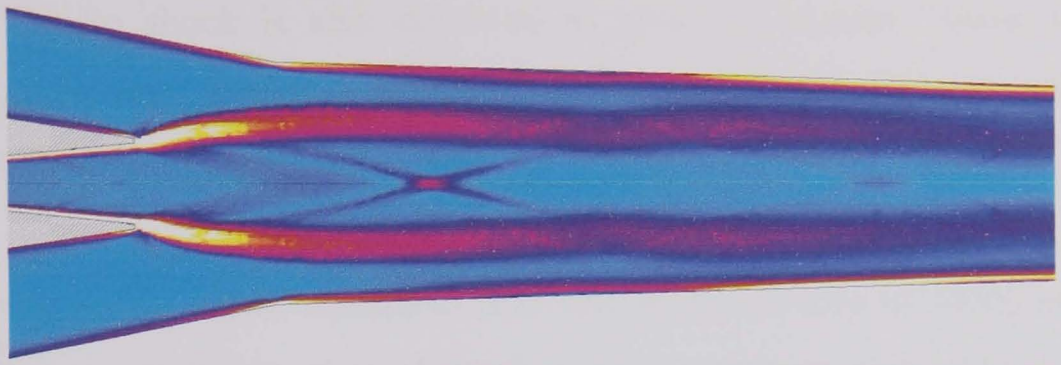

a. – Boiler Temperature = 120°C

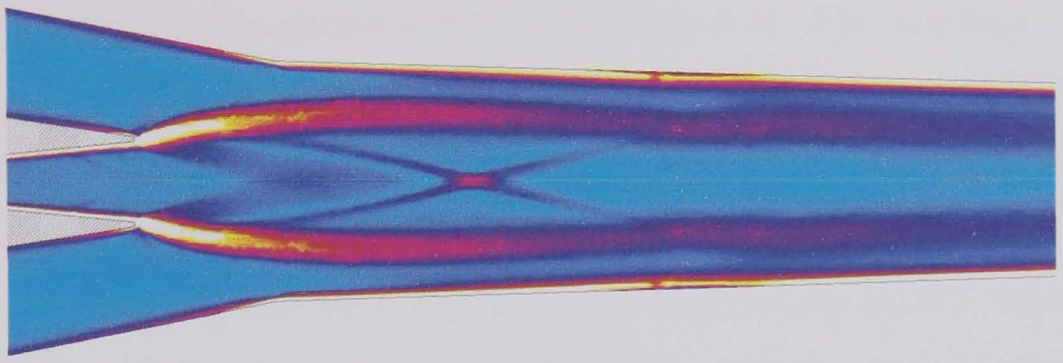

b. – 125°C

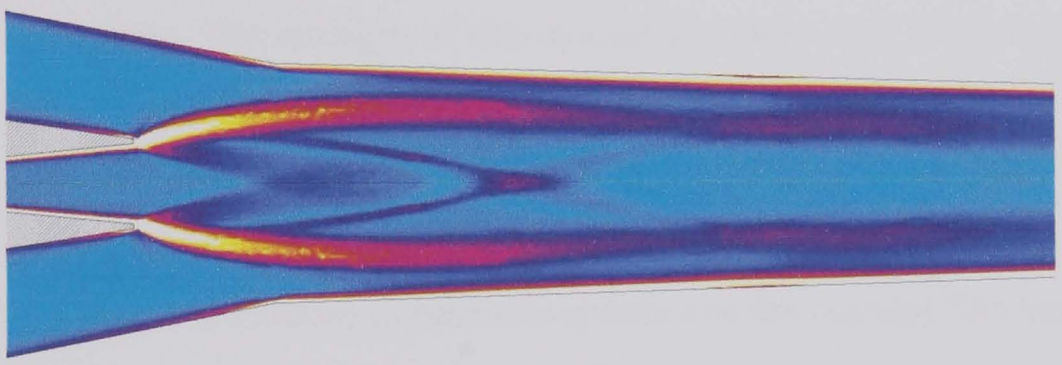

c. – 130°C

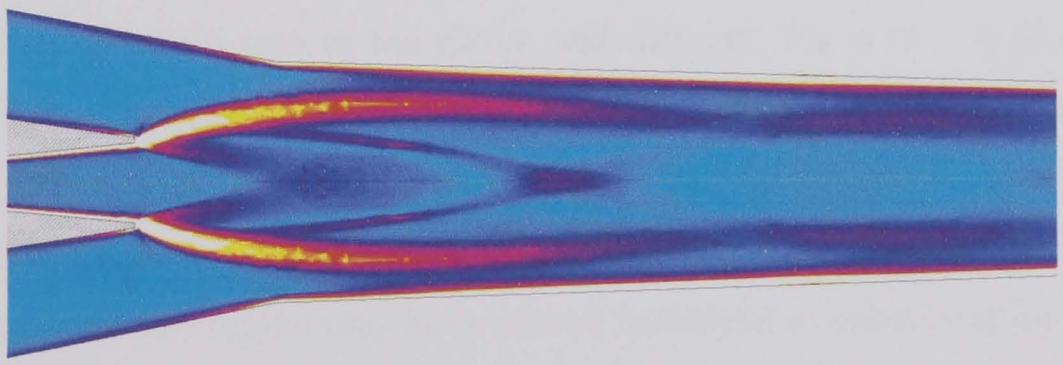

d. – 135°C

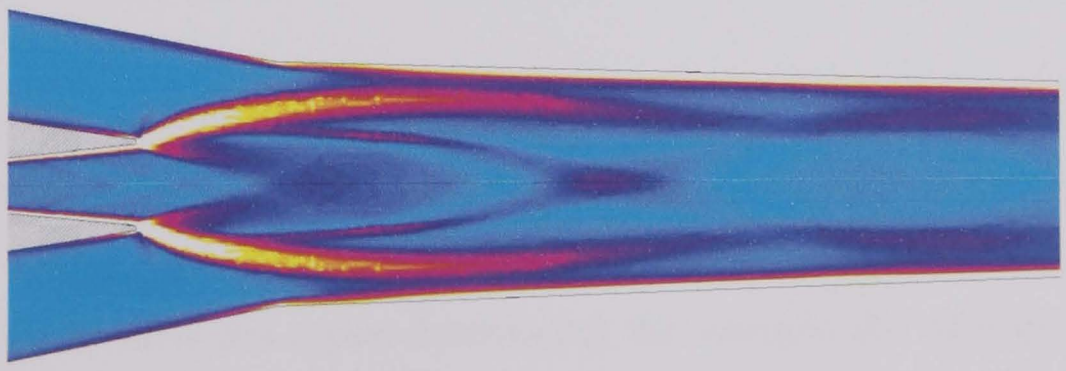

e. – 140°C

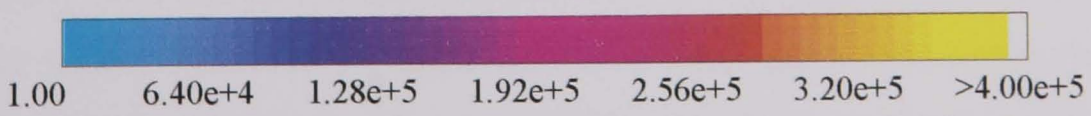

Figure 6.12 – Predicted Strain Rate (1/s) Within Ejector Evaporator Temperature = 5°C

pressure. The lip shock is also observed to grow in severity. Some shock cell structure can be seen further downstream within the mixing chamber however this appears to die out quickly.

The under-expanded nozzle operation, and increasing severity of shock structure at higher boiler temperatures, is confirmed in static pressure plots. These are taken along the centreline of the ejector and shown in Figs 6.13. The customary barrelling effect of the supersonic flow can be seen within the mixing chamber in the oscillatory pressure field, a result of the non-isentropic nozzle expansion. These oscillations occur along the entire length of the mixing chamber, however they decrease in magnitude, and have nearly disappeared by the ejector throat. As the supersonic jet exits the throat, a series of pressure spikes occur which indicate a normal shock system. The strength of this system increases with boiler temperature. This is due to an increase in the velocity of the stream feeding the throat which causes the boundary layer to thicken rapidly. A region of separation and recirculation within the diffuser, and a series of normal reflected shocks of decreasing magnitude result until the flow has reduced to subsonic speeds and the passage fills again.

Contour plots of strain rate in the throat and diffuser, Fig 6.14 – 6.16 show this normal shock system, however the structure is not so clearly defined as in the mixing chamber. Indeed when T_{evap} = 10°C and T_{boiler} = 120°C the shock does not really appear, however once T_{boiler} has increased to 140°C the shock is clearly evident. A finer mesh within this region may have proved beneficial to enhancing the resolution of this system. The thick boundary layer within the throat can also be seen.

The strain rate plots of the mixing chamber (Fig 6.10 – 6.12) indicate that as jet under-expansion increases, the rate at which the jet expands into the mixing chamber increases. This is confirmed in plots of the supersonic flow region within the ejector. Fig 6.17 – 6.19 show this region demarcating the subsonic and supersonic flow. It can be clearly seen that an increase in boiler temperature leads to an expansion of the supersonic region. Also notable is the influence of evaporator temperature, and thus mixing chamber back pressure. A reduction in evaporator temperature also leads to a more extensive supersonic region with a higher degree of expansion.

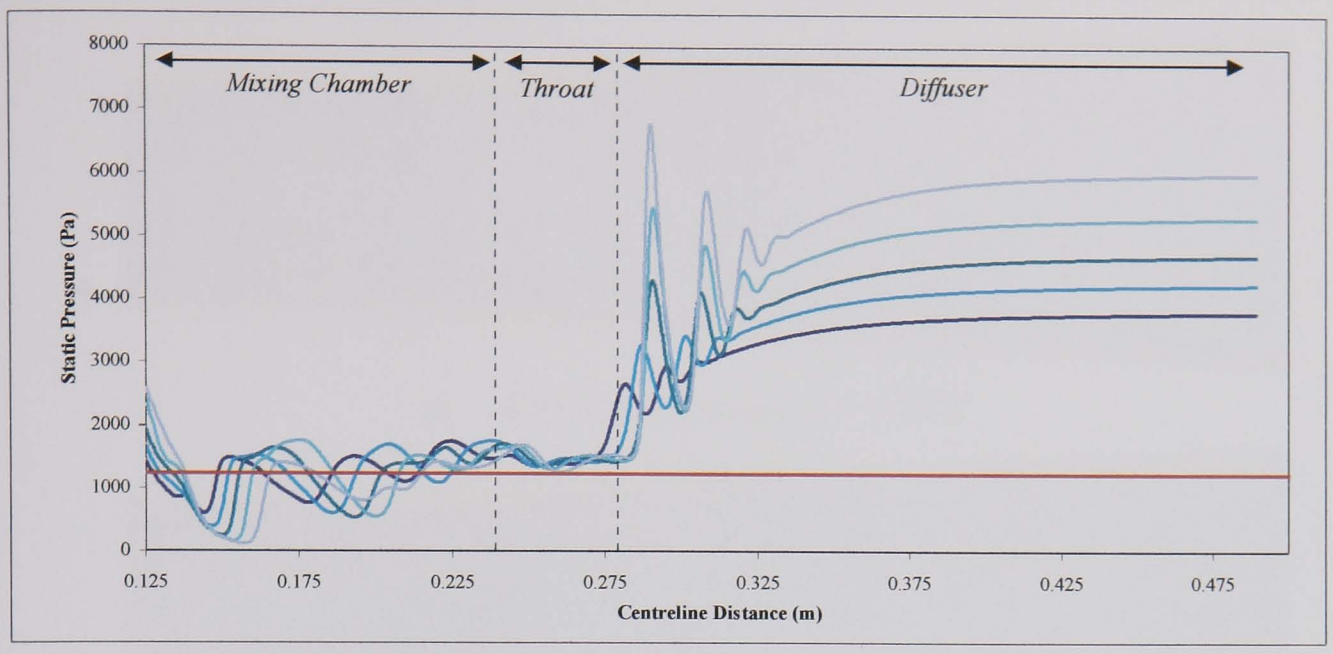

a. - Evaporator Temperature = 10 °C

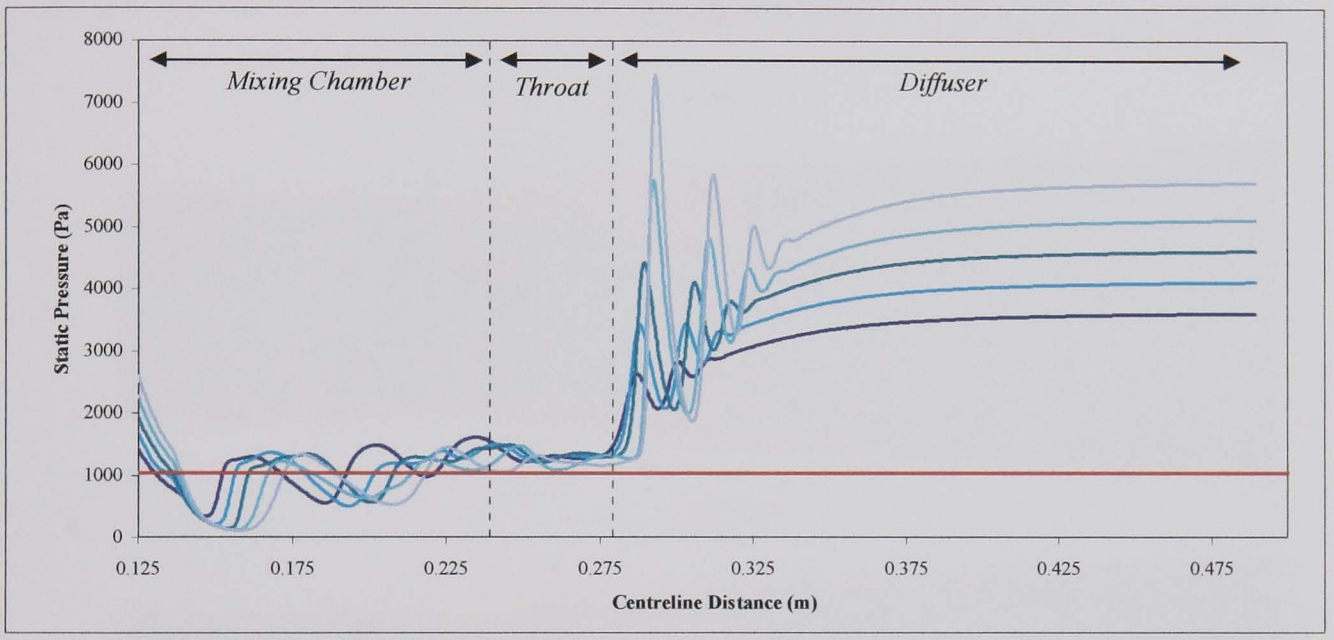

b. - Evaporator Temperature = 7.5 °C

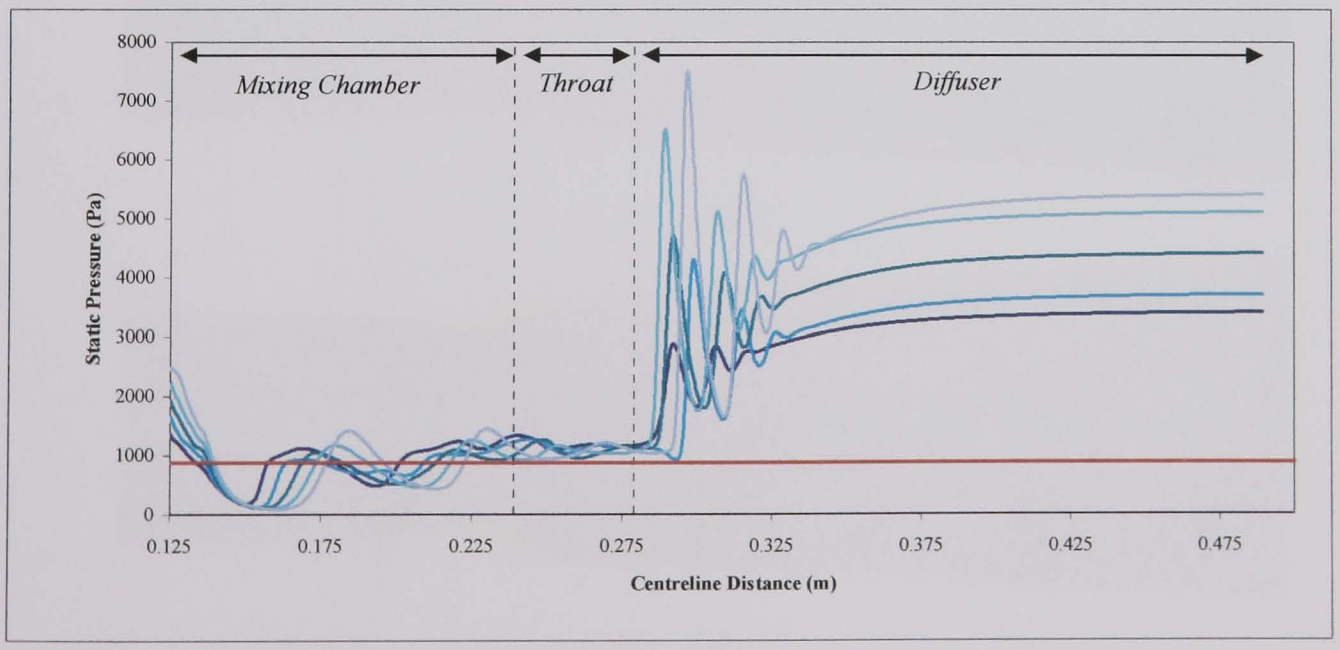

c. - Evaporator Temperature = 5 °C

Figure 6.13 - Effect of Boiler Temperature On Centreline Pressure Distribution

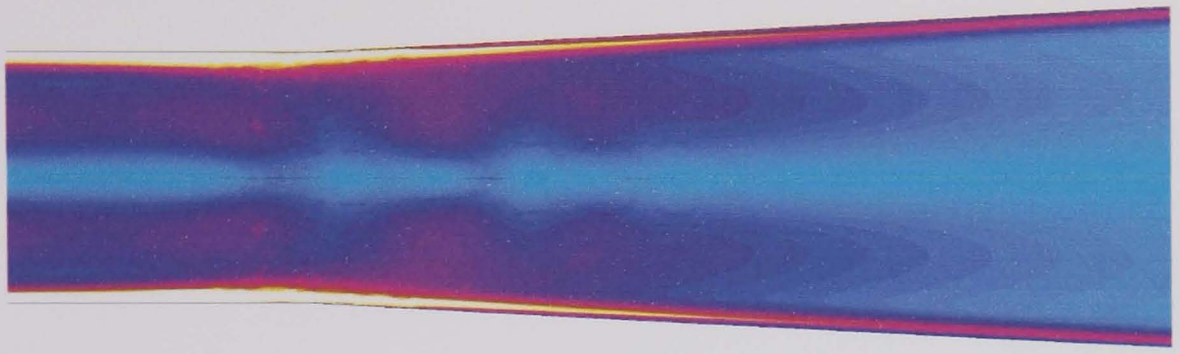

a. – Boiler Temperature = 120°C

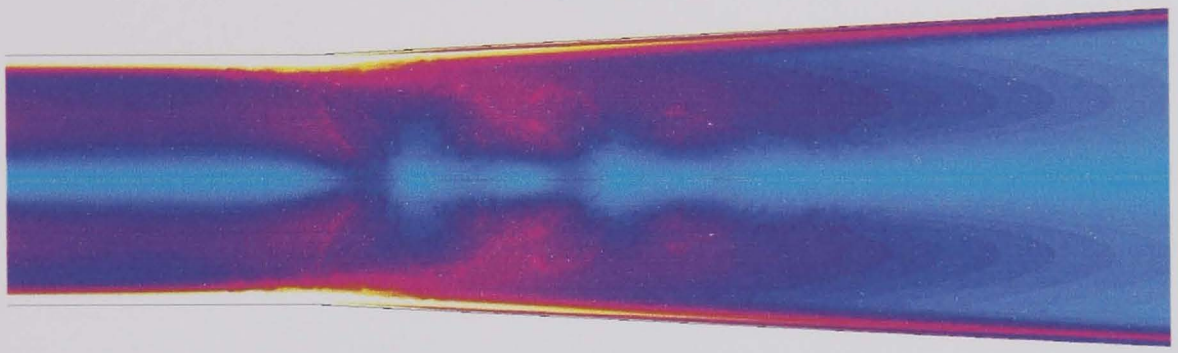

b. – 125°C

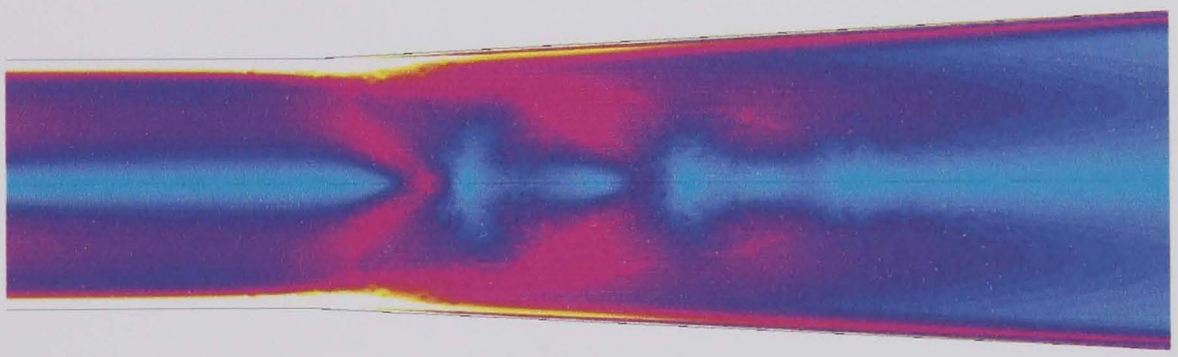

c. – 130°C

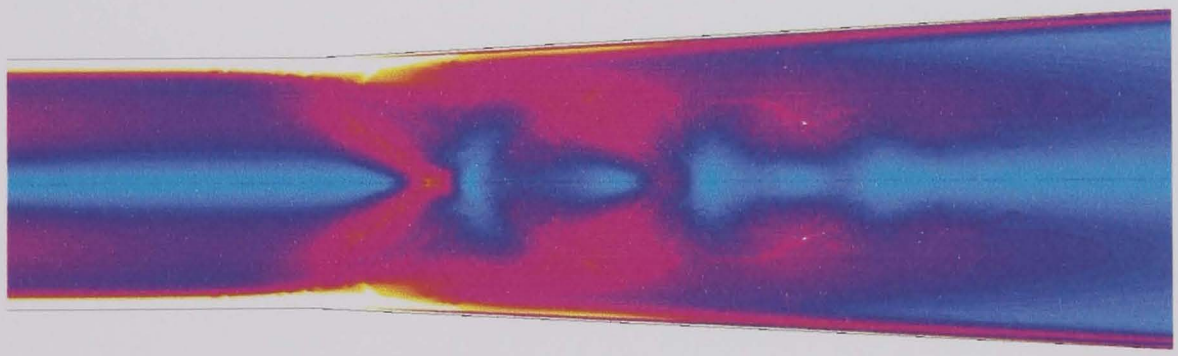

d. – 135°C

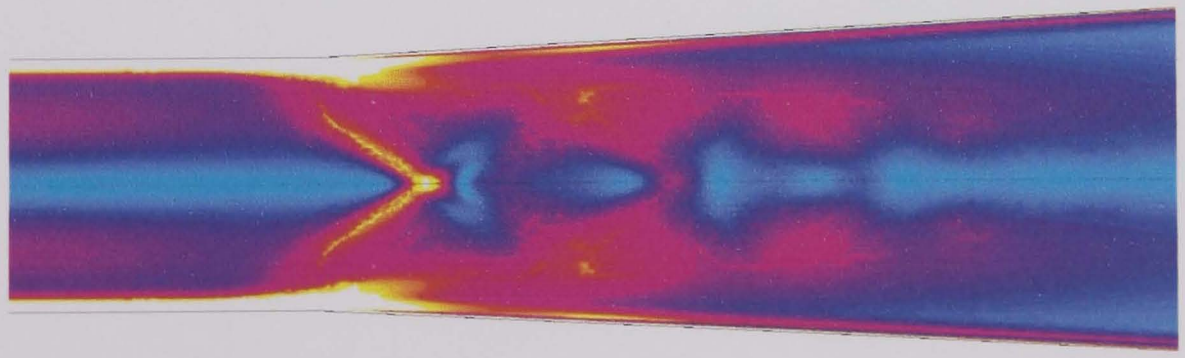

e. – 140°C

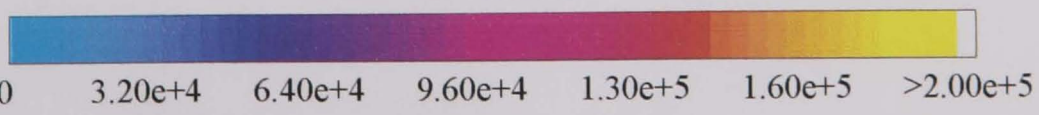

Figure 6.14 – Predicted Strain Rate (1/s) Within Ejector Throat and Diffuser Evaporator Temperature = 10°C

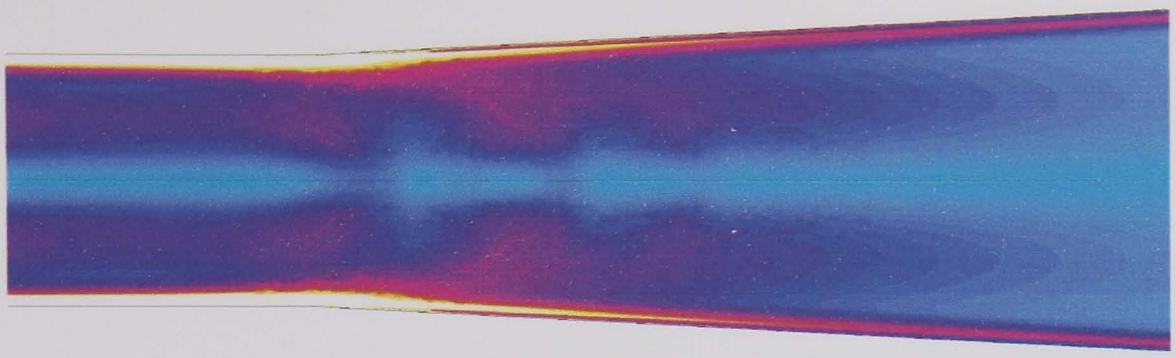

a. – Boiler Temperature = 120°C

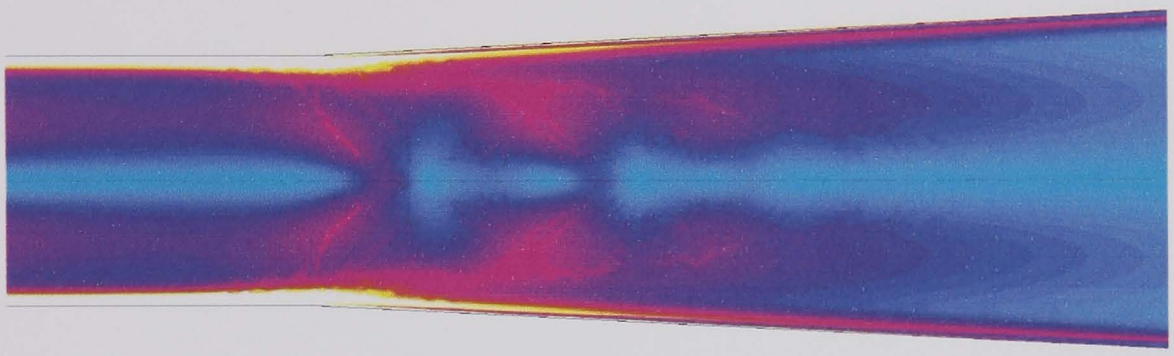

b. – 125°C

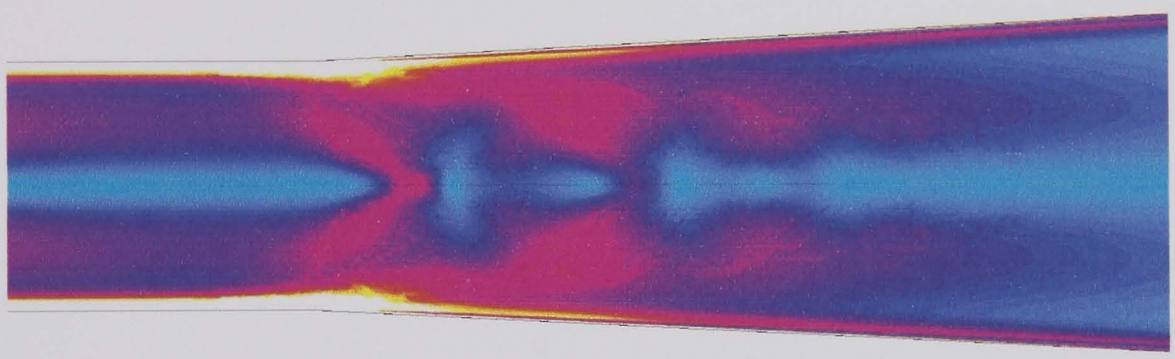

c. – 130°C

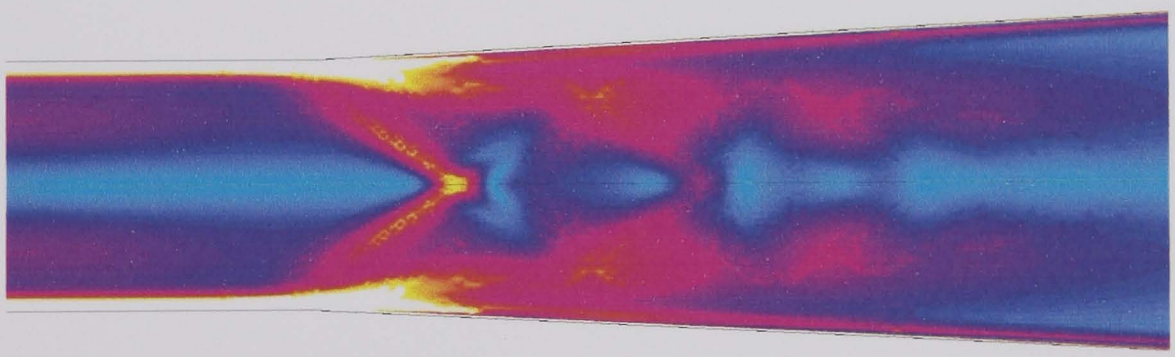

d. – 135°C

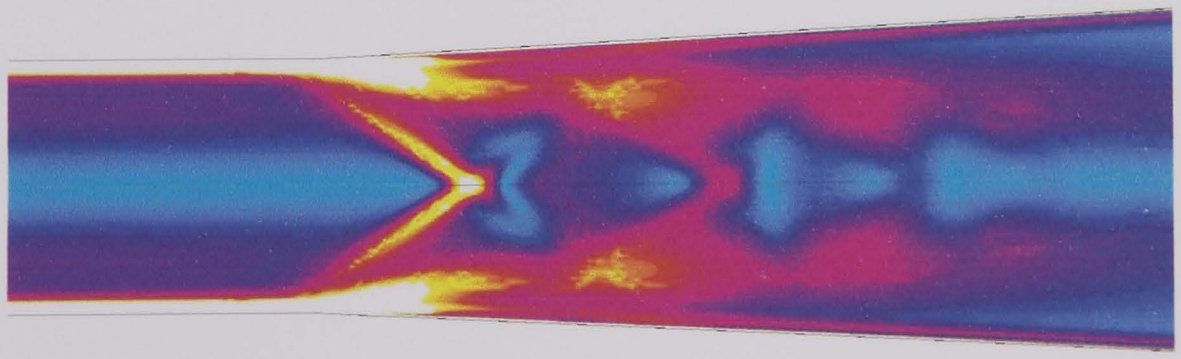

e. – 140°C

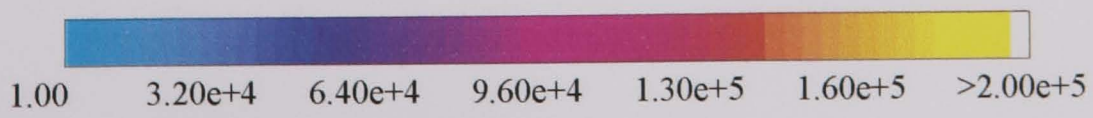

Figure 6.15 – Predicted Strain Rate (1/s) Within Ejector Throat and Diffuser Evaporator Temperature = 7.5°C

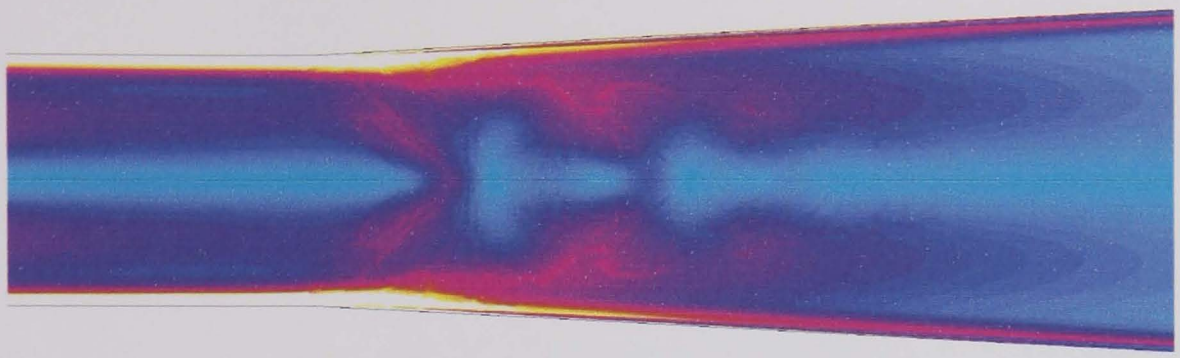

a. – Boiler Temperature = 120°C

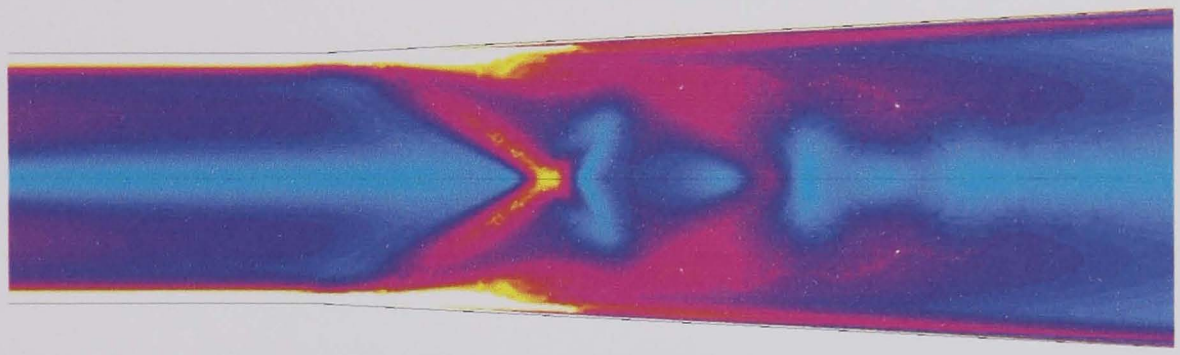

b. – 125°C

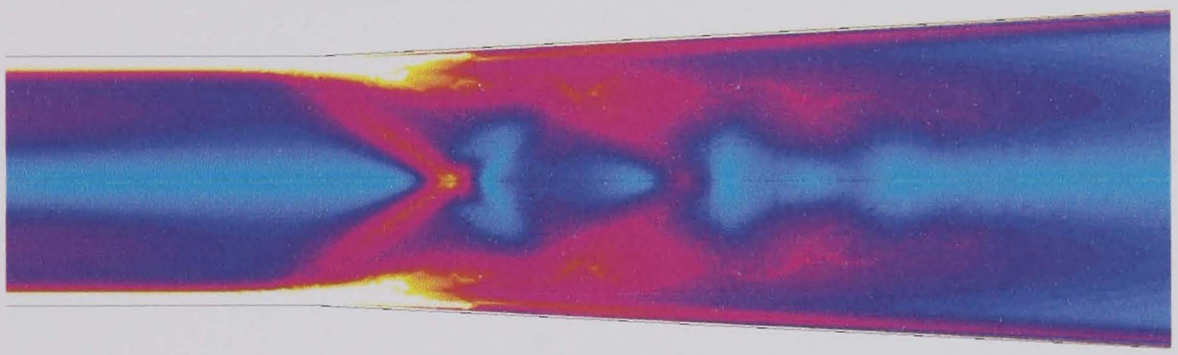

c. – 130°C

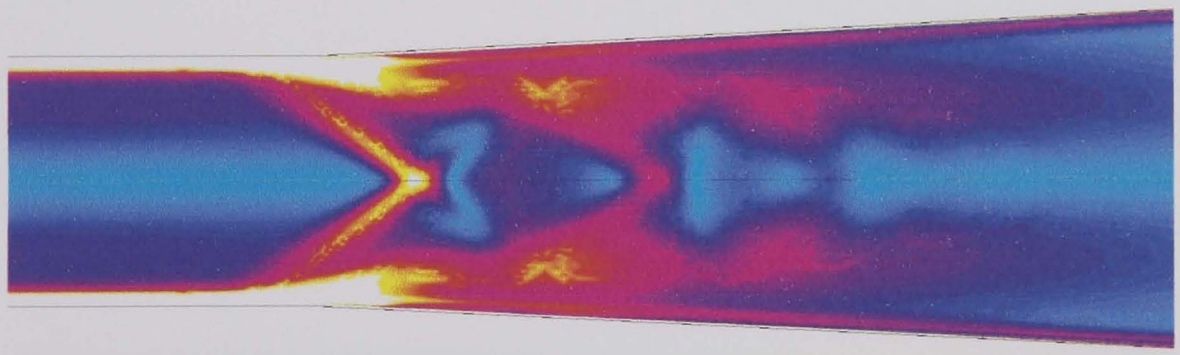

d. – 135°C

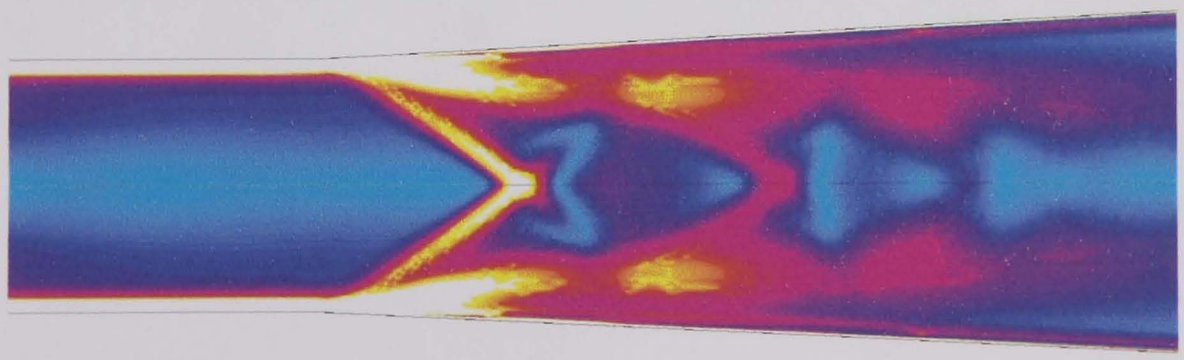

e. – 140°C

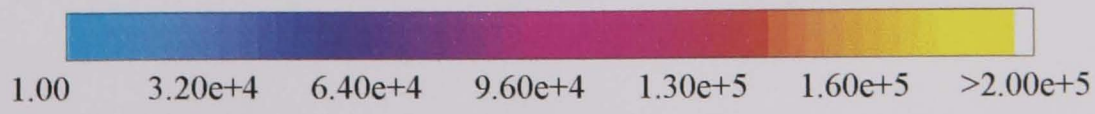

Figure 6.16 – Predicted Strain Rate (1/s) Within Ejector Throat and Diffuser Evaporator Temperature = 5°C

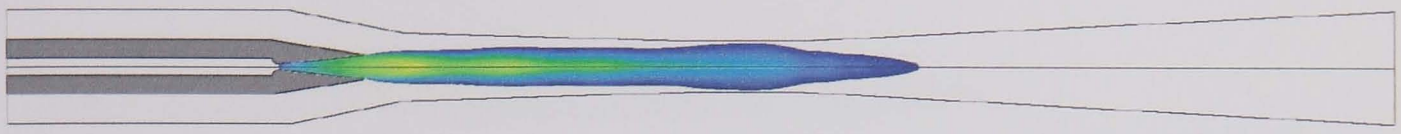

a. – Boiler Temperature = 120°C

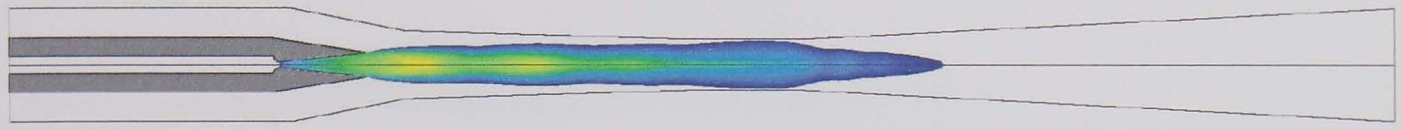

b. – 125°C

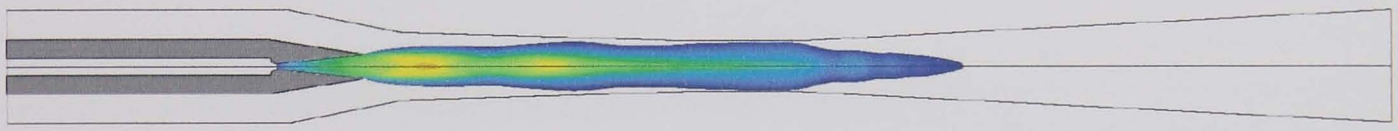

c. – 130°C

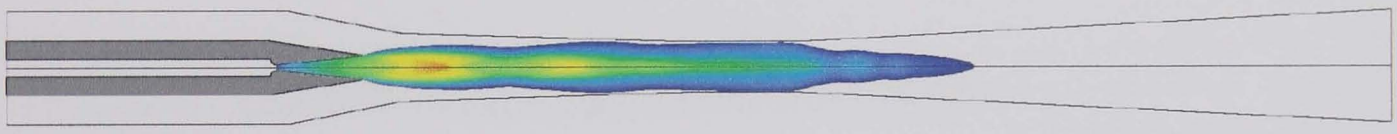

d. – 135°C

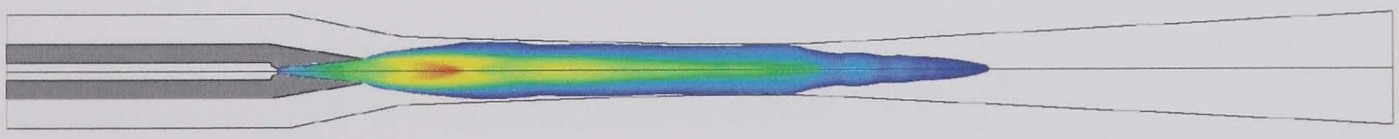

e. – 140°C

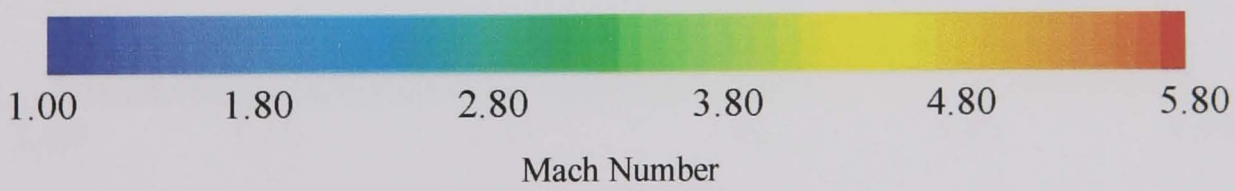

Figure 6.17 – Supersonic Flow Region Within Ejector

Evaporator Temperature = 10°C

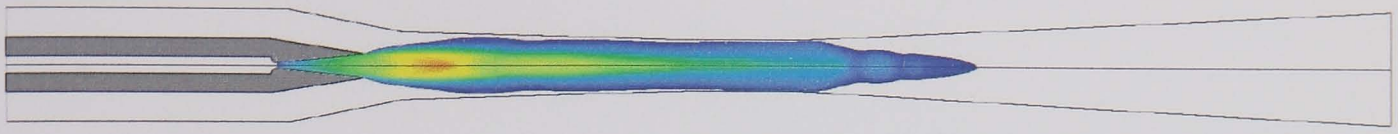

a. – Boiler Temperature = 120°C

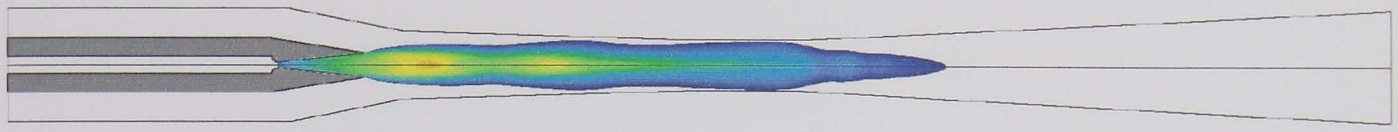

b. – 125°C

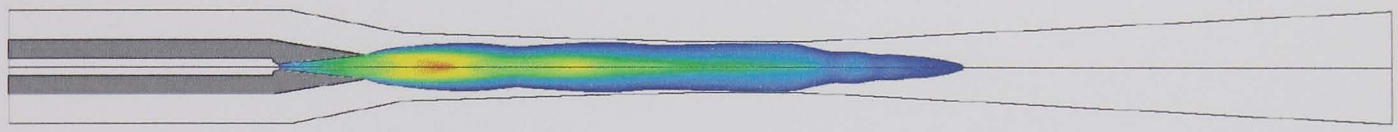

c. – 130°C

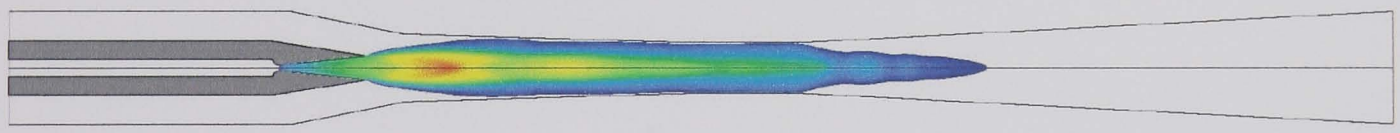

d. – 135°C

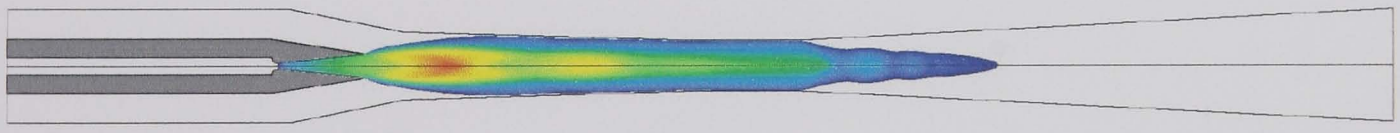

e. – 140°C

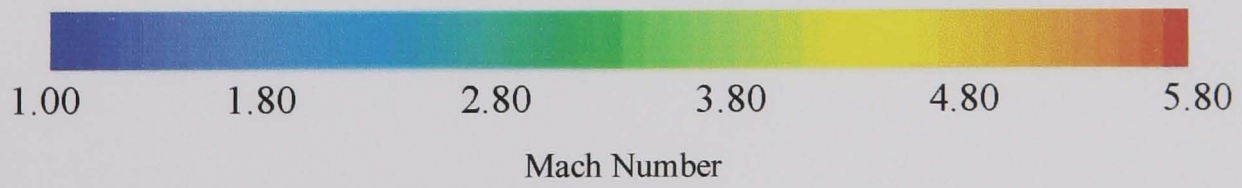

Figure 6.18 – Supersonic Flow Region Within Ejector
Evaporator Temperature = 7.5°C

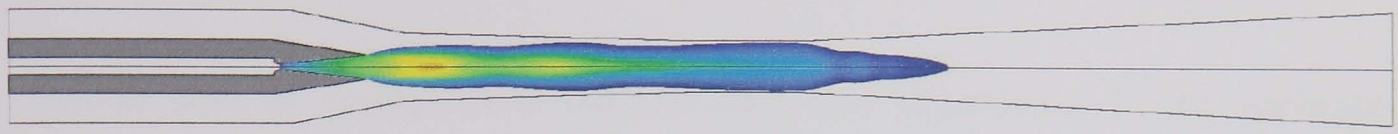

a. – Boiler Temperature = 120°C

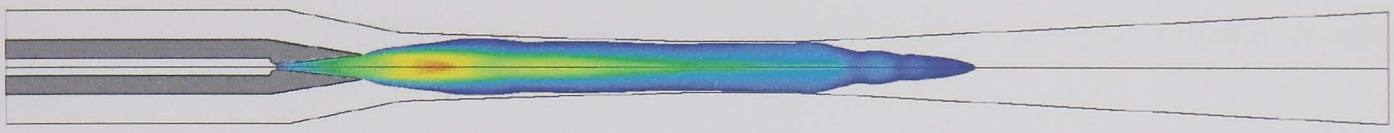

b. – 125°C

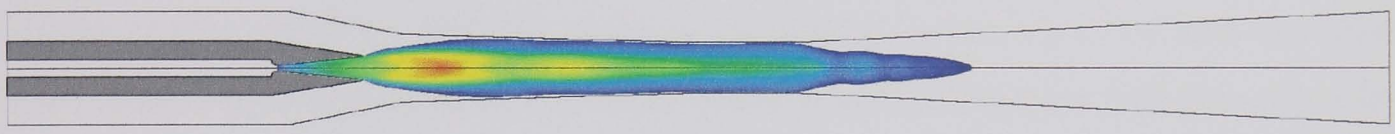

c. – 130°C

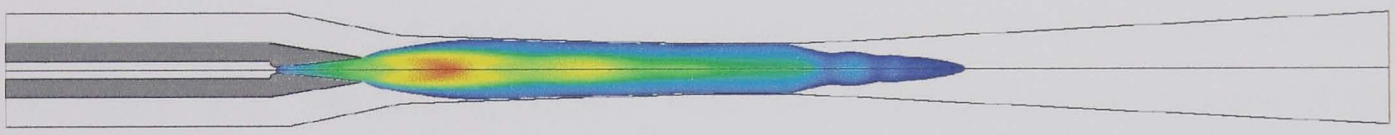

d. – 135°C

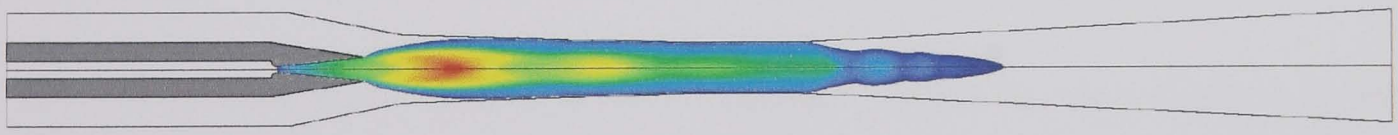

e. – 140°C

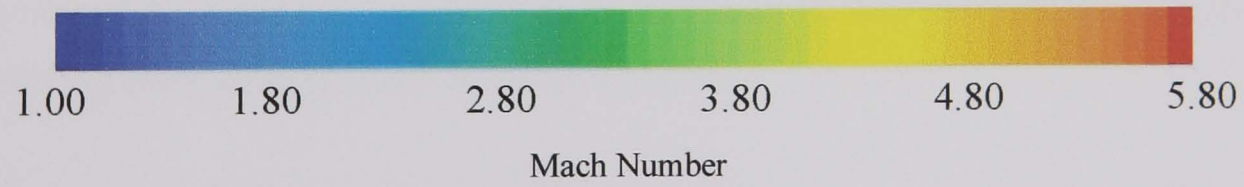

Figure 6.19 – Supersonic Flow Region Within Ejector

Evaporator Temperature = 5°C

The supersonic plots of Fig 6.17–6.19 also show Mach number in the supersonic region. It can be seen that as the primary flow exits the de Laval nozzle it continues to accelerate. At boiler temperatures of 140°C a peak velocity of M = 5.8 is attained.

Contour plots of species mass fraction allow the visualisation of the interaction between the primary and secondary streams within the ejector. Figs 6.20–6.22 show profiles and selective contours of 1%, 10%, 90% and 99% primary fluid species mass fraction. The sonic line separating supersonic and subsonic regions is also shown.

It can be seen from the profiles of primary fluid mass fraction, taken across the width of the mixing chamber, that the majority of mixing occurs on or around the sonic line. This is to be expected as the steep gradient in fluid species will coincide with the steep velocity gradient within this region. The growth in thickness (distance between 1% and 99% contours) of the mixing region is rapid. This rapid growth begins at the nozzle exit where the supersonic jet meets the essentially stationary secondary fluid. The mixing chamber walls and embedded shock structure of the supersonic jet cause further growth until the layer has expanded to fill the entire channel width.

The 1% primary mass fraction contour has been chosen as representative of the subsonic boundary of the mixing layer. In reality turbulence is an intermittent[105] process therefore the exact position of this boundary will fluctuate slightly. This contour will be termed the entrainment boundary as all secondary fluid entrained into the mixing layer must pass through this contour.

The influence of jet expansion on entrainment can be determined by studying Figs 6.20-6.22, the entrainment boundary, and by referring to Fig 6.9. It can be seen in Figs 6.20-6.22 that as the motive jet expands and the sonic line approaches the wall the length of the entrainment boundary is affected. It might be expected that as the expansion rate of the supersonic jet within the mixing chamber increases, that the entrainment boundary between the secondary fluid and mixing layer would reduce in size. However it appears in Fig 6.20-6.22 that this is not quite the case. To confirm

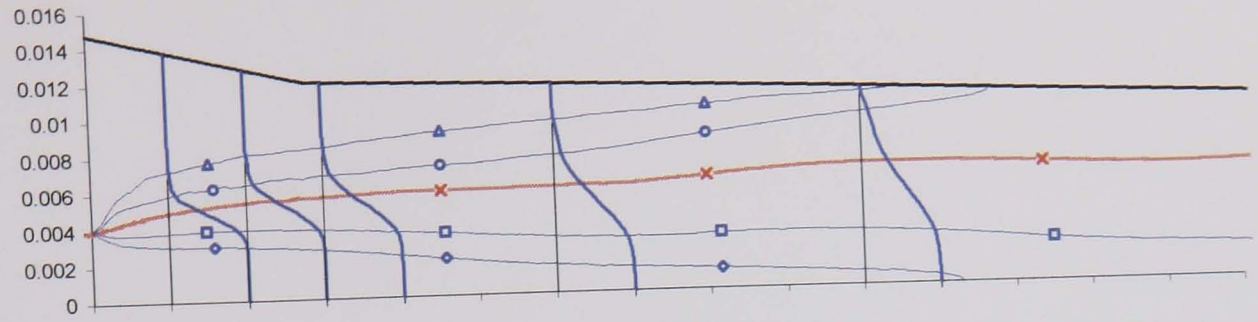

a. - Boiler Temperature = 120 °C

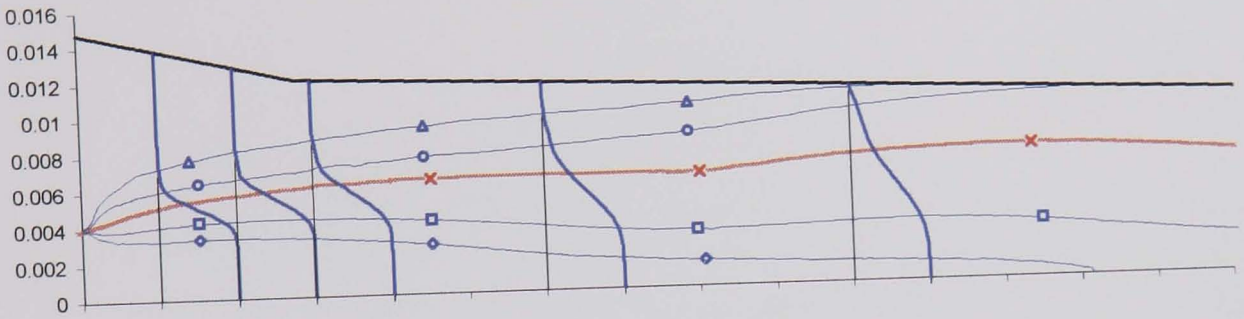

b. - Boiler Temperature = 125 °C

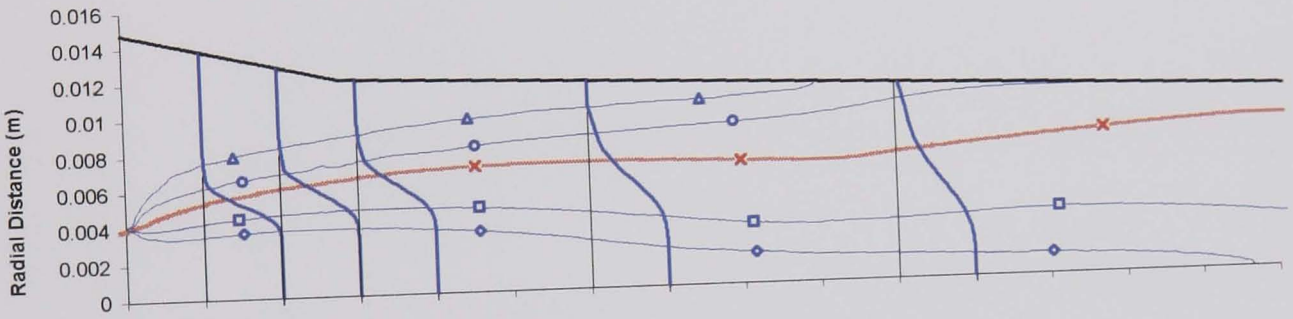

c. - Boiler Temperature = 130 °C

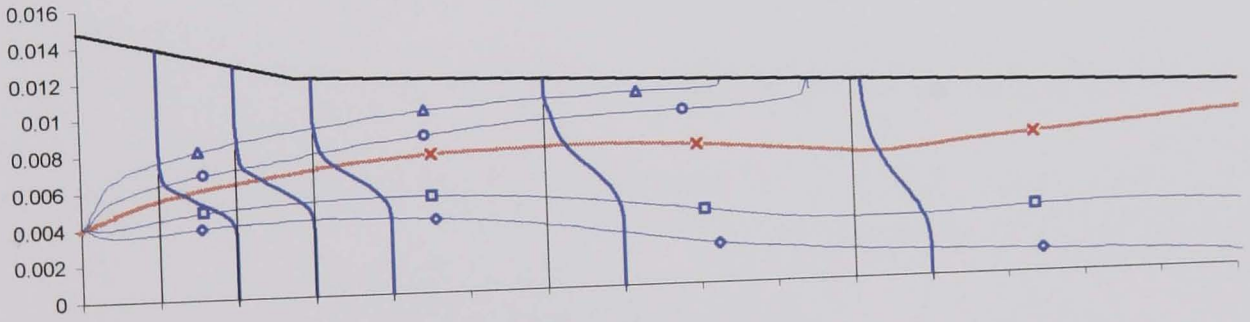

d. - Boiler Temperature = 135 °C

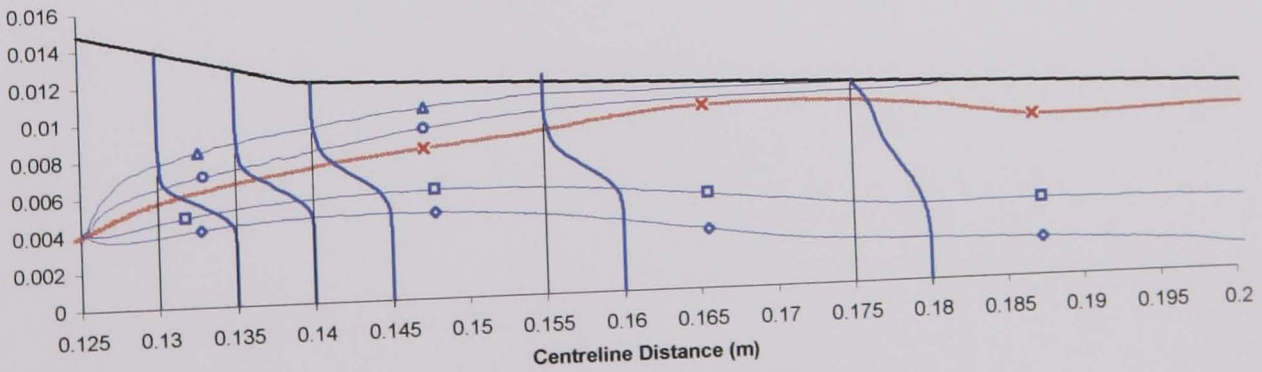

e. - Boiler Temperature = 140 °C

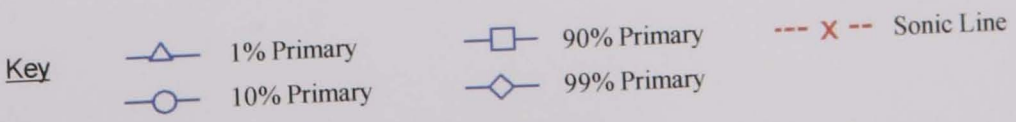

Figure 6.20 - Distribution of Primary Species Mass Fraction Evaporator Temperature Fixed At 10 °C

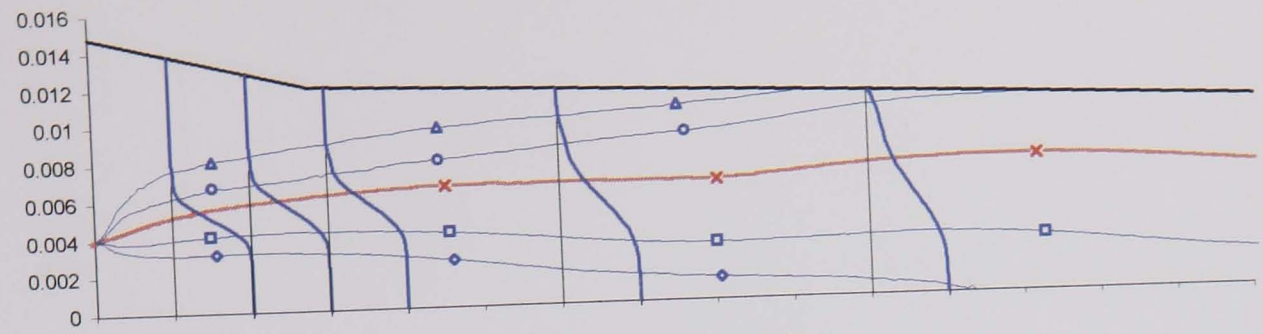

a. - Boiler Temperature = 120 ℃

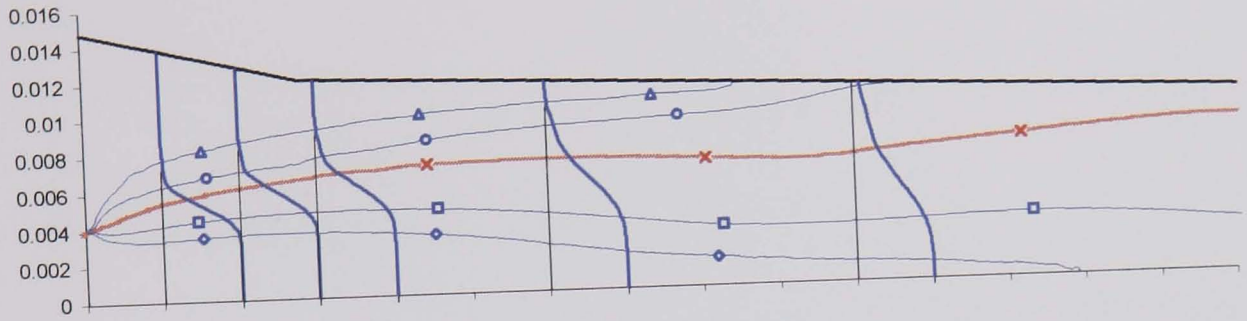

b. - Boiler Temperature = 125 ℃

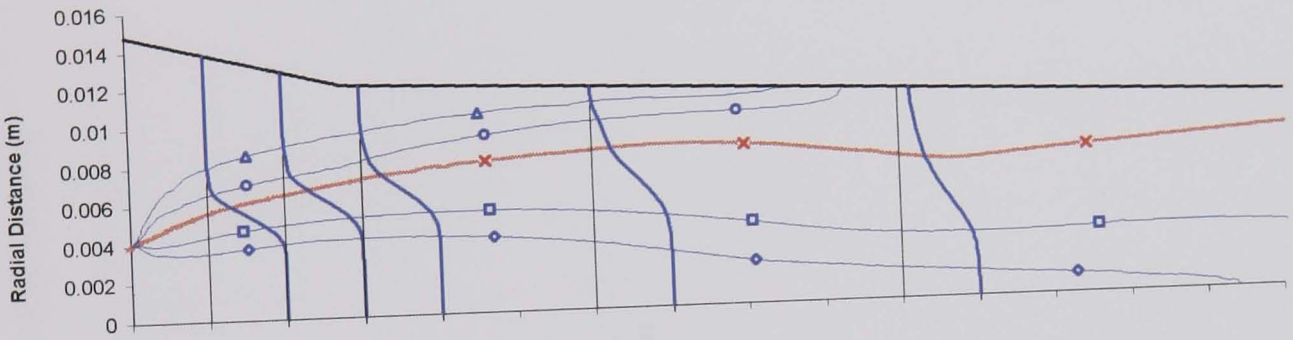

c. - Boiler Temperature = 130 ℃

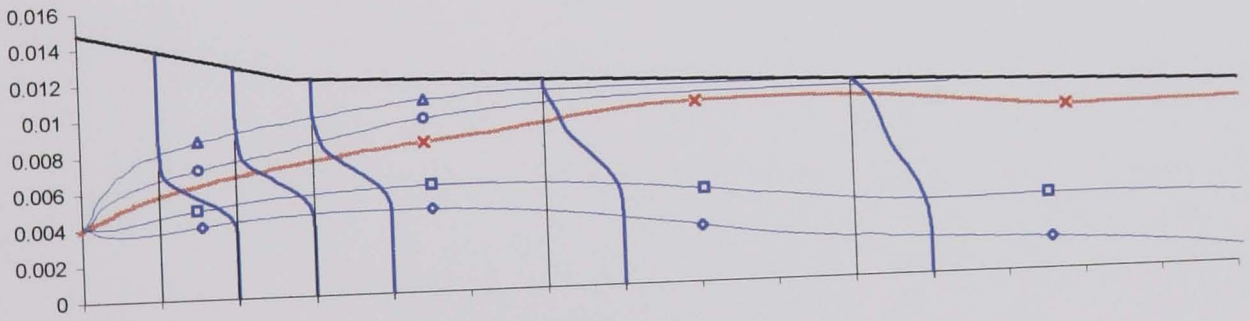

d. - Boiler Temperature = 135 ℃

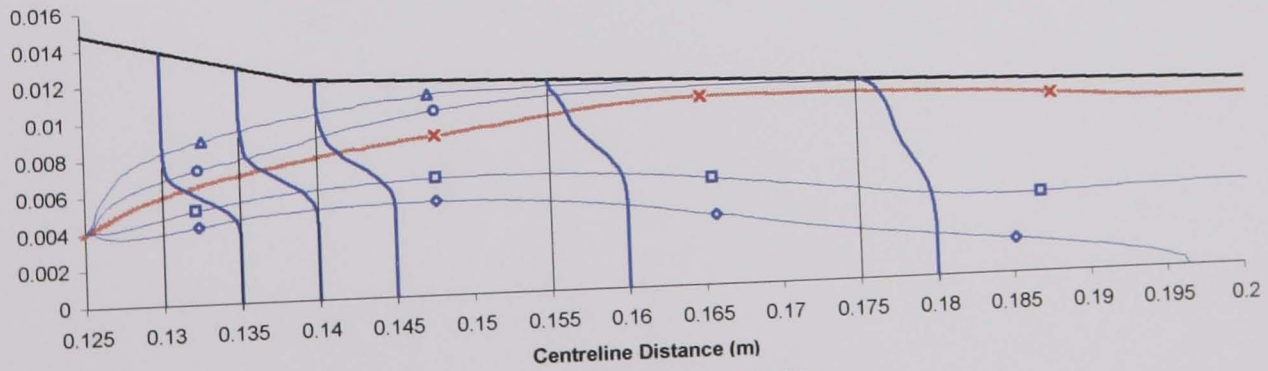

e. - Boiler Temperature = 140 ℃

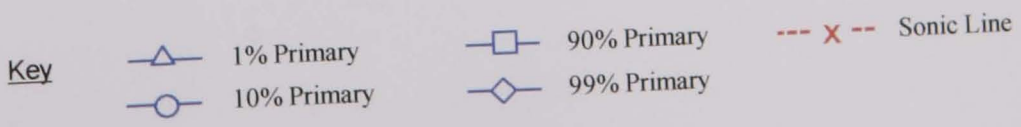

Figure 6.21 - Distribution of Primary Species Mass Fraction Evaporator Temperature Fixed At 7.5 ℃

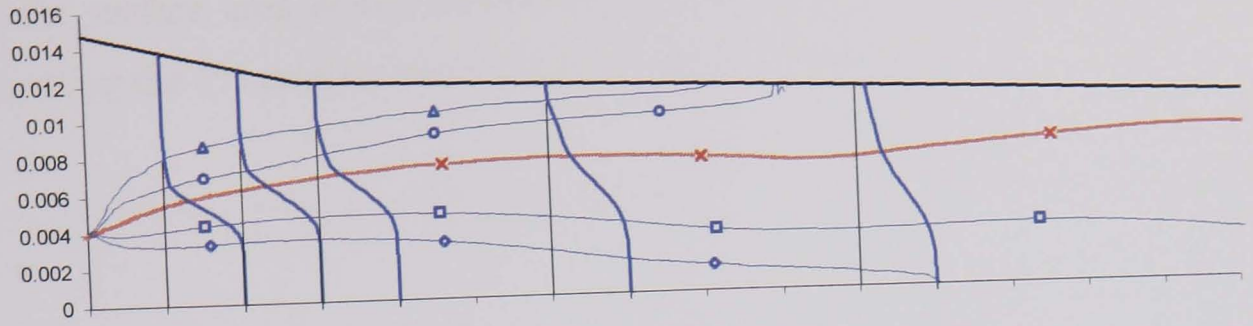

a. - Boiler Temperature = 120 °C

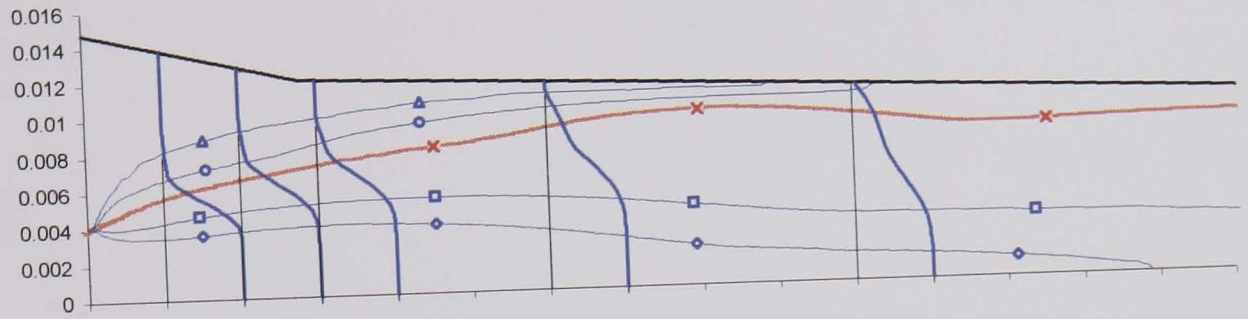

b. - Boiler Temperature = 125 °C

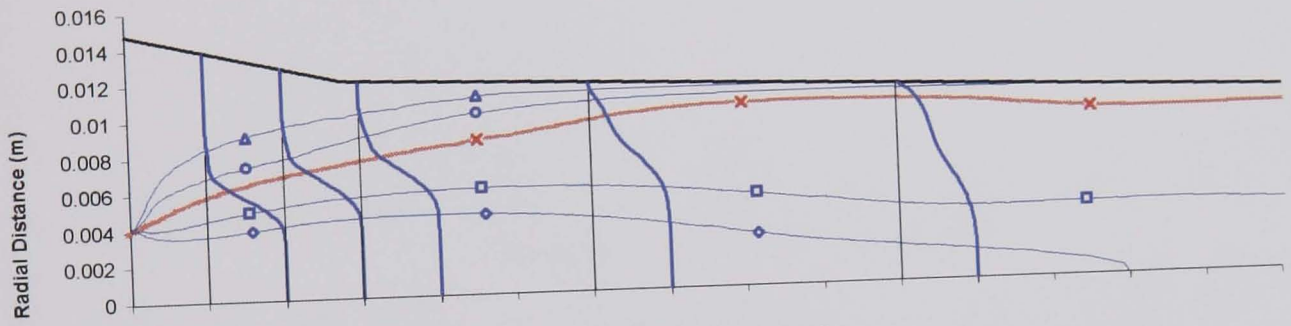

c. - Boiler Temperature = 130 °C

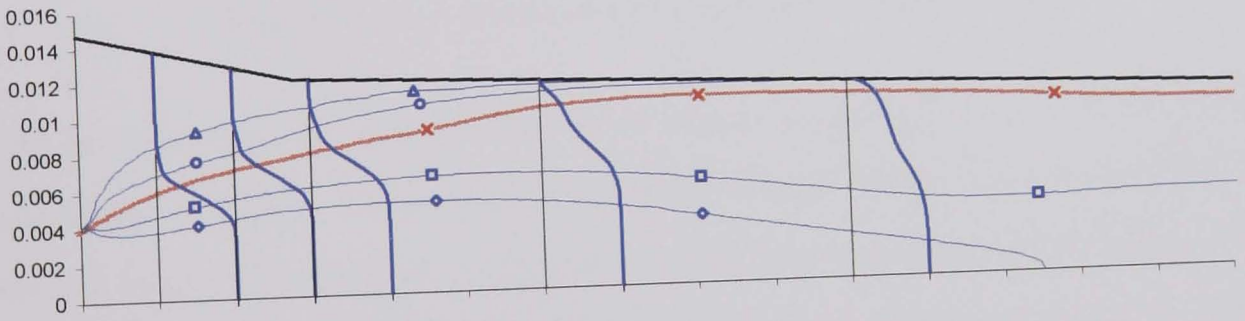

d. - Boiler Temperature = 135 °C

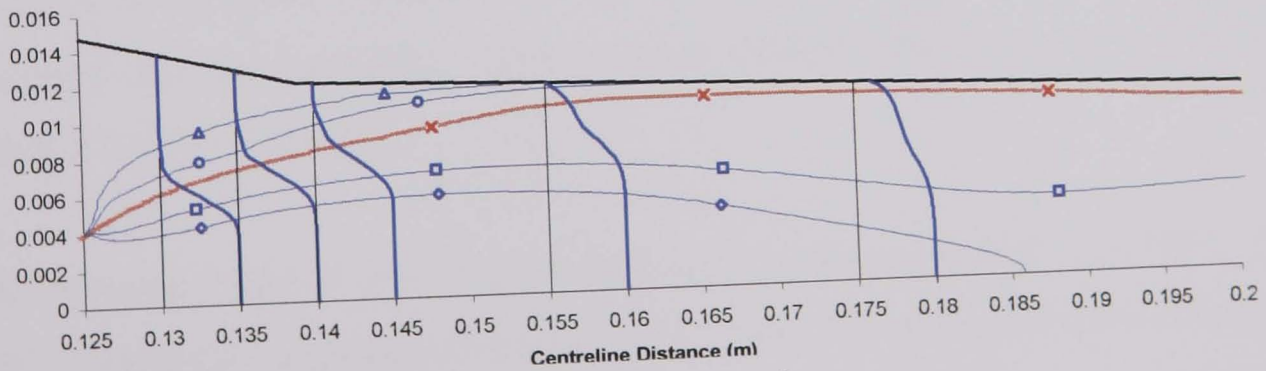

e. - Boiler Temperature = 140 °C

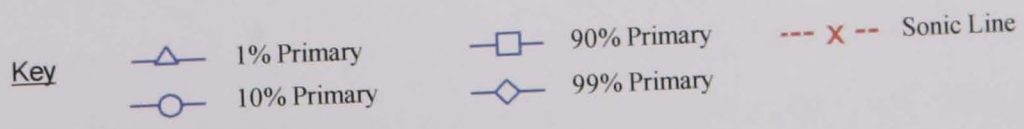

Figure 6.22 - Distribution of Primary Species Mass Fraction Evaporator Temperature Fixed At 5 °C

this the surface area of the entrainment boundary was calculated by plotting and integrating the 1% primary mass fraction contour, Fig 6.23.

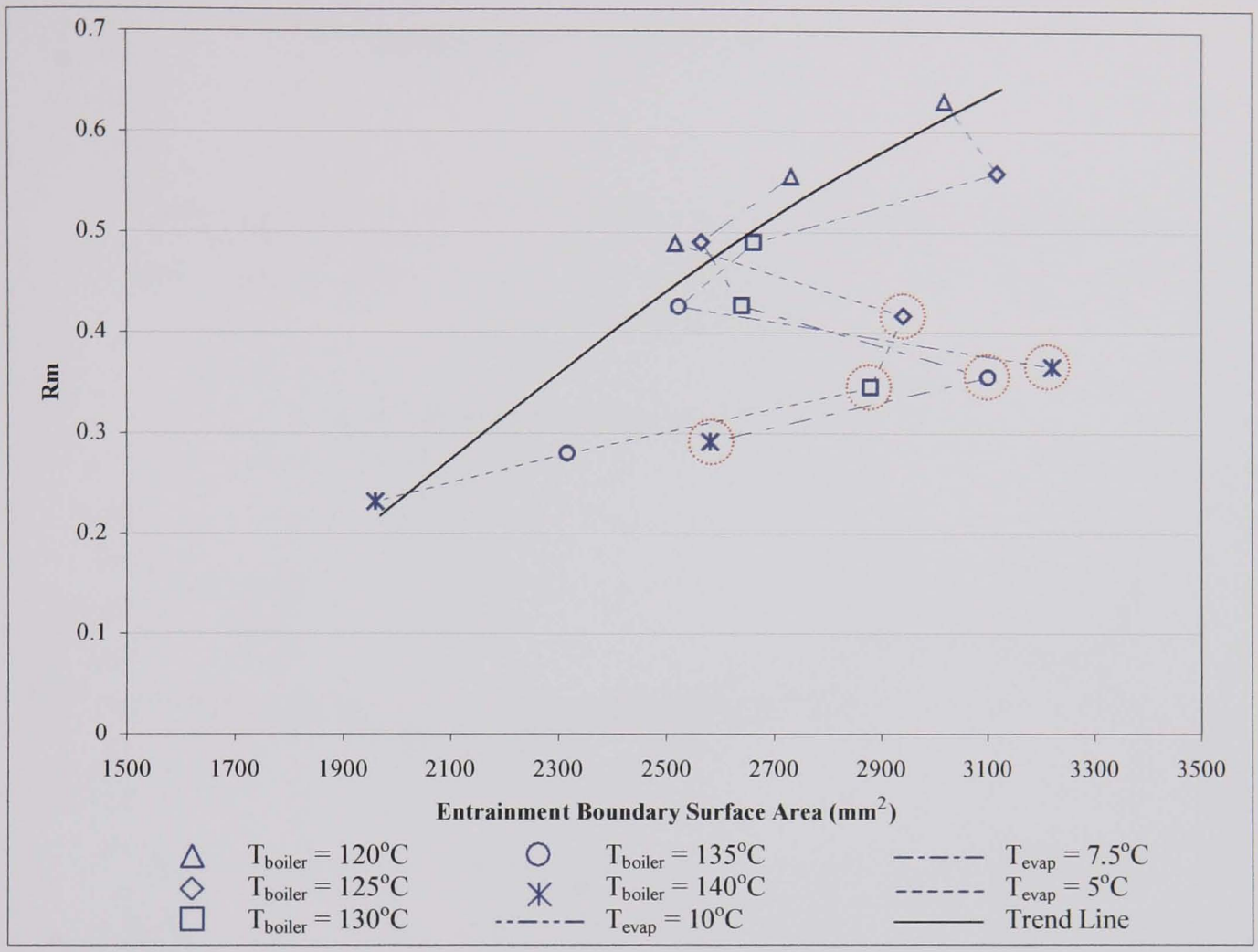

Figure 6.23 – Entrainment Boundary Surface Area

It can be seen that the area of the entrainment boundary fluctuates as the boiler temperature is raised for a fixed evaporator temperature. This behaviour is not restricted to the 1% contour, comparable behaviour was observed between 0.1% to 10% primary fluid mass fraction. Although it may appear that in Fig 6.23 the entrainment boundary fluctuates in an unpredictable manner a trendline can be identified and the fluctuating values (circled-dashed) which do not fall near the trendline can be explained.

The expansion of the motive jet governs the area of the entrainment boundary. As the level of motive jet expansion increases, the surface area of the entrainment boundary at first decreases. However as the jet expands towards the wall, a narrow gap forms between the sonic line and the boundary layer at the wall surface. The proximity of the high velocity jet to the wall causes a pressure drop within the gap. This can be seen in Fig 6.24 that shows pressure distribution along the walls of the mixing

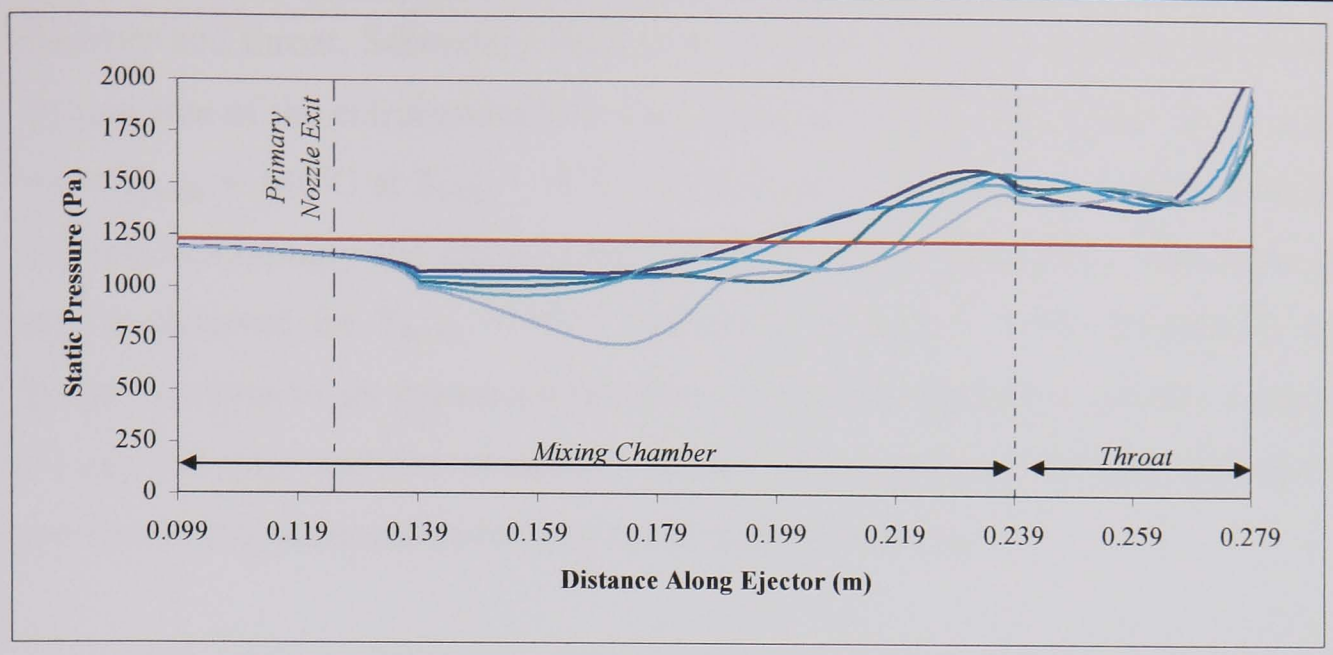

a. - Evaporator Temperature = 10 °C

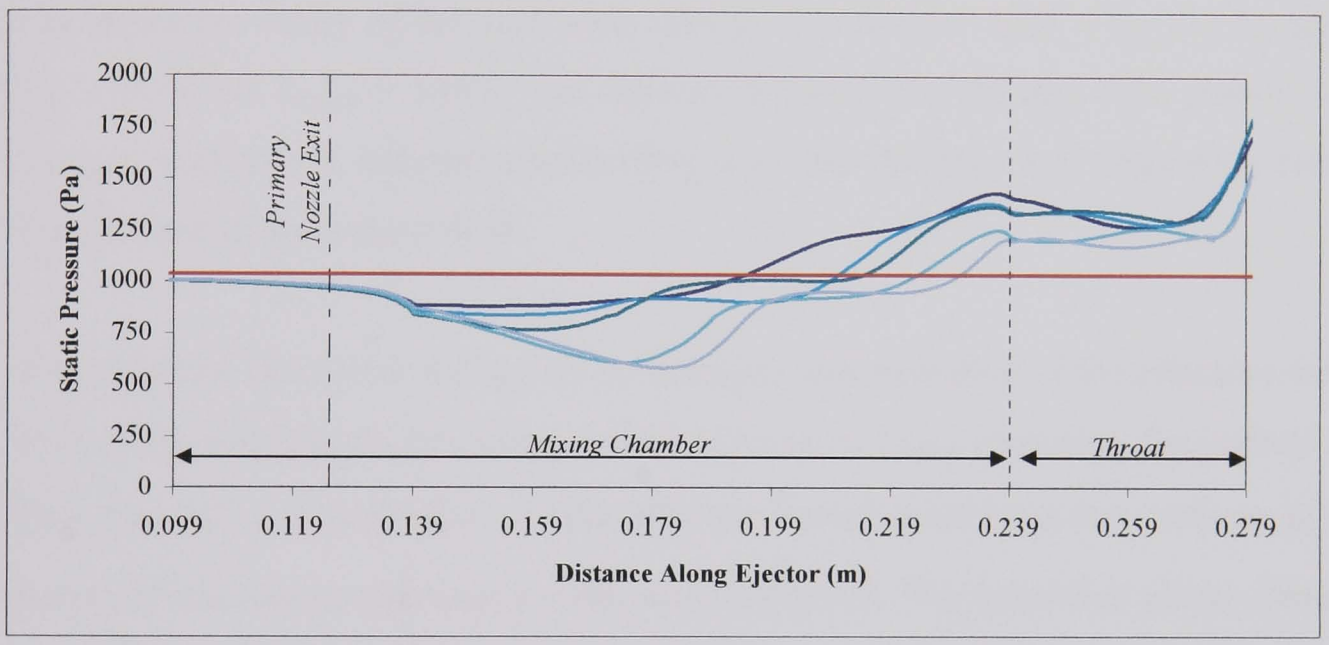

b. - Evaporator Temperature = 7.5 °C

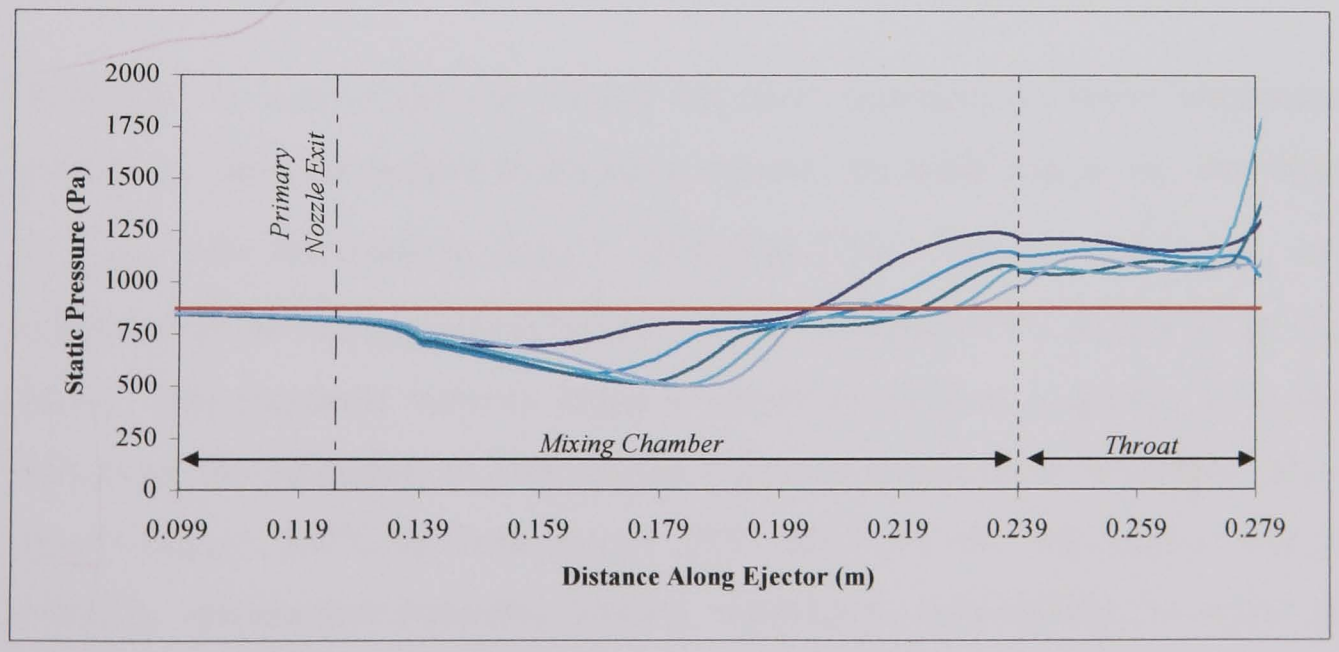

c. - Evaporator Temperature = 5 °C

Figure 6.24 - Effect of Boiler Temperature On Wall Pressure Distribution

chamber and throat. Secondary fluid is drawn into this gap increasing the measured surface area of the entrainment boundary, (circled values – Fig 6.23). As an example when T_{boiler} = 140°C at T_{evap} = 10°C the pressure at the chamber wall is seen to fall and correspondingly the entrainment boundary surface area rises. The same effect can be observed for T_{boiler} =135°C and 140°C at T_{evap} = 7.5°C. Eventually with a further increase in jet expansion the flow within the channel is entirely supersonic, closing the gap, and the measured surface area decreases. Mixing chamber wall pressure is still observed to fall due to the high jet velocity.

The increase in area of the entrainment boundary is not beneficial to entrainment, due to the proximity of the additional area to the chamber wall. This can be seen in Fig 6.20 when T_{boiler} = 140°C, the distance between the 1% and 10% primary mass fraction contours is reduced considerably near the chamber wall indicating reduced entrainment of secondary fluid.

The trendline identified in Fig 6.23 is therefore representative of the effective surface area of the entrainment boundary, which reduces as T_{boiler} increases. Secondary mass flow rate ($\dot{m}_2$) should reduce as the effective entrainment boundary reduces in area, however this was not the case as was seen in Fig 6.9. The behaviour of $\dot{m}_2$ observed in Fig 6.9 can now be explained.

Although the area of the entrainment boundary decreases as boiler temperature is raised, $\dot{m}_2$ does not behave in the same manner. An initial rise in $\dot{m}_2$ was observed as T_{boiler} was increased at T_{evap} = 10°C and 7.5°C. The increase in $\dot{m}_2$ can be attributed to the accompanying increase in exit velocity of the motive jet as T_{boiler} is raised. This increased velocity entrains secondary fluid at a quicker rate, initially offsetting the reduction in size of the effective entrainment boundary. However above T_{boiler} = 130°C for both T_{evap} = 10°C and 7.5°C the reduction in size of the effective entrainment boundary became significant, outweighing the effect of the increased motive jet velocity, thus $\dot{m}_2$ decreased.

At lower evaporator temperatures the motive jet expands at an increased rate due to the lower back pressure in the mixing chamber, hence the level of $\dot{m}_2$ is influenced

more. This could be seen in Fig 6.9 where the fall in $\dot{m}_2$ above T_{boiler} = 130°C is larger for T_{evap} = 7.5°C than at T_{evap} = 10°C. The expansion of the motive jet is severe at T_{evap} = 5°C. When T_{boiler} > 120°C the motive jet expands to fill and eventually choke the entire channel, hence $\dot{m}_2$ decreases for any increase in T_{boiler}.

In these simulations it can be seen that the level of entrainment is predominantly influenced by the primary mass flow rate. The expansion of the motive jet, which accompanies the increase in primary mass flow rate, is only a secondary affect on entrainment. Expansion of the motive jet only has a significant impact on entrainment when the mixing chamber back pressure is low and thus jet expansion is more severe. To enhance entrainment significantly a reduction in primary mass flow rate would therefore be required. However the motive jet must still possess sufficient momentum to choke the ejector throat, ensuring pressure independent operation.

6.2.1 – Low Pressure Studies

A study investigating the operational performance of the Eames[5] ejector at evaporator temperatures less than T_{evap} = 5°C (P_{evap} = 871.9 Pa) has been conducted. Simulations of the ejector operating at T_{evap} = 0.1°C to –40°C, reduced in 10°C intervals, have been performed. Additionally the ejector was simulated operating at evaporator pressures of 200, 100, and 50 Pa for a fixed temperature of 0.1°C.

It is important to determine the performance of the ejector at low evaporator pressures if the ejector was to be applied within sublimation refrigeration processes. Below T_{evap} = 0.1°C the evaporator could contain solid ice which will vaporise at a saturation pressure dependent upon temperature in a sublimation process. Steam vapour properties were not available below T_{evap} = 0.1°C. All properties in simulations where T_{evap} < 0.1°C were set with values corresponding to T_{evap} = 0.1°C. The boiler temperature was fixed at 120°C for all simulations, condenser pressure was set as 2000 Pa. This was an arbitrary value set low enough to ensure the ejector ran in a pressure independent manner with a fully choked throat. It is therefore not possible to calculate a meaningful COP_R value, hence only R_m values will be referred to. Details of applied boundary conditions can be found in Tables 6.4 and physical properties in Appendix D, Table D.3.

The results of the low pressure study are presented in Fig 6.25 and Table 6.4. Predicted entrainment values at evaporator temperatures of 10°C, 7.5°C, and 5°C have been included for comparison purposes.

Nº	Temperature (°C)			Pressure (Pa)		R_m
	Boiler	Evaporator	Condenser	Evaporator	Condenser	CFD
16	120	0.1	25	611.2	2000	0.332
17		-10		259.8		0.132
18		-20		103.8		0.031
19		-30		38.09		-0.005
20		-40		12.88		-0.011
21	120	0.1	25	200	2000	0.095
22		0.1		100		0.029
23		0.1		50		0.000

Table 6.4 - Results of Low Pressure Study

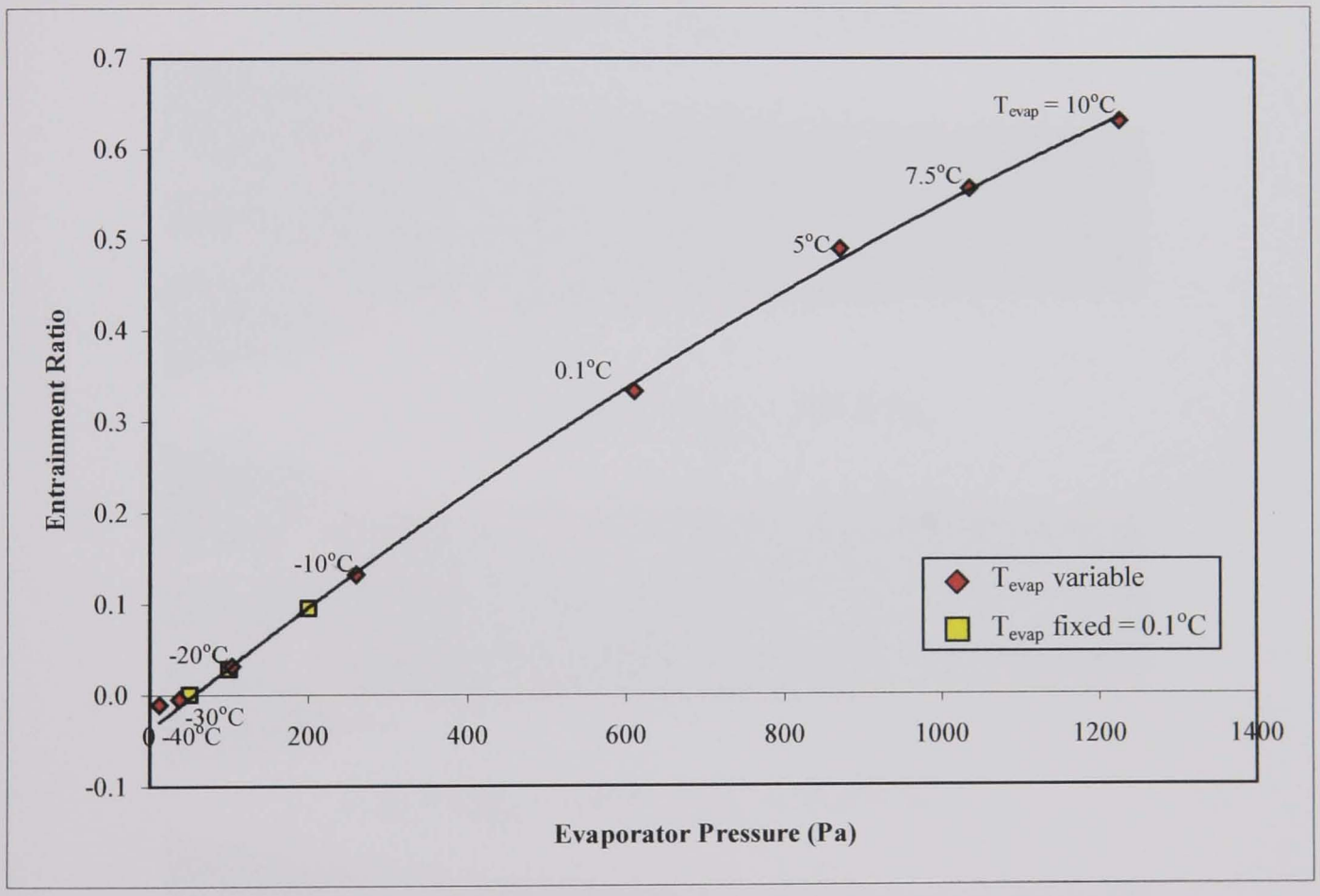

Figure 6.25 - Results of Low Pressure Study

It can be seen from Fig 6.25 that the reduction of evaporator temperature leads to a linear decrease in the predicted entrainment ratio of the ejector. However the line of best fit does not pass through the 0,0 origin. A negative entrainment is predicted once the evaporator pressure is lower than 50 Pa. It may be possible to obtain positive values of entrainment at this pressure or even lower, through the use of lower boiler temperatures.

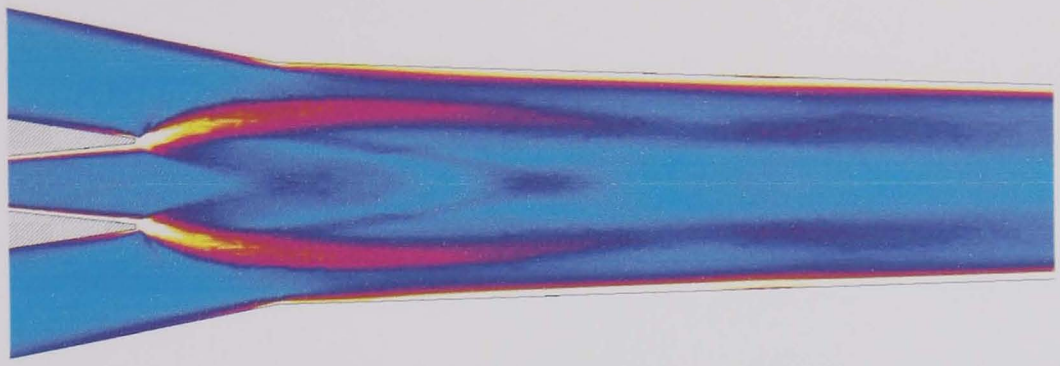

a. – T_{evap} = 0.1°C: P_{evap} = 611.2 Pa

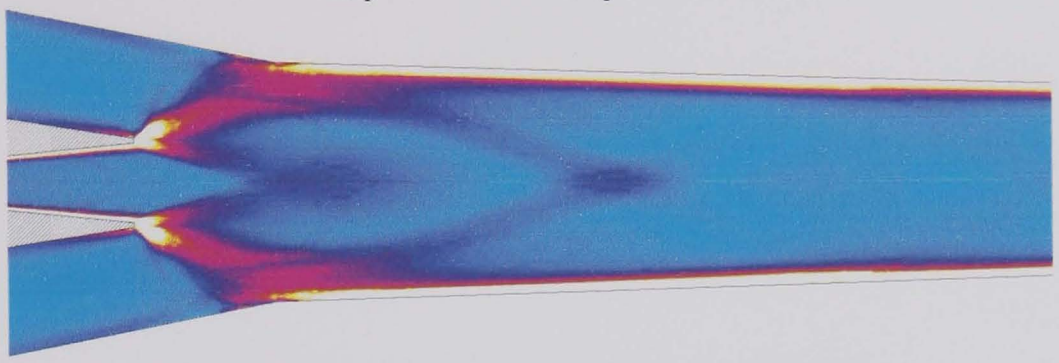

b. – T_{evap} = -10°C: P_{evap} = 259.8 Pa

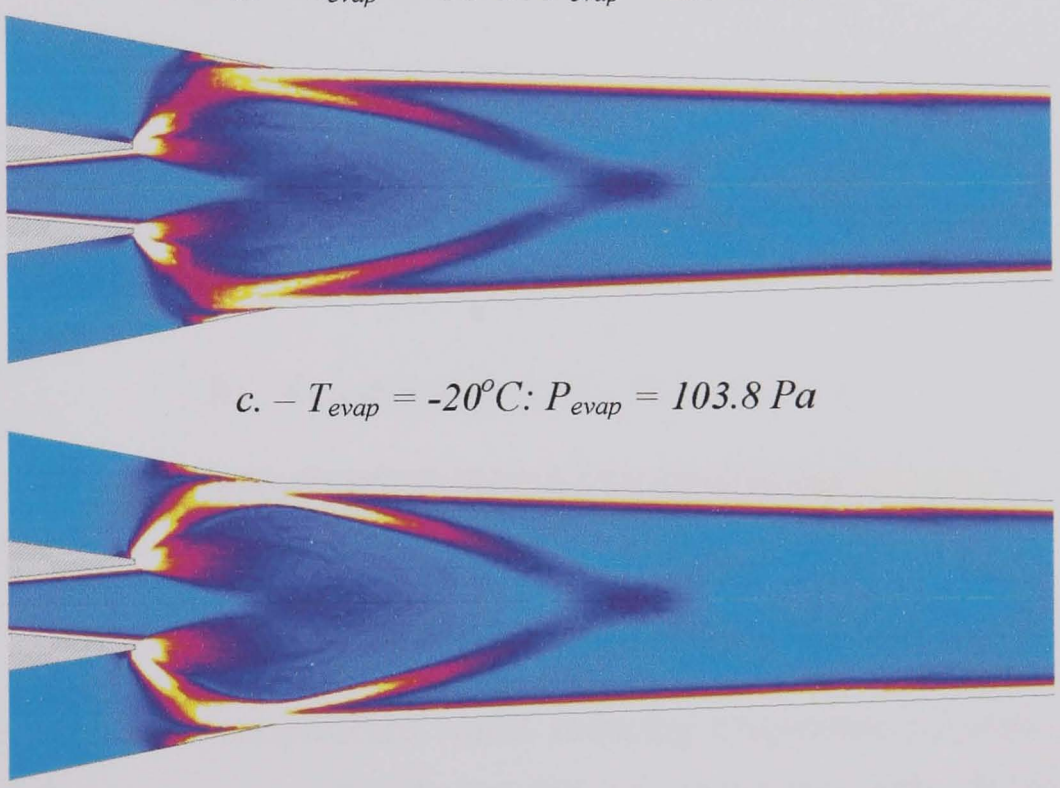

c. – T_{evap} = -20°C: P_{evap} = 103.8 Pa

d. – T_{evap} = -30°C: P_{evap} = 38.09 Pa

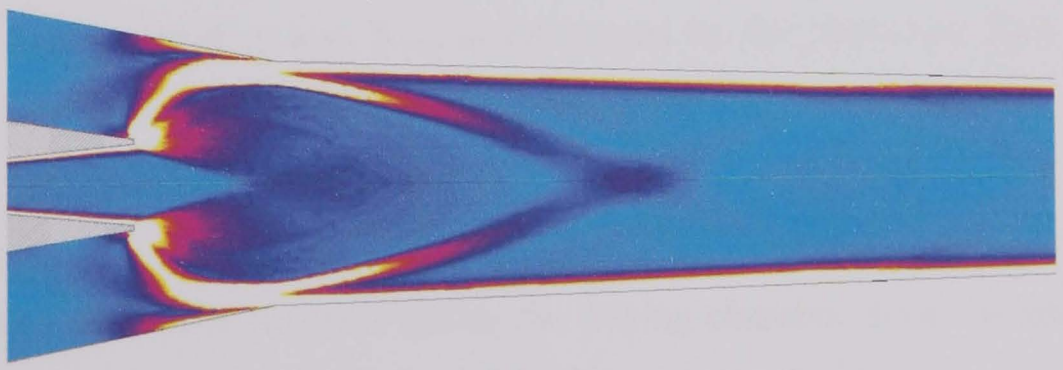

e. – T_{evap} = -40°C: P_{evap} = 12.88 Pa

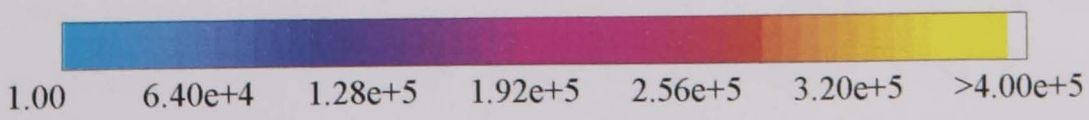

Figure 6.26 (a-e) – Predicted Strain Rate (1/s) Within Ejector

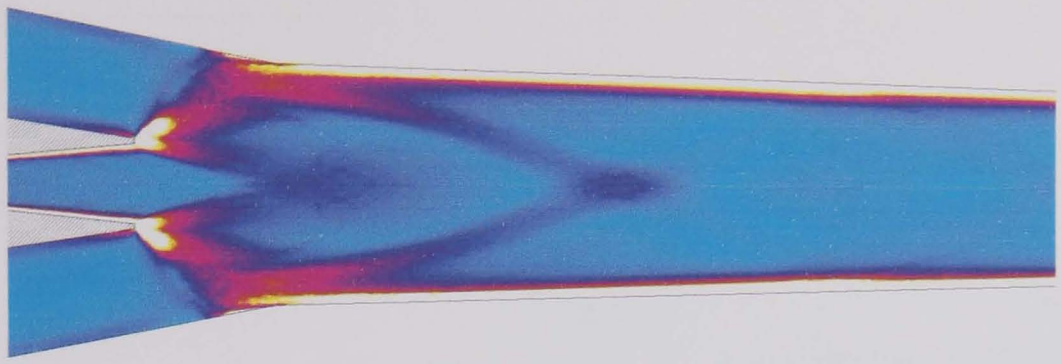

f. – T_{evap} Fixed At 0.1°C: P_{evap} = 200 Pa

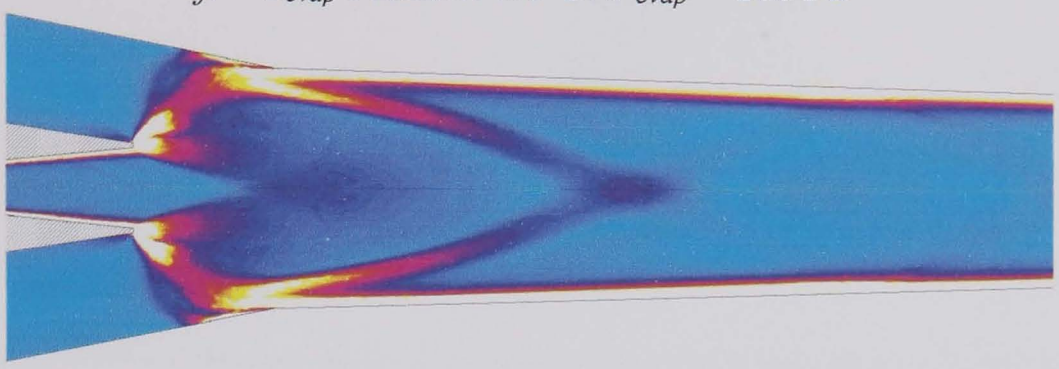

g. – T_{evap} Fixed At 0.1°C: P_{evap} = 100 Pa

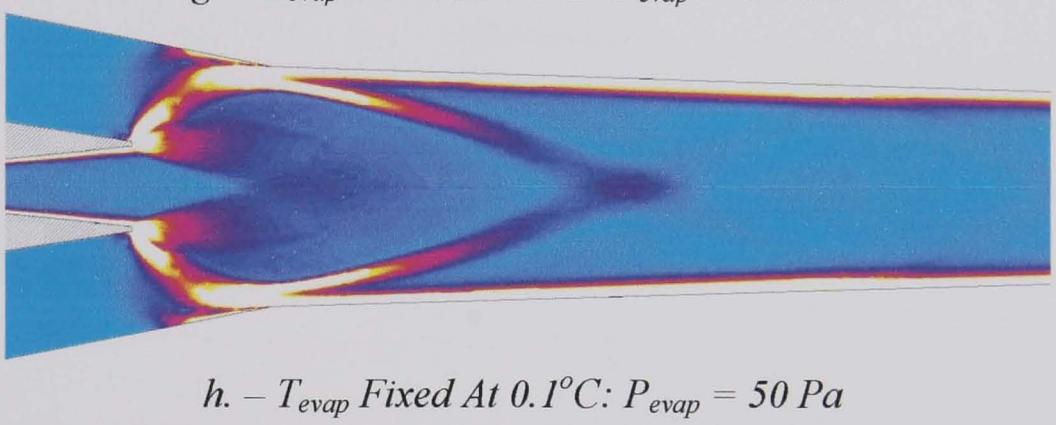

h. – T_{evap} Fixed At 0.1°C: P_{evap} = 50 Pa

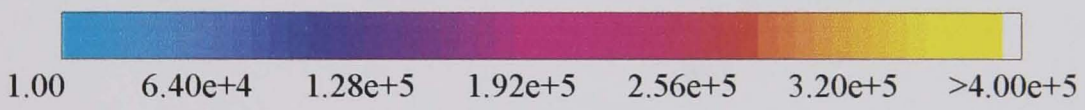

Figure 6.26 (f-h) – Predicted Strain Rate (1/s) Within Ejector

Fixing the evaporator temperature whilst reducing evaporator pressure is seen to have no influence upon predicted entrainment, simulation N^{o}'s 21-23. Thus in simulation, entrainment at low T_{evap} is influenced by the stipulated flow boundary pressure alone. However in reality so long as the secondary fluid is steam, these two properties would be linked regardless.

Fig 6.26 shows the flow structure within the mixing chamber. It can be seen that the reduction in evaporator temperature causes the emerging supersonic jet to expand to a greater and greater extent. The expansion fans at the nozzle exit are seen to increase in strength with reducing evaporator temperature. Once T_{evap} has been reduced to –20°C the jet has expanded to fill the entire mouth of the mixing section.

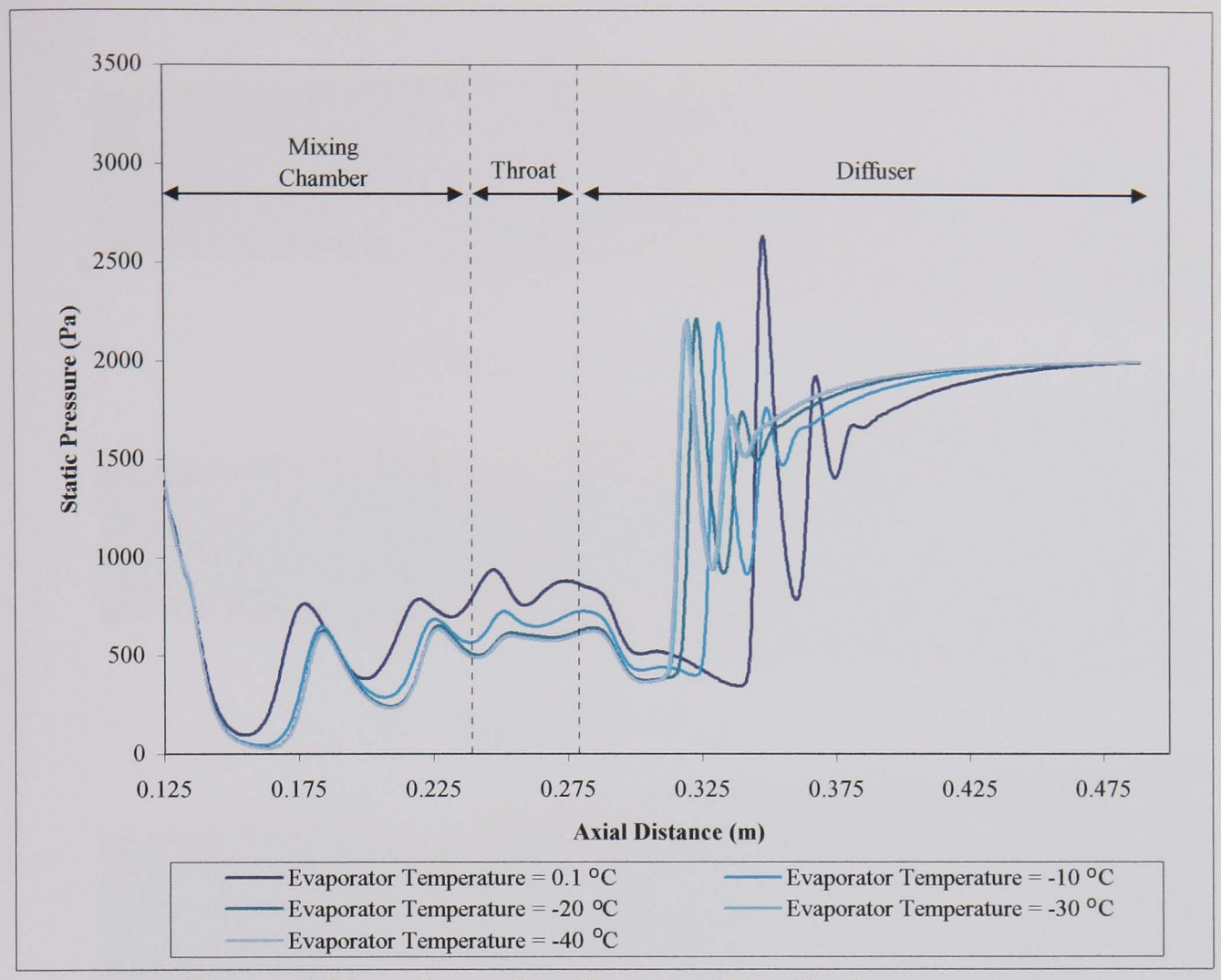

Figure 6.27a - Centreline Pressure Distribution

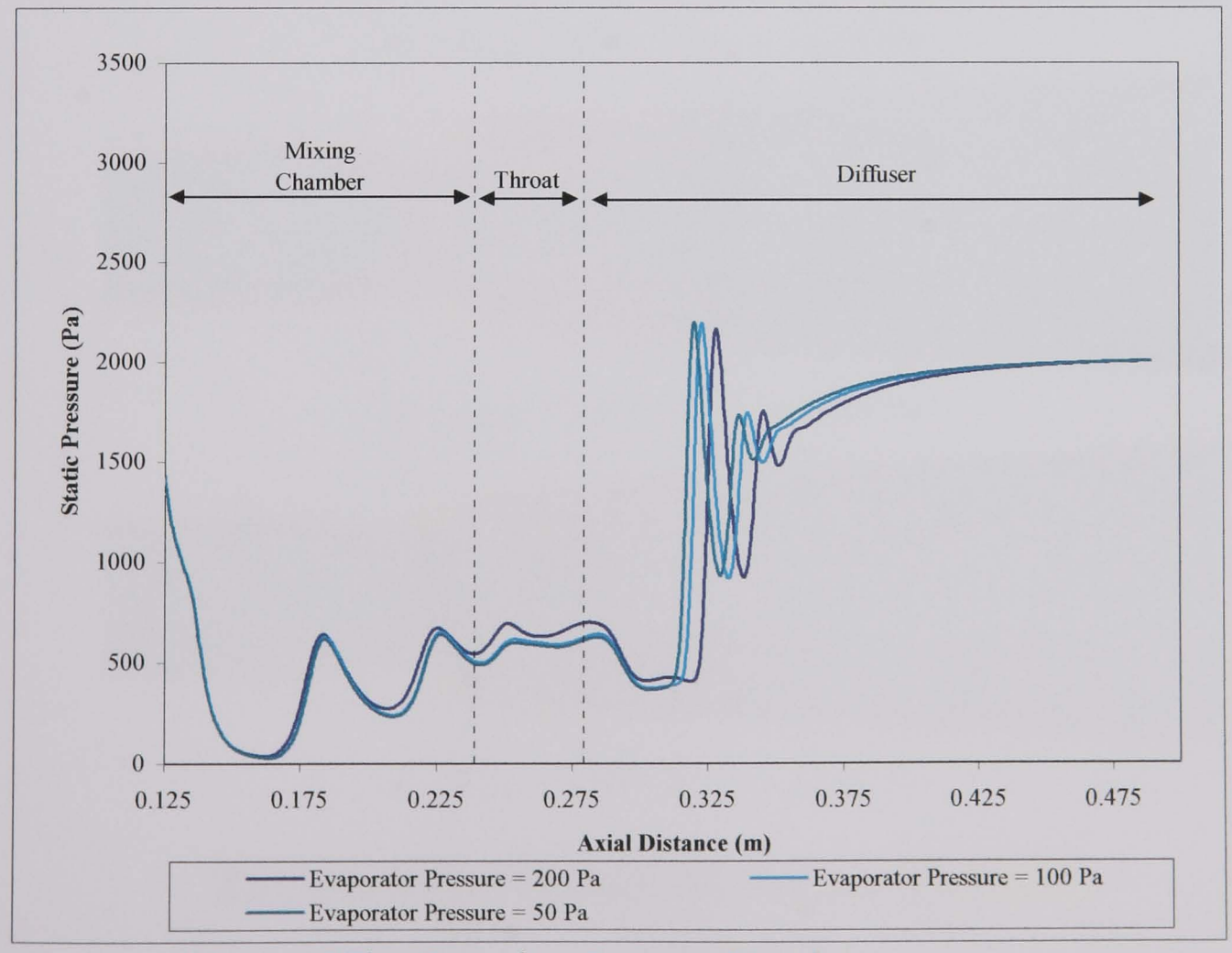

Figure 6.27b - Centreline Pressure Distribution

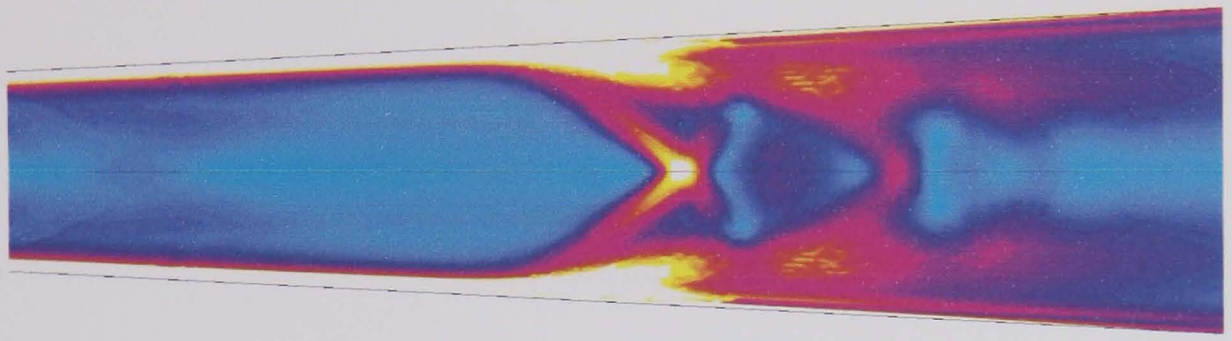

a. – T_{evap} = 0.1°C: P_{evap} = 611.2 Pa

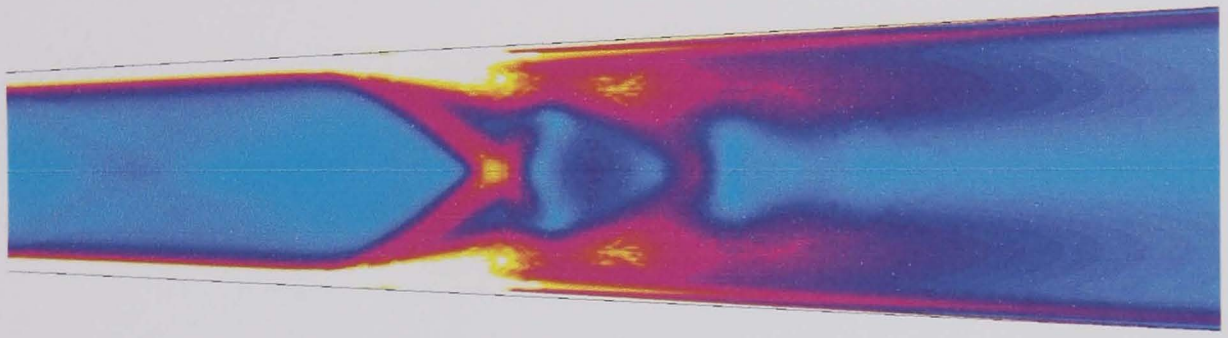

b. – T_{evap} = -10°C: P_{evap} = 259.8 Pa

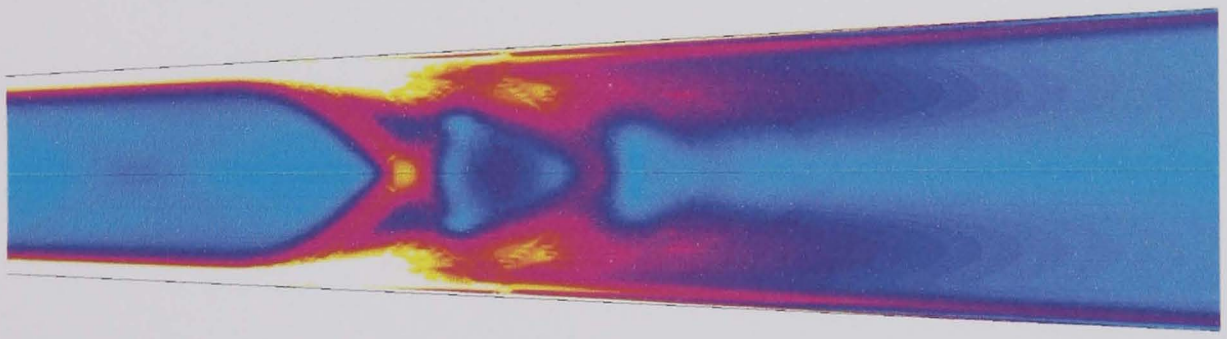

c. – T_{evap} = -20°C: P_{evap} = 103.8 Pa

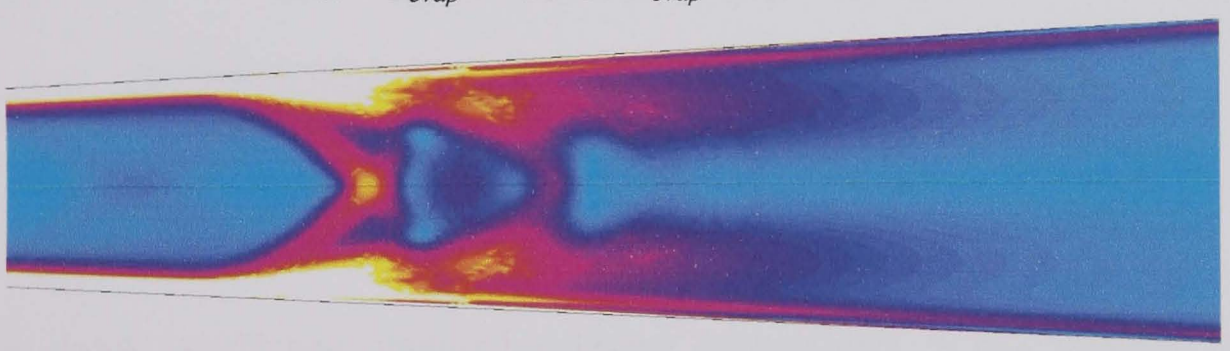

d. – T_{evap} = -30°C: P_{evap} = 38.09 Pa

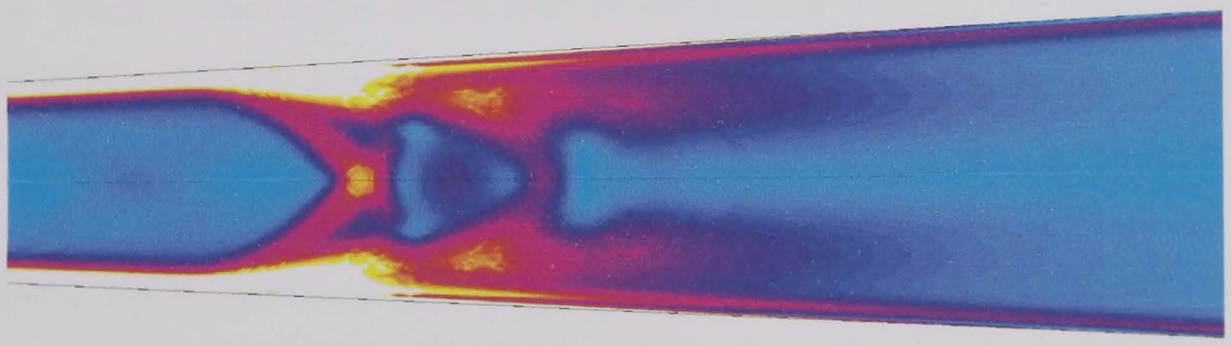

e. – T_{evap} = -40°C: P_{evap} = 12.88 Pa

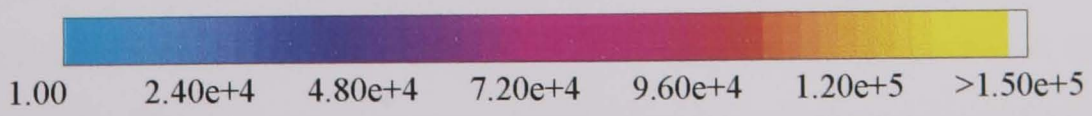

Figure 6.28 (a-e) – Predicted Strain Rate (1/s) Within Ejector Diffuser

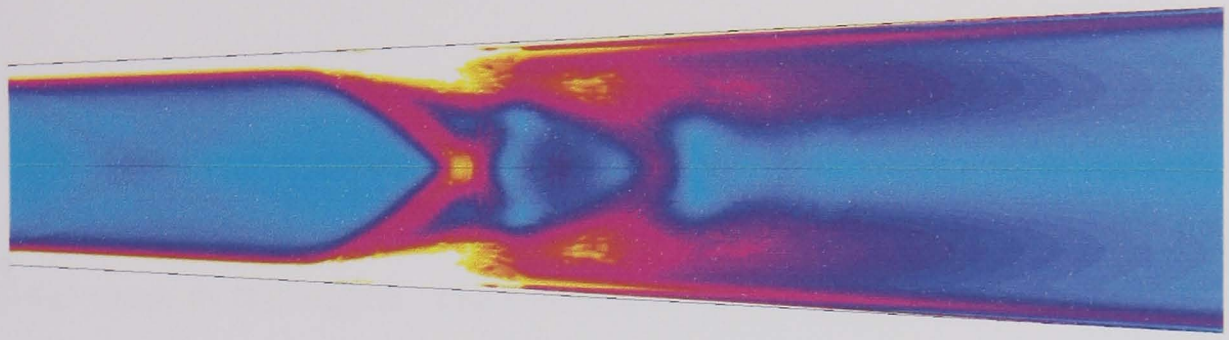

f. – T_{evap} Fixed At 0.1°C: P_{evap} = 200 Pa

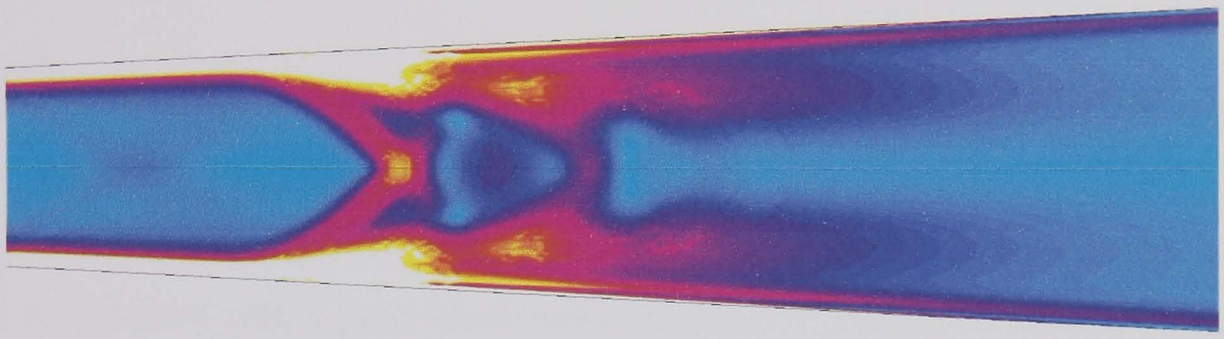

g. – T_{evap} Fixed At 0.1°C: P_{evap} = 100 Pa

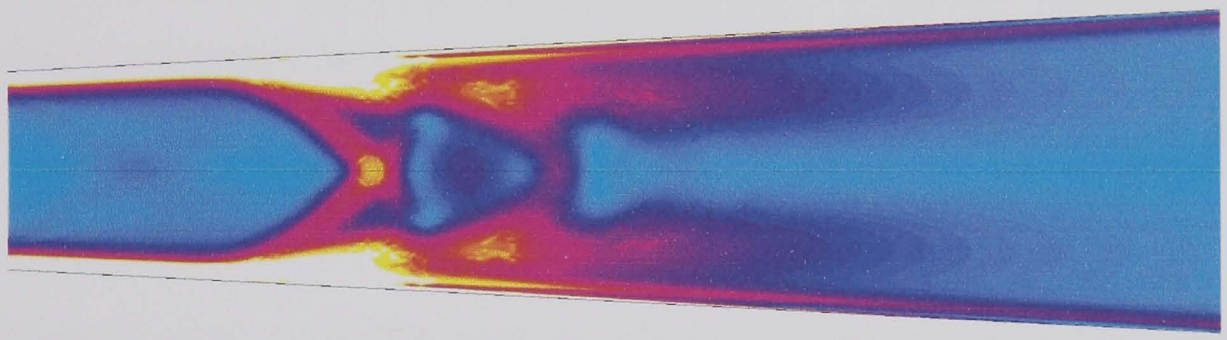

h. – T_{evap} Fixed At 0.1°C: P_{evap} = 50 Pa

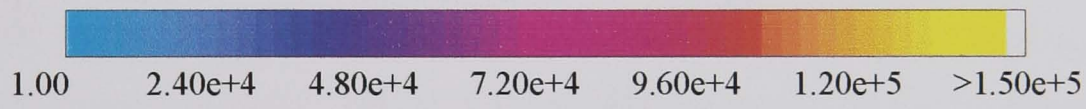

Figure 6.28 (f-h) – Predicted Strain Rate (1/s) Within Ejector Diffuser

The lip shock, which was observed at higher temperatures, is now replaced by an oblique shock. This forms at the wall of the mixing chamber, as the entire flow within the chamber becomes supersonic. After the occurrence of the wall shock the chamber appears to contain no further shock structure.

However it can be seen in plots of centreline pressure, Figs 6.27, that the flow within the chamber does exhibit the characteristic "barrelling" of supersonic flow. Reflections of expansion fan structure are more widely spaced as the channel flow is completely supersonic. The customary normal shock system stands in the entrance of the diffuser. As the evaporator temperature/pressure is reduced the strength of this diffuser normal shock system decreases. This is to be expected as more energy within the jet is expended in the oblique shock at the mixing chamber entrance.

Contour plots of fluid strain rate within the diffuser are shown in Fig 6.28. The thick boundary layer prior to the shock system is visible, however as in Fig 6.14 – 6.16 the resolution of the shock system is poor. Again this could be improved through the use of a finer mesh in this region. The mesh in the diffuser is coarser than in the ejector throat, hence even with mesh refinement the shock is severely smeared.

The increased expansion of the supersonic jet is confirmed in Fig 6.29. The primary jet can be seen to expand rapidly, filling the mixing chamber mouth. The velocity of the flow also increases. Velocities exceeding M = 5 are attained within the first shock / expansion cell, a peak Mach number of M = 6.2 being reached at the lowest evaporator settings. The supersonic jet is observed to decrease in length as the evaporator temperature falls, extending less distance into the diffuser. This again is attributable to the oblique shock at the mixing chamber entrance and higher velocities in the first expansion cell expending more of the jet energy.

The influence of jet expansion upon the mixing and entrainment region within the ejector is shown in Fig 6.30. As the evaporator temperature or pressure settings are reduced the mixing region can be seen to decrease in size. The mixing layer appears to curve back over on itself, until it is eventually perpendicular to the chamber wall. This process is evident in Figs 6.30b & 6.30c. Once T_{evap} is lower than -30°C negative entrainment and reverse flow exist. Primary fluid escapes from the supersonic jet and flows back into the suction chamber.

Fig 6.31 shows the measured decrease in the surface area of the entrainment boundary. As in Section 6.2.1 the 1% primary species mass fraction contour is used as representative of this boundary. Results at evaporator temperatures of 10°C (1227 Pa), 7.5°C (1036.5 Pa), & 5°C (871.9 Pa), have been included for comparison purposes. The surface area is seen initially to gradually decrease as the evaporator pressure falls. As the jet expands to fill the mixing chamber entrance the surface area decreases rapidly as the entrainment boundary reduces. Surface area then remains constant between P_{evap} = 100 Pa to P_{evap} = 250 Pa as the entrainment region curves back over, Figs 6.30b, c, f, & g. Below P_{evap} = 100 Pa a reverse flow condition exists.

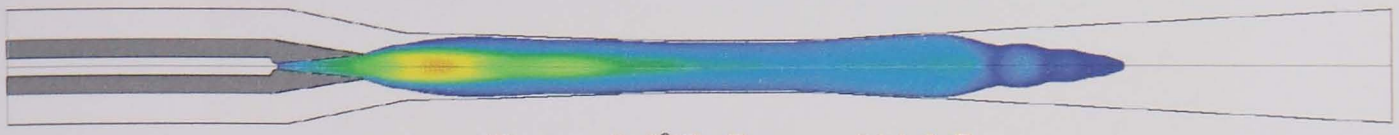

a. – $T_{evap} = 0.1^{o}C$: $P_{evap} = 611.2\ Pa$

b. – $T_{evap} = -10^{o}C$: $P_{evap} = 259.8\ Pa$

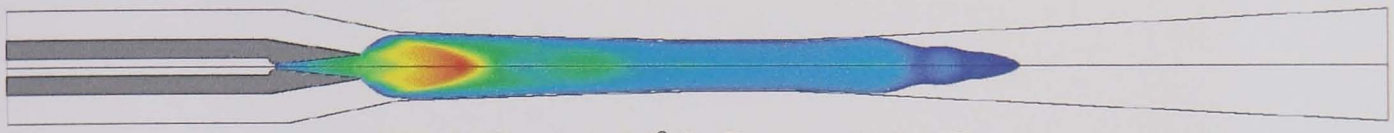

c. – $T_{evap} = -20^{o}C$: $P_{evap} = 103.8\ Pa$

d. – $T_{evap} = -30^{o}C$: $P_{evap} = 38.09\ Pa$

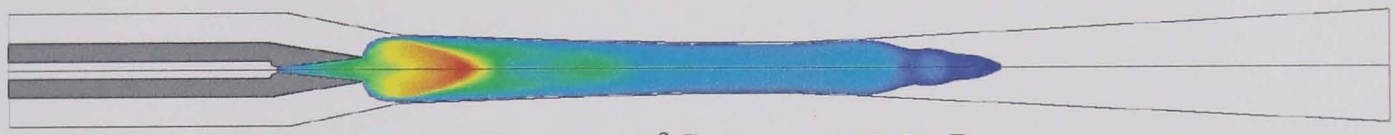

e. – $T_{evap} = -40^{o}C$: $P_{evap} = 12.88\ Pa$

f. – T_{evap} *Fixed At* $0.1^{o}C$: $P_{evap} = 200\ Pa$

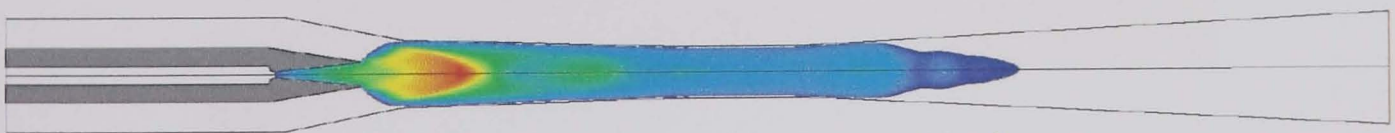

g. – T_{evap} *Fixed At* $0.1^{o}C$: $P_{evap} = 100\ Pa$

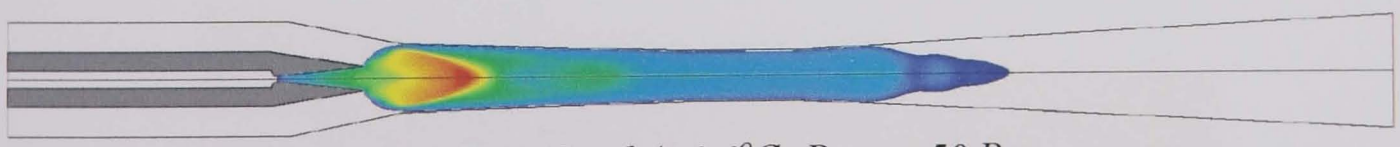

h. – T_{evap} *Fixed At* $0.1^{o}C$: $P_{evap} = 50\ Pa$

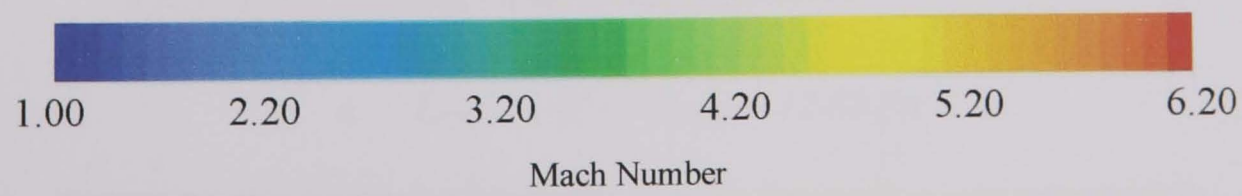

Figure 6.29 – Plots Of Supersonic Flow Region Within Ejector At Low Pressures

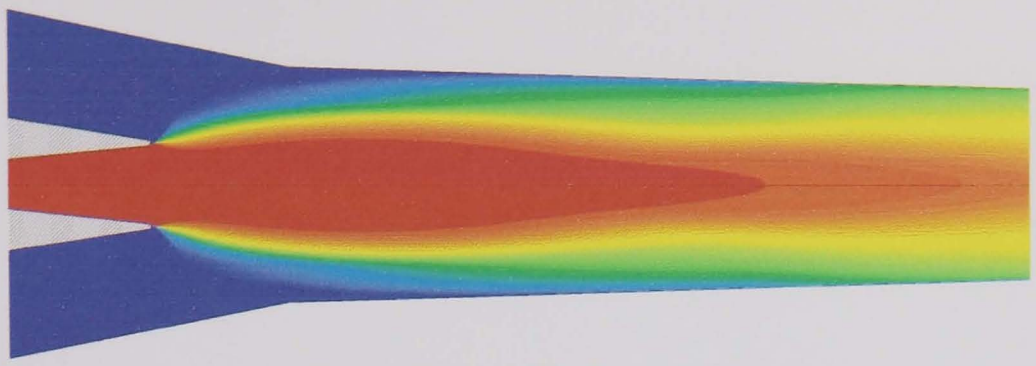

a. – T_{evap} = 0.1°C: P_{evap} = 611.2 Pa

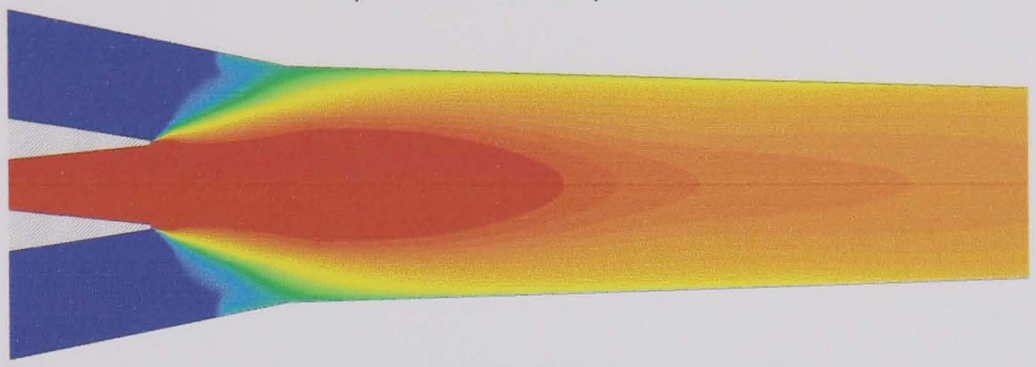

b. – T_{evap} = -10°C: P_{evap} = 259.8 Pa

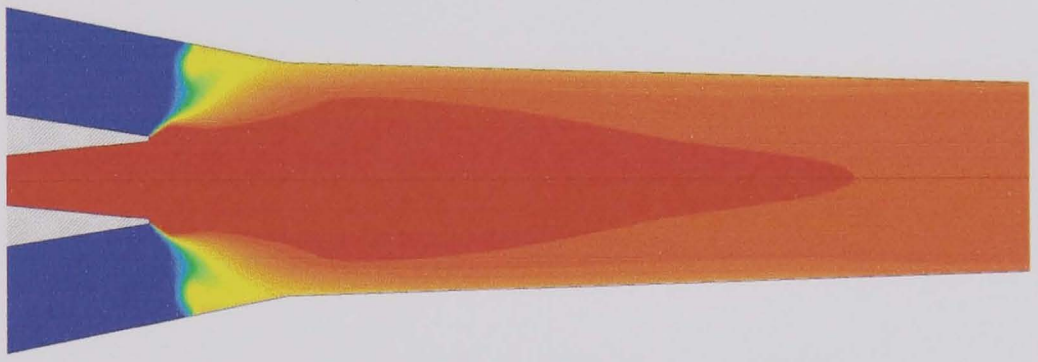

c. – T_{evap} = -20°C: P_{evap} = 103.8 Pa

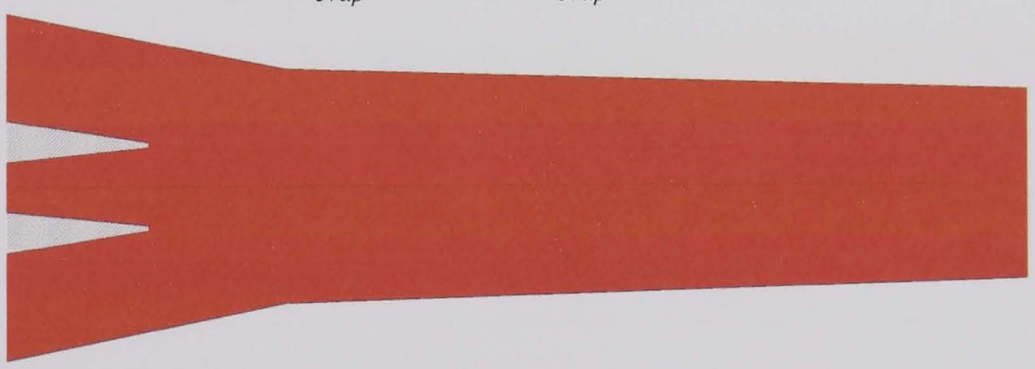

d. – T_{evap} = -30°C: P_{evap} = 38.09 Pa

e. – T_{evap} = -40°C: P_{evap} = 12.88 Pa

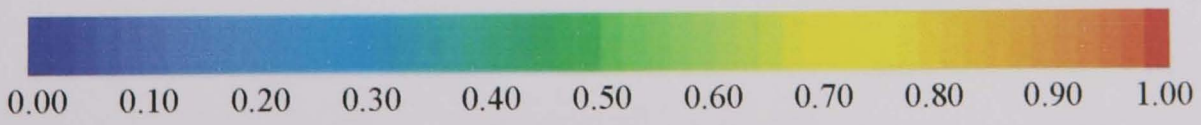

Figure 6.30(a-e) - Distribution of Primary Species Mass Fraction

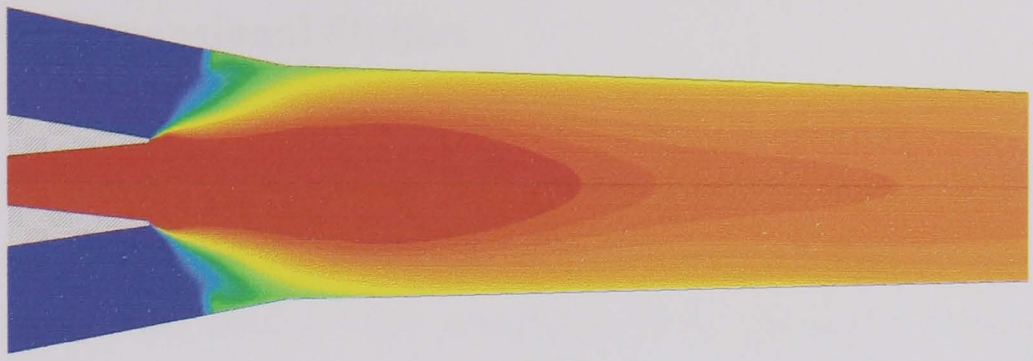

f. – T_{evap} Fixed At 0.1°C: P_{evap} = 200 Pa

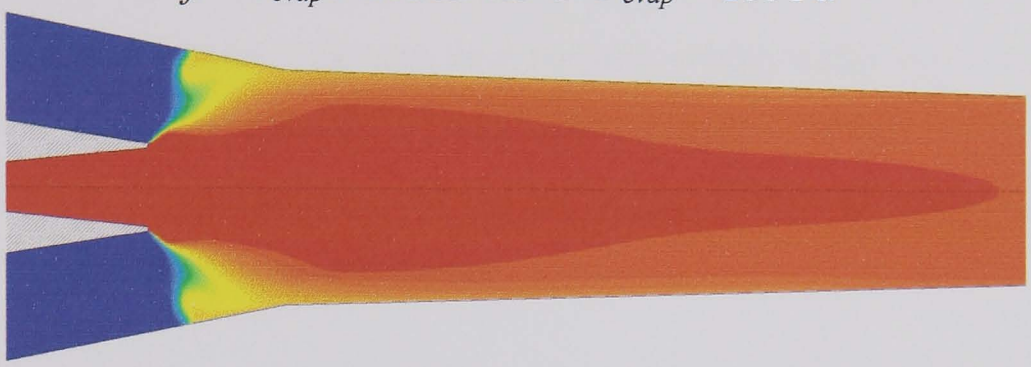

g. – T_{evap} Fixed At 0.1°C: P_{evap} = 100 Pa

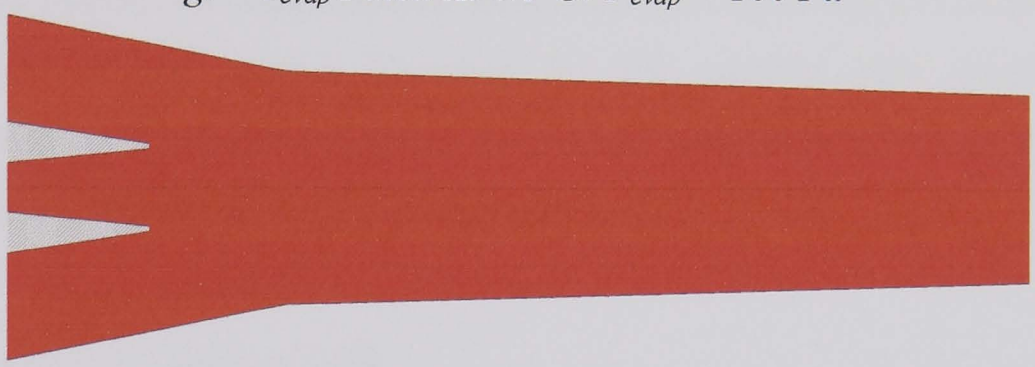

h. – T_{evap} Fixed At 0.1°C: P_{evap} = 50 Pa

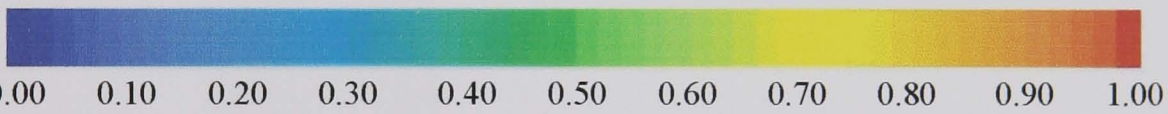

Figure 6.30(f-h) - Distribution of Primary Species Mass Fraction

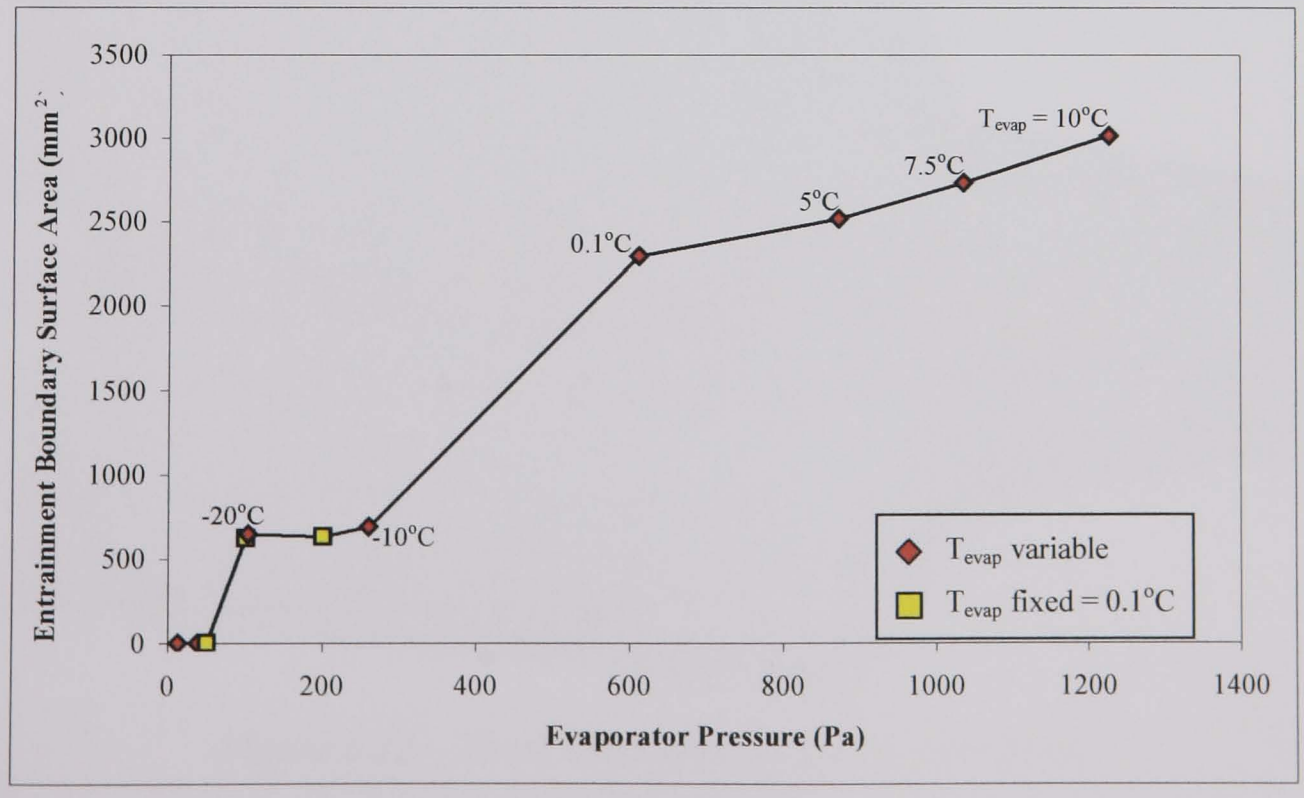

Figure 6.31 – Entrainment Boundary Surface Area

6.3 – Three Dimensional Studies

A three dimensional study of the Eames[5] ejector has been conducted. This allowed determination of whether the previously imposed axisymmetric approximations in the simulation of the ejector were acceptable. Two alternative suction chamber geometries have been modelled. The early Eames ejector design had a narrow suction inlet of 1" diameter. This was later replaced with a wider inlet, in accordance with ESDU[3] recommendations, of equivalent diameter to the suction chamber width. Modelling both inlets allowed the influence of inlet diameter upon ejector operational performance to be ascertained.

The two geometries and computational mesh were generated within Gambit. Fig 6.32 shows detail of the suction chamber for the narrow inlet geometry. The computational mesh comprises 143212 hexahedral and wedge cells, assembled using both structured and unstructured meshing schemes.

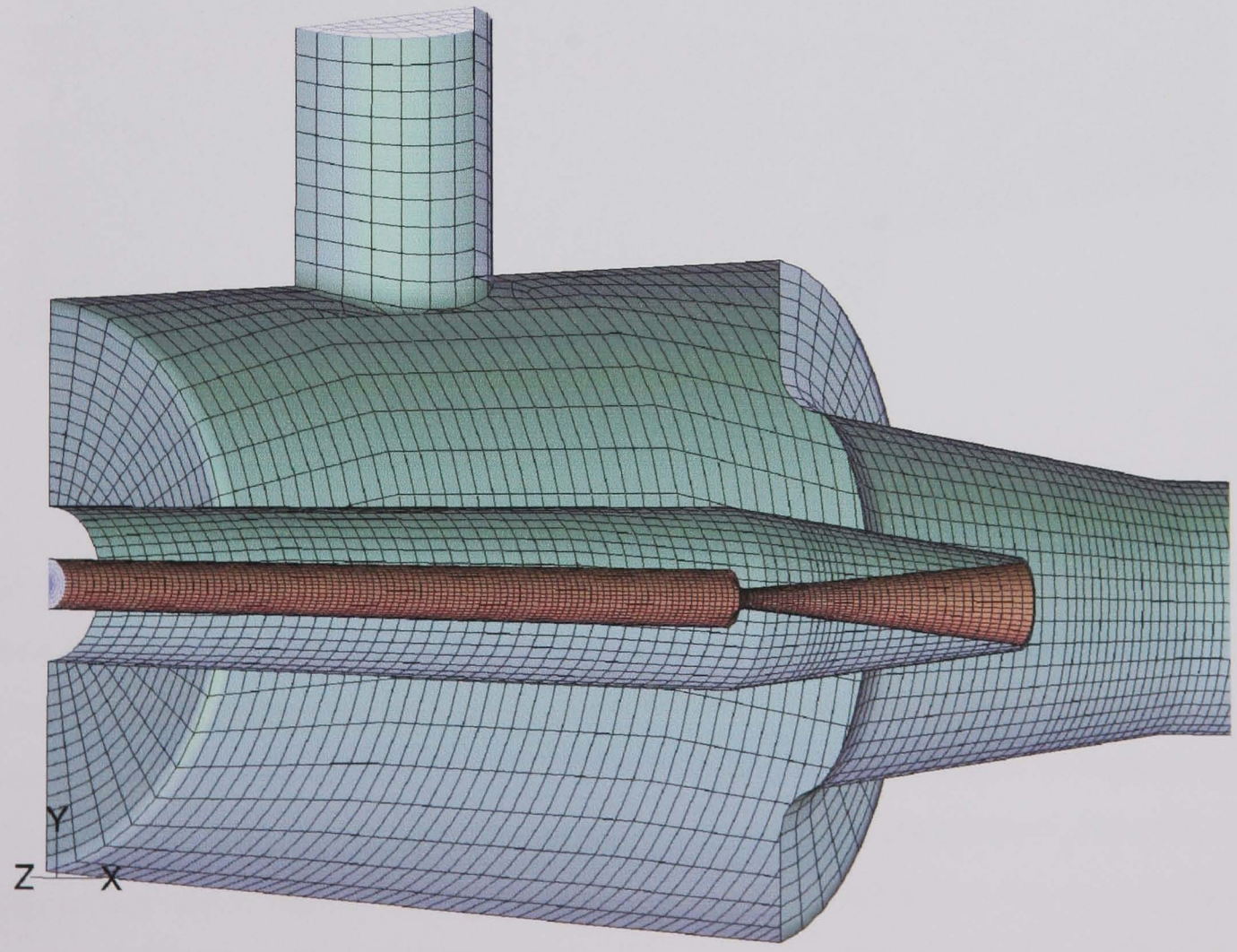

Figure 6.32 – Three Dimensional Narrow Inlet Mesh

Fig 6.33 shows the suction chamber geometry for the wide inlet. Tetrahedral cells were required in the mesh of this geometry due to the manner in which the inlet joins the suction chamber. In total 130180 tetrahedral, hexahedral, and wedge cells were required to mesh the geometry. Although the mesh within the suction chamber differs between the two geometries, the mesh used within the de Laval nozzle, mixing chamber, and diffuser, is identical.

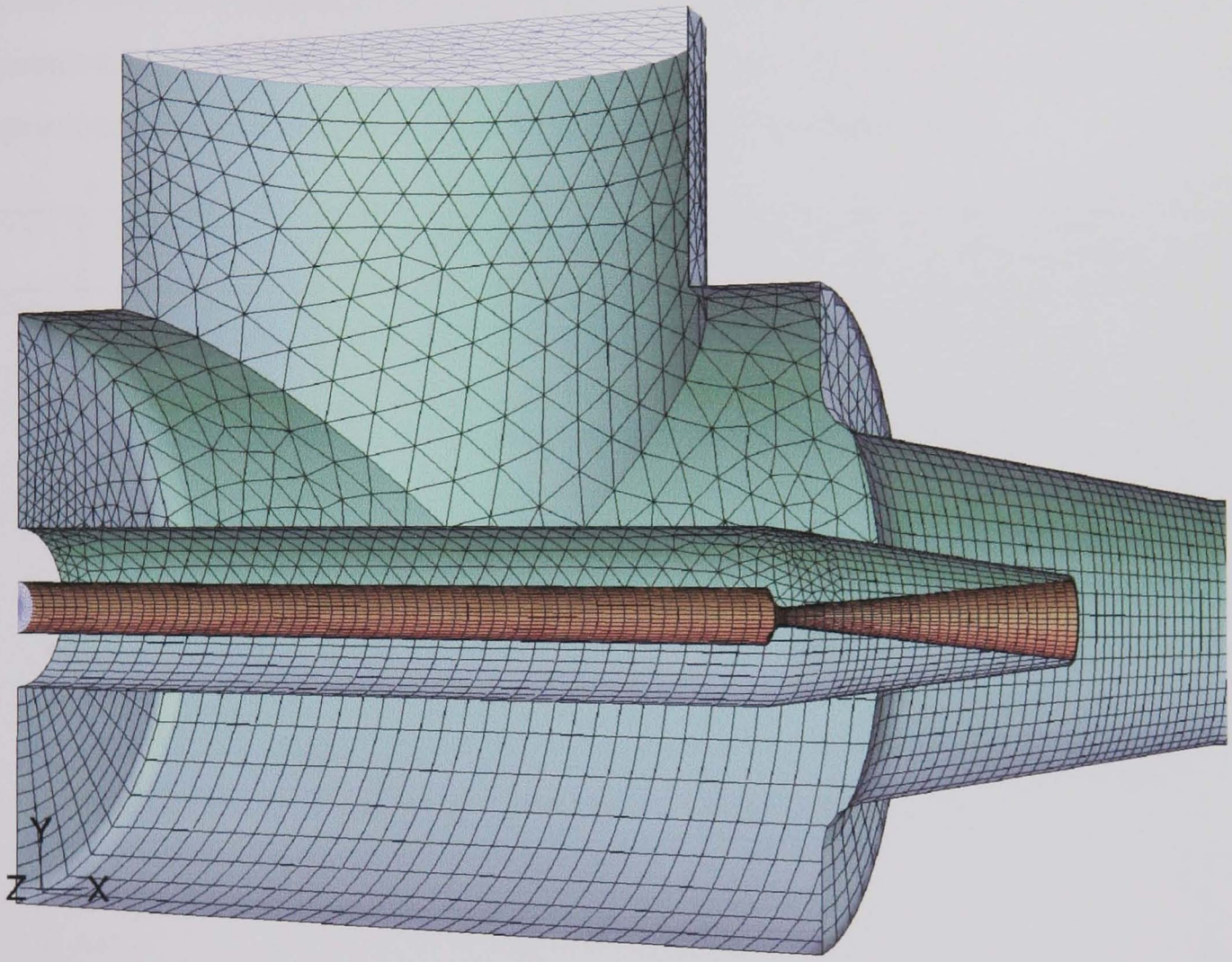

Figure 6.33 – Three Dimensional Wide Inlet Mesh

In comparison to the two dimensional mesh, used within the operating condition investigations (Section 6.2), the three dimensional mesh are relatively coarse. Computational resources limit the size of the mesh which can be solved, as does the number of equations and the nature of the solver adopted, i.e. coupled or segregated. The coupled solver was used in this study and it was the computational demands of this solver which limited the size of mesh. If a segregated solver had been used a mesh of 500000 cells could have been solved. The coarse mesh also affects the choice of near wall model. A standard wall function was used in this region as the

mesh requirements of the two layer zonal method, although preferential, were prohibitive.

The study was based upon three separate sets of critical operating conditions, see Section 2.4.2, taken from the experimental work of Eames et al[5]. Details of applied boundary conditions can be found in Table 6.5 and physical properties in Appendix D, Table D.4. Results of the study are presented within Table 6.5 and Fig 6.34. The results from two dimensional simulations at these modelled operating conditions are included in Fig 6.25 for comparison purposes. The experimental values are based upon studies which utilised an ejector with the wide secondary inlet.

Nº	Inlet	Temperature (°C)			Pressure (mbar)	R_m	COP_R	
		Boiler	Evaporator	Condenser	Condenser	CFD	CFD	Experiment
3D-01	Wide	120	10	28.3	38	0.615	0.571	0.586
3D-02			7.5	27.3	36	0.475	0.438	0.473
3D-03			5	26.5	34	0.369	0.337	0.586
3D-04	Narrow	120	10	28.3	38	0.537	0.498	0.586
3D-05			7.5	27.3	36	0.439	0.407	0.473
3D-06			5	26.5	34	0.338	0.309	0.309

Table 6.5 – Results of Three Dimensional Study

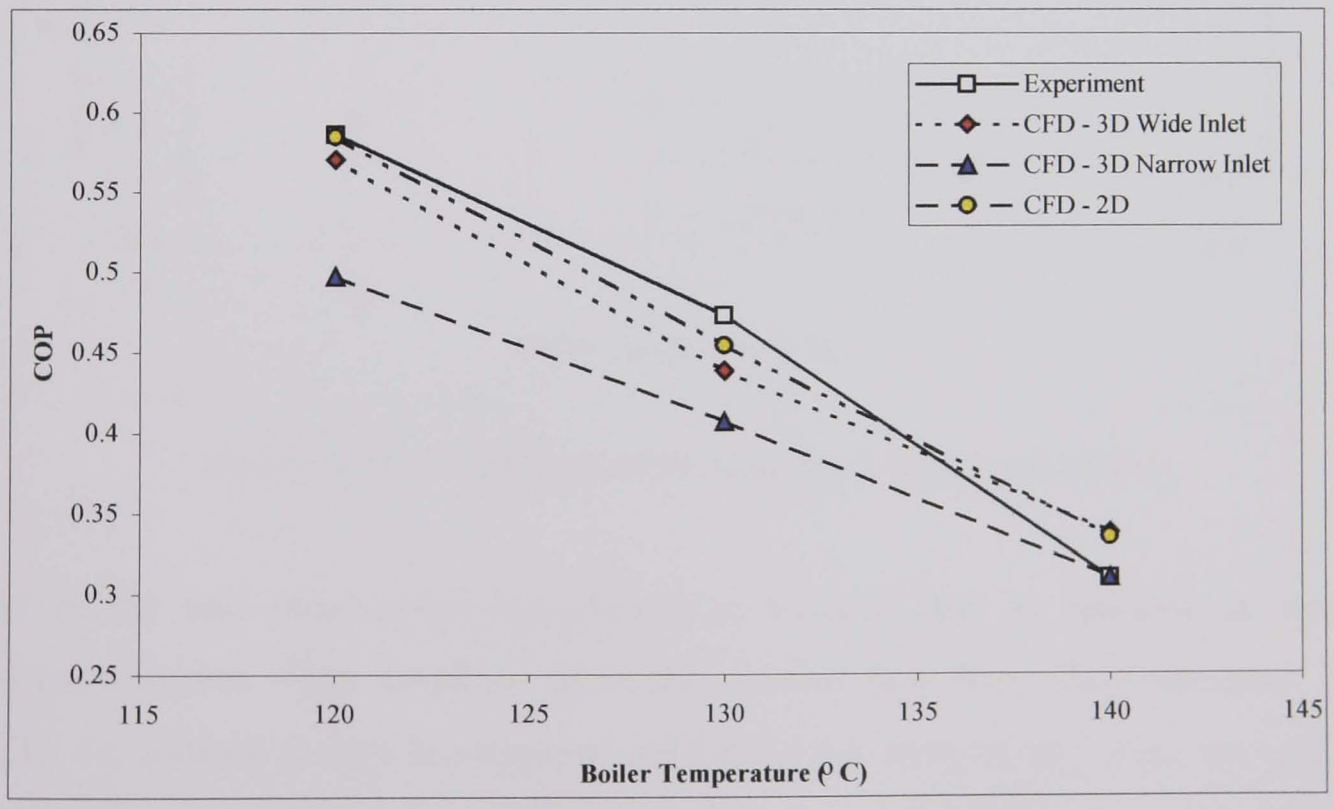

Figure 6.34 – Results of Three Dimensional Study

It can be seen that as with the two dimensional studies, simulations at T_{boiler} = 120°C and 130°C for the wide suction inlet under predict the COP_R of the ejector. The predicted values differ from experiment by –2.6% and –7.38% for T_{boiler} = 120°C and

130°C, respectively. At T_{boiler} = 140°C the COP_R value for the wide suction inlet is over predicted by 9%. The narrow inlet simulations produce COP_R values much lower than those for the wide inlet. Values of 15% & 14% lower than experiment are predicted at T_{boiler} = 120°C and 130°C, respectively. This is in agreement with the ESDU[3] guidelines which state that a generous secondary inlet should be used to guarantee effective operational performance. Simulation of the narrow inlet at T_{boiler} = 140°C produces a COP_R comparable to experiment. However it should be noted that the simulations have been shown to over-predict ejector performance at this boiler temperature, the result therefore is misleading.

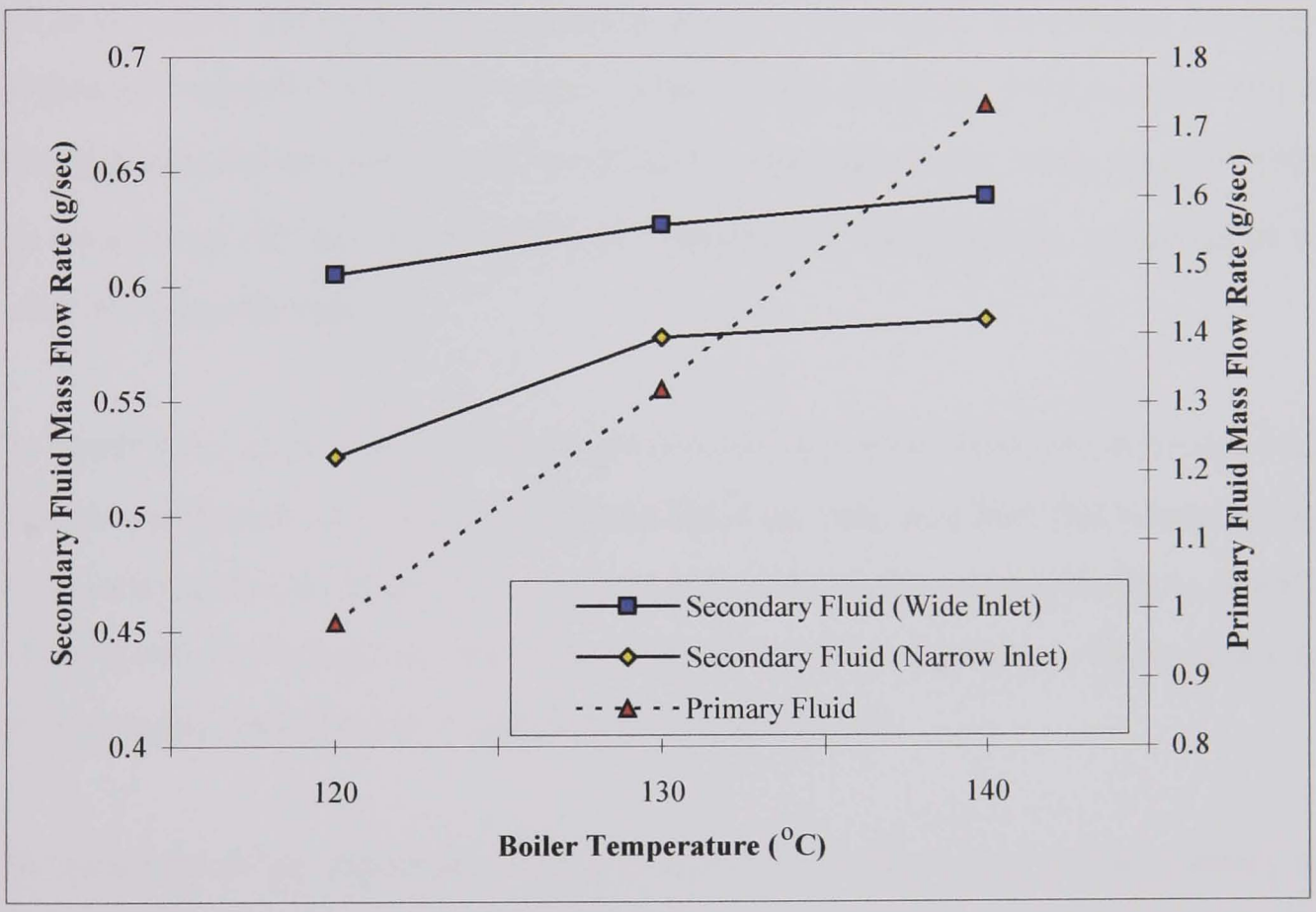

Figure 6.35 – Predicted Mass Flow Rates (3D Simulation)

As in the two dimensional simulations it is clear that an increase in boiler temperature has slight influence upon the induced flow from the evaporator, Fig 6.35. In contrast to two-dimensional simulation the level of $\dot{m}_2$ does not reduce when $T_{boiler} > 130°C$, however the disproportionate increase in primary mass flow rate reduces any potential benefits to predicted entrainment ratio.

It is not possible to use plots of strain rate to view the flow structure within the ejector in the three dimensional study. The mesh that has been used, although

capable of resolving key flow structure, is incapable of clearly resolving shock cell structure within the supersonic flow. It is still possible to visualise the flow within the ejector via other means. Figs 6.36 and 6.37 show plots of the supersonic flow within the ejector, along a symmetrical slice, for the wide and narrow inlets respectively. It can be seen that the supersonic jet does not expand within the ejector throat to the same extent with the narrow inlet as with the wide secondary inlet, for T_{boiler} = 120°C and 130°C. This accounts for the lower entrainment ratio observed with the narrow inlet. The throat appears equally choked for both inlets at T_{boiler} = 140°C. Prediction of a lower entrainment for the narrow inlet at this boiler temperature can be explained by the greater degree of jet expansion external to the de Laval nozzle. However in comparison to two dimensional simulations the motive jet does not expand to the same extent in the mixing chamber. This explains why the three dimensional simulations do not predict a decrease in $\dot{m}_2$ when $T_{boiler} > 130°C$. The benefits of the increased motive jet velocity still outweigh the reduction in size of the entrainment region.

The supersonic jet is seen to be not perfectly axisymmetric. With the wide secondary inlet the supersonic jet is observed to turn up at the end, an effect that becomes more pronounced as boiler temperature is raised. In contrast the supersonic jet is observed to turn down at the end, for the narrow secondary inlet geometry. Again this effect becomes more pronounced at higher boiler temperatures.

The influence of jet expansion upon the interaction and mixing of the primary and secondary fluids can be seen in Figs 6.38 and 6.39 for the wide and narrow inlet geometries, respectively. As in the two dimensional studies the mixing region between the two fluids decreases in area with increasing boiler temperature. However the resolution of the mixing region is not as clear in the 3D studies. This is due to the coarse mesh density used within the mixing chamber. More information regarding the influence of jet expansion upon the mixing region can be obtained by plotting an iso-surface of a mass fraction contour. The 1% primary species mass fraction contour representative of the entrainment boundary was chosen. Figs 6.40 and 6.41 show three dimensional views of this iso-surface for the wide and narrow inlet geometries respectively.

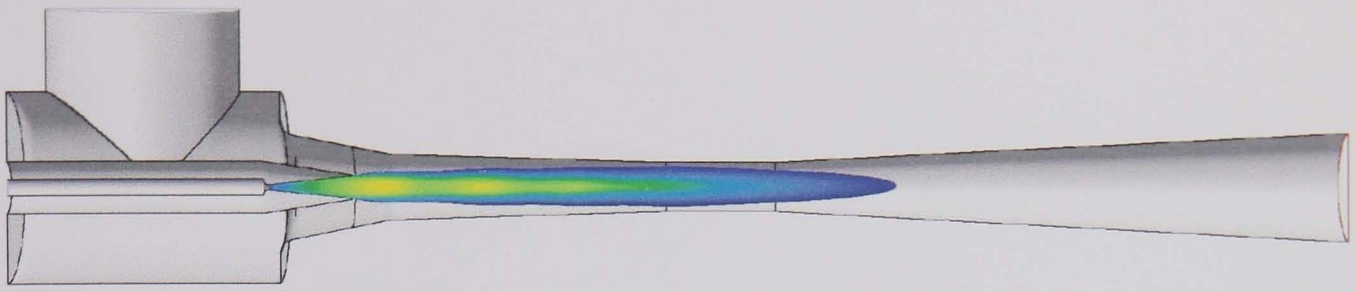

a. – $T_{Boiler} = 120^{o}C$

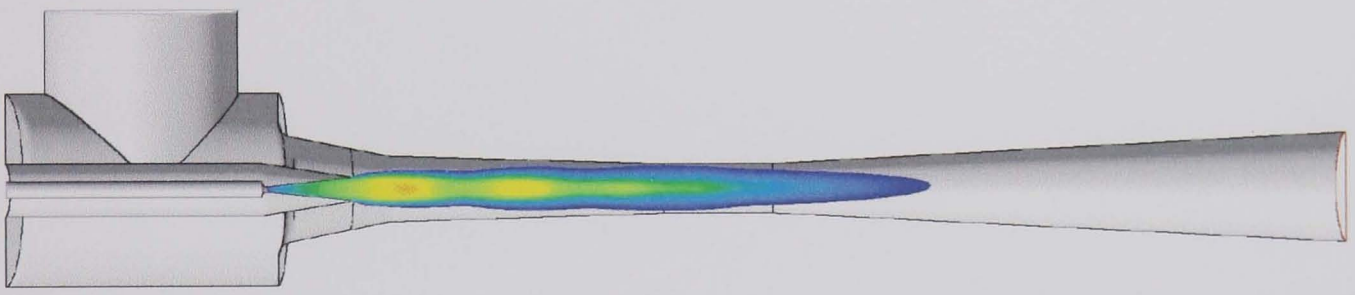

b. – $130^{o}C$

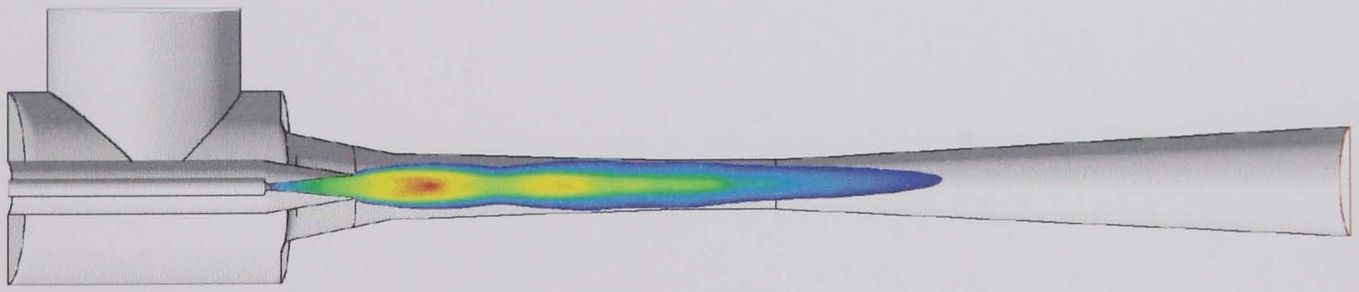

c. – $140^{o}C$

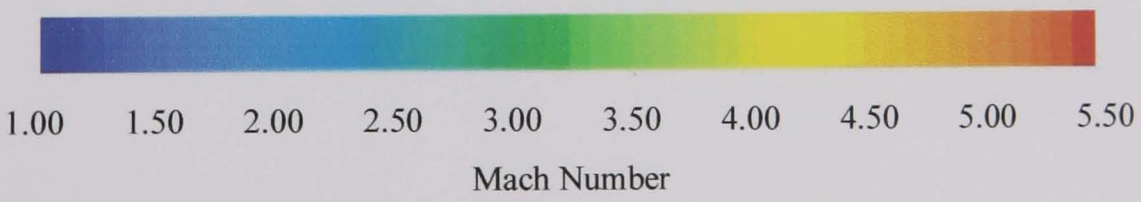

Figure 6.36 - Supersonic Flow Region Within Ejector. Wide Suction Inlet

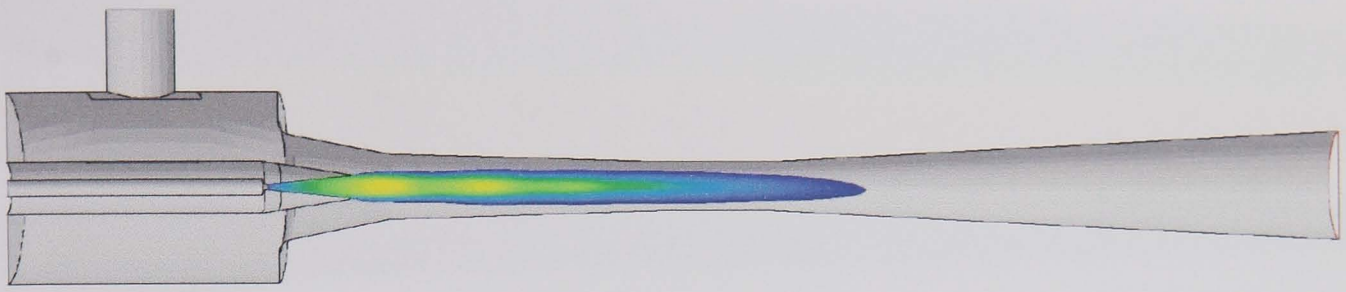

a. – $T_{Boiler} = 120^{o}C$

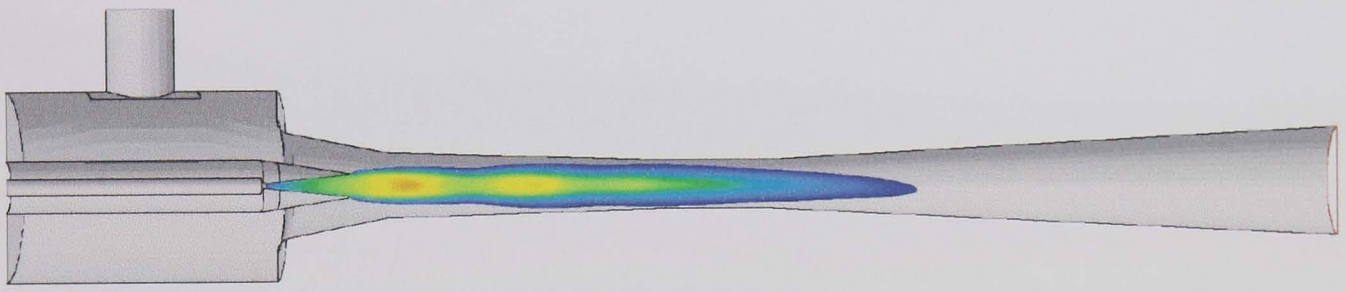

b. – $130^{o}C$

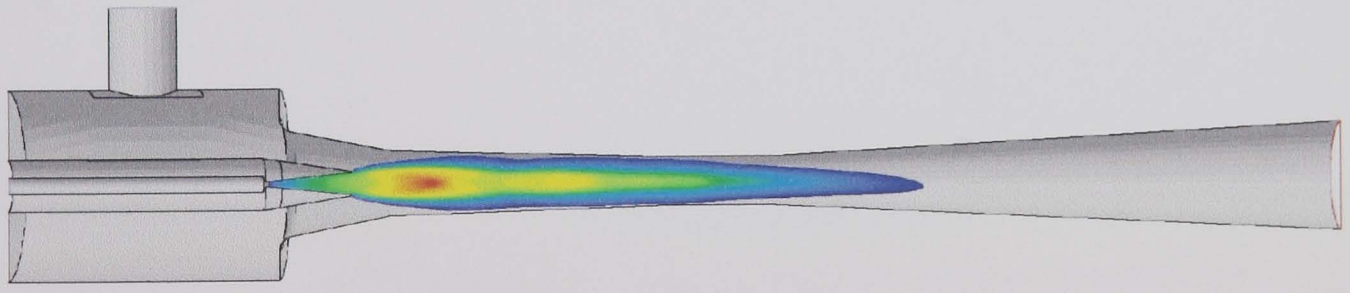

c. – $140^{o}C$

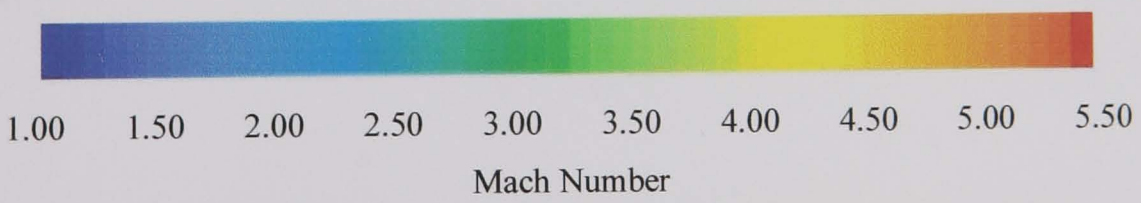

Figure 6.37 - Supersonic Flow Region Within Ejector.
Narrow Suction Inlet

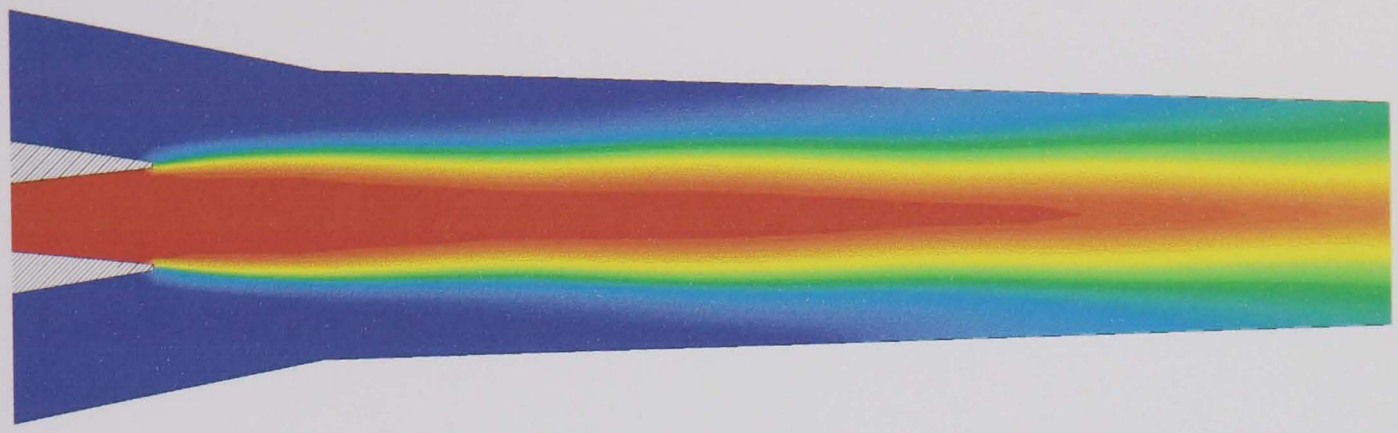

a. – $T_{Boiler} = 120^{o}C$

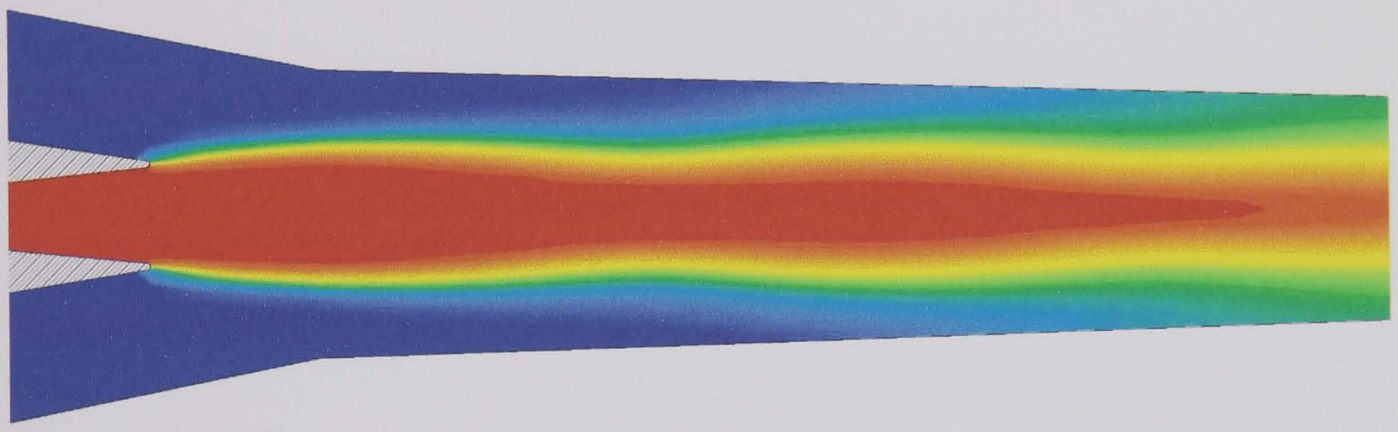

b. – $130^{o}C$

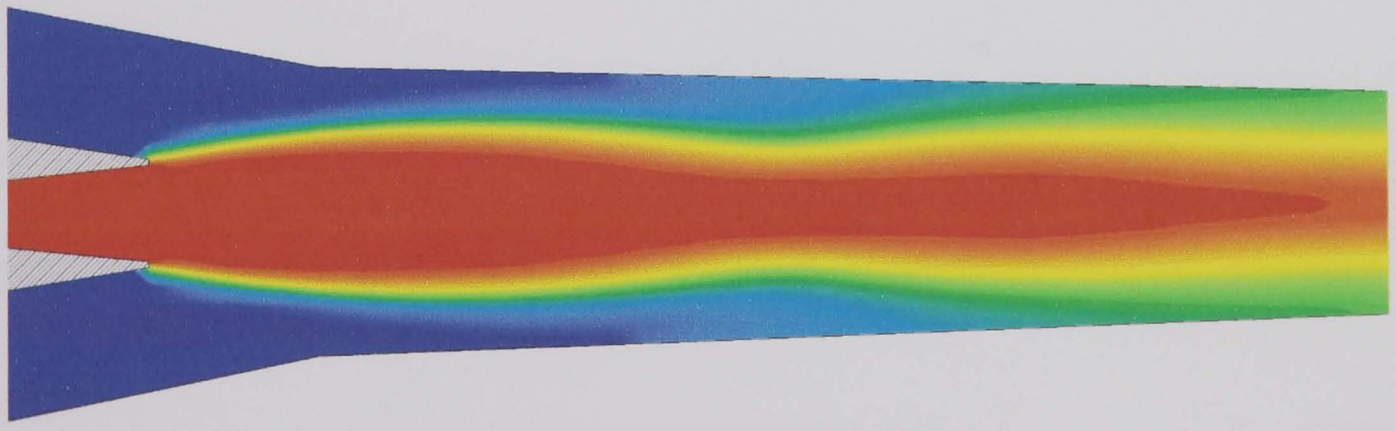

c. – $140^{o}C$

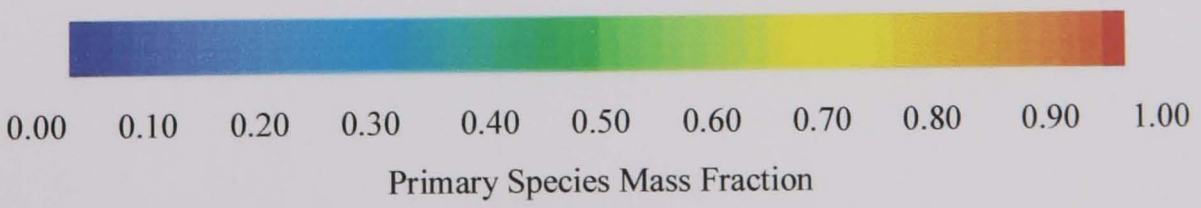

Figure 6.38 - Distribution of Primary Species Mass Fraction. Wide Secondary Inlet.

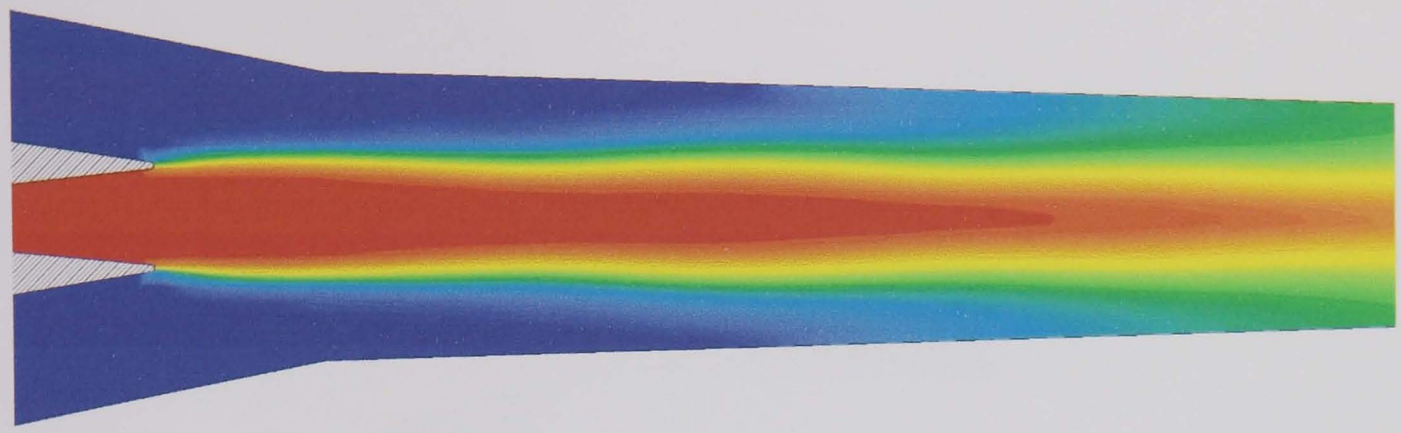

a. – $T_{Boiler} = 120^{o}C$

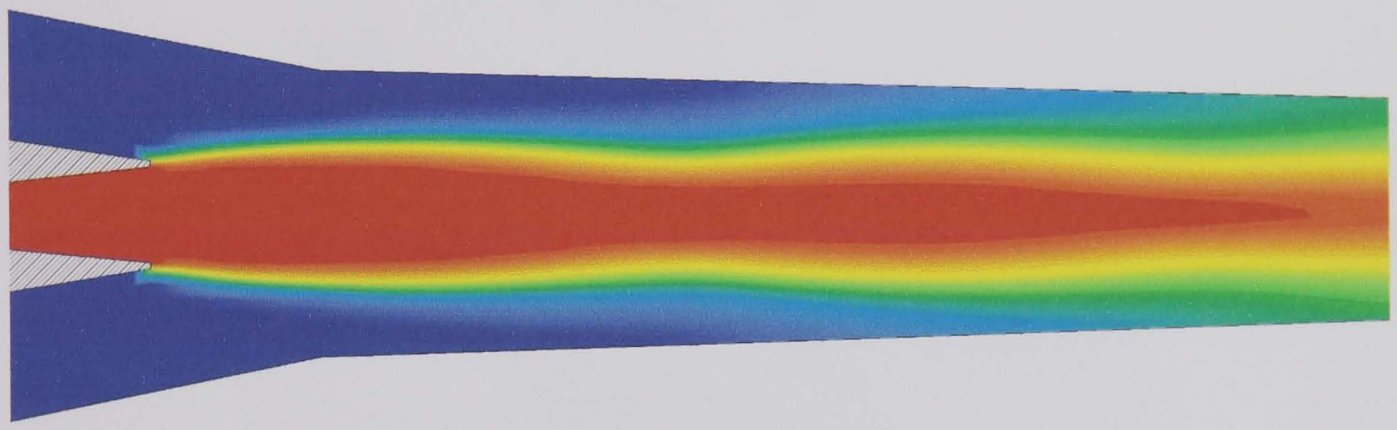

b. – $130^{o}C$

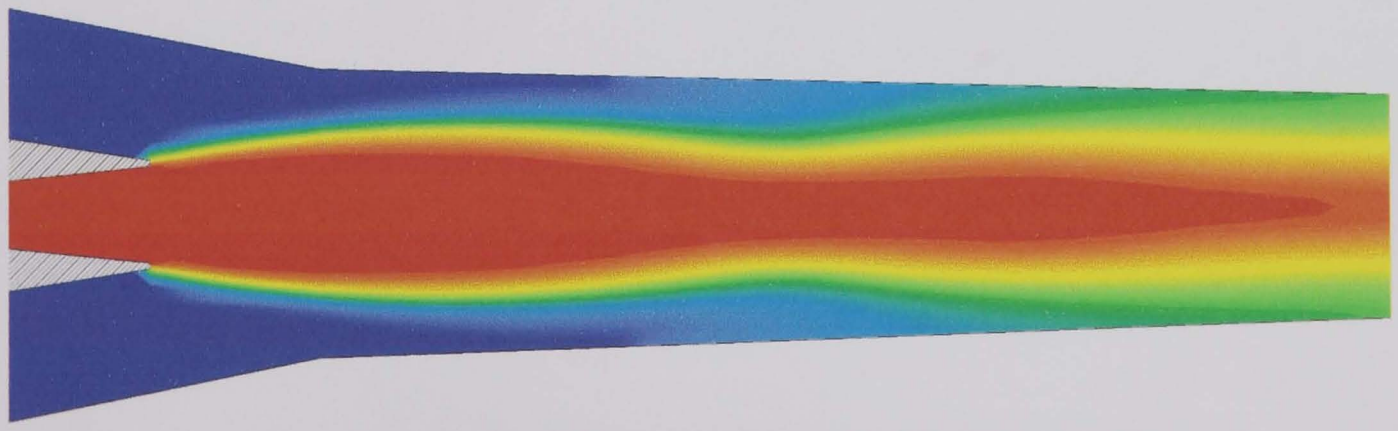

c. – $140^{o}C$

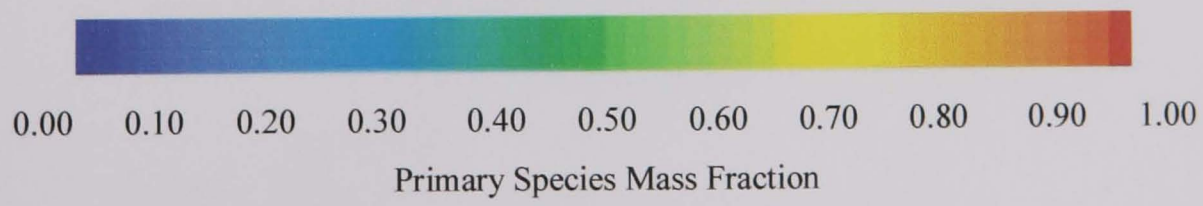

Figure 6.39 - Distribution of Primary Species Mass Fraction. Narrow Secondary Inlet

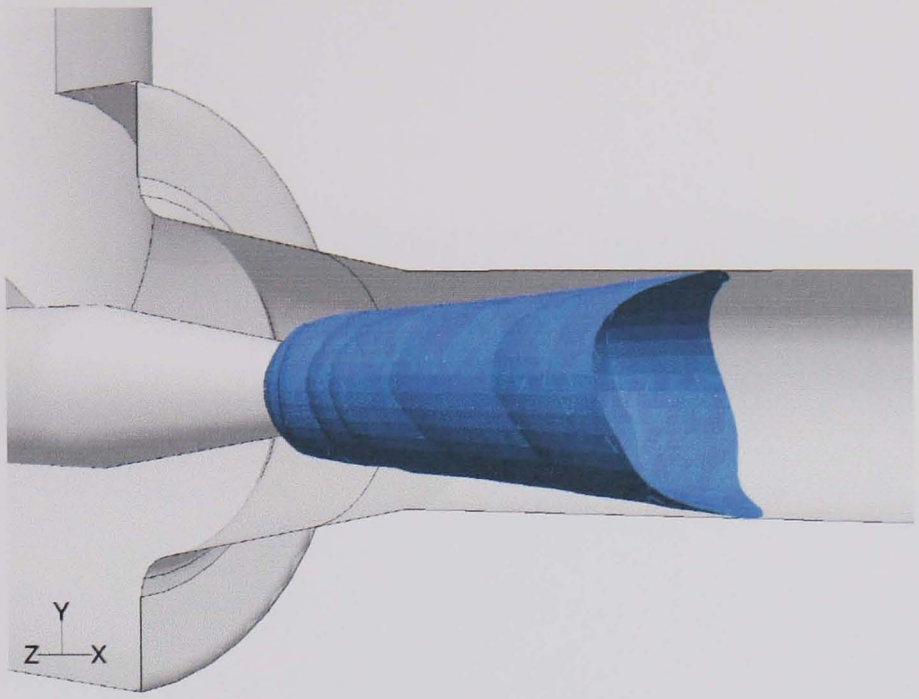

a. – $T_{Boiler} = 120^{o}C$

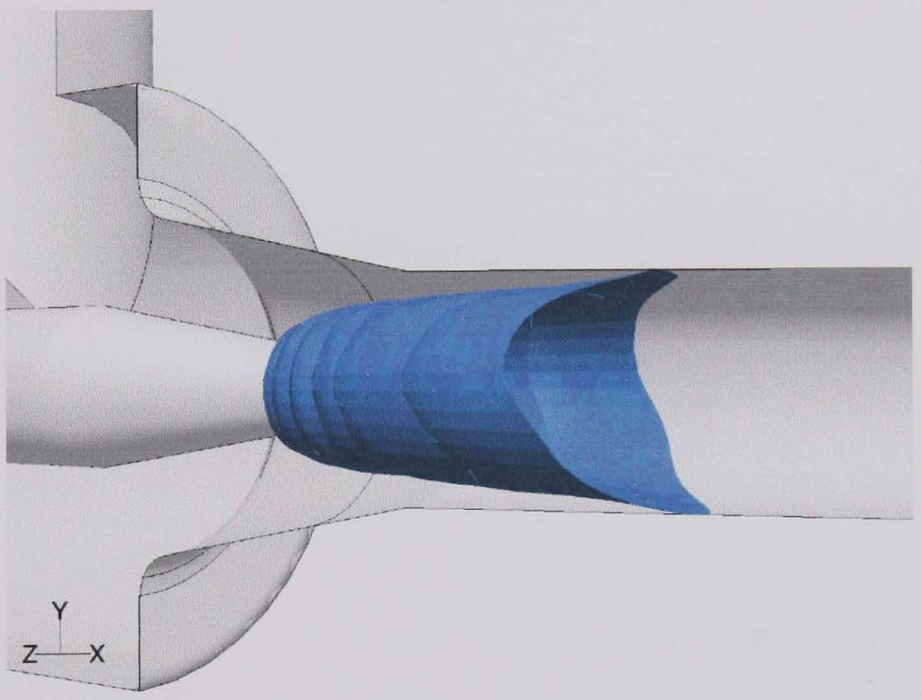

b. – $130^{o}C$

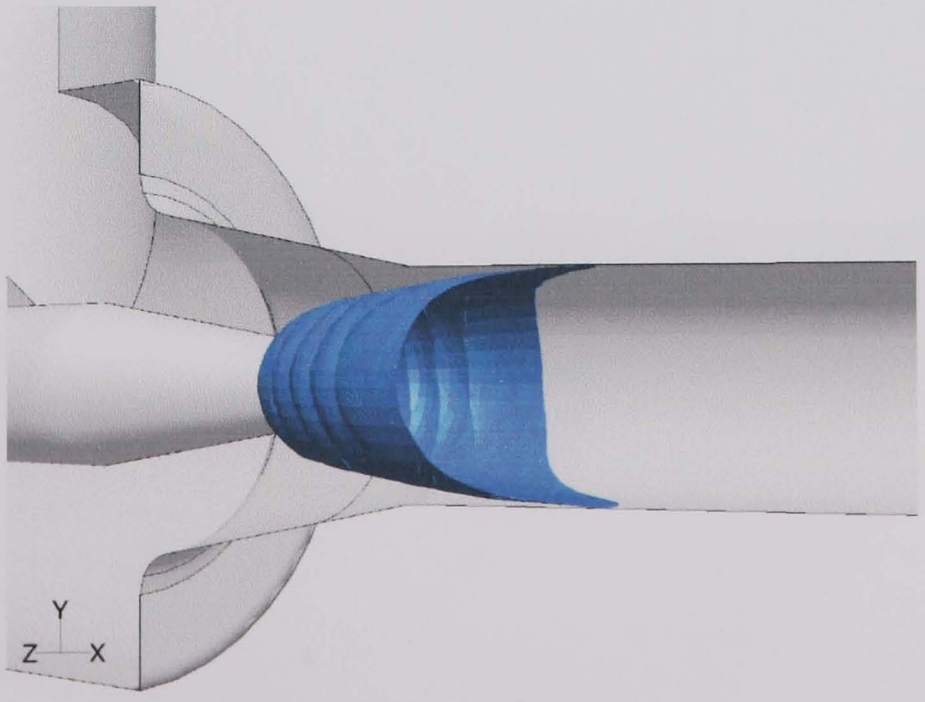

c. – $140^{o}C$

Figure 6.40 - Entrainment Boundary: Wide Secondary Inlet

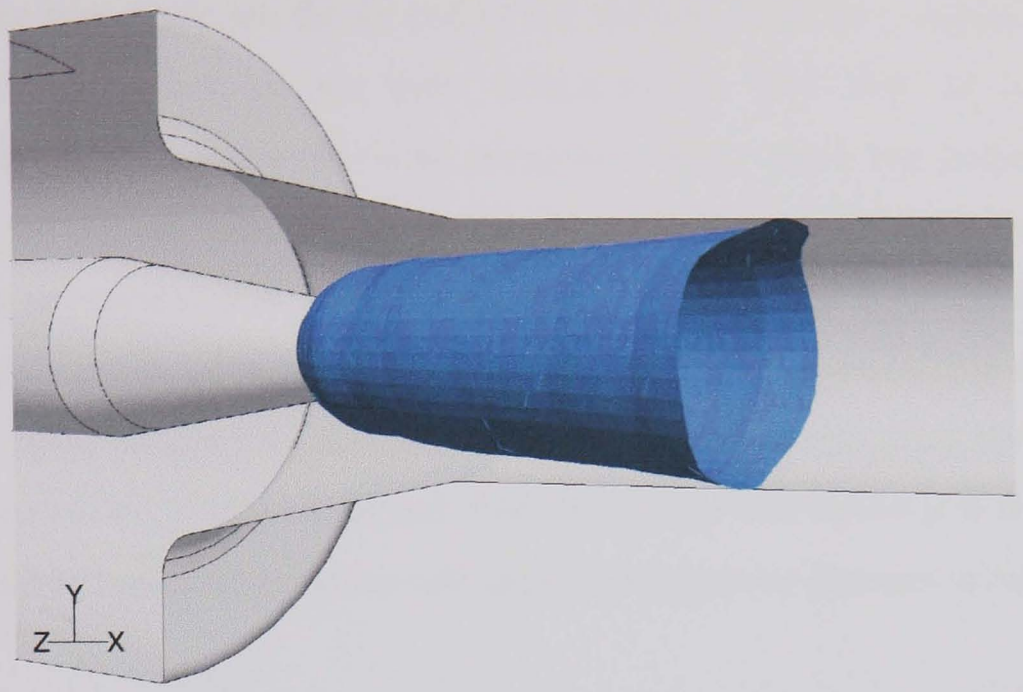

a. – $T_{Boiler} = 120^{o}C$

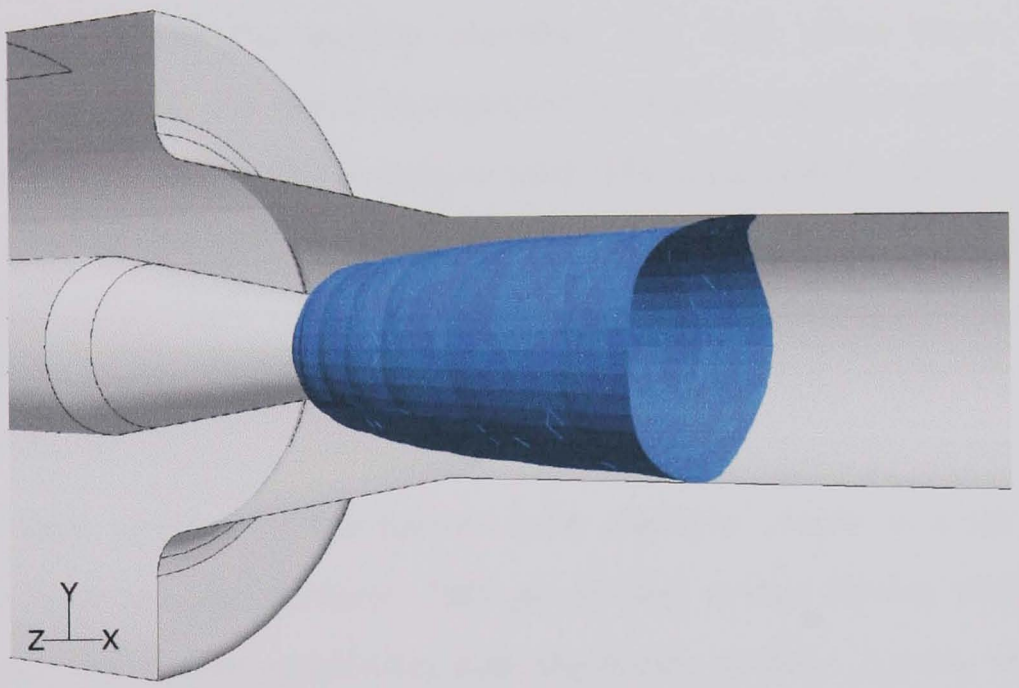

b. – 130°C

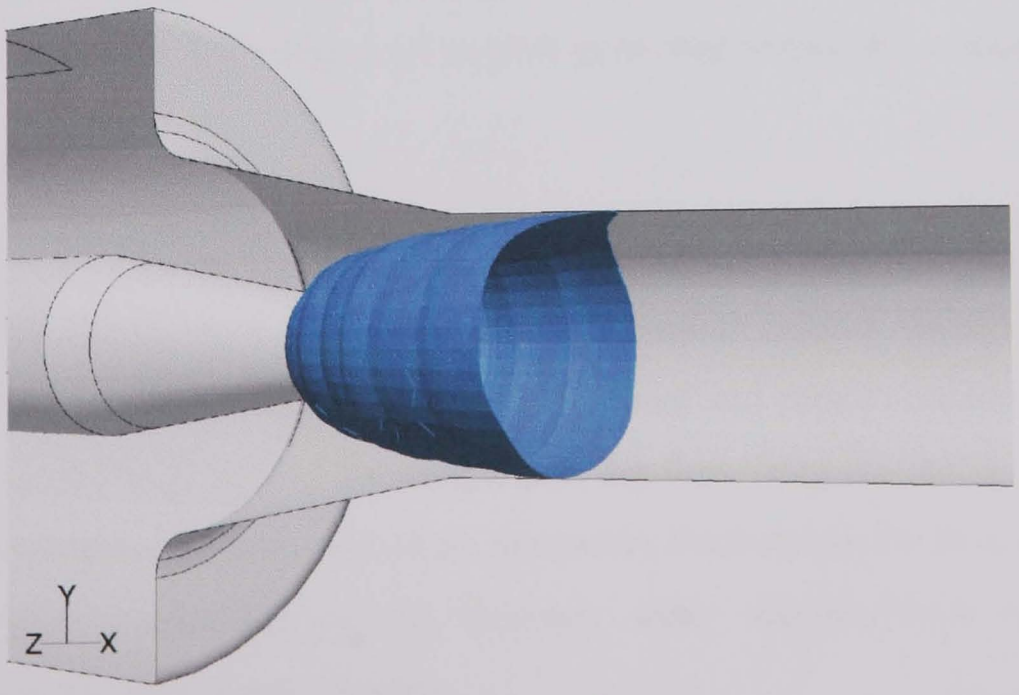

c. – 140°C

Figure 6.41 - Entrainment Boundary: Narrow Secondary Inlet

As with the supersonic jet, the far end of the plotted iso-surface representative of the entrainment boundary is not truly axisymmetric. The lack of uniformity is particularly noticeable for the wide secondary inlet, where the boundary extends further at the top and bottom of the mixing chamber than at the sides. The iso-surface plotted for the narrow inlet is more uniform in shape, though again extends further at the top and bottom of the section. It is believed this non-uniformity has a limited influence upon entrainment as it occurs so close to the mixing chamber wall surface where entrainment would be limited. For both geometries however it is clear that an increase in the boiler temperature will cause this region to decrease in size.

The influence of secondary inlet geometry can be explained by referring to velocity profiles taken across the suction chamber. Fig 6.42 show these for a boiler temperature of 120°C. As would be expected the flow velocities within the wide inlet chamber are lower than with the narrow inlet. The wide inlet has an average chamber entry velocity of ≈16 m/s, in comparison to a velocity of ≈120 m/s for the narrow inlet. The boundary layer within the narrow inlet pipe is particularly evident which is a result of the standard wall function and coarse mesh.

The high inlet velocity of the narrow inlet chamber results in a jet like flow of secondary fluid into the chamber. This jet of fluid strikes the top surface of the de Laval nozzle and further accelerates over the nozzle surface. A peak velocity of 160 m/s is attained. ESDU recommend that secondary fluid should enter a chamber at less than 100 m/s. A high degree of swirl is generated within the suction chamber as a result.

The swirl is evident in Fig 6.43 that show flow lines of secondary fluid within the chamber. Secondary fluid is seen to move in a smooth manner through the chamber with the wide inlet. The degree of swirl is minimal and appears to occur principally beneath the de Laval nozzle. In comparison the flow lines for the narrow inlet are seen to recirculate within the chamber. Secondary fluid strikes the base of the suction chamber and recirculates up the chamber walls. Recirculation is particularly noticeable at the rear of the chamber.

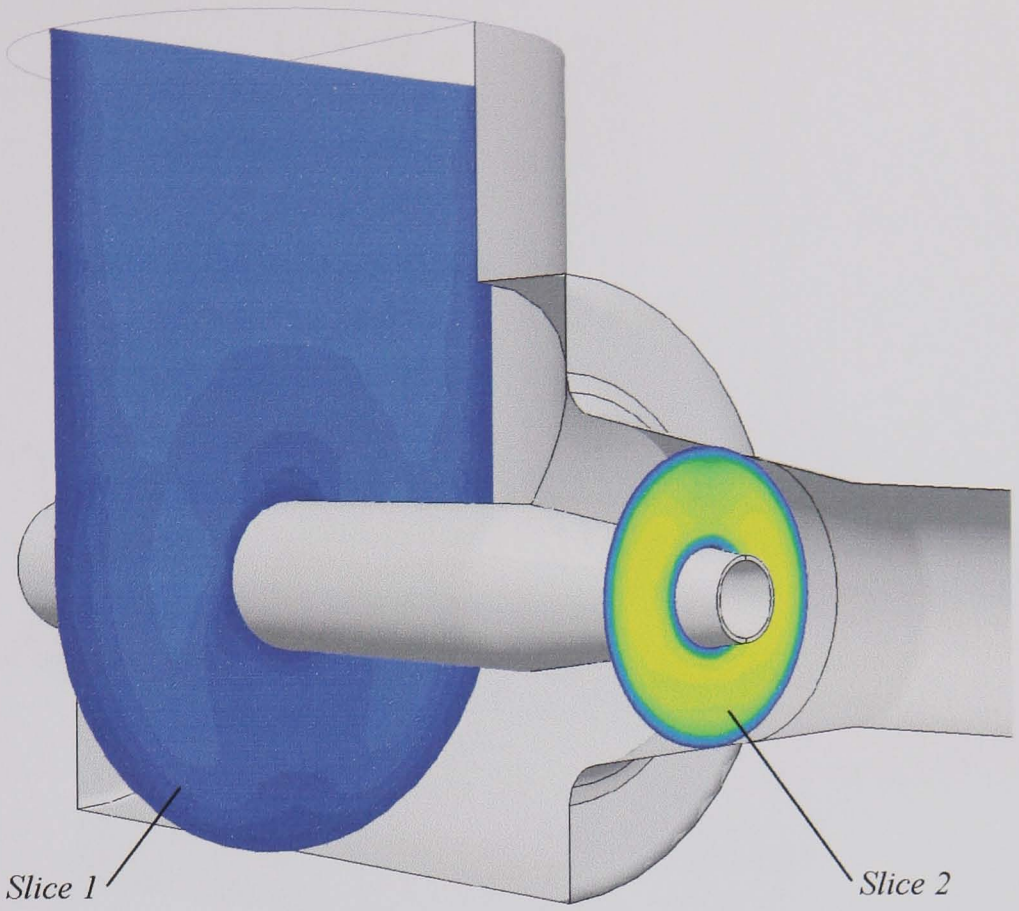

a. – Wide Secondary Inlet

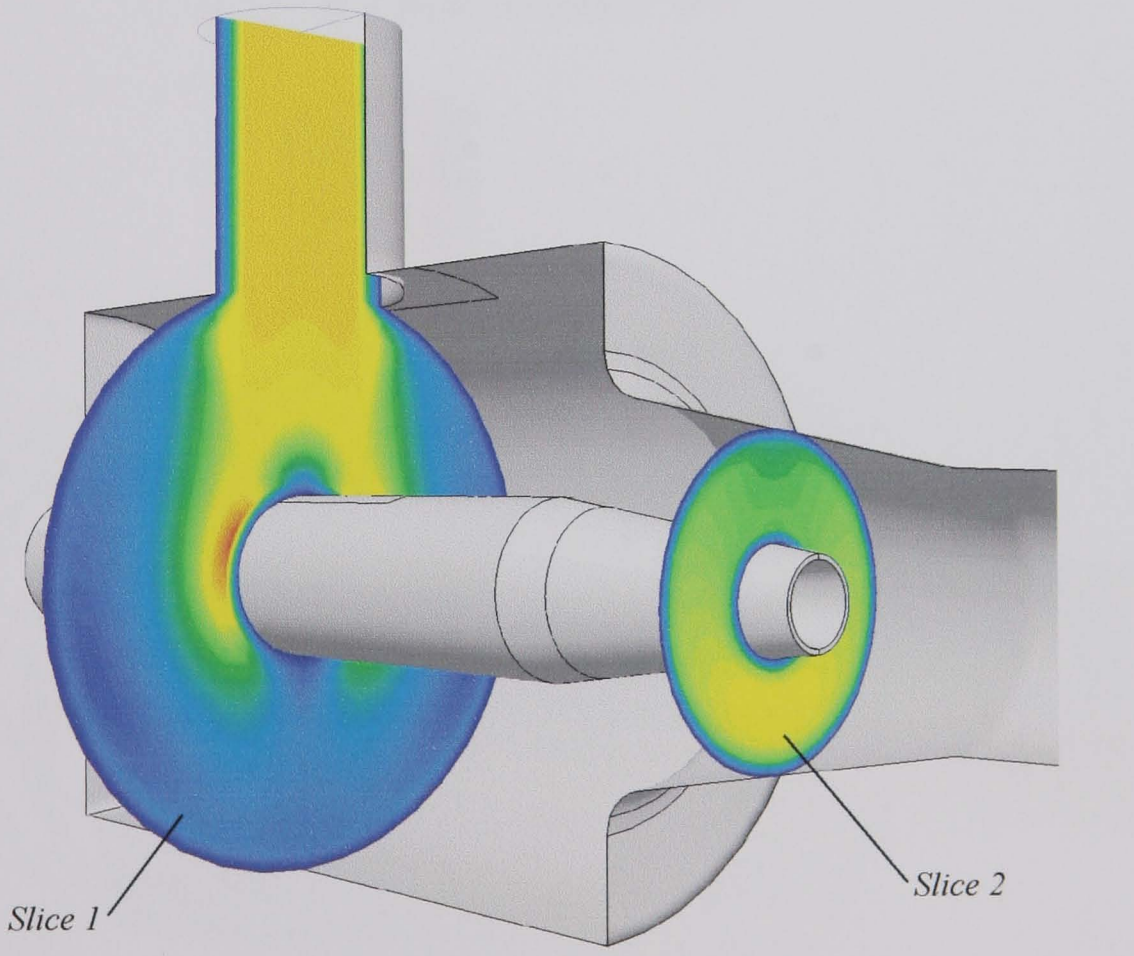

b. – Narrow Secondary Inlet

Figure 6.42 - Flow Velocity Within Suction Chamber

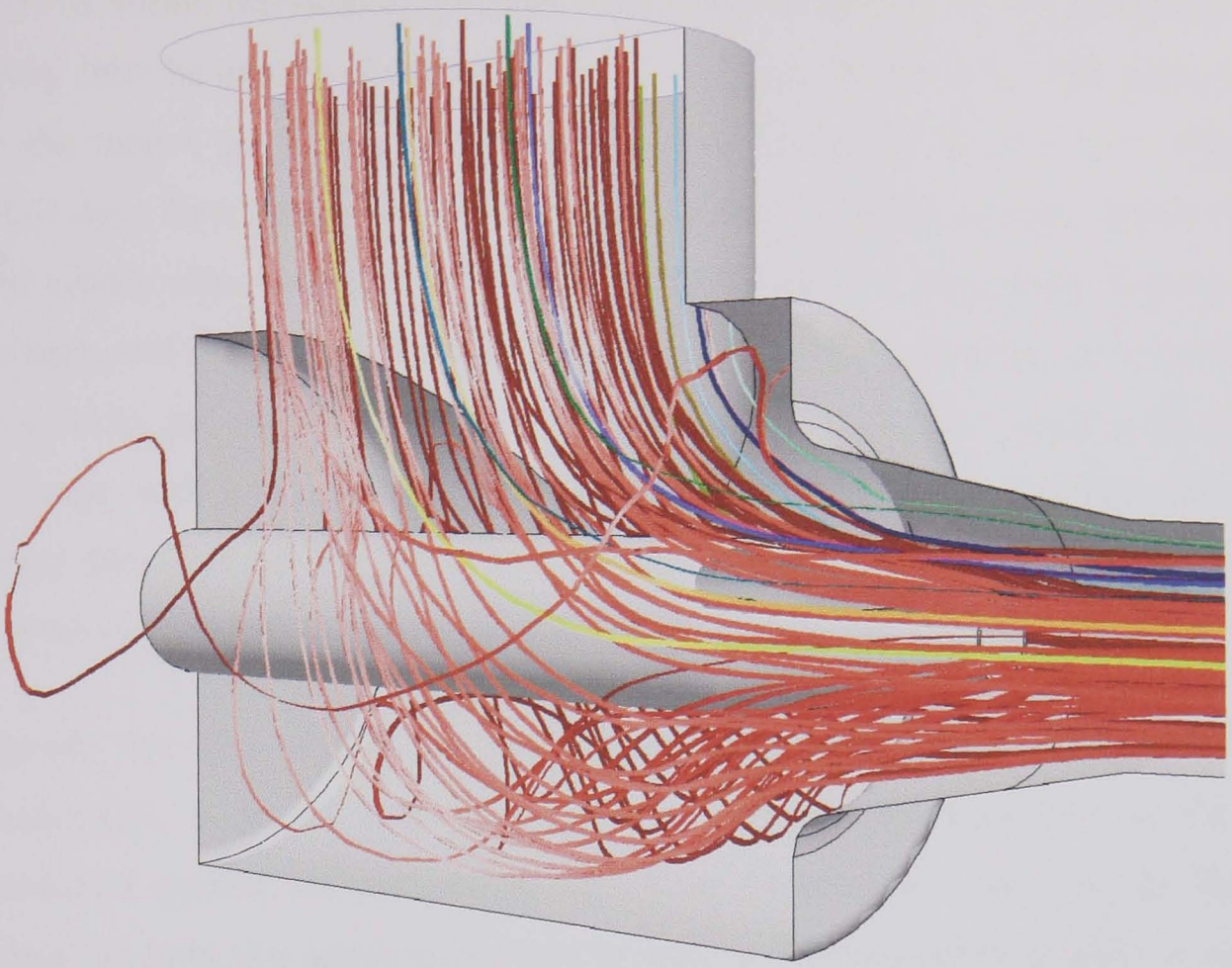

a. – Wide Secondary Inlet

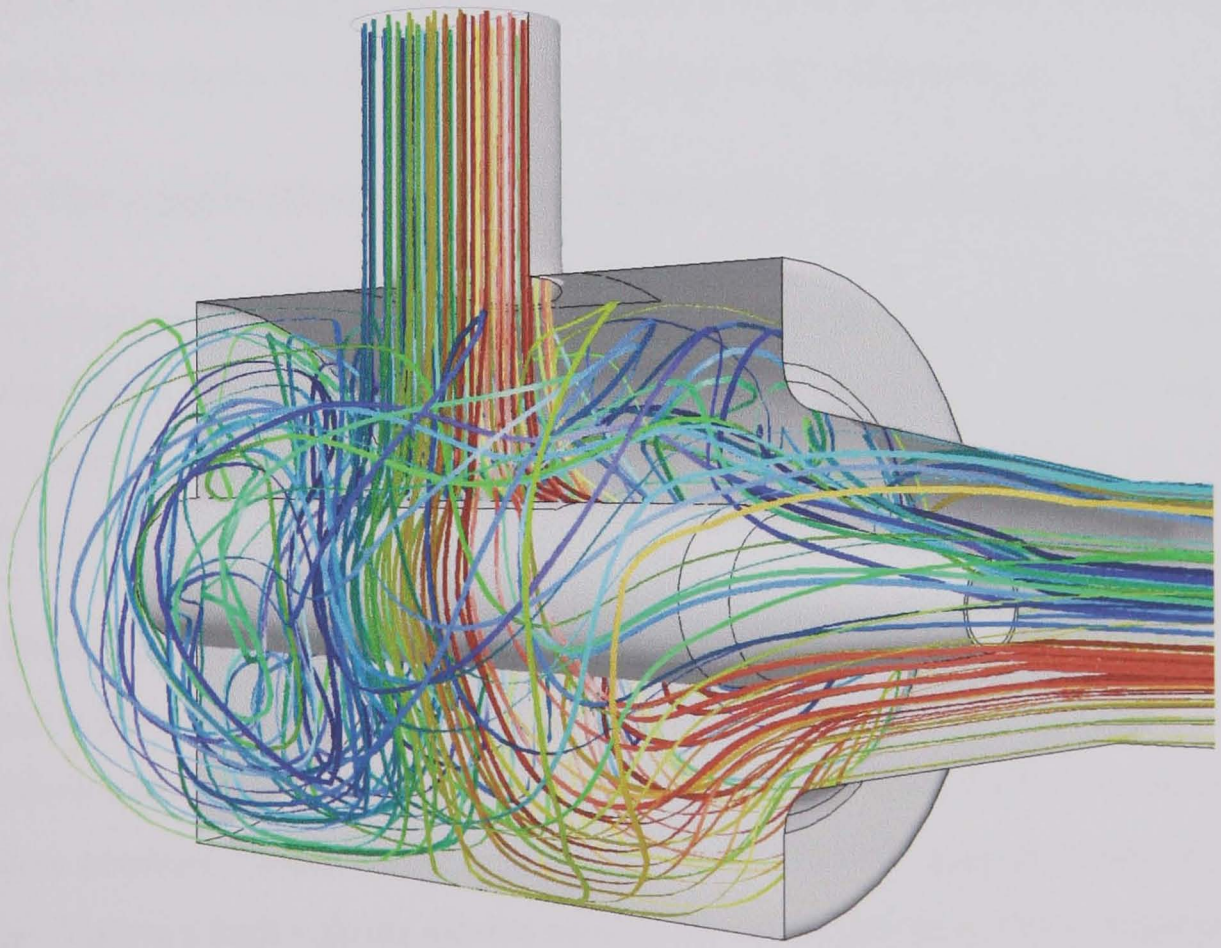

b. – Narrow Secondary Inlet

Figure 6.43 - Flow Path Lines Within Suction Chamber (Path-lines Coloured By Line ID)

The swirl within the suction chamber affects the uniformity of the secondary flow velocity into the mixing chamber, as shown in Fig. 6.42 (Slice 2). This will explain why the motive jet is not purely axisymmetric in Fig's 6.36 and 6.37. With the narrow inlet, flow enters the mixing chamber with a higher velocity below the de Laval nozzle than above. A velocity difference of ≈35 m/s exists between the maximum and minimum velocities at entry to the mixing chamber. In contrast the flow velocity for the wide inlet is more uniform. Peak velocities occur at the side of the nozzle, with a variation of only ≈10 m/s at entry. It is believed that this more uniform flow leads to the higher entrainment. It is the velocity profiles which also affect the entrainment boundary shape.

Although the flow within the ejector has been shown to be not completely axisymmetric, it is felt that the applied axisymmetric assumptions in the two dimensional studies are acceptable. The three dimensional nature of the flow is minimal, so long as a generously sized secondary inlet is used to produce a smooth entry of secondary fluid to the ejector, as recommended within the ESDU[3] guidelines. If this is not the case, and the suction chamber geometry is an issue, then obviously the ejector would have to be modelled in three dimensions.

6.4 – The Application of CFD to Alternative Ejector Designs

The application of CFD, and the general applicability of the numerical method used in simulation of the Eames ejector, to alternative ejector designs has been investigated. Three alternative ejectors have been modelled, taken from the work of Desevaux et al[7], Hickman et al[6], and Watson[1].

The Desevaux[7] ejector is an air-air ejector, using air as both the working fluids (primary and secondary). This ejector operates with ambient conditions at both the secondary inlet and exhaust, and has been used to investigate flow visualisation and intrusive pressure measurement techniques. The Hickman[6] ejector is also an air-air ejector. This is a high volume ejector used in the investigation of thrust augmentation applications. The Watson[1] ejector is a low level vacuum ejector. This uses steam as the primary fluid to entrain air, generating a vacuum within an air tank.

6.4.1 – Desevaux Ejector

The Desevaux[7,62] ejector is a convergent/divergent design although to all intents and purposes can be classed as a constant area ejector. Indeed Desevaux refers to the constant area section, or throat, as the mixing tube. It is the mixing tube which is used to classify ejectors.

The specified dimensions of the Desevaux[7,62] ejector were incomplete, however the key dimensions of the de Laval nozzle, mixing tube, and nozzle exit position were available. The ejector diffuser was modelled using ESDU[3] guidelines, with an included half angle of 4°. More importantly no dimensions were presented for the convergent section of the mixing chamber. This was modelled with an assumed included half angle of 15°. The appropriateness of this assumption is viable as the de Laval nozzle is well advanced within this section, therefore its influence upon the modelled ejector is most likely slight.

The initial computational mesh comprises 17466 quadrilateral cells. This was refined during the solution process using y^+ values and pressure gradient in the provision of refinement criteria. A final refined mesh contained approximately 70000 quadrilateral cells.

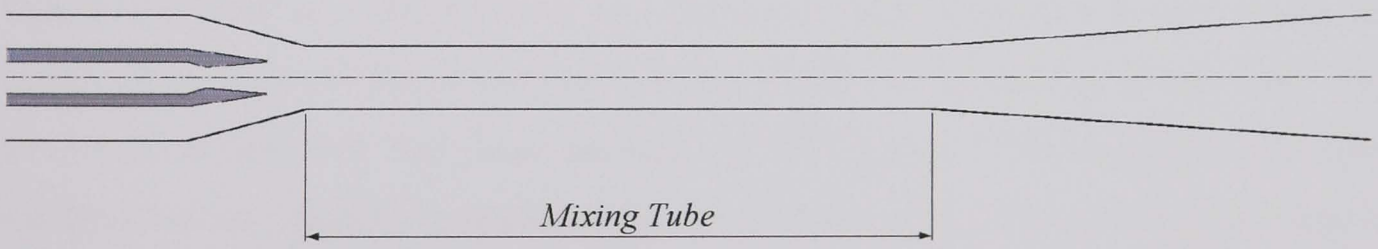

Figure 6.44 – Modelled Desevaux Ejector Geometry

This CFD study was a fixed entrainment study in line with Desevaux's experimental work. Desevaux maintained the level of induced flow by adjusting a flow valve at the secondary inlet. Entrainment values of R_m = 0.47, 0.32, and 0.1 have been simulated. Primary nozzle stagnation pressure was P_1 = 5 bar, the de Laval nozzle is designed to operate with an exit Mach number upto M = 2.3. The level of entrainment was fixed using a mass flux boundary condition for the secondary inlet in-place of a pressure boundary. Secondary mass flow rate ($\dot{m}_2$) was calculated from the desired entrainment level and the primary mass flow rate ($\dot{m}_1$). This value had to

be determined by conducting a simulation with no secondary flow. As the de Laval nozzle is choked $\dot{m}_1$ will remain constant in all simulations. The primary mass flow rate was determined as $\dot{m}_1 = 0.0591$ g/sec.

The prescribed flow rates for the secondary inlet and other boundary conditions are specified in Table 6.6. All thermal boundary conditions were fixed at 283 K. The physical properties of the working fluids, both air, can be found in Table D.5 in Appendix D.

N°	R_m	P_1 (bar)	$\dot{m}_1$ (g/sec)	$\dot{m}_2$ (g/sec)	P_3
D01	0.1	5	0.0591	0.0059	Atmosphere
D02	0.32			0.0189	
D03	0.47			0.0277	

Table 6.6 - Fixed Entrainment Study of the Desevaux Ejector

As the entrainment ratio within the CFD simulations has been fixed it is not possible to determine how accurate the simulations of the Desevaux ejector are through comparison of R_m with experiment. Desevaux however investigated the use of visualisation techniques for studying flow structure within ejectors. It is therefore possible to compare the CFD predicted flow structure with flow visualisation images at the corresponding entrainment ratios, Fig 6.45.

Due to the method of illumination that Desevaux used (illuminating back along the length of the ejector) the convergent portion of the mixing section is not clear. The de Laval nozzle exit has been marked on the images. Unfortunately the flow structure within the mixing section is not particularly clear, however the barrelling of the supersonic jet within the tube is clear. The jet also appears to be over-expanded.

CFD simulations confirm over-expansion, a reflected shock is observed at the de Laval nozzle exit, Fig 6.46. This increases in strength as the fixed entrainment ratio is raised, indicating the jet becomes increasingly over-expanded. Plots of centreline static pressure further confirm this, Fig 6.47, yet it appears that the nozzle exit pressure is slightly higher than the chamber back pressure at $R_m = 0.1$. This is actually the case at the centreline, however pressure distribution across the nozzle exit is not uniform and decreases from the axis to the nozzle wall. Hence the nozzle is actually slightly over-expanding.

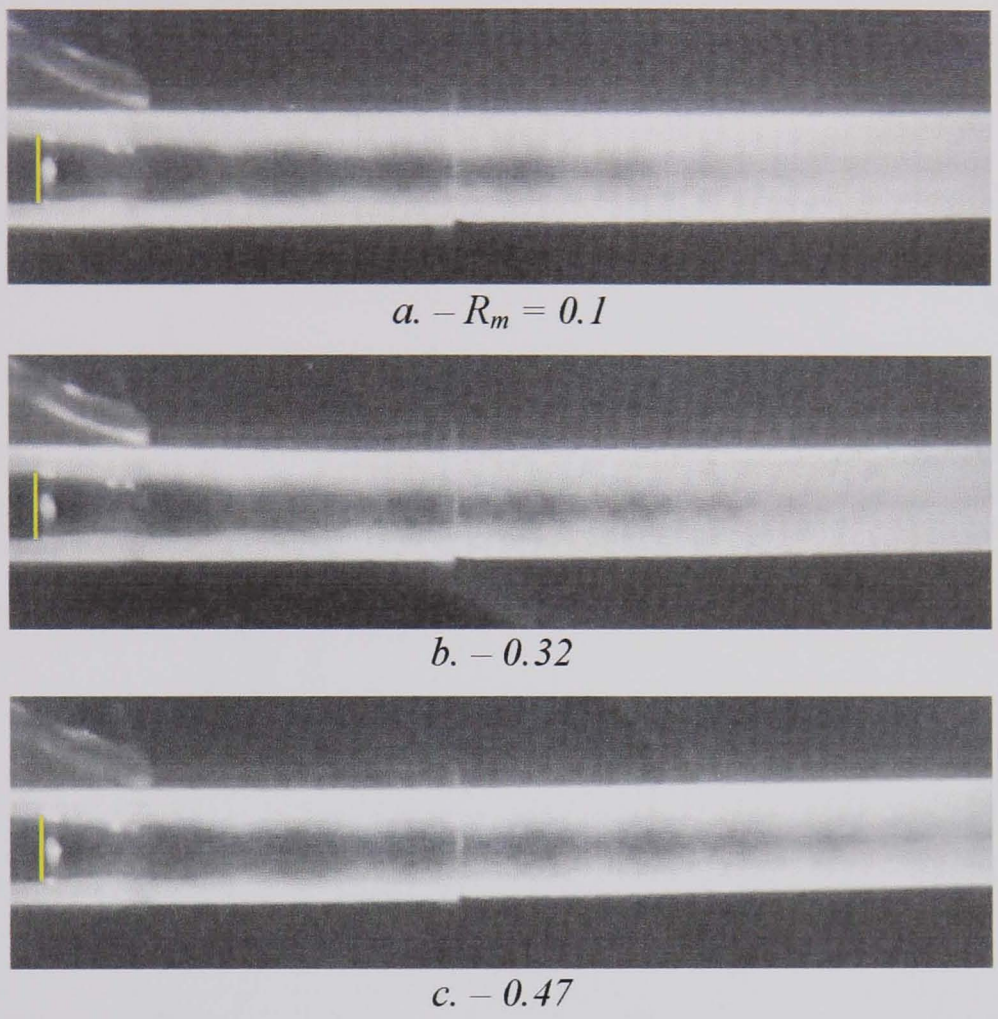

a. – R_m = 0.1

b. – 0.32

c. – 0.47

Figure 6.45 - Flow Visualisation Within The Desevaux Ejector[7]

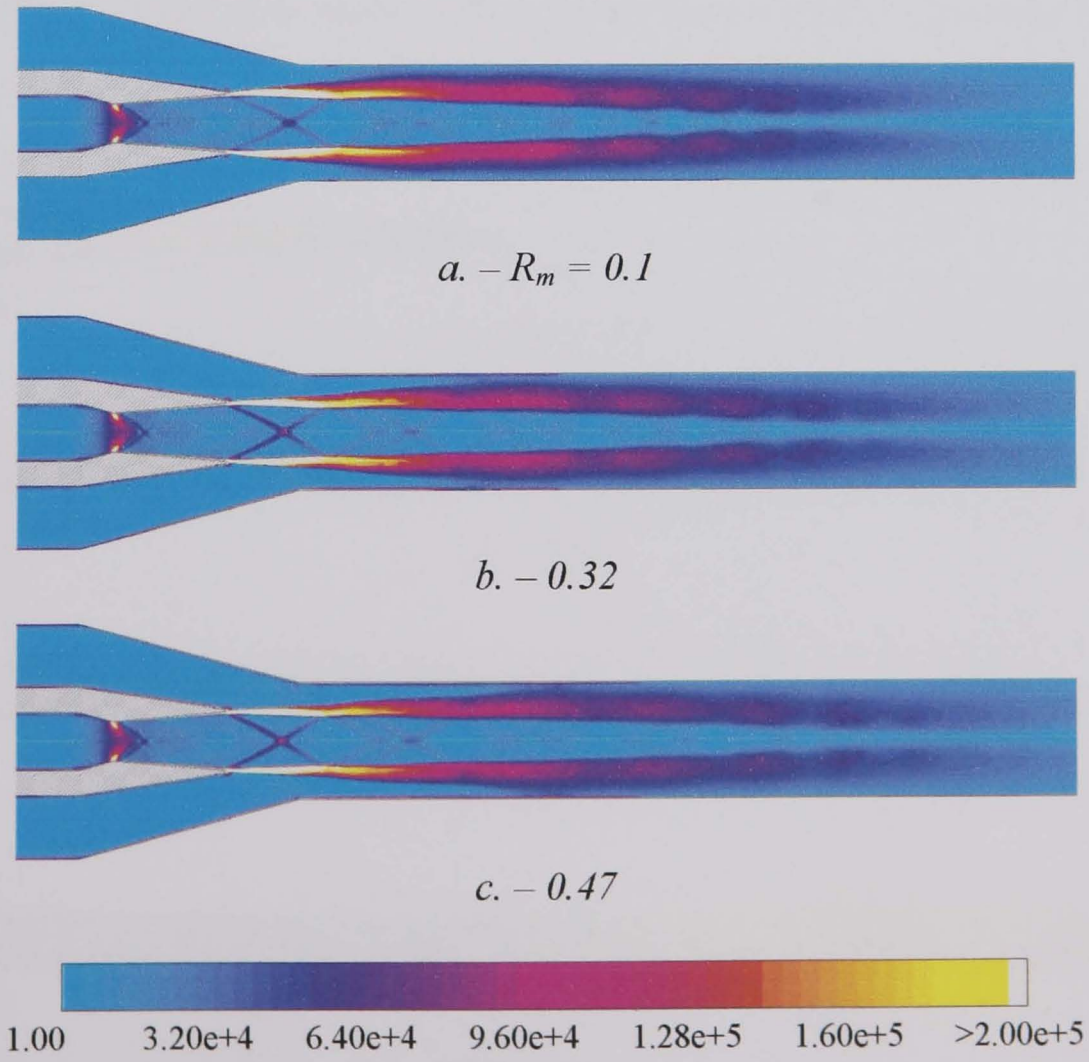

a. – R_m = 0.1

b. – 0.32

c. – 0.47

Figure 6.46 - Predicted Rate of Strain (1/s) Within Desevaux Ejector

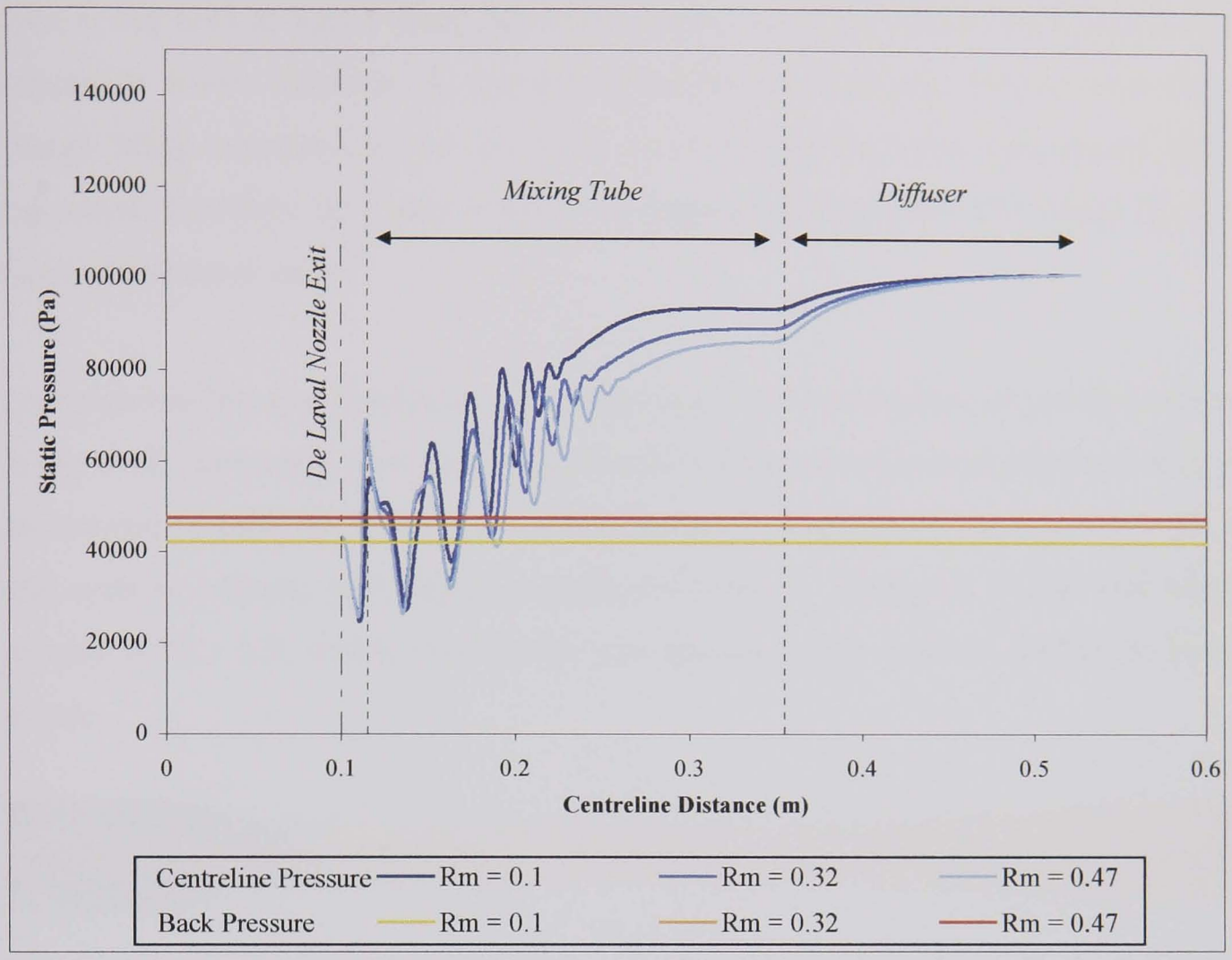

Figure 6.47 – Centreline Static Pressure Distribution Of The Desevaux Ejector

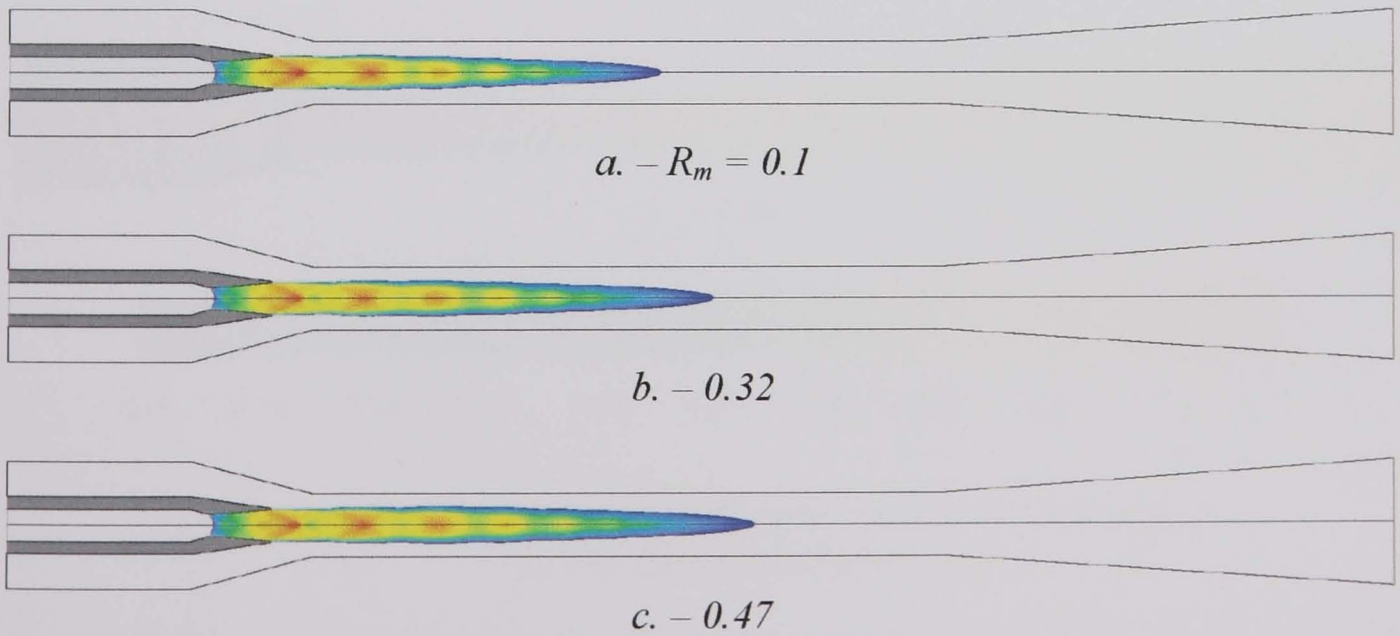

Figure 6.48 – Plots Of Supersonic Flow Region Within Desevaux Ejector

The increase in shock strength for increasing R_m is also confirmed. The jet can be seen in Fig 6.47 to barrel along the mixing tube. After the initial shock subsequent expansion waves decrease in strength as entrainment is raised. This is due to more energy being expended within the shock as the nozzle becomes increasingly over-expanded. However the same number of expansion/reflections still occur at each fixed entrainment value.

Comparisons between the Desevaux images and CFD simulations is perhaps clearer in Fig 6.48, supersonic flow plots. Shock cells within the supersonic flow are seen to correspond to cells within the flow visualisation. The extent of the supersonic jet is also seen to increase with higher entrainment values. Measured nozzle exit Mach number is M = 2.3, which matches the operational design velocity for the de Laval nozzle.

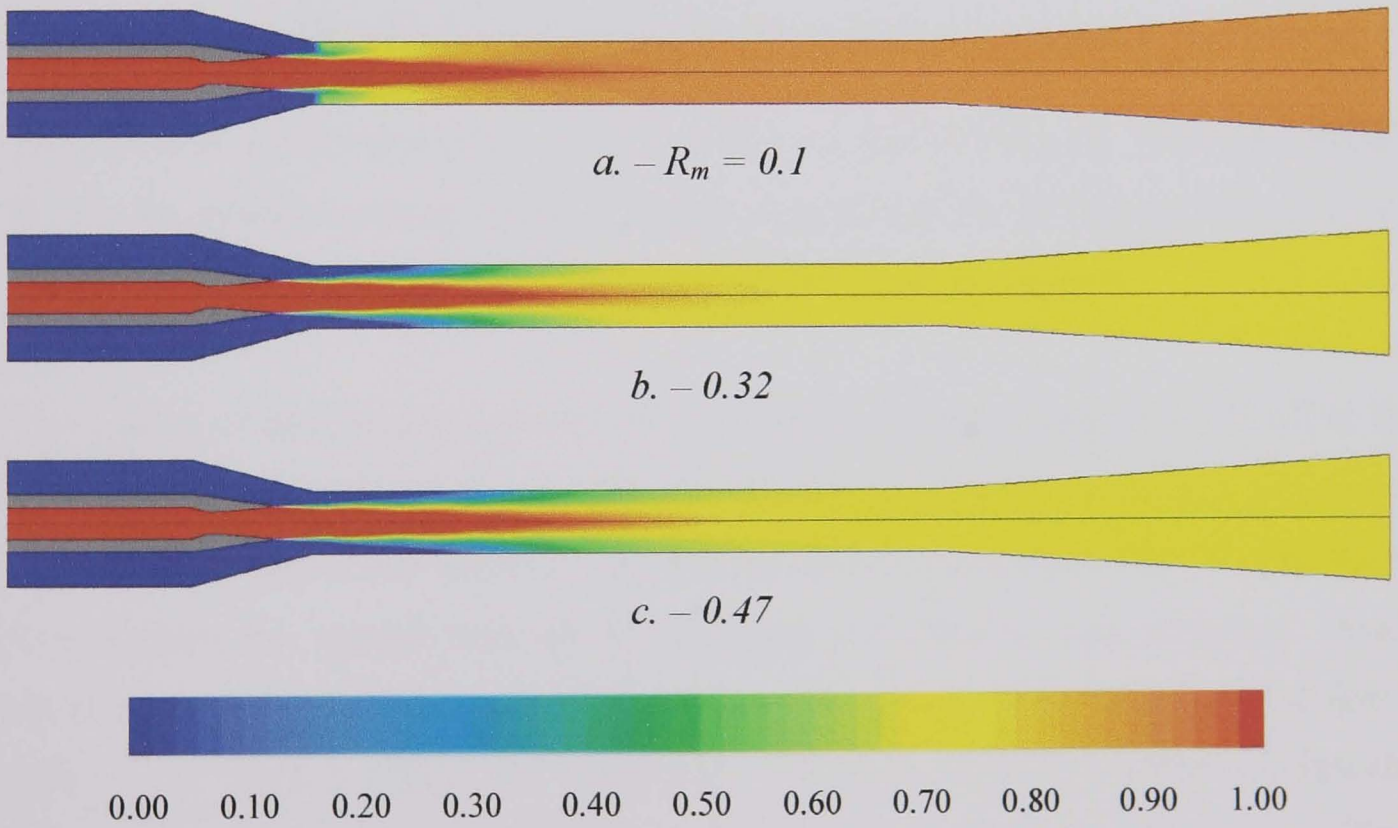

Figure 6.49 - Distribution of Primary Species Mass Fraction In The Desevaux Ejector

The influence of raised entrainment upon the mixing region is shown in Fig 6.49. As would be expected an increase in entrainment extends the distance over which mixing and entrainment occur. When R_m = 0.1 the mixing region is seen to be folding back, suggesting it is at the verge of collapse. This has been observed in all simulations conducted at low entrainment ratios. No differences in flow structure or

mixing are observed between the Desevaux ejector, and the constant pressure design ejectors investigated.

6.4.2 – Hickman Ejector

The Hickman[6] ejector is a convergent/divergent design. Unusually this ejector is fitted with two diffusers in series, separated by a short length of constant area section. The specified dimensions of the ejector are extensive and complete.

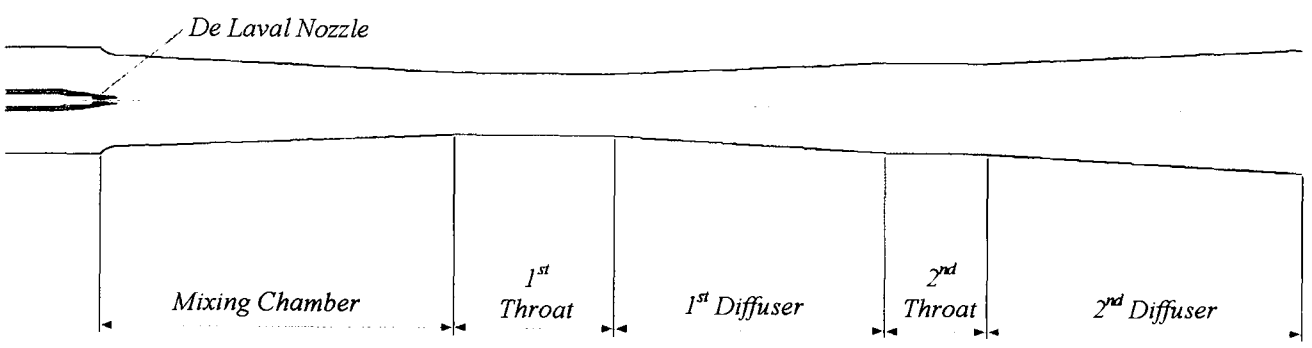

Figure 6.50 - Modelled Hickman Ejector Geometry

The initial computational mesh comprises 46310 quadrilateral cells. This was refined during the solution process using y^+ values as the basis for refinement criterion. A final refined mesh contained approximately 67700 quadrilateral cells.

The ejector is designed to operate with a primary Mach number of 2.72. This is driven by air supplied at 348 psia and a temperature of 807 °F. Secondary air enters the ejector through a bell mouth at 30.06 in Hg and a temperature of 92 °F. The flow rate through the ejector was set by adjusting the diffuser back pressure. Four alternative levels of entrainment were simulated by setting the diffuser back pressure at P_3 = 11.1" H_2O, 7.5" H_2O, 4.7" H_2O, and –1.7" H_2O. Applied boundary conditions are listed in Table 6.8 and physical properties in Table D.6 in Appendix D. The results of the Hickman study are presented in Table 6.7 and Fig 6.51.

Nº	Pressure			R_m	
	Primary Inlet (psia)	Secondary Inlet (in Hg abs)	Diffuser (in H_2O gauge)	Experiment	CFD
H01	348	30.06	11.1	17.0	16.6
H02			7.5	19.4	19.5
H03			4.7	21.0	21.8
H04			-1.7	24.8	24.8

Table 6.7 - Results of Hickman Study

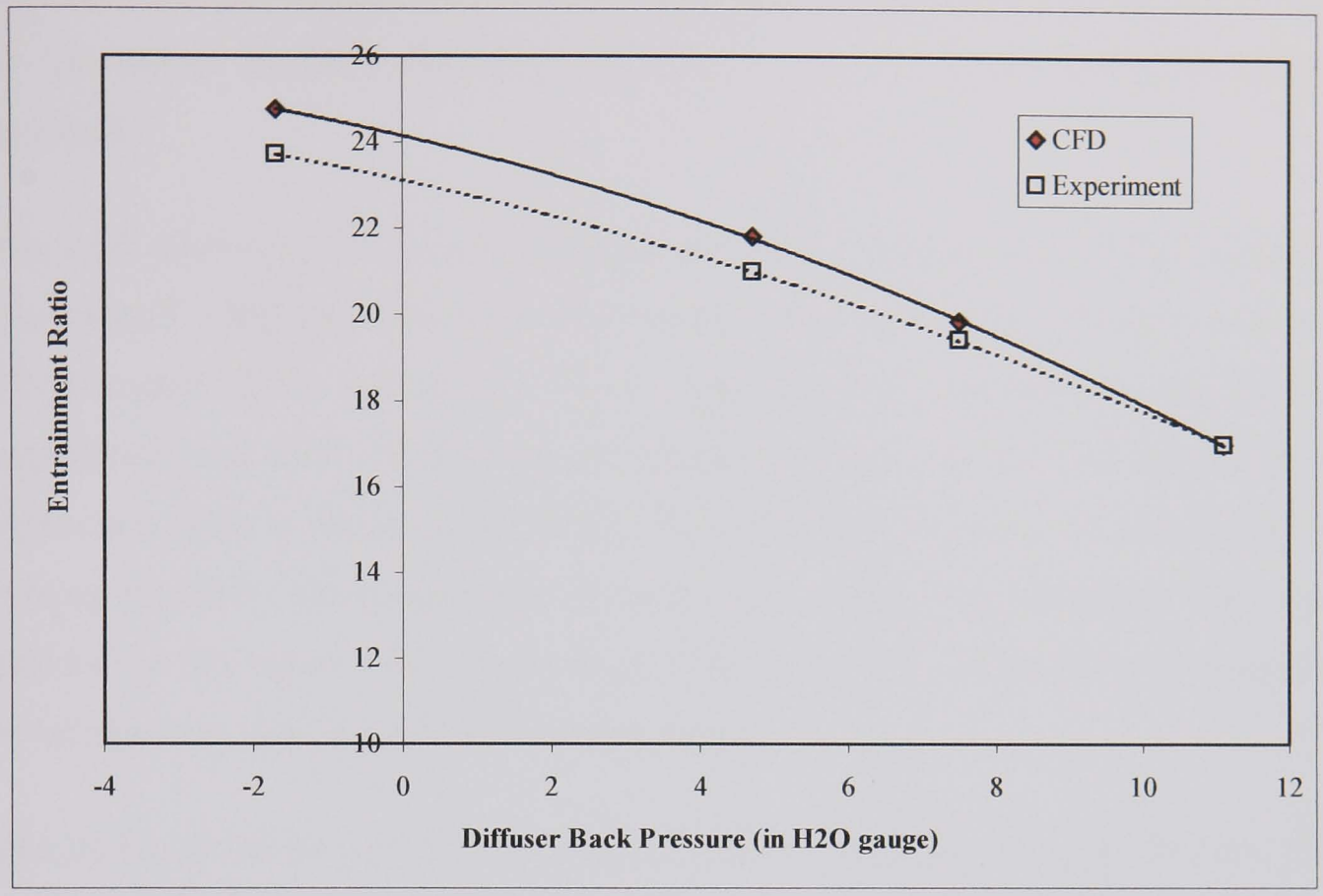

Figure 6.51 - Results of Hickman Study

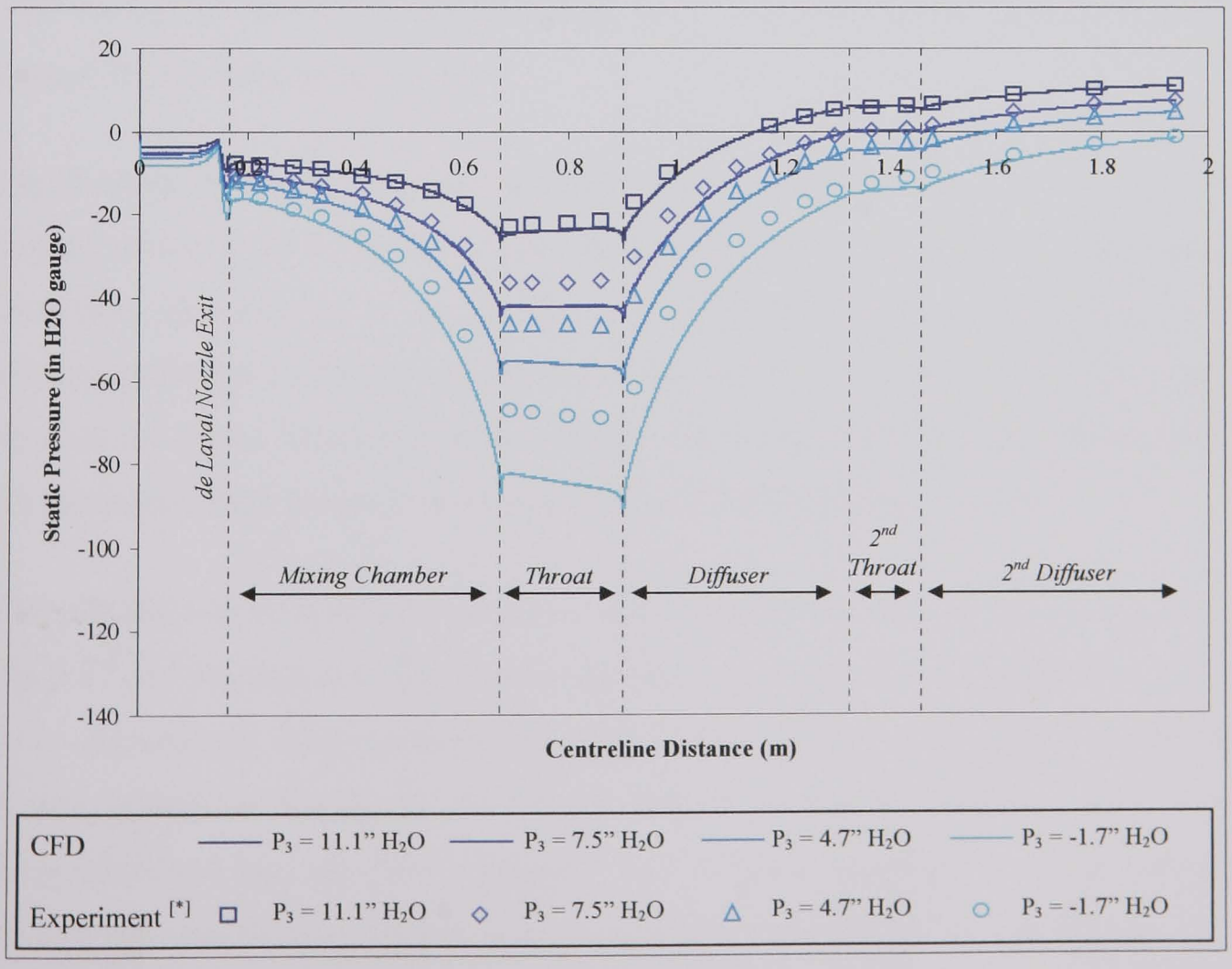

Figure 6.52 - Comparison of Static Wall Pressure Distribution of Hickman Ejector

The difference between the simulated and measured entrainment reduces as the diffuser back pressure is raised. CFD over predicts the level of entrainment by 4.5% at the lowest pressure, however this reduces to –0.1% at the highest diffuser pressure.

Fig 6.52 shows the CFD and experimental static pressure distribution along the ejector wall. CFD predicted static wall pressure distribution are seen to fit measured experimental values well for P_3 = 11.1" H_2O. However the discrepancies between experiment and CFD increase as the diffuser pressure is lowered. Experimental values are close to those predicted by CFD within the diffusers, second throat, and mixing chamber. The largest discrepancies occur within the first throat. The lower pressure in this region will induce a higher secondary flow, hence the over-prediction in entrainment ratio at lower diffuser pressures.

The de Laval nozzle expands isentropically almost perfectly. This can be see in Fig 6.53, no expansion structure is visible within the supersonic jet exiting the de Laval nozzle. The mixing chamber pressure is atmospheric at entry, and the chamber is wide enough to prevent the supersonic jet being influenced by the chamber walls. As a result the jet behaves as a free jet.

The distance between the jet and chamber wall is evident in Fig 6.54. A peak Mach number of M = 2.93 is attained within the first expansion cell of the jet. Although the mass flow rate of the jet is considerably lower than that of the secondary fluid, it still imparts sufficient momentum to the secondary flow to drive the device. The primary jet does not choke the ejector throat, though this is not detrimental to performance as the secondary fluid pressure is almost level with diffuser back pressure.

The influence of diffuser back pressure upon entrainment and mixing can be seen in Fig 6.55, by limiting the minimum visualised primary fluid species mass fraction = 0.01. As diffuser back pressure is reduced the distance over which entrainment occurs extends in length. At the lowest diffuser pressures secondary fluid is still being entrained into the flow within the first diffuser. However it can be seen that mixing between the two streams is predominantly complete by the first throat.

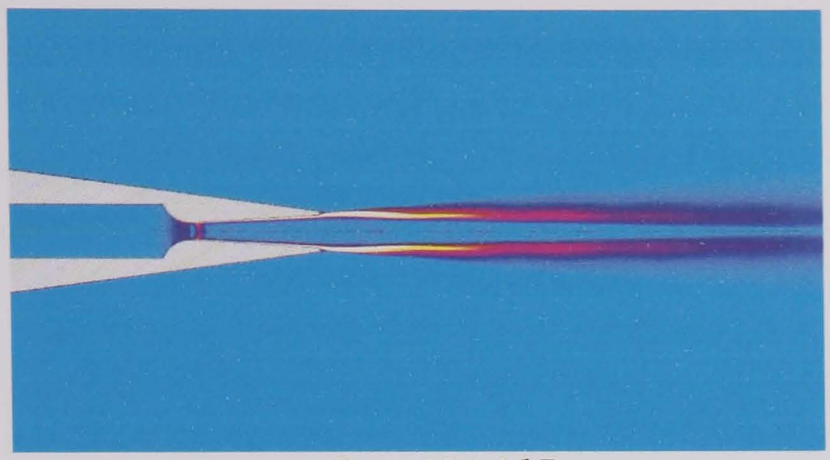

a. – P_3 = 104.1 kPa

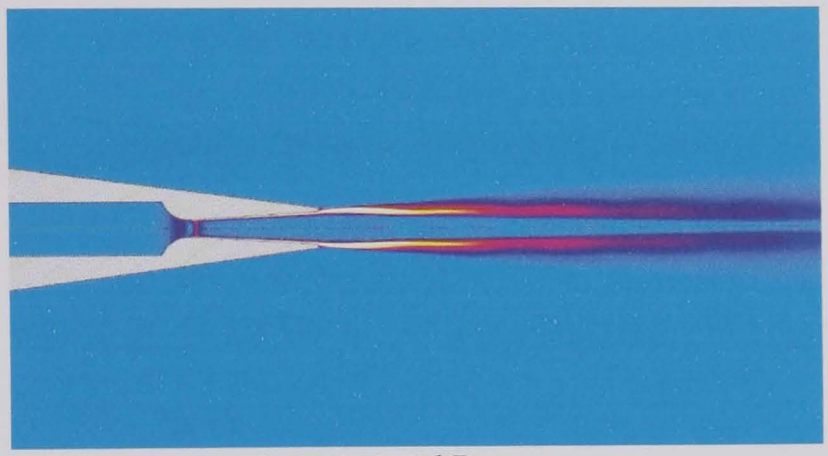

b. – 103.2 kPa

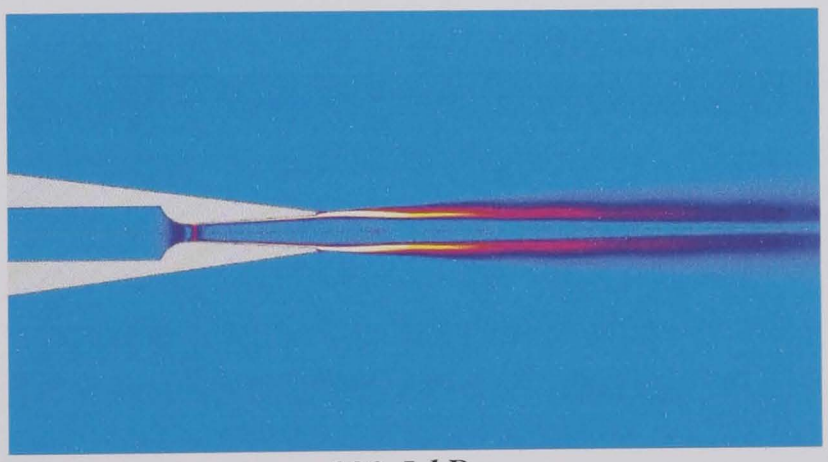

c. – 102.5 kPa

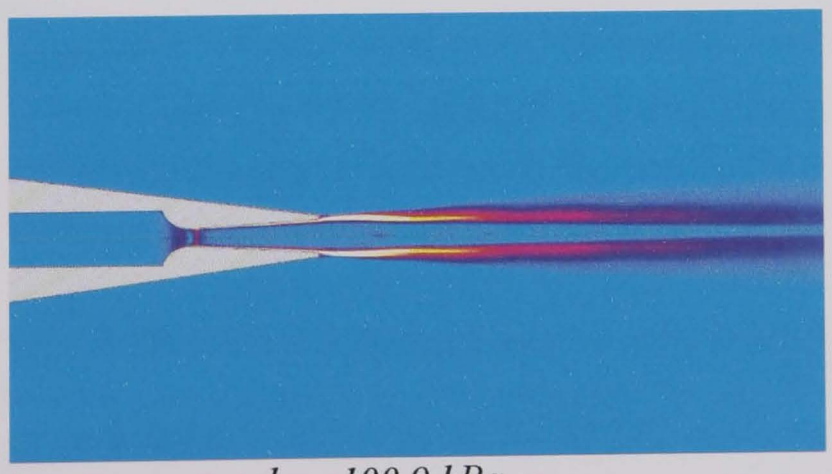

d. – 100.9 kPa

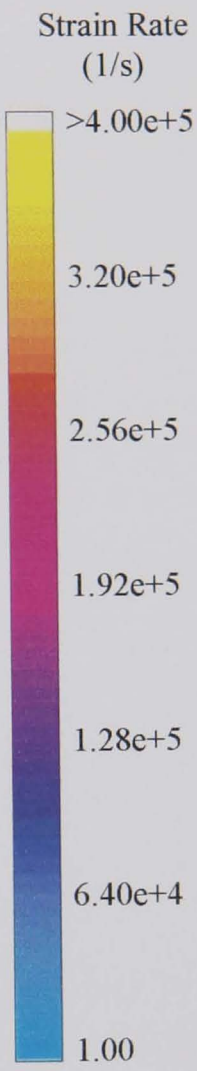

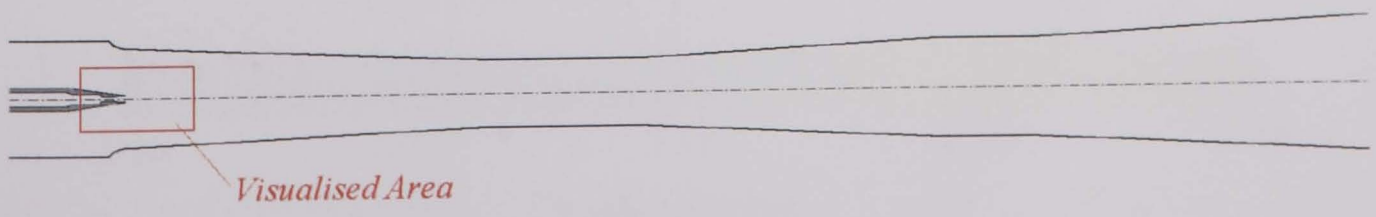

Figure 6.53 - Predicted Rate of Strain (1/s) Within Hickman Ejector

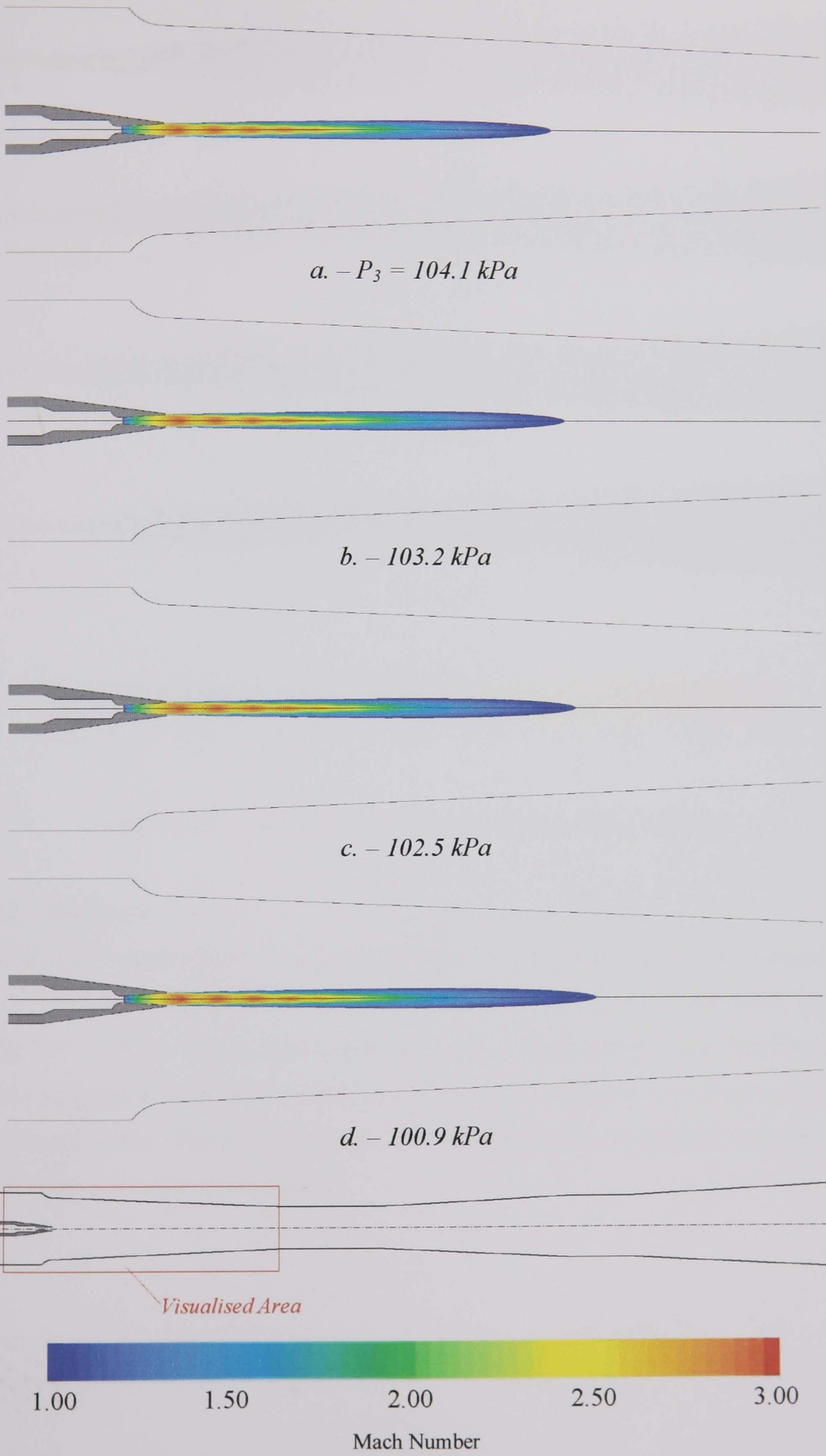

Figure 6.54 - Supersonic Flow Region Within Hickman Ejector

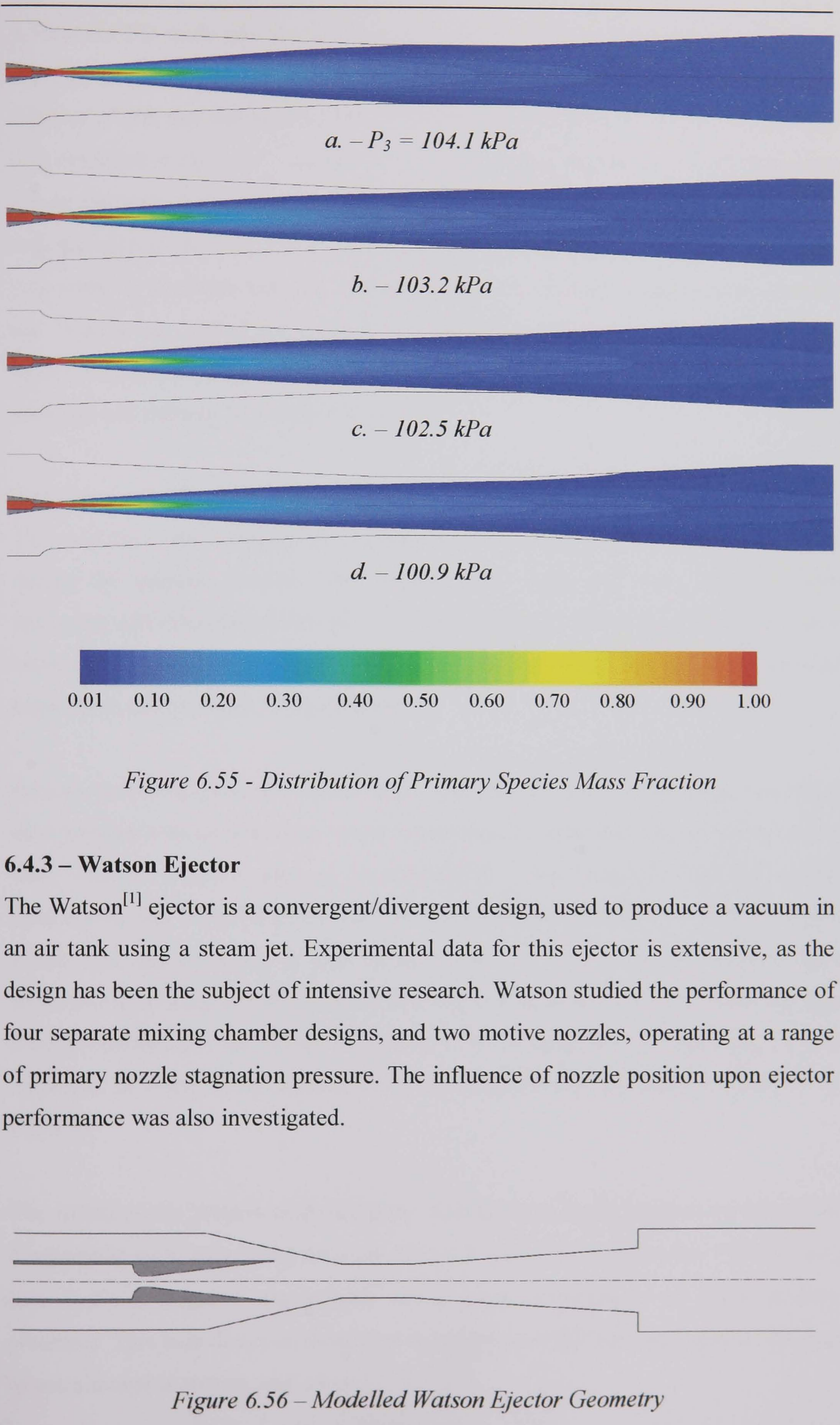

Figure 6.55 - Distribution of Primary Species Mass Fraction

6.4.3 – Watson Ejector

The Watson[1] ejector is a convergent/divergent design, used to produce a vacuum in an air tank using a steam jet. Experimental data for this ejector is extensive, as the design has been the subject of intensive research. Watson studied the performance of four separate mixing chamber designs, and two motive nozzles, operating at a range of primary nozzle stagnation pressure. The influence of nozzle position upon ejector performance was also investigated.

Figure 6.56 – Modelled Watson Ejector Geometry

A limited CFD study of a single mixing chamber design has been performed for two separate primary nozzle positions. The modelled ejector geometry coincides with *Diffuser N° 2B*, and *Steam Nozzle N° 2*, as detailed by Watson[1]. Nozzle exit position was modelled at D_N = 1½", and D_N = 2⅞" where D_N is the distance from the nozzle exit to the start of the mixing chamber throat. A short length of exit pipe (100mm), was included to position the outlet boundary at an appropriate distance. This pipe was wider in diameter than the diffuser outlet that matched Watsons experimental rig. Watson had placed the entire mixing chamber and diffuser assembly within a separate cylinder. This allowed D_N to be altered simply by sliding the mixing chamber and diffuser within the cylinder.

The computational mesh comprised 20676 and 21552 quadrilateral cells for D_N = 1½", and D_N = 2⅞" respectively. No adaptive refinement of this mesh was required during the solution process. The computational mesh had been designed with increasing cell refinement towards walls, and the density of the mesh within the flow channel was sufficient to capture the shock structure within the ejector. Figures of these mesh can be found in Appendix B.

Primary nozzle stagnation pressure (P_{o1}) was varied from 60-140 psig. Secondary inlet pressure was set according to the experimentally measured values within the air tank, diffuser pressure was set as atmospheric. The condenser that the ejector exhausts to, was designed to operate under atmospheric conditions, however Watson stated that the pressure at the diffuser outlet could be slightly higher than atmospheric. A detailed description of the applied boundary conditions and physical fluid properties can be found in Tables C.7-C.8 and D.7 in Appendix C, and Appendix D, respectively. Results of the investigation are presented in Table 6.7 & Fig 6.57.

The results of the Watson study are poor. Although predicted entrainment values are comparable with experiment between 140-120 psig (D_N = 1½") and 140-130 psig (D_N = 2⅞"), negative entrainment values were predicted at all other primary pressures. This is in direct contradiction to experimentally measured values. The loss of entrainment is sudden and severe.

Pressure		D_N (in)	R_m	
Primary Inlet (psig)	Secondary Inlet (Pa)		CFD	Experiment[1]
140	16202	1½	0.099	0.084
130	16877		0.096	0.090
120	23627		0.085	0.095
110	25315		-0.124	0.103
100	35441		-0.097	0.109
80	63118		-0.198	0.114
60	82695		-0.200	0.104
140	18227	2⅞	0.119	0.084
130	17552		0.109	0.090
120	17214		-0.096	0.096
110	39829		-0.219	0.099
100	54005		-0.412	0.101
80	81007		-0.103	0.088
60	91808		-0.247	0.077

Table 6.7 - Results of Watson Study

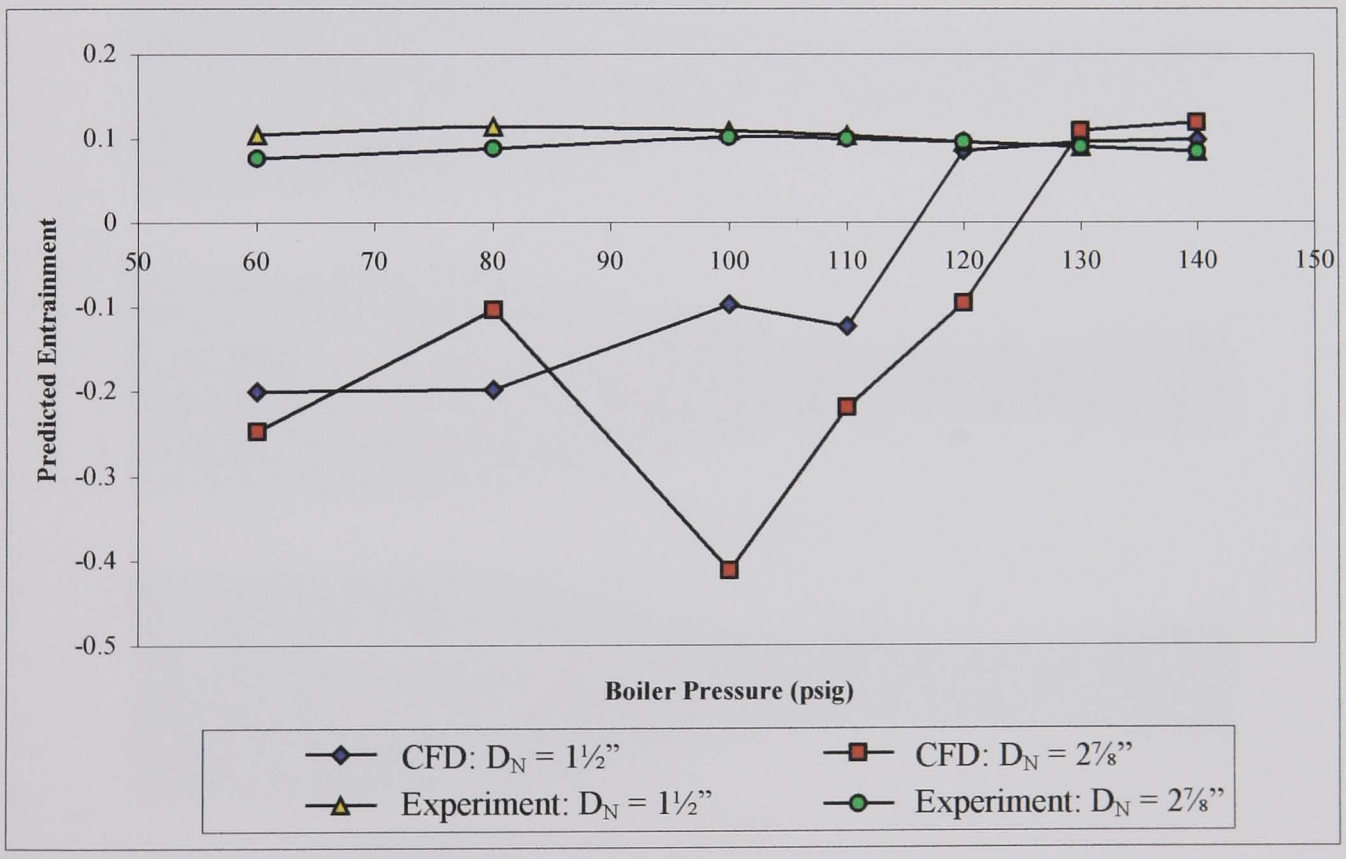

Figure 6.57 - Results of Watson Study

The reason for the prediction of negative entrainment is clearly evident in Figs 6.58 and 6.59. The primary nozzle is over-expanding and as primary stagnation pressure is reduced the diffuser back pressure causes the choke within the ejector throat to collapse, and the motive jet decreases in length. Eventually the rise in diffuser back pressure causes the motive jet to separate from the de Laval nozzle walls, and to further retreat towards the nozzle throat. If the nozzle stagnation pressure was further

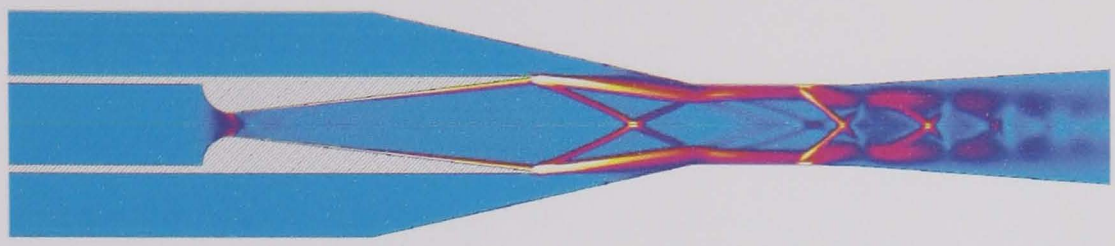

a. – P_{o1} = 140 psig

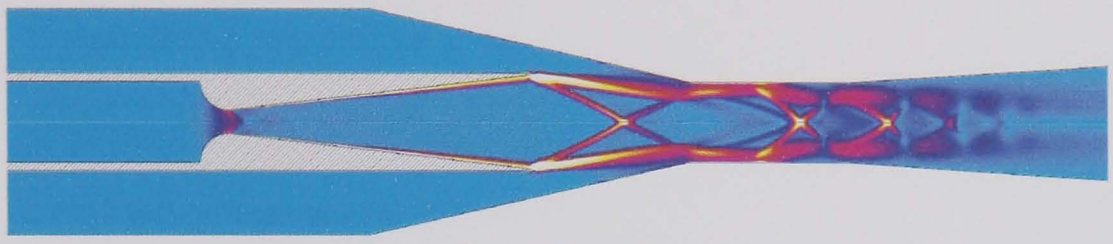

b. – 130 psig

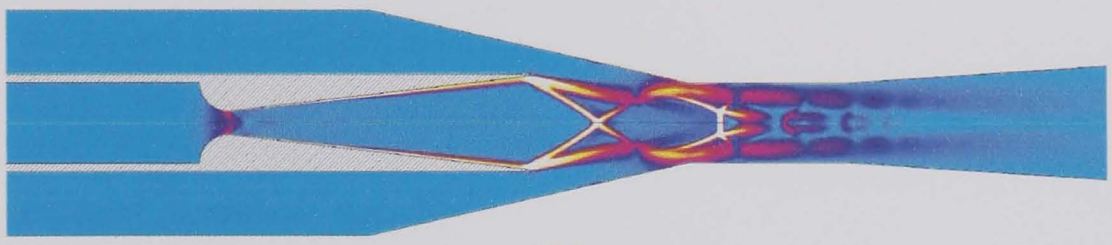

c. – 120 psig

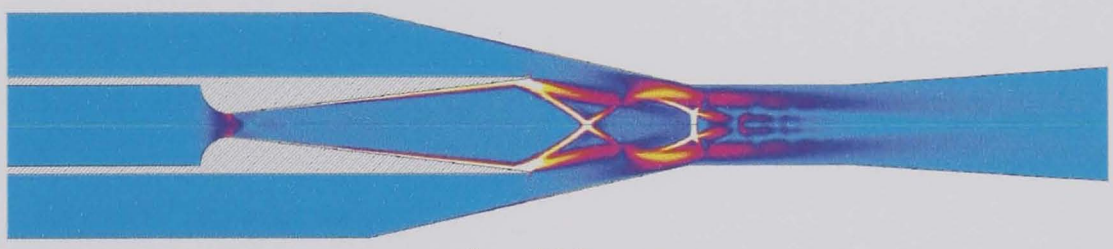

d. – 110 psig

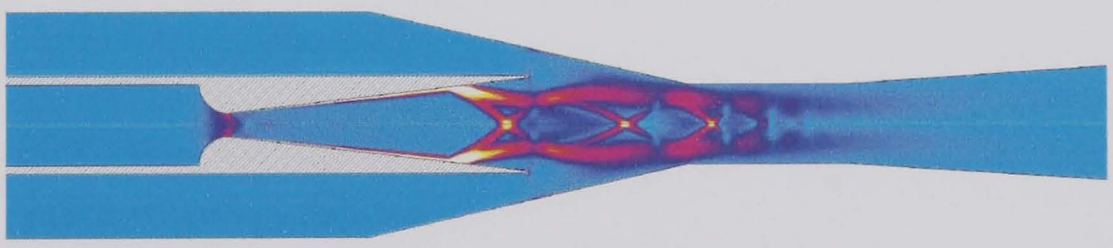

e. – 100 psig

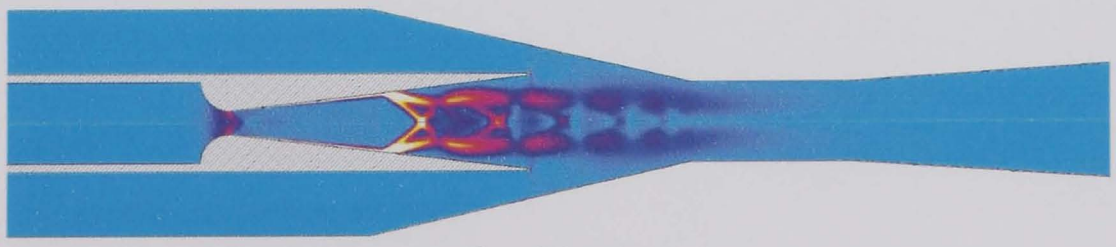

f. – 80 psig

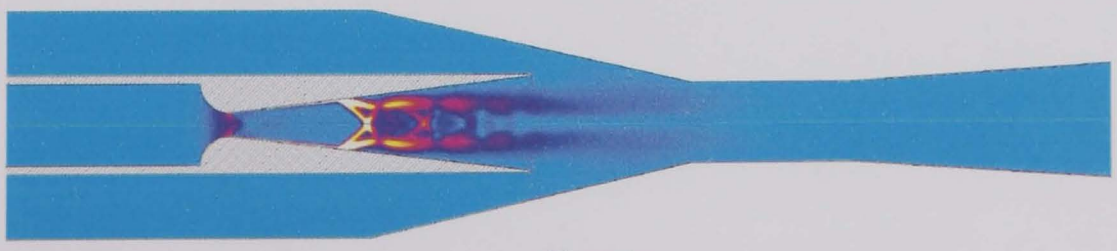

g. – 60 psig

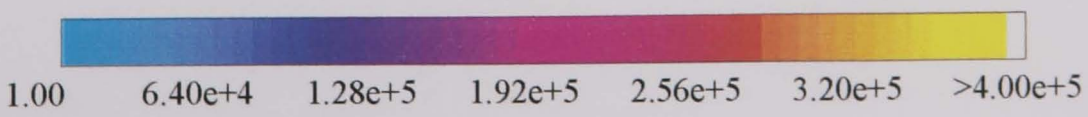

Figure 6.58 - Predicted Strain Rate Within Watson Ejector: D_N = 1½" (1/s)

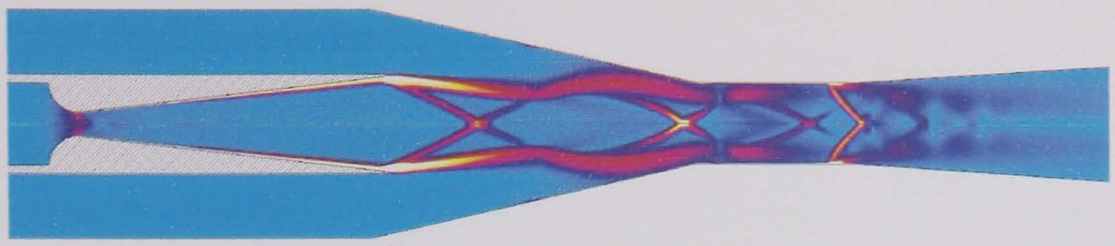

a. – P_{o1} = 140 psig

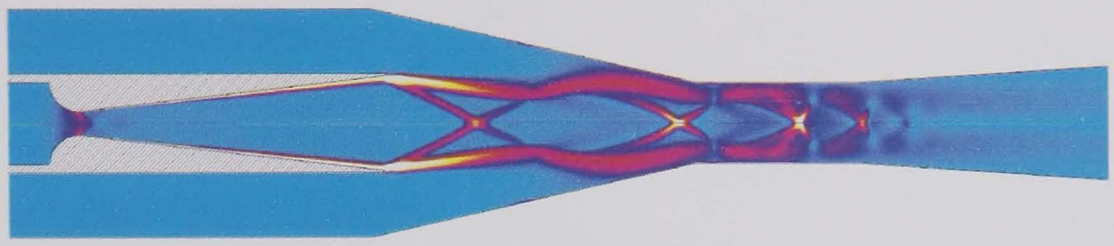

b. – 130 psig

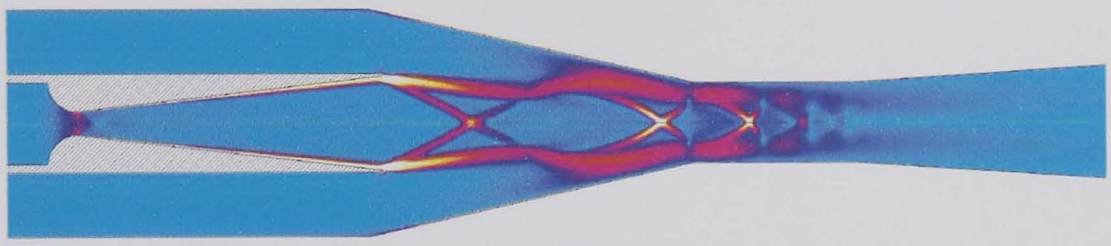

c. – 120 psig

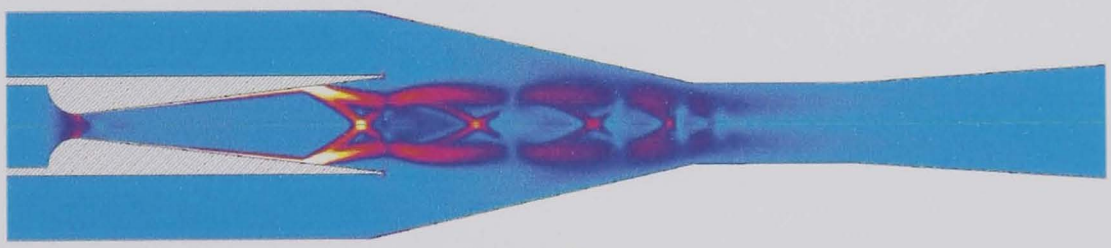

d. – 110 psig

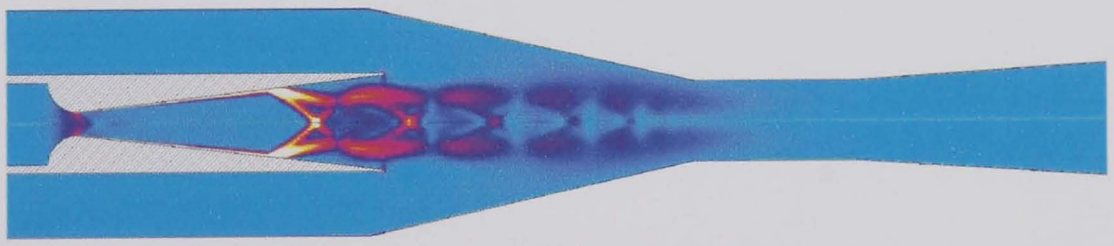

e. – 100 psig

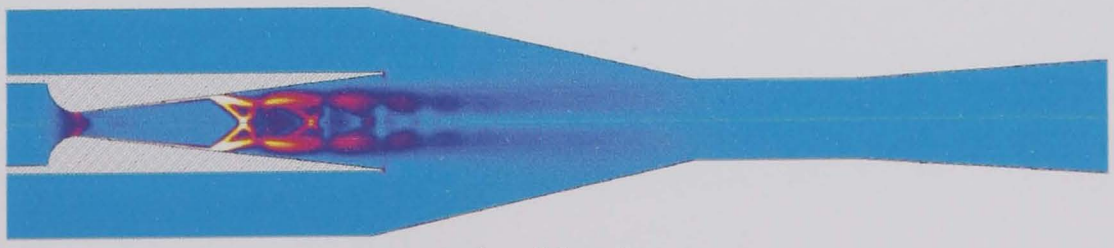

f. – 80 psig

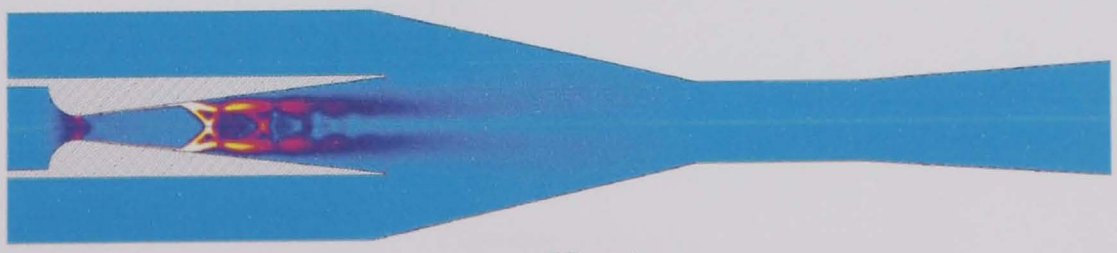

g. – 60 psig

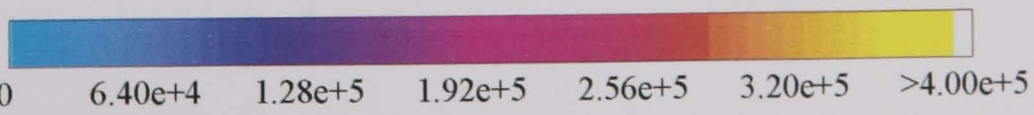

Figure 6.59 - Predicted Rate of Strain Within Watson Ejector: D_N = 2⅞" (1/s)

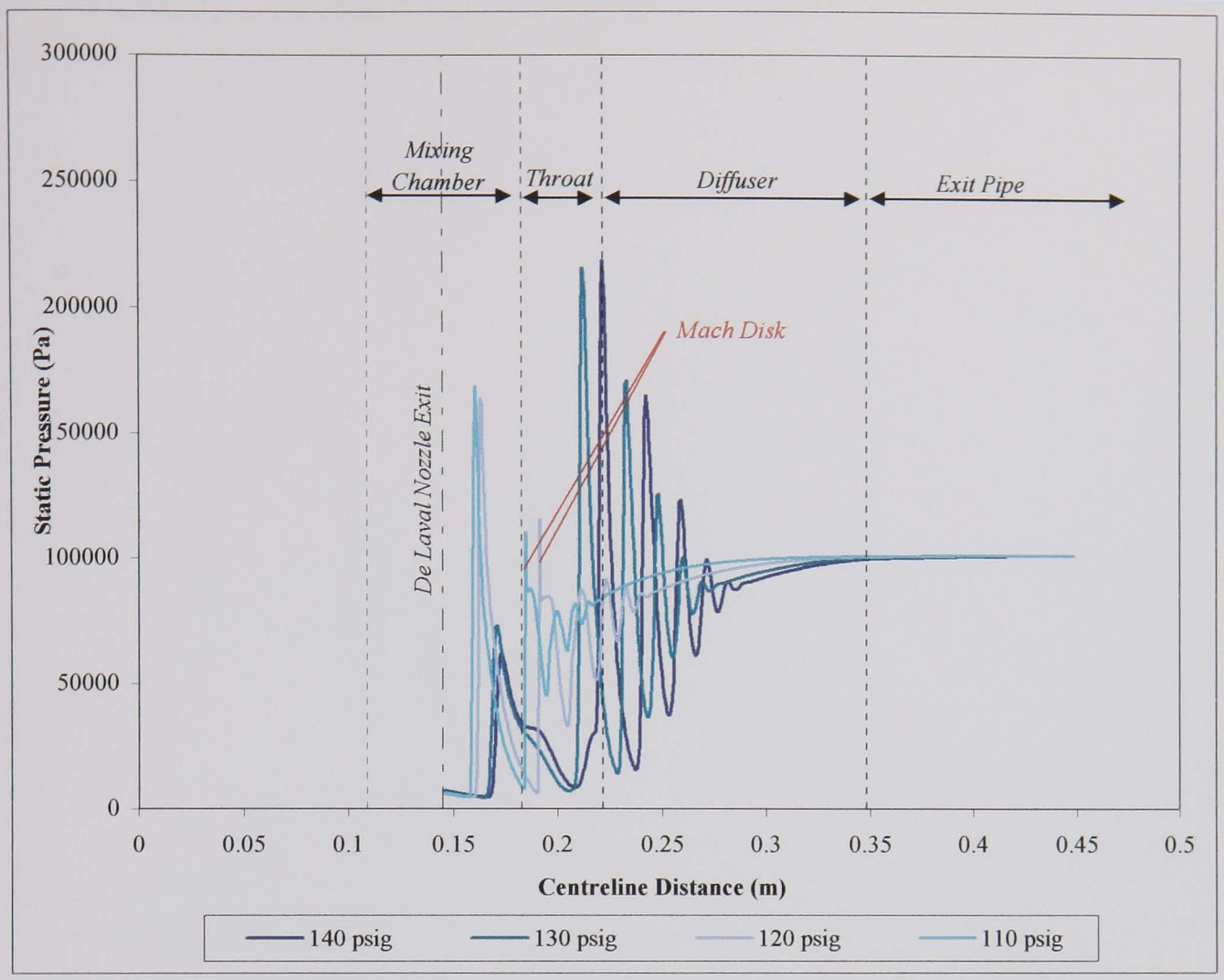

a. - 140 psig - 110 psig

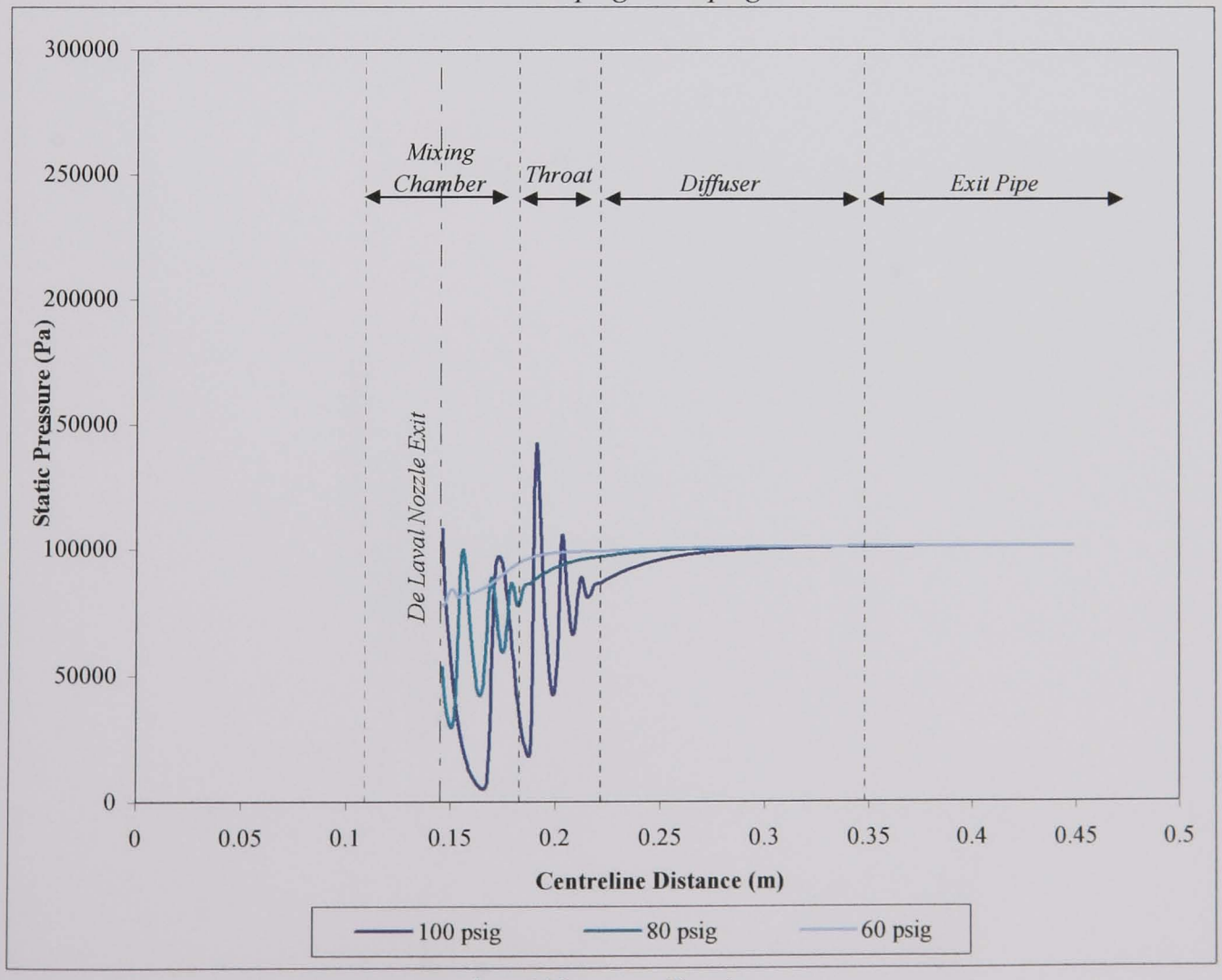

b. - 100 psig - 60 psig

Figure 6.60 - Centreline Static Pressure Distribution: D = 1 1/2"

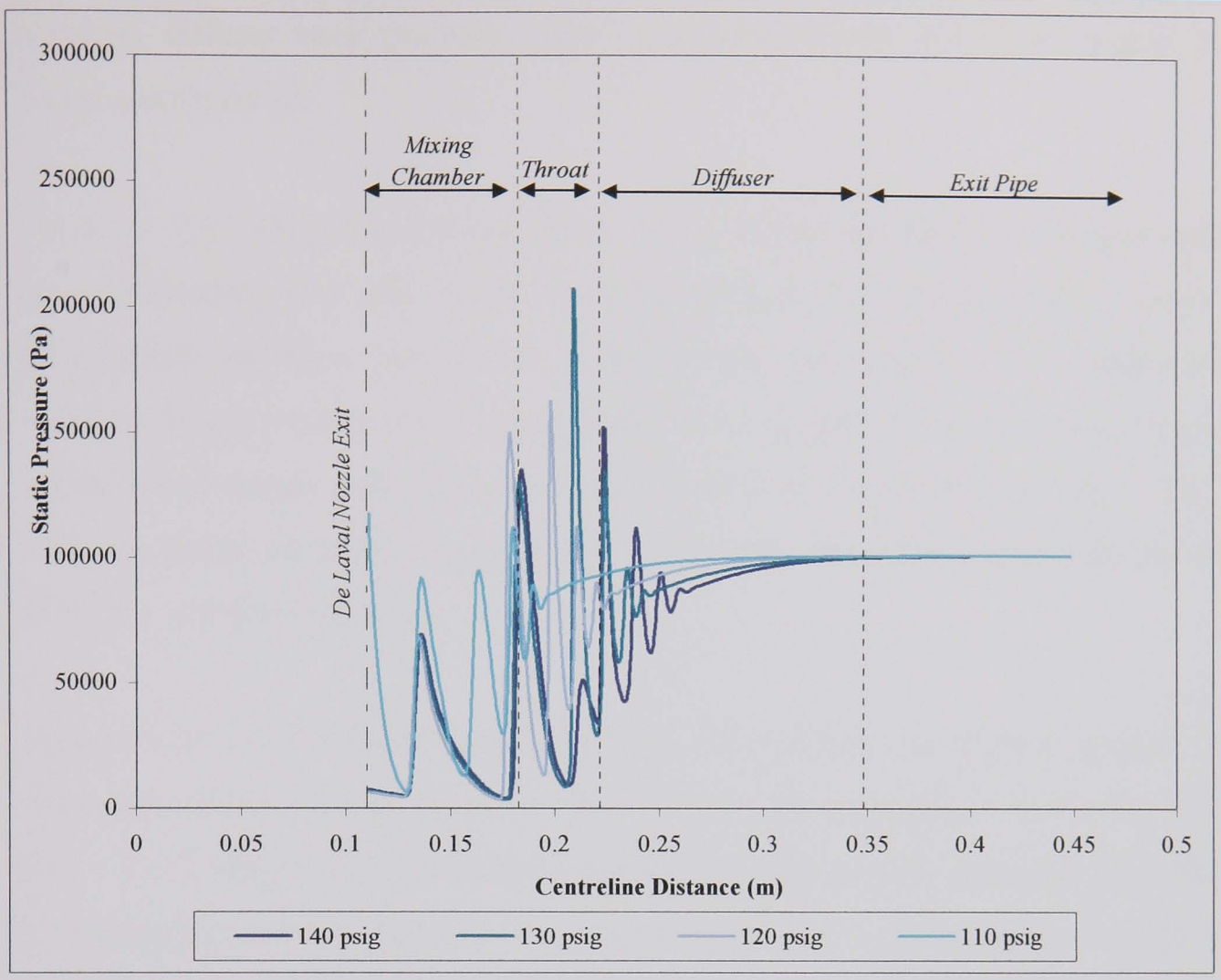

a. - 140 psig - 110 psig

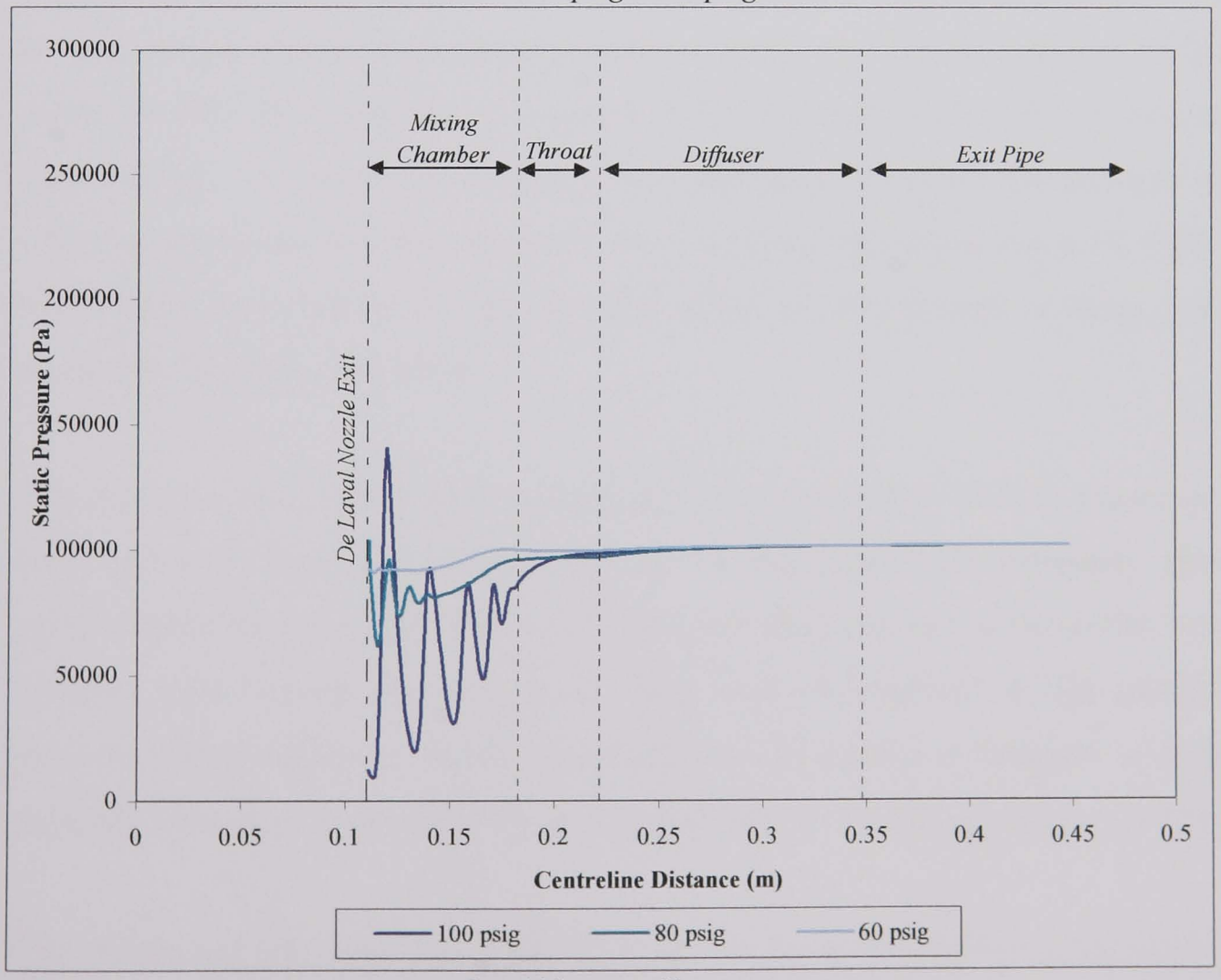

b. - 100 psig - 60 psig

Figure 6.61 - Centreline Static Pressure Distribution: D = 2 7/8"

reduced, diffuser back pressure would eventually unseat the choke within the de Laval nozzle throat.

For D_N = 1½", Fig 6.58, a strong shock stands within the throat at 140 psig and 130 psig, indicating that the throat is fully choked. At 120 psig this shock has disappeared and been replaced by a Mach disk, see Section 2.4.1, within the jet which is clearly evident at 110 psig. Below 110 psig the jet begins to move back into the de Laval nozzle and separates from the wall. In comparison for D_N = 2⅞", Fig 6.58, the throat shock is only observed at 140 psig. The jet collapses into the nozzle when P_{o1} is below 120 psig.

Figures 6.62 and 6.63 show the supersonic flow within the Watson ejector. These show how the jet fails to choke the throat below 120 psig (D_N = 1½") and 130 psig (D_N = 2⅞"), hence the rapid decline in predicted entrainment. Although the reduction in stagnation pressure causes the supersonic jet to decrease in length, the exit Mach number is not influenced until flow separation within the nozzle occurs. This is because the jet velocity is dependant upon the nozzle exit diameter, therefore so long as the jet fills the nozzle the exit velocity will be unaffected. This remains in the region of M = 3.5 until the jet begins to break back. However the strength of the reflected shock due to over-expansion does increase regardless, Fig 6.58–6.61. The Mach disks, and pockets of subsonic flow which sit downstream of these, are also evident in Fig 6.62c and 6.62d.

The influence upon entrainment and mixing of the secondary fluid is shown in Figs 6.64 and 6.65. Both the entrainment and mixing region are extremely short at positive entrainment levels. The entrainment boundary appears to be on the verge of collapse, even though R_m is positive. This is to be expected as the quantity of secondary fluid entrained should be very low as the ejector is designed to maintain vacuum. Obviously when negative entrainment occurs no mixing region is evident.

The collapse of the supersonic jet is attributable to an insufficient stagnation pressure producing a jet incapable of withstanding the diffuser back pressure. However the species distribution within the ejector indicate that the fluid within the ejector as a

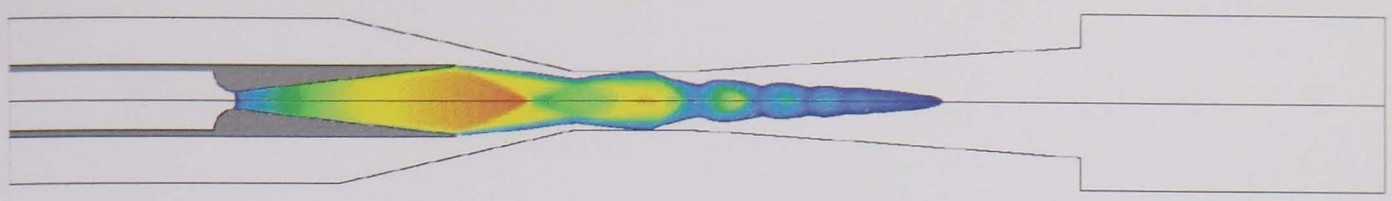

a. – P_{o1} = 140 psig

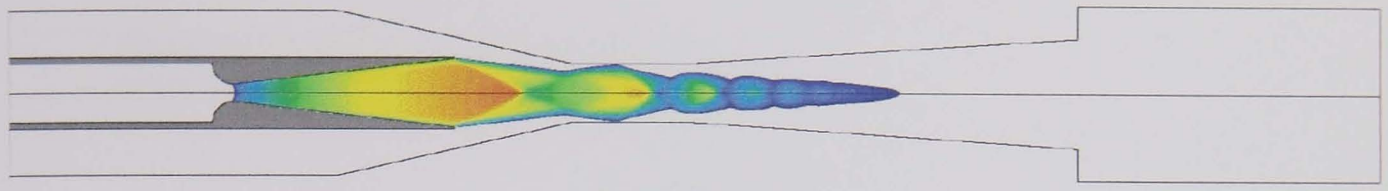

b. – 130 psig

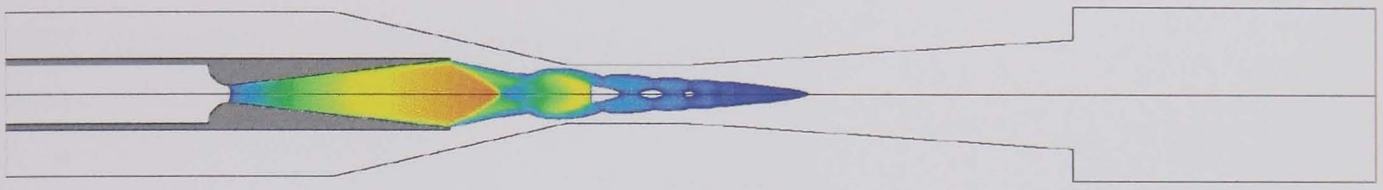

c. – 120 psig

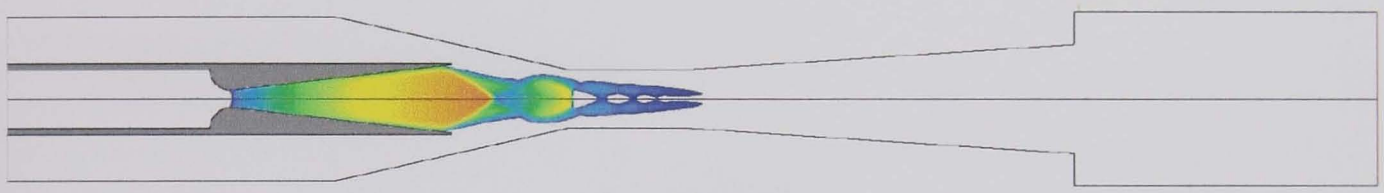

d. – 110 psig

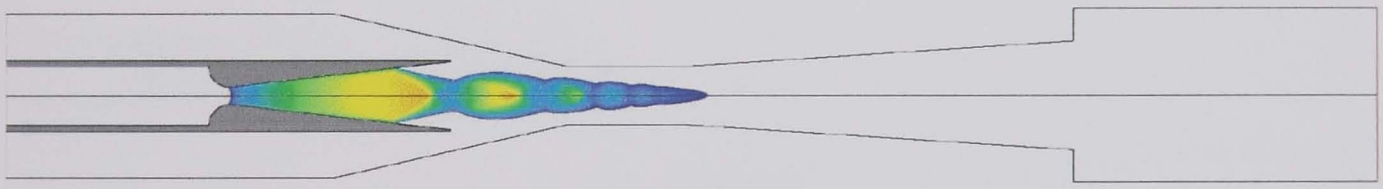

e. – 100 psig

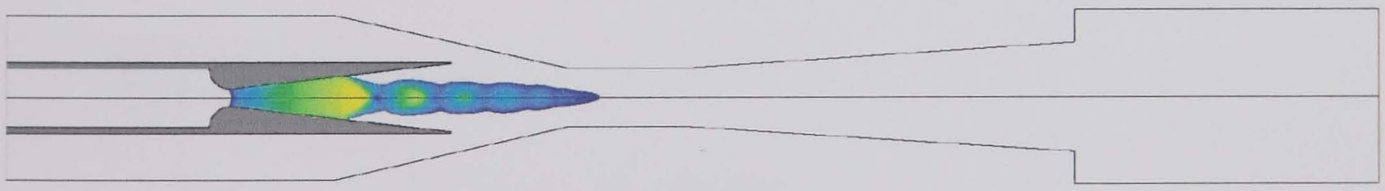

f. – 80 psig

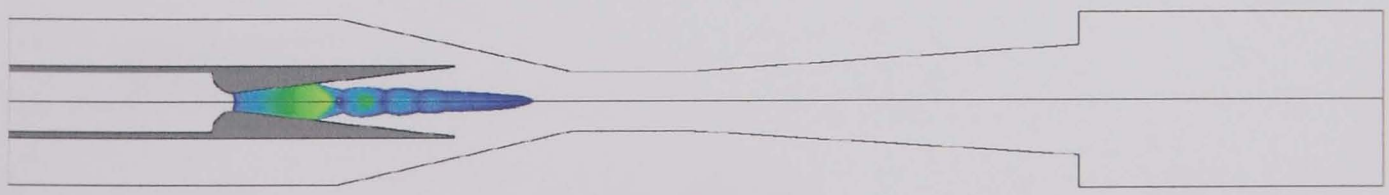

g. – 60 psig

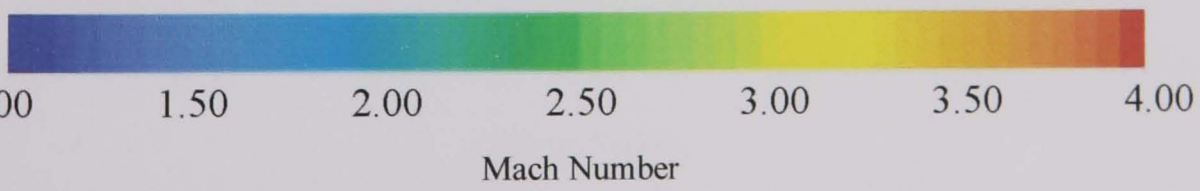

Figure 6.62 - Supersonic Flow Region Within Watson Ejector: D_N = 1½"

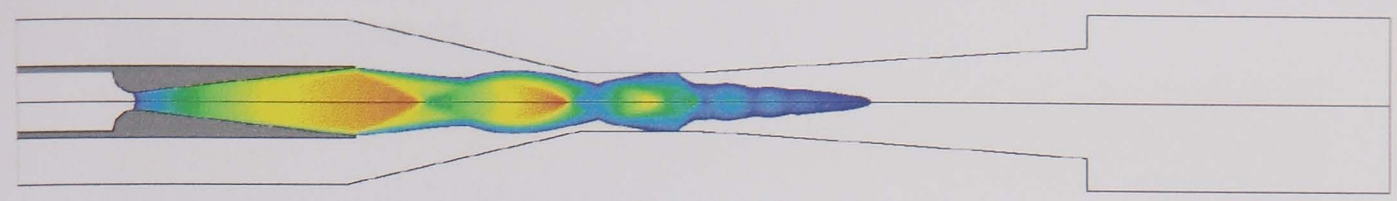

a. – P_{o1} = 140 psig

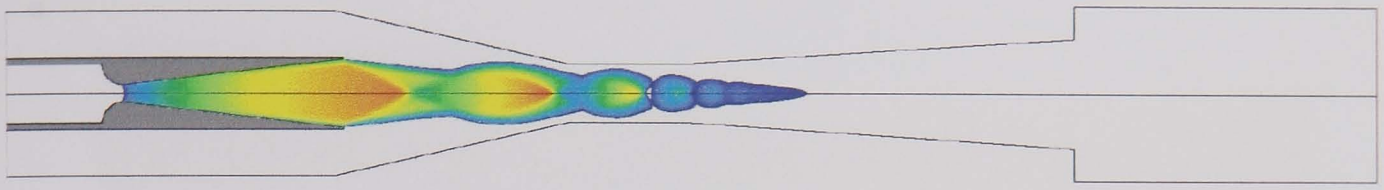

b. – 130 psig

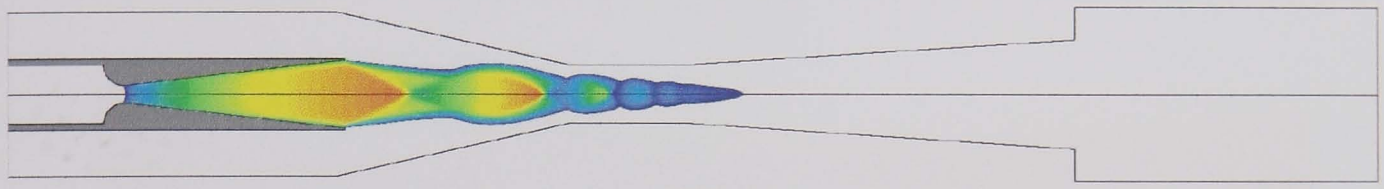

c. – 120 psig

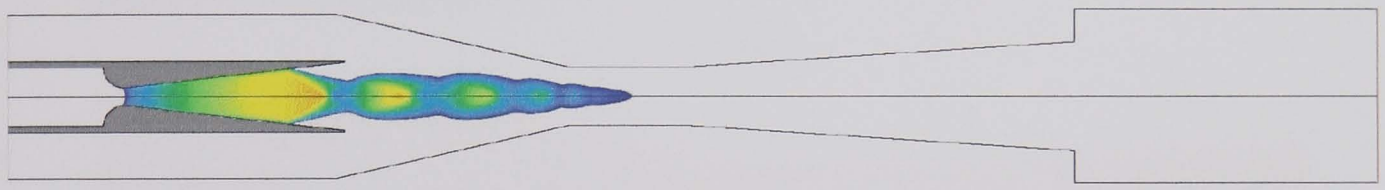

d. – 110 psig

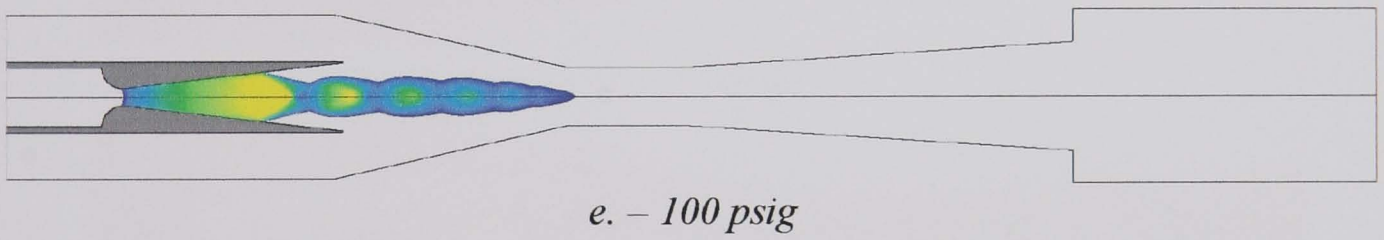

e. – 100 psig

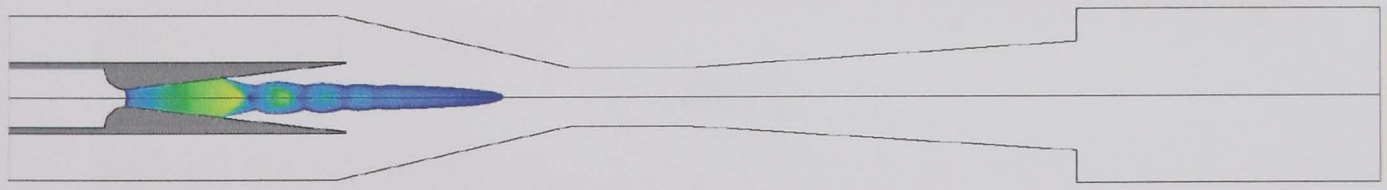

f. – 80 psig

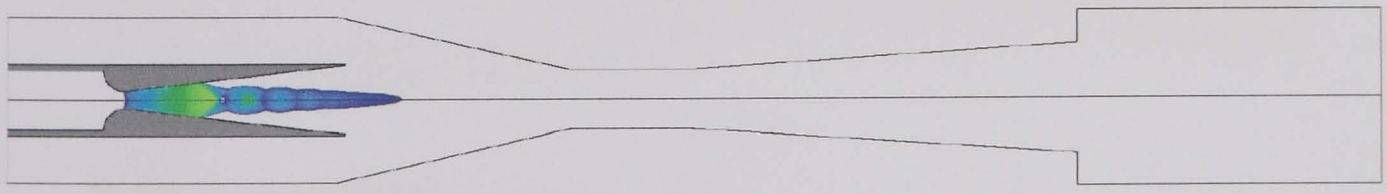

g. – 60 psig

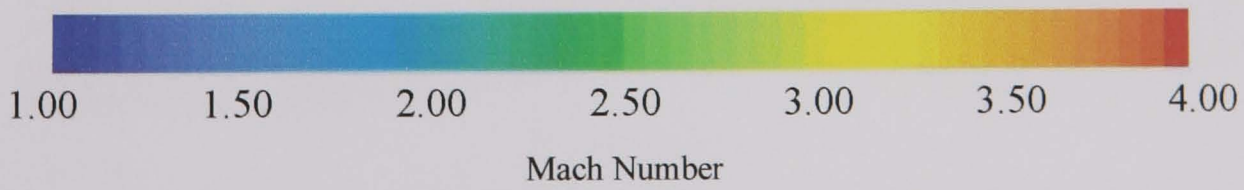

Figure 6.63 - Supersonic Flow Region Within Watson Ejector: $D_N = 2\frac{7}{8}$"

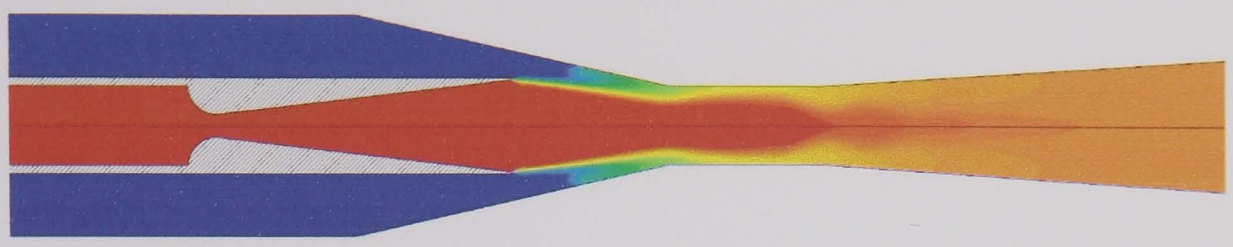

a. – P_{o1} = 140 psig

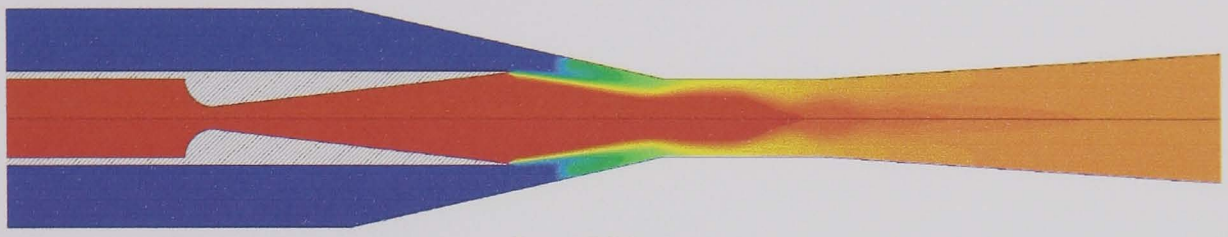

b. – 130 psig

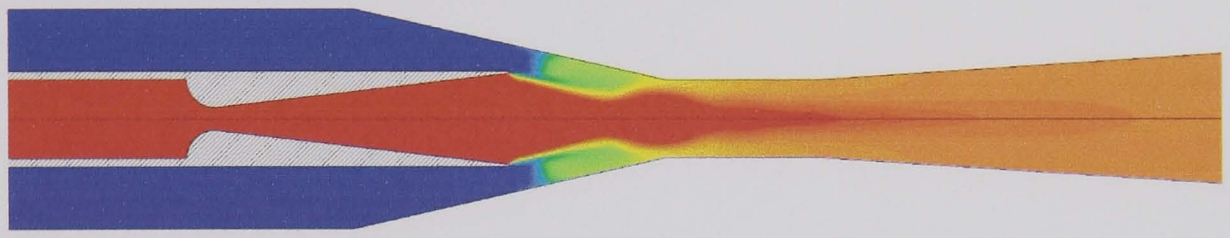

c. – 120 psig

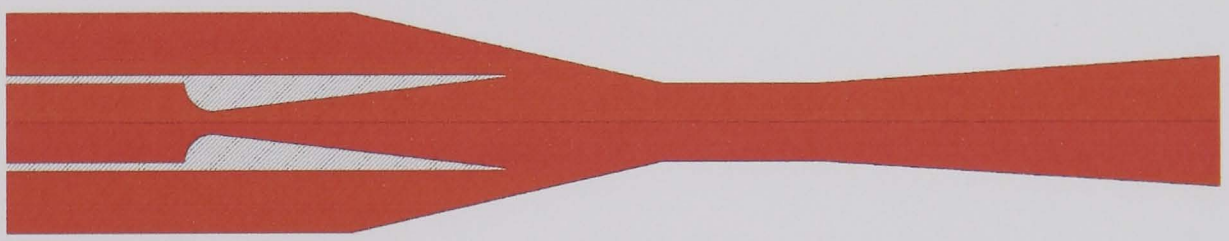

d. – 110 psig

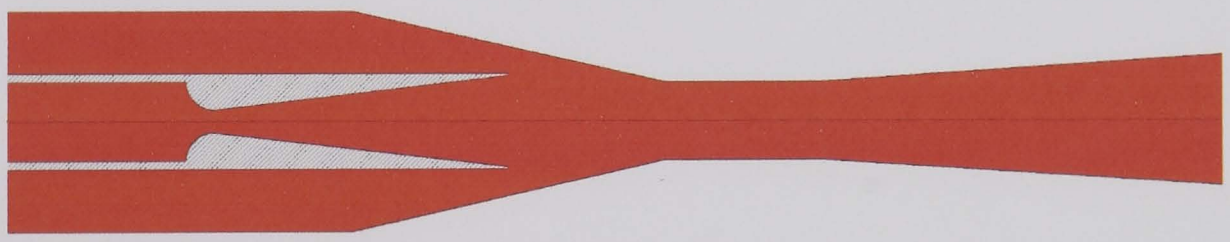

e. – 100 psig

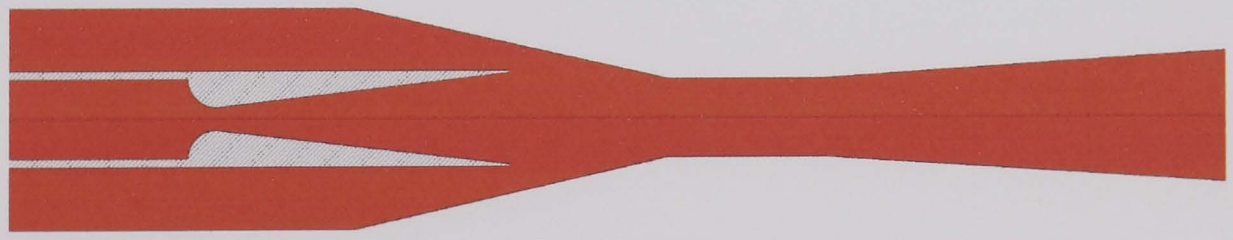

f. – 80 psig

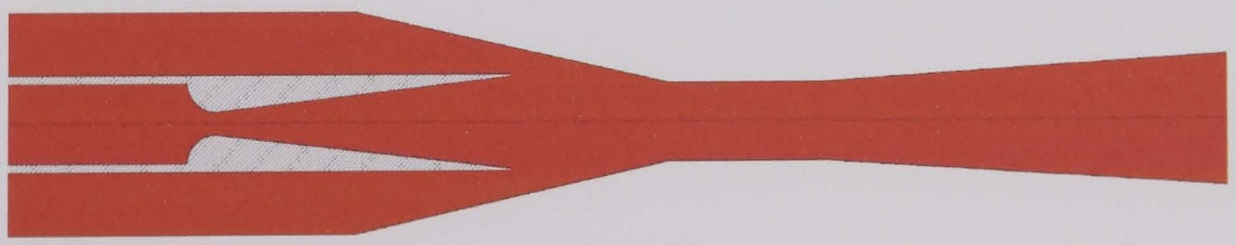

g. – 60 psig

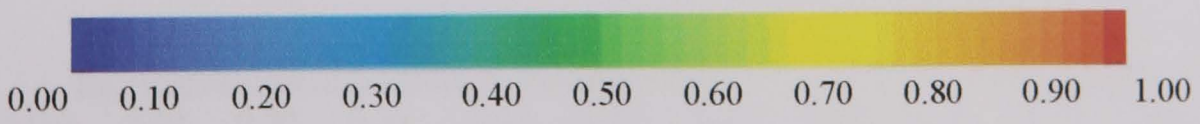

Figure 6.64 - Distribution of Primary Species Mass Fraction: D_N = 1½"

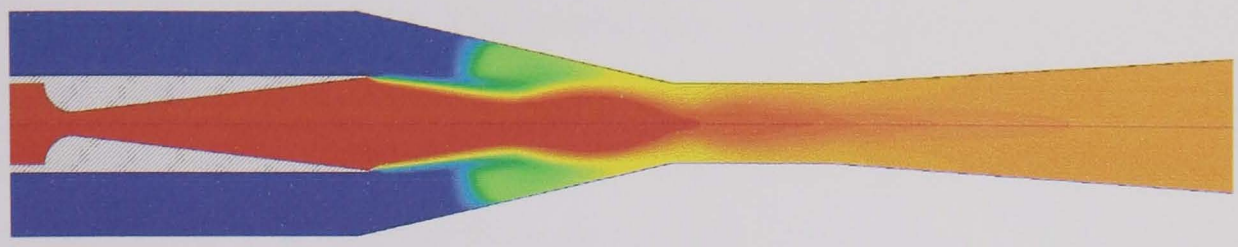

a. – P_{o1} = 140 psig

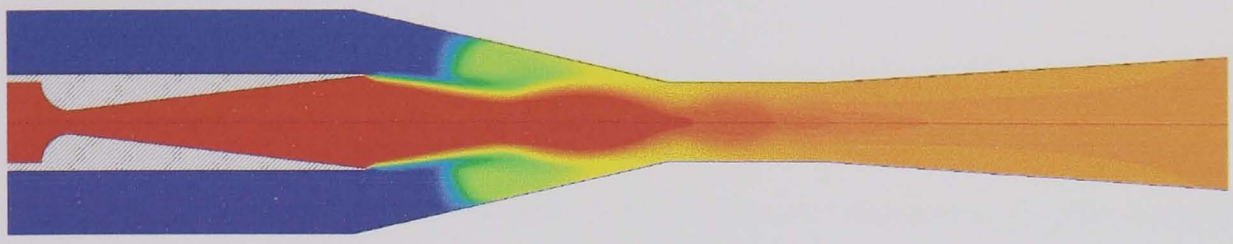

b. – 130 psig

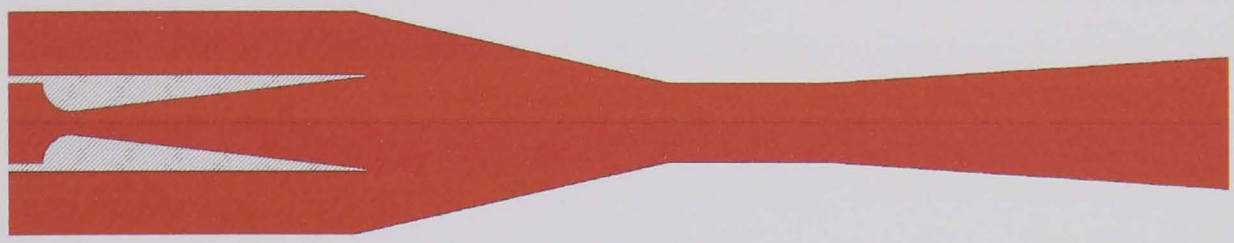

c. – 120 psig

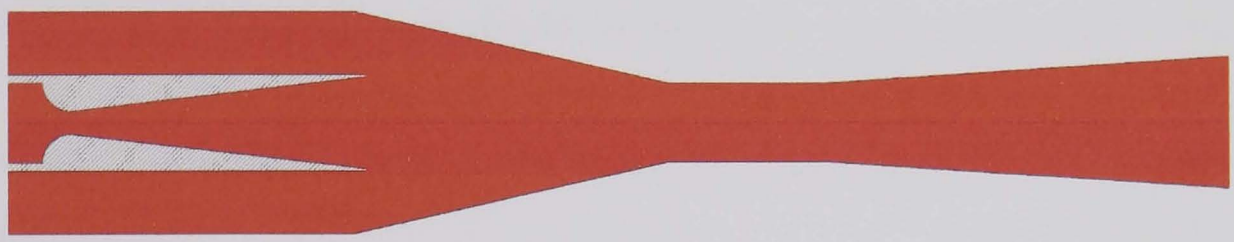

d. – 110 psig

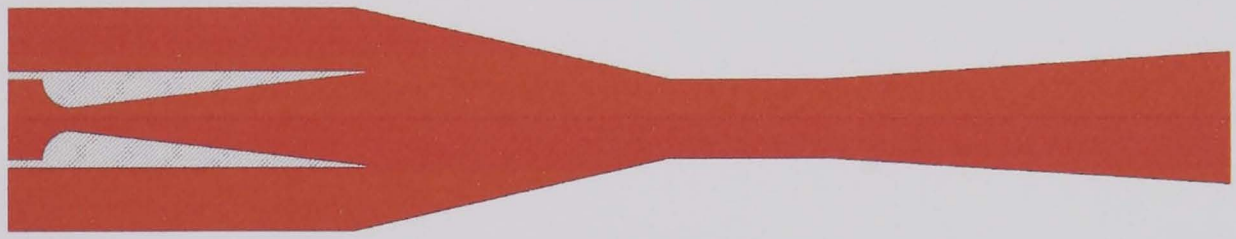

e. – 100 psig

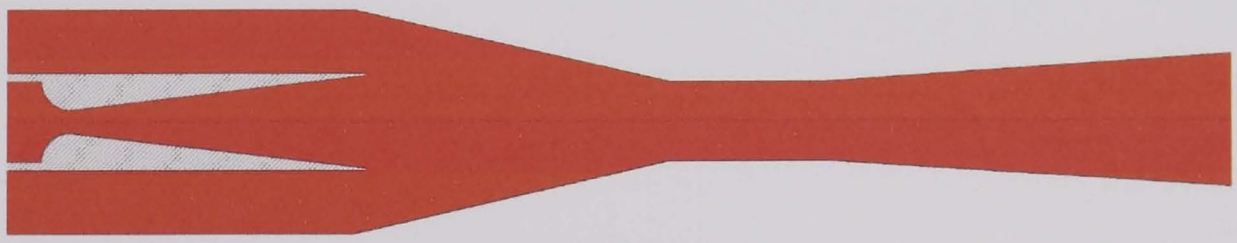

f. – 80 psig

g. – 60 psig

Figure 6.65 - Distribution of Primary Species Mass Fraction: D_N = 2⅞"

whole is purely primary fluid. The reverse flow into the air tank will consist purely of steam originating from the primary nozzle. Even at the reduced stagnation pressures the primary mass flow rate is sufficient to fill the ejector entirely with steam, preventing flow entering from the diffuser.

The reason that CFD is incapable of predicting positive entrainment values at reduced pressures, in contradiction to experiment, is uncertain. It is possible that CFD over predicts the degree of nozzle over-expansion resulting in a jet incapable of driving the ejector at low stagnation pressure. Alternatively the performance of the de Laval nozzle may fluctuate in a time dependent manner at these reduced pressures. It is then possible that CFD is predicting a worse case scenario, and that positive entrainment values are possible but sporadic. Indeed Watson states in his conclusions, that for high vacuum levels to be maintained a primary stagnation pressure greater than 120 psig should be used, low steam pressures having been found unsuitable to maintain high vacuum. This would be in agreement with the CFD predicted results, which found $P_{o1} < 120$ psig incapable of maintaining a vacuum.

Chapter 7 – Discussion

The following chapter discusses the two major aspects of this investigation; the implementation of CFD to the simulation of supersonic ejectors, and the insight gained into ejector operation. Implementation of CFD is first discussed with a general introduction to the benefits that its use can provide. This then progresses to the performance of the assembled numerical parameters. Opportunities and possibilities for improving the performance of the technique are discussed.

Discussion then moves to ejector operation and the knowledge gained of the flow processes that occur. Finally possible methods for the enhancement of ejector performance are considered.

7.1 – Implementation of CFD

The results of this study have shown that CFD has the potential to be an effective and powerful tool in the simulation and further understanding of ejectors. It was also clear that CFD must be carefully optimised and calibrated for such use. Numerical parameters have to be systematically appraised as was detailed in Chapter 5. Indeed it was found that the predicted operational performance of the ejector could vary by as much as 32% through ill-thought application of numerical parameters. Once this process was completed however it was possible to obtain not only qualitative but quantitative results.

CFD though is not the complete solution to ejector analysis and optimisation, which was also evident from the results of this investigation. Discrepancies exist between the utilised experimental data and CFD simulations. Empirical analysis has developed to the extent where it can now be used to design and assess an ejector reliably. It could therefore be argued that there is no real requirement for CFD analysis of ejectors. Empirical analysis will not be surpassed in terms of cost and simplicity in the initial design stage of a new ejector, however CFD should be applied to further refine the initial design.

The results of this investigation have proven that CFD is valuable to the rapid assessment and optimisation of geometrical parameters. However the area of ejector analysis where the major strengths of CFD reside is in the operational analysis of the ejector as a whole. The ability to simulate an ejector operating away from the intended design conditions or with alternative media to determine operational performance is of great value. CFD has been shown capable of performing this task efficiently.

Empirical analysis does not account fully for the complex shock phenomena which occur within ejectors, specifically the shock within the ejector throat which is classically assumed to be a single normal shock. In reality the shock waves in this section are complex and reflective, which was shown in simulation. Additional complex shock and expansion phenomena exist within the supersonic jet, which can severely influence performance and also cannot be assessed fully through empirical analysis. The use of experimental techniques to assess the true impact of these phenomena is not feasible as outlined in Section 2.5, however CFD can recreate and account for such phenomena.

Because of simulation uncertainties it is unlikely that CFD will or should ever completely replace experimental work or analysis. However it can be highly complementary to the design and experimental process. The cost of experimental work can be reduced through prior simulation of parameters of interest.

7.1.1 – Model Performance

Simulation results with good agreement to experiment were obtained for the Eames[5] ejector. Qualitative results could be obtained with either the segregated or coupled solver utilising relatively coarse mesh containing as few as 5500 computational cells. However the coupled solver was also capable of producing quantitative simulations, which was largely attributable to adaptive mesh capabilities.

The optimised numerics of the segregated solver used in qualitative geometrical studies produced a difference of 14.2% to experiment. This was dependent however upon careful assembly of the computational mesh. Assembled mesh should have a cell aspect ratio as near to unity as possible, and a minimum of skewness. This is

particularly important within the mixing chamber and throat where the most complex flow phenomena reside.

The optimised coupled solver used in the critical operating condition studies, Section 6.2.1, over-predicted the experiment by 0.27% to 18.7% (average 7%). The difference increased as evaporator temperature was reduced from 10°C to 5°C. This can be attributed to an under-prediction in the expansion of the motive jet. Simulation of evaporator temperatures less than 5°C, as in the low-pressure investigation of Section 6.2.2, would have resulted in further over-prediction of operational performance. It is therefore likely that a reverse flow condition would have occurred sooner than that predicted at low evaporator temperatures.

Two-dimensional simulation results from the coupled solver were mesh independent. However a quantitative mesh independent solution required approximately 8-10 times the computational time of a qualitative result. Considerable computational savings were obtained through the use of the adaptive meshing tools, which proved invaluable to the attainment of economic mesh independent results. This procedure concentrated the mesh and thus computational resources in areas of interest within the flow. Relatively coarse and economic mesh could be retained in regions with slight influence on the obtained results. A final selectively refined mesh on average consisted of 70000 computational cells; a successive globally refined structured mesh of equivalent resolution could have consisted of more than 280000 cells.

Adaptive meshing also allowed for the economic use of the two-layer zonal wall model. Optimisation studies had shown that if quantitative results of pressure independent ejectors are to be obtained the two-layer zonal wall model must be used. This model allows the boundary layer to grow, unlike the standard wall function, which fixes boundary layer depth. Refinement of the computational mesh in attempts to obtain mesh independent results invalidated the use of the standard wall function. Only the two-layer model remained valid for use in refinement studies, which actually improved the accuracy of this wall model. However the model requires extremely fine mesh at wall surfaces to resolve the boundary layer appropriately making its use computationally expensive. The use of the model approximately increased the required computational time by 75%. This expense was reduced

through selective refinement of cells at wall surfaces using y^+ values as refinement criterion. The standard wall function could still be used to obtain qualitative results, however the computational mesh must be carefully assembled to ensure the model's validity.

A three-dimensional simulation could be performed in the equivalent length of time taken to obtain a mesh independent two-dimensional simulation. However a maximum mesh limit of 150000 cells had to be imposed. Although this mesh was considerably larger than that used in comparable three-dimensional studies outlined in Section 2.6, only qualitative results could be obtained. It is estimated that a mesh consisting in the region of 500000+ cells would have been required to obtain a quantitative mesh independent result.

Regardless of the fact that only qualitative results were obtained, three-dimensional simulations of the Eames[5] ejector produced results which differ from experiment from –2.6% to +9%. These differences were larger than those obtained in the corresponding two-dimensional simulations. This was to be expected as the simulations were mesh dependent, a result of computational resource constraints limiting mesh size. The largest differences were again attributable to an under-prediction in the expansion of the motive jet within the mixing chamber. It is felt that the use of three-dimensional simulation is unnecessary so long as the suction chamber geometry is not influential. Two-dimensional axisymmetric simulations would adequately reproduce ejector performance in this case.

Application of CFD to alternative designs of ejector produced results of varying agreement with experiment. This however may be expected as the applied numerical models were based on the optimised model for the Eames ejector. Additional numerical optimisation was not conducted, save for mesh refinement to ensure a mesh independent result.

The numerical model performed well in the simulations of the Desevaux[7] ejector, Section 6.4.1. This study however was of a fixed entrainment, with secondary fluid levels fixed through the use of a mass flux boundary condition at the secondary inlet. Primary mass flow rate also remained fixed as the de Laval nozzle was choked. The

simulation was effectively forced to deal with a fixed mass of fluid. Simulation results were qualitatively correct in comparison to the experimental visualisations of Desevaux[7]. Simulation results of the Watson[1] vacuum ejector, Section 6.4.3, however were extremely poor. Although at high motive pressure results comparable with experiment were obtained, experimental results at low motive pressure could not be simulated. This is in direct contrast to all other ejectors simulated in the course of this investigation, yet there was nothing significantly different in the Watson ejector design.

Watson[1] had visualised the motive nozzle exhausting into a cylinder at atmospheric conditions. Only the end of the motive jet was visible external of the motive nozzle at 80 psig, as flow separation was occurring within the nozzle. The same behaviour was observed in simulation. The atmospheric back pressure at the diffuser outlet, as specified by Watson, unseated the choke in the throat at low motive pressures causing flow separation in the motive nozzle. This resulted in the occurrence of a reverse flow condition.

The Hickman[6] ejector, Section 6.4.2, was fundamentally different to all other ejectors simulated in this investigation. This was a high volume high-pressure thrust-augmenting ejector designed to operate in a pressure dependant manner. Simulation results for this ejector were good, which is perhaps unsurprising. Predicted difference in the range of –0.004% to 4.4% between simulation and experiment were obtained. In comparison to the other simulated ejectors the Hickman[6] ejector contained little shock structure. The ejector shroud was wide in diameter in comparison to the de Laval nozzle exit, and the motive jet effectively behaved as a free jet unaffected by the presence of the confining chamber walls.

7.1.2 – Visualisation Aspects

A major strength of CFD is the visualisation of flow field data. This allowed the acquisition and interpretation of data that would have been difficult to gain or even unobtainable through experimental methods. The operational mode of the simulated ejector could be identified in plots of supersonic flow. Chokes within the ejector could be clearly identified. Flow and shock patterns could be observed in contour

plots of fluid strain rate. These showed expansion fan and shock structure throughout the mixing chamber and throat.

Image quality was generally good, however the resolution of a shock wave in CFD will always be dependent upon the size of mesh in the vicinity of the shock. A shock will always appear as a smear, as the thickness of the shock will be equivalent in width to the computational cell it falls across. To resolve shock structure properly the computational mesh should be concentrated in the vicinity of the shock wave. Adaptive mesh techniques are particularly useful for this purpose, as it is not always possible to predict the position and form of this structure prior to simulation.

Smearing of shock systems was evident in the throat of the Eames ejector, Fig 6.14-6.16. These images were further complicated by the velocity gradients, which reside in this region. The thick boundary layer interacts with the normal shock system, flow separation occurs at the diffuser wall, and fluid rapidly decelerates. This does not particularly benefit the visualisation of weak shock systems, however strong shock systems are clearly visible and distinguishable. The visualised shock structure in the over-expanding Watson ejector was a good example of this, Fig 6.59-6.60.

The visualisation of the shock structure would benefit from the use of an artificial schlieren technique instead of strain rate. Strain rate had been used in this investigation, as it was an available post-processing variable. To create CFD schlieren it would have been necessary to write and incorporate a subroutine that calculates density gradient. This was beyond the scope of this current project. Visualising density gradient would to a certain extent alleviate additional velocity gradients, un-associated with shock/expansion systems, which complicate the images. It is possible for a velocity gradient to exist in, for example a boundary layer, without a significant change in density.

7.1.3 – Improving Model Performance

The accuracy of CFD simulation may be improved by refining the mathematical model and the numerics in CFD, or through improving processing capabilities. Obviously the CFD user has more control over the mathematical model than CFD

numerics, unless the user so desires to devote time to researching improvements in numerical and solver models.

When considering improvements which could be made to the mathematical model the intended purpose of the simulation results is a significant factor. Simulation may be conducted within an engineering or research environment, and used for geometrical appraisal, operational appraisal, or for detailed analysis of physical processes. Dependent upon environment, and purpose of simulation, there may be no additional benefit to be gained from refining the mathematical model, which would only complicate matters further. This could be particularly relevant in an engineering environment where only rapid qualitative geometrical assessment may be required. The simple mathematical model used with the segregated solver may therefore prove sufficient without further improvement.

The mathematical model however should really be optimised and calibrated for each detailed analysis of an ejector design. This is a time consuming and costly procedure though necessary to ensure accurate simulation. However the optimised mathematical model assembled for simulation of the Eames ejector has demonstrated a general applicability to ejector simulation. This could therefore be used as a suitable starting point for simulation of similar ejectors.

Further improvements to the mathematical model may be achieved through the consideration of additional physical phenomena. Heat transfer processes were omitted from the current investigation through the application of fixed thermal boundaries. The application of heat flux or conduction boundary conditions at wall surfaces may prove beneficial. It was known for example that under certain operating conditions, temperature within the Eames ejector falls low enough for the formation of a ring of ice around the exterior of the ejector mixing chamber. A fixed thermal boundary condition would prevent realistic temperatures at wall surfaces being attained. This may serve to artificially raise the pressure slightly within the ejector.

The specification of individual species fluid properties as functions of temperature and pressure may prove beneficial. Although it was shown in Section 5.6 that no

significant benefits were to be obtained, this was only a single case and low-pressure simulations especially may therefore benefit.

Previous CFD ejector investigations [74,76] have suggested that simulation accuracy may benefit from the addition of phase change to the numerical model. Taylor[88] discussed the possibility of ice formation and accumulation within the de Laval nozzle and throat, outlining the implications of this upon ejector performance. In this investigation a phase change process was omitted. Although pressure and temperature fell below the triple point, it was felt that the extremely short residency times and high shear forces would prohibit particle formation. However omission of phase change at low-pressures might increase simulation errors.

The inclusion of such a phenomenon would complicate the solution process considerably. To model this process fully the implemented model would need to be capable of predicting and dealing with sublimation, nucleation, and the possible accumulation of ice upon surfaces. Thus for general geometrical and operational analysis performed in an engineering environment modelling phase change would be an expensive complication. Inclusion of such a phenomenon may only be justifiable perhaps within detailed flow studies performed in an academic environment.

Computational hardware advances will obviously benefit the simulation of ejectors. A major factor governing accuracy in this investigation was the maximum number of computational cells that could be feasibly solved. The implementation of improved computing facilities would alleviate this problem. This of course would also benefit three-dimensional simulation, though axisymmetric approximations have been found adequate for the majority of simulations.

Advances in turbulence models would perhaps be most beneficial to the solution process. The prediction of turbulent processes which govern entrainment, mixing, and the behaviour of the motive jet are crucial to the accuracy of the solutions. This was particularly evident when testing the available turbulence models. Turbulence model optimisation studies had shown that the Spalart-Allmaras[80], standard k-ε, and RNG k-ε turbulence models had comparable capabilities in the prediction of

turbulent phenomena. A difference of only $\pm 0.5\%$ from experimental data existed between these models. The k-ε realisable model could not recreate the growth of the motive jet. This was ironic, as the realisable model is a modification of the standard k-ε model specifically optimised to deal with compressible jet flows.

Riffat and Everitt[76] claimed that the standard k-ε model was unsuitable for the simulation of ejectors, however in the optimisation studies it marginally out performed RNG. The optimisation studies were axisymmetric and did not calculate swirl, hence in the three dimensional simulations where swirl was evident in the suction chamber RNG may have performed better.

Detailed analysis of the actual entrainment and mixing processes within the ejector could not be performed. One and two-equation turbulence models simulate only one length scale and one velocity scale, assuming isotropic turbulence[105]. This is a hypothetical form of turbulence, as turbulence is well known to be multi-scale in length and time. These models perform rather crude representation of the turbulence effects in the ejector. A more sophisticated approach, e.g. LES, may be the minimum required to fully comprehend the mixing and entrainment processes occurring within the ejector. The use of more sophisticated turbulence models, such as LES, in this investigation was not possible due to their computational demands, see Section 3.2.

7.2 – Entrainment Aspects

Supersonic ejector flow physics are complex, as the results of this investigation have shown. The complex entrainment and mixing interactions between the subsonic and supersonic fluid are further complicated by the confined space within which these processes evolve and develop. This section of the discussion will concentrate predominantly on the insight gained into these processes from CFD investigation of the Eames[5] ejector, however occasional reference will be made to the other ejectors studied here.

The Eames[5] ejector operated in a pressure independent manner with a choked throat. Observed flow patterns in the ejector corresponded to the *fully supersonic*

flow pattern as classified by Matsuo[48], and the *low flow regime* of Addy[44], see Section 2.5.2. The same flow patterns were observed in the Watson[1] ejector, whilst a *mixed flow* pattern as classified by Fabri[65] was observed in the Desevaux[7] ejector.

The Eames[5] ejector could also be observed to behave in the manner postulated by Munday & Bagster[35] to explain the constant capacity characteristics of ejector refrigeration systems. The supersonic motive jet was observed to fan out into the mixing chamber, this created a converging channel between the mixing layer and the shroud wall. Secondary fluid flowed along this channel and was entrained into the mixing layer.

Munday & Bagster[35] also theorised that secondary fluid flowing into this channel would eventually attain sonic velocities forming a choke and retaining its distinct identity from the primary stream. The results of this investigation showed that secondary fluid was fully mixed with the primary flow by the throat where the choke formed in the Eames ejector. If the secondary stream had remained distinct, a flow pattern corresponding to the *choked secondary flow* or *double choked flow* patterns classified by Matsuo[48] would have been observed. These patterns will only be observed in ejectors where the secondary flow rate is high.

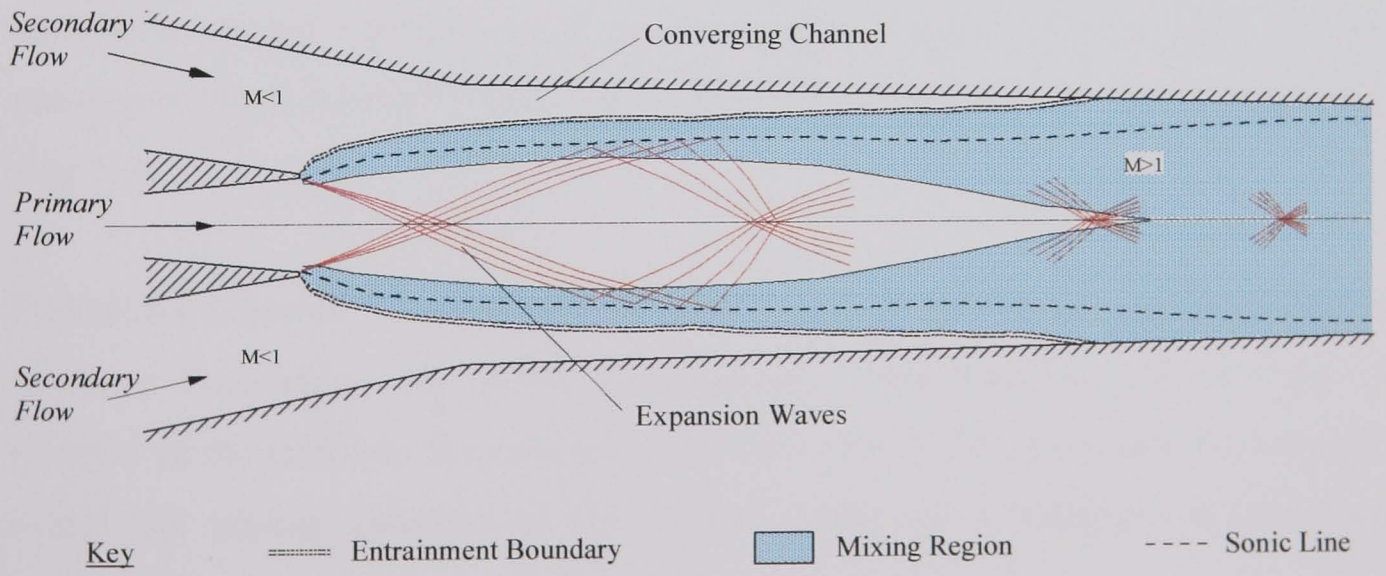

Figure 7.1 – Schematic of Flow Processes Within Eames Ejector

Entrainment occurs along the entire length of the channel formed between the spreading motive jet and the chamber wall. Secondary fluid is entrained into the

mixing layer passing through the entrainment boundary that marks the interface between pure and mixed secondary fluid. The exact position of this boundary will fluctuate in reality as turbulent processes are intermittent[105] in nature. Entrainment could therefore occur across the entire width of the mixing layer if large scale structures are present.

The extent of the entrainment boundary is influenced by expansion of the primary jet. An increase in primary pressure will increase the expansion of the motive jet. This will cause the channel formed to decrease in length and thus the size of the entrainment boundary to reduce. The induced level of secondary fluid however is largely unaffected as the higher velocity of the motive jet, and thus higher entrainment rate, which compensates for the reduction in size of the boundary.

A reduction in secondary inlet pressure will also cause the motive jet to expand at an increased rate. This also serves to decrease the entrainment boundary, however as this does not appreciably increase motive fluid velocity the effect upon entrainment is detrimental.

It is not possible to determine the true turbulent structure of the mixing layer from this investigation, as stated in Section 7.1.3. Turbulent structure cannot yet be visualised feasibly within the ejector using CFD. It is possible however to view turbulence related variables such as turbulence intensity, and to calculate the convective Mach number[52] (M_c) which provides an indication of the structures that may exist.

Turbulence intensity[105] is the ratio between the magnitude of the root mean square turbulent fluctuations and mean flow velocity. This describes the intensity of violence of the turbulent fluctuations in the flow. Fig 7.2 shows turbulence intensity within the mixing chamber of the Eames ejector at a selection of operating conditions.

The highest turbulence intensity values reside within the shear layer, coinciding with the high velocity gradient as would be expected. Peak values occur just external of the de Laval nozzle exit where the shear mixing layer first forms and the velocity

gradient is highest. The high intensity of turbulence in this region causes the rapid growth of the layer width, as secondary fluid is rapidly incorporated into the primary jet. As T_{boiler} is raised the peak value correspondingly increases, a result of the higher velocity gradient. A pocket of high turbulence can also be observed within the motive jet at $T_{boiler} = 140^{o}C$, which is generated by the reflection of shock expansion structure.

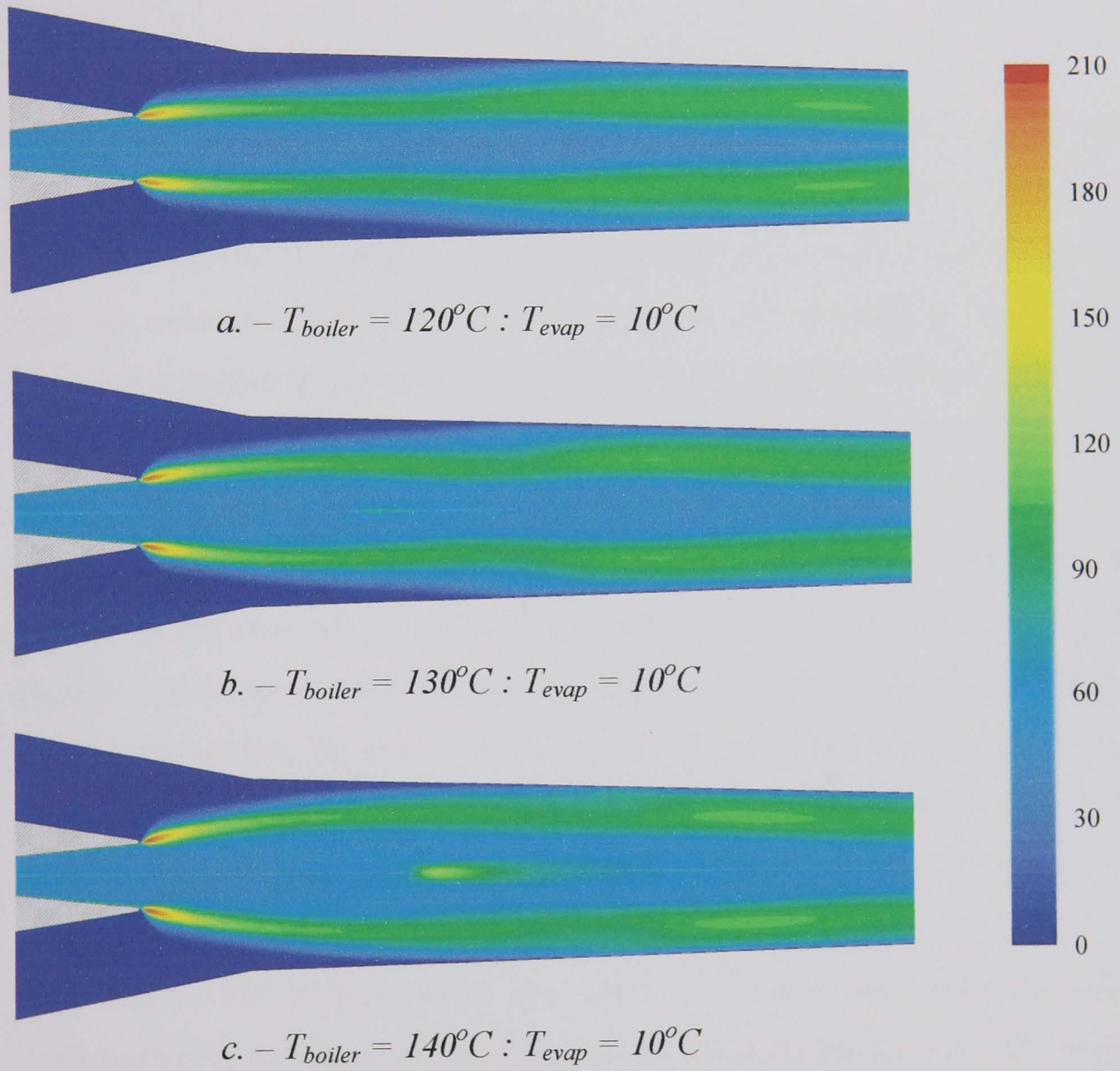

a. – $T_{boiler} = 120^{o}C : T_{evap} = 10^{o}C$

b. – $T_{boiler} = 130^{o}C : T_{evap} = 10^{o}C$

c. – $T_{boiler} = 140^{o}C : T_{evap} = 10^{o}C$

Fig 7.2 – Turbulence Intensity Within Eames Ejector Mixing Chamber

Calculation of M_c[52,106] also suggests that the mixing layer will be dominated by fine scale turbulence. M_c within the Eames ejector was found to be greater than $M_c = 1.7$, and increased as the expansion of the motive jet increased. This shows the layer to be highly compressible and three-dimensional in nature. Large structure of equivalent width to the layer should also exist, though this may be limited. Visualisation studies of supersonic jet shear layers[51], tend to only show fine scale structure within the mixing layer. Large structures, which do form, tend to appear once the mixing layer

has grown to engulf the jet. In the simulations of the Eames ejector by the point where this has occurred the entrainment process is complete.

Additional streamwise vortex structure along the subsonic edge of the shear layer may also be expected. Krothpalli[61] observed streamwise vortices at the boundary of under-expanded supersonic jets, Section 2.4.4, claimed to play a significant role in the entrainment process. The motive jet in the Eames ejector exhibited under-expanded behaviour at all simulated operating conditions.

7.2.1 – Operational Enhancement

To improve the operational performance of the simulated Eames[5] ejector either the entrainment ratio needs to be increased, or/and the maximum operational back pressure needs to be raised. The design of this conventional ejector however has been in existence for more than 100 years, yet significant improvements in operational performance have not been achieved. Researchers have exerted a great deal of experimental effort with the aim of understanding and optimising ejector design. As a result methods and guidelines such as those by ESDU[3] now exist which can be used to design ejectors of reliable performance. This investigation in part reviewed some of the ESDU[3] guidelines, which were found to be well set, if slightly conservative on occasions. A ceiling of attainable operational performance exists however for the conventional ejector design. This will not be exceeded by slight adjustments to these guidelines. A new and maybe even radical approach would be required to improve the performance of the ejector significantly.

This was a belief expounded by Garris[10,11] who has tried to incorporate turbomachinery components into the constant pressure ejector, but with no beneficial aspects to date. Garris[10,11] abandoned a key concept and strength of the ejector, no moving parts. Methods of improving performance whilst retaining this key concept of ejector design however have been tested with varying degrees of success. These methods tend to concentrate on the de Laval nozzle, which is the easiest component to alter within the ejector and which has considerable influence. It is acknowledged that ejector performance can be influenced significantly by adjusting nozzle position[12,17,41] or operating pressure. However enhanced mixing should also lead to

improvements in ejector performance and this is the approach used by most researchers.

Studies using lobed[107,108] nozzles, in thrust augmenting ejectors, and petal[109] nozzles which generate large scale axial vortex structure beneficial to ejector performance have been conducted. However the generation of additional turbulence causes the expansion rate of supersonic jets to increase[110]. The results of this study have shown that an increase in the rate of spread of the motive jet can be detrimental to the performance of the Eames[5] ejector. These methods are maybe therefore best suited to high volume ejectors, such as the simulated thrust augmenting ejector of Hickman[6] where the motive jet can expand. Indeed Chang[109] has shown that petal nozzles are unsuitable for use in ejectors with a throat area ratio less than approximately AR = 150. A conventional de Laval nozzle has been shown superior for use in such occasions. The Eames[5] ejector has an area ratio of AR = 81, suggesting the use of such methods inappropriate.

This investigation has shown that to significantly improve the entrainment ratio of the Eames[5] ejector the primary mass flow rate needs to be reduced, Section 6.2.1. This can be achieved through a reduction in motive jet pressure. However the motive jet still needs to retain a stagnation pressure (P_{o1}) capable of producing a choke within the ejector throat to ensure stable operation. This limits not only the reduction of P_{o1}, but also the maximum allowable diffuser back pressure (P_3). The pressure ratio (P_3/P_2) between diffuser back pressure and secondary fluid (P_2) being another measure of ejector efficiency in certain applications such as refrigeration.

The normal shock system that occurs within the ejector throat wastes valuable energy in the flow. As the supersonic flow rapidly decelerates the accompanying reflective shock system, as observed in the results of this investigation, dissipates energy. This leads to a sudden increase in static pressure and loss in stagnation pressure, limiting the maximum operational back pressure of the ejector. If this loss inducing process could be removed or reduced it would be possible to operate the ejector at higher back pressures, or at the same back pressure with a lower P_{o1} and thus a reduced primary mass flow rate.

This is an approach which has been proposed by Eames[111] who is currently investigating a new design; a constant rate of momentum change (CRMC) ejector. The design abandons the conventional straight sided mixing chamber and diffuser assembly, with distinct sections, in favour of a continuous convergent-divergent design. This results in a curved mixing chamber and diffuser that reportedly removes the normal shock system at design conditions. Eames[110] reports that this ejector can operate with a pressure ratio (P_3/P_2) 48% higher than the conventional design[5,19]. It is also reported that significant improvements in entrainment can be achieved. To date the CRMC ejector of Eames[111] appears to be the most significant and promising advance to the improvement of performance in pressure independent ejectors.

Chapter 8 - Conclusions

The main objectives of this project are; the implementation of CFD to the study of supersonic ejectors, and the investigation of the operational processes that occur within it.

CFD has been shown to be an effective and powerful tool in the simulation and understanding of ejectors. Not only qualitative but quantitative results can be obtained. However for this to be achieved it is also clear that the CFD model must be carefully assembled, then optimised and calibrated. It has been shown that results could vary as much as 32% through the injudicious application of numerical parameters.

Both segregated and coupled solvers have been shown capable of simulating supersonic ejectors. The segregated solver investigated in this study was used to produce qualitative geometrical studies. However its structured nature was prohibitive to the attainment of quantitative results. These could not have been obtained economically without severely compromising the all important quality of the computational mesh.

The coupled solver was used to conduct detailed operational studies of a range of ejector designs. Quantitative results could be viably obtained with this solver due to its powerful mesh adaption capabilities allowing a mesh independent result to be achieved economically. The coupled numerics are more suited to the simulation of the highly compressible processes that occurred within the ejector, as they mimic the highly coupled nature of the flow parameters.

Regardless of the solver formulation the necessary numerical methods and models have to be applied to ensure that even qualitative results are obtained. Without the use of higher order discretisation schemes this is not achievable. The importance of adequately modelling boundary layers at ejector surfaces was clearly apparent. Standard wall functions could be used, however the computational mesh must be

carefully optimised to ensure the validity of the function. The use of the standard function prevents attainment of a mesh independent solution due to the relatively coarse mesh required at wall surfaces to allow its use. Hence only qualitative results are attainable with the standard function. To obtain a quantitative result a two layer zonal model must be applied, allowing mesh refinement without affecting boundary layer thickness. However this method is computationally demanding due to the highly refined mesh required to resolve the boundary layer.

Computational resources can be conserved by other means. Axisymmetric approximations have been shown suitable for use in simulating ejectors if the suction chamber geometry is not influential. Additionally adaptive meshing techniques allowed selective refinement of the computational mesh in regions of interest. This permitted the retainment of economic coarse mesh in regions of slight interest.

The flow processes that occur within ejectors have been shown to be complex. Interactions between supersonic and subsonic phenomena are complicated further by the confined environment in which they occur. CFD allowed clear visualisation and acquisition of data regarding flow phenomena within the simulated ejectors. This would have been difficult to obtain or unobtainable through conventional experimental methods. The operational mode of the simulated ejectors could be readily determined from chokes and the form of shock structure. Adaptive mesh techniques were invaluable for enhancing shock phenomena, the exact position of which could not be fully predicted prior to simulation.

Interaction between supersonic and subsonic fluid could be identified, however it was not possible to fully comprehend the turbulent structure of the mixing and entrainment processes. The turbulence models adopted in this investigation assumed isotropic turbulence removing all but one length scale and velocity scale. A more sophisticated approach such as large eddy simulation may be the minimum required, to obtain this information. Entrainment levels were shown to be influenced predominantly by the mass flow rate of the primary stream, the expansion of the supersonic jet having a secondary influence.

Simulation has shown that the conventional ejector design is effectively at an optimum now. Geometrical studies performed in this investigation have shown the ESDU[3] guidelines to be well set. It was also apparent that significant improvements in ejector performance will not be achieved by slight adjustments to these guidelines. To achieve this a new approach must be taken towards ejector design, and this is now being recognised and investigated. CFD will prove a valuable tool in investigating and furthering these new designs.

In conclusion CFD can be used to gain an in-depth insight of the operational phenomena which occur within supersonic ejectors. The method however is not the complete solution to the investigation of ejectors, though a highly complimentary tool to experimental and empirical analysis. CFD's powerful capabilities can be utilised for the simulation of ejectors within engineering or academic environments, however care should be exercised in its application regardless. This can only be performed if the user fully understands the applied numerics.

References

[1] **Watson, F.R.B.** - "The Production of a Vacuum in an Air Tank by Means of a Steam Jet"., *Proc. I.Mech.E.*, Part I., 2, pp.231-300, 1933

[2] **Parsons, C.A.** - *Engineering.*, 78, pp.500, 1904

[3] **ESDU**. - "Ejectors and Jet Pumps"., Data Item 86030, ESDU International Ltd., 1985.

[4] **Hedges, K.R. & Hill, P.G.** - "Compressible Flow Ejectors. Part 1 - Development of a Finite Difference Model"., *Jn. Fluids Engineering.*, Trans. ASME., 96, pp.272-281, 1974.

[5] **Eames, I.W., Aphornatana, S. & Haider, H.** - "A Theoretical and Experimental Study of a Small Scale Steam Jet Refrigerator"., *Int Jn. Refrig.* 18, 6, pp.378-386, 1995.

[6] **Hickman, K.E., Hill, P.G., & Gilbert, G.B.** - "Analysis and Testing of Compressible Flow Ejectors With Variable Area Mixing Tubes"., *Jn. Basic Eng.*, Trans. ASME., 94, pp.407-416, 1972

[7] **Desevaux, P., Prenel, J.P., & Hostache, G.** – "An Optical Analysis of an Induced Flow Ejector Using Light Polarization Properties"., *Exp. In Fluids.*, 16, pp.165-170, 1994

[8] **Schmitt, H.** – "Diversity of Jet Pumps & Ejector Techniques"., Proc. 2nd Symp. On Jet Pumps & Ejectors and Gas Lifting Techniques., BHRA Fluids Engineering., Cranfield., Bedford UK., Paper No.A4, pp.(A4-35)-(A4-49), 1975

[9] **Nagao, F., Shumamoto, N., Shikata, M., & Toyofuku, H.** – "Application of Exhaust Gas Ejector to Engine Cooling"., *Bull. JSME.*, 12, 53, pp.1153-1162, 1969

[10] **Garris, C.A., & Mavriplis, C.M.** – "1999 Progress Report: A Novel Pressure Exchange Ejector Refrigeration System With Steam as a Refrigerant"., National Center For Environmental Research., Office of Research & Development., U.S. Environmental Protection Agency., 1999

[11] **Garris, C.A., Hong, W.J., Mavriplis, C., & Shipman, J.** – "A New Thermally Driven Refrigeration System with Environmental Benefits"., conference paper, IECEC-98-1088., 33rd Intersociety Engineering Conference on Energy Conversion., Colorado Springs, CO, August 1998

[12] **Keenan, J.H., Neumann, E.P., & Lustwerk, F.** – "An Investigation of Ejector Design by Analysis and Experiment"., *Jn. Applied Mechanics.*, Trans. ASME., 72, pp.299-309, 1950

[13] **Ameri, M., & Dybbs, A.** – "Coanda Ejector – Why it Works"., *Proc. SPIE – Int. Soc. of Optical Eng.*, 2052, pp.289-296, 1993

[14] **Bonnington, S.T., & King, A.L.** - "Jet Pumps and Ejectors, A State of the Art; Review and Bibliography (2nd edn)"., BHRA Fluid Engineering., Cranfield., Bedford UK., 1976

[15] **Sun, D., & Eames, I.W.** - "Recent Developments in the Design Theories and Applications of Ejectors – A Review"., *Jn. of the Institute of Energy.*, 68, 6, pp.65-79, 1995

[16] **ASHRAE.** – "Steam-Jet Refrigeration Equipment"., 1979 Equipment Handbook., Ch. 13., pp.13.1-13.6., ASHRAE., Atlanta Georgia., USA

[17] **Eames, I.W., Wu, S., Worall, M., & Aphornratana, S.** - "An Experimental Investigation of Steam Ejectors for Applications in Jet-Pump Refrigerators Powered by Low-Grade Heat"., *Proc. Instn. Mech. Engrs.*, 213, Part A, pp.351-361, 1999

[18] **Sun, D.** - "Variable Geometry Ejectors and Their Applications in Ejector Refrigeration Systems"., *Energy.*, 21, 10, pp.919-929, 1996

[19] **Aphornratana, S., & Eames, I.W.** - "A Small Capacity Steam-Ejector Refrigerator: Experimental Investigation of a System Using Ejector With Movable Primary Nozzle"., *Int. Jn. Refrig.*, 20, 5, pp.352-358, 1997

[20] **Huang, B.J., Jiang, C.B., & Hu, F.L.** - "Ejector Performance Characteristics and Design Analysis of Jet Refrigeration System"., *Jn. Eng. Gas Turbines & Power.*, Trans. ASME., 107, 7, pp.792-802, 1985

[21] **Huang, B.J., Chang, J.M., Wang, C.P., & Petrenko, V.A.** - "A 1-D Analysis of Ejector Performance"., *Int. Jn. Refrig.*, 22, pp.354-364, 1999

[22] **Huang, B.J., & Chang, J.M.** - "Empirical Correlation for Ejector Design"., *Int. Jn. Refrig.*, 22, pp379-388, 1999

[23] **Yang, T.T., Ntone, F., Jiang, T., & Pitts, D.R.** - "An Investigation of High Performance, Short Shroud Ejectors"., *Jn. Fluids. Eng.*, Trans. ASME., 107, pp.23-30, 1985

[24] **Alperin, M., & Wu, J.J.** - "Thrust Augmenting Ejector, Part 1"., *AIAA Jn.*, 21, 10, pp.1428-1436, 1983

[25] **Alperin, M., & Wu, J.J.** - "Thrust Augmenting Ejector, Part 2"., *AIAA Jn.*, 21, 12, pp.1698-1706, 1983

[26] **Presz, W.M., Morin, B.L., & Gousy, R.G.** - "Forced Mixer Lobe Ejectors"., *Jn. Propulsion.*, 4, 4, pp.350-355, 1988

[27] **Zhou, B., Fleck, B.A., Bouak, F., & Gauthier, J.E.D.** – "Comparison of Turbulence Models For Swirling Effects on Ejector Performances"., conference paper. 8th conference annuelle de la societe canadiene de CFD., CFD2K., Montreal., June 2000.

[28] **Birk, A.M., & Davis, W.R.** – "Suppressing the Infra-Red Signatures of Marine Gas Turbines"., *Jn. Eng. Gas Turbine and Power.*, 111, pp.123-129, 1988

[29] **Birk, A.M., & VanDam, D.** – "Infra-Red Signature Supression for Marine Gas Turbines: Comparison of Sea Trial and Model Test Results for the DRES Ball IRSS System"., *Jn. Eng. Gas Turbine and Power.*, 116, pp.75-81, 1994

[30] **Flűgel G.** - "Berechnung von Strahlapparaten"., VDI Forschungsheft 395., Suppl. To Forschung auf dem Gebiete des Ingenieurwesens., Ausgabe B., 10, pp.1-21, VDI-Verlag., Berlin., 1939

[31] **Elrod, H.G.** - "The Theory of Ejectors"., *Jn. Appl. Mech.*, Trans. ASME., 67, pp.A170-A174, 1945

[32] **Keenan, J.H., & Neumann, E.P.** - "A Simple Air Ejector"., *Jn. Appl. Mech.*, Trans. ASME., 9, 2, pp.A75-A81, 1942

[33] **Work, L.T., & Haedrich, V.W.** - "Performance of Ejectors as a Function of the Molecular Weights of Vapours"., Ind. Eng. Chem., 31, pp.464-477, 1939

[34] **Holton, W.C.** - "Effect of Molecular Weight of Entrained Fluid on the Performance of Steam-Jet Ejectors"., *Trans. ASME.*, 73, 10, pp.905-910, 1951

[35] **Munday, J.T. & Bagster, D.F.** – "A New Ejector Theory Applied to Steam Jet Refrigeration"., *Ind. Eng. Chem., Process Res. Dev.*, 16, 4, pp.442-449, 1977

[36] **Mikhail, S.** – "Mixing of Coaxial Streams Inside a Closed Conduit"., *Jn. Mech. Eng. Sci.*, 2, 1, pp.59-68., 1960

[37] **Hill, P.G.** - "Turbulent Jet in Ducted Streams"., *Jn. Fluid. Mech.*, 22, 1, pp.161-186, 1965

[38] **Hill, P.G.** - "Incompressible Jet Mixing in Converging-Diverging Axisymmetric Ducts"., *Jn. Basic Eng.*, Trans. ASME., 89, 1, 1967

[39] **Hedges, K.R. & Hill, P.G.** - "Compressible Flow Ejectors. Part 2 - Flow Field Measurements and Analysis"., *Jn. Fluids Engineering.*, Trans. ASME., 96, pp.282-288, 1974.

[40] **Hopkins, D.F., & Hill, D.E.** – "Effect of Small Radius of Curvature on Transonic Flow in Axisymmetric Nozzles"., *AIAA Jn.*, 8, 8, pp.1337-1343, 1966

[41] **Hogarth, M.L.** - "The Design and Performance of High Pressure Injectors as Gas Jet Boosters"., *Proc. I.Mech.E.*, 185, 56/71, pp.755-766, 1970/71

[42] **White, F.M.** – "Fluid Mechanics"., 4th Ed., WCB/McGraw-Hill., 1999

[43] **Scroggs, S.D., & Settles, G.S.** – "An Experimental Study of Supersonic Microjets"., *Exp. In Fluids.*, 21, pp.401-409, 1996

[44] **Addy, A.L.** – "The Analysis of Supersonic Ejector Systems"., Agardograph No.163, Supersonic Ejectors, Edited by J.J.Ginoux., Von Karmen Inst. for Fluid Mechanics., Rhode-St-Genèse., Belgium., 1972

[45] **Shapiro, A.H.** - "The Dynamics and Thermodynamics of Compressible Flow", Vol. 1 & Vol. 2, Ronald Press Co., 1953

[46] **Chin, S.B., Hart, J.H., & Eames, I.W.** – "CFD Design of the Throat of a Supersonic Steam Ejector"., conference paper, 8th International Symposium

on Computational Fluid Dynamics., Center of Applied Space Technology and Microgravity., University of Bremen., Germany., September 1999.

[47] **Matsuo, K., Sasaguchi, K., Tasaki, K. & Mochizuki H.** - "Investigation of Supersonic Air Ejectors (Part 1, Performance in the Case of Zero Secondary Flow)"., *Bulletin of JSME.*, 24, 198, pp.2090-2097, 1981.

[48] **Matsuo, K., Sasaguchi, K., Tasaki, K., Kiyotoki, Y., & Mochizuki H.** - "Investigation of Supersonic Air Ejectors (Part 2, Effects of Throat-Area-Ratio on Ejector Performance)"., *Bulletin of JSME.*, 25, 210, pp.1898-1905, 1982.

[49] **Dash, S.M., & Wolf, D.E.** – "Interactive Phenomena in Supersonic Jet Mixing Problems, Part I: Phenomenology and Numerical Modelling Techniques"., *AIAA Jn.*, 22, 7, pp.905-913, 1984

[50] **Brown, G.L., & Roshko, A.** – "On Density Effects and Large Structure in Turbulent Mixing Layers"., *Jn. Fluid Mech.*, 64, part 4, pp.775-816, 1974

[51] **Van Dyke, M.** – "An Album of Fluid Motion"., The Parabolic Press., Stanford. California. US. 1982

[52] **Bogdanoff, D.W.** – "Compressibility Effects in Turbulent Shear Layers"., *AIAA Jn.*, 21, 6, pp.926-927, 1983

[53] **Barre, S., Bonnet, J.P., Gatski, T.B., & Sandham, N.D.** – "Compressible High Speed Flows"., Closure Strategies For Turbulent and Transitional Flows., edited by Launder, B.E., & Sandham, N.D., Cambridge University Press., 2002

[54] **Dimotakis, P.E., Catrakis, H.J., & Fourguette, D.C.** – "Flow Structure and Optical Beam Propagation in High Reynolds Number, Gas-Phase Shear Layers and Jets"., *Jn Fluid Mech.*, 433, pp.105-134, 2001

[55] **Clemens, N.T., & Mungal, M.G.** – "Two- and Three-Dimensional Effects in the Supersonic Mixing Layer"., *AIAA Jn.*, 30, 4, pp.973-981, 1992

[56] **Barlow, R.S., Fourguette, D.C., Mungal, M.G., & Dibble, R.W.** – "Experiments on the Structure of an Annular Compressible Reacting Shear Layer"., *AIAA Jn.*, 30, 9, pp.2244-2251, 1992

[57] **Corrsin, S., & Kistler, A.L.** – "Free-Stream Boundaries of Turbulent Flows"., NACA R-1244, 1955

[58] **Townsend, A.A.** – "The Structure of Turbulent Shear Flow"., 2nd Edition., Cambridge University Press., London., U.K., 1976

[59] **Dimotakis, P.E.** – "Two-Dimensional Shear Layer Entrainment"., *AIAA Jn.*, 24, 11, pp.1791-1796, 1986

[60] **Roshko, A.** – "Structure of Turbulent Shear Flows: A New Look"., *AIAA Jn.*, 14, 10, pp.1349-1357, 1976

[61] **Krothpalli, A., Buzyna, G., & Lourenco, L.** – "Streamwise Vortices in an Underexpanded Axisymmetric Jet"., *Phys. Fluids A.*, 3, 8, pp.1848-1851, 1991

[62] **Desevaux, P., Hostache, G., & Jacquet, P.** – "Static Pressure Measurement Along the Centerline of an Induced Flow Ejector"., *Exp. In Fluids.*, 16, pp.289-291, 1994

[63] **Bauer, B.** – "Theoretische und experimentelle Untersuchungen an Strahlapparaten für kompressible Strőmungsmittel (Strahlverdichter)"., VDI Forschungsheft., 514, VDI-Verlag GmbH, Dusseldorf, 1966

[64] **Desevaux, P.** – "A Method for Visualising the Zone Between Two Co-axial Flows in an Ejector"., *Optics & Lasers in Eng.*, 35, pp.317-323, 2001

[65] **Fabri, J., & Siestrunck, R.** – "Supersonic Air Ejectors"., *Advances in Appl. Mech.*, V, pp.1-34, 1958

[66] **Helmbold, H.B., Luessen, G., & Heinrich, A.M.** – "An Experimental Comparison of Constant Pressure and Constant Diameter Jet-Pumps"., University of Wichita School of Engineering., Engineering Report No.147, 1954

[67] **Croft, D.R., & Lilley, D.G.** – "Finite-Difference Analysis of Jet Pumps"., *AIAA Jn.*, 14, 10, pp.1347-1348, 1976

[68] **De Joode, A.D., & Patankar, S.V.** – "Prediction of Three-Dimensional Turbulent Mixing in an Ejector"., *AIAA Jn.*, 16, 2, pp.145-150, 1978

[69] **Launder, B.E., & Spalding, D.B.** – "The Numerical Computation of Turbulent Flows"., *Comp. Methods in Appl. Mech. & Eng.*, 3, 3, pp.269-289, 1974

[70] **Nilavalagen, S., Ravindran, M., & Radhakrishna, H.C.** - "Analysis of Mixing Characteristics of Flow in a Jet Pump using a Finite-Difference Method"., *The Chem. Eng. Jn.*, 39, pp.97-109, 1988

[71] **Patankar, S.V., & Spalding, D.G.** – "Heat & Mass Transfer in Boundary Layers – A General Calculation Procedure"., 2nd Ed., Inter-Text Books., London., 1970

[72] **Neve, R.S.,** - "Computational Fluid Dynamics Analysis of Diffuser Performance in Gas Powered Jet Pumps"., *Int. Jn. Heat and Fluid Flow.*, 14, 4, pp.401-407, 1993

[73] **Riffat, S.B., Gan, G., & Smith, S.** – "Computational Fluid Dynamics Applied to Ejector Heat Pumps"., *Appl. Thermal Eng.*, 16, 4, pp.291-297, 1996

[74] **Smith, S.J., & Riffat, S.B.** - "Low Pressure Ejectors: Prediction of Performance by Computational Fluid Dynamics"., *Proc. CIBSE A: Building Serv. Eng. Res. Technol.*, 18, 3, pp.179-182, 1997

[75] **Chin, S.B., Eames, I.W., Hunt, J., & Popov, A.** – "Computational Fluid Dynamics Study of a Compressible Steam Ejector Pump Design"., conference paper. Heat Powered Cycles Conference 1997, Nottingham, 1997

[76] **Riffat, S.B., & Everitt, P.** – "Experimental and CFD Modelling of an Ejector System for Vehicle Air Conditioning"., *Jn. Inst. Energy.*, 72, 6, pp.41-47, 1999

[77] **Al-Khalidy, N.** – "CFD Simulation for the Design of Ejector in a Refrigerant Ejector Refrigeration Machine"., Research Report No.1., Cances-ATP., The University of New South Wales., Australia., September 1999

[78] **Anderson, J.D.** – "A History of Aerodynamics and its Impact on Flying Machines"., Cambridge University Press, Cambridge, 1997

[79] Fluent; Users Guide., Version 5., Fluent Inc., Lebanon, N.H., USA., 1999

[80] **Spalart, P., & Allmaras, S.** – "A One-Equations Model For Aerodynamic Flows"., Technical Report AIAA-92-0439., AIAA., 1992

[81] **Launder, B.E., & Spalding, D.B.** – "Lectures in Mathematical Models of Turbulence"., Academic Press., London., UK., 1972

[82] **Choudhury, D.** – "Introduction to the Renormalisation Group Method and Turbulence Modelling"., Technical Memorandum TM-107., Fluent INC., 1993

[83] **Shih, T.H., Liou, W.W., Shabbir, A., & Zhu, J.** – "A New k-ε Eddy Viscosity Model For High Reynolds Number Turbulent Flows – Model Development and Validation"., *Computers Fluids*., 24, 3, pp.227-238, 1995

[84] **Sarkar, S., & Balakrishnan, L.** – "Application of a Reynolds Stress Turbulence Model to the Compressible Shear Layer"., ICASE Report 90-18., NASA CR 182002., 1990

[85] **Wolfstein, M.** – "The Velocity and Temperature Distribution of One Dimensional Flow With Turbulence Augmentation and Pressure Gradient"., *Int. Jn. Heat Mass Transfer*., 12, pp.301-318, 1969

[86] **Hart, J.H.** – "CFD Design of a Supersonic Steam Ejector"., UG Thesis., Dept. Mech. Eng., University of Sheffield., U.K., 1998

[87] **Hunt, J.G.** – "CFD Study of a Supersonic Steam Ejector in a Steam-Jet Refrigeration Cycle"., UG Thesis., Dept. Mech. Eng., University of Sheffield., U.K., 1997

[88] **Taylor, D.** – "Ejector Designs for a Variety of Applications"., Agardograph No.163, Supersonic Ejectors, Edited by J.J.Ginoux., Von Karmen Inst. for Fluid Mechanics., Rhode-St-Genèse., Belgium., 1972

[89] **Warren, R.A.S.** – "CFD Analysis of a Supersonic Steam Ejector"., UG Thesis., Dept. Mech. Eng., University of Sheffield., U.K., 1999

[90] **Versteeg, H.K., & Malasekera, W.** – "An Introduction to Computational Fluid Dynamics – The Finite Volume Method"., 1st Edition., Longman., 1995

[91] **Shaw, C.T.** – "Using Computational Fluid Dynamics", Prentice-Hall, 1992

[92] **Patankar, S.V.** – "Numerical Heat Transfer & Fluid Flow", Hemisphere Publishing Corp., Taylor & Francis Group., New York., USA., 1980

[93] **Anderson, J.D.** – "Computational Fluid Dynamics – The Basics With Applications", McGraw-Hill, New York, 1995

[94] **Leonard, B.P.** - "A Stable and Accurate Convective Modelling Procedure Based on Quadratic Upstream Interpolation"., *Comput Methods Appl. Mech. Eng.*, 19, pp.59-98, 1979.

[95] **Rhie, C.M., & Chow, W.L.** – "Numerical Study of the Turbulent Flow Past an Airfoil with Trailing Edge Separation"., *AIAA Jn.*, 21, 11, pp.1525-1532, 1983.

[96] Fluent; Users Guide., Version 4.5., Fluent Inc., Lebanon, N.H., USA., 1999

[97] **Patankar, S.V., & Spalding, D.B.** – "A Calculation Procedure for Heat, Mass and Momentum Transfer in Three Dimensional Parabolic Flows"., *Int. Jn. Heat Mass Transfer.*, 15, pp.1787, 1972

[98] **Van Doormal, J.P., & Raithby, G.D.** – "Enhancements for the SIMPLE Method for Predicting Fluid Flows"., *Numer. Heat Transfer.*, 7, pp.147-163, 1984

[99] **Issa, R.I.** – "Solution of the Implicitly Discretised Fluid Flow Equations by Operator Splitting"., *Jn. Comp. Phys.*, 62, pp.40-65, 1986

[100] **Issa, R.I., & Lockwood, F.C.** – "Two-Dimensional Supersonic Viscous Interactions"., *AIAA Jn.*, 15, 2, pp.189-187, 1977

[101] **Fisher, E.H., & Rhodes, N.** – "Uncertainty in Computational Dynamics"., *Proc. Instn. Mech. Engrs.*, 210, pp.91-93, 1996

[102] Oxford English Dictionary., Ed. Simpson, J.A., & Weiner, E.S.C., 2nd ed. Oxford: Clarendon Press, 1989. OED Online. Oxford University Press. 4 Apr. 2000.

[103] **Cole, H.W., & Stern, F.** – "Uncertainties and CFD Code Validation"., *Jn. of Fluids Eng.*, 119, pp.795-803, 1997

[104] **Mehta, U.B.** – "Some Aspects of Uncertainty in Computational Fluid Dynamics Results"., *Jn. of Fluids Eng.*, 113, pp.538-543, 1991

[105] **Hinze, J.O.** – "Turbulence: An Introduction to its Mechanism and Theory"., McGraw-Hill, New York, 1959

[106] **Papamoschou, D., & Roshko, A.** – "The Compressible Turbulent Shear Layer: An Experimental Study"., *Jn. Fluid Mech.*, 197, pp.453-477, 1988

[107] **Presz, W.M., Morin, B.L., & Gousy, R.G.** – "Forced Mixer Lobes in Ejector Designs"., *Jn. Prop. & Power.*, 4, 4, pp.350-355, 1988

[108] **Tillman, T.G., Paterson, R.W., & Presz, W.M.** – "Supersonic Nozzle Mixer Ejector"., *Jn. Prop. & Power.*, 8, 2, pp.513-519, 1992

[109] **Chang, Y.J., & Chen, Y.M.** – "Enhancement of a Steam-Jet Refrigerator Using a Novel Application of the Petal Nozzle"., *Exp. Thermal & Fluid Sci.*, 22, 3, 2000

[110] **Gutmark, E.J., Schadow, K.C., & Yu, K.H.** – "Mixing Enhancement in Supersonic Free Shear Flows"., *Annu. Rev. Fluid Mech.*, 27, pp.375-417, 1995

[111] **Eames, I.W.** – "A New Prescription for the Design of Supersonic Jet-Pumps: the Constant Rate of Momentum Change Method"., *App. Thermal Eng.*, 22, 2, pp.121-131, 2002

Appendix A – Geometry

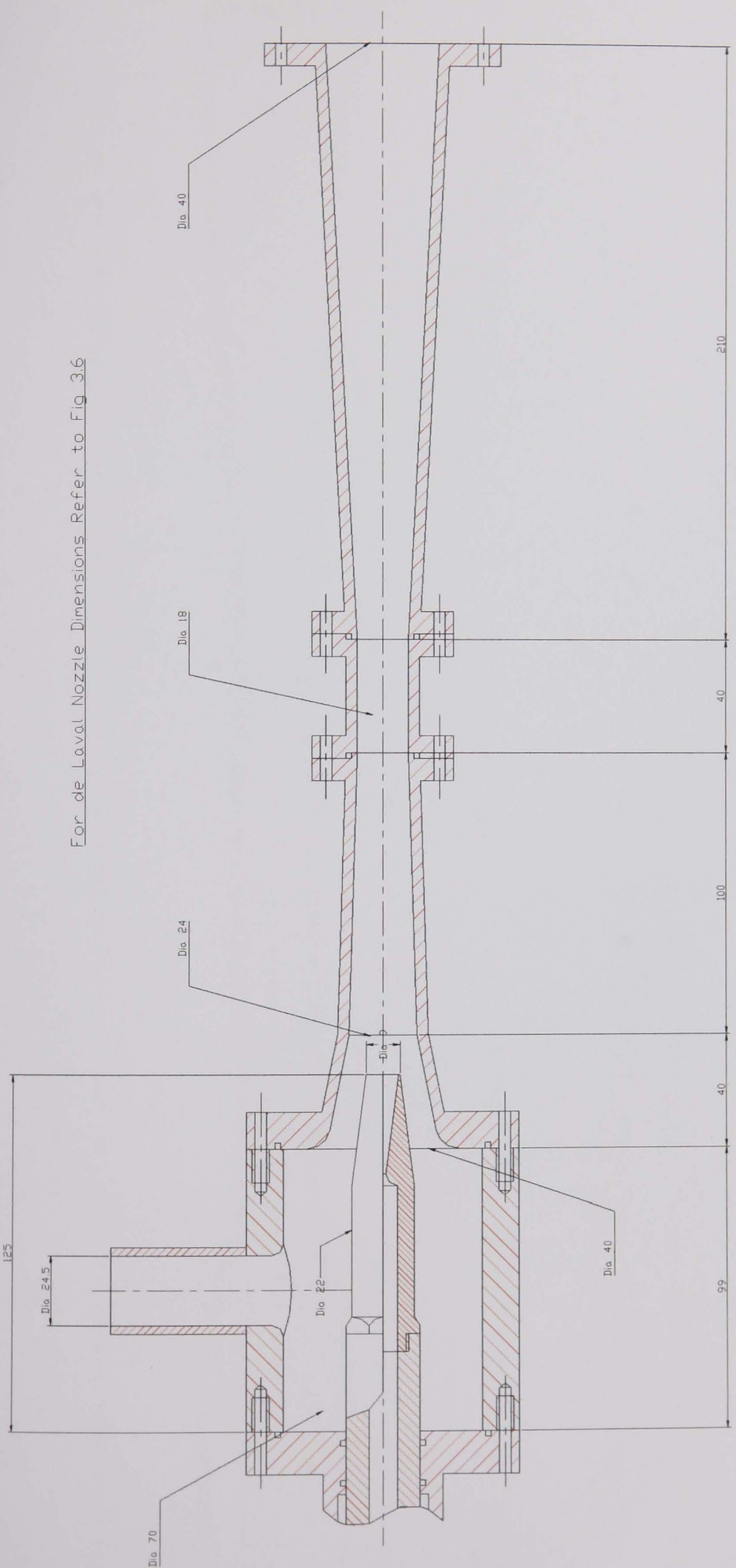

All dimensions in mm.

Figure A-1 – Original Eames Ejector Geometry

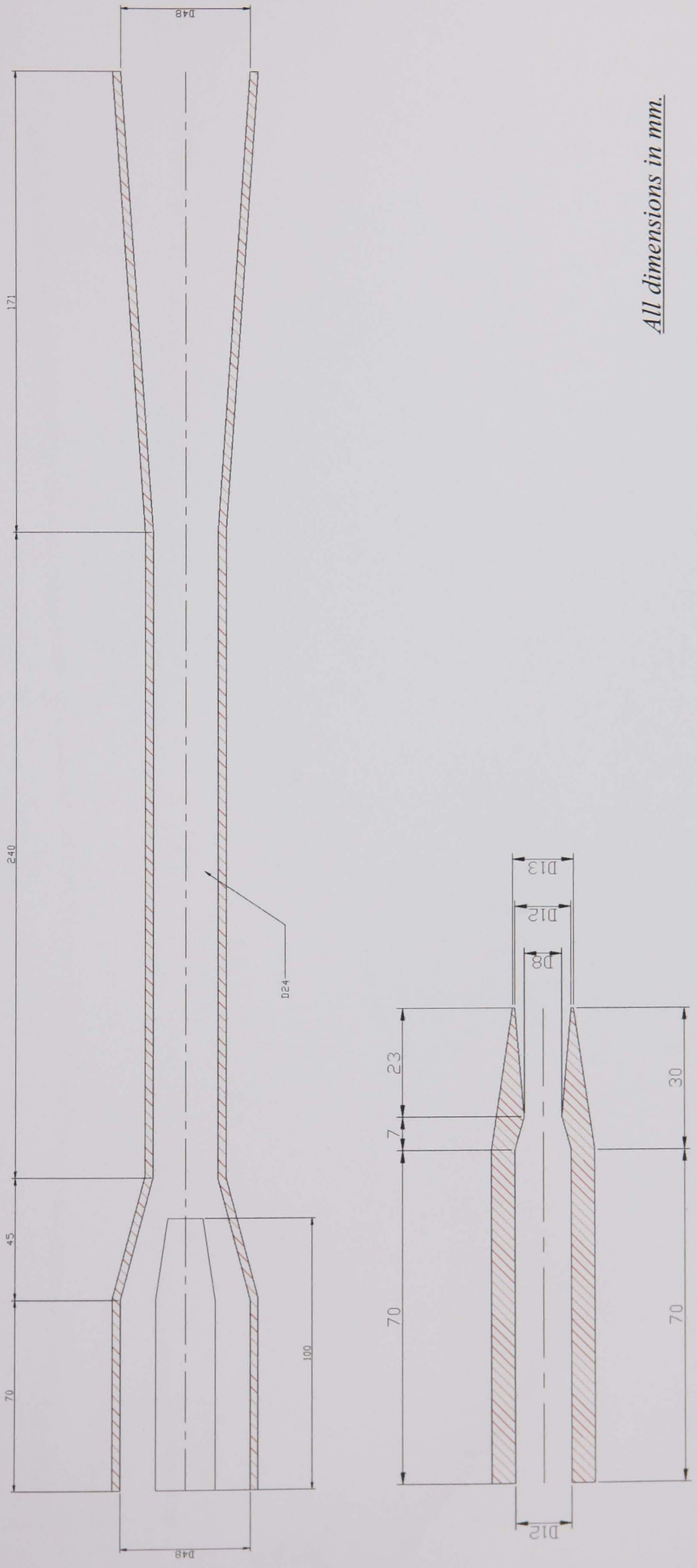

All dimensions in mm.

Figure A-2 – Desevaux Ejector Geometry

All dimensions in mm.

Figure A-3 – Hickman Ejector Geometry

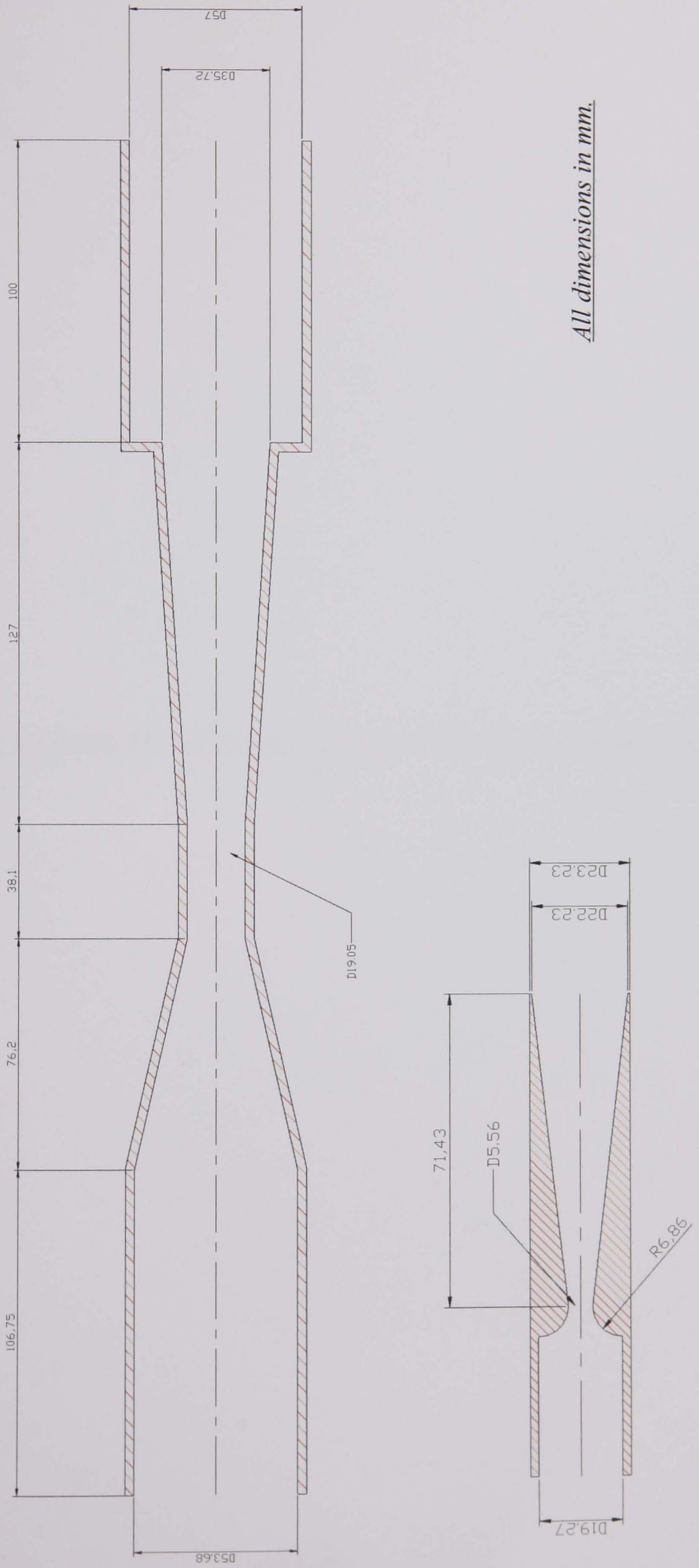

All dimensions in mm.

Figure A-4 – Watson Ejector

Appendix B – Computational Mesh Used in Simulations

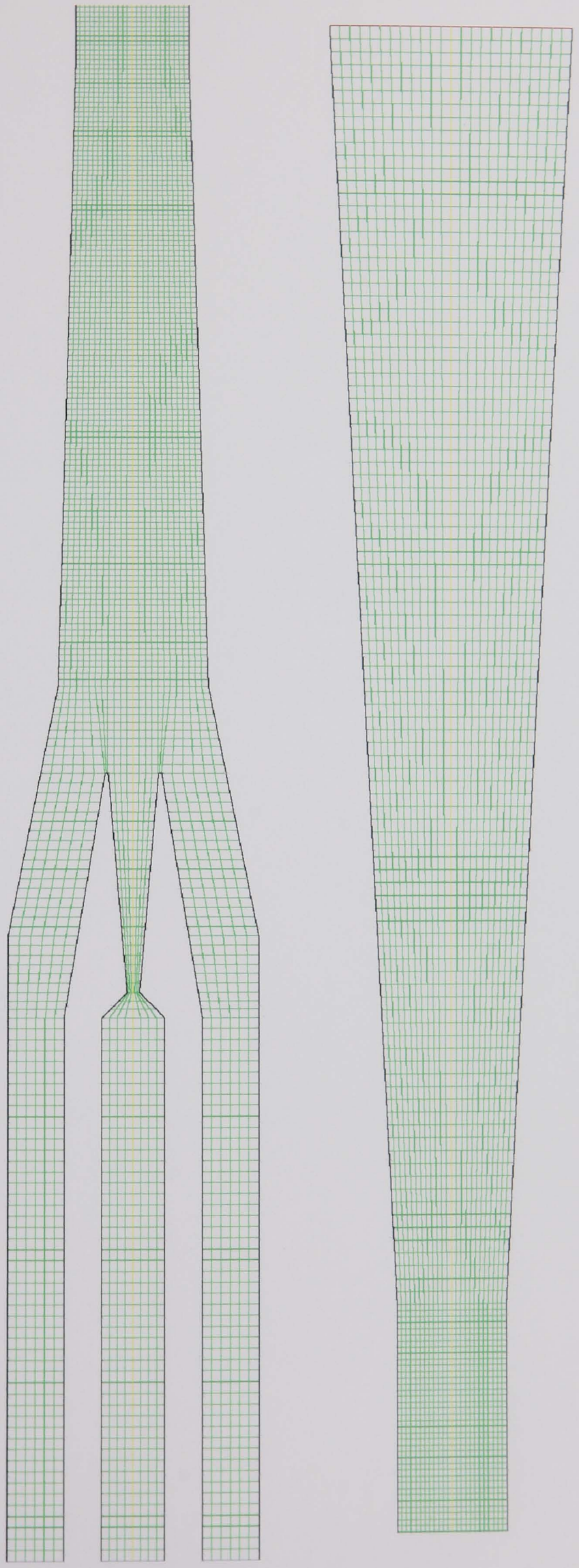

Figure B.1 – Computational Mesh: Msh001

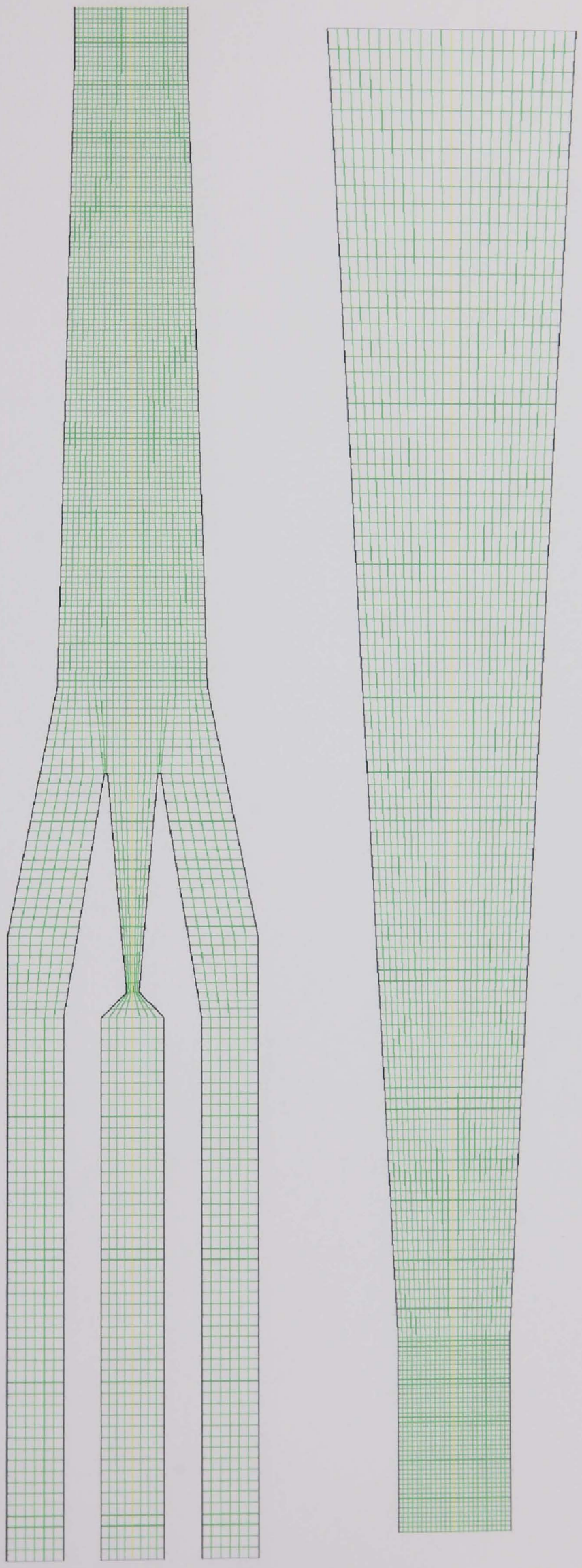

Figure B.2 – Computational Mesh: Msh002

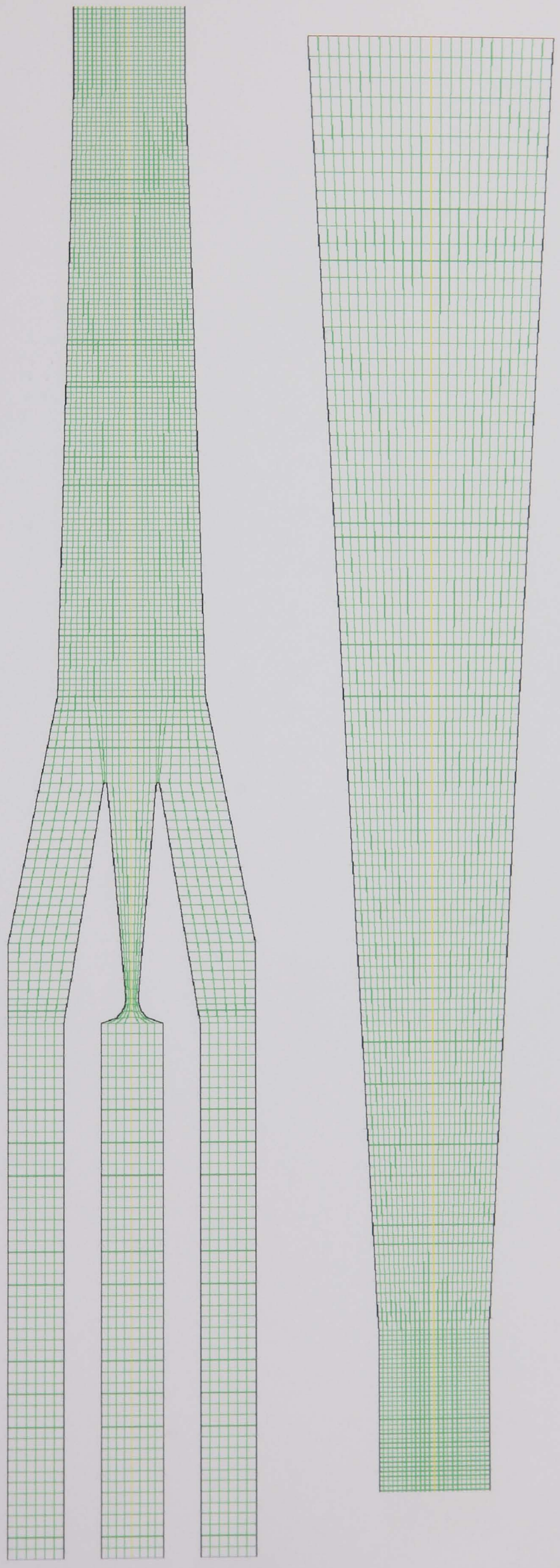

Figure B.3 – Computational Mesh: Msh003

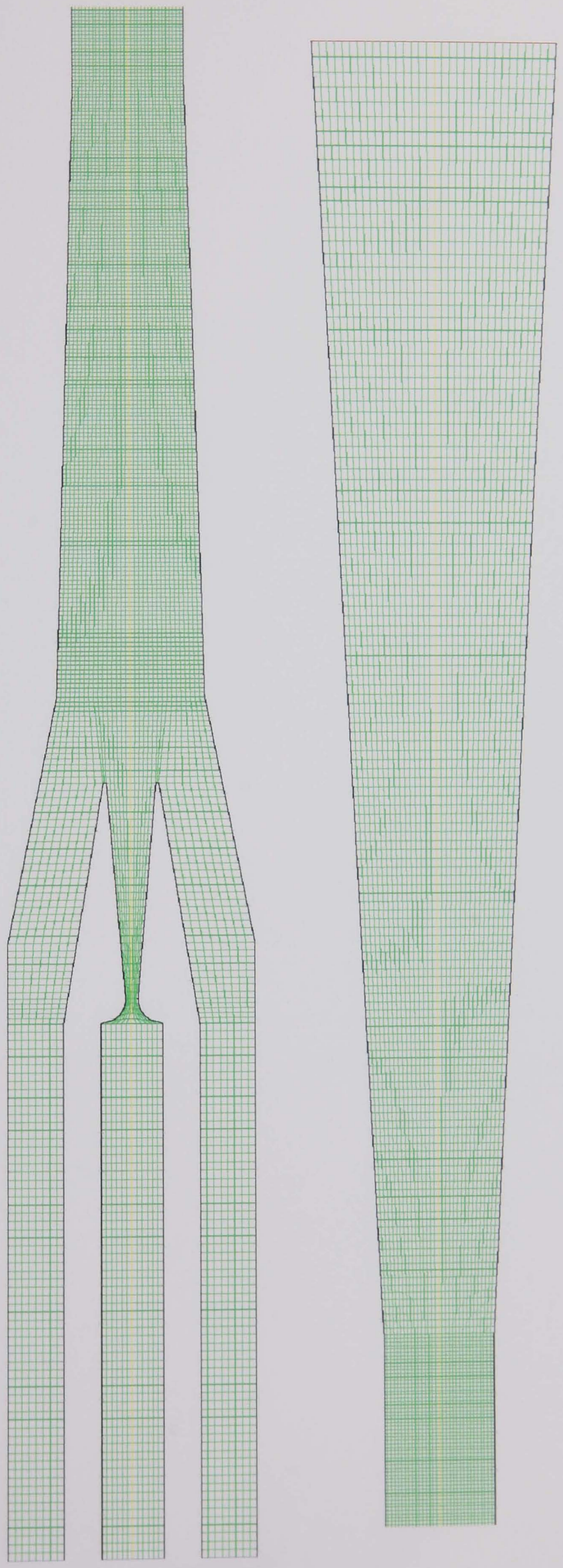

Figure B.4 – Computational Mesh: Msh004

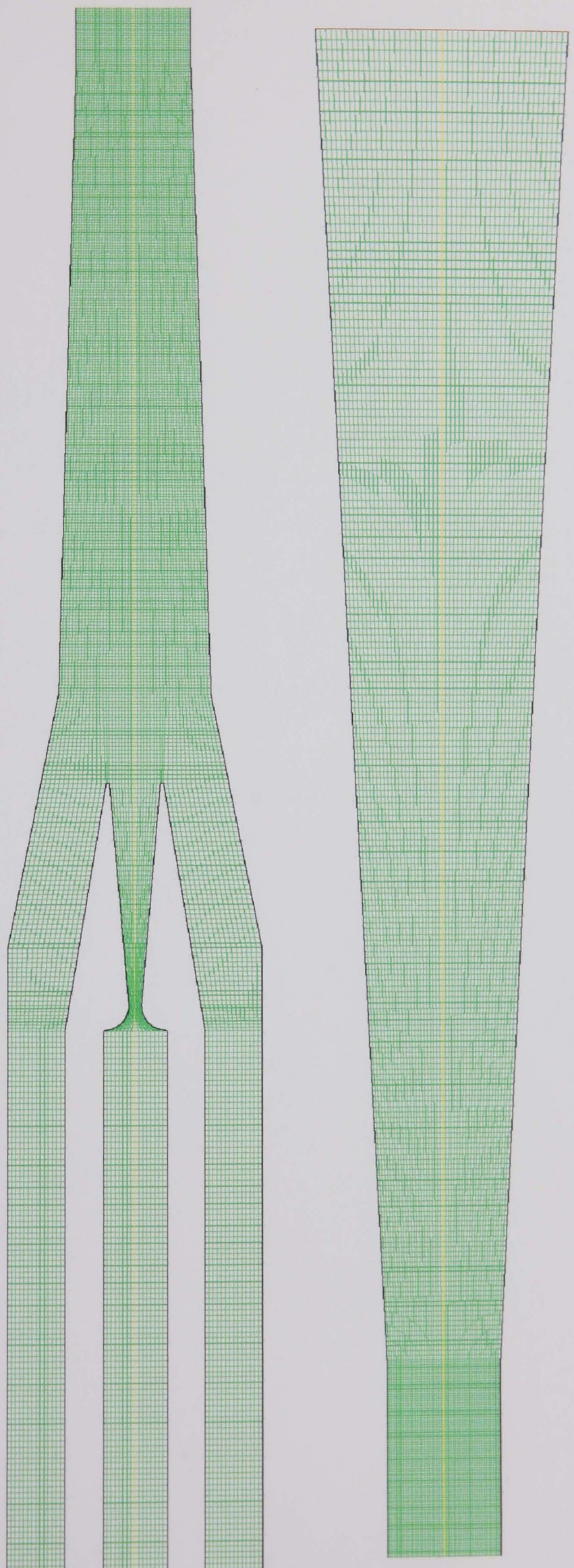

Figure B.5 – Computational Mesh: Msh005

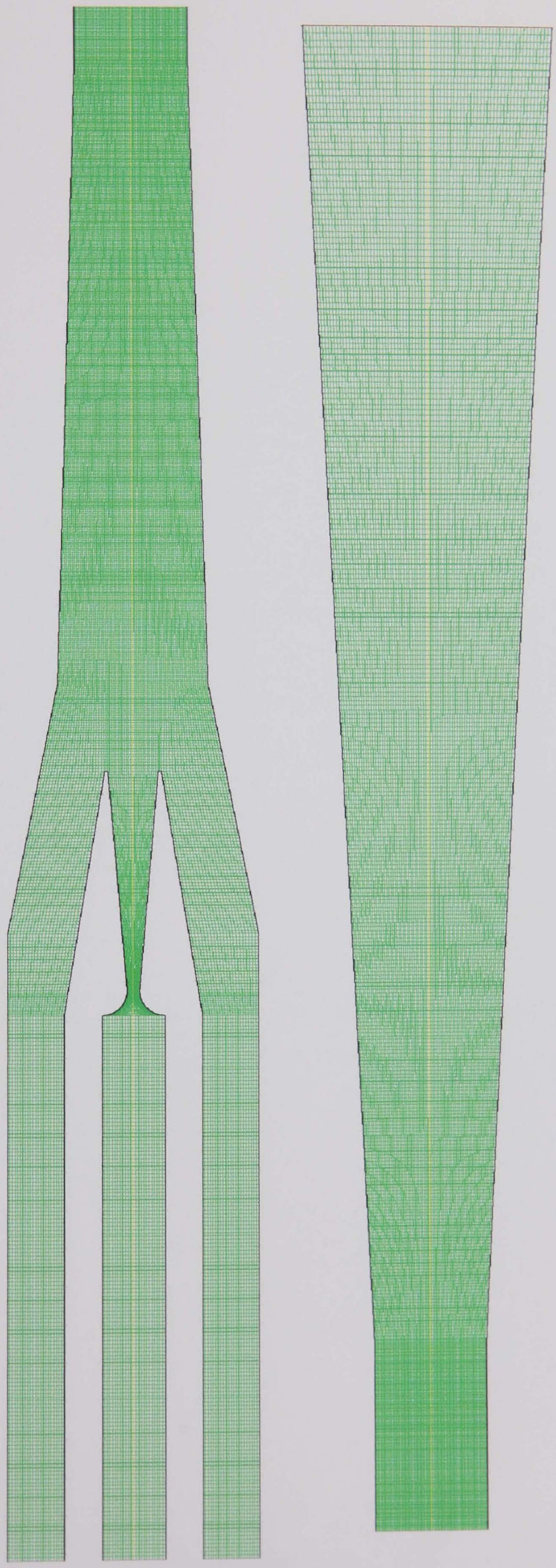

Figure B.6 – Computational Mesh: Msh006

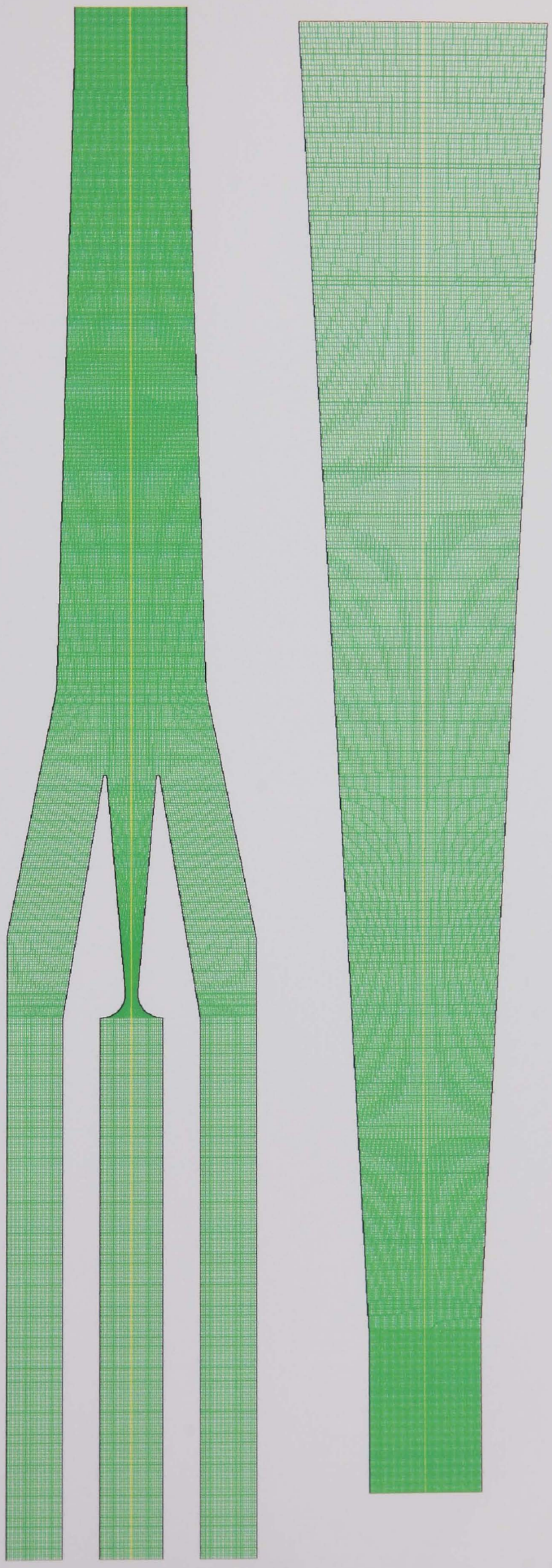

Figure B.7 – Computational Mesh: Msh007

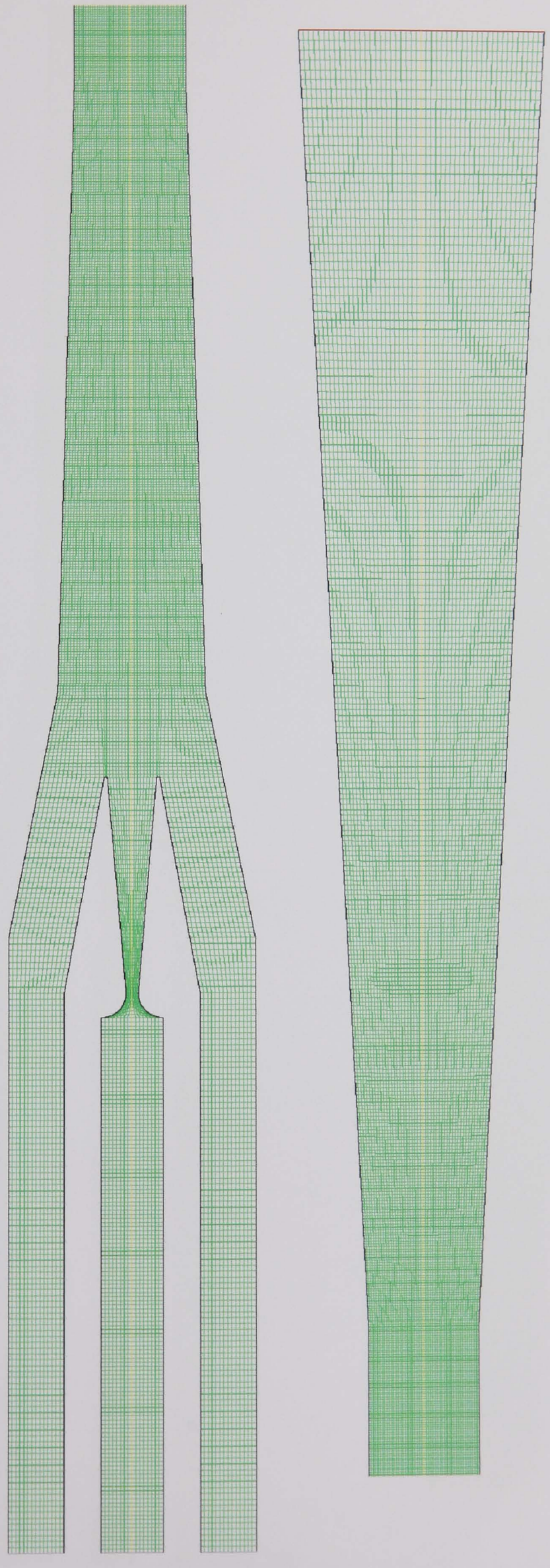

Figure B.8 – Computational Mesh: Msh008

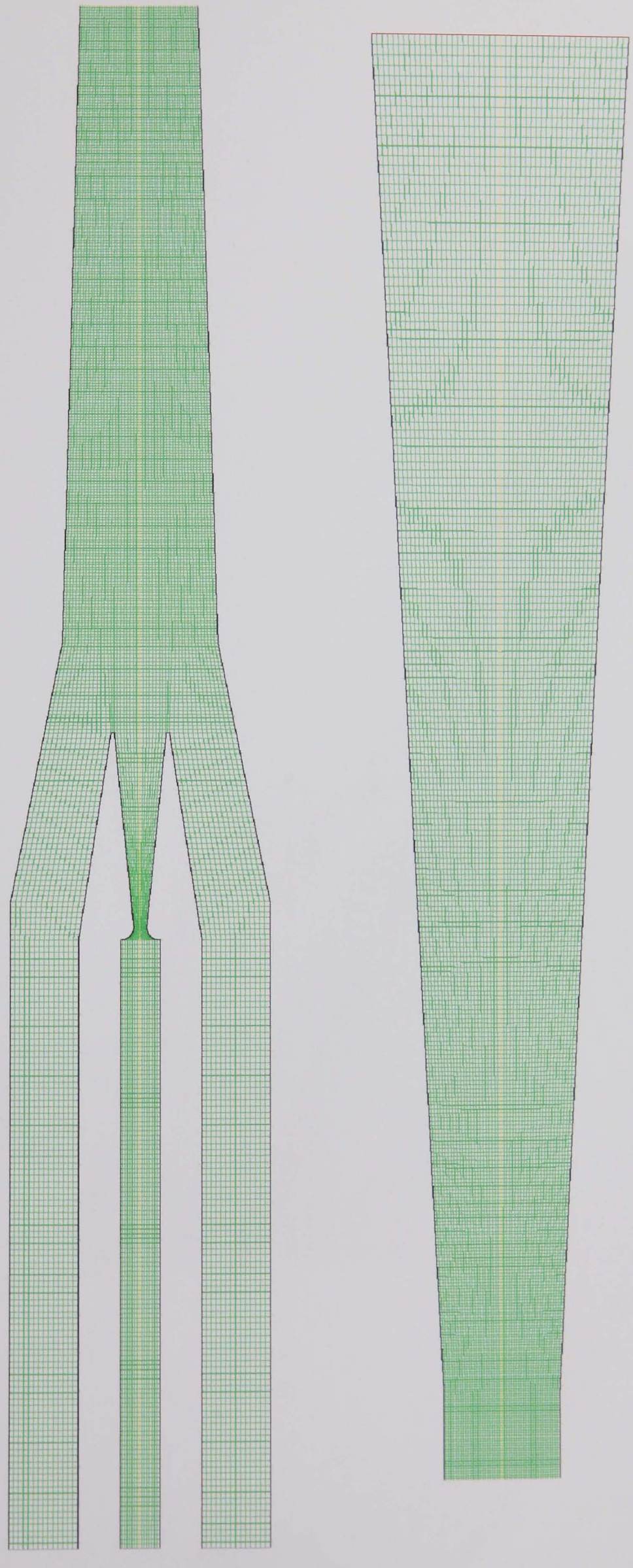

Figure B.9 – Computational Mesh: Msh009

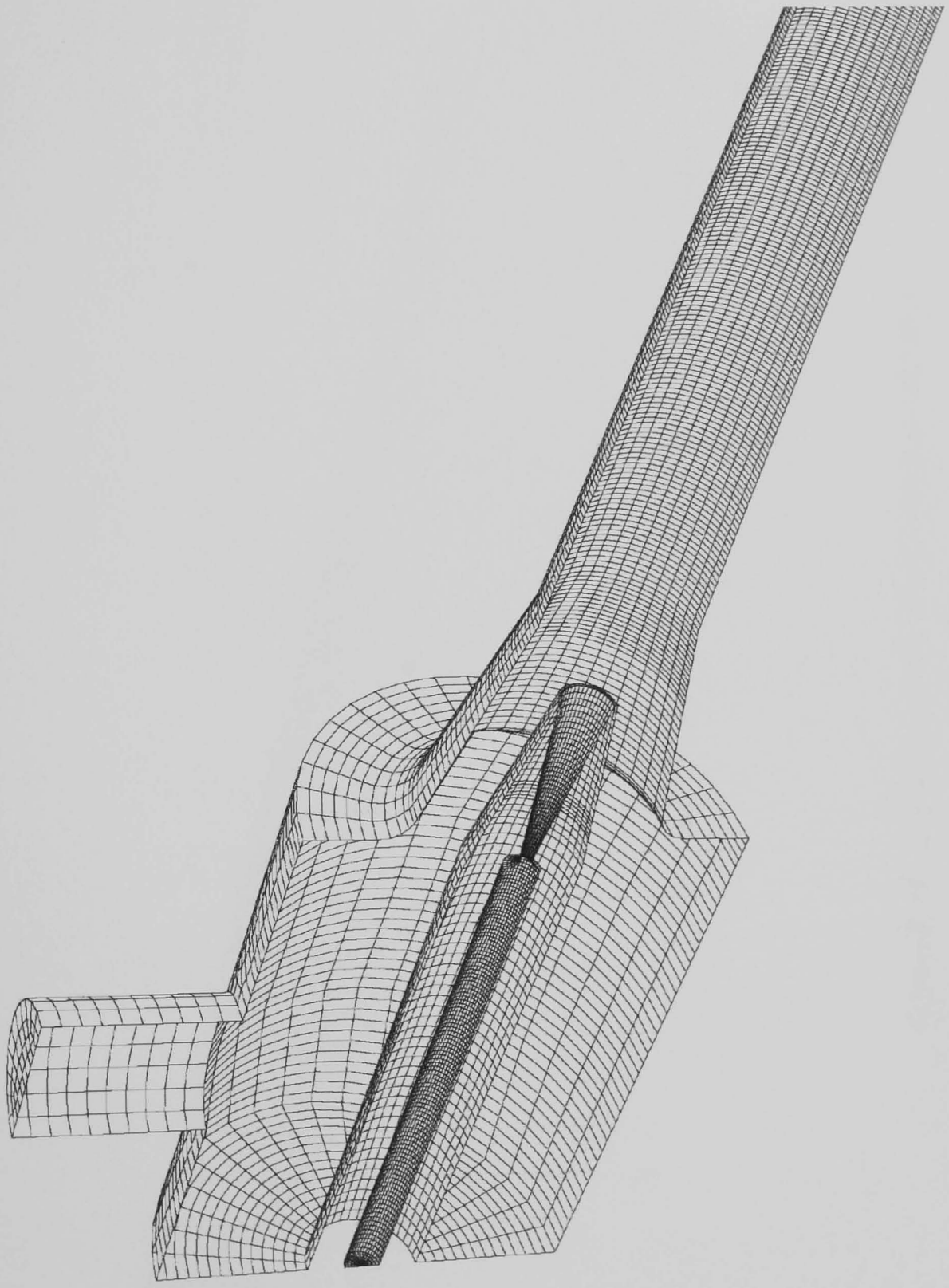

Figure B.10 – 3D Narrow Inlet Mesh (Suction Chamber & Mixing Chamber)

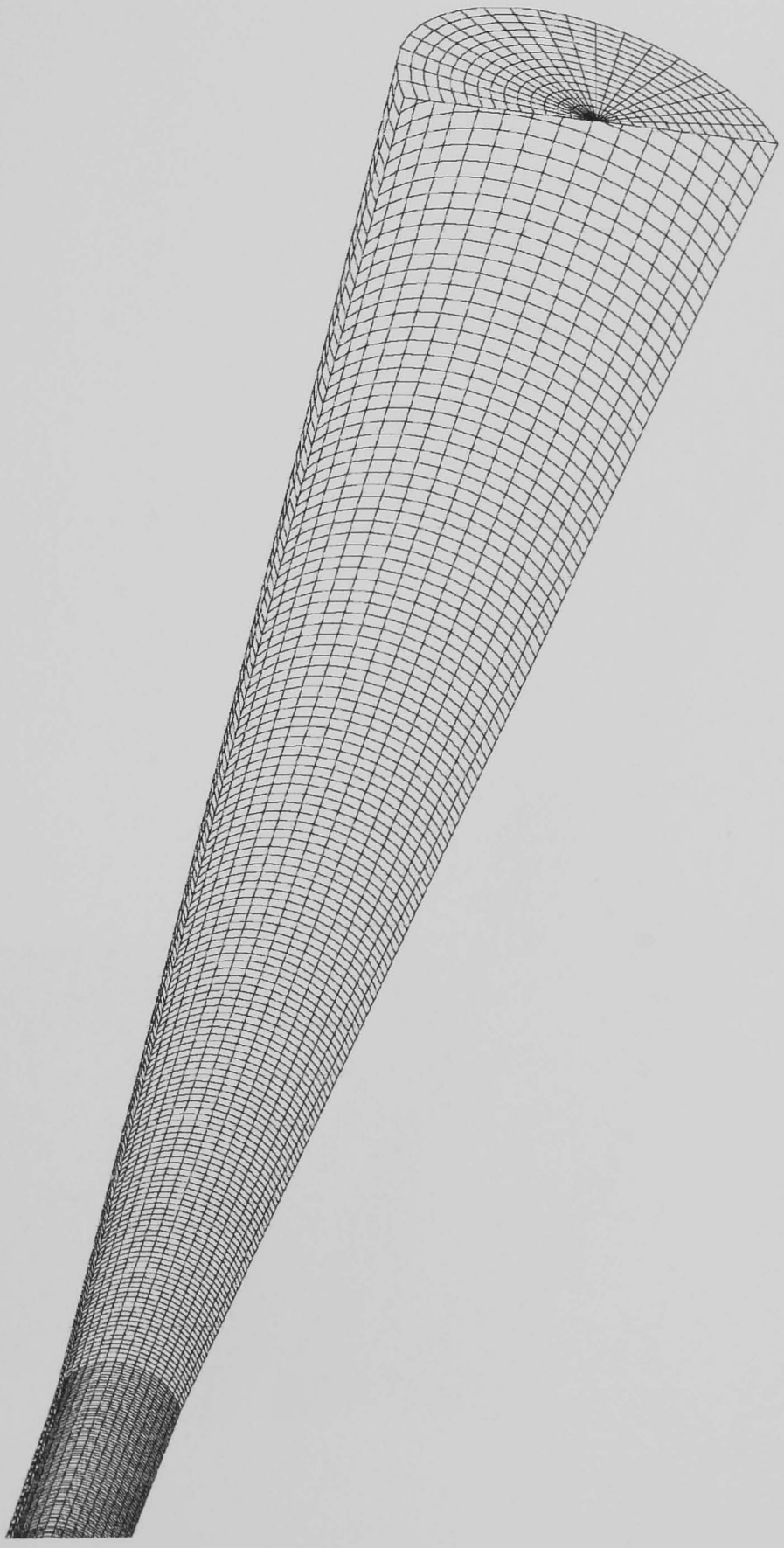

Figure B.11 – 3D Narrow Inlet Mesh (Throat & Diffuser)

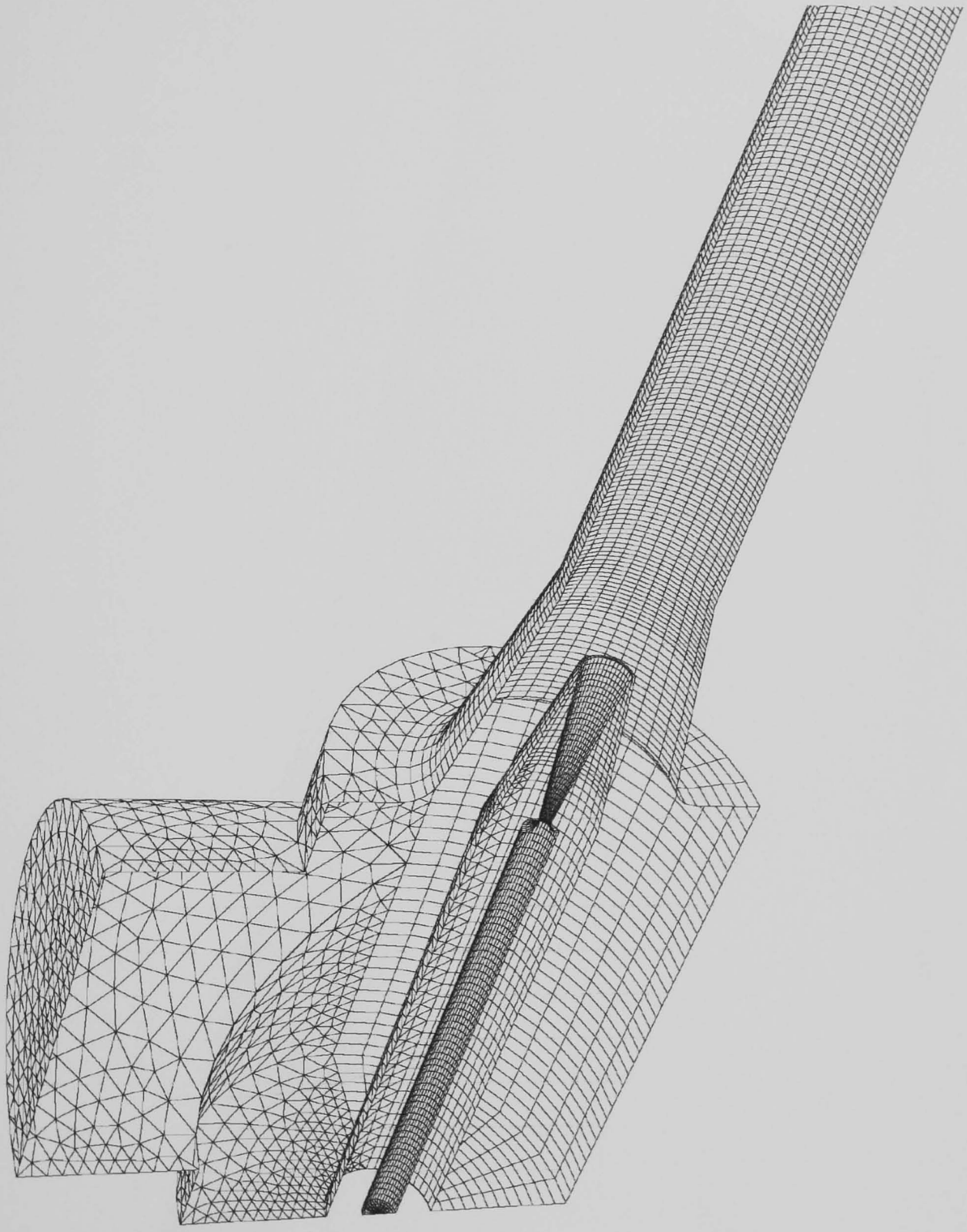

Figure B.12 – 3D Wide Inlet Mesh (Suction Chamber & Mixing Chamber)

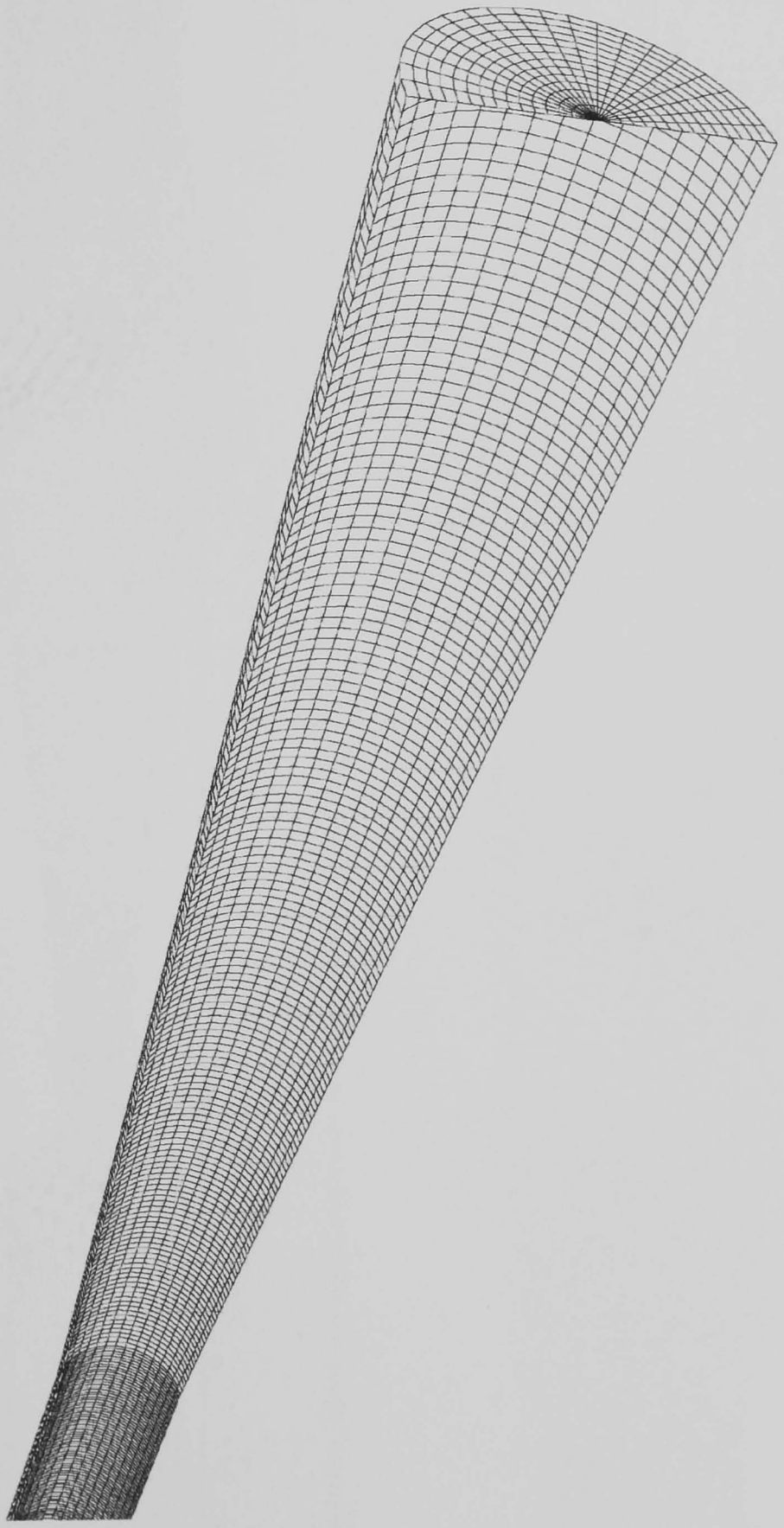

Figure B.13 – 3D Wide Inlet Mesh (Throat & Diffuser)

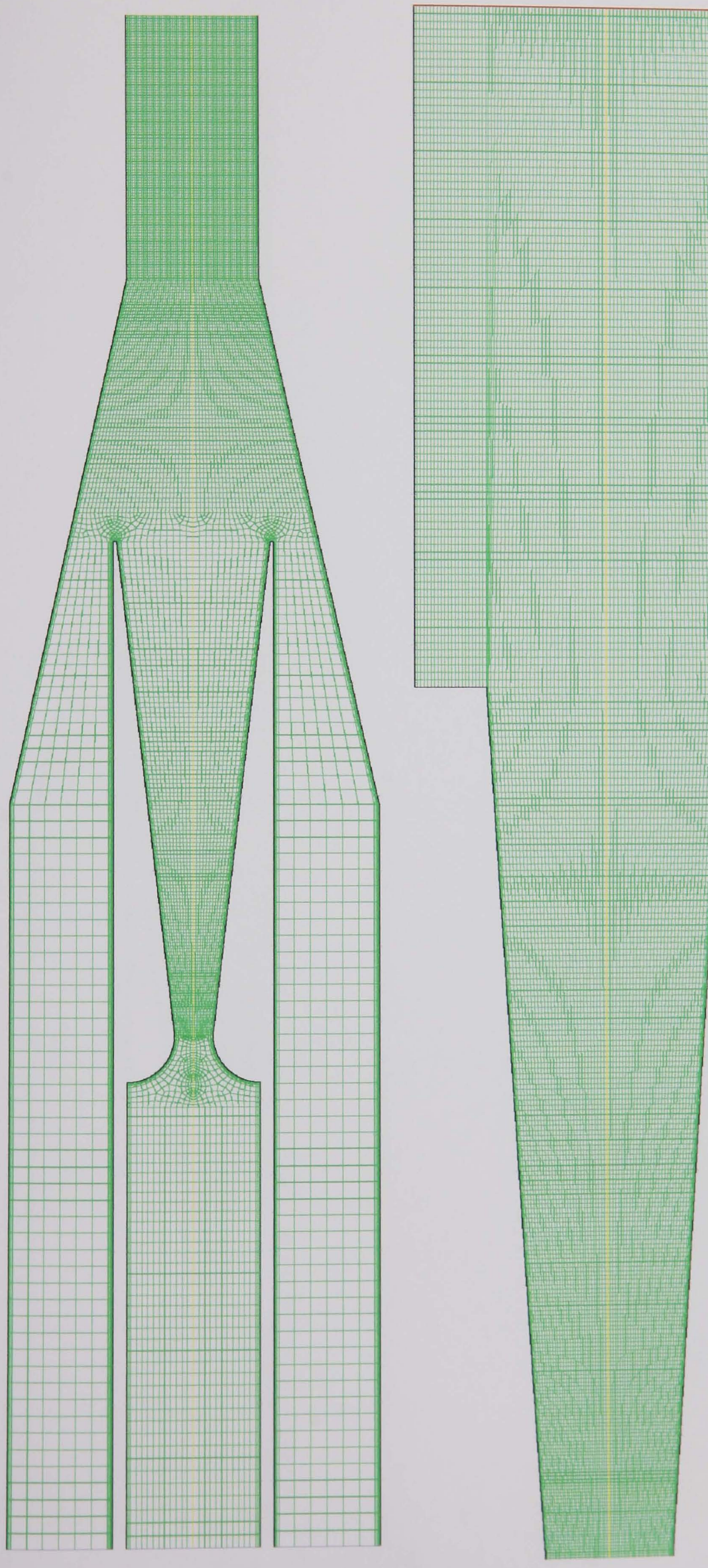

Figure B.14 – Computational Mesh: Watson Ejector D = 1½"

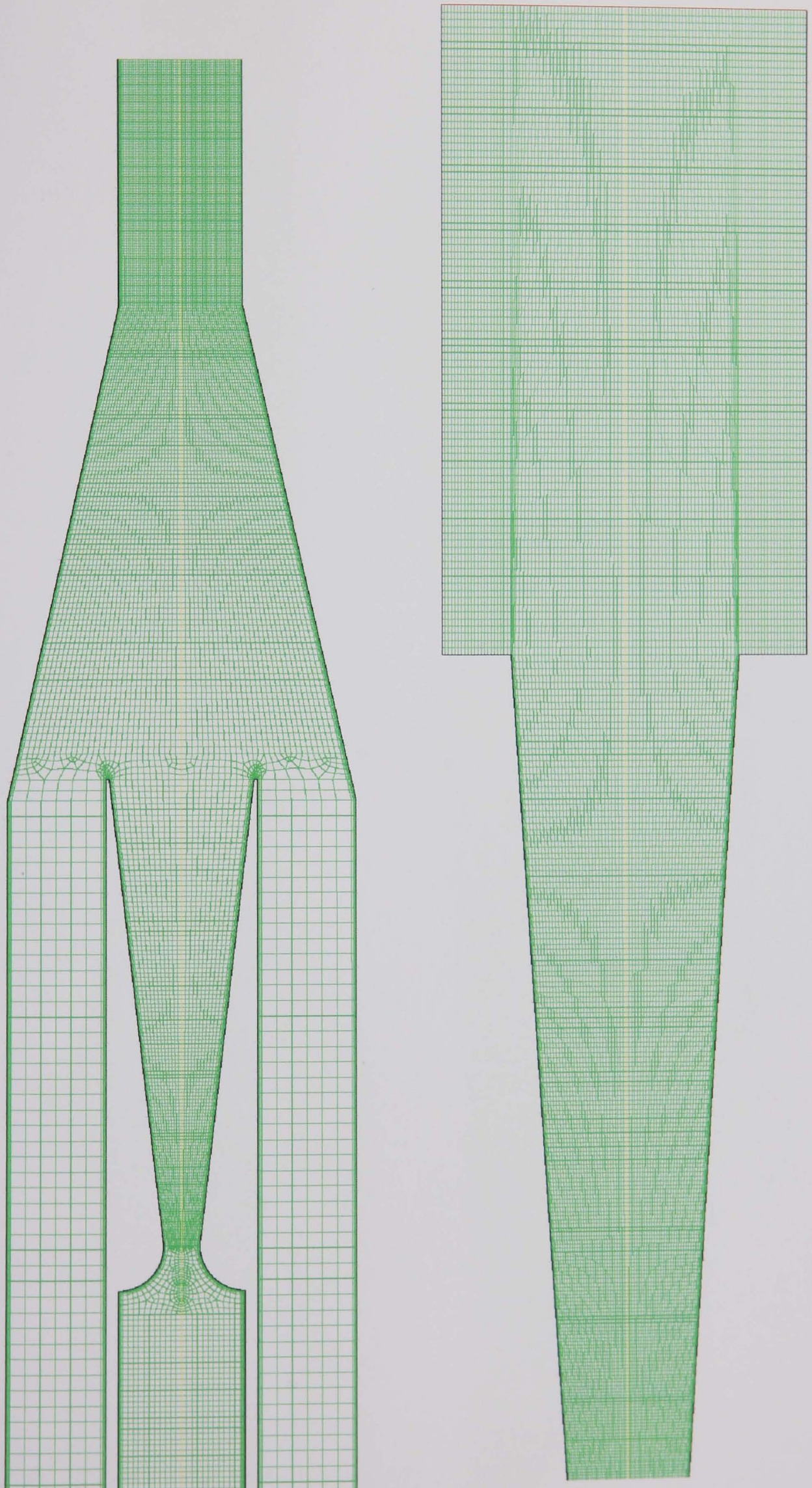

Figure B.15 – Computational Mesh: Watson Ejector D = 2⅞"

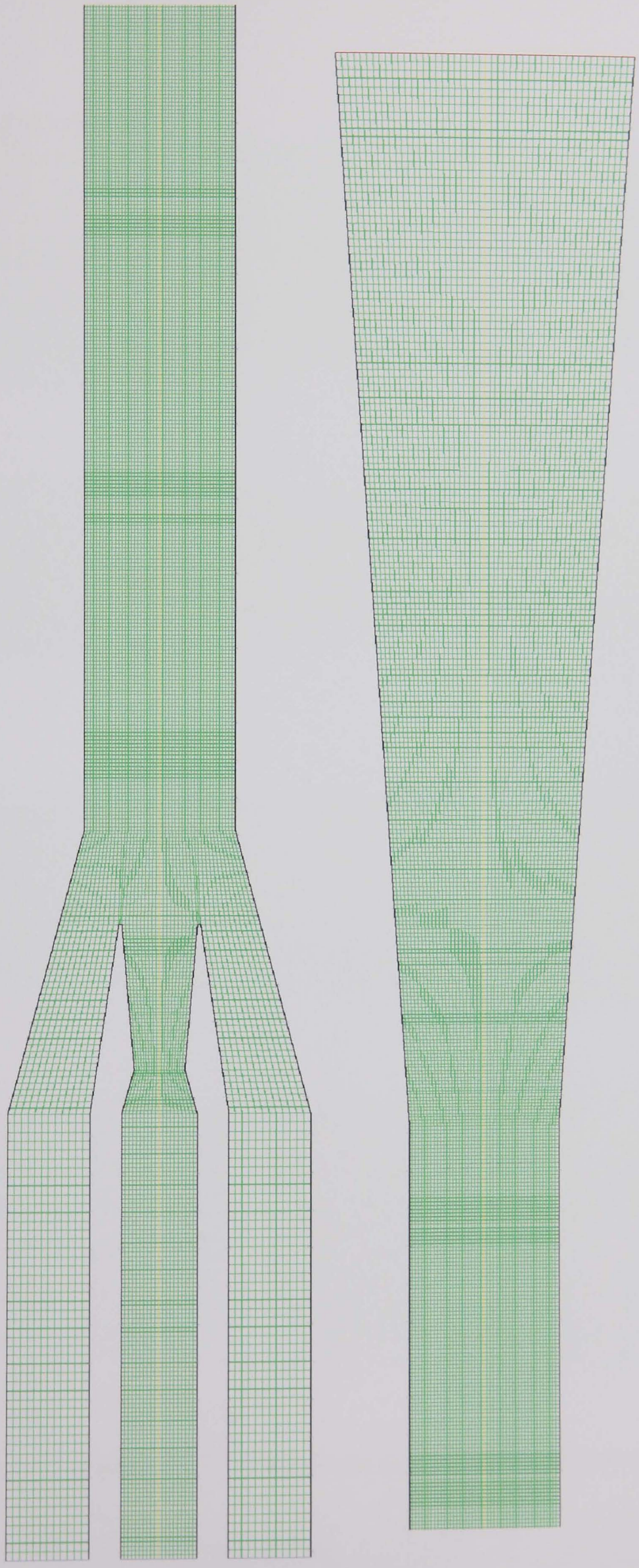

Figure B.16 – Computational Mesh: Desevaux Ejector

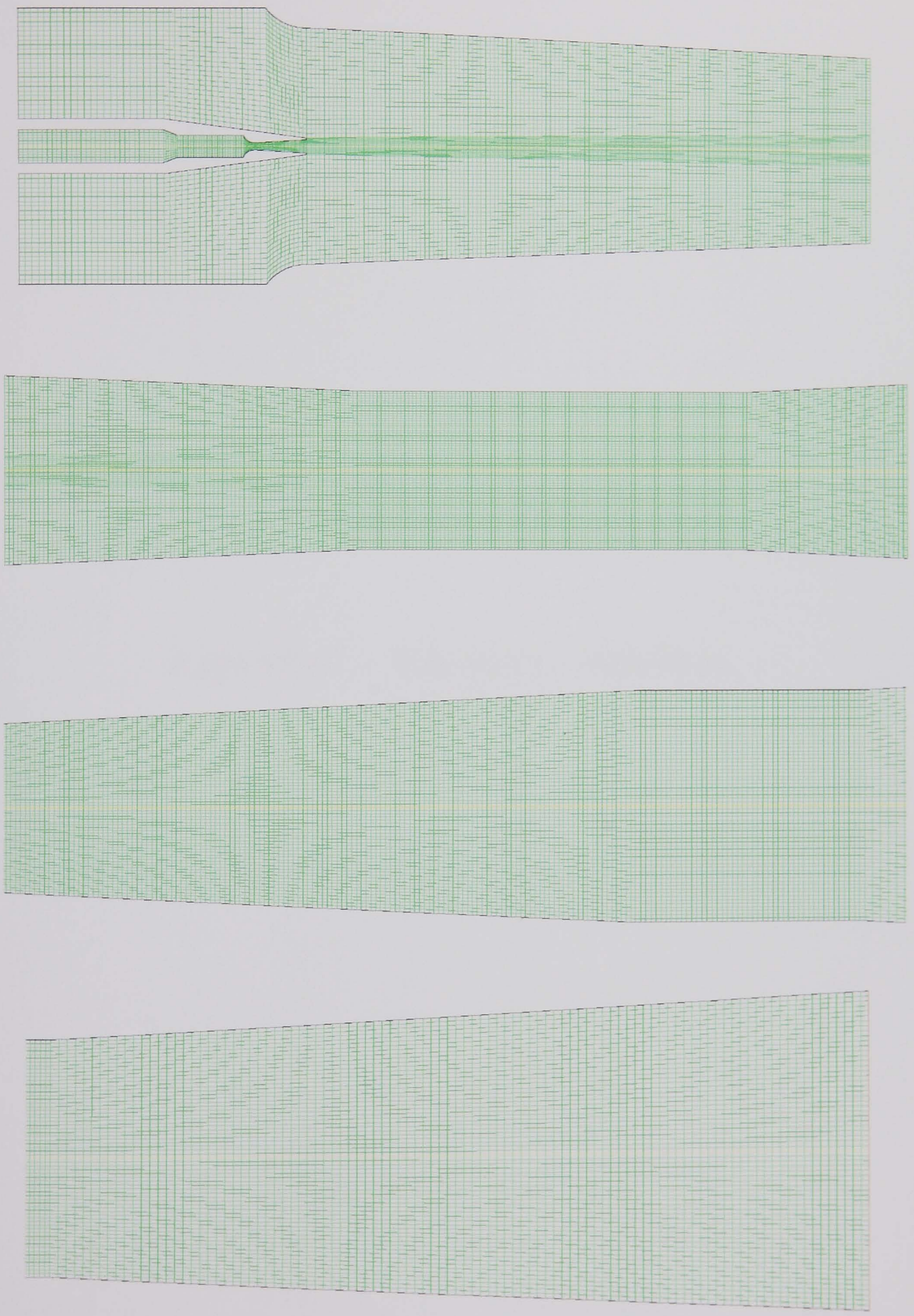

Figure B.17 – Computational Mesh: Hickman Ejector

Appendix C – Boundary Conditions

C.1 – Eames Ejector Studies

C.1.1 – Geometrical Studies

Pressure (Pa)			Temperature (K)		
Primary	Secondary	Outlet	Primary	Secondary	Outlet
198500	1227	3800	393	283	301

Table C.1 – Boundary Conditions: Geometrical Studies

C.1.2 – Critical Operating Conditions Study

Nº	Pressure (Pa)			Temperature (°C)		
	Primary	Secondary	Outlet	Primary	Secondary	Outlet
1	198500	1227	3800	120	10	28.3
2	232100		4200	125		30.0
3	270100		4700	130		31.9
4	313100		5300	135		34.0
5	361400		6000	140		36.3
6	198500	871.9	3600	120	7.5	27.3
7	232100		4100	125		29.5
8	270100		4600	130		31.5
9	313100		5100	135		33.4
10	361400		5700	140		35.3
11	198500		3400	120	5	26.5
12	232100		3700	125		27.8
13	270100		4400	130		30.8
14	313100		5100	135		33.4
15	361400		5400	140		34.4

Table C.2 – Boundary Conditions: Critical Operating Conditions Study

C.1.3 – Low Pressure Study

Nº	Pressure (Pa)			Temperature (°C)		
	Primary	Secondary	Outlet	Primary	Secondary	Outlet
16	198500	611.2	2000	120	0.1	25
17		259.8			-10	
18		103.8			-20	
19		38.09			-30	
20		12.88			-40	
21	198500	200	2000	120	0.1	25
22		100				
23		50				

Table C.3 – Boundary Conditions: Low Pressure Study

C.1.4 – Three Dimensional Studies

Nº	Inlet	Pressure (Pa)			Temperature (°C)		
		Primary	Secondary	Outlet	Primary	Secondary	Outlet
3D-01	Wide	198500	1277	3800	120	10	28.3
3D-02				3600		7.5	27.3
3D-03			871.9	3400		5	26.5
3D-04	Narrow	198500	1227	3800	120	10	28.3
3D-05				3600		7.5	27.3
3D-06			871.9	3400		5	26.5

Table C.4 – Boundary Conditions: 3D Study

C.2 – Desevaux Ejector Study

Nº	R_m	Pressure (Pa)		Secondary Mass Flow (g/sec)	Temperature (°C)		
		Primary	Outlet		Primary	Secondary	Outlet
D01	0.10	500000	101325	0.00591	10	10	10
D02	0.32			0.0189			
D03	0.47			0.0277			

Table C.5 – Boundary Conditions: Fixed Entrainment Study

Nº	Pressure						Temperature				
	Primary		Secondary		Outlet		Primary		Secondary		Outlet
	(psia)	(Pa)	(in Hg) (gauge)	(Pa)	(in H_2O) (gauge)	(Pa)	(°F)	(°C)	(°F)	(°C)	(°C)
H01	348	2399338	30.06	101799	11.1	104090.8	807	430.6	92	33.3	10
H02					7.5	130193.8					
H03					4.7	102496.1					
H04					-1.7	100901.4					

Table C.6 – Boundary Conditions: Hickman Study

C.4 – Watson Ejector Study

C.4.1 – D_N = 1½"

Nº	Pressure					Temperature (°C)		
	Primary		Secondary		Outlet (Pa)	Primary	Secondary	Outlet
	(psig)	(Pa)	(in Hg) (corrected)	(Pa)				
W01	140	1066597	25.2	16201.50	101325	182.5	10	10
W02	130	997649	25	16876.56		179		
W03	120	928701	23	23627.18		176		
W04	110	859753	22.5	25314.83		173		
W05	100	790805	19.5	35440.77		170		
W06	80	652909	11.3	63118.32		161.8		
W07	60	515013	5.5	82695.12		132.7		

Table C.7 – Boundary Condition: Watson Study $D_N = 1\frac{1}{2}$"

C.4.2 – D_N = 2⅞"

Nº	Pressure					Temperature (°C)		
	Primary		Secondary		Outlet (Pa)	Primary	Secondary	Outlet
	(psig)	(Pa)	(in Hg) (corrected)	(Pa)				
W08	140	1066597	24.6	18226.68	101325	182.5	10	10
W09	130	997649	24.8	17551.62		179		
W10	120	928701	24.9	17214.09		176		
W11	110	859753	18.2	39828.67		173		
W12	100	790805	14	54004.98		170		
W13	80	652909	6	81007.46		161.8		
W14	60	515013	2.8	91808.46		132.7		

Table C.8 – Boundary Condition: Watson Study $D_N = 2\frac{7}{8}$"

Appendix D – Physical Properties

D.1 – Eames Ejector Study

D.1.1 – Geometry Studies

Species	Property				
	ρ (kg/m^3)	μ_g (kg/ms) E-6	k_g (kW/mK) E-6	Cp_g (kJ/kgK)	Mol wt
Primary	Ideal Gas	12.8	26.8	2090	18
Secondary		8.83	17.1	1860	
Outlet		9.52	18.7	1880	

Table D.1 – Physical Properties: Geometrical Studies

D.1.2 – Critical Operating Conditions Study

Nº	Species	Property				
		ρ (kg/m^3)	μ_g (kg/ms) E-6	k_g (kW/mK) E-6	Cp_g (kJ/kgK)	Mol Wt
1	Primary	Ideal Gas	12.8	26.8	2090	18
	Secondary		8.83	17.1	1860	
	Mixture		9.52	18.7	1880	
2	Primary	Ideal Gas	13.0	27.3	2120	18
	Secondary		8.83	17.1	1860	
	Mixture		9.52	18.7	1880	
3	Primary	Ideal Gas	13.2	28.3	2180	18
	Secondary		8.83	17.1	1860	
	Mixture		9.52	18.7	1880	
4	Primary	Ideal Gas	13.4	28.3	2180	18
	Secondary		8.83	17.1	1860	
	Mixture		9.7	19.1	1880	
5	Primary	Ideal Gas	13.5	28.8	2210	18
	Secondary		8.83	17.1	1860	
	Mixture		9.7	19.1	1880	
6	Primary	Ideal Gas	12.8	26.8	2090	18
	Secondary		8.74	16.9	1860	
	Mixture		9.44	18.52	1880	
7	Primary	Ideal Gas	13.0	27.3	2120	18
	Secondary		8.74	16.9	1860	
	Mixture		9.52	18.7	1880	
8	Primary	Ideal Gas	13.2	28.3	2180	18
	Secondary		8.74	16.9	1860	
	Mixture		9.52	18.7	1880	
9	Primary	Ideal Gas	13.4	28.3	2180	18
	Secondary		8.74	16.9	1860	
	Mixture		9.642	18.97	1880	
10	Primary	Ideal Gas	13.5	28.8	2210	18
	Secondary		8.74	16.9	1860	
	Mixture		9.7	19.1	1880	
11	Primary	Ideal Gas	12.8	26.8	2090	18
	Secondary		8.66	16.7	1860	
	Mixture		9.35	18.3	1880	
12	Primary	Ideal Gas	13.0	27.3	2120	18
	Secondary		8.66	16.7	1860	
	Mixture		9.42	18.5	1880	
13	Primary	Ideal Gas	13.2	28.3	2180	18
	Secondary		8.66	16.7	1860	
	Mixture		9.52	18.7	1880	
14	Primary	Ideal Gas	13.4	28.3	2180	18
	Secondary		8.66	16.7	1860	
	Mixture		9.64	18.97	1880	
15	Primary	Ideal Gas	13.5	28.8	2210	18
	Secondary		8.66	16.7	1860	
	Mixture		9.7	19.1	1880	

Table D.2 – Physical Properties: Operating Conditions Study

D.1.3 – Low Pressure Study

Nº	Species	Property				
		ρ (kg/m^3)	μ_g (kg/ms) E-6	k_g (kW/mK) E-6	Cp_g (kJ/kgK)	Mol wt
16	Primary	Ideal Gas	12.8	26.8	2090	18
	Secondary		8.49	16.3	1860	
	Outlet		9.52	18.7	1880	
17	Primary	Ideal Gas	12.8	26.8	2090	18
	Secondary		8.49	16.3	1860	
	Outlet		9.52	18.7	1880	
18	Primary	Ideal Gas	12.8	26.8	2090	18
	Secondary		8.49	16.3	1860	
	Outlet		9.52	18.7	1880	
19	Primary	Ideal Gas	12.8	26.8	2090	18
	Secondary		8.49	16.3	1860	
	Outlet		9.52	18.7	1880	
20	Primary	Ideal Gas	12.8	26.8	2090	18
	Secondary		8.49	16.3	1860	
	Outlet		9.52	18.7	1880	
21	Primary	Ideal Gas	12.8	26.8	2090	18
	Secondary		8.49	16.3	1860	
	Outlet		9.52	18.7	1880	
22	Primary	Ideal Gas	12.8	26.8	2090	18
	Secondary		8.49	16.3	1860	
	Outlet		9.52	18.7	1880	
23	Primary	Ideal Gas	12.8	26.8	2090	18
	Secondary		8.49	16.3	1860	
	Outlet		9.52	18.7	1880	

Table D.3 – Physical Properties: Low Pressure Study

D.1.4 – 3D Study

Nº	Species	Property				
		ρ (kg/m^3)	μ_g (kg/ms) E-6	k_g (kW/mK) E-6	Cp_g (kJ/kgK)	Mol wt
3D-01	Primary	Ideal Gas	12.8	26.8	2090	18
	Secondary		8.83	17.1	1860	
	Outlet		9.52	18.7	1880	
3D-01	Primary	Ideal Gas	12.8	26.8	2090	18
	Secondary		8.74	16.9	1860	
	Outlet		9.44	18.52	1880	
3D-01	Primary	Ideal Gas	12.8	26.8	2090	18
	Secondary		8.66	16.7	1860	
	Outlet		9.35	18.3	1880	
3D-01	Primary	Ideal Gas	12.8	26.8	2090	18
	Secondary		8.83	17.1	1860	
	Outlet		9.52	18.7	1880	
3D-01	Primary	Ideal Gas	12.8	26.8	2090	18
	Secondary		8.74	16.9	1860	
	Outlet		9.44	18.52	1880	
3D-01	Primary	Ideal Gas	12.8	26.8	2090	18
	Secondary		8.66	16.7	1860	
	Outlet		9.35	18.3	1880	

Table D.4 – Physical Properties: 3D Study

D.2 – Desevaux Ejector Study

N°	Species	Fluid	Property			
			μ_g (kg/ms) E-5	k_g (kW/mK) E-6	Cp_g (kJ/kgK)	Mol wt
D01	Primary	Air	1.789	24.2	1006.43	28.96
	Secondary					
	Outlet					
D02	Primary	Air	1.789	24.2	1006.43	28.96
	Secondary					
	Outlet					
D03	Primary	Air	1.789	24.2	1006.43	28.96
	Secondary					
	Outlet					

Table D.5 – Physical Properties: Desevaux Study

D.3 – Hickman Study

N°	Species	Fluid	Property			
			μ_g (kg/ms) E-5	k_g (kW/mK) E-6	Cp_g (kJ/kgK)	Mol wt
H01	Primary	Steam	3.332	52.36	1075	28.96
	Secondary	Air	1.789	24.2	1006.43	28.96
	Outlet	Air	1.789	24.2	1006.43	28.96
H02	Primary	Steam	3.332	52.36	1075	28.96
	Secondary	Air	1.789	24.2	1006.43	28.96
	Outlet	Air	1.789	24.2	1006.43	28.96
H03	Primary	Steam	3.332	52.36	1075	28.96
	Secondary	Air	1.789	24.2	1006.43	28.96
	Outlet	Air	1.789	24.2	1006.43	28.96
H04	Primary	Steam	3.332	52.36	1075	28.96
	Secondary	Air	1.789	24.2	1006.43	28.96
	Outlet	Air	1.789	24.2	1006.43	28.96

Table D.6 – Physical Properties: Hickman Study

D.4 – Watson Ejector Study

Nº	Species	Fluid	Property			
			μ_g (kg/ms) E-5	k_g (kW/mK) E-6	Cp_g (kJ/kgK)	Mol wt
W01	Primary	Steam	1.5	34.1	2620	18
	Secondary	Air	1.789	24.2	1006.43	28.96
	Outlet	Air	1.789	24.2	1006.43	28.96
W02	Primary	Steam	1.5	34.1	2620	18
	Secondary	Air	1.789	24.2	1006.43	28.96
	Outlet	Air	1.789	24.2	1006.43	28.96
W03	Primary	Steam	1.486	33.6	2574	18
	Secondary	Air	1.789	24.2	1006.43	28.96
	Outlet	Air	1.789	24.2	1006.43	28.96
W04	Primary	Steam	1.473	33.1	2530	18
	Secondary	Air	1.789	24.2	1006.43	28.96
	Outlet	Air	1.789	24.2	1006.43	28.96
W05	Primary	Steam	1.46	32.6	2490	18
	Secondary	Air	1.789	24.2	1006.43	28.96
	Outlet	Air	1.789	24.2	1006.43	28.96
W06	Primary	Steam	1.43	31.5	2400	18
	Secondary	Air	1.789	24.2	1006.43	28.96
	Outlet	Air	1.789	24.2	1006.43	28.96
W07	Primary	Steam	1.4	30.2	2310	18
	Secondary	Air	1.789	24.2	1006.43	28.96
	Outlet	Air	1.789	24.2	1006.43	28.96
W08	Primary	Steam	1.5	34.1	2620	18
	Secondary	Air	1.789	24.2	1006.43	28.96
	Outlet	Air	1.789	24.2	1006.43	28.96
W09	Primary	Steam	1.5	34.1	2620	18
	Secondary	Air	1.789	24.2	1006.43	28.96
	Outlet	Air	1.789	24.2	1006.43	28.96
W10	Primary	Steam	1.486	33.6	2574	18
	Secondary	Air	1.789	24.2	1006.43	28.96
	Outlet	Air	1.789	24.2	1006.43	28.96
W11	Primary	Steam	1.473	33.1	2530	18
	Secondary	Air	1.789	24.2	1006.43	28.96
	Outlet	Air	1.789	24.2	1006.43	28.96
W12	Primary	Steam	1.46	32.6	2490	18
	Secondary	Air	1.789	24.2	1006.43	28.96
	Outlet	Air	1.789	24.2	1006.43	28.96
W13	Primary	Steam	1.43	31.5	2400	18
	Secondary	Air	1.789	24.2	1006.43	28.96
	Outlet	Air	1.789	24.2	1006.43	28.96
W14	Primary	Steam	1.4	30.2	2310	18
	Secondary	Air	1.789	24.2	1006.43	28.96
	Outlet	Air	1.789	24.2	1006.43	28.96

Table D.7 – Physical Properties: Watson Study

Appendix E – Results

E.1 – Eames Ejector Studies

E.1.1 – Throat Length Study

Throat Length (mm)	Throat Length / D	Mass Flow Rate (g/s)			R_m
		Primary	Secondary	Outlet	
0	0.00	0.1506	0.0426	0.1933	0.283
5	0.28	0.1506	0.0526	0.2033	0.350
10	0.56	0.1506	0.0655	0.2162	0.435
15	0.83	0.1506	0.0752	0.2258	0.500
20	1.11	0.1506	0.0848	0.2353	0.563
25	1.39	0.1506	0.0935	0.2439	0.621
30	1.67	0.1506	0.0991	0.2497	0.658
40	2.22	0.1506	0.1008	0.2514	0.669
50	2.78	0.1506	0.1008	0.2514	0.669
80	4.44	0.1506	0.1008	0.2514	0.669
90	5.00	0.1506	0.1008	0.2514	0.669
100	5.56	0.1506	0.1008	0.2514	0.669
105	5.83	0.1506	0.1008	0.2514	0.669
110	6.11	0.1506	0.0963	0.2471	0.639
120	6.67	0.1506	0.0783	0.2288	0.520
140	7.78	0.1506	0.0641	0.2147	0.426
160	8.89	0.1506	0.0553	0.2058	0.367
180	10.00	0.1506	0.0485	0.1991	0.322

Table E.1 – Results: Throat Length Study

E.1.2 – Mixing Chamber Angle Study

Mixing Chamber		Mass Flow Rate (g/s)			R_m
Half Angle (°)	Length (mm)	Primary	Secondary	Outlet	
1	171.87	0.1506	-0.0145	0.1361	-0.0963
1.074	160.03	0.1506	-0.0034	0.1472	-0.0228
1.228	139.95	0.1506	0.0248	0.1754	0.1648
1.432	120.01	0.1506	0.0713	0.2218	0.4732
1.463	117.46	0.1506	0.1016	0.2522	0.6746
1.494	115.03	0.1506	0.1054	0.2560	0.6999
1.562	110.02	0.1506	0.1040	0.2546	0.6906
1.718	100.00	0.1506	0.1008	0.2514	0.6693
2	85.91	0.1506	0.0967	0.2473	0.6422
3	57.24	0.1506	0.0835	0.2341	0.5544
4	42.90	0.1506	0.0694	0.2200	0.4610
5	34.29	0.1506	0.0586	0.2092	0.3892
6	28.54	0.1506	0.0504	0.2010	0.3349
7	24.43	0.1506	0.0441	0.1946	0.2926
8	21.35	0.1506	0.0392	0.1897	0.2600
9	18.94	0.1506	0.0352	0.1858	0.2337
10	17.01	0.1506	0.0319	0.1825	0.2123

Table E.2 – Results: Mixing Chamber Half Angle Study

E.1.3 – Critical Operating Conditions Study

Nº	Mass Flow Rate (g/s)			R_m	Specific Enthalpy (kJ/kg)			COP_R	
	Primary	Secondary	Outlet		Primary	Secondary	Outlet	CFD	Experiment[5]
1	0.990	0.624	1.614	0.630	2707.0	2519.2	117.3	0.585	0.586
2	1.153	0.645	1.798	0.559	2713.4	2519.2	125.7	0.518	0.537
3	1.335	0.654	1.990	0.489	2720.0	2519.2	133.6	0.452	0.473
4	1.531	0.652	2.183	0.426	2714.9	2519.2	142.4	0.393	0.389
5	1.754	0.642	2.396	0.366	2741.6	2519.2	150.7	0.335	0.309
6	0.990	0.550	1.540	0.555	2707.0	2514.6	114.4	0.514	0.500
7	1.152	0.565	1.717	0.491	2713.4	2514.6	132.0	0.453	0.418
8	1.330	0.568	1.898	0.427	2720.0	2514.6	131.9	0.393	0.355
9	1.531	0.545	2.076	0.355	2714.9	2514.6	139.8	0.328	0.296
10	1.750	0.510	2.260	0.291	2740.6	2514.6	147.7	0.266	0.233
11	0.996	0.487	1.483	0.489	2707.0	2509.9	111.0	0.452	0.404
12	1.160	0.484	1.644	0.417	2713.4	2509.9	116.5	0.385	0.344
13	1.335	0.461	1.796	0.345	2720.0	2509.9	129.0	0.317	0.276
14	1.539	0.430	1.969	0.279	2714.9	2509.9	139.8	0.257	0.251
15	1.755	0.407	2.162	0.232	2740.6	2509.9	144.1	0.211	0.177

Table E.3 - Results: Critical Operating Conditions Study

E.1.4 – Low Pressure Study

Nº	Mass Flow Rate (g/s)			R_m
	Primary	Secondary	Outlet	
16	0.997	0.332	1.329	0.332
17	0.993	0.131	1.120	0.132
18	0.993	0.031	1.024	0.031
19	0.993	-0.004	0.987	-0.004
20	0.993	-0.011	0.982	-0.011
21	0.993	0.094	1.086	0.095
22	0.992	0.028	1.021	0.029
23	0.992	-3.21E-07	0.992	0.000

Table E.4 – Results: Low Pressure Study

E.1.5 – Three Dimensional Study

Nº	Inlet	Mass Flow Rate (g/s)			R_m	COP_R	
		Primary	Secondary	Outlet		CFD	Experiment[5]
3D-01	Wide	0.492	0.303	0.795	0.615	0.571	0.586
3D-02		0.659	0.313	0.973	0.475	0.438	0.473
3D-03		0.868	0.320	1.188	0.369	0.337	0.309
3D-04	Narrow	0.490	0.263	0.753	0.537	0.498	0.586
3D-05		0.659	0.289	0.948	0.439	0.407	0.473
3D-06		0.866	0.293	1.159	0.338	0.309	0.309

Table E.5 – Results: Three Dimensional Study

E.2 – Desevaux Ejector Study

Nº	Mass Flow Rate (g/s)			R_m
	Primary	Secondary	Outlet	
D01	0.0591	0.0059	0.0650	0.1
D02	0.0591	0.0189	0.0780	0.32
D03	0.0591	0.0277	0.0868	0.47

Table E.6 – Results: Desevaux Ejector Study

E.3 – Hickman Ejector Study

Nº	Mass Flow Rate (g/s)				R_m	
	Primary		Secondary		CFD	Experiment[6]
	CFD	Experiment[6]	CFD	Experiment[6]		
H01	0.0533	0.0510	0.8859	0.8700	16.6	17.0
H02	0.0533	0.0510	1.0410	0.9930	19.5	19.4
H03	0.0531	0.0510	1.1596	1.0740	21.8	21.0
H04	0.0533	0.0510	1.3199	1.2120	24.8	23.7

Table E.7 – Results: Hickman Ejector Study

E.4 – Watson Ejector Study

E.4.1 – D_N = 1½"

Nº	Mass Flow Rate (g/s)				R_m	
	Primary		Secondary		CFD	Experiment[1]
	CFD	Experiment[1]	CFD	Experiment[1]		
W01	36.97	41.58	3.65	3.49	0.098	0.084
W02	34.72	38.93	3.32	3.49	0.095	0.089
W03	32.47	36.29	2.77	3.46	0.085	0.095
W04	30.26	33.64	-3.75	3.46	-0.124	0.103
W05	27.98	31.00	-2.73	3.38	-0.097	0.109
W06	23.42	25.70	-4.63	2.94	-0.197	0.114
W07	18.75	20.54	-3.75	2.14	-0.200	0.104

Table E.8 – Results: Watson Ejector Study: D_N = 1½"

E.4.2 – D_N = 2⅞"

Nº	Mass Flow Rate (g/s)				R_m	
	Primary		Secondary		CFD	Experiment[1]
	CFD	Experiment[1]	CFD	Experiment[1]		
W08	36.92	41.58	3.69	3.49	0.119	0.084
W09	34.76	38.93	3.47	3.49	0.109	0.089
W10	32.40	36.29	3.24	3.49	-0.096	0.096
W11	30.17	33.64	3.02	3.35	-0.219	0.099
W12	27.88	31.00	2.78	3.14	-0.412	0.101
W13	23.32	25.70	2.33	2.26	-0.103	0.087
W14	18.65	20.54	1.86	1.57	-0.247	0.076

Table E.9 – Results: Watson Ejector Study: D_N = 2⅞"

Appendix F – Eames Ejector Convective Mach Number

F.1 – Convective Mach Number

Two convective Mach numbers, M_{c1} & M_{c2}, are defined for the supersonic and subsonic sides of the shear layer respectively [105]. Eqn (7.1) and (7.2).

$$M_{c1} = \frac{U_1 - U_c}{a_1} \tag{F.1}$$

$$M_{c2} = \frac{U_c - U_2}{a_2} \tag{F.2}$$

Where

$$\rho_1 (U_1 - U_c)^2 = \rho_2 (U_c - U_2)^2 \tag{F.3}$$

N°	a_1 (m/s)	a_2 (m/s)	ρ_1 (kg/m^3)	ρ_2 (kg/m^3)	u_1 (m/s)	u_2 (m/s)	U_c (m/s)	M_{c1}	M_{c2}
1	265.0	413.4	0.0193	0.0089	1027.0	132.0	852.6	0.658	1.743
2	268.0	413.0	0.0216	0.0088	1038.0	138.0	878.1	0.596	1.792
3	271.7	412.9	0.0243	0.0088	1047.0	142.0	900.2	0.540	1.836
4	274.0	413.0	0.0266	0.0088	1065.0	142.0	925.89	0.507	1.898
5	279.0	413.0	0.0314	0.0088	1073.0	140.7	950.15	0.440	1.959
6	264.8	411.3	0.0192	0.0075	1029.0	138.0	875.65	0.579	1.793
7	267.2	411.0	0.0213	0.0075	1041.0	143.4	898.23	0.534	1.836
8	272.0	411.0	0.0246	0.0075	1050.6	145.8	922.41	0.471	1.889
9	275.4	411.0	0.0277	0.0075	1062.5	139.5	944.34	0.429	1.958
10	279.0	412.0	0.0310	0.0076	1075.9	129.5	965.91	0.390	2.030
11	265.0	409.0	0.0195	0.0064	1028.0	146.3	895.79	0.498	1.833
12	268.0	409.0	0.0220	0.0064	1039.7	147.5	918.70	0.451	1.880
13	271.6	409.6	0.0246	0.0064	1051.0	138.0	938.34	0.415	1.954
14	275.5	410	0.0278	0.0064	1062.0	127.7	959.08	0.370	2.020
15	280.0	411.0	0.0322	0.0065	1072.7	118.0	979.67	0.332	2.096

Table – F.1 – Convective Mach Number in Eames Ejector.